

ERZİNCAN UNIVERSITY JOURNAL OF SCIENCE AND TECHNOLOGY

ISSN: 1307-9085, e-ISSN: 2149-4584

EDITOR IN CHIEF

Assoc. Prof. Dr. Kemal Volkan ÖZDOKUR
Erzincan Binali Yıldırım University

ASSOCIATE EDITORS

Assoc. Prof. Dr. Özlem BARAN ACIMERT
Erzincan Binali Yıldırım University

Ass. Prof. Dr. Fidan ERDEN KARAOĞLAN
Erzincan Binali Yıldırım University

EDITORIAL BOARD

Prof. Dr. Ali Ercan EKİNCİ

Erzincan Binali Yıldırım University

Prof. Dr. Bülent ÇAĞLAR

Erzincan Binali Yıldırım University

Prof. Dr. Suat ÇOLAK

Erzincan Binali Yıldırım University

Prof. Dr. Yeşim KARASULU

Ege University

Assoc. Prof. Dr. Fulya ASLAY

Erzincan Binali Yıldırım University

Ass. Prof. Dr. Agah Oktay ERTAY

Erzincan Binali Yıldırım University

Assoc. Prof. Dr. Neşe ERTUGAY

Erzincan Binali Yıldırım University

Prof. Dr. Salih DOĞAN

Erzincan Binali Yıldırım University

Ass. Prof. Dr. Emre YAVUZ

Erzincan Binali Yıldırım University

Doç. Dr. Tuba AKKUŞ

Erzincan Binali Yıldırım University

Doç. Burcu BOZKURT ÇIRAK

Erzincan Binali Yıldırım University

Ass. Prof. Dr. Vael HAJAHMAD

Erzincan Binali Yıldırım University

Prof. Dr. Süleyman KOÇAK

Manisa Celal Bayar University

Assoc. Prof. Dr. Özgür ARAR

Ege University

**Ass. Prof. Dr. Burçin
TÜRKMENOĞLU**

Erzincan Binali Yıldırım University

Ass. Prof. Dr. Mehmet KUZUCU

Erzincan Binali Yıldırım University

Assoc. Prof. Dr. Tülay ERİŞİR

Erzincan Binali Yıldırım University

Prof. Dr. Öztekin ALGÜL

Mersin University

Ass. Prof. Dr. İrem BOZBEY MERDE

Erzincan Binali Yıldırım University

Ass. Prof. Dr. Arif Onur EDEN

Erzincan Binali Yıldırım University

Ass. Prof. Dr. Mert KARAOĞLAN

Erzincan Binali Yıldırım University

Ass. Prof. Dr. Ali CELEN

Erzincan Binali Yıldırım University

Ass. Prof. Dr. Mehmet Kürşat ÖKSÜZ

Erzincan Binali Yıldırım University

Ass. Prof. Dr. Deniz ELMACI

Dokuz Eylül University

Assoc. Prof. Dr. İsmail TONTUL

Necmettin Erbakan University

Ass. Prof. Dr. Ülgen İlknur KONAK

Avrasya University

Ass. Prof. Dr. Fundagül EREM

Zonguldak Bülent Ecevit University

Ass. Prof. Dr. Takaichi WATANABE

Okayama University

**Ass. Prof. Dr. Ayşenur KELEŞ
DAYAUÇ**

Hitit University

Assoc. Prof. Dr. Aykut ÖZGÜR

Tokat Gaziosmanpaşa University

Ass. Prof. Dr. M. Mustafa ÇETİN

Kadir Has University

Res. Ass. Zehra ÖKSÜZ

Mersin University

**Assoc. Prof. Dr. Kemal
BUHARALIOĞLU**

İzmir Katip Çelebi University

**Assoc. Prof. Dr. Hayrettin Ozan
GÜLCAN**

Eastern Mediterranean University

Prof. Dr. Seyhan ŞAHAN FIRAT

Mersin University

Marin MARİN

Transylvania University of Braşov

Sorin VLASE

Transylvania University of Braşov

Prof. Dr. Alper SEZER

Ege University

AIMS AND SCOPE

The aim of the **Erzincan University Journal of Science and Technology** is to publish original research articles and reviews made in the fields of Science, Engineering in order to create a quality academic contribution in these fields.

Research areas covered in the journal:

- Physics, Chemistry, Biology, Mathematics and related areas
- Mechanical, Electrics-Electronics, Civil and related engineering areas
- Health sciences and related areas

Open Access Policy

Erzincan University Journal of Science and Technology is an open access journal which means that all content is freely available without charge to the user or his/her institution. Users are allowed to read, download, copy, distribute, print, search, or link to the full texts of the articles, or use them for any other lawful purpose, without asking prior permission from the publisher or the author. Erzincan University Journal of Science and Technology signed the Budapest Open Access Declaration (<https://budapestopenaccessinitiative.org/>).

Editor in chief: Doç. Dr. Kemal Volkan ÖZDOKUR

Address: Department of Chemistry, Erzincan Binali Yıldırım University, Erzincan, Türkiye.

E-mail: fbedergierzincan@gmail.com

Publisher: Erzincan Binali Yıldırım University

Address: Erzincan Binali Yıldırım University, Erzincan, Türkiye.

RESEARCH ARTICLES:

Page	Manuscript Title Authors
585-597	Creation of Some Fuzzy Ultranorm Spaces and Examining of Their Properties İbrahim ŞANLIBABA
598-606	The Effect of the Aluminum (Al) Ratio on the Synthesis of the Laminated Mn₂AlB₂ MAB Phase Fatma Nur TUZLUCA YESİLBAG <i>et al.</i>
607-625	Redundant Data Center Planning for Universities Veli ÇAPALI <i>et al.</i>
626-637	Evaluation of Anticancer and Antimicrobial Potentials of <i>Tarantula cubensis</i> Venom (Theranekron® D6) Nazan GÖKŞEN TOSUN <i>et al.</i>
638-649	Efficient Image Retrieval in Fashion: Leveraging Clustering and Principal Component Analysis for Search Space Reduction Başak Esin KÖKTÜRK-GÜZEL
650-662	Fabrication of cZIF-67/Ti₃C₂ Nanocomposites as Sulfur Host for Lithium-Sulfur Batteries Recep YUKSEL
663-677	Preparation of Aloe Vera Gel Containing Solid Lipid Nanoparticles for Treatment of Eczema Hatice ÇETİN <i>et al.</i>
678-687	<i>Zercon kasensis</i> sp. nov., A New Mite Species (Parasitiformes: Zerconidae) from South-Western Türkiye Ayşenur DEMİRDÖVEN <i>et al.</i>
688-702	Determination of Nifedipine in Pharmaceutical Preparations by Square Wave Voltammetry Method Bilal Yılmaz
703-717	Investigation of the Effects of Cetuximab and Agomelatine Drugs on Proliferation and Apoptosis in Prostate Cancer Cells Kevser ALBAYRAK <i>et al.</i>
718-735	Mitigating Osmotic Drought Stress in Rye: Assessing the Ameliorative Effects of Putrecine on Germination, Seedling and Mitotic Index Erdal Eren YELER <i>et al.</i>
736-750	Analyzing Lead Concentrations in Pregnant Women Following Topical Application of Eau de Goulard (2% lead subacetate) via ICP-MS Davut Serdar SAYILGAN <i>et al.</i>

- 751-760 **Antimicrobial Activity and Chemical Composition of Essential Oil Extracted from *Hyoscyamus niger* L. Inflorescence**
Sefa GÖZCÜ *et al.*
- 761-778 **The Effect of Different Storage Conditions on Textural, Microbiological and Color Properties of Phyllo (Yufka)**
Seda COŞKUN *et al.*
- 779-788 **Block-Based Forgery Detection: Performance Comparison Using HOG, LBP and MBF**
Yıldız AYDIN and Yunus BABACAN
- 789-796 **Comparison of Models on Basic Passive Circuit Components**
Murat GÜLNAHAR *et al.*
- 797-810 **Voltage Controlled Oscillator Realisation with Temperature and Source Independent Circuits**
Müslüm GÜR and Yunus BABACAN
- 811-825 **Radioprotective Effect of Umbelliferon Against Radiation-Induced Myocardial Damages**
Nurdan DUMLU *et al.*
- 826-839 **Modeling, Analysis, and Comparison of Rectangular Waveguide Structures Having Glide Symmetrical Step Discontinuity with Periodic Dielectric Loading**
Agâh Oktay ERTAY
- 840-852 **Determination of Uric Acid Using 2D-MoS₂ Modified GCE**
Gülden ASAN and Hüseyin ÇELİKKKAN
- 853-869 **Investigation of Influencing Factors on Power Generation Performance in Reverse Electrodialysis**
Aydın CİHANOĞLU
- 870-883 **Enhanced Classification of Skin Lesions Using Fine-Tuned MobileNet and DenseNet121 Models with Ensemble Learning**
Yasin SANCAR
- 884-904 **A Mobile Secure Content Development Application for Children in the Software Development Life Cycle Framework**
İsakhan KARABAŞ *et al.*

Creation of Some Fuzzy Ultranorm Spaces and Examining of Their Properties

İbrahim ŞANLIBABA^{1*}

¹ Nevşehir Hacı Bektaş Veli University, Faculty of Science and Art, Department of Mathematics,
Nevşehir, Turkey

Received: 31/10/2023 **Revised:** 18/08/2024, **Accepted:** 27/08/2024, **Published:** 31/12/2024

Abstract

In this article, first of all, the definition of fuzzy sets was made, and the different aspects of fuzzy sets from classical sets are underlined. The operations in fuzzy sets are shown. Fuzzy numbers formed by fuzzy sets and fuzzy sequences are emphasized. Fuzzy norm and fuzzy ultranorm definitions are made. The α -cut sequences of fuzzy numbers are shown in figures, and various sequences of fuzzy numbers are given. The definition of ultrametric space is created in fuzzy sets, it is proved that the fuzzy number set is ultrametric space and that it is a complete ultrametric space by researching their completeness. Finally, some fuzzy ultra-sequence sets are defined. Then the set of fuzzy ultra-convergent, fuzzy ultra-null, and fuzzy ultra-bounded sequences are denoted and their coverage states are examined. The differences between fuzzy sequences and fuzzy ultra-sequences are emphasized. In addition, the properties of some fuzzy ultra-sequences created are shown. Fuzzy ultra-bounded sequence spaces are proven to be complete and ultra-isomorphic.

Keywords: Fuzzy set, fuzzy ultrametric spaces, fuzzy ultranorm, fuzzy ultra-sequence, ultra-isomorphic.

Bazı Bulanık Ultranorm Uzayların Oluşturulması ve Özelliklerinin İncelenmesi

Öz

Bu makalede başlangıçta bulanık kümeler açıklanmış, bulanık kümeler ve klasik kümelerin birbirinden farklı yönlerinin altı çizilmiştir. Bulanık kümelerdeki işlemler gösterilmiştir. Bulanık kümeler ve bulanık dizilerden oluşan bulanık sayılar üzerinde durulmuştur. Bulanık norm ve bulanık ultranorm tanımları yapılmıştır. Bulanık sayıların α -kesim dizileri şekillerde gösterilmiş ve çeşitli bulanık sayı dizileri verilmiştir. Ultrametrik uzayın tanımı bulanık kümeler halinde yapılmış olup, bulanık sayı kümesinin ultrametrik uzay olduğu ve tamlıkları araştırılarak tam bir ultrametrik uzay olduğu kanıtlanmıştır. Son olarak bazı bulanık ultra dizi kümeleri tanımlanmıştır. Daha sonra bulanık ultra-yakınsak, bulanık ultra-sıfır ve bulanık ultra-sınırlı diziler kümesi belirtilmiş ve kapsam durumları incelenmiştir. Bulanık diziler ve bulanık ultra diziler arasındaki farklar vurgulanmıştır. Ayrıca oluşturulan bazı bulanık ultra dizilerin özellikleri gösterilmiştir. Bulanık ultra sınırlı dizi uzaylarının tam ve ultra izomorfik olduğu kanıtlanmıştır.

Anahtar Kelimeler: Bulanık küme, bulanık ultrametrik uzaylar, bulanık ultranorm, bulanık ultra diziler, ultra izomorfiklik.

1. Introduction

The concept of fuzzy sets was considered as a generalization of crisp sets and has continued to evolve over time and it has begun to be used in many areas. Because it paved the way for graded evaluation by taking into account the membership degree assigned to each member. Fuzzy logic has been studied by Lukasiewicz and Tarski [1] since the 1920s. Then, the Fuzzy set theory was proposed by Zadeh [2] in 1965. Kaleva [3], Seikkala [4] and Matloka [5] examined fuzzy metric spaces and their properties and obtained significant results. Katsaras [6], C. Felbin [7], and Cheng-Mordeson [8], on the other hand, studied fuzzy metric spaces and fuzzy normed spaces and tried to improve them by Kramosil, Michalek [9]. Bag and Samanta [10] studied fuzzy-bounded linear operators on fuzzy normed spaces in 2005. Fuzzy normed spaces and their topological properties were studied by Kia and Sadeqi [11] in 2009. Xia and Guo [12] investigated the completeness of fuzzy metric space and fuzzy closed set cases. Some new fuzzy sequence spaces were studied by Vakeel A. Khan, Mobeen Ahmad, and Masood Alam [13]. Maria Manuel Clementino and Andrea Montoli were researched and interested in ultrametric groups [14]. Thus, many researchers have developed fuzzy functional analysis and its applications.

Cases of some consequences of metrics induced by a fuzzy ultrametric method were studied by Li [25]. Regarding probability measurement in the category of fuzzy ultrametric spaces, it was examined by Savchenko et al. [26]. Additionally, the completeness of fuzzy metric spaces was examined by Gregori et al. [27]. Fuzzy ultrametric spaces and their applications were also encountered in the decision process, Khameneh et al. [28] worked on the subject. The properties of ultranormed spaces were introduced and studied by Şanlıbaba [29,30]. Intuitionistic fuzzy normed rings and the generation of their basic properties were investigated by Abed Alhaleem et al [31].

With a different approach, we have managed to go even further in this article. Fuzzy norm, fuzzy ultranorm, and fuzzy ultrametric spaces are introduced and their properties are studied. Fuzzy ultranorm spaces created by using ultranorm 3rd property $(N3)' \|u+v\| \leq \max\{\|u\|, \|v\|\}$ are emphasized as a more special case of fuzzy normed spaces, and various interesting results are obtained. Especially in the situations between fuzzy sets and fuzzy ultrametric sets, their coverage conditions are examined. For this reason, it is quite exciting to discover some kind of new type of fuzzy space that can be beneficial for solving various problems in fuzzy work. In addition, some theorems about fuzzy ultrametric space and fuzzy ultra-bounded sequence spaces are proved, and examples are shown.

The structure of this paper is prepared as follows: Some preliminary results and basic definitions are mentioned in section 2. In section 3 fuzzy ultranorm, fuzzy ultrametric, and some fuzzy ultra-sequence spaces are proven and main results are discussed. In section 4 Some of the conclusions emphasized in the article are summarized.

2. Preliminaries

Let X be a universal set, $\mu_A(x)$ is the degree of membership of x in A . Then a fuzzy set A of X is defined by the following transform:

$$\mu_A: X \rightarrow [0,1]$$

With another expressed as:

$$A = \frac{\mu_A(x_1)}{x_1} + \frac{\mu_A(x_2)}{x_2} + \frac{\mu_A(x_3)}{x_3} + \dots + \frac{\mu_A(x_n)}{x_n} = \sum \frac{\mu_A(x_n)}{x_n} \quad [15].$$

As we know, classical sets are in particular fuzzy sets. Many algebraic operations used in classical sets are also valid for fuzzy sets and De Morgan's laws are not always valid in fuzzy sets. Therefore, it is obvious that fuzzy set operations are slightly different from classical set operations.

Let the membership functions of fuzzy sets A and B be $\mu_A(x)$ and $\mu_B(x)$, respectively. The union, intersection, complement, and inclusion of two fuzzy sets are shown below [16].

$$\begin{aligned} \mu_{A \cup B}(x) &= \max\{\mu_A(x), \mu_B(x)\} && \forall x \in X \quad (\text{Union}) \\ \mu_{A \cap B}(x) &= \min\{\mu_A(x), \mu_B(x)\} && \forall x \in X \quad (\text{Intersection}) \\ \mu_{\bar{A}}(x) &= 1 - \mu_A(x) && \forall x \in X \quad (\text{Complement}) \\ \mu_A(x) &\leq \mu_B(x), \quad (A \subseteq B) && \forall x \in X \quad (\text{Inclusion}) \end{aligned}$$

Definition 2.1. Consider a fuzzy subset of the real line $u: \mathbb{R} \rightarrow [0,1]$. Then u is called a fuzzy number if it provides the following conditions:

1. u is normal, i.e., $\exists x_0 \in \mathbb{R}$ with $u(x_0) = 1$;
2. u is fuzzy convex, i.e., $u(tx + (1 - t)y) \geq \min\{u(x), u(y)\}$, $\forall t \in [0,1]$ ve $\forall x, y \in \mathbb{R}$.
3. u is upper semi-continuous on \mathbb{R} . $\forall \varepsilon > 0, \exists \delta > 0$ such that $u(x) - u(x_0) < \varepsilon$ $|x - x_0| < \delta$
4. u is compactly supported, i.e., $\overline{u^0} = \overline{\{x \in \mathbb{R}: u(x) > \alpha\}}$ is compact. [17],[18].

Let's suppose that E_i is the be set of all closed and bounded intervals on \mathbb{R} , $E_i = \{u = [u^-, u^+]: u^- \leq x \leq u^+, u^- \text{ and } u^+ \in \mathbb{R}\}$.

From this definition, $\forall \alpha \in [0,1]$, α -level set defined by $u^\alpha = \{x \in \mathbb{R}: u(x) \geq \alpha\}$ is in E_i , that is $u^\alpha = [u^{\alpha-}, u^{\alpha+}]$ and the set of all fuzzy numbers are denoted by E' .

E' is the set of fuzzy numbers, $f: \mathbb{N} \rightarrow E'$ $k \rightarrow f(k) = u_k$, for $\forall k \in \mathbb{N}$, f is called sequences of fuzzy numbers with $u_k \in E'$,

$$f: \mathbb{N} \rightarrow E' \quad k \rightarrow f(k) = u_k,$$

If the sequences of fuzzy numbers are denoted by $u = (u_k)$ it is clear that u^α is called α – cut sequences given in form $(u^\alpha) = (u_k^\alpha) = (u_1^\alpha, u_2^\alpha, \dots, u_k^\alpha, \dots)$ [19],[20].

Additionally, the sets of sequences of fuzzy numbers are indicated with $w(E') = \{u = (u_k) \in E' : k \in \mathbb{N}\} = \{f: \mathbb{N} \rightarrow E', f(k) = u_k\}$. The algebraic structure of $w(E')$ in Figure 2.1 is as follows:

$$+: w(E') \times w(E') \rightarrow w(E'), u = (u_1, u_2, \dots) \text{ and } (v_1, v_2, \dots) \in w(E')$$

$$(u, v) \rightarrow u + v = u_k + v_k$$

$$= (u_1 + v_1, u_2 + v_2, \dots, u_k + v_k, \dots)$$

$$\cdot : \lambda \in \mathbb{R}, \lambda(u_k) = (\lambda u_k) = (\lambda u_1, \lambda u_2, \dots, \lambda u_k, \dots)$$

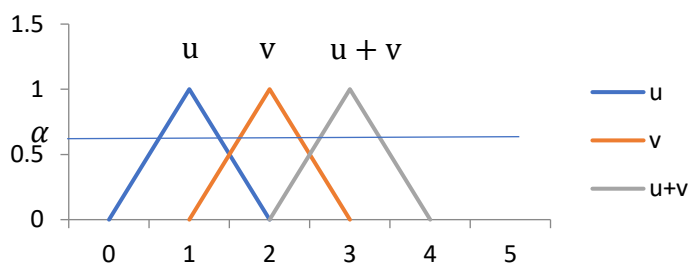


Figure 2.1. α – cut sequence and operations on fuzzy sequences

In scalar multiplication $(u_k) \in w(E')$ and $u_k^\alpha = [u_k^{\alpha-}, u_k^{\alpha+}]$ if α – cuts sequences are taken as:

$$u_k^\alpha = [u_k^{\alpha-}, u_k^{\alpha+}];$$

$$\lambda u_k = \lambda u_k^{\alpha-} = \lambda [u_k^{\alpha-}, u_k^{\alpha+}] = \begin{cases} [\lambda u_k^{\alpha-}, \lambda u_k^{\alpha+}], & \lambda \geq 0 \\ [\lambda u_k^{\alpha+}, \lambda u_k^{\alpha-}], & \lambda < 0 \end{cases}$$

Since the set of closed intervals does not have an inverse with respect to addition, the set of fuzzy numbers in the classical sense has no inverse with respect to addition. Therefore, the same is true for $w(E')$ elements. Therefore, $w(E')$ cannot be transformed into a vector space using scalar multiplication and addition in the Zadeh sense.

3. Main Theorem and Proof

In this section, firstly fuzzy ultrametric spaces and their definitions are given, then the fact that $F(E')$ which is the main subject of the research is an ultrametric space is proved by Theorem

3.1, and its completeness is shown in Theorem 3.2. In the last part, it is proved by Theorem 3.6 that the space of ultra-bounded sequences $l'_\infty(E')$ is ultra-isometric.

3.1. Fuzzy Ultrametric Spaces and Fuzzy Ultra-Sequences

The metric space and completeness of sequences of fuzzy sets have been shown in various articles. In this section, it will be proved that fuzzy numbers are ultrametric space and ultranorm. Then, the definitions of different fuzzy sequence spaces will be made and their properties will be examined.

Definition 3.1. Let G be the set of fuzzy numbers but nonnegative and $u, v \in E'$. The function $d_f: E' \times E' \rightarrow G$ is called fuzzy metric if it satisfies the (F1), (F2), (F3) and (F4) properties:

$$(F1) \quad d_f(u, v) \geq 0$$

$$(F2) \quad d_f(u, v) = 0 \text{ if and only if } u = v$$

$$(F3) \quad d_f(u, v) = d_f(v, u)$$

$$(F4) \quad \text{For all } u, v, w \in E', \quad d_f(u, v) \leq d_f(u, w) + d_f(w, v) \text{ [21].}$$

If is taken (FU4)' $d_{fu}(u, v) \leq \max\{d_{fu}(u, w), d_{fu}(w, v)\}$ instead of (F4) then the function d_{fu} is called fuzzy ultrametric. For any $u, v \in E'$, if d_{fu} is a fuzzy ultrametric on E' , the pair of (E', d_{fu}) is called fuzzy ultrametric space.

Definition 3.2. Let $u = (u_k)$ sequence of fuzzy number and $u, v \in E'$. $\lambda(E')$ the subset of sequences spaces of fuzzy number, H is the set of all nonnegative fuzzy numbers, and $\|\cdot\|: \lambda(E') \rightarrow H$. If the function satisfies the following (N1), (N2), and (N3) properties, it is called a fuzzy norm and fuzzy module [22].

$$(N1) \quad \|u\| = \theta \Leftrightarrow u = \theta$$

$$(N2) \quad \|\alpha u\| = |\alpha| \|u\|$$

$$(N3) \quad \|u + v\| \leq \|u\| + \|v\|$$

$$(N3)' \quad \|u + v\| \leq \max\{\|u\|, \|v\|\}$$

Also, if it satisfies (N1), (N2) and (N3)' properties, it is called fuzzy ultranorm.

Theorem 3.1. The set of all fuzzy numbers is represented by $F(E')$ and $F(E') =$

$\{u | u: \mathbb{R} \rightarrow [0,1]\}$ it is remembered that $F(E')$ is normal, convex, and upper semi-continuous \bar{u}^0 that it is also compact. This is stated from the definition of fuzzy numbers given in definition 2.1. Then, let $d(u, v) = \sup_{\alpha \in [0,1]} \{|u^{(\alpha)-} - v^{(\alpha)-}|, |u^{(\alpha)+} - v^{(\alpha)+}|\}$, for $u, v \in F(E')$. The d function satisfies the ultranorm conditions, and $(F(E'), d)$ is a fuzzy ultrametric space.

Proof. Let $u, v \in F(E')$;

$$d(u, v) = 0 \Leftrightarrow u = v$$

$$d(u, v) = \sup_{\alpha \in [0,1]} \{|u^{(\alpha)-} - v^{(\alpha)-}|, |u^{(\alpha)+} - v^{(\alpha)+}|\} = 0 \Leftrightarrow$$

$$|u^{(\alpha)-} - v^{(\alpha)-}| = 0 \wedge |u^{(\alpha)+} - v^{(\alpha)+}| = 0 \Leftrightarrow u = v$$

$$d(u, v) = \sup_{\alpha \in [0,1]} \{|u^{(\alpha)-} - v^{(\alpha)-}|, |u^{(\alpha)+} - v^{(\alpha)+}|\}$$

$$= \sup_{\alpha \in [0,1]} \{|v^{(\alpha)-} - u^{(\alpha)-}|, |v^{(\alpha)+} - u^{(\alpha)+}|\} = d(v, u)$$

$$d(u, v) = \sup_{\alpha \in [0,1]} \{\max\{|u^{(\alpha)-} - v^{(\alpha)-}|, |u^{(\alpha)+} - v^{(\alpha)+}|\}\}$$

$$= \sup_{\alpha \in [0,1]} \{\max\{|u^{(\alpha)-} - w^{(\alpha)-} + w^{(\alpha)-} - v^{(\alpha)-}|, |u^{(\alpha)+} - w^{(\alpha)+} + w^{(\alpha)+} - v^{(\alpha)+}|\}\}$$

$$\leq \sup_{\alpha \in [0,1]} \{\max\{|u^{(\alpha)-} - w^{(\alpha)-}|, |u^{(\alpha)+} - w^{(\alpha)+}|\}\}, \quad \sup_{\alpha \in [0,1]} \{\max\{|w^{(\alpha)-} - v^{(\alpha)-}|, |w^{(\alpha)+} - v^{(\alpha)+}|\}\}$$

$$= \max\{\sup_{\alpha \in [0,1]} \{|u^{(\alpha)-} - w^{(\alpha)-}|, |u^{(\alpha)+} - w^{(\alpha)+}|\}\}, \max\{\sup_{\alpha \in [0,1]} \{|w^{(\alpha)-} - v^{(\alpha)-}|, |w^{(\alpha)+} - v^{(\alpha)+}|\}\}$$

$$d(u, v) \leq \max\{d(u, w), d(w, v)\}.$$

Since it satisfies the ultrametric axioms $(F(E'), d)$, it is an ultrametric space.

Similarly with $\|u\| = \sup_k |u_k|$, properties (N1), (N2) are clear. Property (N3)' is following denoted.

$$\|u + v\| = \sup_k |u_k + v_k| \leq \sup_k \{\max\{|u_k|, |v_k|\}\}$$

$$= \sup_k \{\max\{|u_k + \theta|, |v_k + \theta|\}\}$$

$$\leq \sup_k \{\max\{\max\{|u_k|, \theta\}, \max\{|v_k|, \theta\}\}\}$$

$$= \max\{\sup_k \{\max\{|u_k|, \theta\}\}, \sup_k \{\max\{|v_k|, \theta\}\}\}$$

$$= \max\{\sup_k d(u_k, \theta), \sup_k d(v_k, \theta)\}$$

$$= \max\{\|u\|, \|v\|\}$$

Consequently, d is fuzzy ultranorm. □

Fuzzy ultranorm spaces are also special cases of fuzzy norm spaces. Now, considering the definitions and theorems explained so far, the relationship between fuzzy metric space, fuzzy ultrametric space, fuzzy ultranorm space, and fuzzy normed spaces is easily shown in diagram 3.1. below.

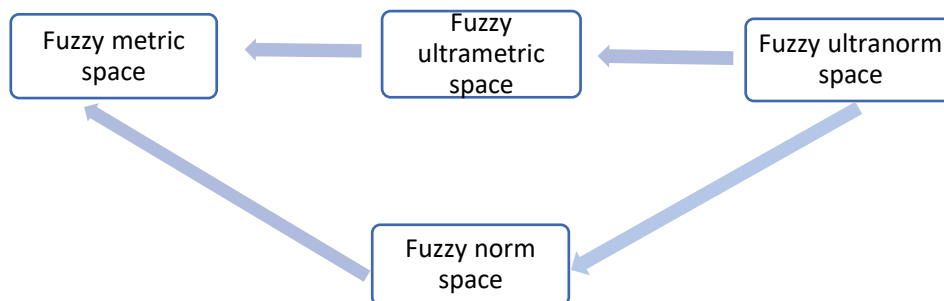


Diagram 3.1. The connection between fuzzy ultrametric space and fuzzy ultranorm space.

Let u be a sequence of fuzzy numbers. For $\forall \varepsilon > 0, \forall k \geq k_0$ and $\exists k \in \mathbb{N}$, if the inequality $d(u_k, u_0) = \sup_{\alpha \in [0,1]} \bar{d}(u_k^\alpha, u_0^\alpha) < \varepsilon$, then (u_k) is called to convergent to $(u_0) \in F(E')$.

$\bar{d}(u_k^\alpha, u_0^\alpha) = \max\{|u_k^{(\alpha)-} - u_0^{(\alpha)-}|, |u_k^{(\alpha)+} - u_0^{(\alpha)+}|\}$. Briefly, it is denoted by $\lim u_k = u_0$. If in the closed interval $d([a, b], [c, d]) = \max\{|a - c|, |b - d|\}$.

Lemma 3.1. Let $E' = \{[a, b] | a \leq b \text{ and } a, b \in \mathbb{R}\}$ be the set of all closed intervals. Since $\tilde{d}: E' \times E' \rightarrow \mathbb{R}, (E', \tilde{d})$ is ultrametric space.

Defined by $([a, b], [c, d]) \rightarrow \tilde{d}([a, b], [c, d]) = \max\{|a - c|, |b - d|\}$, \tilde{d} provides ultrametric properties.

$$\tilde{d}([a, b], [c, d]) = 0 \Leftrightarrow \max\{|a - c|, |b - d|\} = 0 \Leftrightarrow \text{and } a = c, b = d, [a, b] = [c, d].$$

$\tilde{d}([a, b], [c, d]) = \tilde{d}([c, d], [a, b])$ it is clear that.

$$\begin{aligned} \tilde{d}([a, b], [c, d]) &= \max\{|a - c|, |b - d|\} \\ &= \max\{|a - c + e - e|, |b - d + f - f|\} \\ &\leq \max\{|a - e| + |e - c|, |b - f| + |f - d|\} \\ &= \max\{|a - e|, |b - f|\} + \max\{|e - c|, |f - d|\} \\ &\leq \max\{|a - e|, |b - f|\}, \max\{|e - c|, |f - d|\} \\ &= \max\{\tilde{d}([a, b], [e, f]), \tilde{d}([e, f], [c, d])\} \end{aligned}$$

Since it provides ultrametric properties (E', \tilde{d}) , it is an ultrametric space. □

Let's suppose that $u_k = ([x_k, y_k])$ is a Cauchy sequence. So for all $\varepsilon > 0$, it is $\exists n_0 \in \mathbb{N}$ such that for $\forall k, m \geq n_0$ it is $d([x_k, y_k], [x_m, y_m]) < \varepsilon$.

Since $\max\{|x_k - x_m|, |y_k - y_m|\} < \varepsilon$, $|x_k - x_m| < \varepsilon$ and $|y_k - y_m| < \varepsilon$. The sequences (x_k) and (y_k) are also a Cauchy sequence in \mathbb{R} . Because \mathbb{R} is complete, $\lim_k x_k = x_0$ and $\lim_k y_k = y_0$ exist. Since $x_k \leq y_k$ is $x_0 \leq y_0$. So $\lim_k u_k = \lim_k [x_k, y_k] = [x_0, y_0]$. Namely, (u_k) Cauchy sequence is convergent and since it is convergent (E', \tilde{d}) it is a complete ultrametric space.

Theorem 3.2. $F(E')$ is the complete ultrametric space.

Proof. It can be proved that $F(E')$ is also complete using Lemma 2.1. It can be taken as $u \in F(E') \Leftrightarrow u^\alpha = [u^{\alpha-}, u^{\alpha+}]$. Because for $(u_k) \in F(E')$ and $\forall \alpha \in [0,1]$, α -cut (u_k^α) gives a sequence of E' . As a result, it is clear from the complete of E' that $F(E')$ is complete. \square

Definition 3.3. The fuzzy norm of the fuzzy number u is denoted which notation to the fuzzy distance from u to 0, as follows:

$$\|u\|_{E'} = \sup_k \sup_{\lambda \in [0,1]} \lambda [|u_k^- - \bar{0}|, |u_k^+ - \bar{0}|] \tag{3.1}$$

Let $u = (u_k)$ be a sequence of fuzzy numbers, $(u_k) \in E'$ and $\|\cdot\|$ be a fuzzy norm.

It means that the sequences (u_k) converge to $(u_0) \in E'$ with the fuzzy norm $\|\cdot\|$, there is an integer n_0 such that $\|u_k - u_0\| < [\varepsilon, \varepsilon] = \varepsilon$ for $k \geq n_0$, if for any given $\varepsilon > 0$. The sequence (u_k) is said to be fuzzy norm $\|\cdot\|$ if $\sup_k \|u_k\| < \infty$, for all $k \in \mathbb{N}$. Respectively $c(E')$, $c_0(E')$, and $l_\infty(E')$ are written for the the fuzzy sets of all fuzzy convergent, fuzzy null, fuzzy bounded sequences [23].

$$\|\cdot\| \text{ is satisfies the property (N3)' with the norm defined by } \sup_k \|u_k\|. \tag{3.2}$$

$$u_{l'_\infty(E')} (k) = u_{c'(E')} (k) = u_{c'_0(E')} (k).$$

Then the set of fuzzy ultra-convergent, fuzzy ultra-null, and fuzzy ultra-bounded sequences are denoted by $c'(E')$, $c'_0(E')$ and $l'_\infty(E')$ respectively, and defined as follows:

$$c'(E') = \{u = (u_k) \in w(E') : \lim_k \sup_{\lambda \in [0,1]} \lambda [|u_k^- - \bar{0}|, |u_k^+ - \bar{0}|] = \varphi, \varphi \in E' \}$$

$$c'_0(E') = \{u = (u_k) \in w(E') : \lim_k \sup_{\lambda \in [0,1]} \lambda [|u_k^- - \bar{0}|, |u_k^+ - \bar{0}|] = \theta \}$$

$$l'_\infty(E') = \{u = (u_k) \in w(E') : \sup_k \sup_{\lambda \in [0,1]} \lambda [|u_k^- - \bar{0}|, |u_k^+ - \bar{0}|] < \infty \}$$

Theorem 3.3. $c'_0(E') \subset c'(E') \subset l'_\infty(E')$ coverage is available.

Theorem 3.4. $c'_0(E') \subset c_0(E') \subset c'(E') \subset c(E') \subset l'_\infty(E') \subset l_\infty(E')$. It is clear that it has coverage.

Theorem 3.5. $l'_\infty(E') = \{u = (u_k) \in E' : \sup_k \sup_{\lambda \in [0,1]} \lambda[|u_k^- - \bar{0}|, |u_k^+ - \bar{0}|] < \infty\}$ fuzzy ultra-bounded sequences is a complete ultranorm space, with the norm given in (3.2).

Proof. It is easy to prove that a fuzzy ultra-bounded sequence is a fuzzy ultranormed space. Hence it will be proved below that a fuzzy ultra-bounded sequence is complete.

Let's assume that (u_k) is a Cauchy sequence in $l'_\infty(E')$. If (u_k) is a constant sequence then the case is clear. If (u_k) is not a constant sequence then there is an integer n_0 such that $m, n \geq n_0$ and;

$$\|u^m - u^n\| = \sup_k |u_k^m - u_k^n| < \varepsilon \tag{3.3}$$

From here, $|u_k^m - u_k^n| < \varepsilon$ is obtained when $m, n \geq n_0$ for every arbitrary but constant k with $k = 1, 2, \dots$ and $\varepsilon > 0$. So for every constant k , $(u_k^1, u_k^2, u_k^3, \dots)$ is also a Cauchy sequence in E' . Since E' is complete $u_k^m \rightarrow u \in E'$. With the help of these limits to be obtained for each natural number k , the sequence $u = (u_1, u_2, \dots)$ is formed in E' .

$$\begin{aligned} u_1 &= (u_1^1, u_2^1, \dots, u_n^1, \dots) \\ u_2 &= (u_1^2, u_2^2, \dots, u_n^2, \dots) \\ u_3 &= (u_1^3, u_2^3, \dots, u_n^3, \dots) \\ &\vdots \\ u_k &= (u_1^k, u_2^k, \dots, u_n^k, \dots) \\ &\vdots \\ u_m &= (u_1^m, u_2^m, \dots, u_n^m, \dots) \\ &\downarrow \quad \downarrow \quad \downarrow \dots \quad \downarrow \dots \\ u &= (u_1, u_2, \dots, u_n, \dots) \end{aligned}$$

Now it will be denoted that $u_n \rightarrow u$, $n \rightarrow \infty$, and $u \in l'_\infty(E')$. In (3.2) if $n \rightarrow \infty$ is done $\|u_k^n - u_k\|_{l'_\infty(E')} < \varepsilon$ is obtained. Since $u_n = (u_k^n) \in l'_\infty(E')$, there is t_n real sequence such that $\|u_k^n\| \leq t_n$, for $k = 1, 2, \dots$

From the strong triangle inequality $\|u_k\| = \|u_k - u_k^n + u_k^n\| \leq \max\{\|u_k - u_k^n\|, \|u_k^n\|\} \leq \max\{\varepsilon, t_n\} < \infty$. Considering that for all k this inequality is valid, $(u_k) \in l'_\infty(E')$. □

Definition 3.4. $Z' = (z_{nk})$ and given the sequence $u = (u_k)$, consider the transformation $v_k = pu_k + (1 - p)u_{k-1}$, which is called Zweier transformation by the following definition [24].

$$Z'_{nk} = \begin{cases} p, & n = k \\ 1 - p, & n - 1 = k \\ 0, & \text{otherwise} \end{cases}, p \in \mathbb{R} - \{-1\} \quad n, k \in \mathbb{N}$$

Theorem 3.6. Defined by $l'_\infty(E') = \{u = (u_k) \in E' : \sup_k \sup_{\lambda \in [0,1]} \lambda [|u_k^- - \bar{0}|, |u_k^+ - \bar{0}|] < \infty \}$ the set of the fuzzy ultra-bounded sequence is ultra-isomorphic.

Proof.

$Z' : \tilde{l}_\infty(E') \rightarrow l'_\infty(E')$ consider the transformation $u \rightarrow Z'u = v, v = v_k,$

$$v_k = pu_k + (1 - p)u_{k-1} \tag{3.4}$$

i) Z' is linear.

$\forall u, v \in \tilde{l}_\infty(E'), \forall \alpha \in E'$

$$\begin{aligned} Z'(u + v) &= p(u_k + v_k) + (1 - p)(u_{k-1} + v_{k-1}) \\ &= pu_k + pv_k + (1 - p)u_{k-1} + (1 - p)v_{k-1} \\ &= pu_k + (1 - p)u_{k-1} + pv_k + (1 - p)v_{k-1} \\ &= Z'(u) + Z'(v) \end{aligned}$$

$$\begin{aligned} Z'(\alpha u) &= p(\alpha u_k) + (1 - p)(\alpha u_{k-1}) \\ &= \alpha(pu_k + (1 - p)u_{k-1}) = \alpha Z'(u). \end{aligned}$$

ii) Z' bijection.

$Z' : \tilde{l}_\infty(E') \rightarrow l'_\infty(E')$ and $v_k = pu_k + (1 - p)u_{k-1}$

$$\text{When } u = Z'^{-1}v, \text{ every } u = (u_k) = \sum_{j=0}^k (-1)^{k-j} \frac{(1-p)^{k-j}}{p^{k-j+1}} v_j \tag{3.5}$$

The form given has a v element. As a result, it is shown to be a bijection.

iii) In the case of $\tilde{l}_\infty(E')$ and $l'_\infty(E')$ ultranormed spaces, the Z' isomorphic is a linear space isomorphic that preserves the norm, that is, satisfies the $\|Z'u\| = \|u\|$ condition for each u (element) Z' .

In the $u = (u_k) = \sum_{j=0}^k (-1)^{k-j} \frac{(1-p)^{k-j}}{p^{k-j+1}} v_j$ sequence given in (3.5), with (3.4) $v_k = pu_k + (1 - p)u_{k-1}$

$$\begin{aligned} \|Z'u\|_{\tilde{l}_\infty(E')} &= \sup_k \tilde{d}(Z'u_k, \bar{0}) \\ &= \sup_k \tilde{d}(pu_k + (1 - p)u_{k-1}, \bar{0}) \end{aligned}$$

$$\begin{aligned}
 &= \sup_k \tilde{d} \left(p \sum_{j=0}^k (-1)^{k-j} \frac{(1-p)^{k-j}}{p^{k-j+1}} v_j + (1-p) \sum_{j=0}^k (-1)^{k-j} \frac{(1-p)^{k-j}}{p^{k-j+1}} v_j, \bar{0} \right) \\
 &= \sup_k \tilde{d}(u_k, \bar{0}) = \|u\|_{l'_\infty(E')}
 \end{aligned}$$

To summarize, Z' is norm preserving. The spaces $\tilde{l}_\infty(E')$ and $l'_\infty(E')$ are isometric. □

As a result, $l'_\infty(E')$ fuzzy ultra-bounded sequence space is shown to be ultra-isomorphic and the proof is completed.

4. Conclusion

In this study, fuzzy ultrametric space and fuzzy ultranorm definitions were made. It is proved that fuzzy sets are ultrametric space and ultranorm. It was emphasized that fuzzy ultranorm spaces are also special cases of fuzzy norm spaces. Additionally, a relationship was established between fuzzy ultrametric spaces and fuzzy ultranorm spaces. It has been shown that $F(E')$ is a complete ultrametric space. By defining fuzzy ultra-sequence spaces $c'(E')$, $c'_0(E')$, and $l'_\infty(E')$ their coverage states are researched and shown. Finally, the fuzzy ultra-bounded sequence spaces are proven to be complete and ultra-isomorphic.

Ethics in Publishing

There are no ethical issues regarding the publication of this study.

References

- [1] Zimmerman, H. J., (1985) Fuzzy Set Theory and Its Applications, Springer Science Business Media.
- [2] Zadeh, L., (1965) Fuzzy sets. Inf. Control. 8: 338-353.
- [3] Kaleva, O., Seikkala, S., (1984) On fuzzy metric space, Fuzzy Sets and Systems. 12, 215-229.
- [4] Seikkala, S., (1987) On the initial value problem. ric spaces. Fuzzy Sets and Systems, 10.1016/0165-0114(87)90030-3.
- [5] Matloka, M., (1986) Sequence of fuzzy numbers, Busefal. 28, 28_37.
- [6] Katsaras, A. K., (1984) Fuzzy topological vector space II. Fuzzy sets and systems, 12,143-154
- [7] Felbin, C., (1992) Finite dimensional fuzzy normed linear space, Fuzzy Sets and Systems, 48, 239-248.

- [8] Cheng, S.C., Mordeson, J. N., (1994) Fuzzy linear operators and fuzzy normed linear spaces. *Bull. Cal. Math. Soc.* 86 429-436.
- [9] Kramosil, O., and Michalek, J., (1975) Fuzzy metric and statistical metric spaces. *Kybornetika.* 11, 326–334.
- [10] Bag, T., Samanta, S., (2005) Fuzzy bounded linear operators, *Fuzzy sets and Systems*, 151(3):513-547.
- [11] Sadeqi, I., Kia, F., (2009) Fuzzy normed linear space and its topological structure, *Chaos Solitions and Fractals.* 40 (5): 2576-2589.
- [12] Xia, ZQ., Guo, FF., (2004) Fuzzy metric spaces, *JAMC* 16, 371–381.
- [13] Khan, V. A., Ahmad M., Alam M., (2022) A Study of Fuzzy Sequence Spaces, Edited by Constanstin Volosencu 10.5772/intechopen.94202.
- [14] Manuel Clementino, M., Montoli, A., (2021) On the categorical behaviour of V-groups. *Journal of Pure and Applied Algebra* 10.1016/j.jpaa.2020.106550.
- [15] Bede, B., (2013) *Mathematics of Fuzzy Sets and Fuzzy Logic*, Springer-Verlag Berlin Heidelberg (pp. 137-170).
- [16] Bag, T., Samanta, S. K., (2003) Finite dimensional fuzzy normed linear spaces, *The Journal of Fuzzy Mathematics*, vol. 3, pp. 687-705.
- [17] Szmidt, E., (2014) *Studies in Fuzziness and Soft Computing. Distances and Similarities in Intuitionistic Fuzzy Sets*, Springer, International Publishing Switzerland London.
- [18] Diamond, P., Kloeden P., (1994) *Metric Spaces of Fuzzy Sets*, World Scientific Publishing, River Edge, NJ,USA .
- [19] Dubois, D., Prade, H., (1980) *Fuzzy Sets and Systems: Theory and Applications. Mathematics in Science and Engineering*, vol. 144, Academic Press. New York .
- [20] Dutta, P., Boruah, H., Ali, T., (2011) Fuzzy Arithmetic with and without using α -cut method, *A Comparative Study International Journal of Latest Trends in Computing* (E-ISSN: 2045-5364) 99 Volume 2, Issue 1, March.
- [21] Choi, H.C., (1996) The completeness of convergent sequences space of fuzzy numbers, *Kangweon- Kyungki Math. Jour.*, vol. 4, no. 2, pp. 117–124.
- [22] Rano, G., Bag, T., (2012) Fuzzy Normed Linear Spaces. *International Journal of Mathematics and Scientific Computing* (ISSN: 2231-5330), Vol. 2, No. 2

- [23] Şengönül, M., Zararsız, Z., (2011) Some Additions to the Fuzzy Convergent and Fuzzy Bounded Sequence Spaces of Fuzzy Numbers. *Abstract and Applied Analysis*. 10.1155/2011/837584.
- [24] Şengönül, M., (2014) On the Zweier Sequence Spaces of Fuzzy Numbers. *International Journal of Mathematics and Mathematical Sciences*. 10.1155/2014/439169.
- [25] Li, C., (2013) On some results of metrics induced by a fuzzy ultrametric. *Filomat*, 27(6), 1133-1140.
- [26] Savchenko, A., Zarichnyi, M., (2011) Probability measure monad on the category of fuzzy ultrametric spaces.
- [27] Gregori, V., Miñana, J. J., Sapena, A., (2017) Completable fuzzy metric spaces. *Topology and its Applications*, 225, 103-111.
- [28] Zahedi Khameneh, A., Kilicman, A., Md Ali, F., (2021) Revision of Pseudo-Ultrametric Spaces Based on m-Polar T-Equivalences and Its Application in Decision Making. *Mathematics*, 9(11), 1232.
- [29] Şanlıbaba, İ. (2020) Bazı Ultranormlu Uzaylar ve İzomorfikliği. *Bilecik Şeyh Edebali Üniversitesi Fen Bilimleri Dergisi*, 7(1), 265-272.
- [30] Sanlibaba, I. (2019) New Type Ultra-Banach Spaces. *International Journal of Scientific and Technological Research* www.iiste.org ISSN 2422-8702 (Online), DOI: 10.7176/JSTR/5-12-02 Vol.5, No.12.
- [31] Abed Alhaleem, N., & Ahmad, A. G. (2020) Intuitionistic fuzzy normed subrings and intuitionistic fuzzy normed ideals. *Mathematics*, 8(9), 1594.

The Effect of the Aluminum (Al) Ratio on the Synthesis of the Laminated Mn_2AlB_2 MAB Phase

Fatma Nur TUZLUCA YESİLBAG^{1*}, Yasar Ozkan YESİLBAG¹, Ahmed Jalal Salih SALIH² and Ahmad HUSEYİN²

¹Department of Physics, Erzincan Binali Yıldırım University, Erzincan 24100, Turkey

²Erzincan Binali Yıldırım University Graduate School of Natural and Applied Sciences,
Department of Physics, Erzincan 24100, Turkey

Abstract

MAB phases have recently garnered significant interest due to their excellent properties, such as high thermal and electrical conductivity, oxidation resistance, and exceptional corrosion resistance. Although the Mn_2AlB_2 phase has been synthesized using multiple methods recently, it requires long experimental durations (up to 7 days), high costs, and extensive experimental efforts to achieve high purity. In our study, the Mn_2AlB_2 MAB phase was synthesized using Al, B, and Mn as precursor materials. Specifically, we investigated the effect of Al ratios (Al:1.3, Al:3, and Al:10) on the formation of the Mn_2AlB_2 MAB phase. The precursor powders were mixed homogeneously in stoichiometric ratios using ball milling and cold-pressed in a 1-inch die set to form green pellets, which were then sintered in a high-temperature vacuum furnace at 1200°C. The resulting Mn_2AlB_2 MAB phase was characterized in terms of crystal structure, impurity, and microstructure using XRD, FESEM, and EDS.

Keywords: Mn_2AlB_2 MAB phase, crystal structure, XRD and FESEM

Tabakalı Yapıdaki Mn_2AlB_2 MAB Fazının Sentezinde Alüminyum (Al) Oranının Etkisi

MAB fazları iyi termal ve elektriksel iletkenliklerinin yanı sıra oksidasyon direncinin yüksek ve mükemmel korozyon direncine sahip olması gibi mükemmel özelliklerinden dolayı son zamanlarda büyük ilgi görmektedir. Özellikle Mn_2AlB_2 fazı yakın zamanda birden fazla yöntem kullanılarak sentezlenmiş olmasına rağmen, uzun deneysel süre (7 güne kadar), yüksek maliyet ve mükemmel saflıkta sentezlenmesi için deneysel çalışmalara ihtiyaç duyulmaktadır. Yaptığımız çalışmada ise öncü materyaller olarak Al, B ve Mn kullanılarak Mn_2AlB_2 MAB fazı sentezlenmiştir. Çalışmamızda özellikle Al (Al:1.3, Al:3 ve Al:10) oranının Mn_2AlB_2 MAB fazının oluşumuna olan etkisi incelenmiştir. Öncü tozlar stokiyometrik oranlarda bilyalı öğütme ile homojen bir şekilde karıştırılmış ve fiziksel bağların oluşumu için 1 inç'lik die-set ile soğuk preslenerek ham peletler elde edilmiş ve daha sonra 1200 °C'de yüksek sıcaklık vakum fırınında sinterlenmiştir. Elde edilen Mn_2AlB_2 MAB fazının kristal yapısı, safsızlık ve mikro yapısı XRD, FESEM ve EDS kullanılarak karakterize edilmiştir.

Anahtar kelimeler: Mn_2AlB_2 MAB fazı, kristal yapı, XRD ve FESEM

*Corresponding Author: ftuzluca@erzincan.edu.tr

Fatma Nur TUZLUCA YESİLBAG, <https://orcid.org/0000-0003-4383-2432>

Yasar Ozkan YESİLBAG, <https://orcid.org/0000-0002-2519-3078>

Ahmed Jalal Salih SALIH, <https://orcid.org/0000-0002-1760-5423>

Ahmad HUSEYİN, <https://orcid.org/0000-0002-2260-2593>

1. Introduction

Studies have been carried out in recent years on similar MAB phases due to using MAX phases as a leading material in synthesizing 2D structures. Theoretical and experimental studies have proven MAB phases obtained by replacing the carbon and/or nitrogen corresponding to the element X in the MAX phases with boron (Ade and Hillebrecht, 2015; Chai et al., 2015; Bai et al., 2017). Recent studies on MAB phases have mainly focused on single crystal growth and crystal structure determination (Ade and Hillebrecht, 2015), electronic properties (Lu et al., 2017), mechanical properties (Siriwardane et al., 2020), and oxidation resistance (Kota et al., 2016).

MAB phases are layered orthorhombic transition metal borides similar to MAX phases but with higher structural stability. In the MAB phase, M represents the transition metals such as Cr, Mo, W, Fe, Mn, or solid alloys of these elements (FeB, CrB, and MnB), A represents the III-A or IV-A group element, and B represents the boron element. They have shown a unique diversity in crystal chemistry and bonding patterns, where the binding of boron atoms is often determined by the transition metal (M: B) ratio. These can be considered materials consisting of stacked M-B blocks, which consist of face-sharing triangular BM₆ prisms interwoven with planes of A atoms or more complex A sheets between minerals (Kota et al., 2018a). MAB phases have a significant structural diversity. Among them are well-known phases MoAlB, WAlB, Fe₂AlB₂, Cr₂AlB₂, and Mn₂AlB₂, which have attracted significant attention recently. As a result of the atomic structure of MAB phases, the name MAB is given because the thickness of the metal boride layer (n) resembles the large carbide structure of MAX phases. MAB phases have more than one crystal structure (space group). For example, Mn₂AlB₂ (space group C_{mmm}), MoAlB (space group C_{mcm}), Cr₃AlB₄ (space group I_{mmm}), Cr₄AlB₆ (space group C_{mmm}), Cr₄AlB₄ and Ru₂ZnB₂ (space group I4₁/amd). In general, (MB)_{2z}A_x(MB)_{2y}, wherein (z = 1–2, x = 1–2, y = 0–2); M is a transition metal (M = Mo, Cr, Mn, Fe, W, Hf, Ru, Y), A is typically Al, and B is boron. Having the M₂AB₂-type structure (x = 1, y = 0, z = 1), the Mn₂AlB₂ crystallizes in the C_{mmm} space group.

MAB phases can also be synthesized using methods similar to MAX phases (Kota et al., 2018b). The synthesis of MAB phases involves sintering at high temperatures (1000–1500 °C) under an argon (Ar) atmosphere. Elemental (Al, B, Cr, W, Mo, Mn, Fe) or alloy (FeB, CrB, MnB) can be precursor materials. There are few studies in the literature on the synthesis of Mn₂AlB₂. Kota et al. attempted to prepare Mn₂AlB₂ by using hot press sintering technology at 1050 °C, pressure up to 36 MPa, and mixing Mn, Al, and B powders as starting materials (Kota et al., 2018a). In another study, using Mn, Al, and B powders as precursor materials, Mn₂AlB₂ was synthesized by heat treatment sintering at 1050 °C for 15 hours. Despite attempts to synthesize Mn₂AlB₂, the cost of synthesis is high due to the methods used, such as hot-pressure sintering. As for the heat treatment technique, the fact that the experiment lasts approximately 15 hours may cause problems in terms of equipment, and the impurity of the obtained Mn₂AlB₂ MAB phase is relatively low. Therefore, Mn₂AlB₂ synthesis requires new and efficient techniques. In another study, Mn₂AlB₂ was synthesized by arc melting at 1450 °C with Mn:B:Al atomic ratio of 1:1:30 (Ade and Hillebrecht, 2015). Additionally, Zhai et al. obtained Mn₂AlB₂ using arc melting

under the Ar atmosphere at 900 °C for 7 days (168 hours). Mn_2AlB_2 was also produced using Al Flux techniques, where a mixture of Mn, Al, and B (Al:Mn:B = 10:1:2) was heated to 1150 °C for 15 hours (Roy et al., 2023).

In this study, it was aimed to synthesize the Mn_2AlB_2 MAB phase using Al, B and Mn as precursor materials and to investigate the effect of different Al concentrations (Al:1.3, Al:3 and Al:10) on the formation of the phase and to obtain it by high-temperature sintering with a synthesis time that is lower duration than the studies in the literature.

2. Materials and Methods

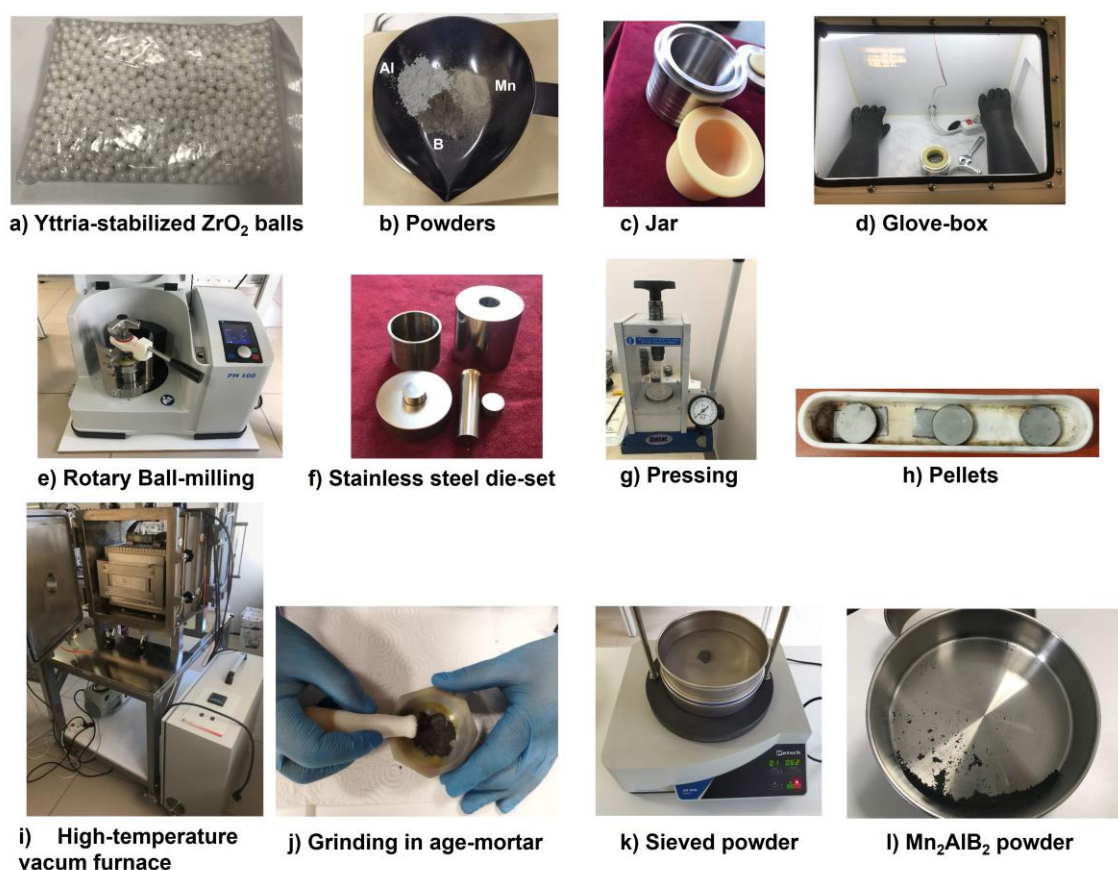


Figure 1. Experimental materials and steps used in the synthesis of Mn_2AlB_2 MAB phase.

As shown in Figure 1, Manganese (99.3 %, 325 mesh), aluminium (99.5 %, 325 mesh), and amorphous boron (98 %, 325 mesh) powders weighed in an atomic ratio of 2:x:2 ($x=1.3, 3$ and 10) respectively. After the precursor materials and yttria-stabilized zirconia (YSZ) balls were placed in the jar, they were sealed in an Argon atmosphere in the glove box. Then, the powders were mixed via rotary ball milling for 18 h. After mixing, the powders were cold-pressed into pellets with loads corresponding to a stress of 15 MPa in a steel die. To react with the pressed pellets at high temperatures, they were placed in an alumina boat, placed in a high-temperature vacuum furnace with a heating rate of 5 °C/min, and sintered for 2 hours at 1200 °C in a pre-vacuumed 200 sccm Argon atmosphere. After cooling at room temperature, the pellets were crushed into fine powders in an agate mortar and pestle and passed through a 325-mesh sieve

for further characterization. The synthesis parameters of the Mn_2AlB_2 MAB phase are given in Table 1.

Tablo 1. Synthesis parameters of Mn_2AlB_2 MAB phase.

Stoichiometric ratio	Diameter of balls (mm)	BPR (Ball to powder ratio)	Mixing powders (rpm)	Time (h)	Pressure (MPa)	Sintering temperature (°C)/Time (h)
Mn:Al:B → 2:x:2 x=1.3, x=3, x=10	5	5:1	200	18	15	1200 °C / 2 h

3. Results and Discussion

When synthesizing MAB phases, Al is added more in molar ratio (Tan et al., 2013; Wang et al., 2021). This is because the melting point of Al is lower than other elements in the MAB phase. However, the effect of Al concentration on the synthesis of the Mn_2AlB_2 phase is not yet fully understood. Therefore, we changed the Al concentration by varying $x=1.3, 3,$ and $10,$ corresponding to $Mn_2Al_{1.3}B_2,$ $Mn_2Al_3B_2,$ and $Mn_2Al_{10}B_2$ labelled samples. Crystalline structures of the samples were investigated in the 2θ range (step size: 0.05°) from 10° to 80° using X-ray diffraction (XRD) patterns obtained from PANalytical Empyrean with Cu- K_α radiation of wavelength (λ) of 1.5406 \AA . The XRD patterns of $Mn_2Al_{1.3}B_2,$ $Mn_2Al_3B_2,$ and $Mn_2Al_{10}B_2,$ corresponding to Al concentrations of $x=1.3, 3,$ and $10,$ respectively, are shown in Figure 2. In XRD patterns, it was observed that most of the peak positions correspond to the orthorhombic (C_{mmm} space group) crystal structure of the Mn_2AlB_2 phase, as indicated by the JCPDS card No: 072-0103 (Figure 3).

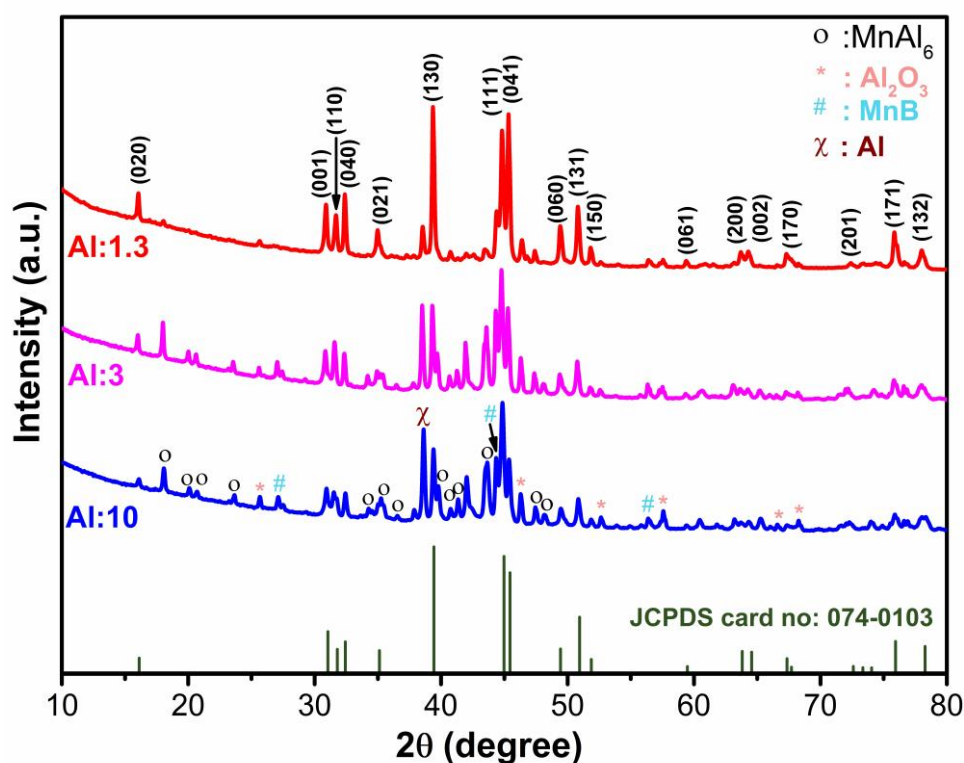


Figure 2. XRD pattern of Mn_2AlB_2 MAB phase according to the amount of Al.

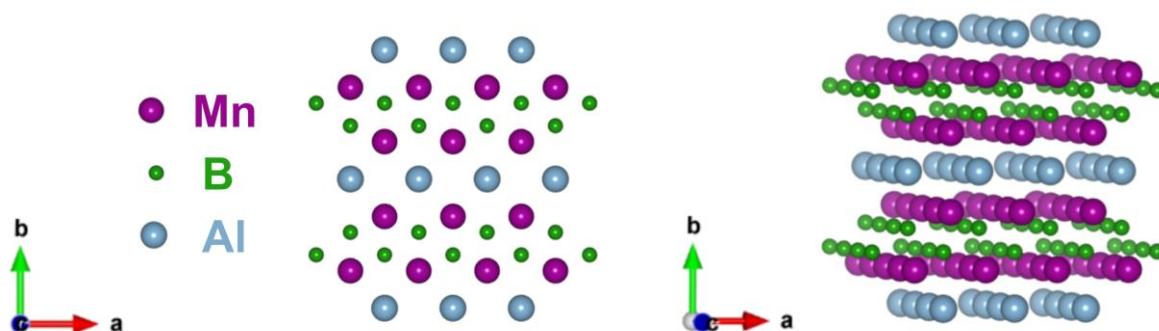


Figure 3. 2D and 3D visualization of the orthorhombic (C_{mmm} space group) crystal structure of 212-type Mn_2AlB_2 MAB phase.

The main phase identified in the sample with an Al content of 1.3 was Mn_2AlB_2 with high purity, alongside minor MnB, MnAl_6 , Al_2O_3 , and Al (Table 2). In contrast, the sample with an Al content of 3 exhibited more MnB, MnAl_6 , Al_2O_3 , and Al impurities compared to the sample with an Al content of 1.3, indicating an increase with higher Al content. However, increasing the initial mixture's Al content to 10 did not effectively enhance the purity of Mn_2AlB_2 ; instead, the quantity of Mn_2AlB_2 MAB phase decreased. As the Al content increased, some characteristics, for example (002), (001), (004), peaks intensity of Mn_2AlB_2 decreased, leading to a higher formation of MnB, MnAl_6 , Al_2O_3 , and Al impurities alongside Mn_2AlB_2 , as observed in Figure 2. In the XRD pattern with an Al content of 1.3, the intensity of reflections from the (002) crystal plane was significantly higher than Al content of 3 and 10, indicating better crystallinity of the Mn_2AlB_2 phase. Additionally, the peak intensity of the (002) crystal plane decreased as the ratio of Al increased. Furthermore, the presence of Al_2O_3 in each sample is likely due to the reaction between Al and O adsorbed on the surfaces of precursor powders.

Tablo 2. Starting mixture with different molar ratios and resulting phases.

Starting mixture	Molar ratio	Resulting phases
Mn/Al/B	2:1.3:2	Mn_2AlB_2 (s), MnAl_6 (w), MnB (w), Al_2O_3 (w), Al (m)
	2:3:2	Mn_2AlB_2 (m), MnAl_6 (m), MnB (m), Al_2O_3 (w), Al (s)
	2:10:2	Mn_2AlB_2 (w), MnAl_6 (m), MnB (m), Al_2O_3 (w), Al (s)

Symbols means: 's':strong; 'm': medium; 'w' weak.

Field Emission Scanning Electron Microscopy (FESEM) measurement and elemental mapping of the MAB phases were performed using the FEI Quanta 450 FEG device and AMETEK Materials Analysis Division on the FESEM device, respectively. In Figure 4, as seen in the low and high magnification, FESEM images of samples passed through a 325-mesh sieve after crushing and grinding steps following sintering, the particle size is less than $38\ \mu\text{m}$. Generally, Mn_2AlB_2 MAB phases where Al is utilized in varying ratios, like commonly synthesized MAX phases, exhibit a well-defined crystalline structure and a morphology resembling a laminated structure.

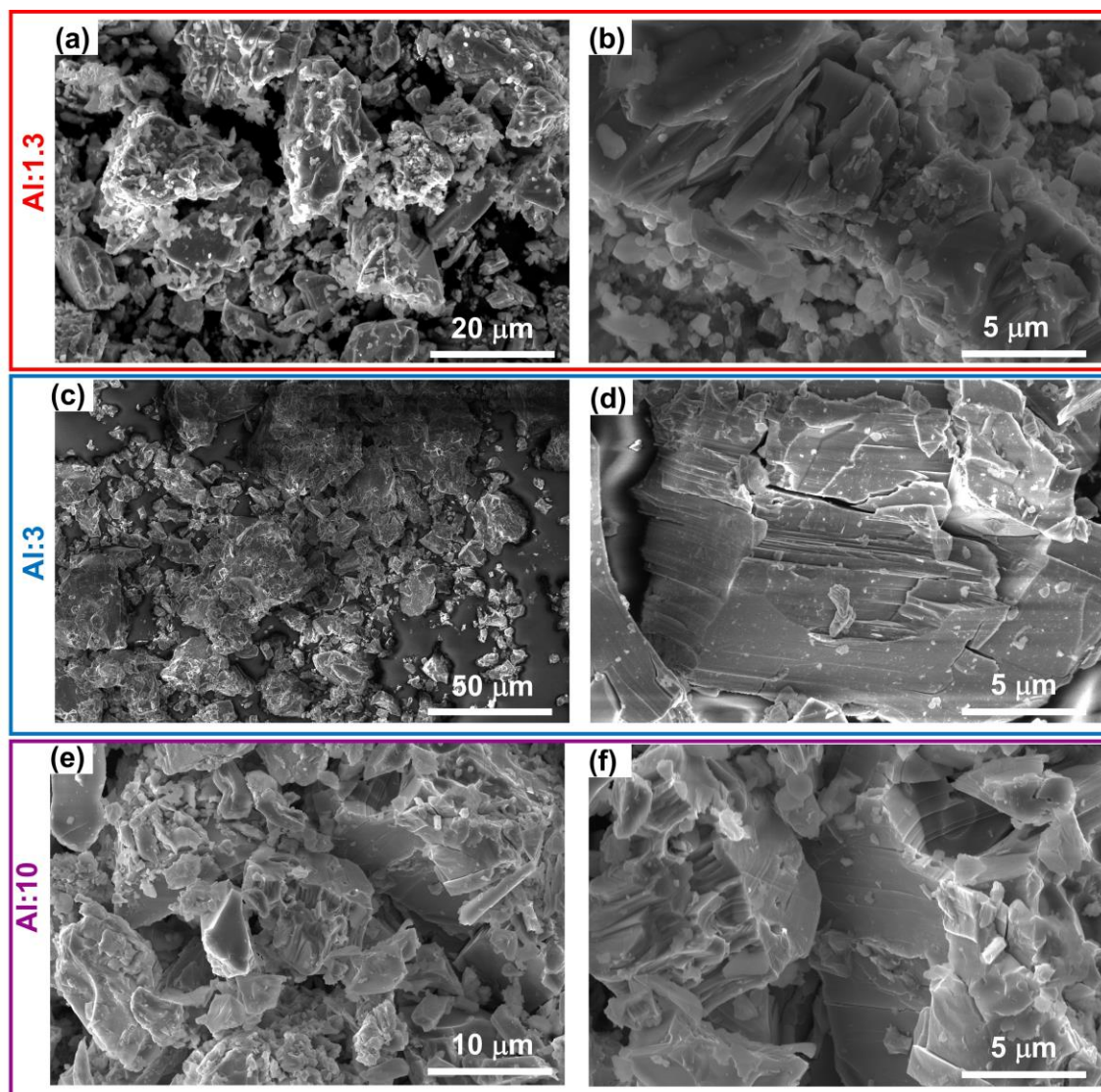


Figure 4. FESEM images of Mn_2AlB_2 MAB phase according to the amount of Al, (a, b) Al:1.3, (c, d) Al:3, and (e, f) Al:10.

EDS analysis was conducted to investigate the effect of varying amounts of Al on forming the Mn_2AlB_2 MAB phase. Figure 5 presents the EDS results regarding the atomic concentration of Mn, Al, and B elements. Generally, no impurities containing different elements were detected in the MAB phases, and full-area measurements indicate a homogeneous distribution of Mn, Al, and B. However, in the MAB phases of samples Al:3 and Al:10, where the Al concentration is increased, a slight increase in the ratio of Al impurity is observed. This phenomenon likely reduces the content of the Mn_2AlB_2 MAB phase in the final compound, as indicated by XRD results within the powder. It is known that adding excessive amounts of Al during the synthesis of MAX phases plays a crucial role in compensating for the loss of Al due to evaporation. However, increasing the amount of Al can reduce the formation rate of MAB phases with low thermal stability or lead to the formation of additional impurities.

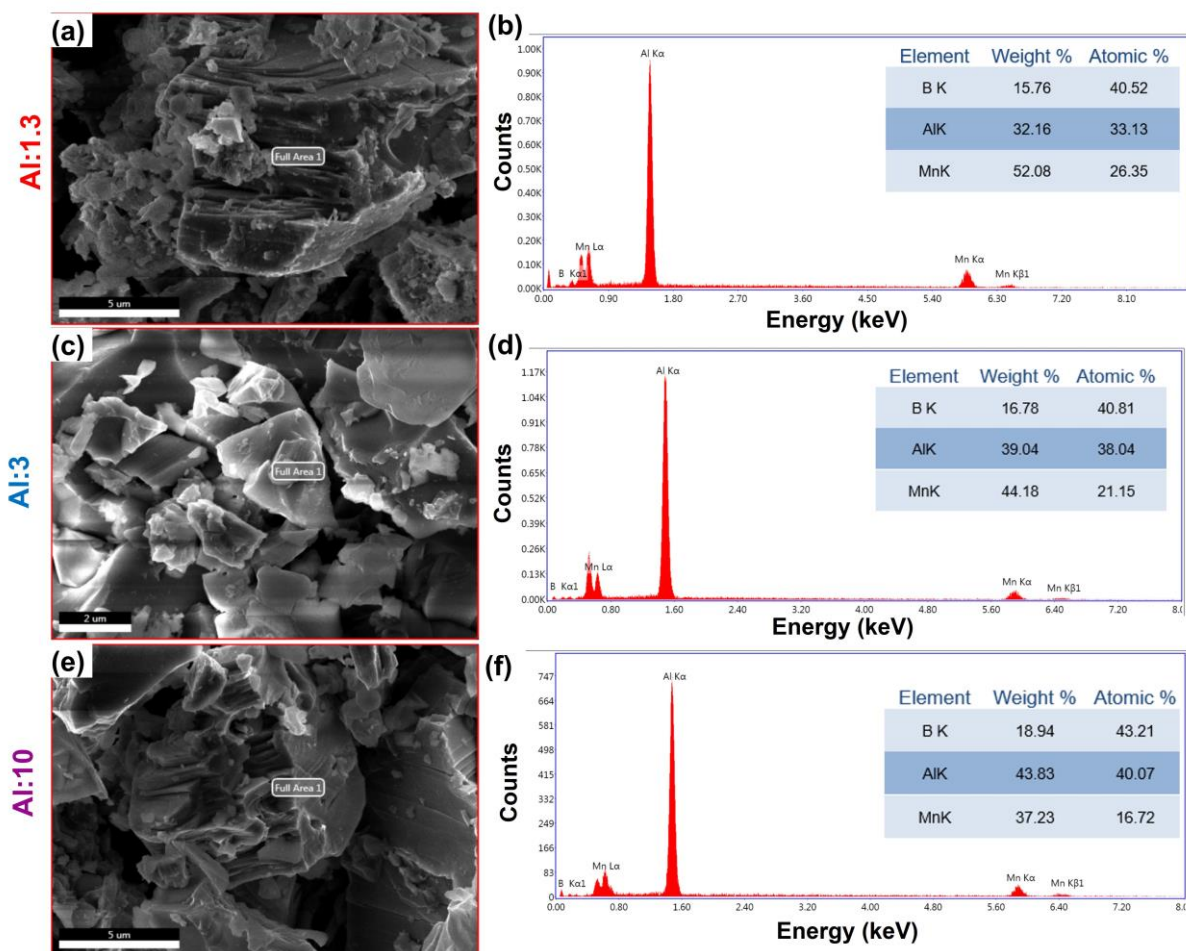


Figure 5. Full area EDS analysis of Mn_2AlB_2 MAB phase with atomic concentrations according to the amount of Al, (a, b) Al:1.3, (c, d) Al:3, and (e, f) Al:10.

4. Conclusion

In this study, the Mn_2AlB_2 MAB phase was obtained by sintering at 1200 °C for 2 hours in a vacuum environment in a high-temperature furnace. The effect of Al content (Al:1.3, Al:3 and Al:10) on the formation of the Mn_2AlB_2 MAB phase was investigated. In the sample with an Al content of 1.3, the main phase Mn_2AlB_2 was obtained in high purity orthorhombic crystal structure and small amounts of MnB, $MnAl_6$, Al_2O_3 and Al impurities were found. As the Al content increases, the proportion of the Mn_2AlB_2 phase decreases, and the proportion of impurities such as $MnAl_6$, MnB and Al_2O_3 increases. XRD and FESEM analyses showed that the Mn_2AlB_2 MAB phase grows perfectly in a layered structure and maintains high crystal quality.

Acknowledgements

This work was supported by the Scientific and Technical Research Council of Turkey, TUBITAK, under Grant Number 120F312.

Ethics in Publishing

There are no ethical issues regarding the publication of this study.

Author Contributions

Fatma Nur Tuzluca Yesilbag: Ideas; formulation or evolution of overarching research goals and aims; Acquisition of the financial support for the project leading to this publication.

Yasar Ozkan Yesilbag: Preparation, creation, and presentation of the published work, specifically visualization/ data presentation.

Ahmad Huseyin: Performing the experiments and data collection.

Ahmed Jalal Salih SALIH: Performing the experiments or data/evidence collection.

5. References

- Ade, M., & Hillebrecht, H. (2015). Ternary borides Cr₂AlB₂, Cr₃AlB₄, and Cr₄AlB₆: the first members of the series (CrB₂)_nCrAl with n= 1, 2, 3 and a unifying concept for ternary borides as MAB-phases. *Inorganic chemistry*, 54(13), 6122-6135.
- Bai, Y., Qi, X., Duff, A., Li, N., Kong, F., He, X., ... & Lee, W. E. (2017). Density functional theory insights into ternary layered boride MoAlB. *Acta Materialia*, 132, 69-81.
- Chai, P., Stoian, S. A., Tan, X., Dube, P. A., & Shatruk, M. (2015). Investigation of magnetic properties and electronic structure of layered-structure borides AlT₂B₂ (T= Fe, Mn, Cr) and AlFe_{2-x}Mn_xB₂. *Journal of Solid-State Chemistry*, 224, 52-61.
- Kota, S. S. (2019). Synthesis and Characterization of the MAB Phases: Ternary, Nanolayered Transition Metal Borides. Drexel University, PhD Thesis.
- Kota, S., Agne, M., Zapata-Solvas, E., Dezellus, O., Lopez, D., Gardiola, B., ... & Barsoum, M. W. (2017). Elastic properties, thermal stability, and thermodynamic parameters of MoAlB. *Physical Review B*, 95(14), 144108.
- Kota, S., Chen, Y., Wang, J., May, S. J., Radovic, M., & Barsoum, M. W. (2018a). Synthesis and characterization of the atomic laminate Mn₂AlB₂. *Journal of the European Ceramic Society*, 38(16), 5333-5340.
- Kota, S., Wang, W., Lu, J., Natu, V., Opagiste, C., Ying, G., ... & Barsoum, M. W. (2018b). Magnetic properties of Cr₂AlB₂, Cr₃AlB₄, and CrB powders. *Journal of Alloys and Compounds*, 767, 474-482.
- Kota, S., Zapata-Solvas, E., Ly, A., Lu, J., Elkassabany, O., Huon, A., ... & Barsoum, M. W. (2016). Synthesis and characterization of an alumina forming nanolaminated boride: MoAlB. *Scientific reports*, 6, 26475.
- Lu, J., Kota, S., Barsoum, M. W., & Hultman, L. (2017). Atomic structure and lattice defects in nanolaminated ternary transition metal borides. *Materials Research Letters*, 5(4), 235-241.

- Roy, C., Mondal, S., Banerjee, P., & Bhattacharyya, S. (2023). Low temperature atmospheric synthesis of WAlB and Mn₂AlB₂ MAB phases by modified molten salt shielded synthesis method. *Advanced Powder Technology*, 34(4), 103983.
- Siriwardane, E. M., Joshi, R., Kumar, N., & Cakir, D. (2020). Revealing the Formation Energy-Exfoliation Energy-Structure Correlation of MAB Phases using Machine Learning and DFT. *ACS Applied Materials & Interfaces*.
- Tan, X., Chai, P., Thompson, C. M., & Shatruk, M. (2013). Magnetocaloric effect in AlFe₂B₂: toward magnetic refrigerants from earth-abundant elements. *Journal of the American Chemical Society*, 135(25), 9553-9557.
- Wang, Y., Yang, L. X., Liu, R. J., Liu, H. J., Zeng, C. L., Zhu, S. L., & Fu, C. (2021). Ternary-layered Cr₂AlB₂ synthesized from Cr, Al, and B powders by a molten salt-assisted method. *Powder Technology*, 387, 354-362.

Redundant Data Center Planning For Universities

Veli ÇAPALI^{1*}, Kadir SÜMER¹, Mevlüt ERSOY²

¹Suleyman Demirel University, Isparta Health Services Vocational School, Department of Medical Services and Techniques

²Suleyman Demirel University, Faculty of Engineering and Nature, Department of Computer Engineering

Received: 01/11/2022 **Revised:** 29/05/2023, **Accepted:** 28/11/2024, **Published:** 31/12/2024

Abstract

During the Covid-19 pandemic period, when remote education and working from home came to the fore, the importance of university information and remote education systems in this process has emerged. The digital transformation process and business continuity in the information technology infrastructure has been of great importance in terms of the services provided to students and staff during the pandemic period. The need for infrastructure for areas such as automation systems, electronic document management systems, online education and learning management systems has suddenly increased during the pandemic process, and it has been a situation faced by universities to meet this need and ensure business continuity by data centers. Because; various applications were made for the criteria to be considered in the design of the data center, redundant infrastructure, security, and later flexibility and business continuity. In this study, Suleyman Demirel University data center planning and business continuity application is given by presenting how the three-location redundant data center planning should be done according to TIER and ISO22301 standards.

Keywords: Data Center, Business continuity, Redundancy, TIER, ISO 22301.

Üniversitelere Yönelik Yedekli Veri Merkezi Planlaması

Öz

Uzaktan eğitim ve evden çalışmanın öne çıktığı Covid-19 pandemi döneminde, üniversite bilgi ve uzaktan eğitim sistemlerinin bu süreçte önemi ortaya çıkmıştır. Bilişim alt yapısındaki dijital dönüşüm süreci ve iş sürekliliği pandemi döneminde öğrencilere ve personele sunulan hizmetler açısından büyük öneme sahip olmuştur. Otomasyon sistemleri, elektronik belge yönetim sistemleri, çevrimiçi eğitim ve öğrenme yönetim sistemleri gibi alanlar için altyapı ihtiyacının pandemi sürecinde bir anda artması, veri merkezlerini bu ihtiyacı karşılaması ve iş sürekliliğini sağlaması üniversitelerin karşı karşıya kaldığı bir durum olmuştur. Bu nedenle; veri merkezi tasarımında dikkat edilmesi gereken kriterler, yedekli altyapı, güvenlik ile sonrasında esneklik ve iş sürekliliğine yönelik çeşitli uygulamalar yapılmıştır. Bu çalışmada, üç lokasyonlu yedekli veri merkezi planlamasının TIER ve ISO22301 standartlarına göre nasıl yapılması gerektiği sunulmuş, Süleyman Demirel Üniversitesi veri merkezleri planlaması ve iş sürekliliği uygulamasına yer verilmiştir.

Anahtar Kelimeler: Veri merkezi, İş Sürekliliği, Yedeklilik, TIER, ISO 22301.

*Corresponding Author: velicapali@sdu.edu.tr

1. Introduction

The Covid-19 virus started an epidemic process that emerged in Wuhan, China in the last days of 2019 and spread throughout the world in a very short time. The World Health Organization has accepted this virus as a very dangerous pandemic that has spread throughout the world. The Turkish state has taken many precautions to prevent the spread of the disease in this process. At the beginning of these; A curfew has been declared for those over 65 and under 20, and education and training at all levels has been suspended for a short period of three weeks.

In Turkey, the Ministry of National Education has included students at every school level within the scope of distance education through television channels and the Education Informatics Network (EBA) as of March 23, 2020. In this way, the courses held via EBA have been made available via the internet, TRT channel and television, and TV and internet-based distance education platforms have been actively used (MEB, 2020). In higher education, this process is left to universities. In terms of universities, the application method was generally carried out with software that provides an online environment. In this direction, some universities have provided online simultaneous education using their existing infrastructure. Some have carried out the distance education process through cloud systems with the service procurement method (YÖK, 2020).

In this period; Internet traffic has increased rapidly in universities using the existing infrastructure, and depending on this increase, network equipment such as servers hosting the services offered and routers and switches used to carry this traffic have to work uninterruptedly. In addition to the increase in data center usage scales, another issue that needs to be analyzed in depth is the reliability level and uninterrupted uptime of these data centers. A single outage event with a 90-minute outage can cost an average of more than half a million euros, including recovery costs, loss of end-user productivity and business interruption (Emerson Network, 2021). An ideal data center management policy should plan to reduce power consumption while maintaining a low failure rate. This planning; It can be provided by standards such as TIER and ISO22301, which show the level of competence and competence that the data center can survive and continue to serve in issues such as electricity, cooling, physical security, fire, building durability, network infrastructure, as well as in natural disasters, disasters and similar extraordinary situations. Upon the determination of the standards of data centers, the Uptime Institute and the International Organization for Standardization (ISO) have set forth various certification methods and standards. The Uptime Institute created the TIER certification standard and the ISO 22301 standard.

The purpose of the TIER system is to measure the availability and availability of data centers. There are 4 levels in the TIER certification method and the minimum required technical competencies and infrastructures are specified for each level value (Uptime Institute, 2022). In Tier certification, documents are given for design and operation. While the Tier design certificate is issued for the construction and design of the data center, the Tier operation certificate is a document for the operation of the data center. Upon submission of all the implementation stages and forms of the project to the Uptime Institute, the projects deemed appropriate are given certificates according to their levels. ISO22301 was standard; It is a

management system standard based on the risk approach for the creation, implementation, monitoring, review, continuity and improvement of business continuity (ISO, 2022; Arief et al., 2019.). ISO 22301 is the world's first international standard for the implementation and maintenance of security and flexibility and business continuity management systems requirements, when published in 2012, and effective business continuity plans, systems and processes, and updated in 2019 and implemented as ISO22301:2019 (TSE, 2022).

In this study, data center planning and business continuity practices at Süleyman Demirel University are given by presenting how the three-location redundant data center planning should be done according to ISO22301 and TIER standards.

1.1. Data Center

Data Centers house critical computing resources in controlled environments and under centralized management, enabling businesses to operate around the clock or according to their business needs. These computing resources are server computers; web and application servers, file and print servers, messaging servers, application software and the operating systems that run them, storage subsystems and network infrastructure, etc. systems (Arregoces and Portolani, 2004). The size of a data center can range from a small cabinet to a high-scale data center. The term high scale refers to a flexible and robust computer architecture capable of increasing computing capability across memory, network and storage resources. Regardless of size and name, all data centers perform one thing: to process and transmit information (Kambhampaty, 2022).

Data centers are designed in various sizes, criticality levels and capacities according to the field of activity in which they are used. The basic components of a data center are as follows:

- Sustainably cooled mechanical system
- Electricity distribution, uninterruptible power supplies and generator systems
- Fire extinguishing systems
- Cabin and cabling systems
- Data center infrastructure systems
- Data center monitoring and management systems
- Disaster recovery and business continuity

1.2. Business Continuity and Redundancy Standards

"Redundancy" provides greater reliability, but has a profound impact on initial investments and ongoing operating costs. This situation is more clearly expressed in the diagram below (Figure 1.3). According to the Tier certification standards of the Uptime Institute, data center redundancy and fault tolerances are determined by the following items.

- N: Basic requirement.
- N +1 redundancy: Having an additional unit, module, bus or system to the minimum requirement.
- N+2 redundancy: Two additional units, modules, paths or systems in addition to the minimum requirement.
- 2N redundancy: Two complete units, modules, paths or systems for everything needed for a base system
- 2(N+1) redundancy: Having two full (N+1) units, modules, paths or systems.

Based on the above, the following levels of TIER certifications are made regarding component redundancy for a data center:

- Tier I Data Center: Basic system
- Tier II Data Center: Redundant components
- Tier III Data Center: Simultaneous maintenance possible
- Tier IV Data Center: Fault Tolerant

In these standards, N+1; It covers the design and implementation of all components of a data center as redundant. Well; a backup of the cooling unit, a backup of the uninterruptible power supply, a backup of the generator, a backup of the electrical infrastructure. 2N redundancy; represents the creation of an exact backup of the existing structure at a different point. If it is 2N+1, it includes that all components are eaten for both points (Choorat and Noimanee, 2022).

In terms of uninterrupted business continuity, there is a Disaster Recovery Center (DRC) in a different location (in a different city) in order to achieve 100% uptime and to ensure that the services of N+1, 2N and 2N+1 data centers do not stop in extraordinary situations (flood, earthquake, etc.). is of great importance. Apart from these, certification and implementation are very important for business continuity. At this point, ISO22301 standards come to the fore. According to ISO22301;

- Asset inventory should be created
- Process inventory should be created
- Risk analysis should be created for assets and processes

- Plan and Process improvements
- Development of disaster recovery plan and process
- Preparation of crisis management plans
- Preparation of exercise management plans

These processes need to be established.

From the analyzes made based on the data in the standards mentioned above, the analysis of the impact of the interruption and/or disaster on the institution, the level of impact and probability are revealed. The final results of the risk assessment describe the sequence of relevant business processes. Taking measures according to these risks ensures that business continuity is kept at the highest level.

2. Redundant Data Center Planning

2.1. Planning Phase

When planning a data center, only the number of servers to be hosted in the data center should not be considered. First of all, general capacity planning should be done. In this context, the services to be hosted should be revealed and a growth plan of at least 10 years should be established. Accordingly, network devices, access and ease of cabling infrastructure, security and accessibility features, amount of heat and cooling system to be released depending on the devices to be housed, and general electrical load of all systems should be calculated (Yüzgeç and Günel, 2015).

While planning the physical server; All of the online systems and automation software offered by the institution should be examined separately as both database and application servers, and disk, ram and processor capacities should be considered depending on their growth capacities. Accordingly, appropriate virtualization infrastructure should be created for the services to be hosted. Table 1 lists the general services and servers used for one of our institutions. By examining this list, the number of physical servers, the number of virtualization servers and storage systems were determined. According to this; Virtualization infrastructure was created with 10 physical servers. For systems that are not included in virtualization, 10 physical servers were planned.

Table 1. Systems to be hosted and resources planned.

Virtual Servers	Ram and CPU Specification	Piece
Data Bases	128Gb Ram, 12 Core Processor	10
Web Servers	12Gb Ram, 4 Core Processor	15
Application Servers	128Gb Ram, 12 Core Processor	10
Otomation Servers	24Gb Ram, 8 Core Processor	10
Service Servers	8Gb Ram, 4 Core Processor	15
E-Mail Services	128Gb Ram, 16 Core Processor	4
Log Store Servers	64Gb Ram, 12 Core Processor	4
Other Servers	24Gb Ram, 4 Core Processor	20
Digital Surveillance (Camera) Recording Servers	32GB Ram 12 Core Processor	4
PACs Systems	64Gb Ram, 12 Core Processor	2

In the light of the data in Table 1, the energy loads of the physical servers were calculated. Data center energy use per server includes energy used by the servers themselves. However, the energy usage calculation of the data center includes the energy used by the servers as well as networking, storage, uninterruptible power supplies for energy redundancy, cooling system, lightings and auxiliary devices. In this context, the heat loads produced by the servers and network devices have been calculated according to their absorbed energy. In this context, a maximum load of 30 kW has been revealed. This load case is the base requirement value expressed as “N”. In order to create a Tier 3 level structure, N+1 level transactions are required. For N+1 redundancy, planning has been made in such a way that at least two uninterruptible power supplies will meet 30kW and two air conditioners with redundancy to meet this temperature. Redundant electrical infrastructure and electrical panel system should be built for this power requirement. Two proposed methods are used for this. The first is parallel connected structures and the second is in the form of two different source feeds in the form of A + B. In this study, A+B double source feeding is planned.

Storage planning varies according to the type of data to be stored. A data storage unit consisting entirely of flash and/or SSD disks should be preferred because the data belonging to application and database servers are processed quickly and are instantly changing data. For less data to be read and written, disk units with SAS and NL-SAS disk structures should be used. Considering today's data compression and deduplication technology, compression and deduplication features should be sought in data storage units. The data in the institution should be analyzed according to their types and the data storage unit should be planned.

Table 2. Selection of appropriate storage size and storage disk type for planned systems.

Virtual Servers	Data Classification	Storage Capacity	Disk Type
Data Bases	Instantly changing, fast, compressed, and singularized data	Total allocated space for all databases 50 TB	SSD / Flash
Web Servers	Instantly changing, fast, compressed, and singularized data	Total allocated space for all web servers 2 TB	SSD / Flash
Application Servers	Instantly changing, fast, compressed, and singularized data	Total allocated space for all application servers 10 TB	SSD / Flash
Automation Servers	Instantly changing, fast, compressed, and singularized data	Total allocated space for all automation servers 5 TB	SSD / Flash
Service Servers	Instantly changing, fast, compressed, and singularized data	Total allocated space for all service servers 1 TB	SSD / Flash
E-Mail Services	Instantly changing, fast, compressed, and singularized data	Total allocated space for all email services 40 TB	SSD / Flash
Log Store Servers	Instantly changing, slow, compressed and deduplicated data	Total allocated space for all log data 20TB	SAS / NLSAS
Other Servers	Instantly changing, fast, compressed, and singularized data	Total allocated space for all other servers 10TB	SSD / Flash
Digital Surveillance (Camera) Recording Servers	Instantly changing, slow, uncompressed, and non-deduplicated video and picture data	Total allocated space for all recordings 250TB	NLSAS
PACs Systems	Instantly changing, slow, uncompressed, and non-deduplicated video and picture data	Total allocated space for all PACs data 100TB	NLSAS

As seen in Table 2, SSD and Flash disks and SAS and NL-SAS disks should be divided into two separate data storage units and used in a separate structure (This structure may change depending on the support of the storage units). The basic requirement, referred to as “N” in this case, is two separate Flash and SAS/NLSAS disk units. In order to create a Tier 3 level structure, N+1 level transactions are required. For N+1 redundancy, one more disk unit should be planned.

It is very important to plan the network infrastructure in order for the server and data storage systems to transfer data to the users in a redundant and fast manner and to receive the data from the user. While making this planning, the number of users and clients should be considered. In addition, the device and network connection types used by the clients should be calculated. Although the number of staff and students varies for universities; Students generally use wireless connection with mobile devices, staff use both wired and wireless connections. Due to serving approximately 50,000 users; At least 10 Gbps network switching between servers, at least 40Gbps between backbones and edge welcome switches, and at least 10Gbps between edge welcome-side switches are planned. In addition to this planning, there should be another backup service other than ULAKNET infrastructure, which is the internet service provider of universities. This service provider should have separate and independent fiber optic lines from the existing infrastructure provider and should be activated without loss of time in case of an interruption in the existing lines.

All of the data in the data storage systems in active use are expressed as hot data and these data can change instantly. Such systems need to be backed up periodically. These hot data should be subject to backup planning according to the type and importance of the services provided.

Table 3. Selection of the appropriate backup plan for the planned systems.

Virtual Servers	Data Classification	Backup Plan
-----------------	---------------------	-------------

Data Bases	Instantly changing, fast, compressed, and singularized data	Every week full, daily incremental
Web Servers	Instantly changing, fast, compressed, and singularized data	Every week full, daily incremental
Application Servers	Instantly changing, fast, compressed, and singularized data	Every week full, daily incremental
Automation Servers	Instantly changing, fast, compressed, and singularized data	Every week full, daily incremental
Service Servers	Instantly changing, fast, compressed, and singularized data	Every week full, daily incremental
E-Mail Services	Instantly changing, fast, compressed, and singularized data	Every week full, daily incremental
Log Store Servers	Instantly changing, fast, compressed, and singularized data	Every week full, daily incremental
Other Servers	Instantly changing, slow, uncompressed, and non-deduplicated video and picture data	Every week full, daily incremental
Digital Surveillance (Camera) Recording Servers	Instantly changing, slow, uncompressed, and non-deduplicated video and picture data	Every week full, daily incremental

With the backup planning in Table 3, it is planned to keep the cold data in a separate storage unit by performing compression and deduplication. In this case, the basic requirement expressed as “N” is the backup unit where the cold data is kept. N+1 level is required to create a Tier 3 level structure, 2N+1 level is required for Tier 4 level to be formed. Backup units should be planned for N+1 and/or 2N+1 redundancy.

An indispensable part of data centers is instantaneous monitoring and security. At this point; All equipment of the data center, usage conditions, performances, temperature, electricity, etc. of the personnel responsible for the operation of the data center. must have a full view and management of the data. In this respect, a data center infrastructure management system (Data Center for Infrastructure Management – DCIM) should be established for data centers. Data center security is provided by adding cabinet lock mechanisms, door lock mechanisms and cameras to these systems. For fire safety, FM200 and/or Novec gas extinguishing systems should be applied. Such systems protect and extinguish all basic fire classes, are also safe, clean and insulating. For this reason, it is planned to use FM200 in data centers.

For universities with Research and Application Hospitals, the planning situation should be structured as 2N or 2N+1 instead of N+1. At this point, the data center structure is planned to be 2N+1. In addition, it is planned to establish a disaster recovery center in a different location (city). In the case of 2N+1, all N+1 plans mentioned above are planned to be configured in pairs to be 2N+1.

TIER standards were prioritized during the commissioning phase of this structure, the planning of which has been completed. Required availability times for systems valid for TIER Standards/levels are listed below.

- Tier 1 – Basic capacity, single supply for cooling and power supplies, no redundancy elements are expected. The estimated annual working time is stated as approximately 99.671%.
- Tier 2 – Redundant system provides for one-way supply for cooling, power supplies, and redundant and redundant components. The estimated annual working time is stated as approximately 99.741%.
- Tier 3 – Simultaneously serviceable system, Predicts Multiple cooling, power and redundancy systems. The estimated annual working time is stated as approximately 99.982%.

- Tier 4 – Physically isolated redundant systems include redundant and fault-tolerant data centers for each component. The estimated annual working time is stated as approximately 99.995%.

2.1.1. Tier 1

In order to meet this standard, it is considered sufficient to have electrical systems and cooling systems in the data center. It is not expected that the systems in the data center will have any redundancy. In other words, we can say that there are N devices in a single line. Figure 1 illustrates this situation on a drawing. It has been studied for a system with 3 cabinets in the drawing. The explanations on Tier2, Tier3, Tier4 will be continued by superimposing this drawing. The estimated annual working time is stated as approximately 99.671%.

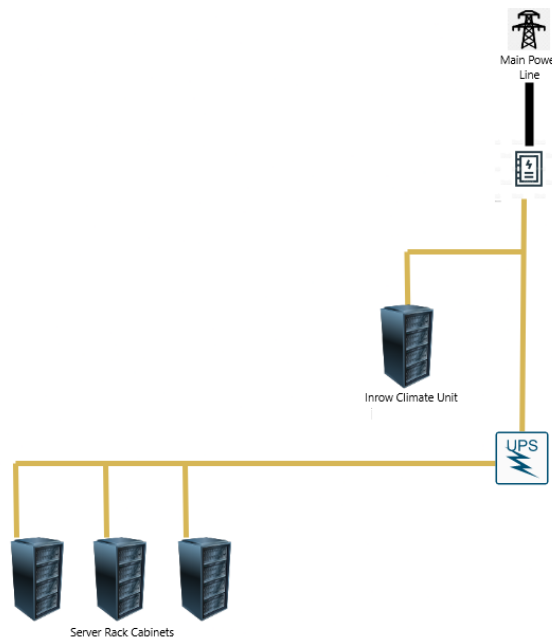


Figure 1. Tier 1 Server Room Requirement Diagram

2.1.2. Tier 2

In order to ensure this standard, redundancy (N+1) of devices with important tasks such as electrical systems and cooling systems in the data center is essential. These units include generator, UPS, cooling systems, etc. can be included. As shown in Figure 2, the incoming power line is supported by a generator and uninterruptible power supplies are backed up. At the same time, redundancy of cooling units is provided. The most important detail in this regard is that each unit is fed from 2 different sources. The estimated annual working time is stated as approximately 99.741%.

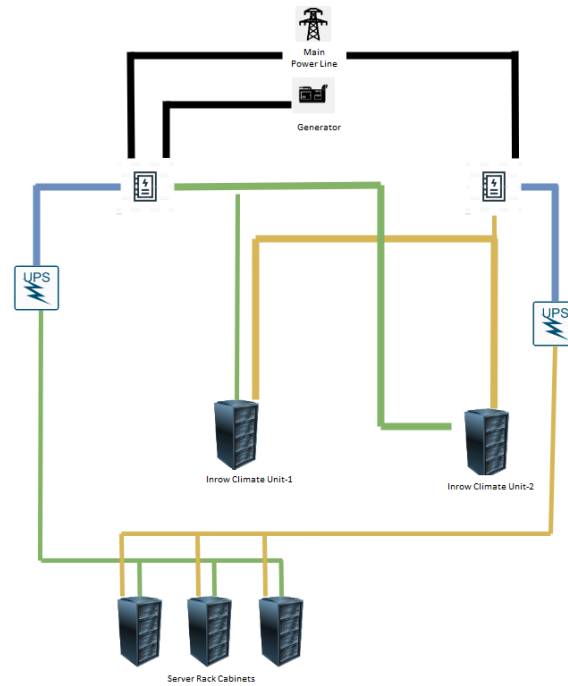


Figure 2. Tier 2 Server Room Requirement Diagram

2.1.3. Tier 3

In order to ensure this standard, it has come to the fore that it can be maintained simultaneously (it will not cause a functional interruption during the necessary maintenance or replacement), as well as the redundancy at the points that have undertaken important tasks such as electrical systems and cooling systems in the data center. In Figure 3, this situation is explained for a single data center with an example drawing. The estimated annual working time is stated as approximately 99.982%.

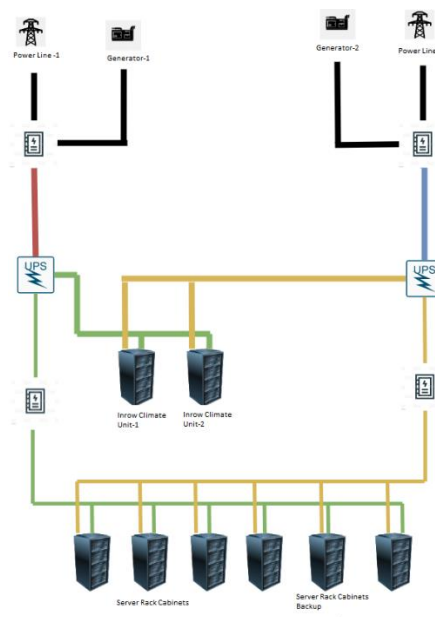


Figure 3. Tier 3 Server Room Requirement Diagram

2.1.4. Tier 4

In order to ensure this standard, in addition to the redundancy at the points that have undertaken important tasks such as electrical systems and cooling systems in the data center, in case of a data center-wide error, the systems do not stop even outside the control of the person (in case of a complete failure at this level while awaited controlled maintenance in Tier 3) is expected. According to Tier standards, we can express this situation as $2N+1$. In Figure 4, this situation is simply explained for a system room. The estimated annual working time is stated as approximately 99.995%.

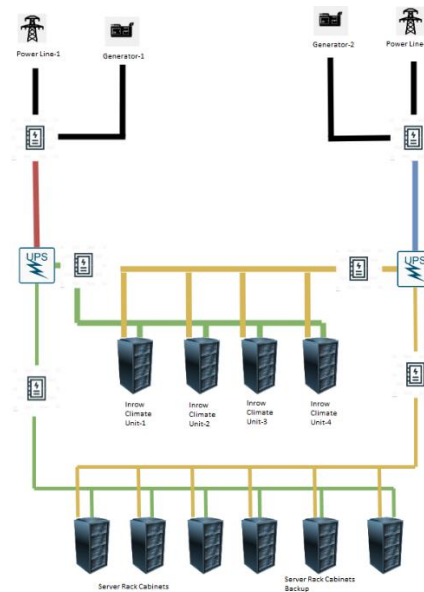


Figure 4. Tier 4 Server Room Requirement Diagram

2.2. Implementation

As stated when planning the data centers of our university, Tier and ISO 22301 standards have been taken into consideration. In order to create a Tier4 $2N+1$ structure, 2 separate areas were selected within the campus and it was planned to provide a $2N$ structure first. In addition to this plan, $N+1$ structuring was also applied for each point and a $2N+1$ arrangement was made. Within the scope of this Plan, two separate data centers in the East and West campuses of Süleyman Demirel University were established with $N+1$ redundancy. 96 core single mode fiber cables were applied between data centers. The third location, the FKM application in a different city, was completed and the structure shown in Figure 5 was created.

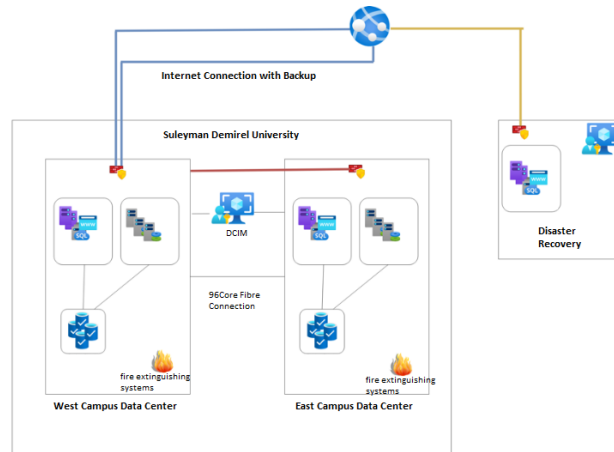


Figure 5. S.D.U. Data Centers

2.2.1. West Campus Data Center

The western data center is considered as two parts, the electrical room and the network-system room, during the architectural planning phase. The high-risk electrical room is isolated from the data center while creating the architectural plan. Cold corridor structure is preferred for the data center. In this structure, instead of raising the base, cabling etc. For the passage of the elements, galvanized panning and cabling are made on the cabinet. The data center layout and drawing are presented in Figure 3.2.1. Copper and fiber cabling is placed as two separate passive cabins, which are kept out of the cold aisle using the mirroring method. Network and cabling operations are separated by creating a NOC (Network Operations Center) structure. Thus, passing into the cold corridor where the systems are located for network works was prevented and both system security was ensured and energy efficiency was achieved by protecting the corridor air circulation. By using card reader lock mechanisms on each of the network cabinets in the NOC environment, the persons who will have access to the network cabinets are separated and authorization definitions are made. The entrance to the corridor, where the systems are located, is also isolated with an automatic door with a card reader, allowing authorized persons to access the card reader here. In addition to these, other processes carried out both in the data center and in the electrical room are explained below.

Table 4. Sensor distribution used in data centers and electrical room

Sensor Type	Location	Piece	Data Center
Wired humidity-temperature sensor	Each cabin was used both at the front and at the back.	26	East/West Data Center and Electrical Room
Wireless temperature sensor	It was used in the room for ambient temperature.	3	East/West Data Center
Liquid Sensor	Used on room floors for liquid contact.	4	East/West Data Center and Electrical Room
Motion sensor	For monitoring the movements in the room and for the cold corridor lighting system.	2	East/West Data Center
IP Cameras	It has been used for monitoring data centers.	8	East/West Data Center and Electrical Room
Door Sensor	Both front and rear doors of each cabin were used in the room entrance doors.	28	East/West Data Center and Electrical Room
Pressure and Airflow Sensor	It is used to measure the air flow and pressure in the cold aisle.	1	West Data Center
Earthquake sensor	For automatic opening of doors and lock systems in case of an earthquake.	2	East/West Data Center
Smoke and Flame Sensors	It is used for fire detection.	11	East/West Data Center and Electrical Room
Vibration Sensor	It is used to detect the situations that may occur due to the vibrations of the air conditioning system.	1	East Data Center
Electrical-Monitoring Analyzers	Each feed is used to monitor the inlet and outlet lines.	8	East Data Center and Electrical Room

Special fire-resistant paints with TS EN 13381-8:2013 certificate were used on the walls of both rooms, and doors with EL120 certificate and 120 minutes fire resistance in accordance with TSE - CE - EN standards were used at the entrances of both rooms.

- FE180 fire resistant cable in accordance with IEC 60331-21/23/25 standards is used in all of the ceiling-top open area wiring of both rooms.

- Lighting, power, sensor, etc. in both rooms. All of the wiring (fire resistant cables) is taken under protection by passing through galvanized pipes.

- Lighting and switching systems; Surface mounted, fire and explosion resistant (exproof) material is preferred in accordance with IP65 standards.

- FM200 fire extinguishing system is integrated with fire detection automation within the data center management. With this integration, air conditioning systems are turned off during a fire and FM200 gas filling is provided by opening the covering ceilings of the cold corridor. In addition to the sensors of the FM200 system, the fire conditions can also be monitored with the sensors on the DCIM system and communication is provided with the FM200 fire control panel. FM200 and DCIM applications were made in the electrical room.

- With 94 sensors on the DCIM system, both east and west data centers and the electrical room are monitored comprehensively from a single point. The sensors used and their places of use are given in Table 4.

With the rules created on the DCIM system, each change in the data centers is communicated to the relevant personnel. This system not only provides monitoring but also automation management. Air conditioning systems are managed through the DCIM system.

Intelligent precision air conditioning systems are used in N+1 construction. Ambient cooling is done by using the data obtained from the temperature and humidity sensors located on the front and rear doors of each cabin. In the same way, N+1 air conditioning was applied in the electrical room. Cooling systems are fed by uninterruptible power supplies separate from server systems.

A front reception room was created before the data center entrance. In this room, the person who will enter the data center is purified and prepared and taken inside. At the same time, both the earthquake sensor and the control panel and tube of the FM200 fire extinguishing system are in this room.

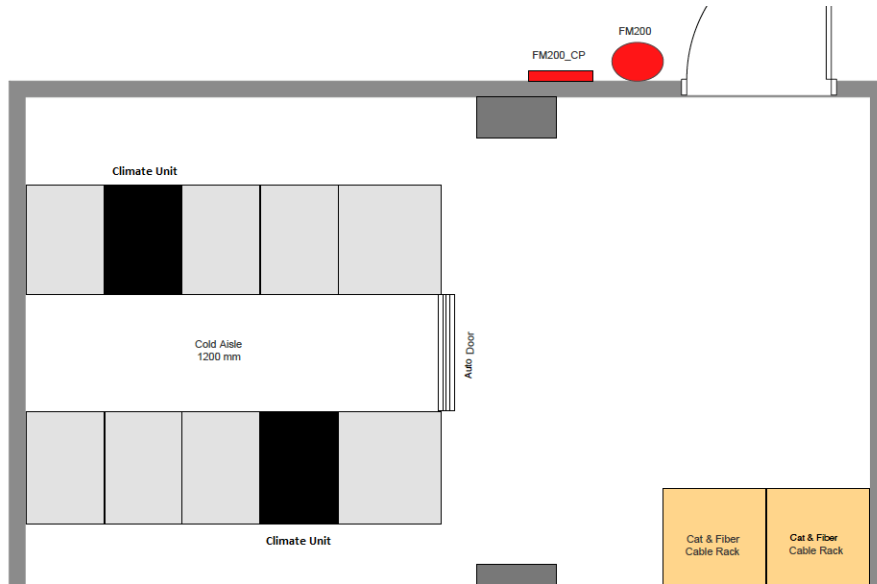


Figure 6. West Campus Data Center Layout Plan



Figure 7. West Campus Data Center

The western data center power distribution is shown schematically in Figure 8. Electricity distribution room planning has been made in order to ensure energy uninterruptedness in the data center. Apart from the generator feeding the building, the positioning of the generator feeding the data center and the two uninterruptible power supplies in the A+B configuration

feeding the system cabinets and a redundant energy line are provided to the double power sourced devices in the cabins. Air conditioning systems are also fed by separate uninterruptible power supplies. There are separate lines from two places to the common busbar of the distribution panel in the electrical room. One of these lines is the line coming from the transformer main panel (the line with the campus common generator), and the other is the line coming from the generator panel of the building. Since these two lines feed the same busbar, they will be controlled by a transfer switch. The priority is the line coming out of the main distribution panel, it is planned to feed the system from the generator of the building in case of a problem on this line. A line taken from this common busbar enters 4 uninterruptible power supplies. The lines coming out of the uninterruptible power supplies are connected to another distribution busbar in the A and B distribution boards. The lines taken from these A and B busbars feed the air conditioners, system and network cabinets. In addition, the lines coming from the A and B busbars are combined with the 40A automatic transfer switch, feeding the card access system, DCIM system, fire detection and extinguishing systems, data center lighting systems.

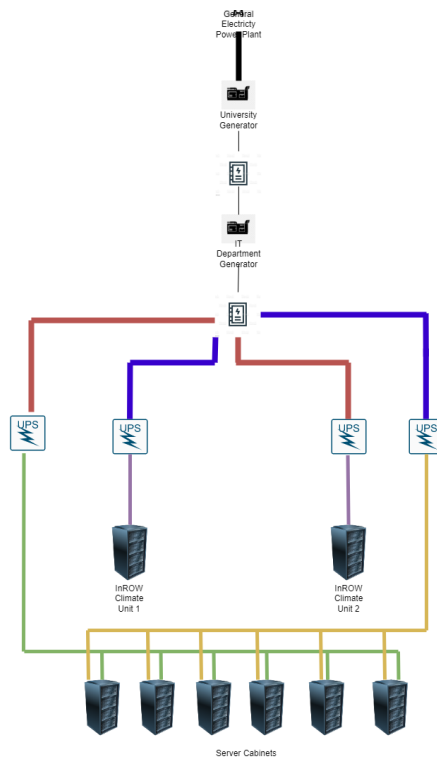


Figure 8. West Campus Data Center Energy Distribution

2.2.2. East Campus Data Center

The eastern data center was planned as a single-storey, single-architectural structure independent of the existing buildings on the campus during the architectural planning phase. For the eastern data center, underfloor cooling structure was preferred. In this structure, a 50 cm high floor was raised and cabling etc. Underfloor galvanized panning and cabling were applied for the passage of the elements. The data center layout and drawing are presented in Figure 9.

Copper and fiber cabling is placed as a passive separate network cabinet using the mirroring method. In addition to these, other processes performed in the data center are explained below.

Fire and moisture resistant special plasterboard in accordance with TS EN 520-A1 standards was used on the walls of the room, and doors with EL120 certificate and 120 minutes fire resistance in accordance with TSE - CE - EN standards were used at the entrance of the room.

In all of the cabling used in the room, FE180 fire resistant cable is used in accordance with IEC 60331-21/23/25 standards.

Lighting, power, sensor etc. inside the room. All of the wiring (fire resistant cables) is taken under protection by passing through galvanized pipes.

Lighting and switching systems; Surface mounted, fire and explosion resistant (exproof) material is preferred in accordance with IP65 standards.

The FM200 fire extinguishing system is integrated with the fire detection automation within the data center management. With this integration, air conditioning systems are turned off during a fire and FM200 gas is filled inside. In addition to the sensors of the FM200 system, the fire conditions can also be monitored with the sensors on the DCIM system and communication is provided with the FM200 fire control panel.

The eastern data center is also located on the common DCIM system.

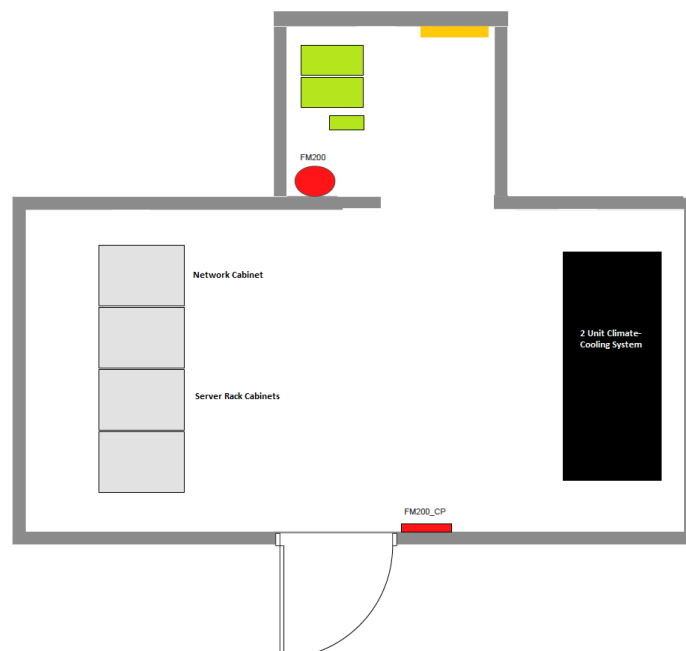


Figure 9. East Campus Data Center Layout Plan

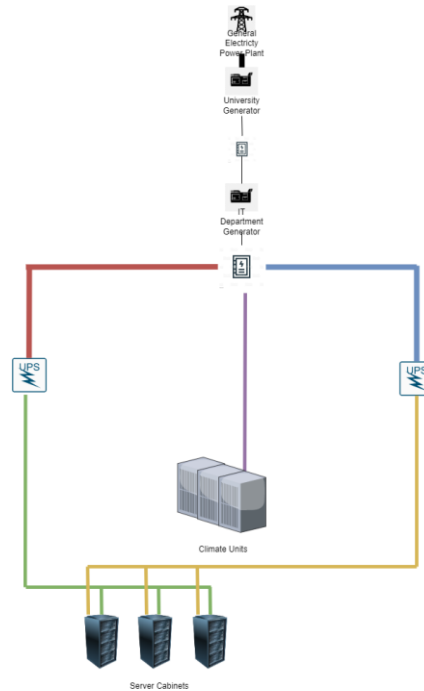


Figure 10. East Campus Data Center energy distribution

The eastern data center energy distribution is shown schematically in Figure 10. Electricity distribution planning was made in order to ensure energy uninterruptedness in the data center. Apart from the generator feeding the building, the positioning of the generator feeding the data center and the two uninterruptible power supplies in the A+B configuration feeding the system cabinets and a redundant energy line are provided to the double power sourced devices in the cabins. Air conditioning systems are fed depending on the generator line. Separate lines are coming from two places to the common busbar of the electricity distribution panel. One of these lines is the line coming from the transformer main panel (the line with the campus common generator), and the other is the line coming from the generator panel of the building. Since these two lines feed the same busbar, they will be controlled by a transfer switch. The priority is the line coming out of the main distribution panel, it is planned to feed the system from the generator of the building in case of a problem on this line. The lines taken from this common busbar enter 2 uninterruptible power supplies. The lines coming out of the uninterruptible power supplies are connected to another distribution busbar in the A and B distribution boards. The lines taken from these A and B busbars feed the system and network cabinets. In addition to A and B uninterruptible power supplies, a third redundant uninterruptible power supply is in the cabinet by using an automatic transfer switch; DCIM system feeds fire detection and extinguishing systems, data center lighting systems.

2.2.3. Disaster Recovery Center

Disaster recovery center (FKM) plays a vital role in restoring the organization's data and providing emergency services from this data center in the event of emergency and dangerous accidents, disasters and large-scale disasters. FKM installation is mandatory for large-scale data centers in public institutions and organizations. Since FKMs come to the fore in large-scale disasters and disasters, they should be installed in a different location than existing data centers,

or even in a different city. Within the scope of the study, Süleyman Demirel University FKM is kept in a data center with Tier 3 certificate in a different city. While our data centers located in the eastern and western campuses of our university work with instant data transfer in an active-passive structure, data is sent from the center to FKM via the tunnel network structure (side to side vpn). A "multi-purpose" backup structure is used, which allows the data in the eastern and western data centers to be restored to multiple sites with multiple methods, with the aim of recovering nearly 90% of the data. All data centers belonging to our university; It is within the scope of large-scale data systems, and transfers are made between data centers with software with special algorithms so that all data can be recovered and restored without a long downtime and complex recovery processes. For an emergency, the FKM scenario is practiced within the scope of ISO quality processes.

3. Results and Discussion

In this study, information about the digital transformation process and business continuity in the informatics infrastructure, which has become prominent in the world and in our country in recent years with the Covid-19 pandemic, the issues to be considered in the planning of data centers, the criteria and certificates related to this subject, will be presented at the end of the study. In this section, the example of Süleyman Demirel University redundant data center design and implementation is presented in general terms. The business continuity situation mentioned in the planning phase of the data centers has been tested with the scenarios for the transfer of data between the data centers and the creation of active-passive redundancy, failure and maintenance situations and the operation of the backup systems, and as a result, the adequacy of the redundant infrastructure necessary to ensure business continuity has been placed. With the advantages of having redundant data centers and FKM in different cities,

- Data centers are not affected by their long-term maintenance that concerns the entire university,
- Isolating data centers from failures caused by other buildings due to the location of data centers in different campuses within the university and separately and independently from existing campus buildings,
- Minimizing the uninterruptedness and downtime by feeding the system by the other uninterruptible power supply in case of a failure in any of them due to the A+B redundancy of the uninterruptible power supplies and electrical infrastructure,
- Earthquake, flood etc. Ensuring business continuity and not losing contact with the outside world, as FKM is located in a different city as an emergency action plan in major disasters,
- Providing instant (25 sec) active-passive mirroring and daily cold data backup, apart from backup only as daily cold data, and returning from backup in case of emergency, business continuity by getting up and running passive systems in the backup data center within minutes, provided.

Ethics in Publishing

There are no ethical issues regarding the publication of this study.

Author Contributions

Authors declare no contributions.

References

- [1] Arief, R., & Putra, Y. H. (2020, January). Design Business Continuity Plan of Data Center Using ISO 22301: 2012. In International Conference on Business, Economic, Social Science, and Humanities–Economics, Business and Management Track (ICOBEST-EBM 2019) (pp. 45-47). Atlantis Press.
- [2] Arregoces, M., & Portolani, M. (2003). Data center fundamentals. Chapter 1:Overview of Data Centers(pp. 5-7). Cisco Press.
- [3] Choorat, P., & Noimanee, S. (2022, March). Design of Cooling System of Tier 3 Standard for Rack Enclosure in the Containerized Data Centers. In 2022 International Electrical Engineering Congress (iEECON) (pp. 1-5). IEEE.
- [4] Power, E. N. (2011). Understanding the cost of data center downtime: an analysis of the financial impact on infrastructure vulnerability. white paper.
- [5] Hwaiyu Geng, P. (2015). Chapter 2: Data Centers—Strategic Planning, Design, Construction, and Operations (pp. 3-14). Data Center Handbook.
- [6] <https://www.iso.org/standard/75106.html>, Eriřim Tarihi: 17.03.2022
- [7] Kambhampaty S., (2022). Infrastructure Architecture Essentials for Data Center and Cloud. Chapter 1:Data Center(3-6). Independently published.
- [8] <https://www.meb.gov.tr/bakan-selcuk-koronaviruse-karsi-egitimalaninda-alinan-tedbirleri-acikladi/haber/20497/tr>, Eriřim Tarihi: 18.03.2022
- [9] <https://www.tse.org.tr/IcerikDetay?ID=2044&ParentID=1064>, Eriřim Tarihi: 19.03.2022
- [10] <https://uptimeinstitute.com/tiers>, Eriřim Tarihi: 17.03.2022
- [11]<https://www.yok.gov.tr/Sayfalar/Haberler/2020/universitelerde-uygulanacak-uzaktan-egitime-iliskin-aciklama.aspx>, Eriřim Tarihi: 18.03.2022
- [12] Yüzgeç, U., & Günel, A. (2015). Üniversitelere Yönelik Bir Veri Merkezinin Enerji Planlaması. Bilecik Şeyh Edebali Üniversitesi Fen Bilimleri Dergisi, 2(2), 17-24.

Evaluation of Anticancer and Antimicrobial Potentials of *Tarantula cubensis* Venom (Theranekron® D6)

Nazan GÖKŞEN TOSUN ¹ Özlem KAPLAN ^{2*} Aykut ÖZGÜR ³

¹Tokat Gaziosmanpaşa University, Tokat Vocational School of Health Services, Department of Medical Services and Techniques, Tokat, Turkey

²Alanya Alaaddin Keykubat University, Rafet Kayış Faculty of Engineering, Department of Genetics and Bioengineering, Antalya, Turkey

³Tokat Gaziosmanpaşa University, Artova Vocational School, Department of Veterinary Medicine, Laboratory and Veterinary Health Program, Tokat, Turkey

Received: 02/04/2024, Revised: 14/08/2024, Accepted: 12/09/2024, Published: 31/08/2024

Abstract

Tarantula cubensis venom (Theranekron®D6) is widely used in veterinary medicine as a drug with anti-tumor, wound healing, anti-inflammatory, antiphlogistic properties. The purpose of the study was to explore Theranekron®D6 (TD6)'s antibacterial activity and its impact on apoptotic cell death in human colon and liver cancer cell lines. TD6 showed a dose and time dependent cytotoxic effect at 12h and 24h in HT-29 and HUH-7 cancer cell lines. The IC₅₀ values of TD6 were calculated as 12.18 µg/mL and 25.10 µg/mL in HT-29 and HUH-7 cell lines at 24h, respectively. TD6 induced apoptosis in HT-29 and HUH-7 cell lines. In these cells exposed to TD6, while the *BAX/BCL-2* ratio and *CASP-3* mRNA level increased, the *HSP90* mRNA and protein level decreased. Also, TD6 exhibited antimicrobial activities against *Pseudomonas aeruginosa*, *Enterococcus faecalis*, *Klebsiella pneumonia*, *Staphylococcus aureus*, *Candida albicans* and *Candida utilis*. Obtained results demonstrated that TD6 has great potentials as alternative therapeutic for cancer and infectious diseases as apoptosis inducer and antimicrobial agent.

Keywords: Cancer, *Tarantula cubensis*, Apoptosis, Antibacterial, Antifungal

Tarantula cubensis Venomunun (Theranekron® D6) Antikanser ve Antimikrobiyal Potansiyellerinin Değerlendirilmesi

Öz

Tarantula cubensis venomu (Theranekron®D6), veteriner tıbbında anti-tümör, yara iyileştirme, anti-enflamatuar, antiflogistik özelliklere sahip bir ilaç olarak geniş bir şekilde kullanılmaktadır. Bu çalışmada, Theranekron®D6 (TD6)'nın antibakteriyel aktivitesi ve insan kolon ve karaciğer kanser hücre hatlarında apoptotik hücre ölümü üzerine etkisini araştırıldı. TD6, HT-29 ve HUH-7 kanser hücre hatlarında 12 saat ve 24 saatte doz ve zaman bağımlı sitotoksik etki gösterdi. TD6'nın HT-29 ve HUH-7 hücre hatlarında 24 saatte hesaplanan IC₅₀ değerleri sırasıyla 12.18 µg/mL ve 25.10 µg/mL olarak bulundu. TD6, HT-29 ve HUH-7 hücre hatlarında apoptozu indükledi. TD6'ya maruz kalan bu hücrelerde, *BAX/BCL-2* oranı ve *CASP-3* mRNA seviyesi artarken, *HSP90* mRNA ve protein seviyesi azaldı. Ayrıca, TD6, *Pseudomonas aeruginosa*, *Enterococcus faecalis*, *Klebsiella pneumonia*, *Staphylococcus aureus*, *Candida albicans* ve *Candida utilis*'e karşı antimikrobiyal aktiviteler sergiledi. Elde edilen sonuçlar, TD6'nın kanser ve enfeksiyon hastalıkları için alternatif bir terapötik olarak büyük potansiyele sahip olduğunu, apoptoz indükleyici ve antimikrobiyal ajan olarak işlev gördüğünü gösterdi.

Anahtar Kelimeler: Kanser, *Tarantula cubensis*, Apoptoz, Antibakteriyel, Antifungal

*Corresponding Author: ozlem.kaplan@alanya.edu.tr

Nazan GÖKŞEN TOSUN, <https://orcid.org/0000-0001-5269-1067>

Özlem KAPLAN, <https://orcid.org/0000-0002-3052-4556>

Aykut ÖZGÜR, <https://orcid.org/0000-0002-4457-1249>

1. Introduction

Natural toxins are important pharmacological resources in the discovery of therapeutic biomolecules. Natural venoms derived from some animals such as snakes, scorpions and spiders have therapeutic potential against many diseases. Spider venoms are a complex mixture of nucleic acids, free amino acids, low molecular weight organic compounds, polypeptides, proteins, neurotoxins, and inorganic salts [1-4]. The biological activity of spider venom is quite impressive. Spider venom has been reported to exhibit potential therapeutic activity against a wide variety of human diseases such as microbial infections, cancer, malaria, and arrhythmia [3, 5, 6].

Tarantula cubensis is a large arachnid from the Theraphosidae spider family. Theranekron® D6 (TD6) is a product made from an alcoholic extract of the entire *tarantula cubensis*. It is a homeopathic drug commonly used in veterinary medicine. TD6 is effectively used in clinical veterinary in the treatment of foot and mouth lesions, pododermatitis, cutaneous papillomatosis and endometritis [7, 8]. A wide range of therapeutic effects of TD6 have been demonstrated in several clinical studies. It has been found to be effective in inhibiting the growth of canine tumors, uterine invasion in cattle, treating genital microbial diseases and oral lesions. According to these studies, TD6 shows antitumor, wound healing, anti-inflammatory, antiphlogistic and necrotizing effects. Additionally, some reports have implied that TD6 has antimicrobial activity [9-18]. Although the antitumor effects of TD6 have been investigated in clinical veterinary medicine, more research is needed to reveal the antitumor action mechanism of TD6.

In this study, anticancer activity of TD6 was investigated in liver (HUH-7) and colon (HT-29) cancer cell lines. The gene expression level of *BAX*, *BCL-2*, *CASP-3* and *HSP90* in cancer cell lines exposed to TD6 was evaluated. *HSP90* protein level in these cells was determined using the ELISA kit. Also, antibacterial and antifungal activities of the TD6 were examined against *Enterococcus faecalis*, *Pseudomonas aeruginosa*, *Staphylococcus aureus*, *Klebsiella pneumonia*, *Candida albicans* and *Candida utilis*. Obtained results demonstrated that TD6 is a potent natural therapeutic in treatment of infectious diseases and cancer.

2. Material and Methods

2.1. Materials

TD6 was supplied from Richter Pharma AG (Wels, Austria). Dulbecco's Modified Eagle's medium (DMEM), Heat-inactivated fetal bovine serum (FBS), penicillin-streptomycin solution, RPMI-1640 medium, trypsin-EDTA, L-glutamine, phosphate buffer saline (PBS), and XTT cell proliferation kit were from Biological Industries. cDNA synthesis kit and SYBR Green master mix was obtained from Bioline. Total RNA isolation was from Favorgen Biotech Corp.. *BCL-2* (PPH00079B), *BAX* (PPH00078B) and *GAPDH* (PPH00150F), *HSP90* (PPH63391B) primers were purchased from Qiagen (Primer Assays; Qiagen, Valencia, CA, USA). *CASP-3* primer was synthesized by Macrogen (forward: 5'-ACATGGAAGCGAATCAATGGACTC-3', reverse: 5'-

AAGGACTCAAATTCTGTTGCCACC-3’). *HSP90* ELISA Kit were purchased from Biont Shangai YL Biotech Co., Ltd. Bacterial strains (*P. aeruginosa* ATCC 27853, *E. faecalis* ATCC 29212, *K. pneumoniae* ATCC 15380, *S. aureus* ATCC 25923), fungal strains (*C. utilis* ATCC 9950, *C. albicans* ATCC 90819), and cancer cell lines (HUH-7 from the Japanese Collection of Research Bioresources (JCRB), HT-29 from the American Type Culture Collection (ATCC)) were obtained from Tokat Gaziosmanpasa University, Department of Bioengineering and Genetics, Turkey."

2.2. XTT Assay

HT-29 cells were cultured in RPMI-1640 medium, while HUH-7 cells were cultured in DMEM high glucose medium. Both cultures were supplemented with 10% fetal bovine serum, 1% L-glutamine, 100 IU/mL penicillin, and 10 mg/mL streptomycin. The cells were cultured under standard conditions at 37 °C in a humidified atmosphere containing 95% air and 5% CO₂. Colorimetric XTT cell proliferation kit was used to analyze the effects of TD6 on cell proliferation. The cells were seeded into 96-well plates at a density of 5×10⁴ cells/mL. After 24 h, the cells were exposed to TD6 at concentrations ranging from 500 µg/mL to 3.9 µg/mL for 24 h. After the exposure period, 50 µL of the XTT reagent was added to each well and incubated for an additional 4 hours. Absorbance was then measured at 450 nm, and cell viability was expressed as a percentage relative to the untreated control group. IC₅₀ values of TD6 were calculated with GraphPad Prism 8.0 software [17].

2.3. Gene Expression Analysis

Expression levels of *HSP90*, *BCL-2*, *BAX* and *CASP-3* genes in cells exposed to TD6 were determined using RT-PCR (Biorad CFX96™). Firstly, IC₅₀ doses of TD6 were applied to HT-29 and HUH-7 cells for 24 hours. Then, the cells were trypsinized and total RNA was isolated from the cells. cDNA synthesis from total RNAs was performed according to the commercial kit protocol. The amplification process was conducted under the following conditions: 1 cycle at 95°C for 10 minutes, followed by 45 cycles at 95°C for 15 seconds and 60°C for 1 minute. The data of RT-PCR were analyzed using the 2^{-ΔΔCt} method and normalization of expression of genes was performed with *GAPDH* [19].

2.4. *HSP90* ELISA Assay

The alteration of *HSP90* protein level under IC₅₀ doses of TD6 were measured in HT-29 and HUH-7 cell line by human ELISA kit following the manufacturer's instructions. The change in the *HSP90* protein level was calculated as a percentage relative to the control.

2.5. Antibacterial and Antifungal Activity Assays

Using the minimum inhibitory concentration (MIC) test, the antibacterial and antifungal properties of TD6 were assessed against *P. aeruginosa*, *E. faecalis*, *K. pneumoniae*, *S. aureus*, *C. utilis*, and *C. albicans*. For this experiment, a 96-well plate was filled with 100 µL of the

nutritional soup in each well and TD6 was applied with two-fold dilutions from 500 $\mu\text{g/mL}$ to 3.9 $\mu\text{g/mL}$. Then, the bacterial and fungal strains (1×10^8 CFU/mL) were added in nutrient broth and incubated overnight at 37°C. A microplate reader was used to detect absorbance at 600 nm at the conclusion of the incubation period and the percent inhibition was calculated compared to control group [20].

2.6. Statistical Analysis

Statistical analysis was conducted using GraphPad Prism 8.0 software, employing two-way ANOVA with Dunnett's and Sidak tests. A significance level of $p < 0.05$ was used to determine statistical significance ($**** < 0.0001$).

3. Results and Discussion

3.1. XTT Assay

The XTT assay was applied to investigate the *in vitro* cytotoxic effect of TD6 on colon and liver cancer. The change in % cell viability of cells exposed to TD6 at different concentrations for 12h and 24h is shown in Figure 1. TD6 exhibited cytotoxic effect on HT-29 and HUH-7 cells in a time and dose dependent manner. IC_{50} values determined from % cell viability data of cells exposed to TD6 are given in Table 1. TD6 showed lower doses of cytotoxic effect in HUH-7 cells than HT-29 at 24h.

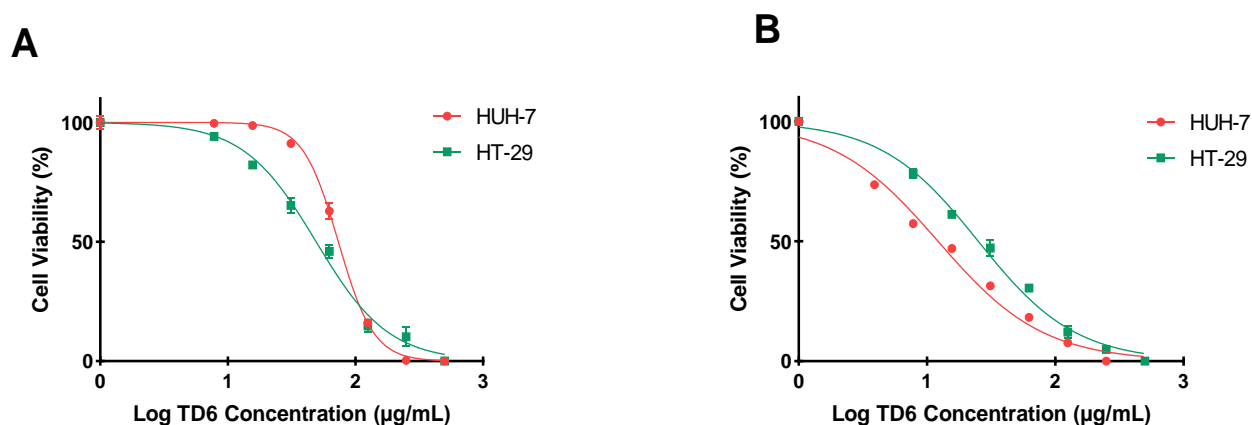


Figure 1 Cell viability of cancer cell lines exposed to TD6 in 12h (A) and 24h (B)

Table 1 IC₅₀ values of TD6 on HT-29 and HUH-7 cancer cell lines

Cell Lines	IC ₅₀ (µg/ml)	
	12 h	24 h
HUH-7	74.47 ± 1.61	12.18 ± 4.23
HT-29	49.23 ± 3.94	25.10 ± 3.05

Colorectal cancer is an important type of cancer and approximately half of colorectal cancer patients die within 5 years [21]. The liver is the most common metastatic site for patients with colorectal cancer, and at least 25%-50% of patients develop colorectal liver metastasis [22]. Resistance to drugs and increase in relapse rate are an important problem in cancer treatment. Therefore, the need to discover new therapeutics in cancer is increasing day by day [23]. The use of natural anticancer agents is seen as powerful resources for overcoming cancer and getting promising results [24]. Poisonous animals play an important role in discovering new therapeutic candidates. Various poisons have been shown to inhibit the proliferation of cancer cells and promote cell death by decreasing or increasing protein expression in inducing apoptosis [25-27]. TD6, which is the venom of *Tarantula cubensis*, is a drug with known anticancer properties in veterinary medicine. In this study, *in vitro* antitumor effect of TD6 on human colon and liver cancer cells was investigated. TD6 caused a dramatic decrease in the viability of colon and liver cancer cells in a time and dose dependent manner.

3.2. Gene Expression Analysis

In order to investigate the apoptotic effects of TD6 on cancer cells, the expression of apoptotic genes was investigated by RT-PCR. Figure 2 shows the change in *BAX/BCL-2*, *CASP-3* and *HSP90* mRNA levels of HUH-7 and HT-29 cells exposed to TD6 for 24 hours.

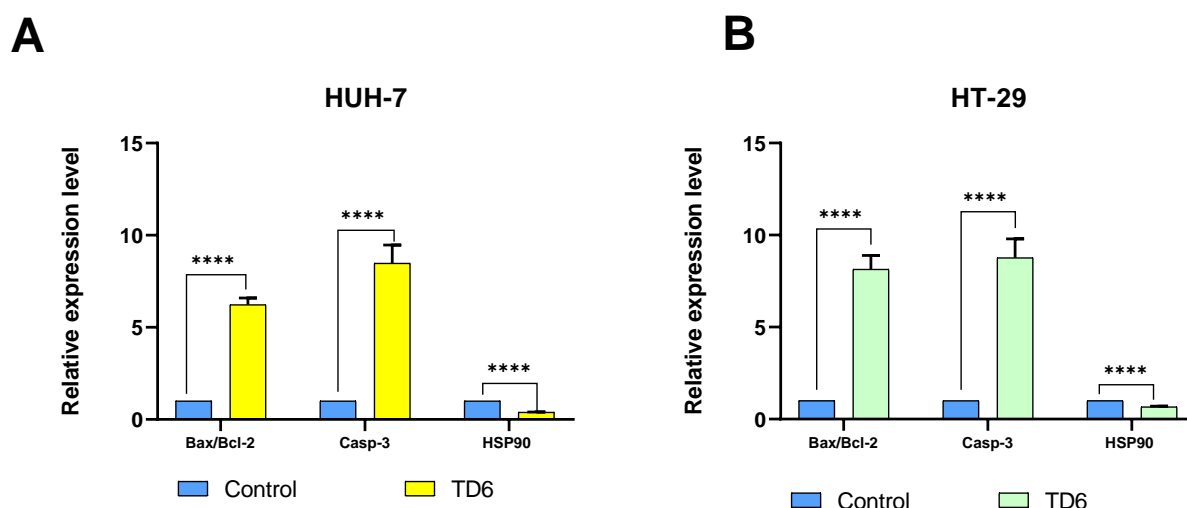


Figure 2 Illustrates the effect of TD6 on the mRNA levels of *HSP90* and apoptotic genes (*BAX/BCL-2*, *CASP-3*) in HT-29 and HUH-7 cell lines.

3.3. *HSP90* ELISA Assay

HSP90 protein level was investigated using *HSP90* ELISA kit in HT-29 and HUH-7 cells exposed to TD6. *HSP90* protein level decreased in TD6 treated HT-29 and HUH-7 cells (**Figure 3**). The decrease in *HSP90* protein level correlated with the decrease in mRNA level.

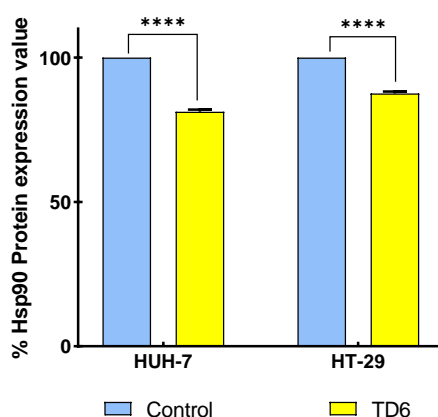


Figure 3 The effect of TD6 on *HSP90* protein level in HT-29 and HUH-7 cell lines

While *BAX/BCL-2* ratio and *CASP-3* mRNA level increased in cells exposed to TD6, *HSP90* mRNA and protein level decreased. *HSP90* plays a role in the metastasis, invasion, vascularization, and proliferation of tumors. In addition, it contributes greatly to the maintenance of oncoproteins, which are involved in the signal transduction pathway of apoptosis [28, 29]. *HSP90* has been found to be overexpressed in hepatocellular carcinoma [30]. In colorectal cancer, the high level of *HSP90* expression causes more aggressive phenotypes of

the tumor [31]. Therefore, *HSP90* represents an attractive therapeutic target for many cancers, including liver and colorectal cancer. In the literature, *HSP90* inhibitors have been shown to induce p53-mediated induction of *PUMA* and *BAX* and apoptotic response *in vitro* and *in vivo* by the mitochondrial pathway in colon cancer cells [32, 33]. In this study, an increase in the ratio of *BAX/BCL-2* and *CASP-3* mRNA level was observed in colon and liver cancer cells exposed to TD6. TD6 also caused a decrease in the *HSP90* mRNA and protein level in these cells. TD6 could potentially induce cellular apoptosis via the mitochondrial pathway, which emerges with the inhibition of *HSP90*. This inhibition results in the reduction of *BCL-2*, increase and stimulation of *BAX*, rendering mitochondrial membranes permeable, cytochrome c release, and caspase activation. Şumnulu et al. investigated the cytotoxic effects of TD6 on HepG2 (human liver cancer) and AML12 (mouse hepatocyte) cell lines. The researchers found an IC₅₀ value of 143 µg/mL for HepG2 cells, resulting in a 31.04% increase in apoptotic and necrotic cells. In contrast, no substantial increase in cell mortality was detected in AML12 cells. Their investigation also found that apoptotic genes such as *BAX*, *CASP-3*, *APAF1*, and *p53* were significantly upregulated in HepG2 cells, but remained mostly unaltered in AML12 cells. Our study found comparable cytotoxic effects on liver cancer cells, with an IC₅₀ value of 12.18 µg/mL in HUH-7 cells at 24 h. TD6 also strongly triggered apoptosis in HUH-7 and HT-29 cells, as demonstrated by increased *BAX/BCL-2* ratios, *CASP-3* expression, and reduced *HSP90* levels. Our research and that of Şumnulu et al. reveal that TD6 may hold potential as a chemotherapeutic treatment for liver cancer, with significant variations in sensitivity between cancer and non-cancerous liver cells [34]. In another study on liver cancer, Vanlı et al. investigated the effects of TD6 and sorafenib on hepatocellular carcinoma in rats. They found that TD6 reduced tumor incidence and size, improved biochemical markers of liver damage, and increased apoptosis markers such as *CASP-10* and *CASP-3*. Similar to Vanlı et al., we observed apoptosis induction in cancer cells through changes in the *BAX/BCL-2* ratio and *CASP-3* levels [35]. Akçakavak and Özdemir investigated the effect of TD6 on colorectal cancer in rats. Their study found that TD6 treatment led to reduced cancer progression. In addition, TD6 decreased the expression of *KRAS* and *β-catenin*, while increasing the expression of *APC* and *p53* genes [36]. In another study, Taspınar investigated the combined antitumor effects of TD6 and cisplatin in neuroblastoma cells (SH-SY5Y). It was found that the co-administration of 100 µM TD6 with 40 µM cisplatin resulted in a significant cytotoxic effect of 60% and a 38% decrease in cell volume. The study also observed a 34.4% early apoptosis rate and an eight-fold decrease in mitochondrial membrane potential in SH-SY5Y cells compared to the control group. These results suggest that TD6 and cisplatin have a synergistic effect and enhance the efficacy of cisplatin. Similar to Taspınar et al., we observed significant apoptosis induction in cancer cells as indicated by changes in *BAX/BCL-2* ratio and *CASP-3* levels [37].

3.4. Antibacterial and Antifungal Activity Assays

Our results demonstrated a significant variation in the antimicrobial activity of TD6 depending on the different bacterial and fungal strains (Figure 4). TD6 exhibited antibacterial and antifungal activities against *E. faecalis*, *P. aeruginosa*, *S. aureus*, *K. pneumonia*, *C. albicans*

and *C. utilis* in dose dependent manner and the MIC values of TD6 were calculated ranged from 60.98 $\mu\text{g/mL}$ to 89.89 $\mu\text{g/mL}$ in these strains (Table 2).

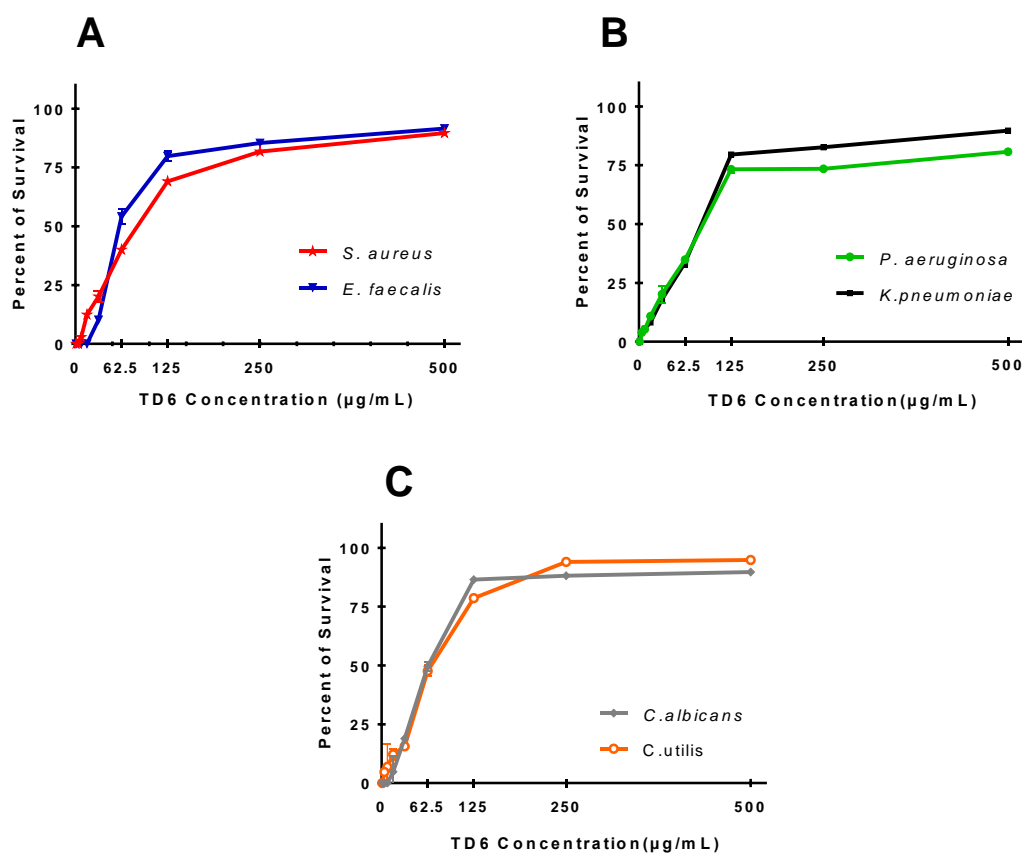


Figure 4 A) Growth curves of pathogen gram-positive bacterial strains, *S. aureus* and *E. faecalis*, with exposure to TD6 B) Growth curves of pathogen gram-negative bacterial strains, *K. pneumoniae* and *P. aeruginosa*, with exposure to TD6 C) Growth curves of pathogen fungal strains, *C. utilis* and *C. albicans*, with exposure to TD6

Table 2 MIC values of TD6 against bacterial and fungal strains

Microorganism	MIC Value of TD6 ($\mu\text{g/mL}$)
<i>E. faecalis</i>	60.98 \pm 4.87
<i>P. aeruginosa</i>	89.89 \pm 6.11
<i>S. aureus</i>	85.21 \pm 7.02
<i>K. pneumoniae</i>	75.00 \pm 6.55
<i>C. albicans</i>	64.12 \pm 3.54

<i>C. utilis</i>	74.64 ± 4.31
------------------	--------------

Antimicrobial activities of venoms against bacterial and fungal strains have been extensively examined in the literature. Peptide and non-peptide-origin components of the animal venoms, including phospholipase A2s (PLA2s), L-aminoacid oxidases (LAAOs), hyaluronidases (HYAs), metalloproteinases, serotonin, histamine, citrate, nucleosides and inorganic ions, exhibit potent antimicrobial activities against different species of microbes [38-40]. In a nutshell, animal venoms have big potent for treatment of cancer and infectious diseases.

Current study is the first comprehensive report of the antimicrobial properties of TD6. TD6 demonstrated dose-dependent antimicrobial activity against four bacterial and two fungal strains. *E. faecalis* (MIC: 60.98 ± 4.87 µg/mL) and *S. aureus* (MIC: 85.21 ± 7.02 µg/mL) are gram-positive bacterial strains which displayed strong sensitivity to TD6. Also, TD6 showed significant antimicrobial activity against *P. aeruginosa* (MIC: 89.89 ± 6.11 µg/mL) and *K. pneumonia* (MIC: 75.00 ± 6.55 µg/mL). Hence, TD6 has a great antimicrobial potential against both gram-negative and gram-positive bacterial strains. Similarly to strains of bacteria tested in this study, fungal strains also exhibited strong sensitivity to TD6. The MIC values for *C. albicans* and *C. utilis* of TD6 were calculated as 64.12 ± 3.54 µg/mL and 74.64 ± 4.31 µg/mL, respectively. This extract displayed antimicrobial activity in *P. aeruginosa*, *E. faecalis*, *K. pneumonia*, *S. aureus*, *C. utilis* and *C. albicans*.

4. Conclusion

Venoms of animals have been used as a therapeutic and healing agent in recent years. Especially, some cancer cell line and microbial strains have been treated with their alcoholic and aqueous extracts *in vitro* studies. In conclusion, we reported the results of antiproliferative activities of TD6 venom on colon cancer cell line and liver cancer cell line, and antimicrobial activity on two pathogenic bacteria and two fungal strains. The findings of this study suggest the therapeutic potentials of TD6 for cancer and infectious diseases. Further investigation of the biological activity of TD6 may contribute to its use as an alternative agent in the treatment of cancer and infectious diseases. However, this study has certain limitations. The *in vitro* nature of the experiments limits the direct applicability of the findings to the clinical practice. The methods by which TD6 exerts its effects, notably its interaction with specific biochemical pathways, have yet to be fully understood. Moreover, the study did not look at potential side effects or toxicity on noncancerous cells, which is crucial for determining the safety profile of TD6. In addition, broadening the study to include various cancer types and microbial strains might offer a more comprehensive understanding of TD6's biological activity. Furthermore, investigating the possible combination of TD6 with existing therapies could increase its efficacy and provide new avenues for treatment strategies.

Ethics in Publishing

There are no ethical issues regarding the publication of this study.

Author Contributions

NGT conceptualized, design and coordinated the investigation. NGT and ÖK performed all the experiments. NGT, ÖK and AÖ analyzed the data. ÖK created the first draft of the manuscript which was edited by all the authors.

Acknowledgements

This research received funding from the Foundation of Scientific Research Projects at Tokat Gaziosmanpaşa University (Project number: 2019/76).

References

- [1] Utkin, Y. N., (2015) Animal venom studies: Current benefits and future developments, *World J Biol Chem*, 6 (2) 28-33.
- [2] Mohamed Abd El-Aziz, T., Garcia Soares, A., and Stockand, J. D., (2019) Snake Venoms in Drug Discovery: Valuable Therapeutic Tools for Life Saving, *Toxins (Basel)*, 11 (10)
- [3] Chatterjee, B., (2018) Animal Venoms have Potential to Treat Cancer, *Curr Top Med Chem*, 18 (30) 2555-2566.
- [4] Chen, N., Xu, S., Zhang, Y., and Wang, F., (2018) Animal protein toxins: origins and therapeutic applications, *Biophys Rep*, 4 (5) 233-242.
- [5] Wu, T. *et al.*, (2019) Spider venom peptides as potential drug candidates due to their anticancer and antinociceptive activities, *J Venom Anim Toxins Incl Trop Dis*, 25 e146318.
- [6] Khusro, A., Aarti, C., Barbabosa-Pliego, A., Rivas-Caceres, R. R., and Cipriano-Salazar, M., (2018) Venom as therapeutic weapon to combat dreadful diseases of 21(st) century: A systematic review on cancer, TB, and HIV/AIDS, *Microb Pathog*, 125 96-107.
- [7] Lotfollahzadeh, S., Alizadeh, M. R., Mohri, M., and Mokhber Dezfouli, M. R., (2012) The therapeutic effect of *Tarentula cubensis* extract (Theranekron(R)) in foot-and-mouth disease in cattle: a randomised trial in an endemic setting, *Homeopathy*, 101 (3) 159-64.
- [8] Dolapcioglu, K. *et al.*, (2013) Theranekron for treatment of endometriosis in a rat model compared with medroxyprogesterone acetate and leuprolide acetate, *Eur J Obstet Gynecol Reprod Biol*, 170 (1) 206-10.
- [9] Gul Satar, N. Y., Cangul, I. T., Topal, A., Kurt, H., Ipek, V., and Onel, G. I., (2017) The effects of *Tarantula cubensis* venom on open wound healing in rats, *J Wound Care*, 26 (2) 66-71.
- [10] Kizilay, Z., Aktas, S., Cetin, N. K., Kilic, M. A., and Ozturk, H., (2019) Effect of *Tarantula Cubensis* Extract (Theranekron) on Peripheral Nerve Healing in an Experimental Sciatic Nerve Injury Model in Rats, *Turk Neurosurg*, 29 (5) 743-749.
- [11] Adib-Hashemi, F. *et al.*, (2016) Retraction note: Anti-inflammatory and protective investigations on the effects of Theranekron(R) "an alcoholic extract of the *Tarantula*

- cubensis*" on wound healing of peritoneal in the rat: an in vivo comparative study, *Diagn Pathol*, 11 (1) 118.
- [12] Gultiken, N. *et al.*, (2015) *Tarantula cubensis* extract alters the degree of apoptosis and mitosis in canine mammary adenocarcinomas, *J Vet Sci*, 16 (2) 213-9.
- [13] Adib-Hashemi, F. *et al.*, (2015) Anti-inflammatory and protective investigations on the effects of Theranekron(R) "an alcoholic extract of the *Tarantula cubensis*" on wound healing of peritoneal in the rat: an in vivo comparative study, *Diagn Pathol*, 10 19.
- [14] Oryan, A., Moshiri, A., and Meimandi Parizi, A., (2012) Alcoholic extract of tarantula *cubensis* improves sharp ruptured tendon healing after primary repair in rabbits, *Am J Orthop (Belle Mead NJ)*, 41 (12) 554-60.
- [15] Cam, Y., Kibar, M., Atasever, A., Atalay, O., and Beyaz, L., (2007) Efficacy of levamisole and *Tarantula cubensis* venom for the treatment of bovine cutaneous papillomatosis, *Vet Rec*, 160 (14) 486-8.
- [16] Richardson-Boedler, C., (2002) The brown spider *Loxosceles laeta*: source of the remedy *Tarentula cubensis*?, *Homeopathy*, 91 (3) 166-70.
- [17] Tosun, N. G., Kaplan, Ö., and Özgür, A., (2021) Apoptosis Induced by *Tarantula cubensis* Crude Venom (Theranekron® D6) in Cancer Cells, *Revista Brasileira de Farmacognosia*,
- [18] Erzurumlu, Y., Dogan, H. K., Catakli, D., and Aydogdu, E., (2022) *Tarantula cubensis* Extract Induces Cell Death in Prostate Cancer by Promoting Autophagic Flux/ER Stress Responses and Decreased Epithelial-Mesenchymal Transition, *Revista Brasileira de Farmacognosia*, 32 (4) 575-582.
- [19] Kaplan, Ö., (2023) Synergistic induction of apoptosis in liver cancer cells: exploring the combined potential of doxorubicin and XL-888, *Medical Oncology*, 40 (11) 318.
- [20] Gökşen Tosun, N. and Kaplan, Ö., (2022) Biosynthesis of Silver Nanoparticles Using White Propolis Extract as a Reduction Agent and Optimized by Box-Behnken Design, *Kahramanmaraş Sütçü İmam Üniversitesi Tarım ve Doğa Dergisi*, 25 (5) 933-945.
- [21] Dekker, E., Tanis, P. J., Vleugels, J. L. A., Kasi, P. M., and Wallace, M. B., (2019) Colorectal cancer, *Lancet*, 394 (10207) 1467-1480.
- [22] Martin, J. *et al.*, (2020) Colorectal liver metastases: Current management and future perspectives, *World J Clin Oncol*, 11 (10) 761-808.
- [23] Falzone, L., Salomone, S., and Libra, M., (2018) Evolution of Cancer Pharmacological Treatments at the Turn of the Third Millennium, *Front Pharmacol*, 9 1300.
- [24] Zainal Abidin, S. A., Lee, Y. Q., Othman, I., and Naidu, R., (2019) Malaysian Cobra Venom: A Potential Source of Anti-Cancer Therapeutic Agents, *Toxins (Basel)*, 11 (2)
- [25] Li, L., Huang, J., and Lin, Y., (2018) Snake Venoms in Cancer Therapy: Past, Present and Future, *Toxins (Basel)*, 10 (9)
- [26] Li, B. *et al.*, (2018) Triggering of cancer cell cycle arrest by a novel scorpion venom-derived peptide-Gonearrestide, *J Cell Mol Med*, 22 (9) 4460-4473.
- [27] Lian, W., Lian, H., Li, Q., Hu, A., and Liu, S., (2018) The venom of spider *Haplopelma hainanum* suppresses proliferation and induces apoptosis in hepatic cancer cells by caspase activation in vitro, *J Ethnopharmacol*, 225 169-177.

- [28] Liu, X., Chen, S., Tu, J., Cai, W., and Xu, Q., (2016) *HSP90* inhibits apoptosis and promotes growth by regulating HIF-1alpha abundance in hepatocellular carcinoma, *Int J Mol Med*, 37 (3) 825-35.
- [29] Boroumand, N. *et al.*, (2018) Therapeutic potency of heat-shock protein-90 pharmacological inhibitors in the treatment of gastrointestinal cancer, current status and perspectives, *J Pharm Pharmacol*, 70 (2) 151-158.
- [30] Nouri-Vaskeh, M., Alizadeh, L., Hajiasgharzadeh, K., Mokhtarzadeh, A., Halimi, M., and Baradaran, B., (2020) The role of *HSP90* molecular chaperones in hepatocellular carcinoma, *J Cell Physiol*, 235 (12) 9110-9120.
- [31] Zhang, S., Guo, S., Li, Z., Li, D., and Zhan, Q., (2019) High expression of *HSP90* is associated with poor prognosis in patients with colorectal cancer, *PeerJ*, 7 e7946.
- [32] He, K., Zheng, X., Zhang, L., and Yu, J., (2013) *HSP90* inhibitors promote p53-dependent apoptosis through PUMA and *BAX*, *Mol Cancer Ther*, 12 (11) 2559-68.
- [33] Gallerne, C., Prola, A., and Lemaire, C., (2013) *HSP90* inhibition by PU-H71 induces apoptosis through endoplasmic reticulum stress and mitochondrial pathway in cancer cells and overcomes the resistance conferred by *BCL-2*, *Biochim Biophys Acta*, 1833 (6) 1356-66.
- [34] Şumnulu, D. (2024) Cytotoxic Effects of Theranekron D6 on HepG2 Hepatocellular Carcinoma Cells, *Cumhuriyet Science Journal*, 45(1) 8-14.
- [35] Vanli, S., Kurtoglu, F., Alan, B. S., Akcakavak, G., and Ozdemir, O. (2024) Investigation of the effects of Theranekron and Sorafenib treatments on carcinogenesis, apoptosis and biochemical profile in hepatocellular carcinoma in rats, *Toxicology Mechanisms and Methods*, 1–11.
- [36] Akcakavak, G., and Ozdemir, O. (2023) Effect of *Tarantula cubensis* alcoholic extract on tumour pathways in azoxymethane-induced colorectal cancer in rats, *Acta Veterinaria Brno*, 92(1) 79-88.
- [37] Taspinar, N. (2023) The Synergistic Effect of Theranekron and Cisplatin on the Neuroblastoma (SH-SY5Y) Cell Line, *Turkish Neurosurgery*, 33(6).
- [38] Campos, L. B., Pucca, M. B., Roncolato, E. C., Netto, J. C., and Barbosa, J. E., (2012) Analysis of phospholipase A2, L-amino acid oxidase, and proteinase enzymatic activities of the *Lachesis muta rhombeata* venom, *J Biochem Mol Toxicol*, 26 (8) 308-14.
- [39] Hiu, J. J. and Yap, M. K. K., (2020) Cytotoxicity of snake venom enzymatic toxins: phospholipase A2 and l-amino acid oxidase, *Biochem Soc Trans*, 48 (2) 719-731.
- [40] Bocian, A. and Hus, K. K., (2019) Antibacterial properties of snake venom components, *Chem. Pap.*, 74 407-419.

Efficient Image Retrieval in Fashion: Leveraging Clustering and Principal Component Analysis for Search Space Reduction

Başak Esin Köktürk-Güzel^{1,2*}

¹İzmir Democracy University, Electrical and Electronics Engineering, Gürsel Aksel Bulvarı No:14
Karabağlar/İZMİR 35350

²Zoi Data Yazılım Danışmanlık Ltd.Şti. İzmir Teknoloji Geliştirme Bölgesi A8 Binası No:8
Urla / İZMİR 34430

Received: 13/06/2024, **Revised:** 05/09/2024, **Accepted:** 16/09/2024, **Published:** 31/12/2024

Abstract

In this study, a novel approach using clustering techniques and Principal Component Analysis (PCA) for reducing the search space in fashion image retrieval systems is introduced. The study focuses on extracting high-dimensional feature vectors from images of clothing items and finding the same or the most similar product using these feature vectors by narrowing the search space. The proposed method employs unsupervised learning algorithms to analyze high-dimensional fashion image feature vectors, grouping them into meaningful clusters. This enhances search efficiency and improves user experience. By reducing the dimensionality of feature vectors with PCA, computational costs are reduced. Experimental results demonstrate that the proposed method significantly improves computation time while maintaining an acceptable level of accuracy.

Keywords: Fashion search, fashion image retrieval, clustering, principal component analysis, Resnet50, VGG19

Modada Etkili Görüntü Arama: Arama Alanını Azaltmak İçin Kümeleme ve Temel Bileşen Analizinden Yararlanma

Öz

Bu çalışmada, moda görüntü arama sistemlerinde arama alanını küçültmek için kümeleme teknikleri ve Temel Bileşen Analizi (PCA) kullanan yeni bir yaklaşım tanıtılmıştır. Çalışmada kıyafet ürünlerine ait görüntülerden yüksek boyutlu öznitelik vektörleri çıkarılmış ve bu öznitelik vektörleri kullanılarak aynı ya da en benzer ürünün bulunması ve arama uzayının daraltılması ele alınmıştır. Önerilen yöntem yüksek boyutlu moda görüntü özellik vektörlerini analiz etmek için denetimsiz öğrenme algoritmaları kullanarak, onları anlamlı kümelere ayırmaktadır. Bu sayede arama verimliliği artırılmakta ve kullanıcı deneyimi iyileştirilmektedir. PCA ile öznitelik vektör boyutları indirgenerek hesaplama maliyeti azaltılmıştır. Deneysel sonuçlar, önerilen yöntemin hesaplama süresini önemli ölçüde düşürürken kabul edilebilir bir doğruluk seviyesini koruduğunu göstermektedir.

Anahtar Kelimeler: Moda arama, moda görüntü arama, kümeleme, temel bileşen analizi, Resnet50, VGG19

1. Introduction

Finding a product in the fashion world can become a challenging problem with the growing amount of data as e-commerce sites upload thousands of new product images every day along with their textual descriptions. The increasing diversity and production speed in the fashion industry make it challenging for customers to choose the right product. In response to these challenges, the use of AI techniques to ensure visual feature compatibility and provide accurate product recommendations is of great importance in the fashion domain [1]. Traditionally, users on e-commerce sites search for products by entering relevant keywords into a search box. The search algorithm matches these keywords with product tags in the database and presents the relevant products to the user. For text-based searches to be effective, it's important for the customer to fully understand/identify the product and know the appropriate keywords to enter. There can be many possible descriptions for an image, making it difficult for a search engine to precisely identify a product, and adding a close-up of the product is much easier. People are good at recognizing images and tend to think visually. Using visual search, customers can instead search for a product using images [2], [3]. Visual search allows customers to find information faster using images instead of words.

A fashion image retrieval task is to find query images or similar images in a database. Despite advancements in technology and deep learning methods, there are specific limitations in real-world applications. A few of these limitations include taking images under uncontrolled circumstances (different lighting, different angles, etc.), displaying multiple fashion products in a single image with some not fully visible (for instance, only half of the model's trousers are visible in a t-shirt image) and being sensitive to shape deformations. [4]. Therefore, there are still problems that need to be solved and automated specifically for fashion images.

In the literature, various studies exist on segmenting and classifying fashion products through images [5], [6], [7] or videos [8], [9]. The methods proposed in these studies have been trained with large, labeled datasets and have utilized different classifiers to create tags for test data. Today, most e-commerce sites still aim to find similar products by creating tags based on images and searching their databases. However, approaching the problem of finding similar products based on images in this way generally requires defining the products with fixed classifiers such as category, collar type, sleeve length, material, length, etc. Yet, searching through these classifiers to find similar products may not always provide the result the user is looking for. Typically, when someone performs a visual search for a product online, they want to find and purchase that exact product. Therefore, searching across images becomes important. For this purpose, Huang et.al. proposed a Dual-attribute perceptual Ranking Network (DARN) for feature learning based on the Siamese network [10]. Also, Berg et.al. used CNN network to find similar product in shop where the input query is a street photo [11]. However, these methods are early research efforts in this innovative area and require further refinement to achieve more precise alignment and improve computational efficiency.

In addition to finding the most similar products, the computational cost associated with image searches can grow exponentially as the number of images in the database increases. To tackle this issue, our study suggests reducing the search space through image clustering. We further investigate the potential of feature reduction via Principal Component Analysis (PCA) to decrease the costs associated with calculating distances between images. This method not only makes the search process more streamlined but also improves efficiency, enabling the effective management of larger datasets.

2. Materials and Methods

In this study, initially, the input image undergoes segmentation to isolate the clothing item from the background. This segmented image is then processed through a deep convolutional neural network, either ResNet50 or VGG19, to extract high-dimensional feature vectors representing the visual characteristics of the item. To manage the high dimensionality and improve computational efficiency, Principal Component Analysis (PCA) is applied to reduce the feature vector dimensions. Subsequently, the reduced feature vector can be optionally assigned to a pre-defined cluster, which helps in organizing the feature space and potentially speeds up the similarity search. This clustering step is particularly useful for large-scale databases, where it can significantly enhance retrieval performance by narrowing down the candidate items. Finally, cosine similarity is calculated between the reduced input feature vector and the reduced feature vectors of candidate items in the relevant clusters to identify the most visually similar items. This approach ensures efficient and accurate retrieval of similar clothing images, facilitating enhanced user experience in fashion-related applications. The block diagram of the proposed method is illustrated in Figure 1, and each block is explained in detail in the subsequent sections.

2.1.Dataset

In this study, BeautifulSoup (BS4) Python library [12] has been used to scrape web pages. Bs4 allows us to read and manipulate HTML codes, as well as search within tags in HTML code. Since each website has its own HTML structure, searching via tags facilitates easier access to images and essential information.

For this project, HTML codes from four major e-commerce websites operating in the global market were scraped using the Bs4 library to extract images of clothing items and related information. A variety of details were extracted from the data, including the title of the product, a hyperlink to the product's image, categories, features, and price. For this research we have only used product images. We have collected 41303 images and since each image has more than one fashion item we have extracted total 81702 product images by segmentation of the fashion products.

All images were downloaded to a local machine to prevent the links from becoming inactive if the products were removed from the website.

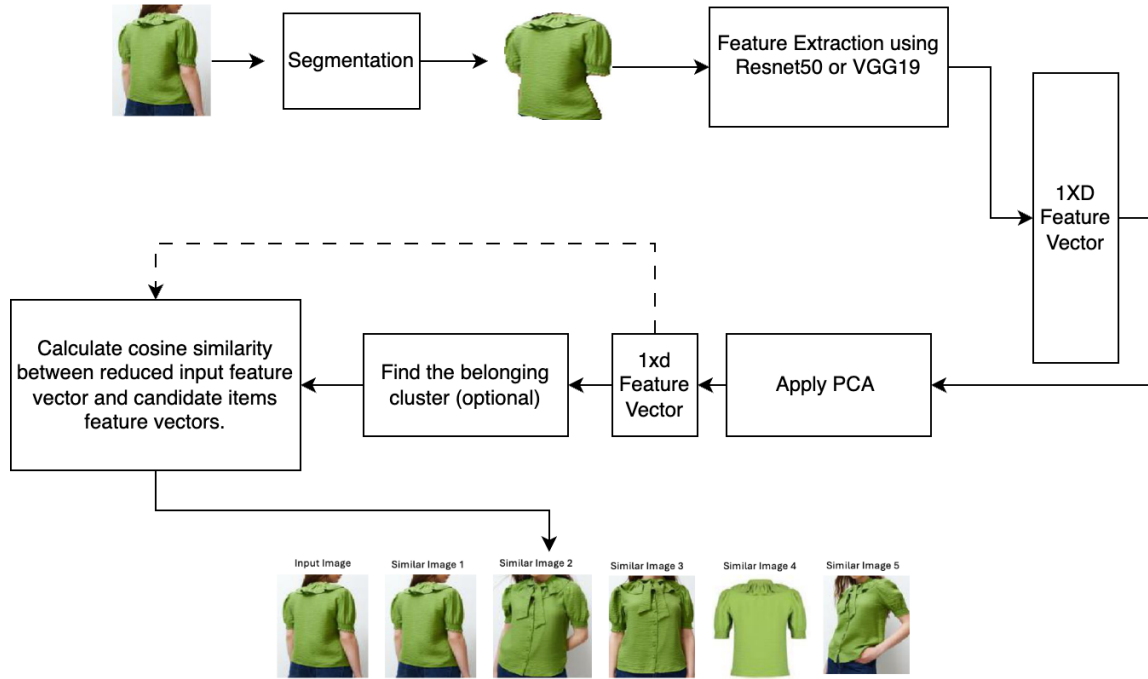


Figure 1 Block Diagram of the Proposed Method

2.2. Segmentation of Fashion Items

Image segmentation is the process of separating different features in an image into distinct regions so they can be differentiated. In this study, we used image segmentation methods to identify a fashion product. Detectron2 [13] is a computer vision tool that can spot objects, segment images, and estimate poses using extensible tools from Facebook AI Research (FAIR). Pre-trained models in Detectron2 save time and compute resources; a modular design simplifies model customization; and its scalable architecture guarantees high performance on large datasets. We tested different image segmentation models like U-net, Attention-Unet, and MaskR-CNN. Detectron2 beats out all the others after comparison evaluations.

Image segmentation methods generally evaluated by calculating Intersection-over-Union (IoU). IoU quantifies the extent of overlap between the predicted region Y and the true region X. The IoU metric returns a value between 0 and 1, where 0 indicates no overlap and 1 indicates perfect segmentation. IoU is given by:

$$IoU = \frac{|X \cap Y|}{|X \cup Y|}$$

We trained and tested various segmentation models on the iMaterialist dataset, which was originally prepared for an image processing competition at CVPR2019 [14]. The dataset contains 6,760 images: 5,408 for training, 676 for testing, and 676 for validation. To ensure an equal distribution of the reduced categories, we used a subset of the iMaterialist dataset. There are 46 categories in the original dataset, making it ideally suited to both classification and segmentation. We have segmented the input image into lower body, upper body, whole body,

accessory, and shoes. The IoU metrics for U-Net and Detectron2 for segmentation results were 0.62 ± 0.36 and 0.79 ± 0.24 respectively. Some segmentation results for our dataset are shown in Figure 2 and Figure 3.



Figure 2 Segmented view of a red blouse and black skirt.



Figure 3 Advanced segmentation of a green dress with lace detailing.

2.3.Feature Extraction

In our study, we employ two distinct convolutional neural networks, ResNet50 (Residual Network [15] with 50 layers) and VGG19 [16], for the feature extraction process to compare their effectiveness in fashion image clustering. Both networks are known for their deep learning capabilities in image recognition tasks but differ significantly in architecture and performance characteristics, which can impact the clustering outcome.

ResNet50 utilizes a series of residual blocks that incorporate skip connections, allowing the model to skip one or more layers. These skip connections help to avoid the problem of vanishing gradients by allowing gradients to flow through a shortcut path during backpropagation. We use a pre-trained ResNet50 model, utilizing weights from the ImageNet dataset, which provides a robust foundational understanding of visual features across diverse categories.

For clustering, we extract features from the last fully connected layer of ResNet50, which contains 2048 deep features encapsulating high-level semantic information from the images. This layer is chosen because it provides a dense representation of the image, capturing both the abstract and detailed aspects, which is ideal for clustering based on visual similarity.

VGG19 has 19 layers, and this architecture is known for its simplicity. Like ResNet50, VGG19 is also pre-trained on the ImageNet dataset. VGG19 employs a stack of convolutional layers with small receptive fields followed by max-pooling layers, which increase the depth of the network while reducing spatial dimensions of the feature maps.

For feature extraction, we use the output from the last fully connected layer of VGG19, which, like ResNet50, provides a feature vector with a comprehensive depiction of the image. However, VGG19's feature vectors tend to be more flattened and less hierarchical compared to those from ResNet50, potentially affecting the granularity and nature of the clusters formed.

The extracted features from both ResNet50 and VGG19 are subsequently used to feature extraction before perform clustering. The choice of different architectures allows us to examine how the depth and structure of a network influence the clustering quality and accuracy. By analyzing the similar product recommendation results obtained from both models, we aim to discern which architectural traits contribute most effectively to grouping fashion images, thus providing insights into the optimal deep learning approach for such applications.

2.4. Clustering Of The Database

After the feature extraction process using ResNet50 and VGG19, we proceed with the clustering of the extracted features using the k-means clustering algorithm. K-means is chosen for its simplicity and effectiveness in grouping data into k distinct clusters based on feature similarity. The algorithm partitions the images by assigning each image to the nearest cluster center, minimizing the within-cluster variance, also known as the inertia.

Using the features extracted from both the ResNet50 and VGG19 models, k-means clustering is applied separately to each set of features. The number of clusters was chosen as 5 through the Elbow Method to finalize the clustering configuration.

The final clusters are analyzed to assess the visual and stylistic similarities within each cluster, validating the effectiveness of the chosen models and clustering techniques. By comparing the outcomes of clustering with features from ResNet50 and VGG19, we gain insights into which feature extraction method is more conducive for fashion image categorization.

2.5. Feature Reduction

Applying Principal Component Analysis (PCA) after clustering reduces the dimensionality of feature vectors extracted from images, thereby enhancing computational efficiency in subsequent operations. PCA is particularly useful when comparing a test image with database images using cosine similarity. Applying PCA to reduce the dimension from D to d results in lower computational costs for image comparisons due to the reduced complexity from $O(D)$ to $O(d)$. This enhancement makes the process more efficient and scalable, particularly useful in systems where real-time image comparisons are necessary.

3. Results and Discussion

To identify similar products, we begin by segmenting images to isolate fashion items. As we stated in previous section, we have trained Detectron2 algorithm with pre-annotated dataset iMaterialist and test on it. Since its segmentation scores are satisfactory level, we have applied our trained segmentation model to collected shop image dataset.

Next, we extracted feature vectors from each segmented product image using the architectures of ResNet50 and VGG19. By omitting the final layer of these models, we obtain a 1x2048 fully connected embedding vector for each product. To visualize these vectors, we employ t-SNE, which helps us plot the feature vectors in a two-dimensional space. A selection of 500 randomly chosen images is displayed in Figure 4, demonstrating that similar products and colors cluster together, particularly when using ResNet50 features. This pattern is also observed with VGG19, reinforcing the use of cosine similarity as a metric for identifying visually similar items.

To find products similar to a given input image, we segment fashion objects within the image, extract their features, and then search our database for similar items by calculating the cosine similarity between the feature vectors of the input product and those in the database. Figure 4 demonstrates that objects sharing similar colors and categories are clustered in proximity within the space. This observation validates the use of cosine similarity as a metric for identifying visually analogous objects in the database.

We calculated the cosine similarity for all images in our database and subsequently grouped the images into clusters. Within these clusters, we specifically identified the group that included our test images. We then calculated the cosine similarity between these test images and others in the same cluster. We also implemented Principal Component Analysis (PCA) with a range of component numbers ($n = 2, 4, 8, 16, 32, 64, 128, 256, 512, 1024$). Afterward, we measured the pairwise cosine similarities and clustered the features post-dimensionality reduction to identify similar products within this condensed feature space. For each scenario, we recorded the computation time and evaluated performance. All experiments were conducted on a workstation equipped with an Intel Xeon W 1270 processor, 64 GB of RAM, a 1 TB hard drive, and an NVIDIA Quadro P2200 graphics card with 5 GB of dedicated memory.

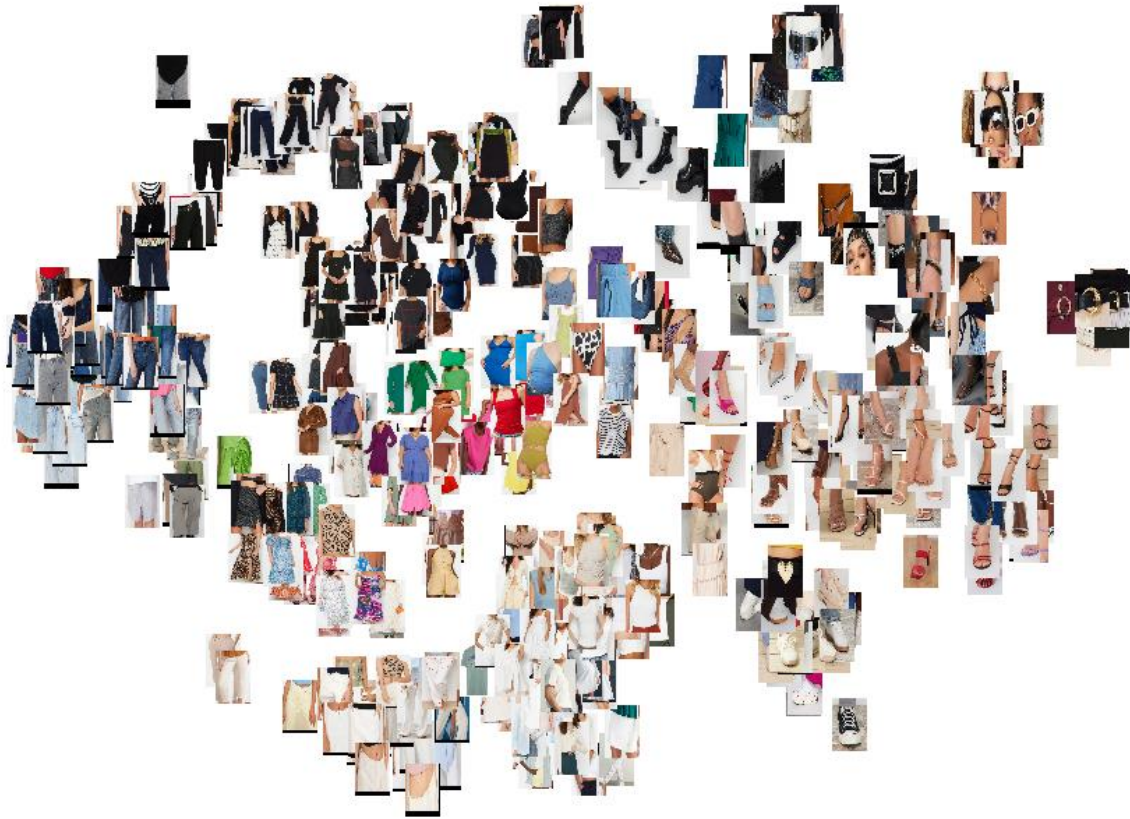


Figure 4 Visualization of 500 randomly selected product images from our dataset after feature extraction using ResNet50 and dimensionality reduction via t-SNE for 2D embedding.

Figure 5 shows the computational time versus the number of principal components. The results indicate that computation time significantly decreases as the number of principal components is reduced. Additionally, when working with a higher number of principal components, clustering further decreases the average computation time because it involves comparing fewer samples. Given the importance of speed on e-commerce web pages, even a small reduction in computation time is highly valuable.

We have multiple images taken from different angles for the same product. For each product, we determine five recommendations. Our success metric is based on how many of these five recommendations are of the same product. Considering that some products do not have five different images, resulting in a lower success rate, our results appear to be sufficiently satisfactory.

As summarized in Figure 6, the prediction performance does not change dramatically when using clustering, which is beneficial for our purposes. The graphs indicate that Resnet50 consistently outperforms VGG19 in terms of prediction accuracy. This is evident as the average number of true product recommendations is higher for Resnet50 across all principal component numbers.

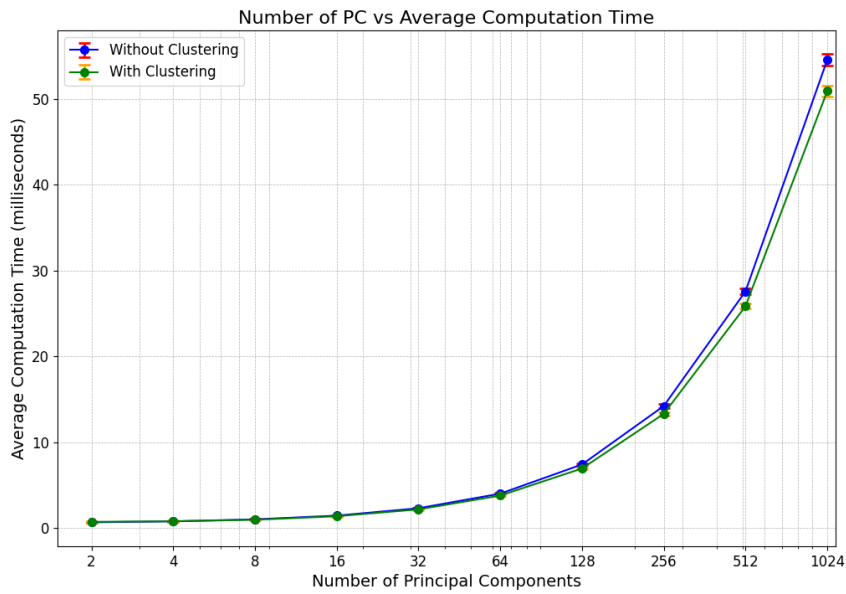
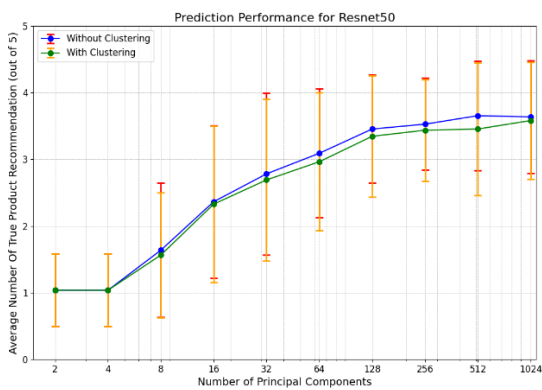
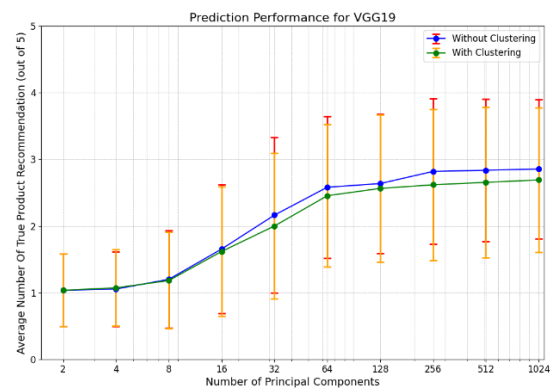


Figure 5 Average computational time for finding the top-5 similar products for a given product.

Additionally, it is important to note that clustering helps in reducing computational time by comparing fewer samples, without significantly impacting the prediction performance. This is crucial for e-commerce applications where speed is a key factor. The slight variations in the number of principal components, as shown in the graphs, demonstrate that while both models improve with more components, Resnet50 maintains a better performance level, making it a preferable choice for our image retrieval system.



(a)



(b)

Figure 6 Average number of true product recommendations for a given product with feature extraction using (a) Resnet50 (b) VGG19.

We have demonstrated some visual results for a given product image in Figure 7. Considering different feature extraction methods, different numbers of PCA components, and whether clustering is applied, there are a total of 40 combinations and 200 recommendations for an input image. Therefore, we did not include all the results in the figure. To illustrate the general structure, we used both ResNet50 and VGG19 for feature extraction with $n=1024$ and included

the top 5 recommended product images. When we look at these, we can say that the ResNet architecture yields better results in finding similar images. Therefore, we only shared the ResNet results to compare the number of PCA components. This example clearly shows that as the number of n components decreases, the performance in finding similar products decreases. All results are provided without clustering since there is only a slight decrease in performance when clustering is applied.



Figure 7 Selected results for various feature extraction architectures and different numbers of principal components.

4. Conclusion

In this study, we presented a novel approach to enhancing fashion image retrieval using clustering methods and Principal Component Analysis (PCA). Our findings emphasize the

significant impact that feature extraction techniques have on the effectiveness of fashion image searches. By grouping similar items, we were able to make the search process faster while maintaining an acceptable level of accuracy. Notably, our experiments demonstrated that ResNet50 outperforms VGG19 in terms of prediction accuracy, particularly when combined with PCA. This combination not only speeds up the retrieval process by reducing the number of necessary comparisons but also proves to be highly beneficial for e-commerce platforms, where user satisfaction is closely tied to the speed and relevance of search results.

However, we acknowledge certain threats to the validity of our findings. The reliance on human evaluation, for instance, introduces subjectivity, as different users may perceive visual similarity differently. Furthermore, traditional evaluation metrics may not fully capture the subtle visual details that are crucial in fashion image retrieval, potentially leading to a gap between algorithmic performance and user expectations. Additionally, the dataset used in our study might not encompass the full diversity of fashion items available in the real world, which could limit the generalizability of our results.

Despite these challenges, our approach demonstrates a clear improvement in both the efficiency and accuracy of fashion image retrieval. By carefully considering these threats to validity and continuing to refine our methods, this research lays a strong foundation for future work in the field. Our approach not only optimizes the search process but also enhances the overall user experience, making it a valuable contribution to the ongoing development of intelligent fashion recommendation systems.

Ethics in Publishing

There are no ethical issues regarding the publication of this study.

Acknowledgements

This project is supported by the KOSGEB's R&D, Product Development, and Innovation Support Program grant number 68KIB.

References

- [1] S. Shirkhani, H. Mokayed, R. Saini, and H. Y. Chai, "Study of AI-Driven Fashion Recommender Systems," *SN Comput Sci*, vol. 4, no. 5, p. 514, 2023, doi: 10.1007/s42979-023-01932-9.
- [2] X. Li, X. Wang, X. He, L. Chen, J. Xiao, and T.-S. Chua, "Hierarchical fashion graph network for personalized outfit recommendation," in *Proceedings of the 43rd international ACM SIGIR conference on research and development in information retrieval*, 2020, pp. 159–168.
- [3] A. Dagan, I. Guy, and S. Novgorodov, "Shop by image: characterizing visual search in e-commerce," *Information Retrieval Journal*, vol. 26, no. 1, p. 2, 2023, doi: 10.1007/s10791-023-09418-1.

- [4] M. Hadi Kiapour, X. Han, S. Lazebnik, A. C. Berg, and T. L. Berg, “Where to buy it: Matching street clothing photos in online shops,” in *Proceedings of the IEEE international conference on computer vision*, 2015, pp. 3343–3351.
- [5] Z. Liu, P. Luo, S. Qiu, X. Wang, and X. Tang, “Deepfashion: Powering robust clothes recognition and retrieval with rich annotations,” in *Proceedings of the IEEE conference on computer vision and pattern recognition*, 2016, pp. 1096–1104.
- [6] M. Jia *et al.*, “Fashionpedia: Ontology, segmentation, and an attribute localization dataset,” in *Computer Vision–ECCV 2020: 16th European Conference, Glasgow, UK, August 23–28, 2020, Proceedings, Part I 16*, 2020, pp. 316–332.
- [7] B. Kolisnik, I. Hogan, and F. Zulkernine, “Condition-CNN: A hierarchical multi-label fashion image classification model,” *Expert Syst Appl*, vol. 182, p. 115195, 2021.
- [8] Z.-Q. Cheng, X. Wu, Y. Liu, and X.-S. Hua, “Video2shop: Exact matching clothes in videos to online shopping images,” in *Proceedings of the IEEE conference on computer vision and pattern recognition*, 2017, pp. 4048–4056.
- [9] N. Garcia and G. Vogiatzis, “Dress like a star: Retrieving fashion products from videos,” in *Proceedings of the IEEE International Conference on Computer Vision Workshops*, 2017, pp. 2293–2299.
- [10] J. Huang, R. S. Feris, Q. Chen, and S. Yan, “Cross-domain image retrieval with a dual attribute-aware ranking network,” in *Proceedings of the IEEE international conference on computer vision*, 2015, pp. 1062–1070.
- [11] M. Hadi Kiapour, X. Han, S. Lazebnik, A. C. Berg, and T. L. Berg, “Where to buy it: Matching street clothing photos in online shops,” in *Proceedings of the IEEE international conference on computer vision*, 2015, pp. 3343–3351.
- [12] L. Richardson, “Beautiful soup documentation,” 2007, *April*.
- [13] Y. Wu, A. Kirillov, F. Massa, W. Y. Lo, and R. Girshick, “Detectron2 [www document],” URL <https://github.com/facebookresearch/detectron2> (accessed 12.12.23), 2019.
- [14] S. Guo *et al.*, “The imaterialist fashion attribute dataset,” in *Proceedings of the IEEE/CVF International Conference on Computer Vision Workshops*, 2019, p. 0.
- [15] K. He, X. Zhang, S. Ren, and J. Sun, “Deep residual learning for image recognition,” in *Proceedings of the IEEE conference on computer vision and pattern recognition*, 2016, pp. 770–778.
- [16] K. Simonyan and A. Zisserman, “Very deep convolutional networks for large-scale image recognition,” *arXiv preprint arXiv:1409.1556*, 2014.

Fabrication of cZIF-67/Ti₃C₂ Nanocomposites As Sulfur Host For Lithium-Sulfur Batteries

Recep YUKSEL ^{1,2,3*}

¹Department of Chemistry, Faculty of Science, Eskisehir Osmangazi University (ESOGU), Eskisehir 26040, Türkiye;

²Nanoscience and Nanotechnology, Graduate School of Natural and Applied Sciences, Eskisehir Osmangazi University (ESOGU), 26040 Eskisehir, Türkiye;

³Advanced Materials Technologies Application and Research Center (IMATEK), Eskisehir Osmangazi University (ESOGU), 26040 Eskisehir, Türkiye.

Received: 22/07/2024, **Revised:** 18/08/2024, **Accepted:** 11/11/2024, **Published:** 31/12/2024

Abstract

It is of great importance to develop high-performance energy storage systems that modern society needs for next-generation technologies such as electric vehicles, consumer electronics, and grid-scale storage. Lithium-sulfur (Li-S) batteries are one of the promising candidates for high-performance energy storage systems due to the high theoretical capacity of the sulfur. On the other hand, some drawbacks, such as the insulating nature of the sulfur and the polysulfide solubility, limit the widespread application of Li-S batteries. Nanocomposite host materials with high surface area and conductive nature can potentially improve the stability of sulfur cathodes. In this study, the MOF-derived heteroatom-doped carbon (cZIF-67) and two-dimensional Ti₃C₂ MXene materials were used to fabricate cZIF-67/Ti₃C₂ nanocomposites. The fabricated cZIF-67/Ti₃C₂ nanocomposites were used as a sulfur host material for Li-S batteries. After the structural and chemical characterizations, S/cZIF-67/Ti₃C₂ nanocomposite cathodes were used in Li-S batteries, and their performance-related properties were examined. The fabricated S/cZIF-67/Ti₃C₂ cathodes eliminate the adverse effects caused by the insulating nature of sulfur and lithium polysulfides.

Keywords: Energy storage, Lithium-sulfur batteries, MOF, MXene

Lityum-Sülfür Bataryalar İçin Kükürt Tutucu cZIF-67/Ti₃C₂ Nanokompozitlerin Üretimi

Öz

Modern toplumun elektrikli araçlar, tüketici elektroniği ve şebeke tipi depolama gibi yeni nesil teknolojiler için ihtiyaç duyduğu yüksek performanslı enerji depolama sistemlerinin geliştirilmesi büyük önem taşıyor. Lityum-sülfür (Li-S) bataryalar, kükürtün yüksek teorik kapasitesi nedeniyle yüksek performanslı enerji depolama sistemleri için umut verici adaylardan biridir. Öte yandan kükürtün yalıtkan doğası ve polisülfür çözünürlüğü gibi bazı dezavantajlar Li-S bataryaların geniş çaptaki uygulamasını sınırlamaktadır. Yüksek yüzey alanına ve iletken doğaya sahip nanokompozit konak malzemeler, kükürt katotlarının stabilitesini iyileştirme potansiyeline sahiptir. Bu çalışmada, MOF'tan türetilmiş heteroatom katkılı karbon (cZIF-67) ve iki boyutlu Ti₃C₂ MXene malzemeler kullanılarak cZIF-67/Ti₃C₂ nanokompozitleri üretilmiştir. Üretilen cZIF-67/Ti₃C₂ nanokompozitler Li-S bataryalar için kükürt tutucu malzeme olarak kullanıldı. Yapısal ve kimyasal karakterizasyonların ardından S/cZIF-67/Ti₃C₂ nanokompozit katotlar Li-S bataryalarda kullanılarak performans ilintili özellikleri incelenmiştir. Üretilen S/cZIF-67/Ti₃C₂ katotlar ile kükürtün yalıtkan yapısından ve lityum polisülfürlerden kaynaklanan olumsuz etkiler ortadan kaldırılmıştır.

Anahtar Kelimeler: Enerji depolama, Lityum-sülfür bataryalar, MOF, MXene.

1. Introduction

Modern society has an increasing energy demand for new technologies such as electric vehicles, smart buildings, and consumer electronics. This demand has also enhanced the need for sustainable and cost-effective production and storage systems [1, 2]. Thus, a global race exists to develop innovative energy production and storage technologies using low-cost and sustainable technologies. The significant success of lithium-ion batteries (LIBs) over the past thirty years has undoubtedly made them the leading battery technology in developing high-capacity energy storage systems. Due to a series of structural limitations, LIBs cannot meet the requirements of next-generation electric vehicles and grid-scale energy storage systems regarding energy density and cost-effectiveness.

Sulfur (S) is one of the few substances found in elemental form in nature and is the 16th most abundant element in the earth's crust, making it widely available. Additionally, sulfur obtained as a by-product during industrial processes is available in large reserves. Sulfur is a cathode material in lithium-sulfur batteries [3]. Sulfur's theoretical specific capacity is 1675 mAh g⁻¹ [4], approximately ten times higher than metal oxide materials commonly used in lithium-ion batteries [5]. All these features show that sulfur is a suitable battery material for developing high-energy-density, low-cost, and sustainable energy systems. Therefore, the emergence of Li-S batteries has generated significant interest in academic and industrial energy storage research.

Lithium-sulfur batteries operate on a significantly different principle from lithium-ion batteries [4]. Li-ion batteries generally use layered or tunnel-type metal oxides (LiMO_x) at the positive electrode. Similarly, negative electrode materials also have layered structures. These structures allow Li⁺ ions to move reversibly between the positive and negative electrodes during the battery's charge-discharge processes. In Li-S batteries, the energy obtained is based on the reaction of Li⁺ with S²⁻. The following equations clearly demonstrate the electrochemical reaction mechanism of Li-S batteries [6]. During electrochemical discharge, elemental sulfur is reduced to a series of soluble lithium polysulfides (LPS) and some solid-phase polysulfides, which are stored in the cathode electrode (Equation (1)) [3]. During charging, all steps of the discharge process occur in reverse. The reactions at the anode electrode involve Li metal's reversible dissolution and deposition (Equation (2)). The overall reaction of a Li-S cell can be simplified as Equation (3).



Most scientific studies on Li-S batteries focus on the S cathode. The main challenges in developing LSBs include the insulating nature of sulfur (25 °C, 5*10⁻³⁰ S cm⁻¹) and a series of unique problems, such as volume expansion during electrochemical processes. More importantly, the migration of soluble polysulfides from the cathode to the anode during charge/discharge, known as the polysulfide shuttle effect, leads to rapid capacity loss [3, 7].

All these issues result in the inefficient and ineffective use of sulfur, reduced LSB lifespan, and significant capacity losses. Therefore, it is necessary to develop host materials compatible with sulfur and capable of holding it for high-performance LSBs [8].

The performance of electrochemical energy storage systems is closely related to the structural properties of device components. The surface area, pore volume, pore size, and many structural and chemical properties of cathode active materials are significantly correlated. Reports in the literature highlight that porous materials with good conductivity can keep sulfur in the cathode [3, 5]. The most effective approach is physically trapping sulfur within a carbon-based host structure. Due to its environmentally friendly, economical, and easy applicability, melt infiltration is the most commonly used method for depositing sulfur onto host structures [9-11]. The high electronic conductivity of carbon structures ensures more efficient and effective use of insulating sulfur. Therefore, developing new materials with desired structural properties is crucial for high-performance Li-S battery systems.

Zeolitic imidazolate frameworks (ZIFs) are a subgroup of metal-organic frameworks (MOFs) and stand out with their large surface area, crystalline structure, high micropore volume, and chemical stability. Among the MOF structures, ZIF-67 is one of the most studied members. They are formed by the Co-N bonds of cobalt (Co) metal centers with 2-methylimidazole (HMIM) ligands. ZIF-67 MOF demonstrates high micropore volume and specific surface area. However, most MOF structures do not exhibit sufficient ionic and electronic conductivity [8]. Carbon materials derived from MOFs obtained by carbonization are much more conductive. MOF-derived carbon structures can retain the structural features of the parent MOF, such as surface area and pore size, which makes them promising materials for energy storage systems [12]. In the literature, it has been reported that ZIF-67-derived carbon materials are used as sulfur hosts in LSBs [13]. Sulfur cathodes, where sulfur is trapped within the microporous carbon structure obtained by carbonizing ZIF-67, have slowed the diffusion of dissolved polysulfides in Li-S batteries. ZIF-67-derived carbon structures with high sulfur content (59 wt% S) have also shown high electrochemical capacity.

On the other hand, MOF-derived carbon hosts in sulfur cathodes examined so far consist of colloidal particles and are generally sub-micrometer in size. In MOF-derived carbon host structures, electron transfer slows down due to the limited electronic conductivity, reduced diffusion kinetics, and increased contact resistance. All these processes can lead to decreased LSB performance and lifespan.

As mentioned earlier, soluble lithium polysulfide compounds formed during electrochemical processes in Li-S batteries migrate from the cathode electrode section to the anode section, causing significant damage to electrochemical performance and capacity. MOF-derived heteroatom-doped carbon structures' important features are their polar and hydrophilic surfaces [14, 15]. Polar carbon structures, i.e., heteroatom-doped carbon structures, are very effective in retaining LPS formed during electrochemical processes within the carbon host. The good wetting of heteroatom-doped structures with the electrolyte solution significantly enhances the sulfur cathode's performance and the electrolyte's electrochemical stability [16]. Therefore, heteroatom-doped carbon structures are potential candidates for developing Li-S batteries.

While using MOF-derived carbon materials as sulfur host structures is an innovative approach for enhancing the electrochemical performance and lifespan of Li-S batteries, achieving the desired electronic and ionic conductivity values and slowing down reaction kinetics have not yet fully shown the desired performance. Therefore, two-dimensional conductive materials are needed to shorten the ion diffusion distance, increase electronic conductivity, facilitate charge transfer, and form a three-dimensional integrated structure with MOFs.

Due to their unique morphologies, two-dimensional (2D) layered materials with atomic thickness and high conductivity, like graphene and metal chalcogenides, are potential cathode materials for high-capacity Li-S batteries [17]. The high capacity values of Ti₃C₂T_x MXene structures result from both the increased number of electrochemically active regions accessible to lithium-ions and the prevention of ion aggregation between MXene layers during intercalation [18]. Using highly conductive MXene and high surface area porous MOF in a nanocomposite structure may result in high energy density LSBs. Combining the high electronic conductivity of two-dimensional Ti₃C₂T_x MXene and the high micropore volume of MOF (ZIF-67) structures can create a more effective sulfur-hosting cathode framework within a 3D nanocomposite structure. This 3D nanocomposite cathode structure is strongly likely to contribute significantly to Li-S battery performance. This is because the three-dimensional porous network structure increases the charge transfer kinetics while maintaining the electronic conductivity of these electrode materials [19].

In this study, a three-dimensional MOF/MXene-based sulfur-hosting composite cathode fabrication is carried out by combining the favorable properties of MOFs and MXenes to obtain high energy density Li-S batteries. The Li-S batteries designed with the produced three-dimensional composite structures have high charge-discharge efficiency, long lifespan, and high energy density, with cathodes possessing high electrical conductivity, excellent electron transfer capability, charge transfer mobility, and a large surface area.

2. Material and Methods

2.1. Nanocomposite Cathode Fabrication

2.1.1 Ti₃C₂T_x MXene Synthesis:

The Ti₃AlC₂ MAX phase in powder form was obtained from a local seller (Nanografi Co.) and used for the Ti₃C₂T_x MXene synthesis. To etch the atomic layers of Al in Ti₃AlC₂, an acid mixture was prepared by adding 5 grams of LiF salt to 9.0 M HCl acid solution. 3.0 grams of MAX powder were slowly added to 40 ml of the acid mixture and stirred at room temperature (<35 °C) at 350 rpm for 24 hours using a magnetic stirrer. Then, the solution was centrifuged at 3500 rpm for 5 minutes repeatedly with deionized water until the pH is neutral. To obtain a homogeneously distributed colloidal MXene solution, Ti₃C₂T_x MXenes were sonicated in an ultrasonic bath for one hour. Then, the dispersed 2D Ti₃C₂T_x MXene sheets were collected by centrifugation and made into a solution at a 2.0 mg/mL concentration.

2.1.2. ZIF-67/ Ti₃C₂T_x Nanocomposite Material Synthesis:

For ZIF-67/ Ti₃C₂T_x nanocomposite production, a homogeneous solution was obtained by adding cobalt nitrate salt to the MXene solution (2.0 mg/mL) and mixing it at high speed with a magnetic stirrer. Following the adsorption of Co²⁺ ions onto the Ti₃C₂ structures, an organic ligand 2-methylimidazole (2-HMIM) solution was added to the initial solution on the magnetic stirrer and stirred at high speed for another 20 minutes. The molar ratio of Co²⁺ salt to 2-HMIM was set to 1:20 for nanocomposite production. Two different mass ratios of ZIF-67/Ti₃C₂ nanocomposites (1:1, and 3:1) were synthesized. The prepared solution was left overnight without disturbing at room temperature to produce the nanocomposite structure. The obtained MOF/MXene nanocomposite structures were purified by centrifugation to remove unreacted ligand groups and metal salts. The synthesized ZIF-67/Ti₃C₂ nanocomposites were freeze-dried to form an aerogel structure.

2.1.3. Thermal Treatment of ZIF-67/Ti₃C₂ MOF/MXene Nanocomposite Structures:

The synthesized ZIF-67/Ti₃C₂ MOF/MXene nanocomposites were then subjected to thermal treatment in an argon gas flow (100 sccm) at low pressure (<20 mbar) in a split tube furnace. The ZIF-67/Ti₃C₂ structures were thermally treated at 600 °C for 2 hours at a ramping rate of 10 °C/min. The resulting nanocomposites were purified by soaking in 2.0 M HCl acid overnight and then washed with deionized water. The obtained cZIF-67/Ti₃C₂ cMOF/MXene nanocomposite structures were dried in a vacuum oven for 24 hours.

2.1.4. Sulfur Loading into cZIF-67/Ti₃C₂ cMOF/MXene Nanocomposite Structures:

Sulfur was loaded into the cZIF-67/Ti₃C₂ nanocomposite using the melt infiltration method. For this purpose, the synthesized nanocomposite material was mixed with sulfur at a mass ratio of 1:3 and placed in a hydrothermal reactor. The hydrothermal reactor was heated at 155 °C for 12 hours, and then the sulfur-loaded material (S/c- ZIF-67/Ti₃C₂) was removed from the reactor.

2.2. Li-S Battery Fabrication

2.2.1. Preparation of Cathode Electrodes:

The synthesized S/cZIF-67/Ti₃C₂ nanocomposite was mixed with a polymeric binder polyvinylidene difluoride (PVDF) and conductive additive carbon black (CB) with a mass ratio of 8:1:1 in N-methyl-2-pyrrolidone (NMP) solvent to form an ink solution. The prepared ink was coated onto aluminum foil as a thin film. Then, the thin film cathode electrodes were dried at room temperature and kept in a vacuum oven at 60 °C for 24 hours. The prepared thin film cathodes were cut into discs (15 mm in diameter) using a disc cutter and made ready for Li-S battery assembly.

2.2.2. Preparation of Electrolyte for Li-S Batteries:

The electrolyte solution for Li-S batteries was prepared by mixing 1.0 M lithium bis(trifluoromethanesulfonyl)imide (LiTFSI) salt in a 1:1 volume ratio of 1,3-dioxolane (DOL) and dimethoxyethane (DME) solvent mixture with 0.5 M LiNO₃ salt additive. The electrolyte preparation processes were carried out in an Argon atmosphere glovebox (O₂ <0.1 ppm and H₂O <0.1 ppm) using a magnetic stirrer and stored in the glovebox.

2.2.3. Li-S Battery Assembly:

The fabricated S/cZIF-67/Ti₃C₂ cathodes and lithium metal foils as anodes were used to assemble 2032 coin-cell Li-S batteries in the glovebox. Commercial Celgard 2400 separators were used to separate the anode and cathode electrodes physically. The electrolyte (μL)/sulfur (mg) ratio for S/cMOF/MXene cathodes was 20 to fabricate Li-S batteries. The fabricated Li-S batteries were rested in ambient conditions for at least 1-2 hours before the electrochemical measurements.

2.3. Characterizations

2.3.1. Structural and Chemical Characterizations:

The structural and chemical characterizations of the fabricated materials and electrodes were done using various methods and techniques. Scanning electron microscopy (SEM) was used to observe the particle size and morphology. X-ray diffraction spectroscopy (XRD) was used for the structural analyses. The BET (Brunauer-Emmett-Teller) method was used to determine the specific surface area. The sulfur content in the nanocomposite structures was determined using thermal gravimetric analysis (TGA).

2.3.2. Electrochemical Characterizations:

The electrochemical performance of the fabricated Li-S batteries was carried out using cyclic voltammetry (CV), galvanostatic charge-discharge (GCD), and cycle life tests. CV measurements were performed in a voltage range of 1.6-2.8 V at scan rates of 0.1-0.5 mV/s. The scan rates were decided based on the position change of sulfur's redox peaks. GCD measurements were performed at 0.1-5.0 C-rates. The 1.0 C-rate was determined based on sulfur's theoretical capacity of 1675 mAh g⁻¹ regarding the sulfur amount used in the cathode electrode.

3. Results and Discussion

Ti₃C₂T_x (or Ti₃C₂) MXenes are well-known materials because of their two-dimensional structures and high electronic conductivity. Ti₃C₂T_x MXenes were obtained from the Ti₃AlC₂ MAX phase using the LiF+HCl etching solution. During exfoliation of Ti₃C₂ sheets, 2D sheets form an accordion-like structure and then are dispersed to a homogeneous

solution using an ultrasonic bath. Since MXene structures are decorated with functional groups, they can be distributed by mechanical processes and form a homogeneous solution. The XRD diffraction pattern of the Ti₃C₂ MXene structures produced from the commercially available MAX phase is shown in Figure 1(a). The obtained XRD diffraction pattern is consistent with studies in the literature [20]. The XRD diffraction pattern of Ti₃C₂ indicates that Al layers were successfully removed from the structure.

The SEM image of the produced 2D Ti₃C₂ MXene structures is shown in Figure 1(b). The SEM image shows that MAX phase is etched well and MXene layers are successfully produced. The SEM and corresponding EDS elemental mapping images of the distributed Ti₃C₂ MXene sheets on a silicon substrate are shown in Figures 1(c)-(d). According to the EDS elemental mapping images in Figure 1(d), titanium and carbon are present in Ti₃C₂ MXene. At the same time, oxygen and fluor elements originate from the surface functional groups on the Ti₃C₂ MXene sheets.

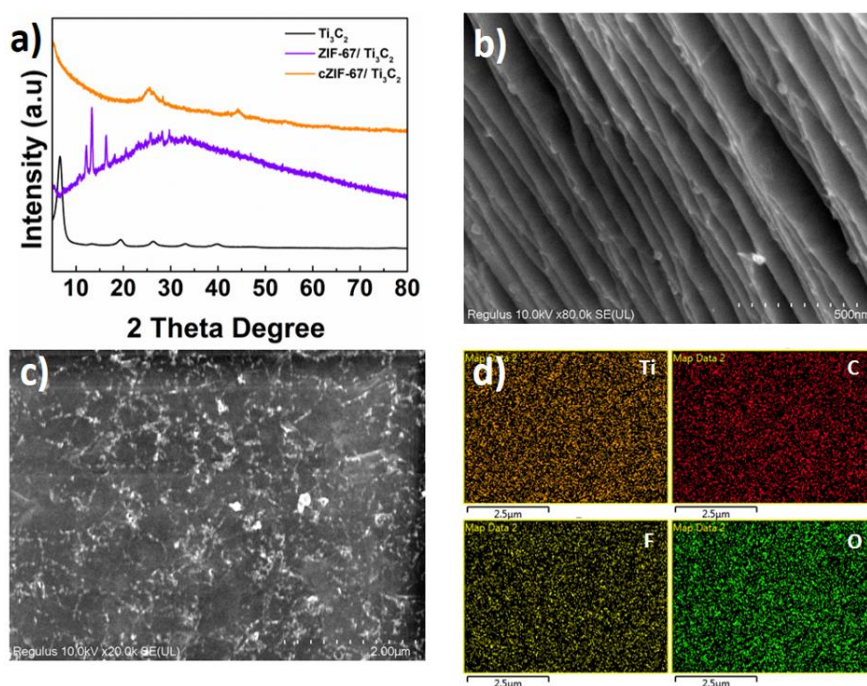


Figure 1. (a) XRD patterns of MXene and ZIF-67/MXene structures. (b)-(c) SEM image of two-dimensional Ti₃C₂ MXenes, and (d) EDS elemental mapping of Ti₃C₂ MXenes.

2D Ti₃C₂ MXenes were combined with ZIF-67 MOFs to form nanocomposite structures. Co⁺² metal ions were mixed with MXene sheets using a magnetic stirrer, and the Co⁺² ions were coordinated onto the MXenes. Then, MOF structures were synthesized on MXene layers in a controlled manner with the ligand groups added according to the 1:20 molar metal ion-to-ligand ratio. Three different mass ratios of ZIF-67/Ti₃C₂ nanocomposites (1:1, and 3:1) were synthesized and then carbonized to obtain c-ZIF-67/Ti₃C₂ nanocomposites. Figure 1(a) shows the XRD patterns of the ZIF-67/Ti₃C₂ nanocomposite structure, containing 3:1 mass ratio of ZIF-67 and Ti₃C₂, and the cZIF-67/Ti₃C₂ after the thermal treatment. The XRD pattern of the nanocomposite with 3:1 mass ratio of ZIF-67 and Ti₃C₂ shows characteristic diffraction peaks of ZIF-67. Due to the well-ordered crystalline structure of MOFs, the strong XRD peaks of ZIF-67 were observed. Figure 1(a) shows the

XRD pattern of the thermally treated nanocomposite structure (c-ZIF-67/Ti₃C₂). The functional groups on the surface of the Ti₃C₂ layers are eliminated at 600 °C under argon gas flow, and the ZIF-67 structures are carbonized, transforming into heteroatom (nitrogen)-doped carbon structures. The XRD pattern of the cZIF-67/Ti₃C₂ nanocomposite demonstrates that the diffraction peaks of ZIF-67 are eliminated, and only the carbon-related diffraction pattern is predominantly obtained. The reason for the significant loss of the ZIF-67 crystalline structure peaks in the XRD pattern after carbonization is that the resulting heteroatom-doped carbon structure is slightly graphitic carbons.

The SEM and EDS elemental mapping images of the fabricated nanocomposite containing 1:1 mass ratio ZIF-67/Ti₃C₂ are shown in Figure 2. ZIF-67 particles are synthesized on MXene layers to form a nanocomposite structure. According to the EDS elemental mapping images shown in Figure 2, titanium is only present in MXene, while cobalt, and nitrogen elements are originated from ZIF-67 structures.

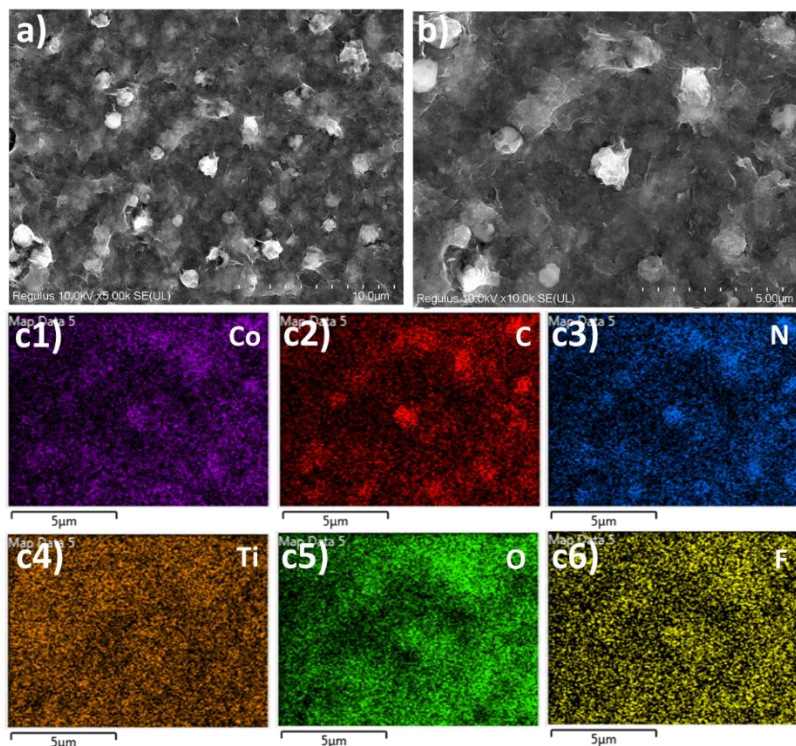


Figure 2. SEM and EDS elemental mapping images of ZIF-67/Ti₃C₂ MXene structures.

Figure 3 shows the SEM and EDS elemental mapping images of the 3:1 cZIF-67/Ti₃C₂ nanocomposite. The SEM images show that the nanocomposite structure has transformed into a three-dimensional porous structure with a high surface area after carbonization. The EDS elemental mapping images show that the samples contain a high amount of nitrogen, indicating that the MOF structures have transformed into carbon structures with a high nitrogen content.

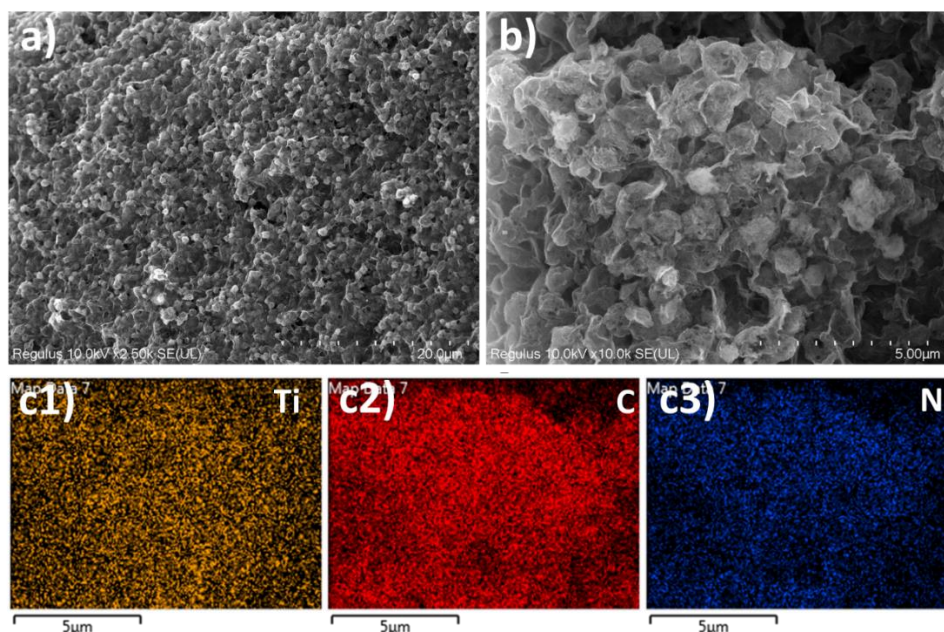


Figure 3. SEM and EDS elemental mapping images of cZIF-67/Ti₃C₂ nanocomposite with 3:1 mass ratio.

Due to the small lateral size and layered structure of MXenes, consisting of three rows of metal and two rows of carbon atoms, they have relatively low specific surface areas than the other 2D materials. On the other hand, the cMOF/MXene structures obtained by nanocomposite formation with two-dimensional MXene and MOF polyhedral particles have high surface areas and pore volumes. Figure 4(a) shows the BET surface area analysis of ZIF-67/MXene nanocomposite structures. The produced ZIF-67/MXene nanocomposite structures with 1:1 and 3:1 ratios have 311 and 340 m²/g surface areas, respectively.

Sulfur impregnation was performed on the heteroatom-doped cZIF-67/Ti₃C₂ structures via melt fusion method, and the sulfur content in the fabricated S/cZIF-67/Ti₃C₂ was determined by TGA analysis. Figure 4(b) shows the TGA results of the S/cZIF-67/Ti₃C₂ nanocomposite structure. The TGA result shows that cZIF-67/Ti₃C₂ nanocomposites mixed with sulfur at three times their mass contain approximately 75 % sulfur.

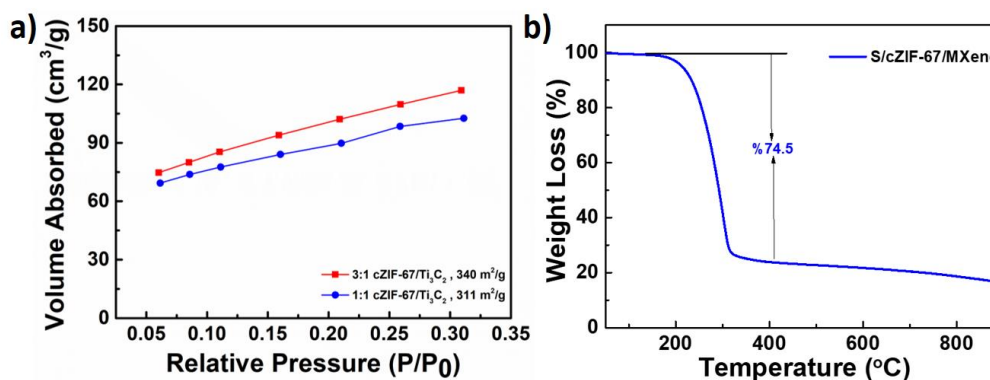


Figure 4. (a) Surface area analysis of ZIF-67/MXene nanocomposite structures. (b) TGA analysis of S/cZIF-67/Ti₃C₂ nanocomposite structures.

Electrochemical energy storage properties of the fabricated cathodes using cZIF-67/Ti₃C₂ nanocomposites with different mass ratios were investigated. Cyclic voltammetry (CV) measurements of the fabricated Li-S cells were done in a voltage window of 1.6-2.8 V. The CV results of the fabricated cathodes at a scan rate of 0.1 mV s⁻¹ are shown in Figure 5(a). The oxidation peaks of sulfur are located around 2.4 V, while the reduction peaks are observed around 2.25 and 1.95 V. The fabricated Li-S batteries with the 3:1 mass ratio cZIF-67/Ti₃C₂ nanocomposite have a sharp oxidation peak, while the other nanocomposite shows combined double peaks. CV results of the fabricated S/cZIF-67/Ti₃C₂ cathodes were also obtained at different scan rates and are shown in Figure 5(b). The obtained CV results show that sulfur's oxidation and reduction peaks shift to higher and lower voltage values as the scan rate increases. The results demonstrate that the produced cathode electrodes have reversible electrochemical performance.

To analyze the charge storage mechanism of the fabricated LSBs more clearly, the CV measurements at different scan rates shown in Figure 5(b) were analyzed and are shown in Figure 5(c)-(e). The diffusive and surface capacitive contribution calculations are analyzed using Equations (4) and (5);

$$i = av^b \quad (4)$$

$$i(v)/v^{1/2} = k_1.v + k_2.v^{1/2} \quad (5)$$

where $k_1.v$ indicates that the surface capacitive contribution is dominant, while $k_2.v^{1/2}$ means the diffusion-based contribution is effective. Generally, high surface area materials show a more widespread surface capacitive effect. When the scan rate decreases, diffusion (purple color) processes are effective, while at high scan rates, the surface capacitive (blue color) is dominant. It is seen that the surface capacitive effect is more pronounced at high scan rates, and the diffusion contribution is more significant at low scan rates for the S/cZIF-67/Ti₃C₂ cathodes.

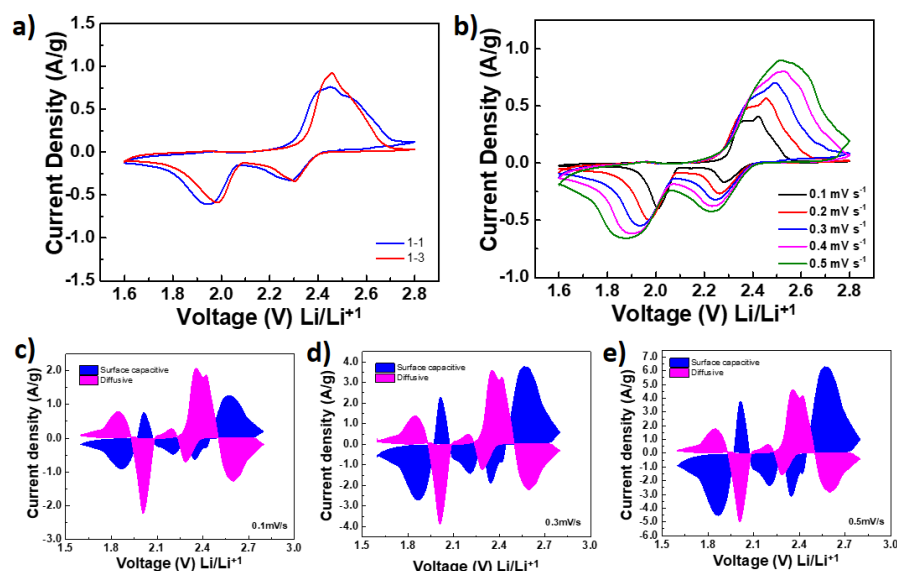


Figure 5. (a) CV measurements of Li-S batteries prepared with S/cZIF-67/Ti₃C₂ cathodes at 0.1 mV/s scan rate. (b) CV measurements of Li-S batteries at different scan rates. (c)-(e) Charge storage mechanism of S/cZIF-67/Ti₃C₂ Li-S battery cathodes.

Figure 6(a)-(b) shows the galvanostatic charge-discharge (GCD) curves of the Li-S batteries at 0.1 C-rate. The fabricated batteries have flat discharge plateaus around 2.3 V and 2.1 V during discharge. Li-S batteries using S/cZIF-67/Ti₃C₂ cathodes reached specific capacity values of approximately 750-780 mAh/g at 0.1 C-rate. GCD measurements were repeated at different C-rates to determine the fabricated Li-S batteries' GCD properties and specific capacities. Figure 6(c) shows the specific capacity change with respect to the C-rate. Battery devices naturally have some capacity drop at high C-rates due to the slow diffusion kinetics. The fabricated Li-S battery devices demonstrated high rate capability at different C-rates. Galvanostatic charge-discharge measurements were also applied to fabricated Li-S batteries at a constant 1.0 C-rate. Figure 6(d) shows the cycle life and capacity retention measurement results at 1.0 C-rate for the fabricated Li-S batteries. After 300 GCD cycles, S cathodes containing 3:1 mass ratio cZIF-67/Ti₃C₂ showed higher electrochemical performance and capacity retention compared to 1:1 mass ratio cZIF-67/Ti₃C₂ cathodes. The obtained results demonstrate that the fabricated nanocomposite structures improved the electrochemical stability and the performance of the Li-S batteries.

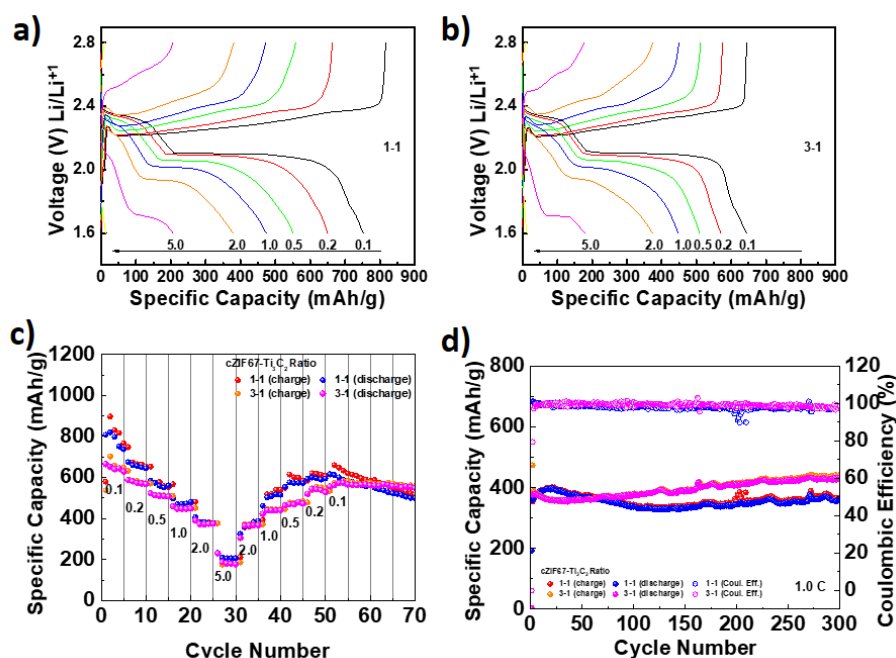


Figure 6. (a)-(b) GCD measurements of the fabricated Li-S batteries with nanocomposite cathodes containing different mass ratios of cZIF-67/Ti₃C₂ at different C-rates. (c) Rate capabilities of the fabricated Li-S batteries. (d) Cycle life and capacity retentions at 1.0 C-rate.

4. Conclusions

cZIF-67/Ti₃C₂ nanocomposite structures with two different mass ratios were synthesized using the wet chemistry method, and their structural characterizations were performed. 3D nanocomposite structures were fabricated by growing high surface area ZIF-67 MOFs on the conductive two-dimensional Ti₃C₂ MXene sheets. The electrochemical charge storage properties of the fabricated Li-S battery devices were carried out using CV and GCD measurements. The fabricated nanocomposite cathodes were found to have potential for use

in Li-S batteries. In GCD measurements, the fabricated Li-S batteries with 1:1 mass ratio S/cZIF-67/Ti₃C₂ cathodes reached a specific capacity of approximately 750 mAh/g. S cathodes containing 3:1 mass ratio cZIF-67/Ti₃C₂ showed higher capacity retention at 1.0 C-rate after 300 GCD cycles. The fabricated cZIF-67/Ti₃C₂ nanocomposite materials demonstrated their potential as a sulfur-host in Li-S batteries with remarkable properties such as high rate capability, capacity retention, and rapid fabrication.

Ethics in Publishing

There are no ethical issues regarding the publication of this study.

Author Contributions

In this study, Recep YUKSEL contributed to scientific literature research, article creation, experimental design, analysis, preparation, and writing of the article results.

Acknowledgments

This study was supported by the Eskişehir Osmangazi University Scientific Research Projects Coordination Unit under project number FBG-2021-1703. The researchers thank the ESOGU BAP coordination for their support.

References

- [1] Yuksel, R., et al., Necklace-like Nitrogen-Doped Tubular Carbon 3D Frameworks for Electrochemical Energy Storage. *Advanced Functional Materials*, 2020. **30**(10): p. 1909725.
- [2] Yuksel, R., et al., Metal-Organic Framework Integrated Anodes for Aqueous Zinc-Ion Batteries. *Advanced Energy Materials*, 2020. **10**(16).
- [3] Pang, Q., et al., Advances in lithium–sulfur batteries based on multifunctional cathodes and electrolytes. *Nature Energy*, 2016. **1**(9): p. 16132.
- [4] Huang, L., et al., Electrode Design for Lithium–Sulfur Batteries: Problems and Solutions. *Advanced Functional Materials*, 2020. **30**(22): p. 1910375.
- [5] Fang, R., et al., More Reliable Lithium-Sulfur Batteries: Status, Solutions and Prospects. *Advanced Materials*, 2017. **29**(48): p. 1606823.
- [6] Boyd, D.A., Sulfur and its role in modern materials science. *Angewandte Chemie International Edition*, 2016. **55**(50): p. 15486-15502.
- [7] Qiu, T., et al., Metal–Organic Framework-Based Materials for Energy Conversion and Storage. *ACS Energy Letters*, 2020. **5**(2): p. 520-532.
- [8] Rana, M., et al., Oriented nanoporous MOFs to mitigate polysulfides migration in lithium-sulfur batteries. *Nano Energy*, 2020. **75**: p. 105009.
- [9] Ji, X., K.T. Lee, and L.F. Nazar, A highly ordered nanostructured carbon–sulphur cathode for lithium–sulphur batteries. *Nature Materials*, 2009. **8**(6): p. 500-506.
- [10] Kim, H., et al., Synthesis of three-dimensionally interconnected sulfur-rich polymers for cathode materials of high-rate lithium–sulfur batteries. *Nature Communications*, 2015. **6**(1): p. 7278.

- [11] Seo, S.-D., et al., "Brain-Coral-Like" Mesoporous Hollow CoS₂@N-Doped Graphitic Carbon Nanoshells as Efficient Sulfur Reservoirs for Lithium–Sulfur Batteries. *Advanced Functional Materials*, 2019. **29**(38): p. 1903712.
- [12] Wang, H., et al., Metal-organic frameworks for energy applications. *Chem*, 2017. **2**(1): p. 52-80.
- [13] Li, G., et al., A microporous carbon derived from metal-organic frameworks for long-life lithium sulfur batteries. *International Journal of Energy Research*, 2020. **44**(3): p. 2126-2136.
- [14] Guan, B., et al., Blocking Polysulfide with Co₂B@ CNT via "Synergetic Adsorptive Effect" toward Ultrahigh-Rate Capability and Robust Lithium–Sulfur Battery. *ACS nano*, 2019. **13**(6): p. 6742-6750.
- [15] Yuksel, R., et al., Necklace-like Nitrogen-Doped Tubular Carbon 3D Frameworks for Electrochemical Energy Storage. *Advanced Functional Materials*, 2020. **30**(10).
- [16] Zhao, M., et al., A Perspective toward Practical Lithium–Sulfur Batteries. *ACS Central Science*, 2020. **6**(7): p. 1095-1104.
- [17] Li, K., et al., 3D MXene Architectures for Efficient Energy Storage and Conversion. *Advanced Functional Materials*, 2020. **30**(47): p. 2000842.
- [18] Liang, X., A. Garsuch, and L.F. Nazar, Sulfur cathodes based on conductive MXene nanosheets for high-performance lithium–sulfur batteries. *Angewandte Chemie*, 2015. **127**(13): p. 3979-3983.
- [19] Zhao, Q., et al., 2D MXene nanosheets enable small-sulfur electrodes to be flexible for lithium–sulfur batteries. *Nanoscale*, 2019. **11**(17): p. 8442-8448.
- [20] Naguib, M., et al., Two-Dimensional Nanocrystals Produced by Exfoliation of Ti₃AlC₂. *Advanced Materials*, 2011. **23**(37): p. 4248-4253.

Preparation of Aloe Vera Gel Containing Solid Lipid Nanoparticles for Treatment of Eczema

Hatice ÇETİN¹, Hüseyin YILMAZ², Güliz AK^{2*}

¹Department of Biochemistry, Graduate School of Natural and Applied Sciences, Ege University, İzmir, Türkiye

²Department of Biochemistry, Faculty of Science, Ege University, İzmir, Türkiye

Received: 06/12/2024 **Revised:** 14/10/2024, **Accepted:** 12/12/2024, **Published:** 31/12/2024

Abstract

Atopic dermatitis, also known as eczema, is a chronic skin disorder that occurs as a result of many diseases and genetic factors. Decreased filaggrin and ceramide levels in the epidermis are considered the prime pathogenesis of atopic dermatitis. Aloe vera contributes to the treatment of atopic dermatitis thanks to its anti-inflammatory, moisturizing and immune response regulating properties. SLN were characterized using UV-Visible Spectroscopy, Fourier Transform Infrared Spectroscopy (FTIR), Scanning Electron Microscopy (SEM). BMV-loaded SLN (BMV-SLN) was analyzed by FTIR and SEM. Release of BMV from nanoparticles and its free solution form was also achieved. The gel formulation of BMV-SLN was developed using Carbopol 940 and Aloe vera. BMV bound to SLN with 87% efficiency, and controlled release of BMV from the nanoparticles was observed. BMV-bound SLN gel was formulated at pH 5.9. This gel formulation has the potential to be used in treatment problems caused by atopic dermatitis.

Keywords: Eczema, solid lipid nanoparticle, betamethasone valerate, Aloe vera gel.

Egzema Tedavisine Yönelik Katı Lipid Nanopartiküller İçeren Aloe Vera Jel Hazırlanması

Öz

Egzama olarak da bilinen atopik dermatit, birçok hastalık ve genetik faktör sonucu oluşan kronik bir cilt rahatsızlığıdır. Epidermisteki azalmış filaggrin ve seramid düzeyleri, atopik dermatitin ana patogenezi olarak kabul edilmektedir. Aloe Vera, anti-inflamatuar, nemlendirici ve immün yanıtı düzenleyici özellikleri sayesinde atopik dermatitin tedavisine katkıda bulunur. SLN, UV-Görünür Spektroskopisi, Fourier Dönüşümlü Kızılötesi Spektroskopisi (FTIR), Taramalı Elektron Mikroskopu (SEM) kullanılarak karakterize edilmiştir. BMV yüklü SLN (BMV-SLN), FTIR ve SEM ile analiz edilmiştir. BMV-SLN'nin jel formülasyonu, Carbopol 940 ve Aloe vera kullanılarak geliştirilmiştir. BMV, SLN'ye %87 verimlilikle yüklenmiştir ve nanopartiküllerden BMV'nin kontrollü salımı gözlemlenmiştir. BMV yüklü SLN jeli, pH 5,9'da formüle edilmiştir. Bu jel formülasyonun atopik dermatitin neden olduğu sorunların tedavisinde kullanılma potansiyeli olduğu söylenebilmektedir.

Anahtar Kelimeler: Egzama, katı lipid nanopartikül, betametazonvalerat, Aloe vera jel.

*Corresponding Author: guliz.ak@ege.edu.tr

Hatice ÇETİN, <https://orcid.org/0009-0001-8702-7200>

Hüseyin YILMAZ, <https://orcid.org/0009-0005-7447-9100>

Güliz AK, <https://orcid.org/0000-0001-9613-6348>

1. Introduction

Atopic dermatitis, also known as atopic eczema, is a chronic inflammatory skin disorder caused by the interaction between multiple genetic and environmental factors. It is characterized by itchy and scaly skin lesions, often localized on the flexural surfaces of the body [1]. Today, the prevalence of atopic dermatitis worldwide is increasing significantly. The disease occurs in 20% of children and 1%-3% of adults [2]. It causes difficulties in the daily lives of patients, reduces their quality of life, and limits their mobility. Atopic dermatitis is a chronic inflammatory skin condition that requires a multifaceted approach to treatment. The aim of treatment is to restore epidermal barrier function and reduce skin inflammation. This can be achieved by moisturizing the skin and using topical anti-inflammatory agents such as topical corticosteroids and calcineurin inhibitors [3].

Betamethasone Valerate is a highly potent topical corticosteroid. Betamethasone is a topically inactive synthetic corticosteroid. To be effective topically, it needs to be administered in the form of esters such as betamethasone 17-valerate or betamethasone 17,21-dipropionate. The esterified form usually has an increased lipophilic structure, which allows the drug molecule to better penetrate through the lipid membrane of the skin. It helps to relieve swelling and irritation of the skin. Since its effects on humans and animals are well known, it is frequently used in adults and children. [2]

Nanoparticles, solid lipid nanoparticles, nanosuspension, nanoemulsion and nanocrystals are important drug delivery systems developed using nanotechnology principles [4]. Solid lipid nanoparticles (SLNs) are aqueous colloidal dispersions with sizes ranging from 10 to 1000 nanometers, consisting of a matrix of solid, biodegradable lipids. SLNs have been developed for peroral, oral, rectal, dermal, and pulmonary applications. SLNs are widely preferred due to their properties such as excellent biocompatibility, lack of cytotoxicity, controlled drug release and drug targeting, increased drug stability, high drug carrying capacity, and better transport of lipophilic drugs [5].

Gel formulations are one of the forms of medication used in the treatment of atopic dermatitis. Gels contain active ingredients dissolved or dispersed in a matrix containing water and other solvents. The use of gel formulations in treatment has many advantages. They are easy to apply and quickly absorbed, as well as ensuring that the active ingredients of the product are effectively absorbed, and the symptoms of the disease are relieved. However, there are some important points to consider. Gels are affected by heat and humidity, so the product should be stored at the appropriate temperature. In conclusion, gel formulations are an effective treatment method in the treatment of atopic dermatitis [6].

The Aloe vera plant has been used for centuries for its health, beauty, medicinal and skin care properties. It contains 77 potentially active compounds, including vitamins, enzymes, minerals, fatty acids, sugar, lignin, saponin, salicylic acid and amino acids. Thanks to the substances it contains, it has healing, protection from ultraviolet and gamma rays, anti-inflammatory,

antiviral, moisturizing, anti-aging, antiseptic and immune system effects. Aloe vera is used in atopic dermatitis due to its anti-inflammatory, moisturizing and immune response regulating effects [7].

The values that make this study unique can be considered as the preparation of the gel form of drug loaded solid lipid nanoparticles, making it easy to apply, increasing the speed of action, efficacy and absorption of the drug from the skin. It is thought that solid lipid nanoparticles could affect the area where the drug should affect at higher rates, reducing the drug dosage that should be used in the treatment, thus protecting patients from possible side effects and providing a positive effect on their economic situation by using the drug for a shorter period of time. In addition the anti-microbial, anti-inflammatory, wound healing, antioxidant and immune-boosting properties of the Aloe vera extract could reduce the treatment of the factors that cause the disease and the possibility of the disease recurring.

The advantage of the study compared to the currently used treatments is that it is loaded into a delivery system, allowing the drug to affect the treated area directly, effectively, quickly and in a controlled manner, thus shortening the recovery period of the patients. Compared to the drug loaded treatment systems used with the Aloe vera gel in its content, it contributes to the healing of the disease with its anti-inflammatory and moisturizing effects. It is shown that this formulation, prepared in a simple and economical way, could contribute to human health by treating the pain, itching and problems that prevent patients from daily life due to eczema more effectively and in a shorter time.

2. Materials and Methods

2.1 Materials

Betamethasone 17-Valerate (BMV), Cetyl Palmitate (CP), Polysorbate 80 and Acetonitrile were purchased from Sigma- Aldrich. Carbopol 940 was bought from Acros Organics and Triethanolamine (TEA) was purchased from Carlo Erba. All other chemicals used were of analytical grade and were used without any further processing or purification.

2.2 Synthesis of Solid Lipid Nanoparticles

Solid lipid nanoparticle synthesis was performed following procedure reported by Ak. et al., 2021 [8]. Solid lipid nanoparticles were formulated using combination of the two techniques named high shear homogenizer and ultrasonication. Aqueous phase, containing Tween- 80, was heated up to 65°C in water bath. 100 mg cetyl palmitate (lipid phase) was heated up to the same temperature separately. Two hot phases were then mixed together just before homogenization, and pre-emulsion was achieved using a high-speed homogenizer (Ultraturrax, Isolab) at 22000 rpm for 2 min. This pre-emulsion continued to be homogenized for 1 min in a sonic bath. Subsequently, the emulsion was quickly cooled to 4°C. The emulsion was left until it reached room temperature. In order to obtain pure nanoparticles, they were placed in a pre-heated

dialysis membrane (12000-14000 MWCO) (Sigma-Aldrich) and they were dialyzed against 50 mL of pure water at room temperature for 4 hours [9].

2.3 Encapsulation of BMV into SLN

The same techniques used for preparing drug-free SLN were applied for the formulation of SLN loaded with BMV. BMV solutions prepared with acetonitrile to final concentrations of 0.25, 0.5, 0.75, 1, 1.25 mg/mL were added to the molten lipid phase at 65 °C and the procedure above was applied. Dialysis procedure was performed to remove free drug and to determine drug loading efficiency. 2 mL of drug loaded SLN were placed in a pre-heated dialysis membrane and dialysis was performed against 50 mL of d-water at room temperature for 4 hours [9]. The dialysis samples analyzed by UV-VIS spectrophotometer (Cary UV Vis 60 spectrophotometer) using calibration graph at 236 nm. The drug loading efficiency (DLE %) was given by the formula 1:

$$\text{Drug loading efficiency (DLE)(\%)} = \frac{[\text{Initial drug amount}(\mu\text{g}) - \text{Unbound drug amount}(\mu\text{g})]}{[\text{Initial drug amount}(\mu\text{g})]} \times 100 \quad (1)$$

2.4 Characterization Studies

The chemical structures of dried SLN and BMV-loaded SLN were analyzed using Fourier transform infrared spectroscopy (FTIR). The sample was compressed into a transparent disk and scanned from 4000 to 400 cm⁻¹ using an average of 16 scans, with a resolution of 1 cm⁻¹. Scanning electron microscopy (SEM) was used to determine the morphological structure and size of gold-coated SLN and gold-coated drug-loaded SLN.

2.5 In vitro Drug Release

In vitro drug release studies were performed using the dialysis membrane with an MWCO value of 12000-14000 (Sigma-Aldrich) in 10 mL 10 mM phosphate buffer (pH 7.4) and 10 mL 10 mM acetate buffer (pH 5.5). 2 mL of BMV-loaded SLN dispersion was taken into the dialysis membrane and dialyzed at 300 rpm at 32°C and 37°C for 48 hours. At the intervals of 0.5, 1, 2, 4, 6, 8, 24 and 48h, all dialysis media replaced with a fresh buffer at the same temperature [10]. The amount of released BMV was determined using UV-VIS spectrophotometer at 236 nm. Cumulative drug release was calculated using the following formula 2:

$$\text{Cumulative release (\%)} = \frac{\text{Amount of drug released } (\mu\text{g})}{\text{Initial drug amount } (\mu\text{g})} \times 100 \quad (2)$$

In vitro free drug release studies were performed using the dialysis membrane in 10 mL 10 mM phosphate buffer (pH 7.4) and 10 mL 10 mM acetate buffer (pH 5.5). BMV was prepared in a mixture of acetonitrile and distilled water 1:1 (v/v) with final concentration 1 mg/mL. 1 mL of drug solution was taken into the dialysis membrane and dialyzed at 300 rpm at 37°C for 24 h. At the intervals of 0.5, 1, 1.5, 2, 2.5, 3, 4, 5, 6, and 24h, all dialysis media replaced with a

warm fresh buffer at the same temperature[10].The amount of released BMV was determined and cumulative drug release was calculated using formula (2).

2.6 Preparation of Aloe Vera Gel Formulation Containing BMV-SLN

Carbopol 940, prepared as 1% (w/v), was stirred with a magnetic stirrer for 24 h[11].In order to form the gel structure TEA was added to the Carbopol 940, which was stirred with the magnetic stirrer at 3000 rpm and the pH was adjusted to 6.00[12].Aloe vera leaves were washed with chlorinated water, cut and the gel inside was collected.The obtained gel was homogenized with a blender. After the homogenization process, the obtained extract was filtered and stored at +4°C[13].5 g of the prepared carbopol gel was taken and 1, 2, 2.5 and 3 mL of Aloe vera extract and 1.8 mg (optimized amount) of BMV containing nanoparticle dispersion were added into the gel. The formulations were evaluated based on pH and spreadability.

3. Results and Discussion

3.1 Synthesis and Characterization of Solid Lipid Nanoparticles

In this study, solid lipid nanoparticles consisting of cetyl palmitate lipid as a solid core coated with aqueous surfactant were obtained. Solid lipid nanoparticles were synthesized by high-speed homogenization and ultrasonication at temperatures above the melting temperature to ensure homogenization of the lipid emulsion [14]. FTIR spectra of the obtained SLN and cetyl palmitate are shown in Figure 1. Several peaks were observed in the FTIR spectrum of SLN in the spectrum range of 400-4000 cm^{-1} .The peak at 1734 cm^{-1} corresponded to C=O tension, the peak at 1462 cm^{-1} was ascribed to C-H bending, the peak at 1090–1300 cm^{-1} corresponded to C-O stretching which were also seen in FTIR data of cetyl palmitate, Tween- 80. The peaks at 2916 and 2848 cm^{-1} were related to aliphatic C-H stretching. The characteristic peaks of cetyl palmitate and Tween 80 are also present in the spectrum of the obtained solid lipid nanoparticles (SLNs), resulting in similar spectra for cetyl palmitate and SLNs. The results are consistent when compared with similar studies [15].

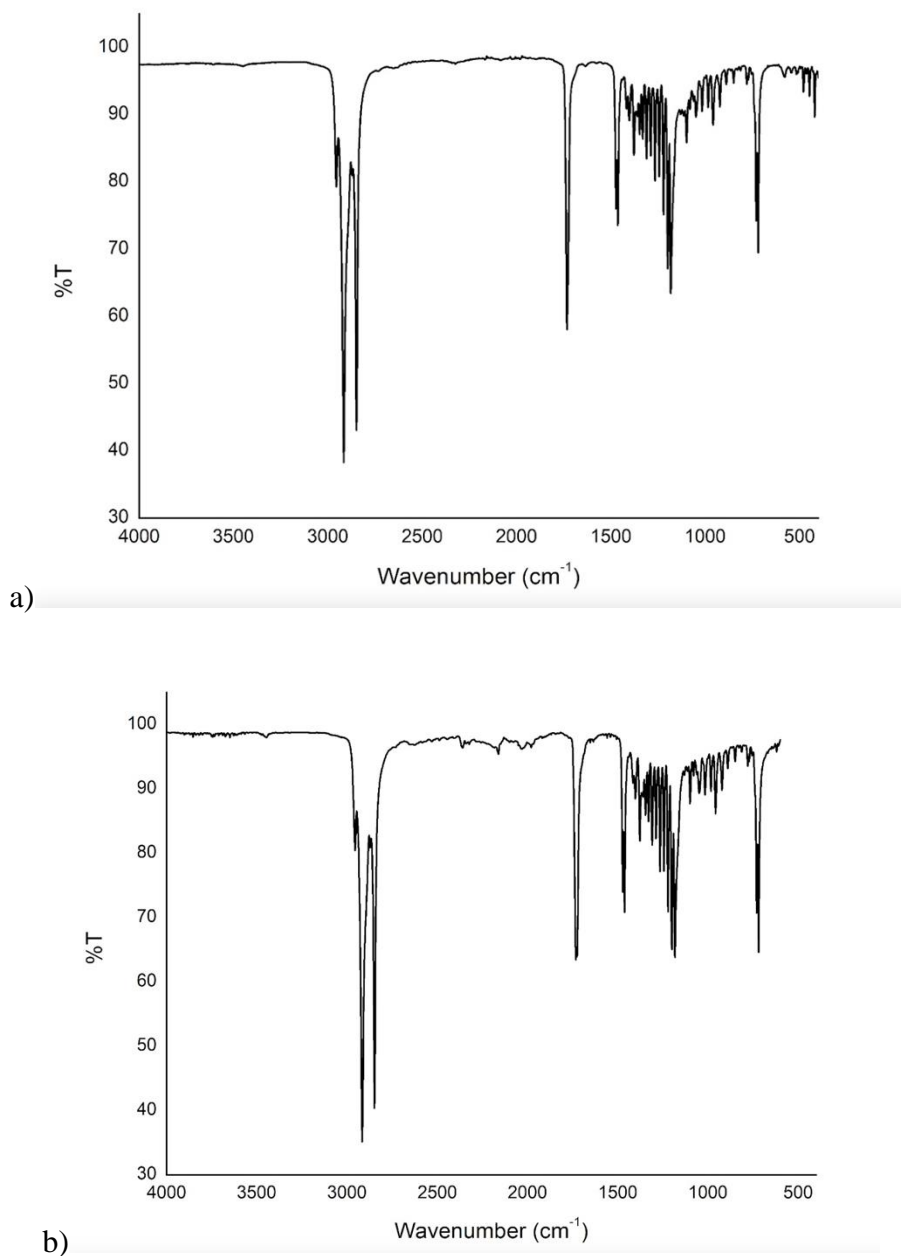


Figure 1. FTIR spectra of a) solid lipid nanoparticles and b) cetyl palmitate.

The morphology of the nanoparticles was investigated by the SEM imaging method and shown in Figure 2. According to the shape, the average size of the nanoparticles was determined to be approximately 200 nm and the structure was found to be spherical, flat and smooth, which is consistent with similar studies in the literature [8].

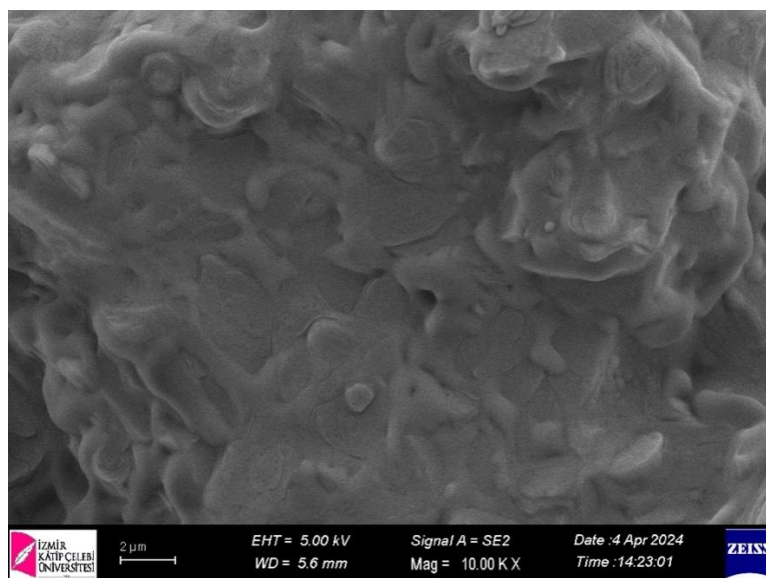


Figure 2. SEM image of solid lipid nanoparticles.

3.2 Encapsulation of BMV into SLN

For the calibration curve of Betamethasone valerate, which has low water solubility, the main stock drug was prepared in acetonitrile-distilled water 1:1 (v/v) mixture and dilutions were made from the main stock at concentrations of 5, 10, 15, 20, 25, 30, and 35 $\mu\text{g/mL}$ [16]. The maximum absorbance peak of the drug was determined as 236 nm. The R^2 of the BMV standard graph was found to be 0.9997. The calibration curve of the drug is given in Figure 3.

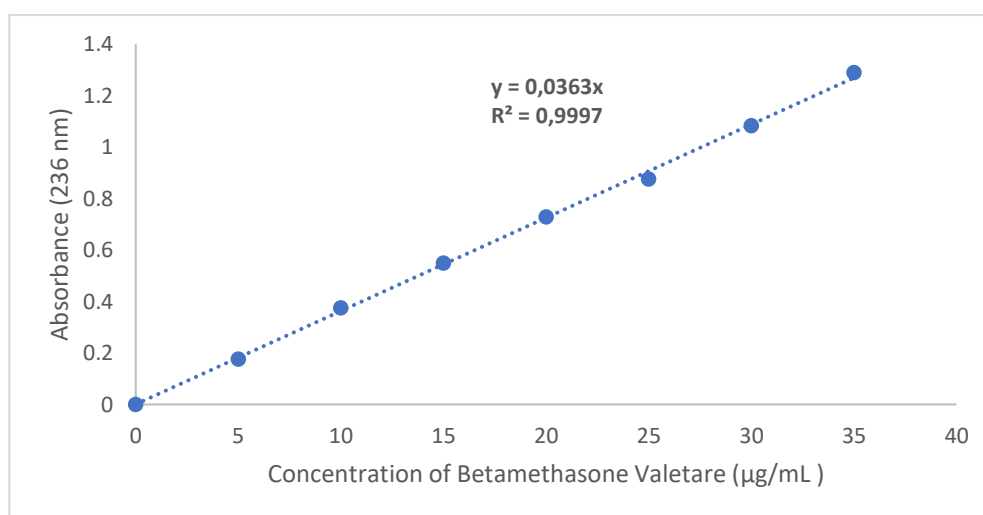


Figure 3. Betamethasone valerate calibration curve.

Solid lipid nanoparticles containing initial dose of BMV at 0.25, 0.50, 0.75, 1.00 and 1.25 mg/ml were prepared. Drug loading efficiencies of the prepared BMV loaded nanoparticles were calculated. The obtained results shown in Table 1. The nanoparticle group (initial BMV dose of 1mg/mL) with the highest drug binding efficiency was selected as optimum for further studies. As reported by Md S. the drug/polymer mass ratio tested were 0.5:1, 0.25:1, 0.17:1, 0.125:1, and 0.1:1. The obtained result depicts that 0.5:1 (drug/polymer) ratio was found to have the highest %EE of $94.39 \pm 1.10\%$ whereas 0.1:1 has the least encapsulation

of $62.43 \pm 6.99\%$. It can be seen that an increase in drug/polymer mass ratio results in an increase in EE. Hence, this proves that the increasing amount of drug in the organic phase remarkably influences the EE due to the higher interaction between the drug and the polymer [17].

Table 1. Encapsulation efficiencies (%) of drug at different concentrations into solid lipid nanoparticles.

Initial BMV Concentration (mg/mL)	Loaded Drug Concentration (mg/mL)	Encapsulation Efficiency (%)
0.25	0.15	58
0.50	0.37	74.5
0.75	0.62	82.1
1	0.90	89.4
1.25	1.10	88.2

3.3 Characterization of BMV loaded SLN

As reported by Pandey et al. the characteristic peaks of BMV appeared at 3422 cm^{-1} ($-\text{OH}$ stretching), 2955 cm^{-1} and 2872 cm^{-1} ($-\text{CH}$ stretching), 1731 cm^{-1} ($\text{C}=\text{O}$ stretching), 1616 cm^{-1} ($\text{C}=\text{C}$ stretching), and 1298 cm^{-1} and 1264 cm^{-1} ($-\text{CF}$ stretching) [18]. The FTIR spectrum of BMV-SLN is represented in Fig. 4. According to FTIR spectrum analysis of BMV-SLN, 2916 and 2847 cm^{-1} ($\text{C}-\text{H}$ tension band), 1732 cm^{-1} ($\text{C}=\text{O}$ tension band), 1464 cm^{-1} ($\text{C}-\text{H}$ bond bending band), 1099 and 1182 cm^{-1} ($\text{C}-\text{O}$ bond tension band), 730 cm^{-1} ($\text{C}-\text{H}$ bond bending vibration) were observed. Spectral analysis showed that the BMV-SLN specific functional groups on the surface of the nanoparticles exhibited almost the same chemical properties as cetyl palmitate and exhibited the main characteristic peaks of the entrapped drug. This study indicates that there is no molecular interaction that could change the chemical structure of BMV [19].

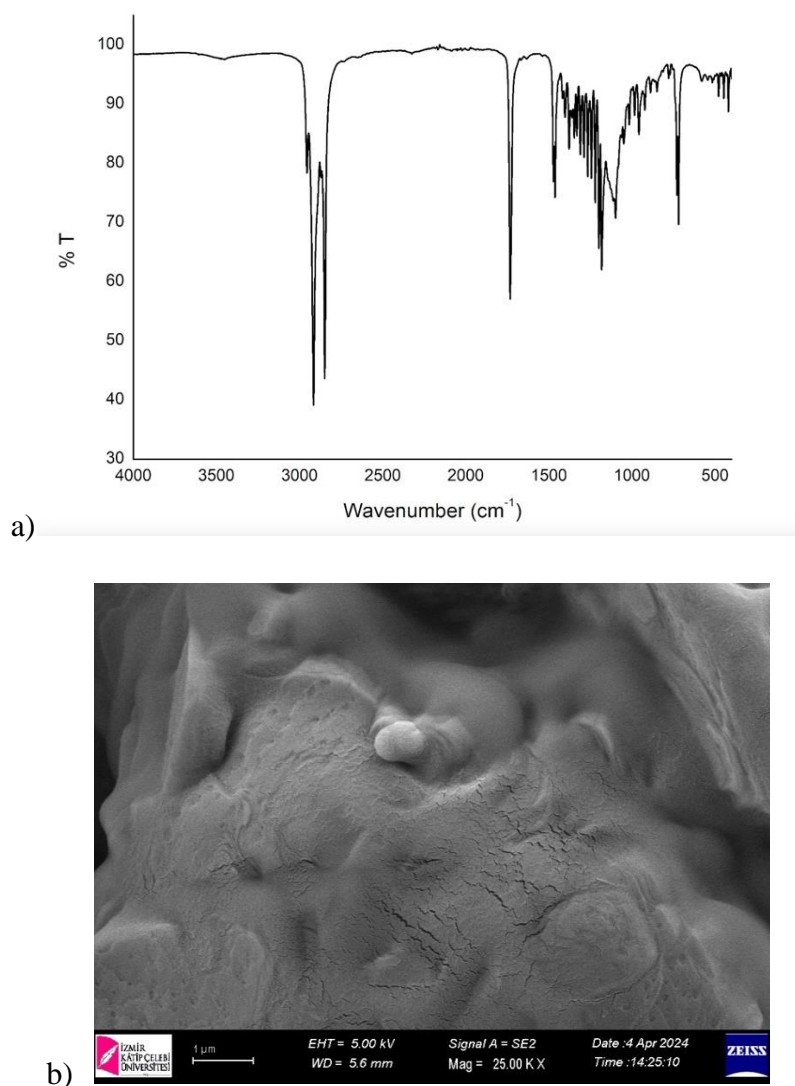


Figure 4. a) FTIR spectrum and b) SEM image of betamethasone valerate loaded solid lipid nanoparticles.

Furthermore, BMV-SLN were morphologically examined with SEM. According to the SEM image, it is seen that the nanoparticle has a shape close to spherical. The size of BMV-CPN also increased a little. According to the literature, as the amount of drug contained in the nanoparticles increases, their sizes also increase[17].

3.4 In vitro Drug Release

The in vitro drug release behavior of nanoparticles was investigated under physiological condition (pH 7.4) and under using simulated skin surface (pH 5.5) at 37°C and 32°C. As a result of the release, at the end of 48 hours at pH 7.4; 18.27% at 37°C, 11.44% at 32°C BMV was released from SLN. At pH 5.5; 24.66% at 37°C, 15.89% at 32°C BMV was released from the SLN at the end of 48 hours. The faster release of BMV in an acidic environment may be due to nanoparticle deterioration[8]. The pH of the skin is acidic. Therefore, more drugs will be released from nanoparticles interacting with the skin topically and a higher concentration of

drug will reach the diseased area. The *in vitro* release of BMV is affected by the lipidic components of SLN, which led to a simultaneous increase in the affinity of lipophilic BMV to lipidic components and caused a relatively low release compared to free release [19]. The results of the release studies are given in Figure 5.

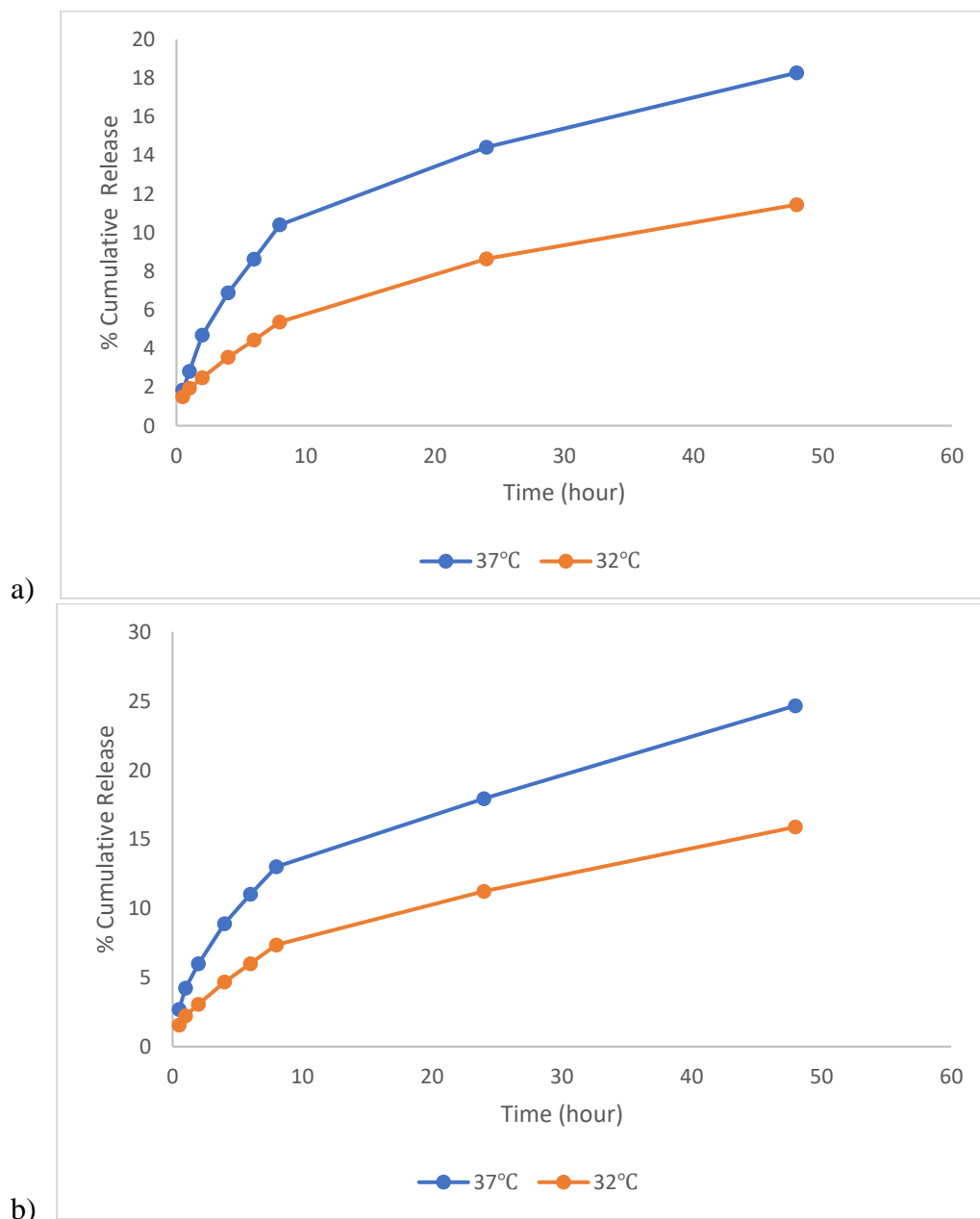


Figure 5. BMV release from nanoparticles in a) pH 7.4 and b) pH 5.5 buffer at 37°C and 32°C.

Free drug release was investigated at both acidic pH and physiological pH at 37°C. At pH 7.4, more than 50% of free BMV was released in the first 2.5 hours, and 84% of free BMV was released after 24 hours. At pH 5.5, more than 50% of free BMV was released in the first 2 hours, and at the end of 24 hours, 99% of free BMV was released. The reason for testing release studies at both pH values is to show that it is suitable for physiological pH values and to show that the

gel was developed for use on the skin surface and that it was worked in an acetate buffer that is close to the skin pH value. The results of the free drug release studies given in Figure 6.

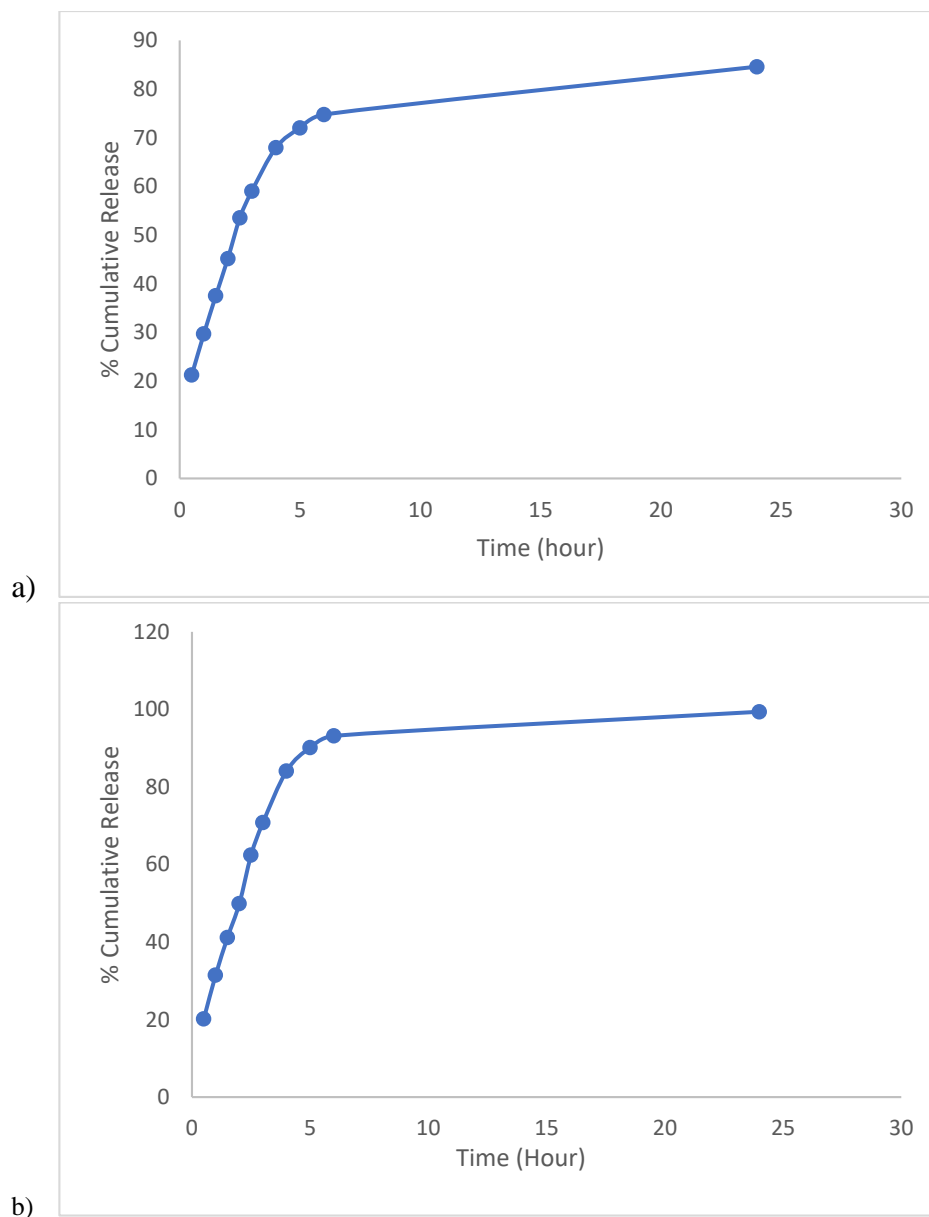


Figure 6. BMV release from free solution in a) pH 7.4 and b) pH 5.5 buffer at 37°C.

For the treatment of eczema, medications must be taken regularly and periodically in a certain dose. Patients usually ignore or forget this when using medications for a long time. When evaluated from this perspective, the controlled slow release of BMV allows for a uniform concentration of medication in the absorption area, allowing plasma concentrations to be maintained in the therapeutic range after absorption. In this way, the side effects of the medication are minimized and the frequency of application is also reduced.

3.5 Preparation of Aloe Vera Gel Formulation Containing BMV-SLN

The pH values of the samples prepared by adding 1, 2, 2.5 and 3 mL of Aloe vera extract and 1.8 g of BMV containing nanoparticle dispersion into 5 g of carbopol gel were measured and are shown in Table 2 and gel photographs are also displayed in Figure 7.

Table 2. Gel pH values obtained after adding Aloe vera extracts and BMV-CPN dispersion.

Contents	pH
BlankGel	6.24
1 mL Aloe vera extract - 2 mL BMV-CPN	6.05
2 mL Aloe vera extract - 2 mL BMV-CPN	5.86
2,5 mL Aloe vera extract - 2 mL BMV-CPN	5.76
3 mL Aloe vera extract - 2 mL BMV-CPN	5.66



Figure 7. Gel formulation photographs; (A) 5 g gel- 3 mL Aloe vera extract- 2 mL BMV-SLN dispersion; (B) 5 g gel- 2,5 mL Aloe vera extract- 2 mL BMV-SLN dispersion; (C) 5 g gel- 2 mL Aloe vera extract- 2 mL BMV-SLN dispersion; (D) 5 g gel- 1 mL Aloe vera extract- 2 mL BMV-SLN dispersion

As seen in Table 2, 2 mL of Aloe vera extract and 2 mL of BMV-CPN dispersion were selected as optimum to be added to the gel. Other ratios can also be accepted as pH suitable for the skin, and after 2 mL of Aloe vera extract, however the fluidity of the gel increased and its structure that can be applied to the skin began to deteriorate.

Studies by Şenyiğit et al. also showed that by using the gel formulation, the concentration of betamethasone valerate can be reduced and a higher flow can still be achieved. This may be a notable advance in terms of reducing dose-dependent side effects and increasing the risk-benefit ratio of betamethasone valerate[20]. The results of a randomized double-blind clinical study by Panahi et al. reported that Olivederma, a combination of Aloe vera and extra virgin olive oil, is superior to topical corticosteroids after 6 weeks of treatment in terms of disease severity, quality of life, and eosinophil count[21]. The data obtained as a result of both these studies and our study show that Aloevera gel formulation can be recommended as a promising alternative system for topical application of betamethasone valerate.

4 Conclusion

In the study, solid lipid nanoparticles were synthesized using cetyl palmitate and Tween-80, and BMV, which has been proven effective to treat eczema, was encapsulated into solid lipids with high efficiency. In this way, BMV, which has a hydrophobic character, was loaded into a lipid carrier; in order to increase the speed of action, effectiveness and skin absorption of the drug. With the anti-microbial, anti-inflammatory, wound healing, antioxidant and immune-boosting properties of the Aloe vera extract, the treatment of the factors that cause the disease and the possibility of the disease recurring can be reduced. With this formulation prepared with a simple and economical method, it is shown that it will contribute to human health by treating the pain, itching and problems that prevent the daily lives of patients due to eczema more effectively and in a shorter time. The study could be used for the benefit of human health and is promising.

Hypertrophic scar inflammation in eczematous lesions creates a strong barrier for dermal penetration of drugs. To overcome this difficulty, various new topical formulations such as solid lipid nanoparticles are quite suitable systems for penetration enhancement and sustained release. It is known that these preparations are not only applied as “drug carriers” but also act as “drug depots” to release active ingredients for a long time. The gel formulation formed by adding BMV loaded SLNs to aloe vera gel was aimed to deliver the drug dermally and thus prevent hepatic first pass metabolism and extensive fluctuations in drug-plasma levels resulting from repeated oral administration of rapidly eliminated drugs. In the future, it is aimed to complete pre-phase studies by determining efficacy, toxicology and biodistribution etc. with in-vivo studies and to reveal the potential of the formulation.

Ethics in Publishing

There are no ethical issues regarding the publication of this study.

Author Contributions

HaticeÇetin: Methodology, Validation, Investigation, Writing,

Hüseyin Yılmaz: Methodology, Investigation

GülizAk: Conceptualization, Methodology, Validation, Investigation, Writing, Supervision

Acknowledgements

This work was supported by Scientific and Technological Research Council of Turkey, TÜBİTAK 2209/A programme (Project No: 1919B012211887). A patent application has been filled with the Turkish Patent Institute for this study (2022/021280) with the support of Ege University.

References

- [1] Berke, R., Singh, A., &Guralnick, M. (2012). Atopic dermatitis: an overview. *American family physician*, 86(1), 35-42.
- [2]Byrne, J. (2018). *Analytical Studies Concerning the Stability of Betamethasone Valerate and Fusidic acid Hemihydrate in Topical Pharmaceutical Preparations*. National University of Ireland, Maynooth (Ireland).
- [3] Chong, M., &Fonacier, L. (2016). Treatment of eczema: corticosteroids and beyond. *Clinical reviews in allergy & immunology*, 51, 249-262.
- [4] Yadav, N., Khatak, S., & Sara, U. S. (2013). Solid lipid nanoparticles-a review. *Int. J. Appl. Pharm*, 5(2), 8-18.
- [5]Lingayat, V. J., Zarekar, N. S., &Shendge, R. S. (2017). Solid lipid nanoparticles: a review. *Nanosci. Nanotechnol. Res*, 4(2), 67-72.
- [6]Mueller, R. S., Bergvall, K., Bensignor, E., & Bond, R. (2012). A review of topical therapy for skin infections with bacteria and yeast. *Veterinary Dermatology*, 23(4), 330-e62.
- [7]Türsen, B., &Türsen, Ü. (2014). Dermatolojide aloe vera. *Dermatoz, c*, 5, 1-11.
- [8]Ak, G., Ünal, A., Karakayalı, T., Özel, B., Günel, N. S., &Şanlıer, Ş. H. (2021). Brain-targeted, drug-loaded solid lipid nanoparticles against glioblastoma cells in culture. *Colloids and Surfaces B: Biointerfaces*, 206, 111946.
- [9]Heydenreich, A. V., Westmeier, R., Pedersen, N., Poulsen, H. S., & Kristensen, H. G. (2003). Preparation and purification of cationic solid lipid nanospheres—effects on particle size, physical stability and cell toxicity. *International journal of pharmaceuticals*, 254(1), 83-87.
- [10]Ak, G., Yilmaz, H., Güneş, A., &HamaratSanlier, S. (2018). In vitro and in vivo evaluation of folate receptor-targeted a novel magnetic drug delivery system for ovarian cancer therapy. *Artificial cells, nanomedicine, and biotechnology*, 46(sup1), 926-937.
- [11]Safitri, F. I., Nawangsari, D., &Febrina, D. (2021, January). Overview: Application of carbopol 940 in gel. In *International Conference on Health and Medical Sciences (AHMS 2020)* (pp. 80-84). Atlantis Press.
- [12]Malik, D. S., Kaur, G. (2018). “Nanostructured gel for topical delivery of azalaic acid. Designing, characterization, and in-vitro evaluation.” *Journal of Drug Delivery Science and Technology*, 4, 123-136

- [13]Shah, S., & Hashmi, M. S. (2020). Chitosan–aloe vera gel coating delays postharvest decay of mango fruit. *Horticulture, Environment, and Biotechnology*, 61, 279-289.
- [14]Venkateswarlu, V., & Manjunath, K. (2004). Preparation, characterization and in vitro release kinetics of clozapine solid lipid nanoparticles. *Journal of controlled release*, 95(3), 627-638.
- [15]Andrade, L. N., Oliveira, D. M., Chaud, M. V., Alves, T. F., Nery, M., da Silva, C. F., ... & Severino, P. (2019). Praziquantel-solid lipid nanoparticles produced by supercritical carbon dioxide extraction: Physicochemical characterization, release profile, and cytotoxicity. *Molecules*, 24(21), 3881.
- [16]Fayed, A. S., Rezk, M. R., Marzouk, H. M., & Abbas, S. S. (2019). Spectrophotometric Assessment of a Spectrally Overlapping Mixture of Cinchocaine Hydrochloride and Betamethasone Valerate in the Presence of Their Degradation Products. *Journal of Applied Spectroscopy*, 86, 176-186.
- [17] S., Kuldeep Singh, J. K. A. P., Waqas, M., Pandey, M., Choudhury, H., Habib, H., ... & Hussain, Z. (2019). Nanoencapsulation of betamethasone valerate using high pressure homogenization–solvent evaporation technique: Optimization of formulation and process parameters for efficient dermal targeting. *Drug development and industrialpharmacy*, 45(2), 323-332.
- [18]Pandey, M., Choudhury, H., Gunasegaran, T. A., Nathan, S. S., Md, S., Gorain, B., ... & Hussain, Z. (2019). Hyaluronic acid-modified betamethasone encapsulated polymeric nanoparticles: fabrication, characterisation, in vitro release kinetics, and dermal targeting. *Drug delivery and translational research*, 9, 520-533.
- [19]Abdelgawad, R., Nasr, M., Moftah, N. H., & Hamza, M. Y. (2017). Phospholipid membrane tubulation using ceramide doping “Cerosomes”: Characterization and clinical application in psoriasis treatment. *European Journal of Pharmaceutical Sciences*, 101, 258-268.
- [20]Şenyiğit, T., Tekmen, I., Sönmez, Ü., Santi, P., &Özer, Ö. (2011). Deoxycholate hydrogels of betamethasone-17-valerate intended for topical use: in vitro and in vivo evaluation. *International journal of pharmaceutics*, 403(1-2), 123-129.
- [21]Panahi, Y., Rastgar, N., Zamani, A., &Sahebkar, A. (2020). Comparing the therapeutic effects of aloe vera and olive oil combination cream versus topical betamethasone for atopic dermatitis: a randomized double-blind clinical trial. *Journal of pharmacopuncture*, 23(3), 173.

***Zercon kasensis* sp. nov., A New Mite Species (Parasitiformes: Zerconidae) From South-Western Türkiye**

Ayşenur Demirdöven¹, Raşit Urhan², Mehmet Karaca^{3*}

¹Department of Biology, The Graduate School of Natural and Applied Sciences, Pamukkale University, Denizli, Türkiye

²Department of Biology, Faculty of Science, Pamukkale University, Denizli, Türkiye

³Denizli Vocational School of Technical Sciences, Pamukkale University, Denizli, Türkiye

Received: 11/09/2024, **Revised:** 11/11/2024, **Accepted:** 11/11/2024, **Published:** 31/12/2024

Abstract

Various biological materials were collected from Saklıkent National Park (Antalya province) for investigation species diversity of the family Zerconidae. The collected materials were transferred to the acarology laboratory, mites were sorted with the Berlese-Tullgren funnels, and specimens of the zerconid mites were selected. Based on the materials collected from *Cedrus libani* and *Quercus coccifera* habitats in the research area, *Zercon kasensis* sp. nov. was described as a new species for the science. The female specimens of the new species were described, drawings were given and various body parts were measured. Males and immature stages of the new species were not found. The new species was compared with other species in the same genus, similarities and differences between the closer species were also presented.

Keywords: Acari, Mesostigmata, systematics, Saklıkent National Park, Antalya

***Zercon kasensis* sp. nov., Güneybatı Türkiye'den Yeni Bir Akar (Acari: Zerconidae) Türü**

Öz

Zerconidae familyasına ait tür çeşitliliğinin araştırılması amacıyla Saklıkent Milli Parkı'ndan (Antalya) çeşitli biyolojik materyaller toplandı. Toplanan materyaller akaroloji laboratuvarına transfer edildi, akarlar Berlese-Tullgren hunileri ile ayıklandı ve zerconid akarlar için örnekler seçildi. Araştırma alanında *Cedrus libani* ve *Quercus coccifera* habitatlarından toplanan materyallere dayanarak, *Zercon kasensis* sp. nov. bilim dünyası için yeni bir tür olarak tanımlandı. Yeni türün dişi örnekleri tanımlandı, çizimleri verildi ve çeşitli vücut kısımları ölçüldü. Yeni türün erkeklerine ve ergin olmayan evrelerine rastlanmadı. Yeni tür aynı cins içindeki diğer türlerle karşılaştırıldı, daha yakın türler arasındaki benzerlikler ve farklılıklar da ortaya konuldu.

Anahtar Kelimeler: Acari, Mesostigmata, sistematik, Saklıkent Milli Parkı, Antalya

*Corresponding Author: karacamehmet@pau.edu.tr
Ayşenur DEMİRDÖVEN, <https://orcid.org/0000-0002-6651-3429>
Raşit URHAN, <https://orcid.org/0000-0002-6548-7927>
Mehmet KARACA, <https://orcid.org/0000-0002-3249-4215>

1. Introduction

Studies aimed at determining biodiversity in protected areas have received the attention of many scientists, leading to a focus on research in these areas. National parks are among the most prominent protected areas in Türkiye. According to recent data, the country has 49 national parks. One of these is Saklıkent National Park, located on the border of Antalya and Muğla provinces with a surface area is 1.643 hectares. The park features maquis vegetation at lower altitudes and coniferous tree communities including Turkish pine, black pine and cedar, at medium and higher elevations. The diversity of landforms and plant species has provided favourable habitats for various life forms, including mites.

Systematic, faunistic, ecological and molecular studies on soil mites are quite common. Especially systematic studies on zerconid mites (members of the family Zerconidae) has been increasing both in Türkiye and worldwide [1-9]. Comprehensive regional and provincial studies are being carried out to document the Zerconidae fauna of the country [10-18]. So far, 92 species belonging to genus *Zercon* have been identified from Türkiye [19-20].

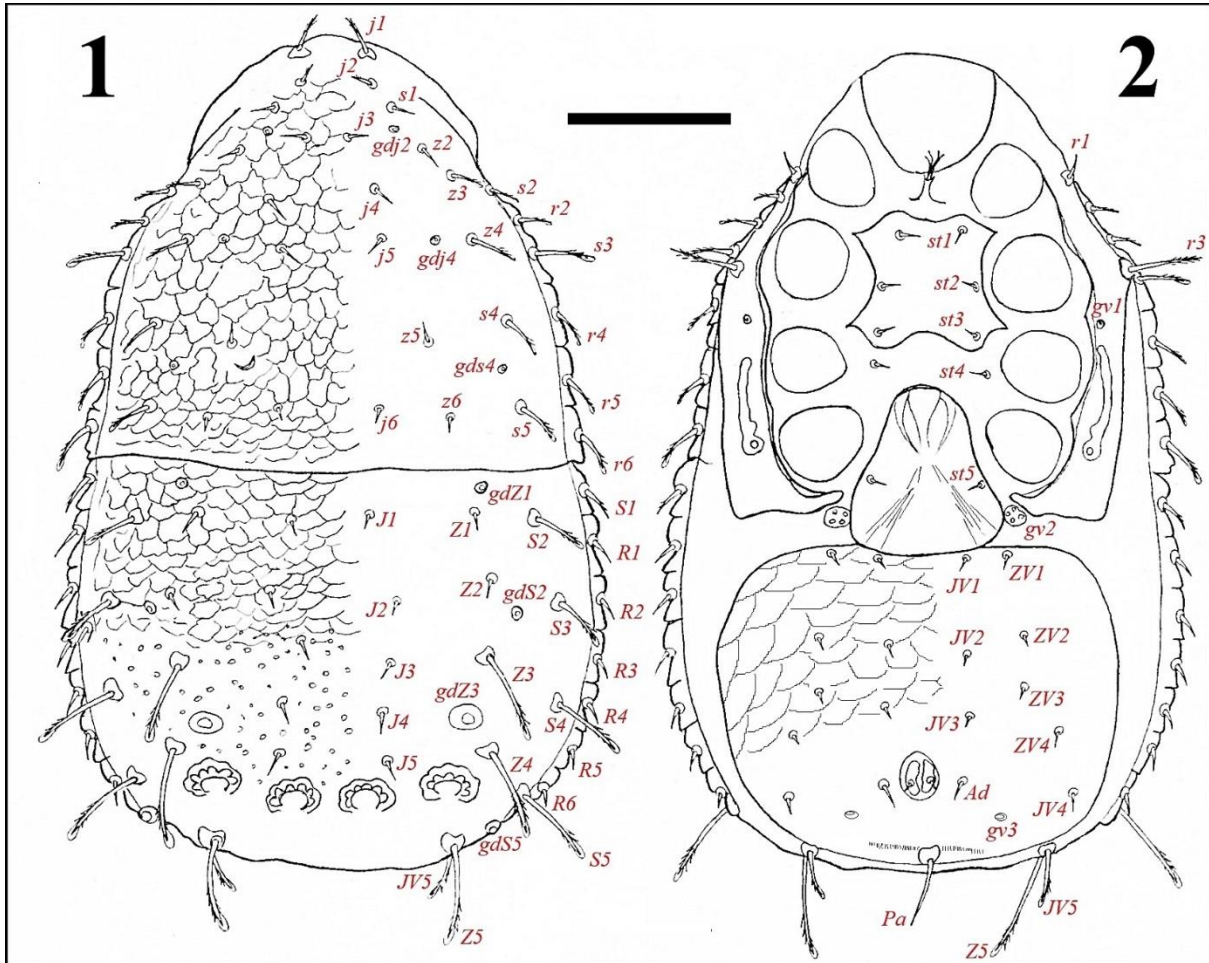
During the examination of zerconid mites specimens collected from Saklıkent National Park, it was observed that two specimens were not resemble any known species of the genus *Zercon*. As a result, they are described here as *Zercon kasensis* sp. nov.

2. Material and Methods

Based on the legal permission received from the General Directorate of Nature Conservation and National Parks (Republic of Türkiye, Ministry of Agriculture and Forestry, No: 21264211-288.04-7093271), soil and litter samples were collected from Lebanese cedar and kermes oak habitats in Saklıkent National Park, Kaş county, Antalya province, south-western Türkiye. At each sampling sites, data on coordinates and altitudes were recorded using a GPS device. All collected materials were then transferred to the Acarology Laboratory at Pamukkale University (PAU), Biology Department, Denizli, Türkiye.

Standard methods were used for extraction, measurement and drawing processes [21]. Terminologies of Lindquist & Evans (1965), Johnston & Moraza (1991) and Lindquist & Moraza (1998) were used in identification of the mite specimens [22-24]. Podonotal setae are shown in lower letters, opisthonotal setae are shown in capital letters. Various measurements (e.g. length and width of idiosoma, lengths of dorsal setae and ranges for setal bases, scale bar of the figures) were taken using a Olympus CX41 light microscope for the new specimens and shown as μm (micrometer). The type specimens of *Zercon kasensis* sp. nov. were stored in the PAU.

3. Results and Discussion



Figures 1-2. Dorsal and ventral appearance of *Zercon kasensis* sp. nov. (female) 1. Dorsum, 2. Venter (scale bar equal to 100)

Family **Zerconidae** Canestrini, 1891

Genus **Zercon** C. L. Koch, 1836

Type species: *Zercon triangularis* C. L. Koch, 1836

For detailed diagnosis, see Urhan and Karaca, 2023 [13].

Zercon kasensis sp. nov. (Figures 1, 2)

Type material. Holotype ♀ from litter and soil under Lebanese cedar: *Cedrus libani* (Pinaceae), 38°28.013' N, 28°28.881' E, 1215 m a.s.l., nearby of Çukur Ardiç plateau, Çamlıköy neighborhood, Kaş, Antalya, TÜRKİYE, 7 March 2023. One paratype ♀ from litter and soil under kermes oak: *Quercus coccifera* (Fagaceae), 36°22.510' N, 29°30.230' E, 885 m a.s.l., nearby of Çamlıova neighborhood, Kaş, Antalya, TÜRKİYE, 15 April 2023. Leg. Ayşenur Demirdöven.

Diagnosis. Two pairs of setae (*JV1* and *ZV1*) in the anterior margin of ventrianal shield. Short and smooth setae on the middle part of podonotum present, finely barbed with hyaline sheaths setae in the lateral part present (except setae *j1*–*2*, both of them finely barbed without hyaline

sheaths). Short and smooth setae in the middle part of opisthonotum present, partially elongated, finely barbed with hyaline sheaths setae present in the lateral part (except marginal setae). Gland pores *gdS2* situated among setae *Z2* and *S3*, closer to *S3*, *gdZ3* larger and more obviously than the other opisthonotal pores, situated among setae *J3* and *Z4*, closer to *Z4*. Dorsal fossae strongly developed and distinct. Tile-like patterns on podonotum and anterior margin of opisthonotum present, remaining parts of opisthonotum punctated.

Female. Length of idiosoma (excluding gnathosoma) 455 and width 300 in holotype; length of idiosoma 450, width 295 in paratype.

Dorsum (Fig. 1). Twenty pairs of setae on podonotal shield present, including *j1–6*, *z2–6*, *s1–6*, *r2* and *r4–5*. Bases of setae *r1* and *r3* on peritrematal shields, both of them inserted ventrally. Setae *j1–2* finely barbed but not having hyaline sheaths, *j3–6*, *z2*, *z5–6*, *s1* short and smooth, remaining podonotal setae (*z3–4*, *s2–5*, *r2* and *r4–6*) finely barbed and having hyaline sheaths. Setae *s3* obviously and more elongated than other podonotal setae. None of setae *j6*, *z6* and *s5* extend the margin of posterior part of podonotum. Tile-like patterns on podonotal shield present. Twenty-one pairs of setae on opisthonotal shield present, including *J1–5*, *Z1–5*, *S1–5* and *R1–6*. Setae *J1–5*, *Z1–2* and *R1–6* short and smooth, all of them resembling in shape (needle-like) and length. Although *S1* finely barbed but not having hyaline sheath, *Z3–5* and *S2–5* elongated, finely barbed and having hyaline sheaths. In the setal rows of opisthonotum (*J*, *Z* and *S*), none of the setae extend the next base of the setae in the related rows. Although setae *S2–3* extend lateral margin of opisthonotum, *Z4–5* and *S4–5* extend beyond margin of opisthonotum. The intervals between *Z5–Z5* 132–135. There is no intervals for setae *Z5–JV5*, their bases are very closer to each other. Tile-like patterns on anterior margin of opisthonotum present, remaining parts of opisthonotum with punctations.

Gland pores *gdj2* situated among setae *z2* and *s1*, closer to *s1*, *gdj4* situated among setae *j5* and *z4*, *gds4* situated among setae *z5* and *s5* or *z6* and *s4*, *gdZ1* situated above the base of seta *Z1*, *gdS2* situated among setae *Z3* and *S3*, closer to *S3*, *gdZ3* larger and more obviously than the other opisthonotal pores, situated among setae *J3* and *Z4*, closer to *Z4*, *gdS5* situated below the base of seta *S5* (Fig. 1).

Venter (Fig. 2). All morphological characters (ornamentation, poroidotaxy, chaetotaxy etc.) of ventral side of the new species are characteristic just as in all species within the genus. On the peritrematal shield, the posterolateral parts extend the level of seta *S1*. Two setae on peritrematal shield present, the first of them *r1* short and smooth, the second *r3* elongated and finely barbed but not having hyaline sheath. Peritreme shaped like inverted comma. Gland pore *gv1* situated above the anterior part of peritreme, at the level of between *coxae II–III*. Three pairs of setae (*st1–3*) on sternal shield present. Only one pair of setae (*st5*) on epigynal shield present. Seta *st4* situated among sternal and epigynal shields, at the level of *coxa III*. All the above-mentioned setae (*st1–5*) short and smooth. Gland pore *gv2* situated among between posterolateral parts of peritrematal shield and anterior part of ventrianal shield, with four opening valves. Because of the presence of setae *JVI* and *ZVI*, four setae on the anterior margin of ventrianal shield. All of the setae (*JVI–4*, *ZVI–4* and *Ad*) on ventrianal shield short and

smooth. Gland pore *gv3* situated closer to the base of adanal setae. Postanal seta (*Pa*) single. Seta *JV5* finely barbed and having hyaline sheaths, resembling to opisthonotal setae *Z5* and *S5*, but shorter them. Anterior part of ventrianal shield with squamous patterns and these extend the level of setae *JV3* and *ZV4*, remaining parts of ventrianal shield smooth.

Various measurements for opisthonotal setae in female specimens of *Z. kasensis* sp. nov., were presented in Table 1.

Table 1. Lengths of setae on opisthonotal shield and distances of the setal bases from each other in the same rows (mean values were given).

Setae	♀	Setae	♀	Setae	♀
<i>J1</i>	10	<i>Z1</i>	10	<i>S1</i>	15
<i>J1–J2</i>	48	<i>Z1–Z2</i>	50	<i>S1–S2</i>	23
<i>J2</i>	10	<i>Z2</i>	10	<i>S2</i>	38
<i>J2–J3</i>	35	<i>Z2–Z3</i>	38	<i>S2–S3</i>	50
<i>J3</i>	13	<i>Z3</i>	45	<i>S3</i>	43
<i>J3–J4</i>	38	<i>Z3–Z4</i>	50	<i>S3–S4</i>	50
<i>J4</i>	18	<i>Z4</i>	58	<i>S4</i>	50
<i>J4–J5</i>	30	<i>Z4–Z5</i>	62	<i>S4–S5</i>	50
<i>J5</i>	18	<i>Z5</i>	75	<i>S5</i>	60

Male and immature stages (deutonymph, protonymph and larva). Not found.

Etymology. Because the female specimens of the new species were collected from the Kaş county of Antalya province (south-western Türkiye), the specific epithet “*kasensis*” was assigned to the new species.

Remarks. General morphological characters of *Zercon kasensis* sp. nov. is considerably like to *Z. albanicus* Ujvári, 2010 [25], *Z. elongatus* Ujvári, 2010 [25], *Z. emirdagicus* Urhan et al., 2016 [26] and *Z. tefenniensis* Urhan, 2010 [27]. The distinctive morphological characters of these related species as in Table 2.

Table 2. Distinguishing features between *Zercon kasensis* sp. nov. and related species within the genus.

Characters	<i>Z. kasensis</i> sp. nov.	<i>Z. albanicus</i> Ujvári, 2010	<i>Z. elongatus</i> Ujvári, 2010	<i>Z. emirdagicus</i> Urhan et al., 2016	<i>Z. tefenniensis</i> Urhan, 2010
Marginal setae on podonotum	having hyaline sheath	not having hyaline sheath	having hyaline sheath	s3 having hyaline sheath, others not having hyaline sheath	s3 having hyaline sheath, others not having hyaline sheath
Podonotal setae z3-4 and s4-5	finely barbed and having hyaline sheaths	s5 finely barbed but not having hyaline sheath, others smooth	short and smooth	short and smooth	short and smooth
Opisthonotal seta S2	having hyaline sheath	short and smooth	short and smooth	having hyaline sheath	having hyaline sheath
Opisthonotal seta S4	having hyaline sheath	having hyaline sheath	having hyaline sheath	having hyaline sheath	absent
Marginal setae on opisthonotum	S1 finely barbed but not having hyaline sheath, others short and smooth	S1 and R1 finely barbed but not having hyaline sheaths, others short and smooth	short and smooth	short and smooth	short and smooth
Opisthonotal pore gdZ3	larger than the others, situated among setae J4-Z4 or J4-S4	about same size with the others, situated among setae J5-Z4, closer to Z4	about same size with the others, situated among setae Z3-4	about same size with the others, situated among setae Z3-4	larger than the others, situated among setae J5-Z4, closer to Z4
Pattern of central surface on opisthonotum	irregular punctated	smooth	smooth	smooth	irregular punctated
Seta JV5 on ventrianal shield	having hyaline sheath	finely barbed but not having hyaline sheath	short and smooth	having hyaline sheath	having hyaline sheath

According to Table 2, all zerconid mites including the new species have four setae on the anterior margin of ventrianal shield. Also, idiosomal setae of *Zercon kasensis* sp. nov. have the full complementary, there is no absence of seta on podonotum or opisthonotum in the related rows.

4. Conclusion

Recently, various studies were carried out on zerconid mites in national park areas in Türkiye and some new species were identified [28-33]. It is expected that studies on various mite groups will be continued in national parks of the country, which are among the most protected areas. Number of known species of the genus *Zercon* increased to 93 with *Z. kasensis* sp. nov. in Türkiye. Species diversity of Zerconidae fauna in the country will increase with new studies to be carried out locally or regionally.

Ethics in Publishing

There are no ethical issues regarding the publication of this study.

Author Contributions

Ayşenur Demirdöven: Collection of specimens (lead), data acquisition (equal), data analysis/interpretation (equal), preservation (lead). Raşit Urhan: Methodology (lead), project administration, supervision (lead), identification, illustration, data acquisition (equal), data analysis/interpretation (equal), critical revision of manuscript (equal), final approval and accountability (equal). Mehmet Karaca: Conception/design of study, collection of specimens (supporting), data analysis/interpretation (equal), drafting manuscript, critical revision of manuscript (equal), final approval and accountability (equal). This paper was prepared based on first author's M.Sc. thesis.

Acknowledgement

We are grateful to the “Republic of Türkiye Ministry of Agriculture and Forestry, General Directorate of Nature Conservation and National Parks” that provided the necessary permissions for field surveys.

References

- [1] Kaczmarek S., Marquardt T., Jangazieva B. (2020) *Zercon utemisovi* sp. n. – a new species of Zerconidae (Parasitiformes, Mesostigmata) from Kazakhstan with notes on *Zercon karadaghiensis* Balan, 1992, International Journal of Acarology, 46(1), 52-59.
- [2] Kaczmarek S., Marquardt T., Seniczak A. (2021) A new species of *Zercon* (Parasitiformes: Mesostigmata) from Norway, with notes on sexual dimorphism in Zerconidae, Systematic and Applied Acarology, 26(9), 1676-1702.
- [3] Marchenko I.I. (2021) Four new species of *Halozircon* (Acari: Mesostigmata: Zerconidae) from South Siberia Mountains (Russia) with a key to all known species, Zootaxa, 4941(2), 151-185.

- [4] Marchenko I.I. (2022) Description of new genus *Baikalozercon* (Acari: Mesostigmata: Zerconidae) with two new species from South Siberia Mountains (Russia), *Zootaxa*, 5120(3), 301-333.
- [5] Moghimi F., Ahadiyat A., Karaca M., Kiadaliri H., Urhan R. (2021) Description of *Prozercon caspiansis* sp. nov. (Acari: Mesostigmata: Zerconidae) from Iran, with descriptions of male and larva of *P. dominiaki* Błazsak, 1979, *Systematic and Applied Acarology*, 26(9), 1703-1720.
- [6] Makarova O.L. (2023) Free-living mites (Acari) of the Franz Josef Land Archipelago, the coldest Old World territory: diversity, geographic distributions, assemblages, *Acarologia*, 63(4), 1163-1186.
- [7] Mohammad-Doustasharaf M., Karaca M., Bagheri M., Urhan R. (2023) A taxonomic study on the zerconid mites (Acari: Zerconidae) in northwestern Iran: descriptions of three new species with three new records, *Systematic and Applied Acarology*, 28(3), 429-438.
- [8] Alinezhad Z., Ostovan H., Hesami S., Gheibi M. (2024) Abundance and diversity of mesostigmatid mites (Acari: Mesostigmata) in Fars Province, Iran, *North-Western Journal of Zoology*, 20(1), 1-13.
- [9] Marquardt T., Kaczmarek S., Seniczak A., Chudaś M. (2024) Biology and ecology of *Zercon hamaricus* Kaczmarek et al. 2021 (Parasitiformes: Zerconidae) with morphological study of all instars, *The European Zoological Journal*, 91(2), 729-747.
- [10] Duran E.H., Urhan R. (2017) Zerconid mites (Acari, Zerconidae) in İstanbul, with four new records for the Turkish fauna, *Turkish Journal of Zoology*, 41(5), 931-939.
- [11] Urhan R., Duran E.H. (2019) Zerconid mites (Acari, Zerconidae) in inner Aegean Region, with a new record for the Turkish fauna, *Zootaxa*, 4568(2), 323-336.
- [12] Urhan R., Karaca M. (2022) Manisa ilinin zerconid akar faunası (Acari: Mesostigmata: Zerconidae). In: *Abalı Y., Minareci O., Kaynar S.Ç. and İncedere L. (Eds), Manisa Akademik Araştırmalar Işığında (Fen Bilimleri & Coğrafya & İktisat)*, Berikan Yayınevi: Ankara, Türkiye, 4, pp. 208-234. (in Turkish)
- [13] Urhan R., Karaca M. (2023) Species diversity of the mite family Zerconidae (Acari: Mesostigmata) in İzmir Province. In: *Demirer A. (Ed), Multifaceted Academic Perspective: Science Research*, SRA Academic Publishing: Klaipėda, Lithuania, 1, pp. 1-26.

- [14] Urhan R., Karaca M. (2023) Aydın ilinin zerconid akar faunası (Acari: Mesostigmata: Zerconidae). In: Beram R.C. (Ed), *Çok yönlü Akademik Perspektif: Fen Bilimleri Araştırmaları*, SRA Academic Publishing: Klaipėda, Lithuania, 5, pp. 89-116. (in Turkish)
- [15] Karaca M., Urhan R. (2023) Zerconid mite fauna (Acari: Zerconidae) of Tekirdağ province, 1. Bilsel International Harput Scientific Research Congress, Elazığ, Türkiye, Proceeding Book, pp. 192-205. (in Turkish)
- [16] Karaca M., Urhan R. (2023) Zerconid mite fauna (Acari: Zerconidae) of Kırklareli province, 2. Bilsel International Ahlat Scientific Research Congress, Bitlis, Türkiye, Proceeding Book, pp. 962-976. (in Turkish)
- [17] Karaca M., Urhan R. (2023) Edirne ilinin zerconid akar faunası (Acari: Zerconidae), Aegean Summit 10. International Congress of Applied Sciences, İzmir, Türkiye, Proceeding Book, pp. 1489-1498. (in Turkish)
- [18] Karaca M., Urhan R. (2023) Balıkesir'den kaydedilmiş zerconid akarlar (Acari: Zerconidae). In: Bayyigit M., Azman M.A., Türker S., Çanakcı M., Yüksel Y. and Abdelghany A.H.A. (Eds), *Cumhuriyetin 100. Yılında Balıkesir'in Kültürel Birikimi, Tarım, Gıda ve Hayvancılık*. Palet Yayınları: Konya, Türkiye, pp. 125-144. (in Turkish)
- [19] Urhan R., Karaca M. (2024) Muğla'dan *Zercon* cinsinin (Acari, Zerconidae) yeni bir türü: *Zercon fethiyensis* sp.nov., Afyon Kocatepe University Journal of Science and Engineering, 24(5), in press. (in Turkish)
- [20] Urhan R., Karaca M., Kassen Z. (2024) A new zerconid mite (Mesostigmata: Zerconidae) from Southwestern Türkiye: *Zercon tripolisensis* sp. nov., *Acarological Studies*, 6(1), 52-59.
- [21] Bulut D.R., Urhan R., Karaca M. (2021) Zerconid mites (Acari, Zerconidae) from eastern parts of Aydın Province (Turkey), with description of *Zercon karacasuensis* sp. nov., *Acarological Studies*, 3(2), 73-81.
- [22] Lindquist E.E., Evans G. O. (1965) Taxonomic concepts in the Ascidae, with a modified setal nomenclature for the idiosoma of the Gamasina (Acarina: Mesostigmata), *Memoirs of the Entomological Society of Canada*, 47, 1-64.
- [23] Johnston D.E., Moraza M.L. (1991) The idiosomal adenotaxy and poroidotaxy of Zerconidae (Mesostigmata: Zerconina). In: Dusbábek F. and Bukva V. (Eds), *Modern Acarology*. Academia: Prague, Czech Republic, 2, pp. 349-356.

- [24] Lindquist E.E., Moraza M.L. (1998) Observations on homologies of idiosomal setae in Zerconidae (Acari: Mesostigmata), with modified notation for some posterior body setae, *Acarologia*, 39, 203-226.
- [25] Ujvári Z. (2010) First records of zerconid mites (Acari: Mesostigmata: Zerconidae) from Albania, with description of three new species, *Opuscula Zoologica (Budapest)*, 41(1), 57-75.
- [26] Urhan R., Duran E.H., Karaca M. (2016) Two new species of the genus *Zercon* C. L. Koch from the Inner Aegean Region of Turkey (Acari: Mesostigmata: Zerconidae), *Zoology in the Middle East*, 62(2), 164-170.
- [27] Urhan R. (2010) Two new species of zerconid mites from Turkey, *Zoology in the Middle East*, 50(1), 111-118.
- [28] Urhan R., Ayyıldız N., Toluk A., Koçođlu E., Taşdemir A. (2007) *Zercon agnostus* Blaszak, 1979 (Acari: Zerconidae) üzerine bir çalışma, *Çankaya University Journal of Science and Art*, 7, 171-179. (in Turkish)
- [29] Urhan R., Karaca M., Öztaş M., Bulut D.R., Tepe M. (2010) Honaz Dađı Milli Parkı (Denizli) zerkonidleri (Acari: Mesostigmata: Zerconidae), 20. National Biology Congress, Denizli, Türkiye, Abstract Book, pp. 831-832. (in Turkish)
- [30] Urhan R., Duran E.H., Karaca M. (2018) The diversity of zerconid mites (Acari, Zerconidae) in Akdađ National Park (Denizli/Turkey), *International Journal of Scientific and Technological Research*, 4(10), 509-517.
- [31] Keçeci B., Urhan R., Karaca M. (2021) Mites of the genus *Prozercon* (Acari, Zerconidae) in Dilek Peninsula-Büyük Menderes Delta National Park (Turkey), with description of a new species, *Acarological Studies*, 3(1), 37-42.
- [32] Bilki K., Urhan R., Karaca M. (2022) Mites of the family Zerconidae (Acari: Mesostigmata) from Southwestern Turkey, with description of three new species, *Acarological Studies*, 4(2), 89-103.
- [33] Urhan R., Karaca M. (2023) Contributions to the Zerconidae (Acari: Mesostigmata) fauna of Dilek Peninsula-Büyük Menderes Delta National Park, Türkiye, *Acarological Studies*, 5(1), 21-33.

Determination of Nifedipine in Pharmaceutical Preparations by Square Wave Voltammetry Method

Bilal Yılmaz^{1*}

¹Department of Analytical Chemistry, Faculty of Pharmacy, Ataturk University, 25240, Erzurum, Turkey

Received: 19/04/2023, **Revised:** 09/12/2024, **Accepted:** 25/12/2024, **Published:** 31/12/2024

Abstract

In the present study, the electroanalytical behaviour of nifedipine was investigated by cyclic voltammetry method. The method was based on nifedipine being electrochemically oxidized at a platinum electrode in nonaqueous solutions. At 1.16 V, the oxidation peak was noted. It was determined that nifedipine's oxidation was diffusion-controlled. Additionally, a quick and easy square wave voltammetry method was developed and validated in this work to determine nifedipine in pharmaceutical preparations. At concentrations between 5 and 50 µg/mL, the calibration curve is linear. The precision was given by relative standard deviation and was less than 3.96%. Accuracy was given with relative error and did not exceed 2.00%. In pharmaceutical preparations, nifedipine had an average recovery of 100.6%. Under the chosen experimental conditions no interference was found. The suggested method is extremely accurate and precise. Therefore, the method is applicable to the measurement of nifedipine in Adalat Crono tablets as pharmaceutical formulation.

Keywords: Nifedipine, voltammetry, validation, tablet

Farmasötik Preparatlarda Nifedipinin Kare Dalga Voltammetri Yöntemi ile Tayini

Öz

Bu çalışmada, nifedipinin elektroanalitik davranışı döngüsel voltametri yöntemiyle incelenmiştir. Yöntem, susuz çözeltilerde bir platin elektrotta elektrokimyasal olarak oksitlenen nifedipine dayanıyordu. 1.16 V'ta oksidasyon piki kaydedildi. Nifedipinin oksidasyonunun difüzyon kontrollü olduğu belirlendi. Ek olarak, farmasötik preparasyonlarda nifedipini belirlemek için bu çalışmada hızlı ve kolay bir kare dalga voltametri yöntemi geliştirildi ve valide edildi. 5 ve 50 µg/mL arasındaki konsantrasyonlarda kalibrasyon eğrisi doğrusaldır. Kesinlik bağıl standart sapma ile verildi ve %3.96'dan azdı. Doğruluk bağıl hata ile verildi ve %2.00'yi geçmedi. Farmasötik preparasyonlarda, nifedipinin ortalama geri kazanımı %100.6'dır. Seçilen deneysel koşullar altında hiçbir girişim bulunmadı. Önerilen yöntem son derece doğru ve kesindir. Bu nedenle yöntem, farmasötik formülasyon olarak Adalat Crono tabletlerdeki nifedipin ölçümüne uygulanabilir.

Anahtar Kelimeler: Nifedipin, voltametri, validasyon, tablet

1. Introduction

Nifedipine (Figure 1) is a calcium channel antagonist of the dihydropyridine class that is frequently used to treat vascular diseases such Raynaud's phenomenon, hypertension, and angina pectoris. When taken orally, the lipid-soluble medication nifedipine is quickly and thoroughly absorbed from the digestive tract. Due to extensive first-pass metabolism, nifedipine has a systematic bioavailability of 50-70%, which may cause significant intersubject pharmacokinetic variability. Nifedipine has a 2 to 5 hour elimination half-life [1].

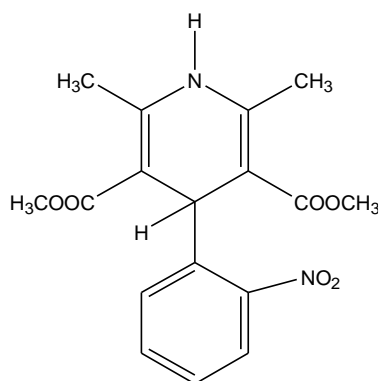


Figure 1. Structure of nifedipine

Several nifedipine determination methods have been published in reports. These include mass spectrophotometric detection, multivariate image analysis, UV or electrochemical detection in conjunction with HPLC [2-5], gas chromatography with electron capture [6-8] and LC-MS/MS [9-10] methods.

According to reports, nifedipine's spectrophotometric detection involves interactions with oxidation of the medication with iron(III) [11,12], subcritical water extraction of the medication [13], reaction of the medication's nitro group with potassium hydroxide in dimethyl sulfoxide medium [14] and reduction of the medication with zinc/naphthalene chloride followed by coupling with N-methyl-1,4-benzoquinon [15]. A thorough review of the literature revealed that there are several chromatographic techniques for determining the presence of nifedipine in human plasma, while the quantitative determination of nifedipine in pharmaceutical formulation samples has only been covered in a small number of other publications [7, 9, 12].

An extensive literature analysis revealed a variety of chromatographic techniques for assessing the presence of nifedipine in human plasma. Endogenous interference, probable drug loss during re-extraction, arduous and time-consuming procedures for preparing and extracting plasma samples, and the requirement for high-end, pricey equipment all had an impact on the revealed procedures.

It's critical to develop a new formula for figuring out how much medication is in pharmaceutical dose forms. Numerous therapeutic substances have been identified using electroanalytical techniques, which have the advantages of frequently not requiring derivatization and being less susceptible to matrix effects than other analytical techniques. Identifying electrode mechanisms is another use of electrochemistry [16-19]. Drugs' redox characteristics may provide

information on their pharmacological effectiveness, in vivo redox activities, or metabolic destiny.

Although the electrochemical behavior and oxidation mechanism of nifedipine have analytical significance, no research on the voltammetric oxidation of nifedipine in nonaqueous media has been published. It is widely known that the electrochemical process and voltammetric response of pharmaceuticals are directly influenced by the experimental and operational parameters. So, it would be interesting to look at how nifedipine oxidizes in aprotic environments. However, the voltammetry method has not yet been used to quantitatively assess nifedipine using a platinum electrode.

This study describes Square Wave Voltammetry (SWV) method using a platinum disc electrode to determine nifedipine using simple, quick, and selective processes that have been completely verified. Also, the method was effectively used to evaluate the consistency of the formulation content and to quantitate a commercially available nifedipine medication for QC.

2. Materials and Methods

2.1. Chemicals and reagents

Nifedipine standard (98 \geq purity), lithium perchlorate (LiClO₄) and acetonitrile were purchased from Sigma (Germany). The nifedipine-containing Adalat Crono tablets were bought at a pharmacy in Erzurum, Turkey.

2.2. Electrochemical instrumentation

Electrochemical experiments were carried out on a Gamry Potentiostat Interface 1000. The single-compartment electrochemical cell used for all tests has a conventional three-electrode setup. Platinum wire served as the counter electrode and a platinum disk served as the working electrode. On microcloth pads, 1.0, 0.3, and 0.05 μm alumina slurries were used to incrementally polish the working electrode. The reference electrode for each potential was made of Ag/AgCl/KCl (3.0 M). The SWV was operated at pulse amplitudes of 25 mV, 10 Hz, 4 mV potential step and 0.1 V s⁻¹ scan rate.

2.3. Preparation of standard and quality control samples

In 0.1 M LiClO₄/acetonitrile, the stock standard solution of nifedipine (100 $\mu\text{g}/\text{mL}$) was prepared. This stock solution was used to prepare working standard solutions. The concentrations of the standard solutions were 5, 7.5, 10, 15, 20, 25, 30, 40 and 50 $\mu\text{g}/\text{mL}$. The QC solutions were made at 7.5, 25 and 45 $\mu\text{g}/\text{mL}$ concentrations.

2.4. Statistical analysis

With the use of a computer program, SPSS V.15.0 was used for the statistical analyses. The nifedipine standard line and calculations were made using regression analyses. The mean and standard deviation of the results were provided.

3. Results and Discussion

3.1. Method development and optimization

At the Pt disc electrode, the electrochemical behavior of nifedipine was studied. The supporting electrolyte in cyclic voltammetry was an acetonitrile solution with 0.1 M LiClO₄. Figure 2 depicts a typical cyclic voltammogram for 100 µg/mL nifedipine at 0.1 V s⁻¹ scan rate. The oxidation peak was seen in the anodic sweep at 1.16 V.

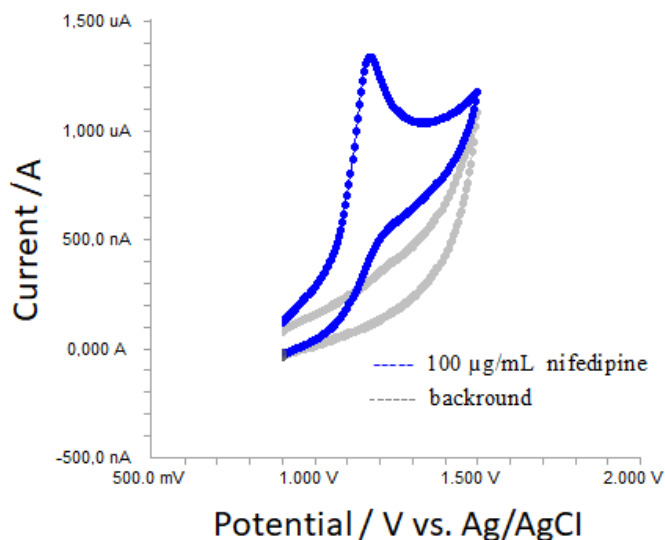


Figure 2. Cyclic voltammogram of nifedipine (100 µg/mL)

The influence of scan rate on the anodic peak currents and peak potentials was investigated in the range of 0.01-1 V s⁻¹ of the potential scan rates in order to better understand the voltammetric waves (Figure 3).

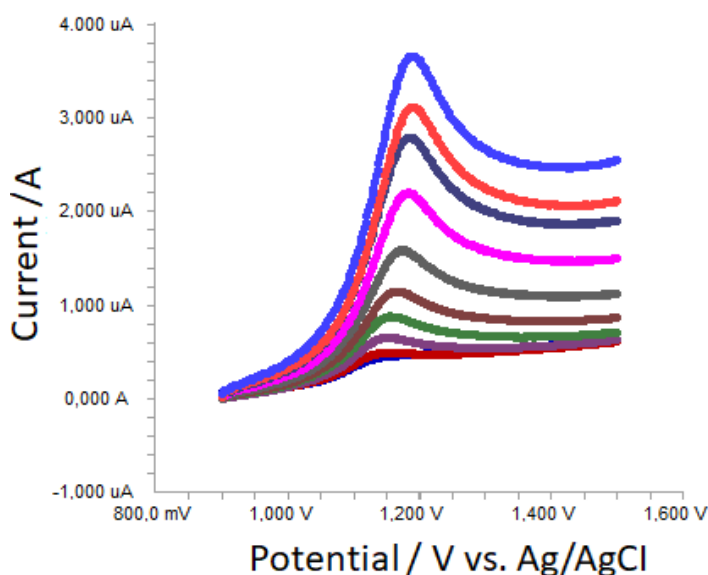


Figure 3. Linear sweep voltammograms of 20 µg/mL nifedipine as a function of scan rate

Figures 4a,b display the linear sweep voltammograms for nifedipine as a function of scan rate. However, the logarithm of peak currents against logarithm of scan rates graphs at nifedipine concentrations of 20 $\mu\text{g/mL}$ show straight lines with a slope of 0.42, which is close to the predicted value of 0.5 anticipated for an ideal diffusion-controlled electrode process [20].

This should be done using the $\log I$ - $\log v$ curve, therefore a diffusional process for the peak should be taken into consideration. The redox species quickly diffuse from the solution rather than precipitate onto the electrode surface, according to these data. This phenomenon may be caused by the solubility of the intermediate species in acetonitrile.

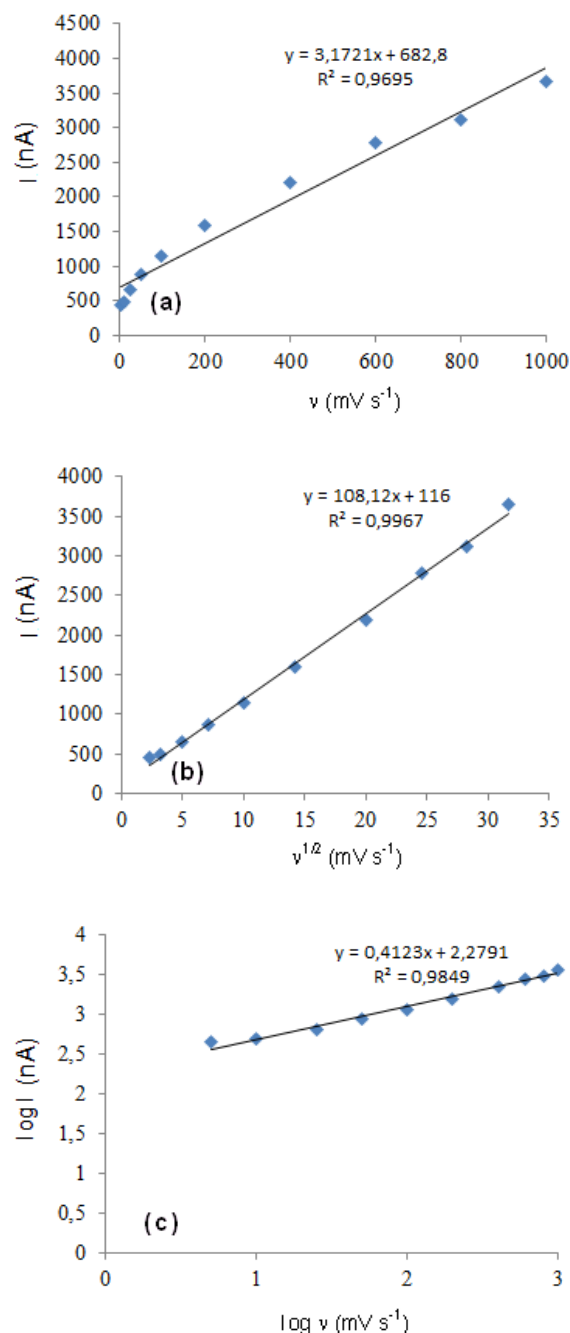


Figure 4(a-c). Scan rate dependence on the peak current (20 $\mu\text{g/mL}$)

As the scan rate is raised, Figure 3 depicts how the oxidation peak potential (E_{pa}) for peaks moves toward more positive values. The equation below describes the relationship between the peak potential and scan rate [21].

$$E_{pa} = E^{0'} + RT / [(1 - \alpha)n_a F] [0.78 + \ln(D^{1/2}k_s^{-1}) - 0.5 \ln RT / [(1 - \alpha)n_a F]] + RT / [(1 - \alpha)n_a F] / 2 \ln v$$

The plots of the oxidation peak potentials against $\ln v$ demonstrate a linear connection in accordance with this equation (Figure 5).

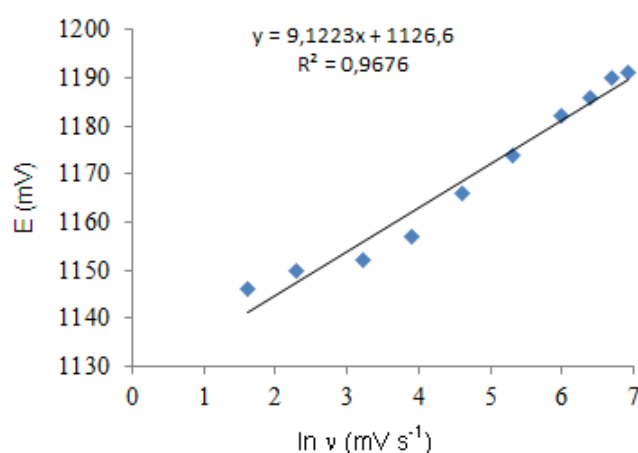


Figure 5. Dependency of the nifedipine anodic peak potentials on the scan rate

The slope indicates that the highest value of αn is 0.75. Additionally, this value shows that the processes of electron transfer are completely irreversible. This outcome demonstrates that the chemical step is a charge transfer and a quick following reaction.

3.2. Validation of the method

ICH Q2B guidelines were followed while determining the validation parameters [22]. These criteria include specificity, linearity, precision, accuracy, recovery, limit of detection (LOD), limit of quantification (LOQ), robustness and stability.

3.2.1. Selectivity

In this study, it was investigated the potential interferences of common excipients and additives. The QC samples were prepared and examined. At the concentrations present in dosage forms, there is no evidence of any interference from these chemicals. The excipient employed in this formulation was one that the pharmaceutical industry employs most frequently. The method's specificity was examined by keeping an eye out for any interference from common tablet ingredients like talc, lactose, sodium chloride, titanium dioxide and magnesium stearate. These exceptions had no negative effects on the suggested method. The procedure might be selective in accordance with the findings of the analysis.

3.2.2. Linearity

Standard solutions at concentration of 5, 7.5, 10, 15, 20, 25, 30, 40 and 50 $\mu\text{g/mL}$ were prepared for SWV (Figure 6). Plotting the nifedipine concentration versus peak current responses allowed for the construction of the calibration curve for the nifedipine (Figure 7).

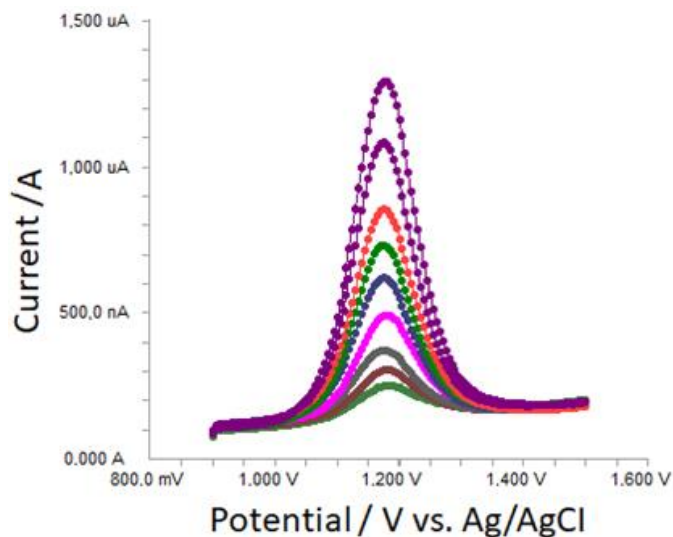


Figure 6. SWV voltammograms of nifedipine (5-50 $\mu\text{g/mL}$)

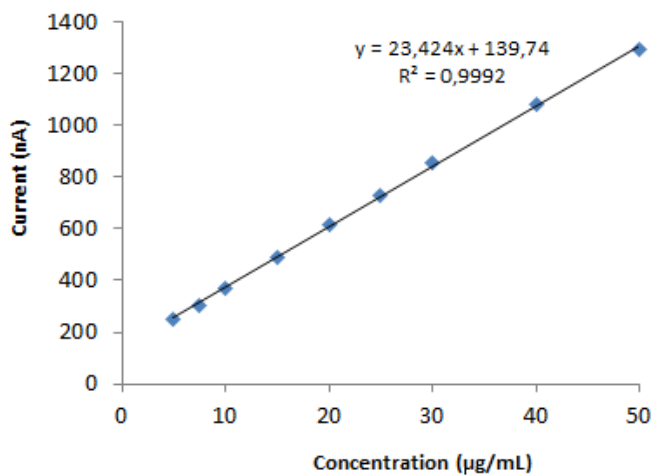


Figure 7. Calibration curve of nifedipine (5, 10, 15, 20, 25, 30, 40 and 50 $\mu\text{g/mL}$)

All of the calibration curves' correlation coefficients (r) were consistently higher than 0.99. Using the least squares method and the Microsoft Excel® application, the linear regression equations were derived and described in Table 1.

Table 1. Linearity of nifedipine

Parameter	Nifedipine
Linearity range ($\mu\text{g/mL}$)	5-50
Slope	23.524
Intercept	139.74
Correlation coefficient	0.9992
LOD ($\mu\text{g/mL}$)	0.90
LOQ ($\mu\text{g/mL}$)	2.70

3.2.3. Precision and accuracy

Using the QC samples, the SWV method's precision and accuracy were assessed for intra-day and inter-day. The same-day analysis of the QC samples served to assess intra-day precision and accuracy. It was able to assess the precision and accuracy between days by contrasting the assays performed on two distinct days. The intra-day accuracy ranged from 0.04% to 1.55%, while the precision ranged from 1.58% to 3.56% (Table 2). It is evident from the results that this process has good accuracy and precision.

Table 2. Precision and accuracy of nifedipine

Added ($\mu\text{g/mL}$)	Intra-day			Inter-day		
	Found \pm SD ^a	Precision % RSD ^b	Accuracy ^c	Found \pm SD ^a	Precision % RSD ^b	Accuracy ^c
7.5	7.38 \pm 0.12	1.58	-1.55	7.47 \pm 0.10	1.38	-0.44
25	25.01 \pm 0.89	3.56	0.04	24.83 \pm 0.98	3.96	-0.67
45	45.33 \pm 1.03	2.28	0.74	45.67 \pm 1.03	2.26	1.48

3.2.4. Recovery

To evaluate the effects of formulation interference, the recovery was investigated at three different concentrations. The recoveries were done by combining nifedipine tablet samples that had already undergone analysis with a known quantity of pure medications. The recoveries were calculated by comparing the amounts recovered from the spiked samples with the actual added concentrations. The results are listed in Table 3.

Table 3. Recovery of nifedipine in tablets (n=6)

Tablet	Found \pm SD	%Recovery	%RSD ^a	Confidence Interval
Adalat Crono (30 mg/tablet)	30.2 \pm 0.51	100.7	1.69	29.2- 31.3
	29.3 \pm 0.44	98.7	1.49	28.6- 30.2
Adalat Crono (60 mg/tablet)	30.8 \pm 0.67	102.3	2.18	29.3- 31.4
	59.2 \pm 1.29	98.8	2.18	58.6-61.2
	61.1 \pm 1.33	101.8	2.21	60.3-62.1
	58.9 \pm 1.22	98.2	2.07	57.9-61.6

3.2.5. LOD and LOQ

The LOD and LOQ values of the proposed method were determined using calibration standards. The computed values for LOD and LOQ were 3.3 and 10/S, respectively [22]. The results are summarized in Table 1.

3.2.6. Ruggedness

The same instrument and standard standard solution were used in this study by a separate analyst to assess the concentration of nifedipine (Table 4). No statistically significant discrepancies between the operators were found in the results, indicating the ruggedness of the developed method.

Table 4. Results of another analyst's studies of nifedipine (n=6)

Added ($\mu\text{g/mL}$)	Found ($\mu\text{g/mL}$) (Mean \pm SD)	% Recovery	% RSD ^a
5	5.1 \pm 0.18	102.0	3.53
15	14.8 \pm 0.25	98.7	1.69
35	35.2 \pm 1.67	100.6	4.74

3.2.7. Stability

The stability of the medication was established since it is known that nifedipine deteriorates in light. Standards of 10, 25 and 50 $\mu\text{g/mL}$ nifedipine were examined for a week under various circumstances in the dark at 4 °C and in the light at room temperature (25 °C) to assess stability. The solutions were reanalyzed against recently generated standard solutions after 2, 4, 8, 12, 24, and 48 h (light, 25°C), and 2, 4, 8, 12, 24, and 48 h (dark, 4°C) respectively (Table 5). The findings demonstrate the stability of nifedipine standards, with recoveries >93% for up to 2 hours when stored in light at 25°C and for up to 2 days when stored in darkness at 4°C.

Table 5. Stability of the nifedipine (n=3)

	Time	Recovery (%)	% RSD ^a
Light (25°C)	Initial	100.1	2.92
	2 h	93.5	1.97
	4 h	87.9	3.67
	8 h	83.6	2.03
	12 h	73.8	3.78
	24 h	68.9	2.47
	Dark (4°C)	Initial	99.8
2 h		98.6	1.99
4 h		97.4	4.04
8 h		96.2	3.01
12 h		95.3	1.67
24 h		95.8	3.16
48 h		94.9	2.93

3.3. Procedure for pharmaceutical preparations

Each Adalat Crono tablets, which contains 30 or 60 milligrams of nifedipine, was precisely weighed and finely powdered. A suitable amount of powder was dissolved in 50 mL of 0.1 M LiClO₄/acetonitrile. Then, the final volume was made up to 100 mL in a balloon flask. Whatman filter (paper no 42) was used to filter the tablet solutions after they had been properly diluted in order to provide a final concentration that was within the linearity constraints of the SWV method (Figure 8). The calibration curve was used to determine the drug concentration for nifedipine.

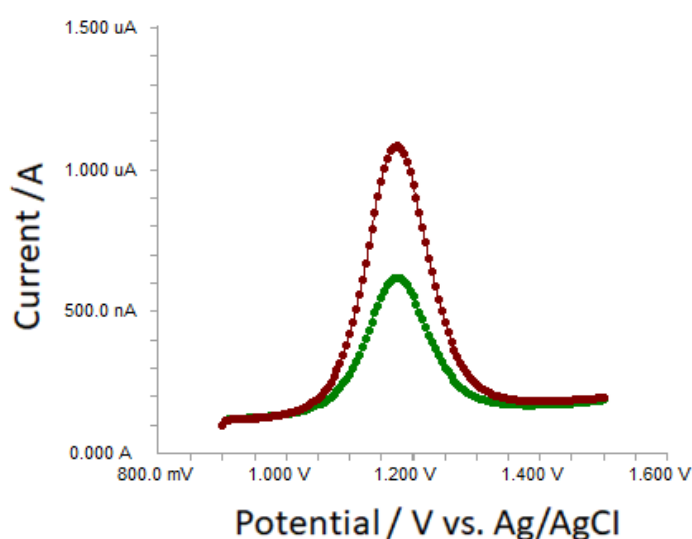


Figure 8. The voltammograms of Adalat Crono tablet containing nifedipine (25 and 40 µg/mL)

Additionally, the presented SWV voltammetric method was statistically evaluated with the reported methods [14-16] using the F-test. The estimated F-values do not surpass the theoretical values at a 95% confidence level (Table 6). Consequently, the differences between the methods are negligible.

Table 6. Comparison of the proposed and reported methods for determination of nifedipine

Parameter	Proposed SWV	Reported Method [14]	Reported Method [15]	Reported Method [16]	Reported Method [24]
Mean (Recovery %)	100.6	99.9-100.1	98.7-100.5	99.5-101.3	99.9-100.1
SD	2.49				
%RSD	2.45	0.52	0.60	1.50	0.72
Variance	5.95				
F-test	3.78				

The analytical findings in this investigation showed that the level of active ingredient in the medicine is within the reported method's recommended range. The developed method was demonstrated to be practical, accurate, and adaptable to drug dose forms. Therefore, developed SWV method can be advised for the routine QC analyses of nifedipine in pharmaceutical preparations.

3.4. Comparison of the methods

Nifedipine is covered in a monograph in the State Pharmacopoeia of Ukraine [25]. The SPhU offers melting point analysis, infrared absorption spectrophotometry, qualitative TLC analysis of the development of azo dye following the earlier restoration of the nitro group to amino group, and quantitative analysis of the content of nifedipine. The definition of nifedipine in pharmaceuticals and tablet form is governed by the United States Pharmacopoeia. Identification is recommended using the definitions of UV-spectrophotometry and infrared absorption spectrophotometry. Nifedipine in pills should be precisely measured using the HPLC method.

An extensive literature analysis revealed a variety of spectrophotometric methods for the determination of nifedipine in pharmaceutical preparations. In these studies, the amount of nifedipine in single and mixed dose forms was estimated using first order [26] and second order [27] derivative spectra, respectively. The amount of the drug was calculated based on its reactions with the folin-Ciocalteau reagent [26] and chloranil [28].

Also, two spectrophotometric methods have been developed based on the drug's interactions with potassium hydroxide in dimethyl sulfoxide and ammonium molybdate in acidic buffer

solution to yield colorful products with absorbance peaks at 430 nm and 830 nm, respectively [14]. A kinetic spectrophotometric method has also been reported [29] based on the drug's oxidation with KMnO_4 at neutral pH. The other spectrophotometric method was based on Rahman et al.'s [15]. $\text{Zn}/\text{NH}_4\text{Cl}$ reduction of the nitro group of nifedipine to hydroxylamino derivatives. Extractive spectrophotometric methods have also been published for the measurement of the drug concentration in pharmaceutical formulations [24]. These methods rely on the colorful drug complex made with dyes such eriochrome black-T, bromocresol green, bromophenol blue and bromothymol blue.

The recommended SWV approach was compared to other methods from the literature. Furthermore, statistical comparisons between the results obtained by the specified method and those produced by the suggested methodology were done [14, 19, 24]. A statistical analysis of the data using the variance ratio F test revealed no appreciable differences between the performance of the suggested and reference procedures (Table 6). We found that the calculated F-values did not significantly surpass the theoretical values, which led us to the conclusion that the suggested method does not significantly deviate from spectrophotometric procedures.

4. Conclusion

The cyclic voltammetry method has been used in the current study to examine the electrochemical behavior of nifedipine in nonaqueous media. Additionally, a fast, accurate, simple and precise SWV method for nifedipine detection in pharmaceutical formulations was developed and validated in the study. The method makes it possible to quickly analyze a number of samples. Therefore, the method can be used to regularly monitor nifedipine, both in its formulations and pure form.

Author Contributions

The author contributed to laboratory examinations and writing manuscripts.

Acknowledgements

The author also appreciates Semih Yilmaz's assistance on proper English usage.

References

- [1] Reetu, Ashutosh, Y., Anita, S., Arun, G., (2021) Enhancement of dissolution rate and bioavailability of nifedipine by chitosan based cocrystallization technique, *Journal of Pharmaceutical Research International* 33(28B), 206-219.
- [2] Hasanuddin, D.N.A., Garmana, A.N., Sasongko, L., (2024) HPLC method for the determination of nifedipine in rat plasma: development, validation, and application to pharmacokinetic drug-herb interaction study, *Pharmacia*, 71, 1-6.
- [3] Choiri1, S., Ainurofiq, A., Ratri, R., Zulmi, M.U., (2018) Analytical method development of nifedipine and its degradants binary mixture using high performance liquid chromatography through a quality by design approach, *Materials Science and Engineering*, 333, 1-6.

- [4] Awad, U.Y., Patel, S.K., Kumar, D., Bari, S.A., (2011) Estimation of nifedipine by reverse phase high performance liquid chromatography tablet dosage form, *International Journal of Pharmaceutical and Life Sciences*, 2, 610-612.
- [5] Guo, Y., Dai, J., Qian, G., Guo, N., Ma, Z., Guo, X., (2007) Determination of nifedipine in human plasma and its use in bioequivalence study, *International Journal of Pharmaceutics*, 341, 91-96.
- [6] Logoyda, L., (2019) Analysis of approaches to the development and validation of the methods of analysis of some active pharmaceutical ingredients from the group of calcium channel blockers in drugs and biological liquids, *International Journal of Applied Pharmaceutics*, 11, 26-34.
- [7] Maurer, H.H., Arlt, J.W., (1999) Screening procedure for detection of dihydropyridine calcium channel blocker metabolites in urine as part of a systematic toxicological analysis procedure for acidic compounds by gas chromatography-mass spectrometry after extractive methylation, *The Journal of Analytical Toxicology*, 23, 73-80.
- [8] Hemmateenejad, B., Mobaraki, N., Shakerizadeh-Shirazi, F., Miri, R., (2010) Multivariate image analysis-thin layer chromatography (MIA-TLC) for simultaneous determination of co-eluting components, *Analyst*, 135, 1747-1758.
- [9] Wang, X.D., Li, J.L., Lu, Y., Chen, X., Huang, M., Chowbay, B., Zhou, S.F., (2007) Rapid and simultaneous determination of nifedipine and dehydronifedipine in human plasma by liquid chromatography-tandem mass spectrometry: Application to a clinical herb-drug interaction study, *Journal of Chromatography A*, 852, 534-544.
- [10] Logoyda, L.S., (2020) LC-MS/MS method development and validation for the determination of nifedipine in human plasma, *Biointerface Research in Applied Chemistry*, 10(5), 6189-6196.
- [11] Rahman, N., Azmi, S.N.H., (2006) Validated spectrophotometric method for the assay of nifedipine in bulk and commercial dosage forms, *Science Asia*, 32, 429-435.
- [12] Hemmateenejad, B., Miri, R., Kamali, R., (2009) A kinetic spectrophotometric method for determination of amlodipine and nifedipine in pharmaceutical preparations, *Journal of the Iranian Chemical Society*, 6, 113-120.
- [13] Richter, P., Toral, M.I., Toledo, C., (2006) Subcritical water extraction and determination of nifedipine in pharmaceutical formulations, *The Journal of AOAC International*, 89, 365-368.
- [14] Rahman, N., Azmi S.N., (2005) New spectrophotometric methods for the determination of nifedipine in pharmaceutical formulations, *Acta Biochimica Polonica*, 52, 915-922.
- [15] Rahman, N., Hoda, M.N., (2002) Spectrophotometric method for the determination of nifedipine with 4-(methylamino) phenol and potassium dichromate, *Il Farmaco*, 57, 435-441.

- [16] El-Hefnawey, G.B., El-Hallag, I.S., Ghoneim, E.M., Ghoneim, M.M., (2004) Voltammetric behavior and quantification of the sedative-hypnotic drug chlordiazepoxide in bulk form, pharmaceutical formulation and human serum at a mercury electrode, *Journal of Pharmaceutical and Biomedical Analysis*, 34, 75-86.
- [17] Corti, P., Corbini, G., Gratteri, P., Furlanetto, S., Pinzauti, S., (1994) Determination of some quinolones in tablets, human plasma and urine by differential-pulse polarography, *International Journal of Pharmaceutics*, 111, 83-87.
- [18] Dogan, B., Ozkan, S.A., (2005) Electrochemical behavior of carvedilol and its adsorptive stripping determination in dosage forms and biological fluids, *Electroanalysis*, 17, 2074-2083.
- [19] Mokhtaria, B., Nematollahia, D., Salehzadehb, H., (2018) Electrochemical simultaneous determination of nifedipine and its main metabolite dehydronifedipine using MWCNT modified glassy carbon electrode, *Journal of Molecular Liquids*, 264, 543-549.
- [20] Alghamdi, A.F., (2024) Validation and application of the square wave voltammetry method for the electrochemical determination of eszopiclone in pharmaceutical formulations and human biological fluids using glassy carbon electrode, *Journal of King Saud University – Science*, 36, 103408.
- [21] Yilmaz, B., Ekinici, D., (2011) Voltammetric behavior of carvedilol in non-aqueous media and its analytical determination in pharmaceutical preparations, *Reviews in Analytical Chemistry*, 30, 187-193.
- [22] Guidance for Industry, Bioanalytical Method Validation, US Department of Health and Human Services, Food and Drug Administration, Center for Drug Evaluation and Research (CDER), Rockville, MD, 2001.
- [23] Rahman, N., Khan, N.A., Azmi, S.N.H., (2004) Extractive spectrophotometric methods for the determination of nifedipine in pharmaceutical formulations using bromocresol green, bromophenol blue, bromothymol blue and eriochrome black T, *Il Farmaco*, 59, 47-54.
- [24] Mallick, S., Gupta, B.K., Ghosal, S.K., (1998) Extractive spectrophotometric determination of nifedipine and verapamil hydrochloride, *East Pharma*, 41, 129-130.
- [25] The State Pharmacopeia of Ukraine in 3 vol. State Enterprise Ukrainian Scientific Expert Pharmacopoeial Center of the Quality of Medicines 2nd iss. Kharkiv: State Enterprise “Ukrainian Scientific and Experimental Pharmacopoeial Center for the Quality of Medicinal Products, 2015, 1128.
- [26] El-Walily, A.F.M., (1997) Simultaneous determination of binary mixture of nifedipine and mefruside using derivative spectroscopy, capillary gas-liquid chromatography and high performance liquid chromatography, *Acta Pharmaceutica Hungarica*, 67, 89-97.

[27] Umapathi, P., (1994) Determination of atenolol, nifedipine, aspirin and dipyridamole in tablet preparations by second order derivative spectrophotometry, *International Journal of Pharmaceutics*, 108, 11-19.

[28] Golcu, A.Y., Serin, S., (1998) Spectrophotometric determination of nifedipine via charge transfer complexes, *Scientia Pharmaceutica*, 66, 341-349.

[29] Vyas, S.P., Goswami, S.K., (1993) A sensitive visible spectrophotometric method for the estimation of nifedipine, *Indian Drugs*, 30, 342-344.

Investigation of the Effects of Cetuximab and Agomelatine Drugs on Proliferation and Apoptosis in Prostate Cancer Cells

Kevser ALBAYRAK¹, Halime TOPAL KIZILOĞLU^{1*}, Rukiye KÖSE¹,
Betül Nur GÜNEY¹, Adem KARA¹

¹Department of Molecular Biology and Genetic, Faculty of Science, Erzurum Technical University, Erzurum/Türkiye.

Received: 05/01/2024, **Revised:** 01/12/2024, **Accepted:** 04/12/2024, **Published:** 31/12/2024

Abstract

Cancer is a complex health problem that occurs as a result of uncontrolled division of cells and includes a series of diseases that depend on evidence and environmental factors. There are more than 100 types of cancer known worldwide. This study used prostate cancer cells, which are the most common disease in men and cause 1,600,000 cases and 366,000 deaths annually. During the cancer treatment process, different medications are used in most cancer patients. In this context, this study examining the proliferation and apoptosis effects of the chemotherapeutic agent Cetuximab (CTX) and the antidepressant Agomelatine drugs on the prostate cancer PC3 cell line emphasizes the great importance of psychological motivation in the treatment process. Focusing on the characteristics and prevalence of prostate cancer, the effects of Cetuximab and Agomelatine on prostate cancer cells were examined.

This research was conducted to understand how the drugs Cetuximab and Agomelatine affect the proliferation and apoptosis in prostate cancer cells. The findings suggest that these drugs may provide potential effects in the treatment of prostate cancer.

Keywords: Prostate cancer, cetuximab, agomelatine, PI3K/AKT/mTOR pathway, gene expression

Cetuximab ve Agomelatin İlaçlarının Prostat Kanseri Hücrelerindeki Proliferasyon ve Apoptoza Etkisinin İncelenmesi

Öz

Kanser, hücrelerin kontrolsüz bölünmesi sonucu ortaya çıkan, delillere ve çevresel faktörlere bağlı bir dizi hastalığı kapsayan karmaşık bir sağlık sorunudur. Dünya çapında bilinen 100'den fazla kanser türü vardır. Bu çalışmada, yılda 1.600.000 vaka ve 366.000 ölümlü sonuçlanan ve erkeklerde en sık görülen prostat kanseri hücreleri kullanılmıştır. Kanser tedavisi sürecinde çoğu kanser hastasında farklı ilaçlar kullanılmaktadır. Bu bağlamda kemoterapötik ajan Cetuximab (CTX) ve antidepressan ajan Agomelatin ilaçları ile prostat kanseri PC3 hücre hattı üzerindeki proliferasyon ve apoptoz üzerindeki etki ile tedavinin önemine odaklandı. Prostat kanserinin özelliklerine ve yaygınlığına odaklanılarak Cetuximab ve Agomelatin'in prostat kanseri hücreleri üzerindeki etkileri incelendi.

Bu araştırma, Cetuximab ve Agomelatin ilaçlarının prostat kanseri hücrelerinde proliferasyonu ve apoptozu nasıl etkilediğini anlamak amacıyla yapıldı. Bulgular, bu ilaçların prostat kanseri tedavisinde potansiyel etkiler sağlayabileceğini düşündürmektedir.

Anahtar Kelimeler: Prostat kanseri, cetuximab, agomelatin, PI3K/AKT/mTOR yolağı, gen ekspresyonu

*Corresponding Author: halimetopal.ht@gmail.com

Kevser ALBAYRAK, <https://orcid.org/0009-0003-1014-485X>

Halime TOPAL KIZILOĞLU, <https://orcid.org/0000-0002-9152-9027>

Rukiye KÖSE, <https://orcid.org/0009-0000-6802-295X>

Betül Nur GÜNEY, <https://orcid.org/0009-0006-9849-3051>

Adem KARA, <https://orcid.org/0000-0002-5766-6116>

1. Introduction

Prostate cancer (PC) is one of the most common types of cancer in men worldwide and causes significant health problems (1). Prostate cancer occurs due to the proliferation and growth of cells in the prostate gland. This type of cancer is associated with various pathophysiological, environmental factors and genetic factors mechanisms (2).

It is the tight expression status of the Epidermal Growth Factor Receptor (EGFR), which is one of the most important factors in the pathogenesis of prostate cancer (3). EGFR is intricately involved in processes such as apoptosis, differentiation process and cellular proliferation (4). Accordingly, monoclonal antibodies such as the therapeutic agent Cetuximab, which targets EGFR, are emerging as a different and important strategy for the treatment of this type of cancer (5, 6).

However, drugs such as Cetuximab, which has a strategic importance, may cause resistance to these and similar treatments over time, despite the initial positive responses for prostate cancer (7, 8). Accordingly, additional treatment or alternative strategies are needed and this emerges as an important issue for the treatment of prostate cancer.

Melatonin regulates mitochondrial functions in cancer cells, reduces reactive oxygen species (ROS) levels, and suppresses tumor growth by arresting the cell cycle via p53/p21 pathways (9, 10, 11). In prostate cancer cells, melatonin activates mitochondrial pathways and triggers apoptosis. It increases the Bax/Bcl-2 ratio, leading to disruption of mitochondrial membrane potential and cytochrome C release. This process induces cell death by activating caspase-3 and caspase-9 (12).

The effects of melatonin on cellular metabolism, cell cycle, metastasis, oxidative stress, apoptosis, and circadian rhythm have been investigated in detail in the context of prostate cancer (13). It has been reported that the disruption of circadian rhythm is associated with the progression of prostate cancer, and melatonin has been shown to suppress the growth and spread of cancer cells by regulating this rhythm. However, more *in vivo* and *in vitro* studies are needed to better understand the mechanisms of these effects (12,13).

Although the effects of melatonin on prostate cancer have been widely studied in the literature, there is no direct study on agomelatine. Agomelatine is an analog of melatonin and has been studied in various types of cancer. This drug, used in the treatment of depressive disorders, may affect important mechanisms in cancer pathogenesis by regulating the circadian rhythm (14). However, more research is needed to elucidate the effects of agomelatine on prostate cancer. The literature also emphasizes that melatonin may affect hormonal regulation and cellular differentiation in prostate cancer cells (12).

This study aims to understand the proliferation and apoptosis effects of drugs on PC3 prostate cancer cells. It is aimed to examine the cellular and molecular responses in detail and explain the pathways. These contribute to knowledge in prostate cancer treatment and research and provide an environment for the development of sustainable treatment strategies.

2. Material and Methods

2.1. Cell Culture

The prostate cancer PC3 cell line used in this study is stored in at -196 °C in Erzurum Technical University, High Technology Application and Research Center (YUTAM), Molecular Cancer Biology Laboratory.

For the PC3 cell line medium, 10% fetal bovine serum (FBS), 1% ml of penicillin-streptomycin (Pen-Strep), 2% L-Glutamine was added to RPMI. The prepared media were stored in 50 ml falcon tubes under +4 °C conditions. Parenteral PC3 monolayer cell lines were incubated in a cell culture medium at 37°C with 5% carbon dioxide (CO₂) and 95% humidity in an incubator (Esco Co., Korea) in 25 cm² flasks under sterile conditions to facilitate cell proliferation.

The cell line, which was kept frozen, was kept in a 37 °C water bath until it was thawed. Then, 3-4 ml of the prepared medium, previously kept at 37 °C, was added into a 15 ml centrifuge tube and centrifugation was performed at 1300 rpm for 5 minutes. Afterwards, the supernatant was removed and the pellet remaining in the centrifuge tube was resuspended in the medium and transferred to a total of 4 ml of medium in a 25 cm² flask.

2.1.3. Passaging of Cells (Subculturing)

Cells that had proliferated and reached a certain confluency (80%) in the cell line were first washed with 2 ml of PBS buffer and then 3 ml trypsin/EDTA (Ethylene Diamine Tetraacetic Acid) was added and kept in a CO₂ incubator for 7-10 minutes to separate the cells from the surface. Then, 8 ml of medium was added and centrifuged at 1300 rpm. The supernatant was removed from the centrifuged cell suspension. 10 ml of medium was added to the pellet and transferred into a 25 cm² flask. The cells whose passaging process was completed were incubated again at 37 °C in a 5% CO₂ incubator with 95% humidity.

2.2. Drug Treatment

2.2.1. Cetuximab and Agomelatine Treatments

Prostate cancer cells (PC3) are prepared together with Agomelatine (Valdoxan, Thymanax, AG0178) and Cetuximab (IMC-C225, Erbitux) cell medium with a concentration of 0.3 µg/ml, 3 µg/ml, 50 µg/ml and cetuximab 50 µg/ml. The concentration used in combined and single study groups are listed in Table 1.

2.3. MTT Assay for Cell Viability

For MTT analysis, 1500 cells were seeded into each well into 2 different plates with 96 wells. Afterwards, it was left for incubation at 37 °C in an oven with 5% CO₂ for 24 hours and 48 hours. MTT (cytotoxicity) analysis was performed to determine the cell viability. The kit was used for this analysis (3-(4,5-dimethylthiazol-2-yl)-2,5-diphenyltetrazolium bromide, Sigma Co. USA) (6-7).

2.3.1. Assay Procedure

MTT analysis is a common colorimetric cytotoxicity test that is frequently used to determine cell viability and results are measured using a spectrophotometer (15). The effects of any therapeutic agent to be used in the MTT method on the desired cell can be determined as cytotoxic or proliferative (16). The MTT kit is used according to its instructions and the possible cytotoxic effect on the PC3 cell line is measured. This method is based on the principle of colorimetric evaluation of the color change in cells incubated with the MTT agent (17).

Agomelatine and/or cetuximab drugs, prepared as serial dilutions kept in the incubator for 24 hours and 48 hours, were divided into groups in series and added to the cell medium. The first column of the A series was set as the cell control and the second column of the A series was set as the medium control. MTT method was then applied to the cells treated with agomelatine and cetuximab, which were incubated for 24 and 48 hours.

Cells were seeded at a density optimized for the detection of cellular metabolic activity and subsequently treated with the drugs. Post-treatment, MTT solution was added, and cells were incubated to facilitate the formation of formazan crystals. The crystals were dissolved, and the absorbance was measured at 570 nm spectrophotometrically. Data were normalized and analyzed to determine the effects of treatments on cellular viability (Multiscan, Thermo, USA).

Based on the results of this analysis, the doses of agomelatine and dose of cetuximab were determined according to previous studies (18, 19).

When these drugs were used together, two combined doses were administered. Afterwards, drug applications at doses appropriate to the determined values were applied to the passaged flasks and incubated for 24 and 48 hours, and these cell flasks were stored for use in qRT-PCR analyses.

2.4. Quantitative Real-Time PCR (qRT-PCR) Analysis

2.4.1. RNA Isolation

Total RNA from PC3 prostate cancer cells treated with drugs was isolated using a commercially available kit according to the manufacturer's instructions (Ambion RNA Mini Kit, USA). The RNA isolation procedure followed a series of necessary steps including cell lysis, homogenization and purification, and a detailed protocol was implemented to ensure the integrity and purity of the isolated RNA. The concentration and purity of the obtained RNA were determined spectrophotometrically using the Nanodrop device (EPOCH Take3 Plate, Biotek), and the RNA samples were stored at -20 °C.

2.4.2. cDNA Synthesis

After RNA isolation, cDNA synthesis was performed using the Maxime RT Premix Kit. The synthesis protocol involves mixing 5 µL of RNA and 15 µL of RNase-free water. Reactions were performed using a Veriti 96-well thermal cycler (Applied Biosystem) with temperature

settings of 45 °C for 60 min and 95 °C for 5 min. Following synthesis, cDNA samples were measured spectrophotometrically and stored at -20 °C.

2.4.3. qRT-PCR Analysis

qRT-PCR analysis Gene expression analysis of EGFR, Bcl-2, Bax, AKT3, PIK3CA, MTOR and GAPDH genes was performed by qRT-PCR using primers specifically designed for each gene (see Table 1 for primer sequences).

Amplification, detection, and data analysis were performed using the Qiagen Rotor-Gene real-time PCR system (Rotor-Gene Q 5plex HRM system) to ensure specificity, efficiency, and reproducibility of the results. Amplification conditions were set at 95°C for 3 min for enzyme activation, 95°C for 5 s (40 cycles) for denaturation, and 60°C for 10 s (40 cycles) for amplification. Relative gene expression was calculated using the $\Delta\Delta CT$ method and provided insight into the molecular mechanisms of cellular responses to drug treatment.

Table 1. List of RT-qPCR primers used for RT-PCR analysis

PRIMER	5'-3' PRIMER SEQUENCES	
BAX	Forward	CGCATCCTGAGGCACCG
	Reverse	TTTCATCCAGGATCGAGCAGGG
GAPDH	Forward	GGTCAATGAAGGGGTCATTGATGG
	Reverse	ATTTGGTCGTATTGGCGCCT
EGFR	Forward	TCGTTGGACAGCCTTCAAGACC
	Reverse	AACACCCTGGTCTGGAAGTACG
BCL	Forward	CGCATCCTGAGGCACCG
	Reverse	TTTCATCCAGGATCGAGCAGGG
AKT3	Forward	GGAAGAATGGACAGAAGCTATTCCA
	Reverse	TCCACTTGCCTTTCTCTCGAAC
MTOR	Forward	GTCAGTGGGACAGCATGGAAG
	Reverse	CCCATATGCCCGACTGTA ACTC

Statistical analyses

MTT and RT-PCR data are expressed as mean \pm standard deviation. Normality analysis was performed using the Shapiro-Wilk test (SPSS 20.0). Differences between groups were determined using the Kruskal-Wallis test. A p value of <0.05 was considered statistically significant.

3. Results and Discussion

3.1. Invert microscopic analysis

MTT analysis provided detailed information about the cell morphology and population density of post-treatment PC3 prostate cancer cells viewed with an inverted microscope. Detailed analysis revealed that survival was significantly reduced in the Agomelatine and Cetuximab treatment groups, with particularly pronounced effects observed at certain doses.

Additionally, the results revealed the possibility of dose- and time-dependent cytotoxic effects of the administered drug. The pooled results of the MTT analysis provide important information to further investigate the potential of Agomelatine and Cetuximab when used alone or in combination as therapeutic agents in the treatment of prostate cancer. The morphology of PC3 cells for the 24 and 48-hour incubation period is seen in Figure 1.

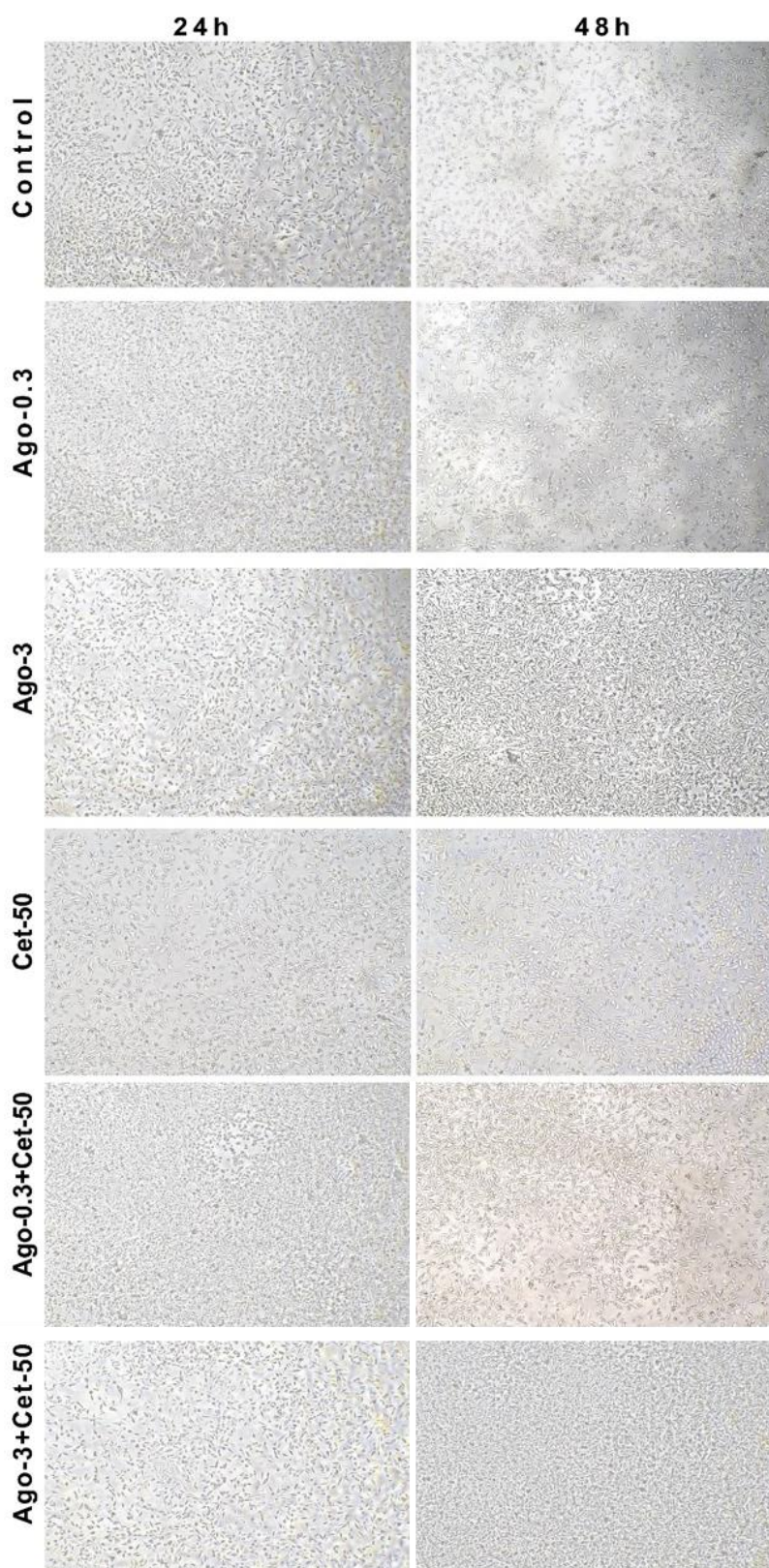


Figure 1. PC3 cells belonging to groups in Agomelatine and/or Cetuximab drug application on an inverted microscope for 24 and 48 hour MTT analysis.

3.2. Cytotoxicity Analysis

The cytotoxic effects of Agomelatine and Cetuximab, alone and in combination, on the PC3 prostate cancer cell line were evaluated by comprehensive analysis. Figure 2 presents the cytotoxicity results obtained when PC3 cells were treated with various dosages of Agomelatine and Cetuximab and then incubated for 24 and 48 hours.

The results show that cell viability was significantly reduced in all treatment groups compared to the control group and varied in a highly dose- and time-dependent manner. In particular, administration of agomelatine at doses of 0.3 $\mu\text{g/ml}$ (Ago-0.3) and 3 $\mu\text{g/ml}$ (Ago-3) significantly reduced cell viability after 24 and 48 h of incubation. Similarly, cetuximab (Cet-50) at a dose of 50 mcg/ml showed strong cytotoxic effects, especially when used in combination with both doses above. Co-administration of Agomelatine and Cetuximab showed significant synergistic effects, especially during the 48-hour incubation period. Cytotoxicity was not only additive but also showed an enhanced effect; this suggested an interaction between the apoptotic and proliferative pathways affected by the two drugs.

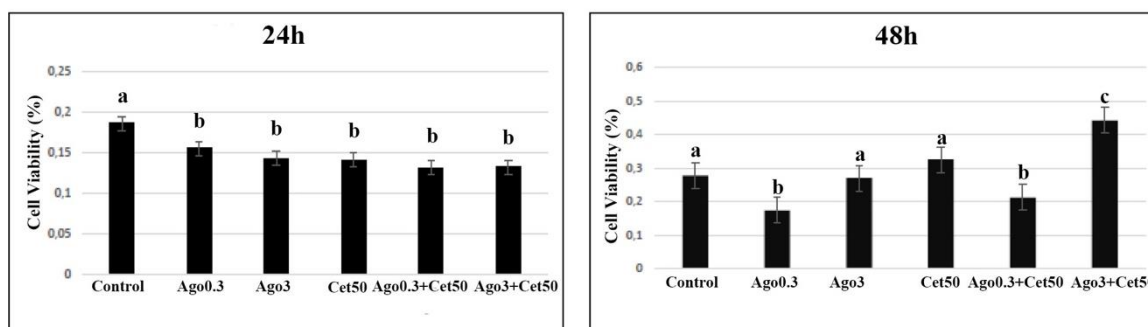


Figure 2. Cytotoxicity results of PC3 prostate cancer cell lines treated with different dosages of agomelatine and/or cetuximab and then incubated for 24 and 48 hours. The data were expressed as mean \pm standard deviation. The letters (a,b,c) indicate the differences between the groups. P value of <0.05 was considered statistically significant.

3.3. Real Time-PCR Analysis Results

Agomelatine and/or Cetuximab interact with EGFR protein at different concentrations and durations, enabling communication between many cancer cells. EGFR, which regulates cell growth and division, is associated with abnormal expression of this gene in multiple types of cancer, such as prostate cancer. When we examine Figure 3, it explains and allows us to observe the EGFR gene expression values for PC3 prostate cancer cells subjected to different concentrations of Agomelatine and Cetuximab drug treatments and durations. When the 24-hour incubated results in the first period were examined, when the Control group was evaluated with the GAPDH gene, the highest EGFR/GAPDH ratio was observed in this period group.

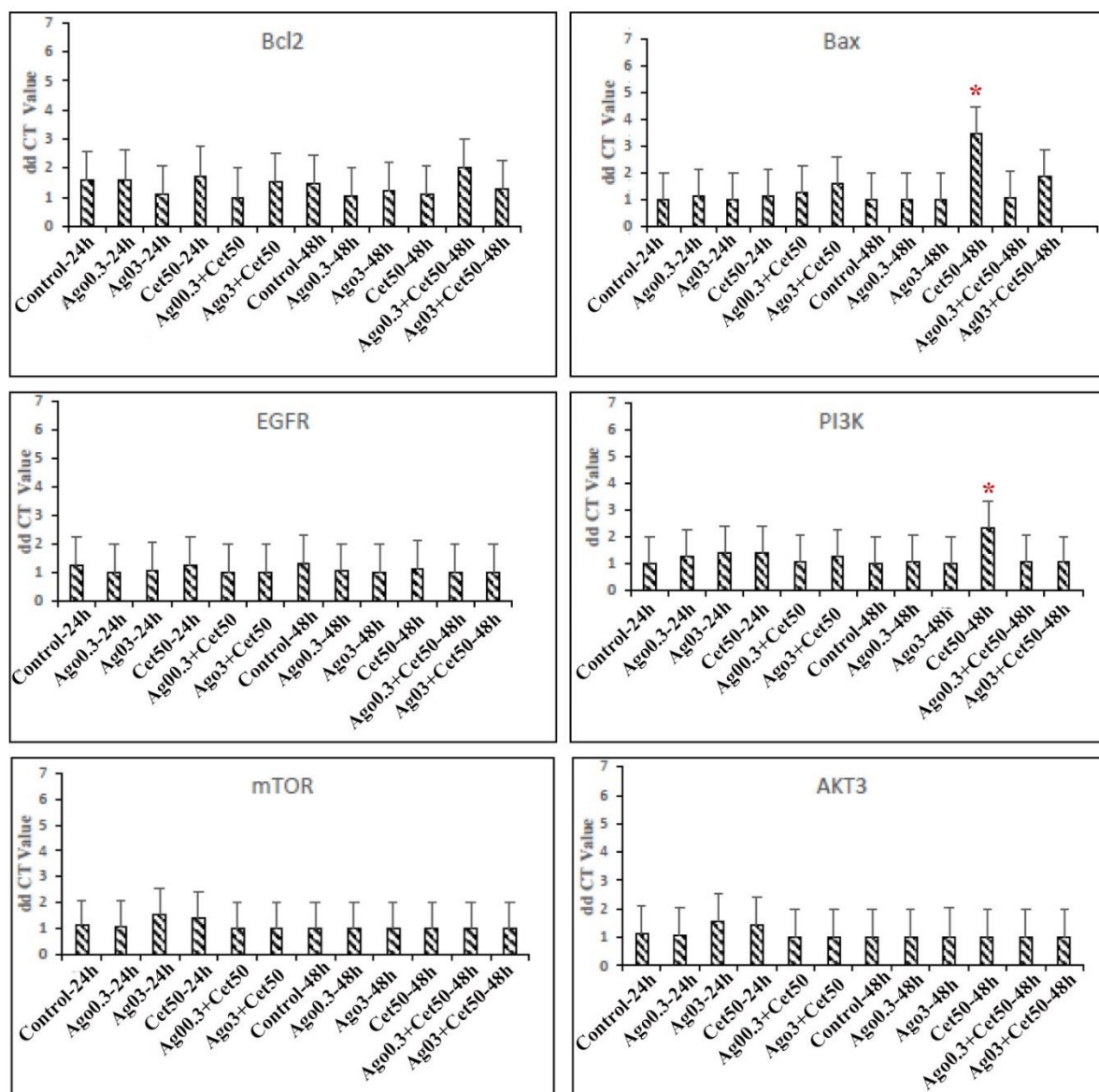


Figure 3. Gene Expression Values of EGFR, PIK3CA, BCL, BAX, mTOR, and AKT3 in PC3 Prostate Cancer Cell Lines Incubated for 24 and 48 Hours with Various Doses of Agomelatine and Cetuximab. The data were expressed as mean \pm standard deviation. The asterisk indicates the differences between the groups. P value of <0.05 was considered statistically significant.

EGFR Gene Expressions

In the study, it was observed that the level of EGFR mRNA expression decreased in the groups administered Agomelatine and/or Cetuximab compared to the control groups. The mRNA expression levels are seen in Fig 3.

PIK3CA Gene Expression

It was observed that PI3K mRNA expression increased more in the Ago3 and Cet 50 groups with 24 hours incubation. It was determined that the increase in the distribution of Agomelatine and Cetuximab in the other 24-hour incubation groups was limited compared to the control

group. PI3K mRNA expression level was determined to be highest in the Cet-50 group with 48 hours incubation (Fig 3).

BCL-2 Gene Expression

While it was determined that Bcl-2 mRNA expression increased in the Ago0.3, Cet-50 and Ago3+Cet 50 groups compared to the control group, mRNA expression in the other groups was determined to be close to the control. Bcl-2 mRNA expression was observed to be at the highest level in the Ago 0.3 +Cet-50 group (Fig 3).

BAX Gene Expressions

It was observed that the mRNA expression level of the BAX gene increased with Ago3 application with an incubation period of 48 hours compared to the control group. It was observed that mRNA levels were close to the control in other groups (Fig 3).

mTOR Gene Expressions

An increase in mTOR mRNA levels was observed in the 24-hour Ago3 and Cet50 groups compared to the control. No significant change was detected in the mTOR mRNA expression levels measured in the other groups and as a result of 48-hour applications compared to the control groups (Fig 3).

AKT3 Gene Expressions

An increase was observed in the Ago3 and Cet50 groups with 24 hours of incubation compared to the control. No change was detected in Akt3 mRNA levels in all other groups (Fig 3).

4. Discussion

Prostate cancer is one of the most common types of cancer in men worldwide and continues to be an important health problem. This type of cancer usually occurs as a disease without visible symptoms and early diagnosis is usually not easy. As cancer progresses, symptoms such as problems in the urinary tract, difficulty urinating, or frequent urination occur (20). For the diagnosis of this type of cancer, regular health checks are required for men in certain age groups. Epidermal Growth Factor (EGF) is a group of proteins that regulate processes such as growth and division in cancer cells (4). Cetuximab, a biological drug used in cancer treatments (21), aims to prevent the growth and proliferation of cancer cells by bonding with the receptor on the cell surface called epidermal growth factor receptor (EGFR). Recently, antidepressant agents can be used as an additional treatment for problems related to mood disorders encountered in cancer patients. Agomelatine, a drug recently used in the treatment of major depressive disorder, has a mechanism that affects serotonergic and melatonergic receptors (22, 23).

Generally, in people diagnosed with cancer, chemotherapy drugs are used for treatment, and in addition to these drugs, drugs such as antidepressants are used to prevent antidepressive disorders (24, 25). Our study aimed to enrich the literature by evaluating the yet undiscovered

treatment effectiveness of Cetuximab, a chemotherapeutic agent, and Agomelatine, an antidepressant additional treatment method, on prostate cancer cells at different concentrations and different incubation periods. This study investigates the effects of single or combined use of 3 µg/ml and 0.3 µg/ml Agomelatine and 50 µg/ml Cetuximab on apoptotic cell death and cell cytotoxicity for the *in vitro* PC3 prostate cancer cell line under 24- and 48-hours incubation. Cell cytotoxicity was determined using the MTT method, which is a colorimetric test. Duplicate groups with EGFR, BAX, BCL2, PIK3CA, mTOR and AKT3 genes were analyzed by real time PCR.

In the study, 6 separate groups were created to better understand the individual and combined effects of cetuximab and/or agomelatine drugs on the cell line. These groups were designed as 1. Control group, 2. Ago0,3 group, 3. Ago3 group, 4. Cet50 group, 5. Ago0,3 + Cet50 group, 6. Ago3 + Cet50 group. As a result of the applications, the division and proliferation of prostate cancer cells have been significantly reduced. In addition, according to the 24-h incubation data of the drugs, it was determined that there was a big difference in combination drug use. According to the 48h cytotoxicity data, it is observed that cell growth is significantly reduced in the low dose of agomelatine drug and in the combination of this group with cetuximab. After determining the antiproliferative role of drugs on prostate cancer cells, protein and mRNA isolations were performed using the same drug doses.

PCR was performed as the second step to investigate the proliferation and apoptosis effects of cetuximab and/or agomelatine drugs at different doses and concentrations applied to PC3 prostate cancer cells. Expression values were determined by subjecting the effects of 6 different primers to multiple tests. As a result of these data, the expression value of these drugs on the *bcl-2* gene is high in the 24h Ago0,3, Ago3 and Cet50 groups and the 48h Ago0,3, Ago3, Cet50, Ago3 + Cet50 groups, showing that we have achieved the expected positive result. The drugs we use, cetuximab and/or agomelatine, increased the effect of the *Bcl-2* gene. Ago3 + Cet50, one of the 24-h incubated groups, also has high expression values on the *Bax* gene of prostate cancer PC3 drug-treated cells. The group with the highest expression value in the groups as a result of 48h incubation is Cet50. The group with the lowest expression value in 24h and 48h incubations is Ago3. This is generally a positive and desired outcome for these values. It was observed that the expression values of the EGFR gene of PC3 prostate drug-treated cells were high in the Ago0,3, Ago3 and Ago0,3 + Cet50 groups as a result of 24h incubation. It was determined that expression values were high in all groups of 48h incubated cells (Ago0,3, Ago3, Cet50, Ago0,3 + Cet50, Ago3 + Cet50). There is no increased expression of the PI3K gene in PC3 prostate cancer drug-treated cells in the 24h and 48h groups. The expression of the 48h Cet50 group increased in the opposite direction. According to the 24-h incubation data of the groups formed with cetuximab and agomelatine drugs in different doses and combinations, it was observed that the expression value of the mTOR gene increased in the Ago3 and Cet50 groups. ddCT values of 48h incubation cells are close to each other and the expression value is not positive. It is observed that the expression values of the last primer, AKT3 gene, in drug-treated prostate cancer cells are high in Ago0,3 and Ago0,3 + Cet50 of the 24h incubation groups. It is shown that the values of the AKT3 gene in the groups incubated for 48 h are close to each other and ineffective.

The apoptotic effects induced by Agomelatine in our study are consistent with similar results observed in prostate cancer cell lines in the literature (26). Melatonin has antitumoral effects in many types of cancer by contributing to the maintenance of metabolic homeostasis through the regulation of circadian rhythm. These effects are associated with reducing cellular oxidative stress, improving mitochondrial functions, and activating apoptotic pathways (17, 23). In addition, melatonin is reported to arrest the cell cycle and suppress tumor growth via the p53/p21 pathways (22). These findings demonstrate that combinations of cetuximab and agomelatine is more effective on apoptotic mechanisms in prostate cancer cell lines and indicate that these molecular mechanisms should be supported by more comprehensive studies.

As a result of these data, it was determined that although the Bcl-2 gene from 6 different primers applied to different doses and combinations of cetuximab and/or agomelatine drugs in PC3 prostate cancer cells was antiapoptotic, the applied drugs had an effect and led the cancerous cells to apoptosis. This shows the desired positive effect of the cetuximab and/or agomelatine drugs used on cancer cells. In the results drawn for the Bax gene, the desired positive result of cetuximab and/or agomelatine drugs could not be achieved due to the low values in the general groups. Since the EGFR gene is a proliferation gene, it is observed that most of the drug groups that are expected to be suppressed show pressure on EGFR. Therefore, it can be thought that the drugs and doses used may slow down cell growth and proliferation. Since PI3K, mTOR, AKT3 genes are genes that trigger proliferation, they are indicated in the graph with the values at which they could not initiate proliferation in all groups administered with cetuximab and/or agomelatine drugs in different doses and combinations. The data on these genes show that cetuximab and/or agomelatine drugs may provide positive results in slowing or stopping the division of PC3 prostate cancer cells and driving the cancerous cells into apoptosis.

5. Conclusion

This study was conducted to determine the temperature of different methods of cetuximab and/or agomelatine drugs on PC3 cell proliferation. The results of the study revealed that there was a significant decrease in the viability of human PC3 prostate cancer cells after separate and combined applications in some groups. However, when the general effect of these applications on apoptosis was investigated, it was seen that apoptosis was stimulated. The suppression of proliferation and induction of apoptosis observed in some experimental setups provides new horizons in the knowledge of the mechanistic basis of survival and death of PC3 cells in response to this treatment.

Based on the results, it seems that new treatment screening processes can be carried out by continuing with genes and mechanisms related to apoptosis and survival. In order to obtain a definitive and complete result, more detailed studies are needed on this subject, both in vitro and in vivo. Apart from these, the current study reveals that cetuximab and/or agomelatine drugs and their services may present a promising additional treatment opportunity in addition to prostate cancer drug treatments.

Ethics in Publishing

There are no ethical issues regarding the publication of this study

Author Contributions

KA, HTK, RK, BNG and AK contributed to project conception, laboratory works and study design. Writing the article (KA, HTK, AK). All authors read and approved the manuscript. KA; Kevser ALBAYRAK, HTK; Halime TOPAL KIZILOĞLU, RK; Rukiye KÖSE, BNG; Betül Nur GÜNEY, AK; Adem KARA.

References

- [1] Ertunç O., Tuna B. (2022), Prostat Kanseri Moleküler Patogenezi. Isparta: Süleyman Demirel Üniversitesi Tıp Fakültesi Dergisi. 29(4), 697-706.
- [2] Lindsey A Torre , Freddie Bray, Rebecca L Siegel, Jacques Ferlay, Joannie Lortet-Tieulent, Ahmedin Jemal, (2012), Global cancer statistics, CA Cancer J Clin, 65(2):87-108.
- [3] Nastały P. et al. (2020), EGFR as a stable marker of prostate cancer dissemination to bones, British Journal of Cancer, 123:1767–1774.
- [4] Uribe M.L, Marrocco L. and Yarden Y., (2021), EGFR in Cancer: Signaling Mechanisms, Drugs, and Acquired Resistance, 13, 2748.
- [5] Zık B. (2004), Epidermal Büyüme Faktörü Reseptörünün (EGFR) Horozların Üropigi Bezinde Immunohistokimyasal Yerleşimi, Uludag Univ. J. Fac. Vet. Med. 1-2-3: 49-53.
- [6] Yue S., Zhang Y., Wei Y., Haag R., Sun H. and Zhong Z., (2022), Cetuximab–Polymersome–Mertansine Nanodrug for Potent and Targeted Therapy of EGFR-Positive Cancers, Biomaterials for Oral Medicine, 23(1), 100-111.
- [7] Dülğar Ö, Yılmaz M, Tural D. (2018), Metastatik Kastrasyona Dirençli Prostat Kanserinde Sistemik Tedavi, Galenos Yayınevi, 4,225-230.
- [8] Vincenzi B. et al., (2008), The biological properties of cetuximab, Critical Reviews in Oncology/Hematology, 68 (2),93-106.
- [9] Megerian MF, Kim JS, Badreddine J, Hong SH, Ponsky LE, Shin J, Ghayda RA, (2023), Melatonin and Prostate Cancer: Anti-tumor Roles and Therapeutic Application, Aging and Disease, 14(3),840-857.
- [10] Reiter RJ., Rosales-Corral, S., Tan, D. X., Acuna-Castroviejo, D., Qin, L., & Yang, S. F. (2017), Melatonin as a mitochondria-targeted antioxidant: One of evolution's best ideas. Cellular and Molecular Life Sciences, 74(21), 3863-3881.

- [11] Hill, S. M., Belancio, V. P., Dauchy, R. T., Xiang, S., Brimer, S., Mao, L., & Blask, D. E. (2015). Melatonin: An inhibitor of breast cancer. *Endocrine-Related Cancer*, 22(3), 183-204.
- [12] Sainz, R. M., Mayo, J. C., Tan, D. X., Leon, J., Manchester, L. C., & Reiter, R. J. (2005). Melatonin reduces prostate cancer cell growth leading to p53- and p21-mediated induction of cell cycle arrest and apoptosis. *Journal of Pineal Research*, 39(3), 234–242.
- [13] Blask, D. E., Dauchy, R. T., Sauer, L. A., Krause, J. A., & Brainard, G. C. (2011). Melatonin, mitochondria, and the metabolic syndrome: Cellular mechanisms, clinical impact, and implications for breast cancer. *Integrative Cancer Therapies*, 10(4), 316–329.
- [14] Maiese, K. (2015), Agomelatine: The role of circadian rhythms in cancer progression." *Molecular Neurobiology*, 52(3), 1017-1025
- [15] Erkekoğlu P, Baydar T. (2021), Güncel In Vitro Sitotoksitesite Testleri. Hacettepe University Journal of The Faculty of Pharmacy. 41(1),45-63.
- [16] Gedikli S. (2013), Melatoninin Mcf-7 Hücre Kültüründeki Apoptoz Aktivasyonunun Ve Sitotoksitesinin Polimeraz Zincir Reaksiyonu (Pcr), Mtt Hücre Canlılık Testi Ve İmmünohistokimya Yöntemleriyle Araştırılması, Atatürk Üniversitesi Sağlık Bilimleri Enstitüsü-Doktora Tezi.
- [17] Polat S. (2015), Kolorektal Kanser Hücrelerinde Melatonin Ve Cisplatin Uygulamasının Otofaji Ve Apoptoz Üzerine Etkilerinin Araştırılması. Atatürk Üniversitesi Sağlık Bilimleri Enstitüsü Tıp Histoloji ve Embriyoloji Anabilim Dalı. Yüksek Lisans Tezi.
- [18] Galeti A.O.C., (2021), Verification of agomelatine in comparison with melatonin as a therapeutic agent to treat breast cancer, *Melatonin Research*, 4 (1) 141-151.
- [19] Hallal R., Lyu N., Wang Y., (2021), Effect of Cetuximab-Conjugated Gold Nanoparticles on the Cytotoxicity and Phenotypic Evolution of Colorectal Cancer Cells, *Molecules*, 26(3), 567.
- [20] Gandaglia G, Leni R, Bray F, Fleshner N, Freedland SJ, Kibel A, Stattin P, Poppel H, Vecchia C, (2021), Epidemiology and Prevention of Prostate Cancer, *European Urology Oncology*, 4(6), 877-892.
- [21] Li R., Liang M., Liang X., Yang L., Su M. and Lai K.P, (2020), Chemotherapeutic Effectiveness of Combining Cetuximab for Metastatic Colorectal Cancer Treatment: A System Review and Meta-Analysis, *Frontiers in Oncology*, 10,868.
- [22] Anderson G., (2023), Tumor Microenvironment and Metabolism: Role of the Mitochondrial Melatonergic Pathway in Determining Intercellular Interactions in a New Dynamic Homeostasis, *International Journal of Molecular Science*, 24(1), 311.

[23] Çetin, D. K. (2013), Metastatik Kolorektal Kanserli Hastaların Tedavisinde Cetuximab Veya Bevacizumab İçeren Kombinasyonların Etkinlik Ve Yan Etkilerinin Değerlendirilmesi. Karadeniz Teknik Üniversitesi.

[24] Tünel M, Vural A, Evlice Y.E. Tamam L. (2012), Meme Kanserli Hastalarda Psikiyatrik Sorunlar, Arşiv Kaynak Tarama Dergisi, 21(3):189-219.

[25] Zheng Y, Chang X, Huang Y, He D, (2023), The application of antidepressant drugs in cancer treatment, Biomedicine & Pharmacotherapy, 157, 113985.

[26] Schroeder JC, DiNatale BC, Murray IA, (2013), The role of melatonin and its analogues in prostate cancer therapy, Cancer Letters, 337(1):1-9.

Mitigating Osmotic Drought Stress in Rye: Assessing the Ameliorative Effects of Putrescine on Germination, Seedling and Mitotic Index

Erdal Eren YELER^{1*}, Metin TOSUN², Aras TÜRKOĞLU³

¹Field Crops Central Research Institute, Meadow-Rangeland and Forage Crops Department, Ankara, Türkiye

²Department of Field Crops, Faculty of Agriculture, Ataturk University, 25240 Erzurum, Türkiye

³Department of Field Crops, Faculty of Agriculture, Necmettin Erbakan University, Konya, Türkiye

Received: 06/02/2024, **Revised:** 28/08/2024, **Accepted:** 03/09/2024, **Published:** 31/12/2024

Abstract

In this study, the impact of putrescine, a polyamine, on the germination, seedling growth, and mitotic index of rye seeds (cv. Aslm-95) was investigated under osmotic drought conditions induced by polyethylene glycol (PEG-6000) application. The experiment involved six different PEG doses (-2, -4, -6, -8, and -10 bars) in combination with putrescine doses of 0.001, 0.01, and 0.1 mM. The concentration of -2 bars of polyethylene glycol, representing osmotic drought, positively influenced some of the studied characteristics. However, the stimulative effect of -2 bars of osmotic drought exhibited minimal changes with PEG 6000 + putrescine combinations. Conversely, as the concentration of osmotic drought (PEG 6000 concentration) increased, all observed traits, especially germination and seedling development, were negatively impacted. All putrescine doses used in combination with PEG-6000 demonstrated positive effects on the examined characteristics and reduced the germination duration. The most significant effect of putrescine on the negative effects caused by osmotic drought was observed at a concentration of 0.1 mM on root dry weight and at a concentration of 0.001 mM on all other characteristics.

Keywords: Rye, PEG 6000, putrescine, germination, seedling, mitotic index.

Çavdarda Ozmotik Kuraklık Stresinin Azaltılması: Putresinin Çimlenme, Fide Gelişimi ve Mitotik İndeks Üzerindeki İyileştirici Etkilerinin Değerlendirilmesi

Öz

Bu çalışmada, polietilen glikol (PEG-6000) uygulamasıyla oluşturulan ozmotik kuraklık koşullarında bir poliamin olan putresinin çavdar tohumlarının (Aslm-95 çeşidi) çimlenmesi, fide büyümesi ve mitotik indeksi üzerine etkisi araştırılmıştır. Bu çalışma, 0,001, 0,01 ve 0,1 mM'lik putresin dozlarıyla kombinasyon halinde altı farklı (-2, -4, -6, -8 ve -10 bar) PEG-6000 dozunu içermektedir. Ozmotik kuraklığı temsil eden -2 bar polietilen glikol konsantrasyonu, incelenen bazı özellikleri olumlu yönde etkilemiştir. Ancak -2 bar ozmotik kuraklığın uyarıcı etkisi PEG 6000 + putresin kombinasyonları ile minimum düzeyde değişiklik göstermiştir. Diğer taraftan, ozmotik kuraklığın (PEG 6000 konsantrasyonu) konsantrasyonu arttıkça özellikle çimlenme ve fide gelişimi olmak üzere gözlemlenen tüm özellikler olumsuz yönde etkilenmiştir. PEG 6000 ile kombinasyon halinde kullanılan tüm putresin dozları incelenen özellikler üzerinde olumlu etki göstermiş ve çimlenme süresini kısaltmıştır. Putresinin ozmotik kuraklığın neden olduğu olumsuz etkiler üzerinde en belirgin etkisi kök kuru ağırlığında 0,1 mM konsantrasyonunda ve diğer tüm özelliklerde 0,001 mM konsantrasyonunda gözlenmiştir.

Anahtar Kelimeler: Çavdar, PEG 6000, putresin, çimlenme, fide, mitotik indeks

1. Introduction

Cereals represent fundamental commodities utilized either directly or indirectly in human nutrition. Globally, over 50% of individuals derive their daily caloric intake from grains. Notably, given that animals predominantly consume plant-based materials, and the contribution of animal-based foods to daily caloric intake is approximately 20%, it becomes evident that humans obtain roughly three-quarters of their daily nutrition from grains [1].

Rye holds significant importance in our country as it serves dual purposes as both bread and fodder due to its high nutritional value. Its robust root system enables efficient water absorption from the soil, surpassing other grains in this aspect. With an annual rainfall requirement of around 150 mm, rye emerges as a viable alternative for cultivation in regions with low precipitation. Moreover, its adaptability extends to sloping, stony, and low-fertility soils where other cultivated plants may not thrive economically. The versatility of rye is further highlighted by its root system's ability to develop either deep or superficially, depending on the specific soil characteristics of the planting location. In our country, rye is cultivated across an area of 99,935 hectares, resulting in a production of 273 thousand tons and a yield of approximately 2.79 t/ha [2].

Environmental stress factors have a detrimental impact on plant development and yield [3]. Drought stress occurs when plants are unable to extract sufficient water from the soil through their roots or when the transpiration rate is excessively high. The repercussions of drought in crop production include challenges such as insufficient plant emergence, reduced development, and decreased yield [4]. The stages of seed germination and subsequent seedling growth are particularly susceptible to adverse environmental conditions, and any damage during these phases can prematurely terminate the plant life cycle [5, 6].

Drought poses a substantial constraint on global crop production, and contemporary climate change exacerbates this issue [7]. The impact of drought conditions on plant growth and grain yield is contingent upon the severity of drought and the developmental stage of the plant when drought occurs. Seedling emergence stands out as a growth period highly sensitive to water deficit. The rate and extent of seedling establishment play pivotal roles in determining yield and time to maturity [8]. Therefore, for successful plant establishment, crucial characteristics such as seed germination, vigor, and coleoptile length must meet adequate standards. In semi-arid regions, low moisture levels during germination present a limiting factor. Some studies suggest that coleoptile length is crucial for the successful establishment of seedlings, especially when seeds are sown deep to reach moisture in dry soils [9]. Researchers often employ chemicals like PEG in studies aiming to assess the drought resistance of seedlings during the early development period, as these substances contribute to intensifying drought severity in controlled environments [10].

Despite advancements in the discovery of new hormones, growth regulators, and insights from plant gene technology, there remains a gap in our understanding of the physiology and biochemistry of seed germination. Consequently, investigating the effects of growth regulators such as triacontanol, brassinosteroids, and polyamines (putrescine, spermine, spermidine, cadaverine) on seed germination becomes particularly intriguing. These regulators have shown efficacy in influencing plant growth and development, holding the potential for significant

advancements in addressing contemporary challenges such as hunger. The primary objective of this study was to assess the impact of artificially induced osmotic drought using PEG 6000 on the germination and seedling development of rye. Additionally, the study aimed to elucidate the potential of putrescine, a growth regulator, in mitigating the adverse effects of osmotic drought on these critical traits. This research has the potential to contribute valuable insights into enhancing crop resilience and productivity in the face of environmental stressors, aligning with the pressing global concern of food security.

2. Materials and Methods

The research was conducted in the Biotechnology laboratory of Atatürk University Faculty of Agriculture, utilizing seeds of the Aslım 95 variety of diploid rye (*Secale cereale* L.) as the primary material. The seeds underwent a thorough preparation process, including washing with tap water, stirring in 70% ethyl alcohol (EtOH) for 3 minutes, followed by three washes with sterile distilled water within a sterile cabinet. Surface sterilization was carried out in a solution containing 10% bleach with a few drops of Tween 20 (Sigma) for 15 minutes. After this process, the seeds were again washed with sterile distilled water and left at room temperature for 24 hours at four different putrescine concentrations [0 (distilled water), 0.001, 0.01, and 0.1 mM] [11]. Following the 24-hour period, the surface-sterilized seeds were washed to remove putrescine and then transferred to blotting papers, where they were dried for 3 hours. Subsequently, 25 dried seeds were sown in each 9 cm diameter petri dish containing two layers of germination paper (Whatman paper number 1). A solution with six different osmotic potentials [0 (pure water), -2, -4, -6, -8, and -10 bar], formed with PEG 6000, was added to the petri dishes. Concentrations of 0, -2, -4, -6, -8, and -10 bar of PEG 6000 solutions were employed to establish osmotic potential [12]. After this setup, the seeds were germinated at 20°C under a 16:8 hours light:dark photoperiod. For the following 10 days, 10 ml of each of the six different doses of PEG 6000 solution was added daily. The experimental design included 4 replicates, following a Completely randomized design. The data obtained from the experiment were subjected to analysis of variance using the SPSS statistical package program, employing a 6 (osmotic potential) × 4 (putrescine dose) factorial arrangement. Subsequently, averages were compared using the Duncan [12] test for further analysis.

Characters examined in the experiment

a. Germination-related characters: Germination rate concerning seed germination [14], germination rate index [15, 16], germination vigor index [17] and mean germination time [18].

b. Seedling-related characters: The total number of embryonal roots, root length, shoot length, root dry weight, and shoot dry weight were investigated in the seedlings obtained in the experiment [19].

c. Mitotic index: The method specified by Sağsöz [20] and Tosun [21] was used to prepare the samples to determine the mitotic index. 5000-6000 cells were counted in each prepared preparation. Cells in prophase, metaphase, anaphase, and telophase were evaluated as dividing cells, and the others as non-dividing cells, and the mitotic index was calculated as % according

to the formula given below [22]. Mitotic index (%) = (number of cells dividing / total number of cells) x 100.

3. Results

3.1. Effects of drought and putrescine application on germination related characters

a) Germination Rate (GR)

The impact of drought, induced with PEG 6000, and putrescine treatments, as well as the interaction between drought and putrescine, exhibited significant effects on the germination rate (GR) of seeds ($P < 0.01$) (Table 1). As the severity of drought, induced by PEG 6000 application, increased, there was a noticeable decrease in the germination rate of seeds. Specifically, the GR, initially at 58.75% in the control, progressively decreased at -2, -4, -6, -8, and -10 bar applications, ultimately reaching 6.00%. Conversely, putrescine application had a positive effect on the germination rate. For instance, the GR, starting at 0.50% in the absence of putrescine, increased to 55.50% at a 0.001 mM dose, 43.66% at a 0.01 mM dose, and 36.33% at a 0.1 mM dose. The differences between all treatments were statistically highly significant. Notably, the effect of putrescine on GR was more pronounced at the 0.001 mM dose compared to other doses. In other words, treatments with doses higher than 0.001 mM significantly enhanced the GR compared to the control, but their effects were less prominent than the 0.001 mM dose. The highest GR of 85.00% was achieved in treatments where drought was not applied, while putrescine was administered at a dose of 0.001 mM (Table 2).

Table 1. Analysis of variance results of the characters related to germination after different doses of PEG 6000 and putrescine applications to seeds.

The average of the squares of the errors					
Variation source	DF	GR	GRI	GVI	MGT
Drought (D)	5	6344.00**	31.30**	14143658.69**	23.69**
Putrescine (P)	3	13467.11**	10.09**	3227973.68**	35.42**
D x G	15	796.71**	0.43**	289791.39**	2.09**
Error	72	6.55	0.06	9839.28	0.07
Total	96				

** Significant at the $P < 0.01$ level.

Table 2. Data on some characters related to germination after PEG-6000 and putrescine treatments to seeds.

Drought (bar)	Putrescine (mM)	GR (%)	GRI	GVI	MGT (day)
0	0	3.00 c ¹	18.60 d	1966.00 d	5.57 a
	0.001	85.00 a	20.06 a	3604.00 a	4.20 c
	0.01	82.00 a	19.91 b	3354.00 b	4.32 c
	0.1	65.00 b	19.66 c	2709.00 c	4.54 b
	Mean	58.75 A²	19.56 A	2908.00 A	4.65 F
-2	0	0.00 c	18.10 d	1905.00 d	6.12 a
	0.001	71.00 a	19.73 a	3539.00 a	4.49 c
	0.01	60.00 b	19.57 b	3320.00 b	4.62 c
	0.1	58.00 b	19.40 c	2655.00 c	4.88 b
	Mean	47.25 B	19.20 B	2854.00 B	5.02 E

Mitigating Osmotic Drought Stress in Rye: Assessing the Ameliorative Effects of Putrescine on Germination, Seedling and Mitotic Index

-4	0	0.00 b	17.70 c	1219.68 d	6.82 a
	0.001	58.00 a	19.21 ab	2084.00 a	5.22 b
	0.01	56.00 a	19.38 a	179.44 b	4.76 c
	0.1	55.00 a	19.18 b	1553.00 c	5.20 b
	Mean	42.25 C	18.87 C	1661.45 C	5.50 D
-6	0	0.00 c	17.31 c	995.00 c	7.80 a
	0.001	55.00 a	18.82 a	1476.30 a	5.55 b
	0.01	42.00 b	18.16 b	1171.96 b	5.49 b
	0.1	40.00 b	18.61 a	1053.12 bc	5.76 b
	Mean	34.25 D	18.22 D	1172.49 D	6.15 C
-8	0	0.00 c	16.78 b	511.92 b	10.03 a
	0.001	40.00 a	17.50 ab	796.28 a	5.42 c
	0.01	22.00 b	17.64 a	760.26 a	5.72 c
	0.1	0.00 c	17.11 ab	647.52 ab	8.00 b
	Mean	15.50 E	17.26 E	681.26 E	7.29 B
-10	0	0.00 b	14.92 c	98.56 d	10.29 a
	0.001	24.00 a	17.11 a	453.60 a	5.62 c
	0.01	0.00 b	15.78 b	309.68 b	7.04 b
	0.1	0.00 b	15.51 b	193.16 c	7.63 b
	Mean	6.00 F	15.83 F	246.10 F	7.64 A
Mean of Putrescine	0	0.50 D	17.23 D	986.78 D	7.77 A
	0.001	55.50 A	18.74 A	1850.50 A	5.08 D
	0.01	43.66 B	18.41 B	1624.09 B	5.32 C
	0.1	36.33 C	18.24 C	1333.86 C	6.00 B

¹. Differences between means shown with the same lowercase letter in the same column for each application are insignificant.

². Differences between means with the same capital letter in the same column are insignificant.

b) Germination rate index (GRI)

The impact of drought and putrescine treatments induced by PEG 6000 on the Germination Rate Index (GRI) was found to be highly significant ($P < 0.01$), with a similarly significant interaction observed between drought and putrescine ($P < 0.01$) (Table 1).

The GRI exhibited a continuous decrease in response to the increasing severity of drought. Specifically, the GRI, starting at 19.56 in the control group, decreased to 19.20 at -2 bars, 18.87 at -4 bars, 18.22 at -6 bars, and 17.26 at -8 bars. Beyond this, at -10 bars, the GRI experienced a much more significant decrease, reaching 15.83. Contrastingly, the effect of putrescine application on GRI while statistically highly significant, remained at a limited level. For instance, the GRI, initially at 17.23 in the control group without putrescine application, increased to 18.74 with the application of 0.001 mM putrescine. At higher doses of 0.01- and 0.1-mM putrescine, the GRI exhibited slight decreases to 18.41 and 18.24, respectively. Considering the drought x putrescine interaction, the highest GRI (20.06) was determined at the 0.001 mM putrescine application dose in the group where drought was not applied (Table 2). This suggests a nuanced interplay between drought and putrescine in influencing the germination rate index.

c) Germination vigour index (GVI)

As depicted in Table 1, the effects of drought induced by PEG 6000, putrescine, and the interaction between drought and putrescine on the the GVI were found to be highly significant ($P<0.01$). The impact of drought induced by PEG 6000 on the GVI decreased significantly with the escalation of drought severity (PEG 6000 concentration). The GVI, initially at 2908.00 in the absence of drought, steadily declined to 246.10 at the -10 bar dose. Notably, the most substantial decrease occurred at doses of -8 and -10 bars. When evaluating the effect of putrescine applied in combination with PEG 6000 on the germination vigour index, it was observed that putrescine had a positive influence on the GVI. Specifically, the GVI, averaging 986.78 at 0 mM putrescine, reached its highest value at 1850.50 with the application of 0.001 mM putrescine, approximately doubling. There was a slight decrease in GVI at putrescine concentrations beyond this. For instance, the GVI was 1624.09 at 0.01 mM putrescine and 1333.86 at 0.1 mM putrescine. Consistent with other traits the most significant effect of putrescine on the GVI was observed at the dose where PEG 6000 was applied at a concentration of -10 bars. For example, the GVI. starting at 98.56 when putrescine was not applied at this dose. significantly increased to 453.60 with the application of 0.001 mM putrescine (Table 2).

d) Mean germination time (MGT)

The impact of drought, putrescine, and the interaction between drought and putrescine on the Mean Germination Time (MGT) of diploid rye seeds was found to be highly significant ($P<0.01$) (Table 1). It was observed that the MGT increased with the concentration of PEG 6000. Specifically, the MGT values were 4.65, 5.02, 5.50, 6.15, 7.29 and 7.64 days at PEG 6000 concentrations corresponding to osmotic pressures of 0, -2, -4, -6, -8 and -10 bars. respectively. Notably, at doses of -8 and -10 bars.,the germination time was significantly longer compared to other doses indicating a notable delay in germination under more severe drought conditions. When analyzing the effect of putrescine on the MGT, it was observed that the MGT was significantly reduced at different concentrations. For instance, the MGT, initially at 7.77 days in the control group, decreased to 5.08 days with 0.001 mM putrescine treatment. Additionally, the MGT was 5.32 and 6.00 days at 0.01 and 0.1 mM putrescine concentrations, respectively. The most significant effect of putrescine on the MGT was observed at -8 and -10 bar doses of PEG 6000. For example, the MGT, initially at 10.29 days with no putrescine applied at -10 bars, decreased to 5.62 days with the application of 0.001 mM putrescine (Table 2). This suggests that putrescine has a notable impact in reducing the mean germination time. particularly under more severe drought conditions.

3.2. Drought and putrescine application on seedling-related characters

a) Number of embryonal roots (NER)

The effect of drought, putrescine, and the interaction between drought and putrescine on the Number of Embryonal Roots (NER) was found to be highly significant ($P<0.01$) (Table 3). With the increase in the severity of drought induced by PEG 6000 application, the number of roots in seedlings decreased. The NER, starting at 4.66 in the control group without PEG 6000

Mitigating Osmotic Drought Stress in Rye: Assessing the Ameliorative Effects of Putrescine on Germination, Seedling and Mitotic Index

treatment, steadily decreased at -2, -4, -6, -8 and -10 bar treatments, reaching 4.51, 4.16, 3.78, 3.57, and 3.40, respectively. The difference between the group without PEG 6000 (control) and the -2-bar dose was statistically insignificant, grouping these two treatments together. However, the other doses (-4, -6, -8, and -10 bars) formed distinct groups. In contrast, putrescine application had a positive effect on the NER. For instance, the NER, initially at 3.90 in the absence of putrescine, increased to 4.35 at 0.001 mM, 4.01 at 0.01 mM, and 3.79 at 0.1 mM dose of putrescine. Upon closer examination of the drought x putrescine interaction, a small decrease was noted in -4 bar + 0.01 mM, -4 bar + 0.1 mM, -6 bar + 0.001 mM, -6 bar + 0.01 mM, and -6 bar + 0.1 mM interactions compared to the control. The most significant effect of putrescine on the NER was observed at -10 bar, like other traits. At this dose, the average number of embryonal roots was 4.00 in the 0.001 mM putrescine treatment, compared to 3.00 in the control (Table 4). This underscores the potential of putrescine in mitigating the adverse effects of severe drought on the number of embryonal roots.

Table 3. Variance analysis results of seedlings and some related characters after different doses of PEG 6000 and putrescine were applied to the seeds

The average of the squares of the errors							
Varyasyon kaynağı	DF	NER	RL	SL	RDW	SDW	MI
Drought (D)	5	20.99**	1520.85**	2600.13**	0.009**	0.015**	20388.66**
Putrescine (P)	3	7.23**	402.04**	626.01**	0.004**	0.018**	9491.71**
D × P	15	1.06**	25.14**	57.39**	0.003**	0.002**	962.31**
Error	72	0.48	1.31	0.98	0.001	0.001	60.23
Toptal	96						

** Significant at P<0.01 level.

Table 4. Data on some seedling characters after PEG 6000 and putrescine treatments.

Drought (bar)	Putrescine (mM)	NER (number)	RL (cm)	SL (cm)	RDW (mg)	SDW (mg)	MI (%)
0	0	4.40 b ¹	8.80 d	10.86 c	0.0186 d	0.0511 d	26.53 c
	0.001	4.95 a	15.80 a	20.24 a	0.0384 a	0.0756 a	60.40 a
	0.01	4.80 ab	13.89 b	19.65 a	0.0288 b	0.0686 b	65.58 a
	0.1	4.50 ab	11.36 c	15.73 b	0.0252 c	0.0624 c	45.32 b
	Average	4.66 A²	12.46 B	16.62 A	0.0277 B	0.0644 A	49.46 B
-2	0	4.55 ab	10.40 d	8.65 c	0.0309 b	0.0413 d	23.95 c
	0.001	5.00 a	17.30 a	18.09 a	0.0602 a	0.0685 a	72.30 a
	0.01	4.40 b	15.05 b	18.15 a	0.0421 ab	0.0624 b	67.10 a
	0.1	4.10 b	12.15 c	14.40 b	0.0327 ab	0.0581 c	45.86 b
	Average	4.51 A	13.72 A	14.82 B	0.0414 A	0.0575 AB	52.30 A
-4	0	4.20 b	6.10 d	6.22 d	0.0219 b	0.0479 a	20.42 c
	0.001	4.70 a	11.40 a	9.44 a	0.0219 b	0.0612 a	50.35 a
	0.01	3.80 c	9.80 b	8.48 b	0.0171 b	0.0527 a	35.19 b
	0.1	3.95 bc	8.28 c	7.25 c	0.0394 a	0.0447 a	32.47 b
	Average	4.16 B	8.89 C	7.85 C	0.0250 BC	0.0516 BC	34.61 C
-6	0	3.85 a	5.38 c	4.17 c	0.0077 b	0.0291 c	11.88 c
	0.001	3.80 a	8.35 a	7.19 a	0.0164 b	0.0586 a	38.36 a
	0.01	3.80 a	7.80 a	6.32 b	0.0096 c	0.0511 b	26.69 b
	0.1	3.70 a	6.48 b	4.49 c	0.0568 a	0.0318 c	14.42 c
	Average	3.78 C	7.00 D	5.54 D	0.0226 BC	0.0426 C	22.84 D
-8	0	3.40 a	4.20 c	2.91 d	0.0151 b	0.0227 b	7.71 c

Mitigating Osmotic Drought Stress in Rye: Assessing the Ameliorative Effects of Putrescine on Germination, Seedling and Mitotic Index

	0.001	3.70 a	5.70 a	6.01 a	0.0159 b	0.0870 a	23.61 a
	0.01	3.70 a	5.10 b	4.78 b	0.0114 b	0.0315 b	14.78 b
	0.1	3.50 a	4.70 bc	3.82 c	0.0256 a	0.0269 b	7.61 c
	Average	3.57 CD	4.92 E	4.38 E	0.0170 CD	0.0420 C	13.43 E
-10	0	3.00 c	1.57 c	1.95 c	0.0053 b	0.0198 b	4.02 b
	0.001	4.00 a	3.10 a	4.10 a	0.0181 a	0.0322 a	7.17 a
	0.01	3.60 b	2.80 a	3.52 b	0.0077 b	0.0306 a	6.78 a
	0.1	3.00 c	2.10 b	2.29 c	0.0081 b	0.0219 b	4.64 b
	Average	3.40 D	2.39 F	2.96 F	0.0098 D	0.0261 D	5.65 F
Average Put	0	3.90 BC	6.07 D	5.79 D	0.0214 BC	0.0353 C	15.75 D
	0.001	4.35 A	10.27 A	10.84 A	0.0254 AB	0.0638 A	42.03 A
	0.01	4.01 B	9.07 B	10.15 B	0.0178 C	0.0494 B	36.02 B
	0.1	3.79 C	7.51 C	8.00 C	0.0310 A	0.0409 C	25.05 C

¹. Differences between means shown with the same lowercase letter in the same column for each application are insignificant.

². Differences between means with the same capital letter in the same column are insignificant.

b) Root length (RL)

As evident from Table 3, the effects of drought, putrescine, and the interaction between drought and putrescine induced by PEG 6000 on the Root Length (RL) were statistically very significant ($P < 0.01$). The average RL generally decreased with the increase in the concentration of PEG 6000 applied to induce drought. However, the RL, measured at 12.46 cm in the control group, slightly increased to 13.72 cm in the -2 bar application, with the difference between these two groups being statistically very significant. Conversely, the RL decreased to 8.89, 7.00, 4.92, and 2.39 cm in -4, -6, -8, and -10 bar treatments, respectively, with statistically significant differences observed between these groups. Examining how putrescine application altered the effect of drought induced by PEG 6000 on root length revealed that the RL, averaging 6.07 cm in the control group, increased with putrescine application, reaching the highest value of 10.27 cm at a dose of 0.001 mM. Additionally, the RL was 9.07 cm and 7.51 cm at 0.01 and 0.1 mM doses, respectively. The most significant effect of putrescine on RL was observed at the 0.001 mM dose. While there was an increase compared to the control at other doses, there was a slight decrease compared to the first dose. Moreover, the most pronounced effect of putrescine on RL was observed at -10 bar drought, where the RL reached approximately twice (3.10 cm) that of the control (1.57 cm) when putrescine was applied at a dose of 0.001 mM (Table 4). This highlights the potential of putrescine in significantly enhancing root length under severe drought conditions.

c) Shoot length (SL)

The effect of drought and putrescine treatments on the Shoot Length (SL) induced by PEG 6000 was observed to be highly significant ($P < 0.01$), with the drought x putrescine interaction also exhibiting significant effects ($P < 0.01$) (Table 3).

The SL exhibited a continuous decrease with the increasing severity of drought treatment (PEG 6000 dose). The average shoot length, initially at 16.62 cm in the control group, decreased to 14.82 cm at -2 bars, 7.85 cm at -4 bars, 5.54 cm at -6 bars, 4.38 cm at -8 bars, and 2.96 cm at -10 bars.

When analyzing the effect of putrescine application on shoot length, it was observed that the SL, initially at 5.79 cm in the control group (0 mM putrescine), doubled to 10.84 cm at a dose

of 0.001 mM and reached 10.15 cm at a dose of 0.01 mM. The average SL was 8.00 cm at 0.1 mM putrescine dose. The most significant interaction effect between drought and putrescine treatment was found in the -10 bar group. In this group, the SL, initially at 1.95 cm in the absence of putrescine, more than doubled to 4.10 cm at the putrescine dose of 0.001 mM (Table 4). This emphasizes the potential of putrescine in mitigating the adverse effects of severe drought on shoot length, particularly under extreme conditions.

d) Root dry weight (RDW)

The effect of drought (PEG 6000) and putrescine treatments, as well as the interaction between drought and putrescine on the Root Dry Weight (RDW), one of the seedling characters examined in diploid rye, was found to be highly significant ($P < 0.01$) (Table 3). The highest RDW value (mean 0.0414 mg) was determined at -2 bar drought, and the difference with the control group (0.0277 mg) was highly significant. However, the RDW decreased continuously at -4, -6, -8, and -10 bar drought doses, reaching 0.0098 mg at -10 bars. Examining the effect of putrescine on RDW to determine its role in reducing the negative effects caused by drought, unlike other characters, the highest values were determined at 0.1 mM concentration (0.0310 mg), followed by 0.001 mM dose with 0.0254 mg, with the difference between the two being insignificant. It was followed by the control group with 0.0214 mg and 0.01 mM concentration with 0.0178 mg. The most significant effect of putrescine on RDW was observed at -6 bars of osmotic drought. At this dose, the RDW, initially at 0.0077 mg when putrescine was not applied, increased more than seven times to 0.568 mg at 0.1 mM dose of putrescine. This effect was followed by the control group and -2 bars of osmotic drought. In these two groups, the increase compared to the control was almost doubled at 0.001 mM dose (Table 4). This underscores the potential of putrescine in significantly influencing the Root Dry Weight, particularly under severe drought conditions.

e) Shoot dry weight (SDW)

The effect of drought (PEG 6000) and putrescine treatments on the Shoot Dry Weight (SDW) was highly significant ($P < 0.01$). Similarly, the interaction between drought and putrescine also significantly influenced the SDW ($P < 0.01$) (Table 3). In terms of drought mean values, the SDW exhibited a continuous decrease with increasing drought severity, and this decrease was statistically significant. The SDW, initially at 0.0644 mg in the control group, decreased to 0.0575 mg at -2 bars, 0.0516 mg at -4 bars, 0.0426 mg at -6 bars, 0.0420 mg at -8 bars, and 0.0261 mg at -10 bars. The first two doses of putrescine, applied in combination with PEG 6000 to mitigate the negative effects of drought, significantly increased the SDW that had decreased due to drought ($P < 0.01$). For example, the SDW with different doses of putrescine was 0.0353 mg in the control group (0 mM), increasing to 0.0638 mg at 0.001 mM dose, with the highest value obtained in this group. The 0.01 mM dose showed a significant decrease compared to the first dose, reaching 0.0494 mg, but this value was still higher than the control. Similarly, the 0.1 mM dose of putrescine resulted in an increase (0.0409 mg) compared to the control, but this value was lower than the first two doses. The highest SDW was found in the 0.001 mM putrescine application at all drought doses. The most significant positive effect of putrescine was observed at -8 bars considering all drought doses. In this group, the SDW, initially at 0.0227

mg in the control, increased approximately four times to 0.0870 mg in the 0.001 mM putrescine treatment (Table 4). This highlights the potential of putrescine in significantly influencing Shoot Dry Weight, particularly under severe drought conditions.

3.2. Effects of putrescine application on mitotic index

The effect of drought and putrescine treatments induced by PEG 6000, as well as the interaction between drought and putrescine on the mitotic index, was highly significant ($P < 0.01$) (Table 3). The mitotic index, initially at 49.46% in the control group without PEG 6000, slightly increased to 52.30% at the -2 bar dose compared to the control. However, at -4, -6, -8, and -10 bar drought doses, the mitotic index exhibited a continuous decrease, reaching 34.61%, 22.84%, 13.43%, and finally, 5.65%, respectively. Notably, there was a significant decrease in the mitotic index, especially at -8 and -10 bars. When analyzing the effect of putrescine on the mitotic index in terms of mean values, it was observed that putrescine application caused an increase in the mitotic index compared to the control group. However, this increase was not parallel to the dose increase. The mitotic index, initially at 15.75% in the control group without putrescine, significantly increased at 0.001 mM putrescine dose, reaching the highest value of 42.03%, and then slightly decreased with increasing doses. Accordingly, the mitotic index was 36.02% and 25.05% at 0.01 and 0.1 mM putrescine doses, respectively, with all doses in statistically different groups. The effect of putrescine on increasing the mitotic index, promoting cell division, was more pronounced, especially at -6 and -8 bar drought doses compared to others. In both drought doses, the highest increase was observed at 0.001 mM concentration of putrescine, nearly three times higher than the control. The highest mitotic index was 72.30% at -2 bar + 0.001 mM putrescine dose (Table 4). This suggests that putrescine has a significant role in promoting cell division, particularly under drought stress conditions.

4. Discussion

The research findings indicate that the germination rate, germination rate coefficient, and germination rate index decreased with the increasing concentration of PEG 6000, reflecting the escalating severity of osmotic drought. Simultaneously, the average germination time, representing the duration of germination, increased. These results align with observations in a study on the Norstar winter wheat variety, where prolonged germination periods were noted due to a decrease in soil water potential (-0.20 Mpa; -1.5 Mpa). In that study, the germination rate, initially higher than 80% in other stress levels, decreased to 56% in the -1.5 Mpa application [23]. Another study involving 64 wheat genotypes found that the germination strength index varied between 2331.1-5028.2 in the control application. The germination strength index decreased by 82.5% in -5 bar osmotic potential application, and germination did not occur in any wheat genotypes in -10 and -15 bar osmotic potential applications [24]. Additionally, it was reported that the germination strength index of 30 bread wheat genotypes at -10 bar stress level ranged between 146.2-585.6. with the highest rate of decrease (85.8%) observed in the germination strength index compared to other parameters and the control [25]. Under stress conditions (15% PEG), a study recorded that the seed vigor index decreased by 60.1-76.6% according to genotypes when compared to control groups [26]. These consistent

findings across various studies emphasize the negative impact of osmotic drought on germination-related parameters in different plant varieties.

In this experiment, the germination vigor index and germination rate showed a slight increase at -2 bar osmotic drought compared to the control. However, significant decreases were observed in these characters at -4 bar and higher doses of osmotic drought. The marginal increase observed at -2 bar might be attributed to the fact that low doses of the stress treatment stimulated the mentioned characters. A similar phenomenon was reported in a study involving ethyl methanesulfonate (EMS), a chemical mutagen, where low doses of EMS acted as a stress factor and stimulated plant regeneration *in vitro*. It was noted that low doses of EMS application stimulated regeneration in mature embryo culture in wheat, causing an increase in shoot length, coleoptile length, seedling height, root wet and dry weight, and shoot dry weight compared to the control [16]. The literature information presented here suggests that low doses of stress application can stimulate growth, leading to an increase in the mentioned characters compared to the control. In a study investigating the response of 10 summer wheat genotypes to drought stress during germination and the seedling period, it was found that the germination rates of the varieties decreased by 0.0-34.1%, 0.0-64.4%, and 51.3-100.0% in -5.9, -8.2, and -11.3 bar drought (osmotic potential) treatments, respectively. The variety x treatment interaction was also significant in this study [27]. These findings highlight the complex and variable responses of different plant varieties to drought stress, emphasizing the importance of considering specific genotypes and stress conditions in research. In another study, where 5 different osmotic stresses (0, -2, -4, -6, -8 bar) were applied to 2 wheat genotypes, it was observed that the germination rates of the varieties decreased with the increasing stress level [28]. Similarly, in a study involving 9 bread wheat genotypes, the germination rates were reported as 89.7%, 55.6%, 41.7%, and 24.1% at 0, -2, -4, -6, and -8 bar osmotic stress levels respectively [29]. These findings highlight the negative impact of osmotic stress on germination rates in wheat, with a clear trend of decreasing germination rates as stress intensity increases. In a study conducted with 16 wheat varieties, the effects of different concentrations of PEG 6000 (control, 150 g PEG 6000/850 ml pure water, 200 g PEG 6000/800 ml pure water, and 250 g PEG 6000/750 ml pure water) on germination and early seedling development were investigated. Significant differences were observed among the genotypes in terms of the examined characters, and it was noted that the germination rate decreased significantly with the increasing concentrations of PEG [8]. This aligns with the general understanding that higher concentrations of osmotic stressors, such as PEG, can negatively impact germination rates and early seedling development in various plant species.

A study conducted on three durum wheat cultivars, the effects of -0.15, -0.58, -1.5, and -1.57 MPa osmotic potential applications created with PEG 6000 on germination were investigated. The results showed a significant decrease in germination rate at increasing stress levels, and germination was completely inhibited at the -1.57 MPa stress level [30]. This underscores the sensitivity of durum wheat germination to severe osmotic stress conditions.

Considering the averages of different concentrations of putrescine in our study, it was observed that germination rate, germination rate coefficient, germination rate index, germination strength, and germination strength index increased as putrescine concentration increased, while germination time shortened. These findings align with a study conducted in pistachio, where positive results were obtained on germination speed, germination rate, and other seedling

growth parameters because of indolebutyric acid (IBA) application at different doses [33]. The positive impact of putrescine on germination-related parameters suggests its potential role as a growth regulator in mitigating the effects of stress on seed germination and early seedling development. The findings from this study reveal that the number of embryonal roots, shoot length, and coleoptile length decreased continuously with the increasing severity of osmotic stress induced by PEG 6000 application. This aligns with previous research in wheat and other crops under similar osmotic stress conditions. For instance, a study on wheat seeds exposed to osmotic potential conditions created with PEG 4000 found that water uptake gradually decreased at lower osmotic potentials, leading to varying emergence rates of seeds. The grass sheath (coleoptile) germination was reported to be more sensitive to low water potential than rootlet germination [34]. Similarly, another study on bread wheat genotypes showed a decrease in embryonal root numbers and root growth rates under stress conditions induced by PEG 6000 [33]. Moreover, studies on durum wheat cultivars subjected to different osmotic potential treatments with PEG 6000 reported a significant decrease in the number of roots and seedling length at increasing stress levels [32]. In addition, research on 30 bread wheat cultivars under -10 bar osmotic stress conditions created with PEG 6000 solution indicated a decrease in root length, shoot length, and grass sheath length, with an increase in root-shoot length ratio [26]. Similarly, a study on 16 wheat varieties exposed to different concentrations of PEG 6000 reported significant decreases in root length, shoot length, and coleoptile length with increasing PEG concentrations, along with a significant increase in root/shoot length ratio [8]. These consistent findings across various studies emphasize the detrimental effects of osmotic stress on root and shoot development in wheat, providing valuable insights into the physiological responses of plants to water deficit conditions.

The additional studies you mentioned further support the observed trends in this research. In a study applying six different osmotic stress levels to wheat, it was found that root length decreased significantly at stress levels higher than -6 bar [36]. Another study noted a similar trend, reporting that root length decreased with increasing stress level in terms of low water potential [37]. Moreover, a study on wheat genotypes exposed to different stress environments found a substantial reduction in shoot length in stress treatments compared to the control. Specifically, the average shoot length decreased by 70.02% and 85.34% in environments with -0.6 and -0.8 Mpa stress, respectively [37]. Additionally, in barley, it was observed that as osmotic pressure created with PEG 6000 increased, characters such as coleoptile length, shoot length, and root length decreased [38]. These findings are consistent with these results and further underline the impact of osmotic stress on root and shoot development in various cereal crops, providing a comprehensive understanding of the physiological responses to water deficit conditions.

The findings regarding root and shoot weights in our study align with existing research, supporting the impact of osmotic drought stress on these parameters. In our study as in previous investigations, osmotic drought stress induced by PEG 6000 significantly decreased root wet weight, root dry weight, shoot wet weight and shoot dry weight. Interestingly we observed a significant increase in root wet weight and root dry weight under -2 bar osmotic drought stress conditions, followed by a decrease under subsequent increasing osmotic drought stress. This initial increase at -2 bar may indeed be attributed to the growth-stimulating effect of low-level stress conditions, as noted in other studies [28]. In a study on bread wheat researchers found

that root weights decreased by 17.2-44.4%, and coleoptile weights decreased by 44.9-73.3% compared to the control under -0.67 Mpa stress conditions induced by PEG 6000 [35]. Similarly, it was reported that root length, wet and dry root weights decreased significantly as the severity of osmotic stress increased in wheat genotypes [8]. Consistent with our findings, in barley, the shoot wet and dry weights, along with proportional water content, decreased significantly as the osmotic pressure created by different concentrations of PEG 6000 increased [38]. These consistent results across different cereal crops highlight the general impact of osmotic stress on root and shoot development.

The positive effects of putrescine application on various germination and seedling growth parameters in response to osmotic drought stress are noteworthy. Putrescine significantly increased the germination rate, germination rate coefficient, germination rate index, germination power, germination power index. and shortened germination time. This indicates that putrescine played a crucial role in mitigating the negative effects of osmotic drought on germination. Moreover, considering the averages of putrescine concentrations, it was observed that putrescine significantly increased the number of embryonal roots, root length, shoot length, coleoptile length, seedling length, root wet weight, shoot wet weight and shoot dry weight. The highest impact of putrescine on these characters, except for root dry weight, was observed at 0.001 mM concentration, followed by 0.01 and 0.1 mM concentrations. In the case of root dry weight, the most effective dose was 0.1 mM, although the difference between this dose and 0.001 mM dose was statistically insignificant. These findings suggest that putrescine application has a positive influence on seed germination and early seedling growth under osmotic drought conditions, providing valuable insights for potential applications in agricultural practices to enhance stress tolerance in crops. The polycationic structure of polyamines, such as putrescine, spermidine and spermine, is a key feature contributing to their biological activity [39]. Numerous studies have demonstrated that the external application of polyamines can enhance abiotic stress tolerance in plants.

In line with the findings of this study, a similar investigation was conducted to assess the impact of drought and putrescine hormone on seed germination in wheat [17]. Different doses of PEG 6000 were applied to induce osmotic drought of varying severities (0, -2, -4, -6, -8, and -10 bar), and these doses were combined with 0, 0.01, 0.1, and 1 mM doses of putrescine. The research revealed that as drought severity increased, germination rate, root and shoot length decreased and germination time increased. Importantly, it was observed that the application of 1 mM putrescine mitigated these negative effects of drought. In a related study by the same researchers [17], PEG 6000 and putrescine (at doses of 0, 0.01, 0.1, 1 mM) were applied to wheat and their effects on various seedling characters were investigated. The experiment demonstrated that PEG 6000 negatively impacted seedling growth parameters at different doses and notably, the 1 mM dose of putrescine alleviated the adverse effects of drought. These findings underscore the potential of putrescine to mitigate the impact of drought stress on seed germination and seedling growth in wheat, providing valuable insights for strategies aimed at enhancing stress tolerance in crops.

Indeed, polyamines play crucial roles in various fundamental cellular processes, contributing to the regulation of essential functions within plant cells. These functions include DNA replication, transcription, translation, cell growth, enzyme activity regulation, cellular cation-anion balance maintenance and membrane stability [40, 41]. Additionally, polyamines are key

participants in numerous growth and development processes. such as cell division. breaking tuber dormancy, seed germination, stimulation, support and development of flower buds, fruit formation and ripening, embryogenesis, plant morphogenesis and responses to both biotic and abiotic stresses. Polyamines have been recognized for their effectiveness in enhancing plant tolerance to a range of stresses, including high and low temperatures, salinity, hyperosmosis, hypoxia and exposure to atmospheric pollutants [42, 43]. The multifaceted involvement of polyamines in these physiological processes highlights their significance in shaping plant responses to environmental challenges and their potential as important components in strategies for improving stress resilience. As mentioned earlier, the specific application of putrescine in this study aligns with the broader context of polyamine involvement in plant stress mitigation. The reported membrane-stabilizing effect of externally applied polyamines, including di-, tri-, and tetra-amines, is significant in protecting plant cell membranes from damage under stress conditions [42, 44]. Additionally, intrinsic polyamines play a role in maintaining membrane integrity [45]. In *Allium fistulosum*, the external application of putrescine has been shown to reduce oxidative damage by increasing antioxidant capacity [44]. The researchers observed a reduction in superoxide radical (O₂⁻) and H₂O₂ contents, leading to less oxidative stress in plant cells as a result of externally applied putrescine. In a study involving *Malus domestica* Borkh. (apple), which exhibits embryonal dormancy, the effects of different doses of spermidine (spd) on primary root length, cell shape, and mitotic index in maize were investigated [47]. The study found that low concentrations of putrescine and spermidine, such as 0.1 and 1 mM, stimulated germination. However, higher doses, such as 5 mM, were found to be ineffective and even inhibitory in germination. This underscores the importance of optimal concentrations when applying polyamines, as excessively high doses may not yield the desired effects and could even have adverse consequences on germination and other physiological processes.

5. Conclusion

The study results indicate that the dose of polyethylene glycol (PEG) 6000 applied to induce osmotic drought at -2 bar had a positive impact on some of the examined characters. However, the stimulatory effect of osmotic drought at -2 bar showed a minor change compared to the combinations of PEG 6000 + putrescine applied in conjunction with PEG 6000. Beyond this dose, all characters were negatively affected by the increasing severity of osmotic drought (PEG 6000 concentration). In contrast, all doses of putrescine applied in combination with PEG 6000 demonstrated positive effects on all the examined characters and contributed to the reduction of germination time. The highest impact of putrescine was observed at a dose of 0.1 mM in root dry weight and at a dose of 0.001 mM in all other characters. Consequently, the study suggests that higher doses of osmotic drought stress had a significantly negative effect on germination and seedling development. However, all doses of putrescine were able to partially alleviate the adverse effects of osmotic drought induced by PEG 6000.

Ethics in Publishing

There are no ethical issues regarding the publication of this study

Author Contributions: Idea – M.T; Data Collection and/or Processing – E.E.Y; Analysis and/or Comment – A.T; Literature Review – E.E.Y; Posted by – E.E.Y; Critical Review – M.T. A.T.

REFERENCES

- [1] Kün, E., Çiftçi, CY., Birsin, M., Ülger, AC., Karahan. S., Zencirci. N., Öktem. A., Güler, M., Yılmaz, N., Atak, M. (2004) Tahıl ve yemeklik baklagiller üretimi. Türkiye Ziraat Mühendisliği VI. Teknik Kongresi - 31.12.2004.
- [2] Anonim. (2022) https://data.tuik.gov.tr/Kategori/GetKategori?p=Tarim_11.12.01.2024
- [3] Khan, NA., Singh, S. (2008) Abiotic Stress and Plant Responses. IK International. New Delhi.
- [4] Saxena, NP., Johansen. C, Saxena, MC., Silim, SN. (1993) Selection for drought and salinity tolerance in cool-season food legumes. Breeding for stress tolerance in cool-season food legumes. Eds: K.B. Singh and M.C. Saxena. United Kingdom. 245-270.
- [5] Mooring, M.T., Cooper, AW., Senaca. ED. (1971) Seed germination response and evidence for height ecophenes in *Spartina alterniflora* from North Carolina. American Journal of Botany, 58: 48-55.
- [6] Bozcuk, S. (1978) Domates (*Lycopersicum esculentum* Mill), arpa (*Hordeum vulgare* L.) ve pamuk (*Gossypium hirsutum* L.) bitkilerinin büyüme ve gelişmesinde tuz kinetin etkileşimi üzerinde araştırmalar. Doçentlik tezi. Hacettepe Üniversitesi. Fen Fakültesi. Botanik Bölümü. Ankara.
- [7] Pan, XY., Wang, YF., Wang, GX., Cao, QD., Wang, J. (2002) Relationship between growth redundancy and size inequality in spring wheat populations mulched with clear plastic film. Acta Phytopathologica Sinica, 26: 177-184.
- [8] Rauf, M., Munir. M., Ul-Hassan, M., Ahmed., M., Afzal, M. (2007) Performance of heat genotypes under osmotic stress at germination and early seedling growth stage. African Journal of Biotechnology, 6 (8): 971-975.
- [9] Dilday, R., Mgonja, M., Amonsilpa, S., Collins, F., Wells, B. (1990) Plant height vs. mesocotyl and coleoptile elongation in rice: linkage or pleiotropism? Crop Science. 30 (4): 815-818.
- [10] Lagerwerff, J., Ogata, G., Eagle, HE. (1961) Control of osmotic pressure of culture solutions with polyethylene glycol. Science, 133 (3463): 1486-1487.
- [11] Gupta, S., Gupta, N. (2011) Field efficacy of exogenously applied putrescine in wheat (*Triticum aestivum* L.) under water-stress conditions. Indian Journal of Agricultural Sciences, 81(6): 516-9.

- [12] Duncan, DB. (1955). Multiple range and multiple F tests. *Biometrics*, 11(1): 1-42.
- [13] Michel, BE., Kaufmann, MR., (1973) The osmotic potential of polyethylene glycol 6000. *Plant Physiology*, 51 (5): 914-916.
- [14] Elkoca, E., (1997) Fasulye (*Phaseolus vulgaris* L)'de tuza dayanıklılık üzerine bir araştırma. Atatürk Üniversitesi Fen Bilimleri Enstitüsü. Yüksek Lisans Tezi. Erzurum.
- [15] Maguire, JD., (1962) Speed of germination aid in selection and evaluation for seedling emergence and vigor. *Crop Science*, 2 (2): 176-177.
- [16] Aydın, M., Hossein Pour, A., Haliloğlu, K., Tosun, M. (2015) Effect of application of putrescine on seedling growth and cell division of wheat (*Triticum aestivum* L.) under drought stress. *Yuzuncu Yıl University Journal of Agricultural Sciences*, 26(3): 319-332.
- [17] Abdul-Baki, AA., Anderson, JD. (1970) Viability and leaching of sugars from germinating barley. *Crop Science*, 10 (1): 31-34.
- [18] Kaya, MD., Okçu, G., Atak, M., Çıkılı, Y., Kolsarıcı, Ö. (2006) Seed treatments to overcome salt and drought stress during germination in sunflower (*Helianthus annuus* L.). *European Journal of Agronomy*, 24(4): 291-295.
- [19] Hossein Pour, A. (2016) Kimyasal mutagen uygulamalarının buğdayda bazı invitro karakterler ve kuraklığa tolerans üzerine etkileri. Atatürk Üniversitesi Fen Bilimleri Enstitüsü Tarla Bitkileri Ana Bilim Dalı, Doktora Tezi. 57 s.
- [20] Sagsöz, S. (1974) Diploid İngiliz çiminden tetraploid İngiliz çiminin elde edilmesi imkanları. Bu bitkilerde mitoz ve meioz kromozomları ile bazı morfolojik özelliklerin mukayesesi. Atatürk Üniv. Yay. No: 325. Zir. Fak. Yay. No: 159. Araş. Serisi No: 95. Erzurum.
- [21] Tosun, M. (1995) Heksaploid triticales çeşit/hatlarında tane verimini etkileyen bazı sitolojik ve morfolojik özelliklerin belirlenmesi. Atatürk Üniversitesi Fen Bilimleri Enstitüsü Tarla Bitkileri Ana Bilim Dalı, Doktora Tezi. 112 s.
- [22] Reiger, R., Michaelis, A., Green, MM. (1968) *A. Glassory Genetics and Cytogenetics*. Springer-Verbig, 507 p.
- [23] Lafond, GP., Fowler, BD. (1989) Soil temperature and water content. seedling depth. and simulated rainfall effects on winter wheat emergence. *Agronomy Journal*, 81: 609-614.
- [24] Taskesenligil, B. (2016) Düşük su potansiyelinde çimlenme hücre membran hasarı ve paraquata tolerans ölçütleri ile buğday genotiplerinin erken dönem kuraklığa dayanıklılık yönünden karakterizasyonu. Atatürk Üniversitesi Fen Bilimleri Enstitüsü Tarla Bitkileri Ana Bilim Dalı, Yüksek Lisans Tezi. Erzurum.

- [25] Dhanda, SS., Sethi, GS., Behl, RK. (2004) Indices of drought tolerance in wheat genotypes at early stages of plant growth. *Journal of Agronomy and Crop Science*, 190 (1): 6-12.
- [26] Baloch, MS., Nadim, MA., Zubair, M., Awan, IU., Khan, EA., Ali, AS. (2012) Evaluation of wheat under normal and late sowing conditions. *Pakistan Journal Botany*, 44 (5): 1727-1732.
- [27] Pius, J., George, L., Eapen, S., Rao, P. (1994) Evaluation of somaclonal and mutagen induced variation in finger millet. *Plant Breeding*, 112 (3): 239-243.
- [28] Blum, A., Sinmena, B., Zıvr, O. (1980) An evaluation of seed and seedling drought tolerance screening tests in Wheat. *Euphytica*, 29 (3): 727-736.
- [29] Gholamin, R., Khayatnezhad, M., Somarin, S., Mahmoodabad, RZ. (2010) Effects of polyethylene glycol and NaCl stress on two cultivars of wheat (*Triticum durum*) at germination and early seedling stages. *American Eurasian Journal of Agricultural and Environmental Science*, 9 (1): 86-90.
- [30] Rezzaq, A., Ali, Q., Qayyum, A., Mahmood, MA., Rasheed, M. (2013) Physiological responses and drought resistance index of nine wheat (*Triticum aestivum* L.) cultivars under different moisture conditions. *Pakistan Journal of Botany*, 45 (S1): 151-155.
- [31] Almansouri, M., Kinet, JM., Lutts, S. (2001) Effect of salt and osmotic stresses on germination in durum wheat (*Triticum durum* Desf.). *Plant and Soil*, 231 (2): 243-254.
- [32] Akkuş, G., (2009) Farklı dozlardaki (GA₃) ve IBA hormonlarının bazı standart antep fıstığı (*Pistacia vera* L.) tohumlarının çimlenme oranı ve hızı üzerine etkisi. Yüzüncü Yıl Üniversitesi Fen Bilimleri Enstitüsü Bahçe Bitkileri Ana Bilim Dalı, Yüksek Lisans Tezi. Van.
- [33] Hızarcı, Y., (2001) Karaerik üzüm çeşidinde katlama ve GA₃ uygulamalarının tohum çimlenmesi ve dinlenmesi üzerine etkileri. Atatürk Üniversitesi Fen Bilimleri Enstitüsü Bahçe Bitkileri Anabilim Dalı, Yüksek lisans tezi. 54 s.
- [34] Naylor, REL., Gurmu, M. (1990) Seed vigour and water relations in wheat. *Annals of Applied Biology*, 117 (2): 441-450.
- [35] Barutçular, C., Koç, M., Genç, İ. (1994) Ekmeklik buğdayda çimlenme ve ilk büyümenin PEG-6000 yardımı ile oluşturulan su geriliminden etkilenişi. Türkiye I. Tarla Bitkileri Kongresi. İzmir.
- [36] Jajarmi, V. (2009) Effect of water stress on germination indices in seven wheat cultivar. *World Academy of Science. Engineering and Technology*, 49: 105-106.
- [37] Ahmadizadeh, M., Valizadeh, M., Zaefizadeh, M., Shahbazi, H. (2011). Evaluation of interaction between genotype and environments in term of germination and seedling growth in durum wheat landraces. *Advances in Environmental Biology*, 5 (4): 551-558.

- [38] Ugur, Ö. (2015) Kuraklık stresinin arpada ilk gelişme dönemi üzerine etkileri. Yüzüncü Yıl Üniversitesi Fen Bilimleri Enstitüsü Tarla Bitkileri Anabilim Dalı, Yüksek Lisans Tezi. Van.
- [39] Valero, D. Perez-Vicente, A. Martinez-Rormero, D., Castillo, S., Guillen, F., Serrano, M., (2002) Plum Storability improved after calcium and Heat postharvest treatments: role of polyamines. *Journal of Food Science*, 67: 2571-3.
- [40] Bonchetau, A., Aziz, A., Larher, F., Martin-Tanguy, J. (1999) Polyamines and environmental challenges: Recent Development *Plant science*, 140: 103-25.
- [41] Groppa, MD., Benavides, MP. (2008). Polyamines and abiotic Stress: recent advances. *Amino acids*, 34: 35-45.
- [42] Liu, JH., Kitashiba, H., Wang, J., Ban, Y., Moriguchi, T. (2007) Polyamines and their ability to provide environmental stress tolerance to plants. *Plant Biotechnology*, 24: 117-26.
- [43] Garcia-Jimenez, P., Just, PM., Delgado, AM., Robaina, RR. (2007) Transglutaminase activity decrease during acclimation to hyposaline conditions in marine seaweed *Gratelonpiadoryphora (Rhodophayta. Halymeniaceae)*. *Journal of plant physiology*, 164: 367-70.
- [44] He, L., Ban, Y., Inoue, H., Matsuda, N., Liu, J., Moriguchi, T. (2008) Enhancement of spermidine content and antioxidant capacity in transgenic pear shoots overexpressing apple spermidine synthase in response to salinity and hyperosmosis. *Phytochemistry*, 69(11): 2133-2141.
- [45] Borell, A., Carbonell, L., Ferras, R., Puig-Parellada, P., Tiburcio, AF. (1997) Polyamines inhibit lipid peroxidation in senescing oat leaves. *Physiologia Plantarum*, 99(3): 385-390.
- [46] Yiu, JC., Juang, LD., Fang, DYT., Liu, CW., Wu, SJ. (2009) Exogenous putrescine reduces flooding-induced oxidative damage by increasing the antioxidant properties of Welsh onion. *Scientia Horticulturae*, 120(3): 306-314.
- [47] Sinska, I., Lewandawska, U., (1991) Polyamines and ethylene in the removal of embryonal dormancy in apple seeds. *Physiologia Plantarum*, 81(1): 59-64.

Analyzing Lead Concentrations in Pregnant Women Following Topical Application of Eau de Goulard (2% lead subacetate) via ICP-MS

Davut Serdar Sayılğan¹, Tugrul Cagri Akman^{2*}, Alptug Atila³,
Gamze Nur Cimilli Senocak⁴

¹Erzurum Regional Criminal Police Laboratory Directorate, Erzurum, Turkey

²Department of Analytical Chemistry, Faculty of Pharmacy, Erzincan Binali Yildirim University, Erzincan, Turkey

³Department of Analytical Chemistry, Faculty of Pharmacy, Ataturk University, Erzurum, Turkey

⁴Department of Gynecology and Obstetrics, Faculty of Medicine, Ataturk University, Erzurum, Turkey,

Received: 29/04/2024, Revised: 26/11/2024, Accepted: 11/12/2024, Published: 31/12/2024

Abstract

Lead compounds having cytotoxic and genotoxic properties can enter the body via the skin. Although Eau de Goulard (EDG), which contains lead subacetate, is used to prevent edema and phlebitis, it raises concerns about lead exposure. In the study, lead levels in the whole blood of 10 pregnant women were measured by inductively coupled plasma mass spectrometry before and 120 minutes after topical application of the EDG. Upon analysis of the whole blood samples, the average lead concentration was found to be 12.763 µg/L at 0 minutes and 15.823 µg/L at 120 minutes. Statistical analysis using the Paired-Samples *t*-test indicated a significant correlation between lead levels in whole blood and time elapsed after the topical EDG application ($R: 0.981$, $p < 0.05$). The study showed that even short-term application significantly increased the lead concentration in the whole blood of pregnant women ($p < 0.05$). This application carries potential health risks due to lead exposure. The study revealed that the topical EDG application threatens both maternal and fetal health and that safer medical practices are needed to prevent phlebitis and edema.

Keywords: ICP-MS, Lead, Eau de Goulard, Trace elements, Validation

Eau de Goulard'ın (2%kurşun subasetat) Topikal Uygulanmasının Ardından Gebe Kadınlarda Kurşun Konsantrasyonlarının ICP-MS ile Analizi

Öz

Sitotoksik ve genotoksik özelliklere sahip kurşun bileşikleri deri yoluyla vücuda girebilir. Kurşun subasetat içeren Eau de Goulard (EDG), ödem ve flebiti önlemek için kullanılsa da kurşun maruziyeti konusunda endişeler yaratmaktadır. Çalışmada, 10 hamile kadının tam kanındaki kurşun seviyeleri, EDG'nin topikal uygulamasından önce ve uygulamadan 120 dakika sonra indüktif eşleşmiş plazma kütle spektrometresi ile ölçüldü. Tam kan örneklerinin analizinde ortalama kurşun konsantrasyonu 0. dakikada 12.763 µg/L, 120. dakikada ise 15.823 µg/L olarak belirlendi. Paired-Samples *t*-testi kullanılarak yapılan istatistiksel analiz, tam kandaki kurşun seviyeleri ile topikal EDG uygulamasından sonra geçen süre arasında anlamlı bir korelasyon olduğunu gösterdi ($R:0,981$, $p:0,000$). Çalışma, kısa süreli uygulamanın bile hamile kadınların tam kanındaki kurşun konsantrasyonunu önemli ölçüde artırdığını gösterdi ($p < 0.05$). Bu uygulama kurşuna maruz kalma nedeniyle potansiyel sağlık riskleri taşır. Çalışma, topikal EDG uygulamasının hem anne hem de fetus sağlığını tehdit ettiğini, flebit ve ödemin önlenmesi için daha güvenli tıbbi uygulamalara ihtiyaç duyulduğunu ortaya koydu.

Anahtar Kelimeler: ICP-MS, Kurşun, Eau de Goulard, Eser elementler, Validasyon

*Corresponding Author: eczcagri87@gmail.com

Davut Serdar SAYILGAN, <https://orcid.org/0000-0001-7385-9244>

Tugrul Cagri AKMAN, <https://orcid.org/0000-0002-5439-950X>

Alptug ATILA, <https://orcid.org/0000-0001-7027-809X>

Gamze Nur Cimilli SENOCAK, <https://orcid.org/0000-0002-6750-9210>

1. Introduction

In hospitals, intravenous injection (IV) is the most preferred method of medication administration. Peripheral intravenous catheters are used for 83% of hospitalized patients receiving intravenous bolus/push medication [1]. IVs are multipurpose devices that may be used to provide nutrients, fluids, drugs, and imaging-related contrast chemicals. However, despite these varied IV applications, complications such as edema, phlebitis, infiltration, burning sensation, and excessive fluid volume make it impossible to continue therapy [2].

Especially, phlebitis is characterized by inflammation of the vessel wall and symptoms such as erythema, pain, and edema, along the affected vessel or surrounding the catheter insertion site. Thus, patients with phlebitis endure greater pain, need to stay in the hospital longer, and spend more money on their medical care [3]. To prevent edema and phlebitis among hospitalized patients, a standard practice involves the regular administration of Eau de Goulard (EDG) solution, which contains 2% lead subacetate. This therapeutic approach is used together with antibiotic and anti-inflammatory creams. The reason for including EDG is that the lead subacetate component in the solution reduces the symptoms of edema with its vasoconstrictor effect in vascular complications [4–11].

Lead (Pb) compounds have toxic effects at the cellular level, negatively affecting many organs and systems. Their genotoxicity can cause DNA damage, disrupt cellular replication and pave the way for serious health problems such as cancer [12]. The use of EDG raises concerns due to the toxic nature of Pb. Pb exposure can potentially cause severe complications during pregnancy and also adversely affect the health of fetus [13,14]. The topical application of EDG may release Pb into the bloodstream of pregnant women by absorption from the skin. So, this situation may threaten the health of the mother and the fetus. To eliminate this risk, minimizing Pb exposure of pregnant will be an effective method to safeguard the health of the fetus [15,16]. Therefore, monitoring Pb concentrations in the blood following topical application of EDG is crucial to determine the safety of this therapeutic application for pregnant.

Blood is responsible for transporting trace elements between tissues. Therefore, it is an important source of information about the amount and metabolism of trace metals in the human body [17,18]. Whole blood, serum and plasma have been used in recent biological research for the analysis of trace metals [19–22]. In the literature, some studies for trace metal analysis in pregnant women have been reported. In these studies, whole blood [22–28], plasma [20,22,29], serum [19,30], and urine [21,31] samples were used. There have been no published investigations on the reliability of topical EDG use and its relationship to Pb concentrations.

The purpose of this study was to examine whether Pb from the topical application of Eau de Goulard (2% lead subacetate solution) reaches the bloodstream after being applied to the catheter area. To accomplish this, Pb concentration in the whole blood of pregnant women was measured before and after the first EDG was applied, using Inductively Coupled Plasma Mass Spectrometry (ICP-MS). Pb levels before and after the application were then analyzed statistically.

2. Materials And Methods

2.1. Study Population

The study adheres to the principles of the World Medical Association Declaration of Helsinki (WMADH). Ten pregnant women, aged between 18 to 40 years, seeking medical attention at Atatürk University Faculty of Medicine, Department of Obstetrics and Gynecology, between March 2020 and September 2020, were enrolled as participants. The study population consisted of pregnant patients at risk of premature birth with a mean age of 30.32 ± 5.3 years and a BMI $> 30 \text{ kg/m}^2$.

Written informed consent was obtained from each patient. The study was carried out in accordance with the Declaration of Helsinki and approved by the Atatürk University Clinical Research Ethics Committee on 07.11.2019 (Permission Number: B.30.2.ATA.0.01.00, Decision Number: 65/482). The study included pregnant women who were at risk of premature birth and were administered IV medication (Ritodrine) via the catheter. To prevent phlebitis and edema around the catheter on the left arm, nurses soaked sterile hydrophilic gauze with EDG solution and pressed the gauze on the catheter area for fifteen minutes every hour. A qualified nurse collected a 3-mL blood sample from the right arm of each participant both prior to and two hour following the first administration of EDG. These samples were collected in evacuated tubes (BD Vacutainer[®]), which were free of trace metals and contained heparin as an anticoagulant. 2 mL of blood was transferred to an Eppendorf tube which was previously cleaned in a 100-clean room. Before analysis, the blood sample was immediately frozen at $-80 \text{ }^\circ\text{C}$.

During the study period, all patients were closely monitored and their treatment continued in the Gynecology and Obstetrics Service. All participants were provided with comprehensive high-risk pregnancy care, including regular uterine ultrasonography and fetal heart monitoring.

2.2. Reagents and standard solutions

All aqueous solutions utilized in the study were prepared using purified water obtained through the Milli-Q Advanced A 10 purification system (Millipore, USA). To prevent contamination during sampling, storage, and analysis, all equipment, including tubes, glass bottles, and micropipette tips, used in the study were cleaned. This ensured the elimination of potential contaminants that could affect the accuracy and reliability of the results. Whole blood samples, the solutions of internal standard and standard were prepared using a mixture solution consisting of 65% HNO_3 (Merck, USA) and 33% H_2O_2 (Sigma Aldrich, Germany) ($>99\%$). This solution served as the medium for dissolving and diluting the respective samples, maintaining consistency in the analytical process. To create the calibration curve, a standard stock Pb solution was prepared at a concentration of 100 ppm by diluting the Agilent[®] Trace Elements (USA) solution. By utilizing increasing concentrations of 2% nitric acid solution, both standard Pb samples in the range of 1-500 $\mu\text{g/L}$ and quality control samples (25, 200 and 400 $\mu\text{g/L}$) were prepared. The internal standard stock solution containing 10 ppm Bismuth was prepared. Each sample contained the internal standard at a concentration of 1 $\mu\text{g/L}$ to adjust for calibration curve deviations during analysis.

2.3. Instrumentation

The ICP-MS method was used for quantification of Pb in the whole blood samples [32]. The drying process was carried out using an oven (Milestone connect ETHOS UP microwave), and ultra-pure water was obtained with Direct-Q 8 UV Ultrapure Water systems. To analyze the samples, and process the data, the Agilent 7800 Quadrupole ICP-MS device, equipped with an Integrated Sample Introduction System (ISIS 3) and SPS 4 Autosampler, along with Mass Hunter 4.2 Workstation Software 7800 ICP-MS Top C.01.02, was used. The device was calibrated using Agilent tune solution (1 ppm Ce, Co, Li, Mg, Tl, Y). For Pb analysis, the helium (He) collision mode was employed, with argon (Ar) gas used as the carrier gas. The ICP-MS system was run at 1550 W of radio frequency power. The detailed settings and operating parameters of the ICP-MS system applied in the method are provided in Table 1. Values for the measured concentrations ($\mu\text{g/L}$) were recorded.

Table 1. Agilent 7800 Quadrupole ICP-MS operating parameters

Parameter	Value
Plasma conditions	Forward power 1200W
Plasma gas flow	15.0 L/min
Carrier gas flow	0.99 L/min
Carrier gas pressure	1.45 kPa
Dilution gas flow	1 L/min
He gas flow	4.5 mL/min
QP bias	-15 V
Oct bias	-18 V
Cell entrance	-40 V
Cell exit	60 V
Deflect	-0.8 V
Plate bias	-60 V
Nebulizer pump speed	0.30 rps
Sample uptake rate	1.5 mL/min

2.4. Sample Preparations

In the sample preparation process, measures were taken to prevent atmospheric particle contamination. In accordance with the publication by Meyer et al.[32], the sample processing methodology was optimized. To prevent contamination from air particles, the whole blood samples were prepared for ICP-MS analysis using the Milestone Connect ETHOS UP microwave oven and Direct-Q 8 UV Ultrapure Water equipment. Initially, the the whole blood samples were homogenized by vortexing for one minute. A 15 ml polypropylene tube with a screw cap (VWR labs) was filled with 0.5 mL of whole blood. After adding 0.5 mL of hydrogen peroxide (H_2O_2) and 1 mL of 65% nitric acid (HNO_3), the liquid was quickly vortexed. Tubes were then placed in a heating system and heated to 130°C for 60 minutes in order to dissolve.

Following incubation, ultrapure water was added to the digested sample volume until it reached 15 milliliters. For sample preparation and analysis, around 18 MΩ cm⁻¹ ultrapure water was utilized. Samples were prepared for measurement after centrifugation (3 min/ 2500 rpm) and vortexing. To eliminate particulate matter, the prepared samples were filtered using a 0.45 μm syringe tip. The filtered samples were subjected to ICP-MS analysis six times, and the results were averaged to ensure accuracy and precision in the measurements. The standard and whole blood samples were diluted at the same ratio using ultrapure water. Parameters such as final volume, sample volume, and dilution coefficient were accurately entered into the calculation section of the total dilution sub-tab in the software. The dilution factor, calculated using the formula: "Dilution factor = (final weight or volume / sample quantity or volume) * dilution coefficient," was used to verify the analytical process's accuracy. Table 2 shows the ramping conditions for the microwave program in the degradation process.

Table 2. The ramping conditions of the microwave program.

Step	Time	T1	T2	Pressure	Power
1	00:10:00	200 °C	100 °C	45 bar	Max power*
2	00:15:00	200 °C	100 °C	45 bar	Max power*

*Max power: 1500W for Ethos and 1200W for Start units.

2.5. Method Validation

The validation of the ICP-MS method involved a series of assessments to determine the accuracy, precision, and sensitivity of the method.

Standard samples (1-500 μg/L) were analyzed, and a calibration curve was established by performing linear regression analysis on the obtained results. The curve equation and correlation coefficient (R) were determined, providing an indication of the method's linearity. The sensitivity of the method was evaluated through the determination of the limit of detection (LOD) and the limit of quantification (LOQ) values. LOD and LOQ values were calculated as three and ten times the standard error of the curve slope, respectively, signifying the minimum concentration of Pb that could be reliably detected and quantified.

Intra-day and inter-day precision and accuracy of the ICP-MS method were assessed using three replicates of the quality control (25, 200 and 400 μg/L) samples. The accuracy and precision of the method were examined through the calculation of percent relative error (RE%) and percent relative standard deviation (RSD%) values, respectively, for both intra-day and inter-day analysis results of the control samples. Acceptance criteria required values below 15% to indicate satisfactory precision and accuracy.

The range of 80–120% is the acceptable range for the percent recovery value. This criteria further validates the method's applicability and reliability for the analysis by verifying that the amount of Pb recovered from the samples was within an acceptable range.

2.6. Statistical Analysis

The statistical analysis was performed using the SPSS 15.0 package program to evaluate the impact of topical EDG application on whole blood Pb levels. The mean and standard deviation values of whole blood Pb levels before and after the application were computed using the Paired-Samples *t*-test. This analysis aimed to evaluate any significant changes in Pb concentrations resulting from the application. $p < 0.05$ was considered significant. Any observed *p*-value below this threshold indicated a statistically significant difference in the Pb levels between before and after the application.

3. Results and Discussion

Before the analyses, the method was validated by evaluating in terms of accuracy, precision, linearity, sensitivity and percentage recovery parameters in the study. Finally, it was successfully applied to the whole blood samples of the pregnant women for Pb analysis.

Standard Pb samples prepared in the range of 0.1-1000 $\mu\text{g/L}$ were analyzed by the method. The results were plotted against concentrations. In the linear regression analysis, the equation of the calibration curve was determined as $y = 33242.1153x + 6031.6467$. This showed that there was a strong linear relationship between the measured values and the Pb concentration in the samples. The correlation coefficient was calculated as 0.9999, confirming the excellent fit of the data to the calibration curve (Figure 1). Determining the linear working range of the developed ICP-MS method between 1-500 $\mu\text{g/L}$ (1, 10, 50, 100, 250, 500 $\mu\text{g/L}$) reveals the concentration range in which accurate and precise quantitative analysis of Pb levels can be made reliably.

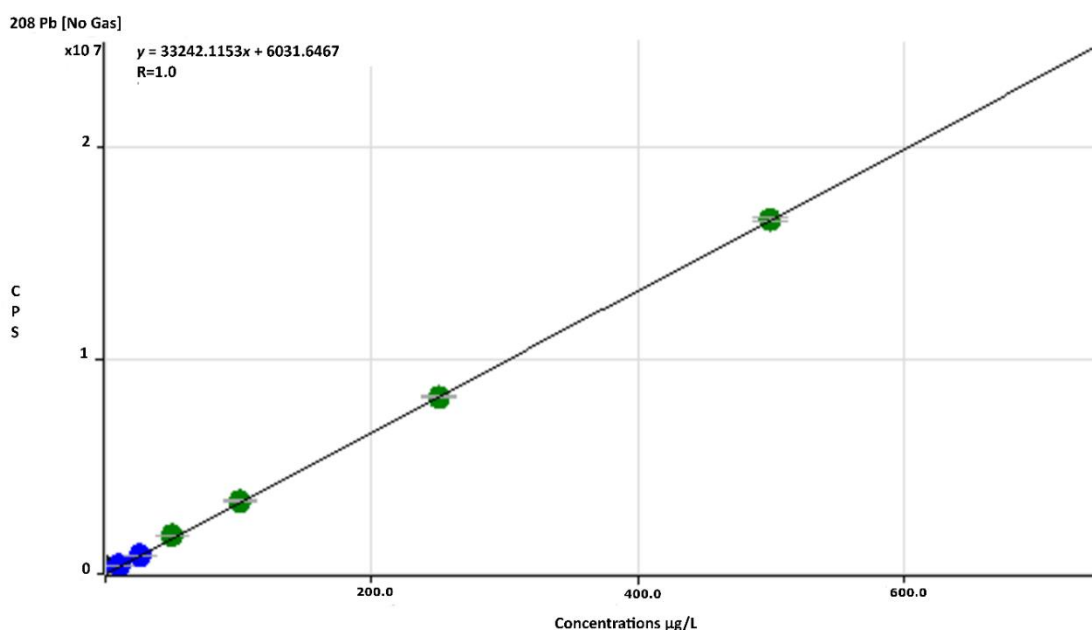


Figure 1. Calibration curve of standard Pb solutions at 1-500 $\mu\text{g/L}$ (Agilent® Trace Elements)

Additionally, the sensitivity of the method was evaluated by determining the LOD and LOQ values. LOD and LOQ values were found to be 0.0418 and 0.1395 µg/L, respectively. These values indicate the minimum concentration of Pb that the method can detect and reliably quantify, further affirming the method's high sensitivity for trace element analysis.

To assess the accuracy and precision (intraday and inter-day) of the ICP-MS method, quality control samples were analyzed three times. According to the analysis results, RSD% and RE% values were found to be 0.662% and 1.540%, respectively. The method has high accuracy and precision for the quantitative analysis of Pb in whole blood samples.

Recovery experiments were carried out at two different concentrations (25, 200 and 400 µg/L). Calculated recovery values (100.2%) were within the acceptable range of 98-102%; This result proves the reliability of the method in accurately recovering and quantifying trace elements in samples. Additionally, the repeatability of the method was evaluated by analyzing 25, 200 and 400 µg/L samples in ten replicates. The results were found to be the same over 95%. (24.96±0.161 µg/L, 200.35±2.425 µg/L and 403.94±1.295 µg/L)

To eliminate differences in analyte sensitivity caused by matrix components in the sample, internal standards must be used in trace element analysis. In this study, a 1 µg/L concentration of bismuth was added to each sample. Consequently, the normalizing of matrix-induced waves allowed the ICP-MS approach to reach excellent sensitivity.

The validated ICP-MS method was applied to the whole blood of women. Table 3 lists the Pb concentrations at two different times. At the 0th and 120th minute, the average Pb concentrations were determined to be 12.763 µg/L and 15.823 µg/L, respectively (Figure 2, Table 4).

Table 3. Pb concentrations in whole blood samples at 0 and 120 minutes following EDG application (mean ± standard deviation, n=10)

Patients	0. minute (µg/L)	120. minute (µg/L)
1	12.763 ± 1.04	15.822 ± 3.04
2	14.363 ± 0.82	14.976 ± 2.19
3	11.999 ± 0.39	16.432 ± 1.38
4	14.379 ± 2.13	13.973 ± 0.76
5	13.337 ± 0.01	17.452 ± 1.51
6	12.975 ± 1.41	14.838 ± 1.68
7	12.273 ± 1.38	16.137 ± 0.43
8	11.678 ± 0.93	16.346 ± 0.69
9	11.869 ± 0.86	17.176 ± 1.14
10	11.974 ± 2.62	15.135 ± 1.76

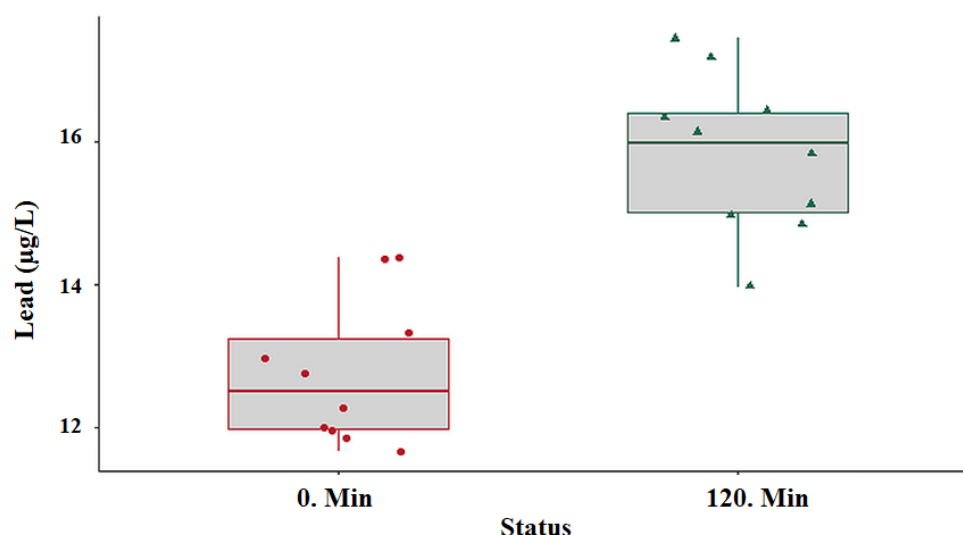


Figure 2. Boxplot showing change in the Pb concentrations with topical application of EDG

Table 4. Mean levels of Pb in whole blood of ten patients at 0. and 120. minutes

Paired Samples Statistics				
Groups	Mean (µg/L)	n	Standard Deviation	Standard Error Mean
0. minute	12.7630	10	8.25083	2.60914
120. minute	15.8225	10	10.30786	3.25963

The Paired Sample *t*-test was used to determine whether or not this increase was statistically significant. It was found that there was a considerable rise in Pb concentration following EDG treatment (<0.05, Table 5).

Table 5. Statistical analysis results with the Paired Samples *t*-test

Time	Paired Differences				<i>t</i>	df	Sig. (2-tailed)	R*	
	Mean	SD*	Std. Error Mean	95% CID*					
				Lower					Upper
0. min/120. min	-3.059	2.719	.860	-5.005	-1.114	-3.557	9	.006	0.981

*R: Correlation coefficient, CID: Confidence Interval of the Difference, SD: Standard Deviation

Pb exposure is a global public health concern. Pb is the second most dangerous environmental toxic agent due to its high toxicity and widespread presence. According to the World Health Organization, the maximum acceptable concentration for Pb has not yet been determined. Additionally, it is stated that the estimated contribution of Pb to the "global burden of disease" is 0.6%. According to a number of studies, high blood Pb levels are associated with cognitive problems such as memory loss, difficulty focusing, learning challenges, and even reduced IQ, particularly in the developing brain [33,34].

IV is the most preferred method of administering large amounts of fluid into a vein via a catheter in hospitalized patients. However, this method causes complications such as phlebitis, thrombophlebitis, and edema [3]. For the well-being of the patient and the successful progression of treatment, topical Eau de Goulard solution is frequently used in hospitals [4–11]. Lead subacetate contained in the Eau de Goulard solution causes safety concerns with this method. Determination of Pb levels in patients after administration will provide important information about the reliability of EDG.

In this study, whole blood samples of patients who applied EDG around the catheter for 15 minutes were analyzed using the validated ICP-MS method. Intra-day and inter-day RSD% and RE% values of quality control solutions were below 15%. As a result, the results obtained from the ICP-MS method had high accuracy and precision. The sensitivity of the ICP-MS method was high because the LOD and LOQ values are at low levels such as 0.0418 and 0.1395 $\mu\text{g/L}$. The correlation coefficient found close to 1 showed that there was a strong positive correlation between the concentrations and the analysis results. Recovery values calculated by analysis of standard Pb samples at three different concentrations were within the acceptable range (80–120%).

The ICP-MS method had advantages compared to many studies reported in the literature. The method had a large linear range (1–500 $\mu\text{g/L}$) for determination of Pb [22,23,30]. Compared to other studies, the method allowed to determination with high accuracy (RE%: 1.54%) of Pb in the whole blood volume as low as 0.5 mL [22,24,28]. Since whole blood samples were used in the study, samples were prepared for ICP-MS analysis in a short time of approximately 1 hour, without the need for serum and plasma separation processes [22,24,28,29]. $\text{HNO}_3\text{:H}_2\text{O}_2$ (2:1) mixture was used for sample preparation and high recovery was achieved. To eliminate the masking problem and minimize the matrix effect in the determination of Pb, samples were prepared by diluting with distilled water as an analyte-free matrix compared to an acid or alkali mixture. In this way, the analysis of Pb in whole blood samples was performed with higher sensitivity (LOD: 0.0418 $\mu\text{g/L}$) [22,24,26,29,30].

EDG treatment increased the mean Pb concentration in the whole blood of patients by 3.05950 $\mu\text{g/L}$ after 2 hours (Table 4). Statistical analysis of the analysis results with the Paired-Samples *t*-test showed that there is a significant correlation between Pb levels in the whole blood and the time elapsed after Pb exposure (R : 0.981; $p < 0.05$, Table 5). It was determined that there was a significant difference in Pb concentrations before and after application (Figure 2). As a result, EDG, applied topically for 15 minutes to prevent phlebitis and edema, significantly increased the Pb concentration in the whole blood according to the Paired-Samples *t*-test ($p < 0.05$, Table 5).

Percutaneous absorption is important in assessing the risk of exposure to toxic substances such as Pb. They are known to both accumulate in the skin and widely penetrate the body and cell membranes after long-term topical application. It is well-established that prolonged contact or topical application can lead to Pb absorption through the skin. However, it has not been reported in any study that Pb enters the systemic circulation after short-term topical application [35–38]. Unlike the literature, this study showed that short-term Pb exposure increased Pb concentration

in whole blood. Various factors also contribute to the increase of Pb concentration in whole blood by topical EDG application. Application duration and frequency, concentration of the EDG (lead subacetate) solution and physical properties of the skin are among these factors. Each of these factors can affect the absorption of Pb from the skin and subsequently lead to the accumulation of Pb in the bloodstream, tissue, and bones [38]. In this study, the effect of EDG solution applied to the skin for 15 minutes on Pb concentrations, especially in pregnant women was investigated. The results conclusively showed that this practice led to a significant increase in participants' whole blood Pb concentrations, threatening the health of pregnant women and fetuses.

The presence of Pb salts at parts per billion raises serious concerns about fetal health even if they are poorly soluble. Recent studies have demonstrated a strong correlation between cord blood Pb levels and maternal blood Pb levels [39]. There have been important scientific findings that Pb exposure can cause metabolic, neurological and psychological problems in pregnant women and fetuses. It has been reported that in cases where the maternal blood level is approximately 10 µg/dl, hypertension, spontaneous abortion and cognitive development of the fetus are negatively affected in pregnant women. Studies show that maternal Pb exposure is associated with serious outcomes such as low birth weight, preterm birth, stillbirth, spontaneous abortion, congenital defects and hypertension. Pb exposure in the intrauterine period can lead to serious health problems such as fetal growth retardation, nervous system disorders, postnatal mental retardation, motor skill disorders and renal dysfunction [39–43]. Studies conducted by the United States Centers for Disease Control and Prevention (CDC) have determined the acceptable blood Pb level as 50 ng/mL in children. However, no lower threshold has been reported for pregnant women. To avoid the reported effects of Pb, it is critical to identify the factors that may contribute to increased Pb exposure and immediately execute preventive measures against these causes. For example, the development of safer and more effective Pb-free treatment methods that can replace EDG is a critical part of this effort [44]. In the context of alternative treatment options, hot-cold and dry-wet compresses, nonsteroidal anti-inflammatory drugs (NSAIDs), topical products containing heparinoids and herbal creams (such as *Aesculus hippocastanum* and *Arnica montana*) have been shown in various studies to be effective in preventing phlebitis and relieving symptoms [45–47]. In addition, blood Pb tests for confirmation and monitoring purposes should be performed in accordance with the protocols determined by the CDC, and maternal blood or umbilical cord blood Pb levels should be measured during delivery. Women with blood Pb levels above 450 ng/mL should be treated by specialists experienced in the management of complications related to Pb toxicity and high-risk pregnancies [39,41–43].

It is known that skin thickness, contact time, and pregnancy can all influence lead absorption. Thicker skin may act as a barrier, reducing lead absorption, however longer contact times may enhance absorption. Furthermore, pregnancy can impact lead absorption and distribution in the body by generating metabolic changes such as hormonal alterations, higher blood pressure, and abnormalities in nutrient transport. Although this study did not directly investigate these factors, it is obvious that these limitations may have an impact on the generalizability of our findings and that more research into lead exposure is required.

4. Conclusion

In this study, the effect of topically applied Eau de Goulard (2% lead subacetate) solution on lead concentration in whole blood was investigated. A validated ICP-MS method was employed for whole blood samples in the study. Through this method, a notable elevation in lead concentrations within the whole blood of pregnant women was determined. The findings of the study drew attention to the potential threat that topical application of Eau de Goulard poses to both maternal and fetal health. The sensitivity of the ICP-MS method played a pivotal role in detecting even low concentrations of lead absorbed through the skin into the systemic circulation. Eau de Goulard can be applied topically for shorter periods and at longer intervals to reduce lead exposure and prevent lead from reaching the bloodstream. In addition, the use of Eau de Goulard solutions with lower lead concentrations may be a viable strategy. However, this study suggests that safer, lead-free treatment methods should be the first choice for pregnant women who are a vulnerable population, rather than Eau de Goulard, which has been shown to increase lead exposure. In conclusion, the study emphasizes the necessity for in-depth investigations into the toxic effects of topical Eau de Goulard application. This step is crucial for shedding light on the potential health risks associated with this common medical practice. Finally, the study represents an important step toward advocating for safer medical protocols and enhancing awareness about lead exposure, particularly among sensitive populations like pregnant women.

Limitation of the study

The small number of patients limits the study. Comprehensive studies with large numbers of participants are needed to more clearly determine the safety and toxicity of Eau de Goulard solution. In addition, the application of multivariate analyses that take into account factors such as age, BMI, and skin condition that may affect lead absorption through the skin, as well as the increasing number of participants, will provide stronger results.

Ethics in Publishing

Written informed consent was obtained from each patient. The study was carried out in accordance with the Declaration of Helsinki and approved by the Atatürk University Clinical Research Ethics Committee on 07.11.2019 (Permission Number: B.30.2.ATA.0.01.00, Decision Number: 65/482).

Conflict of Interest

The authors declare no competing interests.

Acknowledgements

The authors are grateful to Atatürk University for support of this study.

Author Contribution

A.A. conceived and designed the research. T.C.A. and D.S.S. conducted experiments and analyzed the data statistically. G.N.C.S. collected the whole blood samples. A.A. and T.C.A. evaluated the analysis results. T.C.A, D.S.S. and A.A. drafted the manuscript. All authors have read and agreed to the published version of the manuscript.

References

- [1] Piredda, M., Biagioli, V., Barrella, B., et al., (2017) Factors affecting difficult peripheral intravenous cannulation in adults: a prospective observational study, *Journal of Clinical Nursing*, 26, 1074–1084. <https://doi.org/10.1111/JOCN.13444>
- [2] Lee, S., Kim, K., Kim, J.S., (2019) A Model of Phlebitis Associated with Peripheral Intravenous Catheters in Orthopedic Inpatients, *International Journal of Environmental Research and Public Health*, 16, 3412–3416. <https://doi.org/10.3390/IJERPH16183412>
- [3] Sofia, A., Nobre, P., Delmina, M., Martins, S., (2018) Prevalence of peripheral intravenous catheter-related phlebitis: associated factors, *Revista de Enfermagem Referência*, 127–138. <https://doi.org/10.12707/RIV17058>
- [4] Gómez, L.A., Tuta-Quintero, E., Briceño-Balcázar, I., et al., (2021) Surgery through time. Saturn extract: an 18th century medical prescription, *Cirugía y cirujanos*, 89, 135–139. <https://doi.org/10.24875/CIRU.20000745>
- [5] Morgado-Carrasco, D., Bosch-Amate, X., Fustà-Novell, X., Giavedoni, P., (2020) Úlcera de Lipschütz. Una úlcera genital aguda no infecciosa para tener en cuenta en mujeres adultas, *Actas Dermo-Sifiliográficas*, 111, 624–626. <https://doi.org/10.1016/J.AD.2018.12.011>
- [6] Eserdağ, S., (2023) Labiaplasty, *Aesthetic and Functional Female Genital Surgery*. Eserdağ, S., 97–141. Springer Nature, Switzerland. https://doi.org/10.1007/978-3-031-16019-6_9
- [7] Bilkay, U., Bicer, A., Ozek, Z., Gurler, T., (2021) Augmentation of the calf region with autologous fat and platelet-rich plasma-enhanced fat transplants: A comparative study. *Turkish Journal of Plastic Surgery*, 29, 21. https://doi.org/10.4103/TJPS.TJPS_67_20
- [8] Türkyılmaz, Ç., Batukan, C., Özgün, M.T., Atakul, T., Bilateral Massive Vulvar Edema Due to Severe Preeclampsia: a Case Report. *Journal of Clinical Practice and Research*, 30, 194–197
- [9] Duran, B., Şalk, S., Erden, Ö., et al., (2003) Gebelikte Behçet Hastalığına Bağlı Vulvar Ödem: Olgu Sunusu. *Journal of Clinical Obstetrics & Gynecology*, 13, 463–465
- [10] Karabay, Ö., Yetkin, U., Önol, H., et al., (2004) Üst Ekstremitede Bulgulanan Derin Venöz Tromboz Olgularına Yaklaşım* Approach to upper extremity deep vein thrombosis cases, *15th Annual Meeting of the Mediterranean Association of Cardiology and Cardiac Surgery*, 18(1), 81–86.
- [11] Karabay, O., Yetkin, U., Onol, H., (2004) Upper extremity deep vein thrombosis:

- Clinical and treatment characteristics, *Journal of International Medical Research*, 32, 429–435. <https://doi.org/10.1177/147323000403200413>
- [12] Hemmaphan, S., Bordeerat, N. K. (2022). Genotoxic effects of lead and their impact on the expression of DNA repair genes. *International journal of environmental research and public health*, 19(7), 4307. <https://doi.org/10.3390/ijerph19074307>
- [13] Taylor, C., Golding, J., Emond, A., et al., (2013) Lead, cadmium and mercury levels in pregnancy: The need for international consensus on levels of concern The 1986 Jamaica Perinatal Morbidity and Mortality Survey View project ALSPAC View project Lead, cadmium and mercury levels in pregnancy: the need for international consensus on levels of concern, *Journal of Developmental Origins of Health and Disease*, 5(1), 16-30. <https://doi.org/10.1017/S2040174413000500>
- [14] Arpa, Y., Cengiz, A., (2016). Determining of the knowledge levels of healthcare staff in the diagnosis and prevention of development of phlebitis and thrombophlebitis associated with intravenous infusion therapy. *Journal of Education and Research in Nursing*, 13(1), 21-26. <https://doi.org/10.5222/HEAD.2016.253>
- [15] Ettinger, A.S., Wengrovitz, A.G., Portier, C., (2010). Guidelines for the identification and management of lead exposure in pregnant and lactating women. *US Department of Health and Human Services, Centers for Disease Control and Prevention, National Center for Environmental Health/Agency for Toxic Substances and Disease Registry*.
- [16] Abadin, H., Ashizawa, A., Lladós, F., & Stevens Y.W., (2007) Toxicological Profile for Lead, *Agency for Toxic Substances and Disease Registry, USA*.
- [17] Wang, T., Fu, J., Wang, Y., et al., (2009) Use of scalp hair as indicator of human exposure to heavy metals in an electronic waste recycling area, *Environmental Pollution*, 157, 2445–2451. <https://doi.org/10.1016/j.envpol.2009.03.010>
- [18] Robinson, M.F., McKenzie, J.M., Thompson, C.D., Van Rij, A.L., (1973) Metabolic balance of zinc, copper, cadmium, iron, molybdenum and selenium in young New Zealand women, *British Journal of Nutrition*, 30, 195–205. <https://doi.org/10.1079/bjn19730025>
- [19] Krachler, M., Rossipal, E., Micetic-Turk, D., (1999) Concentrations of trace elements in sera of newborns, young infants, and adults, *Biological Trace Element Research*, 68, 121–135. <https://doi.org/10.1007/BF02784401>
- [20] Pasha, Q., Malik, S.A., Shaheen, N., Shah, M.H., (2010) Investigation of trace metals in the blood plasma and scalp hair of gastrointestinal cancer patients in comparison with controls, *Clinica Chimica Acta*, 411, 531–539. <https://doi.org/10.1016/j.cca.2010.01.010>
- [21] Wilhelm, M., Ewers, U., Schulz, C., (2004) Revised and new reference values for some trace elements in blood and urine for human biomonitoring in environmental medicine. *International Journal of Hygiene and Environmental Health*, 207, 69–73. <https://doi.org/10.1078/1438-4639-00260>
- [22] Smith, D., Hernandez-Avila, M., Téllez-Rojo, M.M., et al., (2002) The relationship between lead in plasma and whole blood in women. *Environmental Health Perspectives*,

- 110, 263–268. <https://doi.org/10.1289/ehp.02110263>
- [23] Telišman, S., Čolak, B., Pizent, A., et al., (2007) Reproductive toxicity of low-level lead exposure in men, *Environmental Research*, 105, 256–266. <https://doi.org/10.1016/j.envres.2007.05.011>
- [24] Guo, J., Lv, N., Tang, J., et al., (2018) Associations of blood metal exposure with thyroid hormones in Chinese pregnant women: A cross-sectional study, *Environment International*, 1185–1192. <https://doi.org/10.1016/j.envint.2018.10.038>
- [25] Kresovich, J.K., Argos, M., Turyk, M.E., (2015) Associations of lead and cadmium with sex hormones in adult males, *Environmental Research*, 142, 25–33. <https://doi.org/10.1016/j.envres.2015.05.026>
- [26] Lewis, R.C., Meeker, J.D., (2015) Biomarkers of exposure to molybdenum and other metals in relation to testosterone among men from the United States National Health and Nutrition Examination Survey 2011-2012, *Fertility and Sterility*, 103, 172–178. <https://doi.org/10.1016/j.fertnstert.2014.09.020>
- [27] Niederberger, C., (2010) Environmental exposure to metals and male reproductive hormones: Circulating testosterone is inversely associated with blood molybdenum, *The Journal of urology*, 184, 1083. <https://doi.org/10.1016/j.juro.2010.04.057>
- [28] Lozoff, B., Jimenez, E., Wolf, A.W., et al., (2009) Higher Infant Blood Lead Levels with Longer Duration of Breastfeeding, *The Journal of Pediatrics*, 155, 663–667. <https://doi.org/10.1016/j.jpeds.2009.04.032>
- [29] Henríquez-Hernández, L.A., Romero, D., González-Antuña, A., et al., (2020) Biomonitoring of 45 inorganic elements measured in plasma from Spanish subjects: A cross-sectional study in Andalusian population, *Science of the Total Environment*, 706, 135750. <https://doi.org/10.1016/j.scitotenv.2019.135750>
- [30] Mohammed, N.A, Chin, S.F., Jamal, R., (2020) Simultaneous analysis of 25 trace elements in micro volume of human serum by inductively coupled plasma mass spectrometry (ICP-MS). *Practical Laboratory Medicine*, 18, e00142. <https://doi.org/10.1016/j.plabm.2019.e00142>
- [31] Zeng, Q., Zhou, B., Feng, W., et al., (2013) Associations of urinary metal concentrations and circulating testosterone in Chinese men. *Reproductive Toxicology*, 41, 109–114. <https://doi.org/10.1016/j.reprotox.2013.06.062>
- [32] Laur, N., Kinscherf, R., Pomytkin, K., et al., (2020) ICP-MS trace element analysis in serum and whole blood, *PLoS One* 15, e0233357. <https://doi.org/10.1371/JOURNAL.PONE.0233357>
- [33] World Health Organization. (2023). Preventing disease through healthy environments: exposure to lead: a major public health concern.
- [34] Owsianowska, J., Kamińska, M.S., Bosiacki, M., et al., (2020) Depression, changes in peripheral blood cell count, and changes in selected biochemical parameters related to lead concentration in whole blood (Pb-B) of women in the menopausal period, *Journal of Trace Elements in Medicine and Biology*, 61, 126501.

<https://doi.org/10.1016/J.JTEMB.2020.126501>

- [35] Kennedy, C.C., Lynas, H.A., (1949) Lead poisoning by cutaneous absorption from lead dressings, *Lancet*, 254, 650–652. [https://doi.org/10.1016/S0140-6736\(49\)91281-7](https://doi.org/10.1016/S0140-6736(49)91281-7)
- [36] Cohen, A.J., Roe, F.J.C., (1991) Review of lead toxicology relevant to the safety assessment of lead acetate as a hair colouring, *Food and Chemical Toxicology*, 29, 485–507
- [37] French, L.R., Williams, A.N., Campbell, R.G., (1985) Lead toxicity, *Minnesota Medicine*, 68, 899–901.
- [38] Pan, T.L., Wang, P.W., Al-Suwayeh, S.A., et al., (2010) Skin toxicology of lead species evaluated by their permeability and proteomic profiles: A comparison of organic and inorganic lead, *Toxicology Letters*, 197, 19–28. <https://doi.org/10.1016/j.toxlet.2010.04.019>
- [39] Al-Saleh, I., Shinwari, N., Mashhour, A., Mohamed, G.E.D., Rabah, A., (2011). Heavy metals (lead, cadmium and mercury) in maternal, cord blood and placenta of healthy women. *International journal of hygiene and environmental health*, 214(2), 79-101. <https://doi.org/10.1016/j.ijheh.2010.10.001>
- [40] Elmugabil, A., Hamdan, H.Z., Elsheikh, A.E., Rayis, D.A., Adam, I., Gasim, G.I. (2016). Serum calcium, magnesium, zinc and copper levels in sudanese women with preeclampsia. *PloS one*, 11(12), e0167495. <https://doi.org/10.1371/journal.pone.0167495>
- [41] Esteban-Vasallo, M. D., Aragonés, N., Pollan, M., López-Abente, G., Perez-Gomez, B., (2012). Mercury, cadmium, and lead levels in human placenta: a systematic review. *Environmental health perspectives*, 120(10), 1369-1377. <https://doi.org/10.1289/ehp.1204952>
- [42] Şimar, S., Karahan, N., (2021). Doğumda kordon kanında kurşun ve kadmiyum düzeyleri. *Kocatepe Tıp Dergisi*, 22(4), 287-293. <https://doi.org/10.18229/kocatepetip.705336>
- [43] Yüksel D., (2015). İntrauterin gelişme geriliğinde maternal kan, kordon kanı ve plasentada ağır metal düzeyi.
- [44] Sonçağ, A., Yurdakök, K., (2010). İntrauterin toksik ağır metal etkilenimi. *Cocuk Sagligi ve Hastaliklari Dergisi*, 53(2).
- [45] Dost T., Tosun N., (2023) Evidence Based Nursing Practices in Preventing the Development of Phlebits Due to Peripheral Venous Catheter: Traditional Review. *Turkiye Klinikleri Journal of Nursing Sciences*, 15, 1207–16.
- [46] Yetkin, H., Başak, P.Y. (2006). Herbal therapy in dermatology, *Turk Derm*, 40(2): 40-45.
- [47] Erdoğan, B. C., Baykara, Z. G. (2020). Periferik intravenöz katater ilişkili flebit gelişimini önlemede hemşirelik bakımı. *Gazi Sağlık Bilimleri Dergisi*, 5(1), 30-36.

Antimicrobial Activity and Chemical Composition of Essential Oil Extracted from *Hyoscyamus niger* L. Inflorescence

Sefa Gözcü^{1*}, Zeynep Akşit², Hüseyin Akşit³

¹Department of Pharmacognosy, Faculty of Pharmacy, Erzincan Binali Yildirim University, 24100, Erzincan, Türkiye, e-mail: sgozcu@erzincan.edu.tr

² Department of Hotel, Restaurant and Service, Tourism and Hospitality Vocational School, Erzincan Binali Yildirim University, 24100, Erzincan, Türkiye, e-mail: zeynep.aksit@erzincan.edu.tr

³ Department of Analytical Chemistry, Faculty of Pharmacy, Erzincan Binali Yildirim University, Erzincan, 24100 Türkiye, e-mail: huseyin.aksit@erzincan.edu.tr

Received: 25/07/2024, Revised: 19/11/2024, Accepted: 20/11/2024, Published: 31/12/2024

Abstract

This study aimed to analyze the chemical composition and evaluate the antibacterial activity of essential oil extracted from the *Hyoscyamus niger* L. inflorescence collected from Erzincan, Türkiye. The essential oil was extracted using hydrodistillation and analyzed by GC-MS, identifying 23 components, with major constituents being 10-heneicosene (35.72%), phytol (20.50%), and acetic acid, butyl ester (10.10%). The antibacterial activity was tested against six bacterial strains, including *Staphylococcus aureus*, *Clostridium perfringens*, *Enterococcus faecalis*, *Bacillus cereus*, *Listeria monocytogenes*, and *Escherichia coli*, using the disc diffusion method. The *H. niger* inflorescence essential oil exhibited moderate antibacterial activity, specifically against *C. perfringens*, with a zone of inhibition of 11.7 ± 1.2 mm compared to the positive control imipenem (17.0 ± 1.0 mm). The results suggest that *H. niger* inflorescence essential oil has potential as an antibacterial agent, highlighting the importance of exploring plant-derived compounds as alternatives to traditional antibiotics in combating multidrug-resistant bacteria.

Keywords: *Hyoscyamus niger* L., Essential oil, Antibacterial, GC-MS

Hyoscyamus niger L. Çiçeklerinden Elde Edilen Uçucu Yağın Antimikrobiyal Aktivitesi ve Kimyasal Bileşimi

Öz

Bu çalışmada, Erzincan, Türkiye'den toplanan *Hyoscyamus niger* L. çiçek durumlarından elde edilen uçucu yağların kimyasal bileşimi ve antibakteriyel aktivitesi incelenmiştir. Uçucu yağlar hidrodistilasyon yöntemiyle elde edilmiş ve kimyasal bileşenleri GC-MS ile analiz edilmiştir. Analiz sonucunda, uçucu yağda toplam 23 bileşen tespit edilmiştir; majör bileşenler 10-heneikosan (%35,72), fitol (%20,50) ve asetik asit, bütül ester (%10,10) olarak belirlenmiştir. Antibakteriyel aktivite, disk difüzyon yöntemi kullanılarak *Staphylococcus aureus*, *Clostridium perfringens*, *Enterococcus faecalis*, *Bacillus cereus*, *Listeria monocytogenes* ve *Escherichia coli* dahil olmak üzere altı bakteri suşuna karşı test edilmiştir. *H. niger* çiçek durumlarından elde edilen uçucu yağ, pozitif kontrol imipenem (17.0 ± 1.0 mm) ile karşılaştırıldığında 11.7 ± 1.2 mm'lik inhibisyon alanıyla özellikle *C. perfringens*'e karşı kabul edilebilir seviyede antibakteriyel aktivite sergilediği gözlenmiştir. Sonuçlar, *H. niger* çiçek durumlarından elde edilen uçucu yağın antibakteriyel potansiyele sahip olduğunu ve çoklu-antibiyotik dirençli bakterilerle mücadelede doğal kaynaklı bileşiklerin antibiyotiklere alternatif olarak araştırılmasının önemi vurgulanmıştır.

Anahtar Kelimeler: *Hyoscyamus niger* L., Uçucu yağ, Antibakteriyel, GC-MS

*Corresponding Author: sgozcu@erzincan.edu.tr

¹ Sefa GÖZCÜ, <https://orcid.org/0000-0002-0735-4229>

² Zeynep AKŞİT, <https://orcid.org/0000-0002-0349-0223>

³ Hüseyin AKŞİT, <https://orcid.org/0000-0002-1509-851X>

1. Introduction

The genus *Hyoscyamus* (Solanaceae) comprises six species in the flora of Turkey: *Hyoscyamus aureus* L., *Hyoscyamus albus* L., *Hyoscyamus muticus* L., *Hyoscyamus niger* L., *Hyoscyamus pusillus* L., and *Hyoscyamus reticulatus* L. [1]. *H. niger* (black henbane) is the most renowned species of the *Hyoscyamus* genus. It has been utilized as a medicinal plant since ancient times in both Greece and Türkiye [2-4]. The mature corolla of *H. niger* is a lurid yellow, typically veined with purple; the fruiting calyx is constricted in the middle; and the upper cauline leaves are amplexicaul [1].

H. niger is used in folk medicine as an antiasthmatic, anthelmintic and for toothaches [2-5]. Phytochemical investigations show that all parts of *H. niger* contain hyoscyamine and scopolamine [6]. In addition to these compounds, lignanamide, tyramine derivative, and non-alkaloid compounds were isolated from *H. niger* seeds, and many secondary metabolites were identified in its essential oil [7,8]. Previous studies have reported the antibacterial, antifungal antiviral, and insecticidal activities of *H. niger* seeds [1, 7-10]. Additionally, the essential oil of *H. niger* has been reported to exhibit antibacterial and antioxidant properties. [8].

Recent studies have demonstrated the wide-ranging pharmacological effects of essential oils, driven by their complex mixtures of monoterpenes, sesquiterpenes, phenolics, and other volatile compounds. For instance, essential oils from medicinal plants have been shown to exhibit significant antimicrobial, anti-inflammatory, and antioxidant activities, with potential applications against antibiotic-resistant pathogens [11–13]. Advances in analytical techniques, such as GC-MS and LC-MS, have enabled the precise characterization of these oils, linking their bioactivities to specific chemical constituents [14].

Antibiotic resistance has become a serious problem affecting millions of people globally. Because of this resistance, there has been an increase in research into alternative solutions, such as medicinal plants [15,17]. As a result, the World Health Organization (WHO) has published a list of global priority diseases caused by multidrug-resistant bacteria to discover novel effective drugs [16]. The aim of this study is to investigate the chemical composition of the essential oil from *H. niger* inflorescence collected in Erzincan, Türkiye, and to evaluate their antibacterial activity against six bacterial strains: five gram-positive strains, *Staphylococcus aureus*, *Clostridium perfringens*, *Enterococcus faecalis*, *Bacillus cereus*, *Listeria monocytogenes*, and one gram-negative strain, *Escherichia coli*.

2. Materials And Methods

a. Plant Material

The plant material was collected in June 2024 at inflorescence stage from Kurutilek village in Erzincan, Türkiye (39° 46' 33.47" N, 39° 29' 38.57"E), located at an altitude of 1740 m. Fresh inflorescences of *Hyoscyamus niger* were used for the essential oil extraction. The herbarium specimens were prepared by drying the collected plant material under shaded conditions with adequate ventilation to ensure preservation and prevent degradation of morphological and

chemical characteristics. The authentication of voucher specimens was conducted by Prof. Dr. Ali Kandemir and deposited at the Herbarium of Erzincan Binali Yıldırım University in Erzincan, Türkiye (EBYU 000005).

b. Essential Oil Extraction

A total of 500 grams of fresh *Hyoscyamus niger* inflorescence (HN) were mixed and subjected to hydrodistillation for 3 hours using a Clevenger apparatus according to the method recommended in the European Pharmacopoeia. The extraction procedure was carried out in triplicate. Subsequently, the essential oil were carefully collected and stored in sealed sample tubes, which were then kept at 4 °C until analysis [31].

2.3. GC-MS Analysis Conditions

GC-MS analyzes were carried out utilizing a Thermo Scientific Trace 1310 GC-MS (Trace 1310, Thermo Scientific, Milano, Italy) system equipped with an HP-5MS capillary column (30 m x 0.25 mm and 0.25 m ID), in accordance with previously reported techniques [17,18]. In split mode, helium was employed as the carrier gas, with a 50:1 ratio and a constant rate of flow of 1.2 mL/min. The mass transfer line and injection site were both set to 280 °C. Starting at 60 °C for three minutes, the temperature of the column oven was set to increase to 200 °C at a rate of 3 °C/min for 0 minutes, and then ramp up to 240 °C at a rate of 5 °C/min for five minutes. The mass spectrometer was set up with the following parameters: electron ionization (EI) mode was used with an ionization energy of 70 eV, and the ion source temperature was maintained at 280 °C. Based on a homolog n-alkane series (C8–C40), the Van den Dool and Kratz equation was used to compute the retention index (RI) for each secondary metabolite. Chemical identity was validated using NIST2004 MS libraries and Wiley. The relative peak area percentages of each chemical were calculated using the peak areas from the MS chromatograms.

2.4. Antibacterial Activity

Staphylococcus aureus (ATCC 6538), *Clostridium perfringens* (ATCC 13124), *Enterococcus faecalis* (ATCC 8459), *Bacillus cereus* (ATCC 10876), *Listeria monocytogenes* (ATCC 51774) and *Escherichia coli* (ATCC 25922) were examined for antibacterial activities. The standard protocol was followed for performing the disc diffusion test [19]. Sterile blank discs measuring 6 mm were put on Nutrient Agar medium after 100 µL of bacteria (10^8 cells/ml) was added. A blank disc was injected with 5 µL of the sample, and a positive control disc containing the antibiotic imipenem was put on the medium. Plates were incubated for 24 hours at 37 °C. A digital caliper was utilized to measure the inhibitory zones and report the mean diameter ± standard deviation of three replications in millimeters.

3. Results and Discussion

3.1. The composition of *Hyoscyamus niger* Essential oil

The hydrodistillation technique was used to produce essential oil from *Hyoscyamus niger* inflorescence (HN) with a yield of 0.06% (yellow oil). There were 23 components found in the essential oil of HN, accounting for 97.17% (v/w) of the total oil. In total, 22 secondary metabolites in the essential oil obtained from the aerial parts of *H. niger*. It was also reported that 42 secondary metabolites were identified in the essential oil obtained from the *H. niger* seeds [8]. It is known that the difference observed in these yields is due to the climate and environmental conditions in which the plants grow [21]. Table 1 presented the chemical composition of essential oil along with the percentage of each secondary metabolites, retention index (RI), and retention time (RT). Acetic acid, butyl ester (10.10%), 10-heneicosene (35.72%), and phytol (20.50%) were determined to be the major components (Table 1). In the study conducted on *H. niger* aerial parts essential oil, hexahydrofarnesyl acetone (19.19%) and phytol (52.09%) were reported as major components. In the same study again conducted on *H. niger* seeds essential oil, the major component was reported to be hexahydrofarnesyl acetone (46.36%) [8]. In the presented study, hexahydrofarnesyl acetone was found to be 0.11%. In another study, it was reported that the major components of the essential oil obtained from *H. niger* leaves were *n*-Eicosane and phytol [30]. These results support the presented study. Although borneol was detected as the major secondary compound in the essential oils of *Hyoscyamus* sp., borneol was not identified in the presented study [20, 29]. Additionally, In the presented study, the presence of 20 compounds was identified in the essential oil of HN for the first time (Acetic acid, butyl ester, ethylbenzene, *p*-xylene, styrene, methylbutyl propanoate, α -pinene, eucalyptol, linalool, camphor, caryophyllene, γ -elemene, nerolidol, germacrene B, dodecanoic acid, 8-heptadecene, 2-hexadecanol, 9-nonadecene, 9-eicosene, 10-heneicosene, 9-octadecenoic acid) [8,30].

Table 1. Chemical constituents identified in the *H. niger* L. essential oil

Compounds	RT	RI	RI (NIST)	Composition (%)
Acetic acid, butyl ester	3.69	813	814	10.10
Ethylbenzene	4.58	865	867	0.94
<i>p</i> -xylene	4.73	883	882	4.99
Styrene	5.18	894	895	3.68
Methylbutyl propanoate	5.52	969	968	0.22
α -pinene	7.23	945	945	0.20
Eucalyptol	8.68	1043	1045	0.67
Linalool	10.56	1101	1102	0.15

Antimicrobial Activity and Chemical Composition of Essential Oil Extracted from *Hyoscyamus niger* L. Inflorescence

Camphor	11.83	1145	1145	1.84
Caryophyllene	19.21	1443	1442	0.32
γ -elemene	19.52	1445	1440	0.15
Nerolidol	20.05	1531	1533	0.11
Germacrene B	22.55	1562	1559	0.69
Dodecanoic acid	22.70	1571	1572	0.52
8-heptadecene	25.13	1678	1678	1.49
2-hexadecanol	27.22	1705	1706	0.13
Hexahydrofarnesyl acetone	28.67	1848	1847	0.11
9-nonadecene	29.23	1894	1892	3.55
9-eicosene	29.74	1914	1916	9.42
10-heneicosene	33.49	2060	2061	35.72
9-octadecenoic acid	34.29	2125	2125	0.11
Phytol	34.70	2149	2148	20.50
Phytol, acetate	35.25	2227	2228	1.56
Total				97.17

RT: Retention time, RI: Retention index, RI (NIST): RI literature (NIST webbook)

3.2. Antibacterial Activity

Antibacterial activity test results of *Hyoscyamus niger* inflorescence (HN) essential oil are presented in Table 2. In this context, it was determined that HN essential oil (5 μ L) exhibited moderate antibacterial activity against all bacterial chains compared to the positive control imipenem (10 mcg). Inci et al. reported in their study that HN essential oil exhibited higher activity against *E. coli* (inhibition zone: 32 mm) and *S. aureus* (inhibition zone: 21 mm) compared to the positive control streptomycin (zone inhibition: 30 mm- 20mm, respectively) [8]. This difference is attributed to the difference in the components of essential oil in the presented study. In a different study, the methanol extract extracted from the seeds of *H. niger* has been found to have significant antibacterial activity (inhibition zone: 25.0 mm) against *S. Aureus* [22]. Chalabian et al. also reported that the alkaloid extract obtained from *H. niger* root and aerial parts had strong antibacterial activity [23]. Vanitha et al. tested the antibacterial activity of 10-heneicosene, the major component of HN essential oil, on *S. pneumoniae* and *A. fumigatus*. Vanitha et al. reported that 10-heneicosene has strong antibacterial activity [24]. When we look at the antibacterial activity studies on the other major component, phytol, it has been reported that it has strong antibacterial activity on *E. coli* [25] and *P. aeruginosa* [26]

bacterial chains (growth inhibition MIC: 62.5 µg/mL-19 µg/mL, respectively). In another study conducted on phytol, it was shown that it exhibited strong antibacterial activity on *Clostridium sporogenes*, *Sarcina lutea*, and *E. faecalis* bacterial chains [27]. It has been emphasized that phytol exerts antibacterial effects by dysregulating the function of eukaryotic cells through a series of effects, including disruption of membrane permeability and depolarization of the mitochondrial membrane [24-28]. According to this information, the antibacterial activity and antibacterial activity mechanism of HN essential oil can be explained.

Table 2. Disc diffusion results (mm) of *H. niger* L. essential oil for tested pathogenic bacteria

Bacterial strains	HN (5 µL)	Imipenem* (10 mcg)
<i>Staphylococcus aureus</i>	14.3±0.5	45.3±0.6
<i>Clostridium perfringens</i>	11.7±1.2	17.0±1.0
<i>Enterococcus faecalis</i>	13.0±0.9	45.0±1.0
<i>Bacillus cereus</i>	13.3±1.2	30.0±1.0
<i>Listeria monocytogenes</i>	7.0±1.7	36.3±2.1
<i>Escherichia coli</i>	15.7±1.5	35.3±2.1

HN: *Hyoscyamus niger* inflorescence essential oil, *: Positive control (Imipenem)

4. Conclusion

The chemical compounds identified in this study using GC-MS analysis were produced through hydrodistillation, which was followed by an examination of their chemical variation and antibacterial activity. Despite the broad geographical distribution of *Hyoscyamus niger* inflorescence (HN), there were small variations in the essential oil composition and showed efficacy against various bacterial strains. According to scientists, the search for antibiotic alternatives is critical since the antibiotic era is ending. HN essential oil may be effective antibacterial agents. Furthermore, the war against multidrug-resistant bacteria must be fought by means other than antibiotics, and volatiles may play an essential role in this.

Ethics in Publishing

There are no ethical issues regarding the publication of this study.

Conflict of Interest

The authors declare no competing interests.

Acknowledgements

We thank Professor. Dr. Ali Kandemir for the taxonomic description of the plant samples. This research did not receive any specific grant from funding agencies in the public, commercial, or not-for-profit sectors

Author Contribution

S.G. conceived and designed the research. S.G., Z.A, and H.A. conducted experiments. Z.A. and H.A. evaluated the analysis results. S.G. and H.A. drafted the manuscript. All authors have read and agreed to the published version of the manuscript.

References

- [1] Küpeli Akkol, E., Ilhan, M., Kozan, E., Güragaç Dereli, F. T., Sak, M., Sobarzo-Sánchez, E. (2020). Insecticidal activity of *Hyoscyamus niger* L. on *lucilia sericata* causing myiasis. *Plants*, 9, 655-665. <https://doi.org/10.3390/plants9050655>
- [2] Gözcü, S., Korkmaz, M., Çorlu, S., Tuysuz, S. (2024). Traditional uses of medicinal plants in Erzincan province, Türkiye. *Journal of Faculty of Pharmacy of Ankara University*, 48(1), 34-45. <https://doi.org/10.3390/plants905065510.33483/jfpau.1329957>
- [3] Ghorbanpour, M., Hatami, M., Hatami, M. (2015). Activating antioxidant enzymes, hyoscyamine and scopolamine biosynthesis of *Hyoscyamus niger* L. plants with nano-sized titanium dioxide and bulk application. *Acta Agriculturae Slovenica*, 105(1), 23-32. <https://doi.org/10.14720/aas.2015.105.1.03>
- [4] Yiğit, B. M., & Gözcü, S. Ethnobotanical study of medicinal plants in ađri province, türkiye: exploring traditional knowledge and therapeutic potential. *Journal of Faculty of Pharmacy of Ankara University*, 48(2), 486-497. <https://doi.org/10.33483/jfpau.1402467>.
- [5] Honda, G., Yeşilada, E., Tabata, M., Sezik, E., Fujita, T., Takeda, Y., Tanaka, T. (1996). Traditional medicine in Turkey VI. Folk medicine in West Anatolia: Afyon, Kütahya, Denizli, Muğla, Aydın provinces. *Journal of Ethnopharmacology*, 53(2), 75-87. [https://doi.org/10.1016/S0378-8741\(96\)01426-2](https://doi.org/10.1016/S0378-8741(96)01426-2).
- [6] Çırak, C., Kevseroglu, K., Sağlam, B. (2004). Physical and physiological dormancy in black henbane (*Hyoscyamus niger* L.) seeds. *Journal of Plant Biology*, 47, 391-395. <https://doi.org/10.1007/BF03030556>
- [7] Ma, C. Y., Liu, W. K., Che, C. T. (2002). Lignanamides and nonalkaloidal components of *Hyoscyamus niger* seeds. *Journal of natural products*, 65(2), 206-209. <https://doi.org/10.1021/np010073b>
- [8] İnci, Ş., Sancar, P. Y., Demirpolat, A., Kirbag, S., Civelek, S. (2022). Chemical

- compositions of essential oils, antimicrobial effect and antioxidant activity studies of *Hyoscyamus niger* L. from Turkey. *bioRxiv*, 2022(8), 503024. <https://doi.org/10.1101/2022.08.07.503024>
- [9] Dulger, B., Hacıoglu, N., Goncu, B. S., Gucin, F. (2010). Antifungal activity of seeds of *Hyoscyamus niger* L. (Henbane) against some clinically relevant fungal pathogens. *Asian Journal of Chemistry*, 22(8), 6321.
- [10] Al-Snafi, A. E. (2018). Therapeutic importance of *Hyoscyamus* species grown in Iraq (*Hyoscyamus albus*, *Hyoscyamus niger* and *Hyoscyamus reticulatus*)-A review. *IOSR Journal of Pharmacy*, 8(6), 18-32.
- [11] Gandhi, G. R., Hillary, V. E., Antony, P. J., Zhong, L. L., Yogesh, D., Krishnakumar, N. M., & Gan, R. Y. (2024). A systematic review on anti-diabetic plant essential oil compounds: Dietary sources, effects, molecular mechanisms, and safety. *Critical reviews in food science and nutrition*, 64(19), 6526-6545. <https://doi.org/10.1080/10408398.2023.2170320>
- [12] Zhang, J., Zhang, M., Bhandari, B., & Wang, M. (2024). Basic sensory properties of essential oils from aromatic plants and their applications: A critical review. *Critical Reviews in Food Science and Nutrition*, 64(20), 6990-7003. <https://doi.org/10.1080/10408398.2023.2177611>
- [13] Dhifi, W., Bellili, S., Jazi, S., Bahloul, N., & Mnif, W. (2016). Essential oils' chemical characterization and investigation of some biological activities: A critical review. *Medicines*, 3(4), 25-46. <https://doi.org/10.3390/medicines3040025>
- [14] Ertas, A., Yilmaz, M. A., & Firat, M. (2015). Chemical profile by LC–MS/MS, GC/MS and antioxidant activities of the essential oils and crude extracts of two *Euphorbia* species. *Natural product research*, 29(6), 529-534. <https://doi.org/10.1080/14786419.2014.954113>
- [15] Bakal, S. N., Bereswill, S., Heimesaat, M. M. (2017). Finding novel antibiotic substances from medicinal plants—antimicrobial properties of *Nigella sativa* directed against multidrug resistant bacteria. *European Journal of Microbiology and Immunology*, 7(1), 92-98. <https://doi.org/10.1556/1886.2017.00001>
- [16] Shrivastava, S. R., Shrivastava, P. S., Ramasamy, J. (2018). World health organization releases global priority list of antibiotic-resistant bacteria to guide research, discovery, and development of new antibiotics. *Journal of Medical Society*, 32(1), 76-77. https://doi.org/10.4103/jms.jms_25_17
- [17] Gözcü, S., Akşit, Z. Chemical Composition and Antibacterial Activity of Three Volatile Oils Extracted from *Nigella sativa* L. Seeds. *Black Sea Journal of Health Science*, 6(4), 662-666. <https://doi.org/10.19127/bshealthscience.1318520>

- [18] Aksit, H., Bayar, Y., Simsek, S., Ulutas, Y. (2022). Chemical composition and antifungal activities of the essential oils of *Thymus* species (*Thymus pectinatus*, *Thymus convolutus*, *Thymus vulgaris*) against plant pathogens. *Journal of Essential Oil-Bearing Plants*, 25(1), 200-207. <https://doi.org/10.1080/0972060X.2022.2043189>
- [19] Wayne, P., Melvin, P (1999) Performance Standards for Antimicrobial Susceptibility Testing, 9th International Supplement, M100-S9. Wayne, P(Ed), 120-135. National Committee for Clinical Laboratory Standards. Malvern, Pennsylvania, USA.
- [20] Ayari-Guentri, S., Djemouai, N., Gaceb-Terrak, R., Rahmania, F. (2017). Chemical composition and antioxidant activity of *Hyoscyamus muticus* L. subsp. *falezlez* (Coss.) Maire from Algeria. *Journal of Essential Oil-Bearing Plants*, 20(5), 1370-1379. <https://doi.org/10.1080/0972060X.2017.1396930>
- [21] Mehalaine, S., & Chenchouni, H. (2021). Quantifying how climatic factors influence essential oil yield in wild-growing plants. *Arabian Journal of Geosciences*, 14(13), 1257. <https://doi.org/10.1007/s12517-021-07582-6>
- [22] Dulger, B., Goncu, B. S., Gucin, F. (2010). Antibacterial activity of the seeds of *Hyoscyamus niger* L. (Henbane). *Asian Journal of Chemistry*, 22(9), 6879-6883.
- [23] Chalabian, F., Majd, A., Mehrabian, S., Falahian, F. (2002). A study of growth inhibitory effect of alkaloids of two species of genus *Hyoscyamus* on some kinds of microbes of skin. *Journal of science (Islamic Azad University)*, 12(3), 3371-3378.
- [24] Vanitha, V., Vijayakumar, S., Nilavukkarasi, M., Punitha, V. N., Vidhya, E., Praseetha, P. K. (2020). Heneicosane—A novel microbicidal bioactive alkane identified from *Plumbago zeylanica* L. *Industrial Crops and Products*, 154, 112748. <https://doi.org/10.1016/j.indcrop.2020.112748>
- [25] Ghaneian, M. T., Ehrampoush, M. H., Jebali, A., Hekmatimoghaddam, S., Mahmoudi, M. (2015). Antimicrobial activity, toxicity and stability of phytol as a novel surface disinfectant. *Environmental Health Engineering and Management Journal*, 2(1), 13-16.
- [26] Pejin, B., Ciric, A., Glamoclija, J., Nikolic, M., Sokovic, M. (2015). *In vitro* anti-quorum sensing activity of phytol. *Natural product research*, 29(4), 374-377. <https://doi.org/10.1080/14786419.2014.945088>
- [27] Pejin, B., Kartali, T., Stanimirović, B., Karaman, M. (2014). Phytol may inspire new medicinal foods for the treatment of heart disease. *Asian Journal of Chemistry*, 26(23), 8261-8262.
- [27] Bakkali, F., Averbek, S., Averbek, D., & Idaomar, M. (2008). Biological effects of essential oils—a review. *Food and chemical toxicology*, 46(2), 446-475. <https://doi.org/10.1016/j.fct.2007.09.106>

- [29] Elsharkawy, E. R., Ed-dra, A., Abdallah, E. M., & Ali, A. M. (2018). Antioxidant, antimicrobial and antifeedant activity of phenolic compounds accumulated in *Hyoscyamus muticus* L. *African Journal of Biotechnology*, 17(10), 311-321. <https://doi.org/10.5897/AJB2017.16316>
- [30] Sadeghi, B. (2016). Extraction and comparative identification of essential oil components of different *Hyoscyamus* species using hydro-distillation and GC-MS. *The 23rd Iranian Seminar of Analytical Chemistry*, 328
- [31] Karakaya, S., Yilmaz, S. V., Özdemir, Ö., Koca, M., Pinar, N. M., Demirci, B., & Baser, K. H. C. (2020). A caryophyllene oxide and other potential anticholinesterase and anticancer agent in *Salvia verticillata* subsp. *amasiaca* (Freyn & Bornm.) Bornm.(Lamiaceae). *Journal of Essential Oil Research*, 32(6), 512-525. <https://doi.org/10.1080/10412905.2020.1813212>

The Effect of Different Storage Conditions on Textural, Microbiological and Color Properties of Phyllo (Yufka)

Seda COŞKUN ¹, Mehmet Murat KARAOĞLU ^{1*}, Aslıhan HANOĞLU ¹,
Yeşim BEDİR ¹

¹Atatürk University, Faculty of Agriculture, Department of Food Engineering, Erzurum/Turkey

Received: 01/08/2024, Revised: 29/11/2024, Accepted: 02/12/2024, Published: 31/12/2024

Abstract

The effects of different storage conditions on textural, microbiological and color properties of phyllo were investigated. Phyllo samples were stored at room temperature (20°C) for 3, 5 and 7 days, in refrigerator (4°C) for 7, 14 and 21 days, and in deep freezer (-18°C) for 20, 40 and 60 days. It was determined that phyllo samples stored in the deep freezer exhibited higher L* color values (82.33-82.97), followed by samples stored in the refrigerator (78.53-81.75) and samples stored at room temperature (75.74-77.75), respectively. A statistically similar and lower total color change (ΔE) occurred in the phyllo samples stored at room temperature and in the refrigerator compared to the samples stored in the deep freezer. The samples stored in the refrigerator exhibited higher hardness, chewiness and gumminess values, while the samples stored in the deep freezer exhibited lower values. Most of the samples produced were similar to the control sample in terms of springiness property. In terms of relaxation time, the samples stored at room temperature and in the deep freezer exhibited statistically similar and lower values than the samples stored in the refrigerator. Additionally, the samples stored in the deep freezer had higher breaking force and breaking length values. The total mesophilic aerobic bacteria count of the samples varied between 3.38-12.30 log cfu/g, and mold and yeast count varied between <2.00-6.87 log cfu/g.

Keywords: Phyllo (yufka), storage, textural properties, microbiological properties, color

Farklı Depolama Koşullarının Yufkanın Dokusal, Mikrobiyolojik ve Renk Özellikleri Üzerine Etkisi

Öz

Farklı depolama koşullarının yufkanın dokusal, mikrobiyolojik ve renk özellikleri üzerine etkisi araştırılmıştır. Yufka örnekleri oda sıcaklığında (20°C) 3, 5 ve 7 gün, buzdolabında (4°C) 7, 14 ve 21 gün ve derin dondurucuda (-18°C) 20, 40 ve 60 gün boyunca depolanmıştır. Derin dondurucuda depolanan yufka örneklerinin daha yüksek L* renk değerlerine (82.33-82.97) sahip olduğu ve bunu sırasıyla buzdolabı (78.53-81.75) ve oda sıcaklığında depolanan örneklerin (75.74-77.75) izlediği belirlenmiştir. Oda sıcaklığı ve buzdolabında depolanan yufka örneklerinde, derin dondurucuda depolanan örneklere kıyasla istatistiksel olarak benzer ve daha düşük seviyede toplam renk değişimi (ΔE) meydana gelmiştir. Buzdolabında depolanan örnekler daha yüksek, derin dondurucuda depolanan örnekler daha düşük sertlik, çignenebilirlik ve sakızimsılık değerleri sergilemiştir. Üretilen örneklerin çoğu elastikiyet özelliği bakımından kontrol örneğine benzerdir. Gevşeme süresi bakımından oda sıcaklığında ve derin dondurucuda depolanan örnekler buzdolabında depolanan örneklere göre istatistiksel olarak benzer ve daha düşük değerler göstermiştir. Ayrıca derin dondurucuda depolanan örnekler daha yüksek kopma kuvveti ve kopma uzunluğu değerlerine sahiptir. Örneklerin toplam mezofilik aerobik bakteri sayısı 3.38-12.30 log kob/g ve küf ve maya sayısı ise <2.00-6.87 log kob/g arasında değişmiştir.

Anahtar Kelimeler: Yufka, depolama, dokusal özellikler, mikrobiyolojik özellikler, renk

*Corresponding Author: mmurat@atauni.edu.tr

Seda COŞKUN, <https://orcid.org/0000-0002-0688-9280>

Mehmet Murat KARAOĞLU, <https://orcid.org/0000-0002-9919-8824>

Aslıhan HANOĞLU, <https://orcid.org/0000-0002-4772-5944>

Yeşim BEDİR, <https://orcid.org/0000-0003-4756-7269>

1. Introduction

Cereals and cereal-based products have an important role in human nutrition as they provide a significant portion of the daily energy needed [1]. Phyllo, also called yufka or fyllo, has a special position among cereal-based products due to its being a ready-to-use, practical [2] and easily accessible product and creating a feeling of fullness. It is a semi-finished product obtained by rolling out and partially baking the dough prepared using baklava and pastry type of wheat flour, drinking water, edible salt and additives when necessary [3]. Phyllo is a single-layered, cream-colored and 1–2 mm thick product [4] and can be produced in different shapes and sizes according to need [2].

Phyllo attracts attention especially due to its practical use [5] and is used as an intermediate product in the preparation of many pastries such as börek, flatbread [2], baklava, and pies like kasseropita and spanakopita [6], as well as desserts, samosas, and other delicious dishes [7]. It offers the opportunity to produce various food products in a short time and is widely preferred by consumers in modern living conditions, especially by people who have a busy work life and limited time to spare for food preparation and consumption [5]. For this reason, the demand for phyllo, which already has a wide consumption geography spanning the Middle East, Balkans, Caucasus and Turkey, is constantly increasing [8]. It is also stated that phyllo has become one of the most popular foods in many US, Asian and European countries due to its ease of cooking and taste [7, 9].

The most important quality characteristics of phyllo are surface color, proper baking degree and uniform diameter and thickness [10]. Additionally, textural properties are known to be extremely important for phyllo, especially in terms of the quality of the final product to be prepared using phyllo. It is expressed that phyllo must have perfect springiness and flexibility. It must also have excellent extensibility, all of which are desirable to provide the ability to fold and roll during processing [2, 4, 10]. In addition, phyllo should be neither be sticky nor so weak that it tears easily. If phyllo does not meet the appropriate textural properties, the final products cannot be properly produced, or even if they are produced, significant quality problems may arise in the final product, leading to substantial economic losses.

Phyllo generally has a short shelf life due to its neutral pH (6-7) and comparatively high water activity (0.6-0.8 aw), which make it a suitable substrate for aerobic microorganisms. This requires keeping the phyllo under appropriate storage conditions; which it is typically stored at 4-6°C in retailers and/or frozen in supermarkets [6]. However, the effect of different storage conditions on the textural properties, one of the most important quality parameters of phyllo, is still not well known. In this study, the effects of different storage temperatures and periods on the textural properties of phyllo were investigated. Phyllo samples were also examined in terms of color and microbiological properties during the storage period.

2. Material and Methods

2.1. Material

Flour (Çevikler Altınyazma) and salt used in phyllo production were obtained from Erzincan local market. Drinking tap water was used in preparing the phyllo. The properties of the flour were as follows; moisture content: 13.0%, wet gluten: 29.70%, dry gluten: 10.41%, gluten index: 92.75%, falling number: 1.035 s, Zeleny sedimentation: 35 mL. The L*, a* and b* color values of the flour were 85.50, -0.57 and 9.13, respectively. The farinograph parameters were as follows; water absorption: 69.1%, stability: 17.2 min., development time: 15.8 min., degree of softening: 35 FU. The extensograph parameters were as follows; extensibility: 114 mm, maximum resistance: 682 BU, energy: 91 cm².

2.2. Methods

2.2.1. Phyllo Production

Phyllo production was carried out by İrem Yufka company operating in Erzincan province (Figure 1). Firstly, 50 kg of flour was sifted, and 30 liters of water and 2 kg of salt were added. The mixture was kneaded for 30 min., the obtained dough was rested for 30 min., and then divided into balls of 130 g in size. After they were rolled out to a diameter of 60-70 cm, they were placed on a hot sheet and baked for 15 seconds on both sides. Then, they were soaked and rested for 2 hours. The rested phyllo samples were packaged in polyethylene bags with low moisture permeability and stored for short, medium and long periods in different storage conditions (3, 5 and 7 days at room temperature (20°C); 7, 14 and 21 days in refrigerator (4°C); 20, 40 and 60 days in deep freezer (-18°C)). The non-stored sample, i.e. the first day of production, was considered as the control sample.

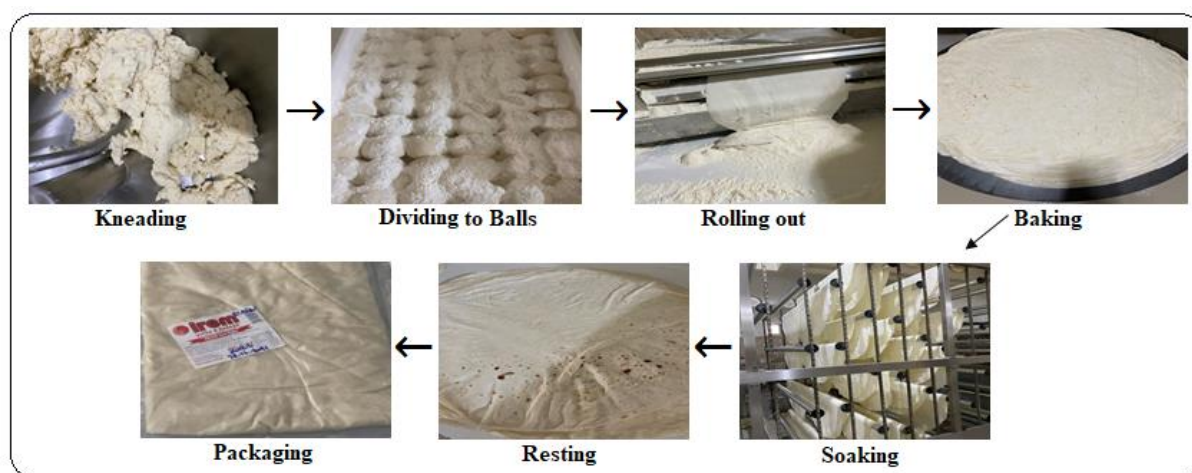


Figure 1. Phyllo production flow chart

2.2.2. Analysis of Phyllo Samples

2.2.2.1. Color Measurement

The color measurement of phyllo samples was carried out using the color analyzer (Minolta, CR-200, Japan) and measuring L*, a* and b* color values. Total color change (ΔE) was calculated as follows:

$$\Delta E = [(L_0 - L_1)^2 + (a_0 - a_1)^2 + (b_0 - b_1)^2]^{1/2}$$

where, L₀, a₀, b₀ are L*, a* and b* color values of control phyllo sample (non-stored sample; first day of production), and L₁, a₁, b₁ are L*, a* and b* color values of stored phyllo samples, respectively.

2.2.2.2. Texture Profile Analysis (TPA)

Texture profile analysis in the phyllo samples (25 mm diameter, 4 layers (4x1 mm thickness)) was performed using a texture analyzer (TA.XTplus, Stable Micro Systems Ltd, Godalming, Surrey, U.K.) equipped with a 5 kg load cell and cylindrical metal probe (36 mm) (P/36). TPA test was carried out under conditions: 0.5 mm/s pre-test speed, 0.2 mm/s test and post-test speed, 30% compression rate, 20 g trigger force. The obtained results were expressed as hardness (N), cohesiveness, springiness, chewiness (N) and gumminess (N).

2.2.2.3. Stress Relaxation Test

The stress relaxation test was performed on phyllo samples with a texture analyzer (TA.XTplus, Stable Micro Systems Ltd, Godalming, Surrey, U.K.) equipped with Tortilla/Pastry Burst Rig under the following conditions: pre-test and test speed: 1 mm/s; post-test speed: 5 mm/s; holding time: 120 s; distance: 5 mm; trigger force: 5 g. Maximum force (g), minimum force (g) and relaxation time (s) values (time required for the maximum force to decrease to its 80%) were calculated from the obtained curve.

2.2.2.4. Stretching Test

The stretching test was performed on phyllo samples with a texture analyzer (TA.XTplus, Stable Micro Systems Ltd, Godalming, Surrey, U.K.) equipped with Tortilla/Pastry Burst Rig under the following conditions: pre-test and test speed: 1 mm/s; post-test speed: 10 mm/s; distance: 30 mm; trigger force: 5 g. Breaking force (g), breaking length (mm) and deformation modulus (g/mm) (breaking force/breaking length) were calculated from the obtained curve.

2.2.2.5. Microbiological Analysis

For the microbiological analysis, 90 ml of sterile physiological saline solution (0.85% NaCl) was added to 10 g of the sample and homogenized for 50 seconds. Plate Count Agar (PCA) and spreading method were used to determine total mesophilic aerobic bacteria count (TMAB). Petri dishes were incubated at 30°C for 48 hours. To determine total number of yeast and mold, Potato Dextrose Agar (PDA) and spreading method were used. Incubation was carried out at

28-30°C for 120 hours. The results were expressed as log colony forming units/g (log cfu/g) [11].

2.2.3. Statistical Analysis

All analyzes were carried out in triplicate. The data obtained were subjected to variance analysis using IBM® SPSS Statistics software version 22.0.0.0. The averages of main variation sources found to be important ($p < 0.05$) were compared with the Duncan Multiple Comparison Test. The results were expressed as mean \pm standard error. Pearson's Correlation Test was applied to determine the correlation among textural characteristics of phyllo samples.

3. Results and Discussion

3.1. Results of Color Measurement

Color is one of the most important criteria for food products [12]. Color, a physical characteristic that customers use to assess product quality [13], indicates the composition and freshness of the food products and provides information about whether there is falsification or not [12]. L^* , a^* and b^* color values and total color change (ΔE) of phyllo samples are given in Table 1. L^* value indicates the dark-light density of a product, and the closer to 100, the lighter the color [14]. Storage temperature significantly affected the L^* color values of the samples ($p < 0.01$). In general, the phyllo samples stored in the deep freezer exhibited higher L^* color values, followed by the samples stored in the refrigerator and samples stored at room temperature, respectively. It is expressed that color change in the baked product originates from Maillard reactions which occur between proteins and reducing sugar and the increase in melanoidin concentration resulting from these reactions gives brownness to the product [15]. As known, the increasing the temperature causes the rate of the Maillard reaction to increase [16]. This situation explains why the highest level of L^* color value was measured in the deep freezer temperature and the lowest level at room temperature. Although there was no statistically significant difference between the samples belonging to the short and medium period storage process in terms of the L^* color value, an increase in storage time led to an increase in the L^* color values of the samples stored at room temperature. Similarly, an increase was observed in the L^* color values of the samples stored in the refrigerator due to the increase in the storage time. In the samples stored in the deep freezer, the increase in the storage time firstly increased the L^* color value of the phyllo samples and then decreased this value. Nevertheless, the L^* color values of the samples stored under deep freezer conditions were statistically close to each other and higher than the control sample in all three storage periods. It is thought that the degradation of color pigments over time may be effective in the increase in L^* color values depending on storage time. On the other hand, it is known that color has a crucial importance on the acceptability of bakery products involving dough-based preparations, and a bright and clear appearance is generally desired [9]. Therefore, it can be said that the storage process and increasing the storage time in the refrigerator and deep freezer conditions provided positive changes in the phyllo samples in terms of L^* color value, since its increase indicates increased brightness and clarity as desired.

Table 1. L*, a* and b* color values and total color change (ΔE) of phyllo samples^a

Storage Temperature	Storage Time (Days)	L*	a*	b*	ΔE
	0 (Control)	77.61±0.33d	-0.53±0.03b	16.86±0.07a	-
20°C	3	75.74±0.19e	-1.05±0.00f	13.42±0.12e	3.96±0.01bc
	5	76.60±0.39e	-0.94±0.01d	13.73±0.46e	3.33±0.55cd
	7	77.75±0.75d	-1.23±0.01g	14.12±0.02de	2.93±0.06cd
	GA	76.93±0.35C**	-0.94±0.10B**	14.53±0.52C**	3.40±0.24B**
4°C	7	78.53±0.14d	-1.34±0.01h	13.96±0.91e	3.16±0.88cd
	14	79.70±0.19c	-0.86±0.03c	16.41±0.07ab	2.17±0.21d
	21	81.75±0.18b	-0.43±0.00a	14.47±0.03cde	4.79±0.14ab
	GA	79.40±0.59B**	-0.79±0.13A**	15.43±0.50B**	3.37±0.54B**
-18°C	20	82.39±0.07ab	-1.34±0.00h	15.07±0.05cd	5.17±0.09ab
	40	82.97±0.02a	-1.00±0.00e	16.58±0.02ab	5.39±0.02a
	60	82.33±0.01ab	-1.06±0.03f	15.54±0.03bc	4.94±0.01ab
	GA	81.33±0.82A**	-0.98±0.11C**	16.01±0.28A**	5.17±0.09A**
P		**	**	**	**

^a Means with different lowercase and uppercase letters in the same column are statistically different ($p < 0.05$).

**P < 0.01, GA: General Average.

a* value indicates the red/green color density of a product (+a: red, -a: green) [14]. The a* color values generally decreased in the stored samples compared to the control sample. Storage temperature affected the a* color values of the samples at a statistically significant level ($p < 0.01$). In general, the phyllo samples stored in the refrigerator had higher a* color values, while the samples stored in the deep freezer had lower a* color values. When the storage period reached the middle period, a* color values of the phyllo samples increased in all storage temperatures. On the contrary, further increase in the storage time, which means that the storage time reached the long period, caused these values to decrease again in the samples stored at room temperature and in the deep freezer. However, in the samples stored in the refrigerator, a* color value increased when the long period was reached. b* value indicates the yellow/blue color density (+b: yellow, -b: blue) [14]. The b* color values generally decreased in the stored samples compared to the control sample. It was determined that the storage temperature affected the b* color values of the samples at a statistically significant level ($p < 0.01$). In general, the phyllo samples stored in the deep freezer had higher b* color values, followed by the samples stored in the refrigerator and samples stored at room temperature, respectively. Although it was not statistically significant, the increasing the storage time caused an increase in b* color values of the samples stored at room temperature. In the samples stored in the refrigerator and deep freezer, medium period storage process caused an increase in b* color values, while the long period storage process caused a decrease.

It was determined that a statistically similar and lower total color change (ΔE) occurred in the phyllo samples stored at room temperature and in the refrigerator compared to the samples stored in the deep freezer. It is known that pigments can ordinarily degrade easily due to the many factors such as temperature, pH, light, etc. [17], however, they can be preserved at low temperatures away from these factors [18]. On the other hand, some studies have reported that exposure to low temperatures in different food samples can result in pigment damages such as

carotenoid degradation [19], decrease in chlorophyll content [20], etc. Therefore, it is thought that in this study, storage process in the deep freezer may have caused relatively more damage to the color pigments of the samples due to the low temperature effect, and therefore caused more total color change and variations in a^* and b^* values. In the samples stored at room temperature, the increasing the storage time decreased the total color change. In the samples stored in the refrigerator, medium period storage process caused a decrease in the total color change, while the long period storage process caused an increase. The opposite effect was observed in the samples stored in the deep freezer. That is, medium period storage process caused an increase in the total color change of the samples, while the long period storage process caused a decrease, however, all three values were statistically close to each other, especially the samples stored for short and long periods. When the color measurement parameters were examined in general and natural color of the phyllo was taken into consideration, it was concluded that although the total color change reached its maximum level, the deep freezer conditions, in which the highest L^* color values were obtained, were better in terms of color properties, since a bright and clear appearance is desired [9].

3.2. Results of Texture Profile Analysis

The textural properties are very important for phyllo, especially in terms of quality of final product to be prepared using phyllo. The phyllo must have good flexibility and springiness properties. In addition, it must have good extensibility and be neither sticky nor weak enough to tear. All these features are desirable to supply it the ability to fold and roll during processing [2, 4, 10]. Hardness, cohesiveness and springiness values of phyllo samples are given in Figure 2. Hardness is the force required to deform a sample to a certain level [21]. Both very hard and very soft structures are undesirable in the phyllo as it affects the quality of the final product to be prepared using phyllo. The hardness values generally decreased in the stored samples compared to the control sample. The decrease in the hardness values of the samples due to the storage process was probably related to amylolytic and proteolytic enzymes present in the flour, which were activated by water during dough preparation and originated from microbial activity (Table 5), and phase transformations of water. In general, the phyllo samples stored in the refrigerator exhibited higher hardness values, followed by the samples stored at room temperature and samples stored in the deep freezer, respectively. The freezing process is one of operation that significantly affects dough quality [22]. During the freezing process, water molecules bond with hydrogen bonds to form a hexagonal crystal structure, leading the volume increases by approximately 9% [23]. The formed ice crystals negatively affect especially proteins in the dough system, as a result, three-dimensional gluten network is damaged by ice crystals [22]. Moreover, when thawing, which is necessary for rehydration of the gluten matrix in the frozen dough, is carried out at a certain temperature, condensation phenomenon takes place on the dough surface because the dough has a lower temperature than surrounding air [22], that is, the dough cannot regain all the water it lost. All these cases lead to significant decreases in the strength of dough [22] and, therefore the hardness of samples stored in the deep freezer decreases further. In addition, it is thought that the reason why the samples stored at room temperature had lower hardness values than the samples stored in the refrigerator may primarily due to higher enzyme activity. As it is known that enzymes have optimal temperature

requirements for maximum activity. Most of the enzymes work optimally between 30-70°C [24]. The low temperature ranges do not generally meet the needed activation energy, leading to the decreases in enzyme activity [25]. The increasing the storage time caused a significant decrease in the hardness values of the samples stored at room temperature and in the deep freezer. This decrease appears to be due to a general increase in the microbial activity linked to enzyme activity (Table 5). Although there was no statistically significant difference between medium and long period storage processes, the increase in the storage time had an increasing effect on the hardness values of the samples stored in the refrigerator. This may be due to the environment being relatively unfavorable in terms of temperature for enzymes activity. In addition, it is thought that the increase in the hardness values of the samples stored in the refrigerator depending on the storage time may have caused by partial retrogradation. It is mainly responsible for the hardness that occurs over time in foods containing starch [26] and occurs either too slow or too dense at extreme temperatures due to Brownian motion mechanism of macromolecules [27], which this range, where the highest hardness was measured, was a relatively medium temperature degree in this study.

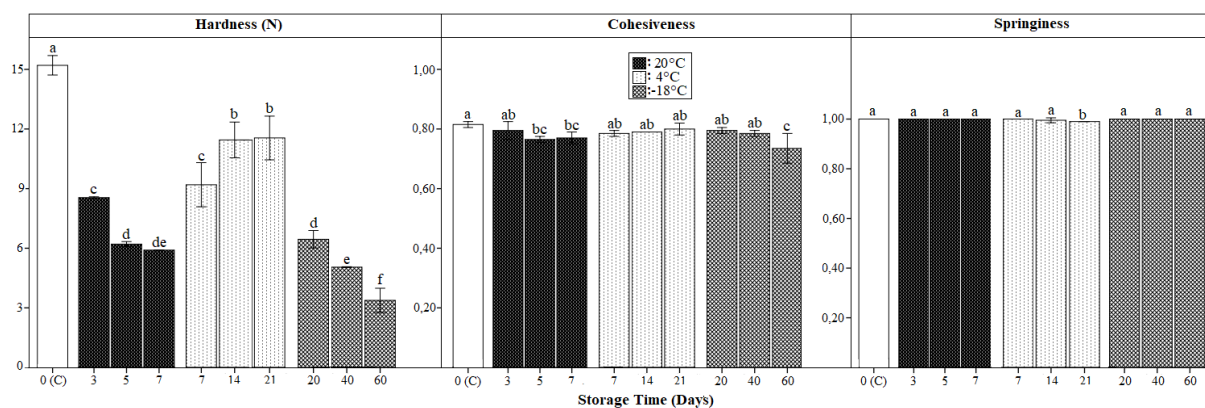


Figure 2. The effect of different storage temperatures and periods on the hardness, cohesiveness and springiness values of phyllo samples, respectively (C: Control)

Cohesiveness is described as the density of internal bonds in the structure of food [28]. It was determined that the storage process caused the phyllo samples to tend to exhibit lower cohesiveness values in general. The samples stored in the refrigerator had higher cohesiveness values, followed by the samples stored at room temperature and samples stored in the deep freezer in general, however, it was not statistically significant. The increasing the storage time had a reducing effect on the cohesiveness values of the samples stored at room temperature and in the deep freezer in general. The opposite effect was observed in the samples stored in the refrigerator, but it was not statistically significant. It was determined that the changes in the cohesiveness values of the samples depending on the storage time and temperature were similar to the changes in the hardness values in general. Therefore, it is thought that the occurrences that damage the hardness properties of samples such as breakdown of proteins, which gluten is mainly responsible for cohesiveness of bakery products [29], and carbohydrates due to microbial and enzyme activity, ice crystal formation [22] and failure to completely rehydration during thawing caused similar injuries, weakening the internal structure of the samples and leading to loss of dough strength. It was already determined that there was a significant correlation between the hardness and cohesiveness values of the phyllo samples ($r = 0.802^{**}$)

(Table 4). In addition, it is expressed that the decrease in the cohesiveness due to the increase in the storage time is caused by instability of protein macromolecular colloid originated from the freezing concentration effect such as changes in solubility and denaturation of protein and cohesion force among the protein molecules, and this case tends to the increase with the increase in the storage time, as seen in deep freezer storage process in this study. Supportively our findings, it is stated that longer frozen storage periods have also an unfavorable effect on interactions among starch and gluten network [30].

Springiness is an expression of how well a sample springs after initial deformation [31]. As mentioned earlier, phyllo must have a good springiness to obtain optimum processing properties. It was determined that the samples stored at room temperature and in the deep freezer exhibited statistically similar and higher values than the samples stored in the refrigerator. Only the sample stored in the refrigerator for 21 days exhibited a statistically lower springiness value than the other samples. Nevertheless, there was no numerically sharp decrease in the springiness value of this sample, meaning that all phyllo samples had similar springiness properties to the control group in general. It can be said that the fact that different storage conditions, including long periods and wide temperature ranges, do not significantly affect the springiness property, which is essential for phyllo, is a quite positive and desirable result for this study.

Table 2. Chewiness and gumminess values of phyllo samples^a

Storage Temperature	Storage Time (Days)	Chewiness (N)	Gumminess (N)
	0 (Control)	12.37±0.22a	12.39±0.22a
20°C	3	6.77±0.13c	6.80±0.14c
	5	4.71±0.01de	4.72±0.00de
	7	4.45±0.00ef	4.43±0.03ef
	GA	7.08± 1.21B**	7.09± 1.21B**
4°C	7	7.19±0.39c	7.22±0.41c
	14	9.75±0.25b	9.75±0.25b
	21	9.90±0.30b	9.88±0.31b
	GA	9.80±0.70A**	9.81±0.70A**
-18°C	20	5.13±0.14d	5.14±0.14d
	40	3.94±0.02f	3.95±0.02f
	60	2.47±0.14g	2.48±0.14g
	GA	5.98±1.44C**	5.99±1.44C**
	P	**	**

^a Means with different lowercase and uppercase letters in the same column are statistically different ($p < 0.05$).

** $P < 0.01$, GA: General Average.

Chewiness and gumminess values of phyllo samples are given in Table 2. Generally, both chewiness and gumminess decreased in the stored samples compared to the control sample. It was determined that the storage temperature affected the chewiness and gumminess values of the samples at a statistically significant level ($p < 0.01$). In general, the phyllo samples stored in the refrigerator had higher chewiness and gumminess values, while the samples stored in the deep freezer had lower values. In the samples stored at room temperature and in the deep freezer, the increase in the storage time decreased the chewiness and gumminess values. In the

samples stored in the refrigerator, chewiness and gumminess values increased with increasing the storage time, however, there was no statistically significant difference between medium and long storage periods. Chewiness is defined as the measure of energy required to make solid foods ready to be swallowed while being chewed in the mouth [32]. It is calculated by multiplying the hardness, cohesiveness and springiness parameters. Gumminess is the measure of the energy required to make semi-solid foods ready to swallow. It is calculated by multiplying the hardness and cohesiveness parameters [21]. Chewiness and gumminess are secondary textural parameters derived from primary textural attributes. Consequently, these parameters are influenced by fundamental factors, particularly hardness, as the hardening of food texture typically indicates an increase in the energy required to make the food ready for swallowing. Therefore, the changes in the hardness values of the phyllo samples, depending on storage temperature and duration, were directly reflected in the chewiness and gumminess values. Consistently, positive and significant correlations were observed between hardness and chewiness ($r = 0.997^{**}$), hardness and gumminess ($r = 0.997^{**}$), and chewiness and gumminess ($r = 1.000^{**}$) (Table 4).

3.3. Results of Stress Relaxation Test

The stress relaxation test, used to investigate the viscoelastic properties of foodstuffs, is based on measuring the force required to maintain deformation under a certain stress value over time [33]. Relaxation time, maximum force and minimum force values of phyllo samples, that are the basic textural parameters obtained from the stress relaxation test, are given in Table 3. Relaxation time value expresses to the time required for the maximum force to decrease to its 80% for this study. It was determined that the storage temperature affected the relaxation time values of the phyllo samples at a statistically significant level ($p < 0.01$). The samples stored at room temperature and in the deep freezer exhibited statistically similar and lower relaxation time values than the samples stored in the refrigerator. As the storage time increased, the relaxation time value firstly decreased and then increased in the samples stored at room temperature and in the deep freezer. However, they could not reach their levels in the short period storage time, in which case it can be said that the increase in the storage time had a generally decreasing effect on the relaxation time values of these samples. In the samples stored in the refrigerator, the increasing the storage time caused relaxation time values to increase. It is thought that the changes in the relaxation time values of the stored samples due to temperature and period variation sources may be caused by changes in the hardness properties of the samples. The lower relaxation time is associated with the material that shows liquid-like property, on the contrary, the higher relaxation time is associated with a more solid property [34]. Based on this, it is thought that the samples stored in the refrigerator, which had higher hardness values (Figure 2), exhibited higher relaxation time values. In addition, the samples stored at room temperature and in the deep freezer may have exhibited close and lower relaxation time values, since they had close and lower hardness values than the samples stored in the refrigerator even if statistically different. Similarly, as storage time increased, the relaxation time values of the samples stored at room temperature and in the deep freezer generally decreased, while the relaxation time values of the samples stored in the refrigerator increased, which a similar change trend was also observed in the hardness values of the samples.

Table 3. Relaxation time, maximum force and minimum force values of phyllo samples^a

Storage Temperature	Storage Time (Days)	Relaxation Time (s)	Maximum Force (g)	Minimum Force (g)
	0 (Control)	8.63±0.22d	33.83±0.05f	24.74±0.12f
20°C	3	11.06±0.00b	41.02±0.50c	33.52±0.49c
	5	8.68±0.02cd	37.71±0.37e	31.92±0.33d
	7	9.53±0.13bcd	39.38±0.28d	30.66±0.66d
	GA	9.48±0.37B**	37.99± 1.02B**	30.21± 1.26B**
4°C	7	8.48±0.06d	42.30±0.20b	36.55±0.55b
	14	9.29±0.52cd	43.17±0.18b	37.35±0.55b
	21	17.61±1.28a	50.98±0.79a	41.46±0.50a
	GA	11.00±1.47A**	42.57±2.30A**	35.03±2.36A**
-18°C	20	11.01±0.32b	32.10±0.10g	25.35±0.25ef
	40	9.71±0.00bcd	31.60±0.40g	26.37±0.14e
	60	10.38±0.61bc	31.45±0.45g	25.80±0.56ef
	GA	9.93±0.36B**	32.24±0.38C**	25.57±0.26C**
	P	**	**	**

^a Means with different lowercase and uppercase letters in the same column are statistically different ($p < 0.05$).

**P < 0.01, GA: General Average.

It was determined that the storage temperature significantly affected the maximum force values of the phyllo samples ($p < 0.01$). While the samples stored at room temperature and in the refrigerator showed higher maximum force values than the control sample, the samples stored in the deep freezer showed lower values. Among the samples subjected to storage process, the samples stored in the refrigerator exhibited higher maximum force values, followed by the samples stored at room temperature and samples stored in the deep freezer, respectively. For the samples stored at room temperature, the increasing the storage time initially decreased and then increased the maximum force values, though there was a general trend of decrease. Although there is no statistically significant difference between the short and medium period storage process, the increase in the storage time had an increasing effect on the maximum force values of samples stored in the refrigerator. It had also a decreasing effect on the maximum force values of samples stored in the deep freezer, however, it was not statistically significant. The storage process was generally effective in increasing the minimum force values of the phyllo samples compared to the control sample. The storage temperature affected the minimum force values of samples at a statistically significant level ($p < 0.01$). In general, the samples stored in the refrigerator had higher minimum force values, while the samples stored in the deep freezer had lower values. Although there was no statistically significant difference between the samples stored in the medium and long period, the increasing the storage time caused a decrease in the minimum force values of samples stored at room temperature. In the samples stored in the refrigerator, the increasing the storage time caused an increase in the minimum force values of samples, however, there was no statistically significant difference between the samples stored in short and medium period. In the samples stored in the deep freezer, the minimum force value firstly increased and then decreased with the increase in the storage time, however, the minimum force values in all three storage periods were statistically similar. Similar to relaxation time, the trends in maximum and minimum force values can also be attributed to changes in the hardness of the samples. The maximum force refers to the measure of the initial resistance of

the sample to deformation in the course of stress relaxation analysis, while the minimum force refers to the measure of the ultimate resistance measured at the end of the analysis. The increase in mentioned values, which are closely connected with the hardness of food structure, implies that the material shows a more solid-like property and requires higher deformation amount [35]. For this reason, the changes in hardness values of the samples depending on storage temperature and period were generally reflected in maximum and minimum force values (Figure 2).

3.4. Results of Stretching Test

The effects of different storage temperatures and periods on the breaking force, breaking length and deformation modulus values of phyllo samples are given in Figure 3, respectively. It was determined that the samples stored in the deep freezer exhibited higher breaking force values, while those stored in the refrigerator generally showed lower values. As the storage time increased, the breaking force values of the samples stored at room temperature decreased significantly. A general decrease was also observed in the samples stored in the deep freezer, however, the breaking force values of the samples stored medium and long period were statistically insignificant. In the samples stored in the refrigerator, when the storage period arrived to the middle period, the breaking force value increased, but further increase decreased this value again. It was determined that the breaking force values of the phyllo samples had a negatively correlation with the maximum force ($r = -0.645^*$) and minimum force ($r = -0.657^*$) values (Table 4), suggesting that changes in breaking force values of the samples may depend on this relationship. That is, the samples with higher maximum and minimum force values, which was previously stated to indicate a harder sample structure, exhibited easier breakable property due to their harder structure, and this situation caused them to exhibit lower breaking force values. As another pointer, it is clearly seen in Figure 2 that the samples with higher hardness values had lower breaking force values, while the samples with lower hardness values had higher breaking force values when comparing on the group basis.

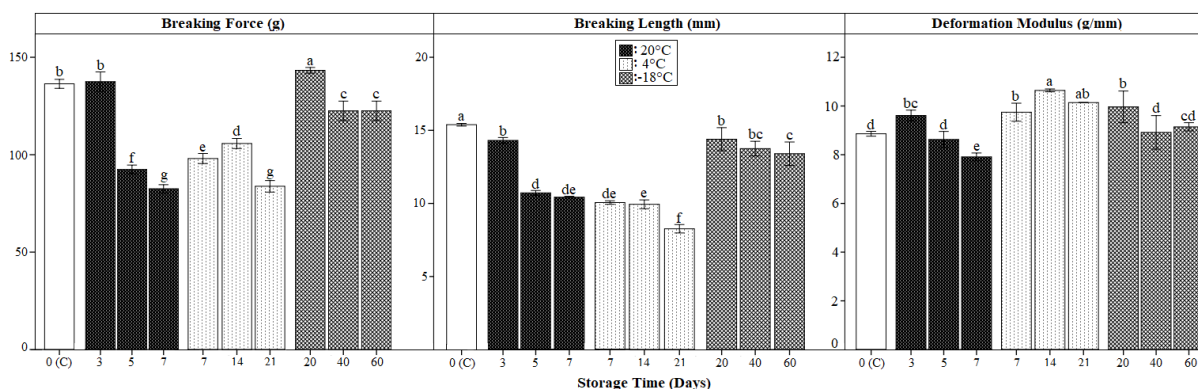


Figure 3. The effect of different storage temperatures and periods on the breaking force, breaking length and deformation modulus values of phyllo samples, respectively (C: Control)

Breaking length refers to the average distance required for the breaking process, and the increasing this distance means that the dough extensibility increases [36]. It was determined that the storage process caused the breaking length values of all samples to decrease, which expresses that the control sample had the highest breaking length value. In general, the samples stored in the deep freezer exhibited higher breaking length values, followed by the samples

stored at room temperature and samples stored in the refrigerator, respectively. At all three storage temperatures, there was a general decrease in the breaking length values of the samples in parallel with the increase in the storage time. The changes in the breaking length values of the samples can be generally attributed to the close relationship between breaking length and breaking force values ($r = 0.926^{**}$) (Table 4). As stated in the previous section, the decrease in the breaking force values of the samples is due to the increase in the breaking ability resulting from the increase in the hardness of the sample structure, facilitating the breaking action. That is, the decrease in the breaking force means that the breaking action ends faster, leading to a decrease in the breaking length value expressing the distance required for breaking. Therefore, the samples with lower breaking force values exhibited lower breaking length values, while the samples with higher breaking force values exhibited higher breaking length values. For these reasons, phyllo samples with higher springiness, which implies that they can tolerate the applied deformation better and do not immediately deform/rupture/break, exhibited higher breaking length values ($r = 0.656^*$) (Table 4).

It was determined that the samples stored in the refrigerator had higher deformation modulus values, followed by the samples stored in the deep freezer and samples stored at room temperature, respectively. As the storage time increased, the deformation modulus values generally decreased in the samples stored at room temperature and in the deep freezer. In the samples stored in the refrigerator, the deformation modulus values firstly increased and then decreased to a similar statistical level depending on the storage time. Deformation modulus is a parameter obtained by using the breaking force and breaking length values, stating that it is characterized by these values, and gives an idea about the processability properties of the phyllo. When the stretching/tearing properties of phyllo are considered, the deformation modulus is desired to be low, while the breaking force and breaking length values are desired to be high, which enables that the phyllo is not too weak to tear in order to obtain optimum processing performance. In this context, it can be said that storage process in the deep freezer conditions was generally more suitable, as the samples stored in that condition had relatively higher breaking force and breaking length values with a moderate deformation modulus.

Table 4. Pearson's correlation coefficient of textural characteristics of phyllo samples

	Hardness	Cohesiveness	Springiness	Chewiness	Gumminess	Max. Force	Min. Force	Relaxation Time	Breaking Force	Breaking Length
Cohesiveness	0.802**	-	-	-	-	-	-	-	-	-
Springiness	-0.441	-0.292	-	-	-	-	-	-	-	-
Chewiness	0.997**	0.799**	-0.500	-	-	-	-	-	-	-
Gumminess	0.997**	0.800**	-0.497	1.000**	-	-	-	-	-	-
Maximum Force	0.465	0.304	-0.783**	0.493	0.491	-	-	-	-	-
Minimum Force	0.350	0.190	-0.738*	0.381	0.380	0.968**	-	-	-	-
Relaxation Time	0.150	0.207	-0.809**	0.199	0.197	0.583	0.489	-	-	-
Breaking Force	0.025	0.253	0.460	0.010	0.013	-0.645*	-0.657*	-0.226	-	-
Breaking Length	-0.088	0.128	0.656*	-0.119	-0.116	-0.801**	-0.844**	-0.367	0.926**	-
Deformation Modulus	0.376	0.362	-0.577	0.421	0.422	0.437	0.512	0.391	0.165	-0.216

* $p < 0.05$ ** $p < 0.01$

3.5. Results of Microbiological Analysis

Total mesophilic aerobic bacteria (TMAB), and yeast and mold count of phyllo samples are given in Table 5. Compared to the control sample, storage process at room temperature and in

the refrigerator caused an increase in the total mesophilic aerobic bacteria count of the samples, while the deep freezer conditions caused a decrease. In general, the samples stored at room temperature had higher total mesophilic aerobic bacteria count, followed by the samples stored in the refrigerator and deep freezer, respectively. As it is known, microorganisms have certain temperature requirements for growth and reproduction, and each microorganism has optimum temperature ranges in which it reproduces at the maximum level [37]. In general, mesophilic bacteria reproduce at 37°C at an optimum level [38], while molds and yeasts reproduce at 25-30°C [37]. Reproduction of microorganisms decreases as environment temperature moves away from these limits [39] as in this study. As expected, the increasing the storage time at all three storage temperatures generally led to an increase in the total mesophilic aerobic bacteria numbers of the samples and it was especially higher at room temperature. The change trend in the yeast and mold count was partially similar for similar reasons. Storage process at room temperature and in the refrigerator caused an increase in the total yeast and mold count of the phyllo samples compared to the control sample. An increase was also observed in the samples stored in the deep freezer conditions, but, it was relatively lower. The increasing the storage time resulted in an increase in the total number of yeast and mold in the samples stored at room temperature and in the refrigerator. In the samples stored in the deep freezer, the increase in the storage time firstly increased and then decreased the total number of yeast and mold. The increase in microbial load due to prolonged storage time, which is one of the stages that should be given importance in terms of microbiological stability [40], has also been observed in different food samples [41]. Considering the effect of the storage process on the microbial load of the phyllo samples, it was concluded that the storage process in the deep freezer conditions was more promising due to a relatively lower total mesophilic aerobic bacteria and mold and yeast count with a relatively lower overall rate of increase.

Table 5. Total mesophilic aerobic bacteria (TMAB) and yeast and mold count of phyllo samples

Storage Temperature	Storage Time (Days)	TMAB (log cfu/g)	Total Number of Yeast and Mold (log cfu/g)
	0 (Control)	6.61	<2.00
20°C	3	7.94	4.72
	5	9.81	6.41
	7	12.30	6.65
	7	8.69	3.79
4°C	14	8.38	3.98
	21	8.98	6.87
	20	3.38	<2.00
-18°C	40	4.27	3.04
	60	4.43	2.69

4. Conclusion

Phyllo is an important cereal-based semi-product. Phyllo, which has an important role in human nutrition, is generally stored in cold storage conditions due to its short shelf life. In this study, the effect of different storage conditions on the textural, microbiological and color properties of phyllo was investigated. In general, the phyllo samples stored in the deep freezer exhibited higher L* color values, followed by the samples stored in the refrigerator and samples stored at

room temperature, respectively. A statistically similar and lower total color change (ΔE) occurred in the phyllo samples stored at room temperature and in the refrigerator than the samples stored in the deep freezer. The samples stored in the refrigerator exhibited higher hardness values, followed by the samples stored at room temperature and samples stored in the deep freezer, respectively. The storage temperature did not affect statistically significantly the cohesiveness values of the samples. Most of the phyllo samples were similar to the control sample in terms of springiness property. The samples stored in the refrigerator had higher chewiness and gumminess values, while the samples stored in the deep freezer had lower values. In terms of relaxation time value, the samples stored at room temperature and in the deep freezer exhibited statistically similar and lower values than the samples stored in the refrigerator. In addition, the samples stored in the deep freezer generally had higher values in terms of the breaking force and breaking length. For microbiological properties, the storage process in the deep freezer conditions was more appropriate by reason of a relatively lower total mesophilic aerobic bacteria and yeast and mold count with a relatively lower overall rate of increase.

As a result, it was concluded that the deep freezer conditions were more suitable for preserving the color and microbial properties of phyllo. Considering textural properties of phyllo, it was determined that the refrigerator conditions were more suitable in terms of hardness, chewiness, gumminess, relaxation time, maximum force and minimum force values, while the deep freezer conditions were more suitable in terms of springiness, breaking force and breaking length. Overall, considering the textural quality of phyllo, it would be more appropriate to recommend deep freezer conditions, as the springiness and stretching properties of phyllo are relatively more important in terms of processability.

Ethics in Publishing

There are no ethical issues regarding the publication of this study.

Author Contributions

This article is a part of Seda COŞKUN's Master's Thesis titled "Effects of different storage conditions on textural and microbiological properties of yufka" under the supervisor of Prof. Dr. M. Murat KARAOĞLU. Aslıhan Hanoğlu and Yeşim Bedir contributed to the laboratory studies of this study and the writing of this article.

Acknowledgements

This study was supported in the scope of Atatürk University Scientific Research Project (FYL-2021-9426).

References

[1] Elgün A., Ergutay Z., (2011). Tahıl İşleme Teknolojisi. Atatürk Üniversitesi Yayınları, No:718, Erzurum.

- [2] Erbaş, M., Uslu, M. K., Demir, M., Certel, M. (2010). Effects of extraction rates of wheat flour on phyllo (Yufka) properties at different storage temperatures. *Cereal Chemistry*, 87(5), 398-402.
- [3] Anonim, (2018). TS 10443 Yufka Standardı. Türk Standartları Enstitüsü, Ankara.
- [4] Peighambardoust, S. H., Davarani, A. K., Fasihnia, S. H. (2024). Effect of active antimicrobial films on quality parameters and shelf-life of fresh yufka dough. *Heliyon*, 10(4).
- [5] Çapçioğlu, G., (2007). The effect of different process techniques applied for the production of laminated dough on the product quality. Master's Thesis, Trakya University, Institute of Science, Trakya.
- [6] Tsiraki, M. I., El-Obeid, T., Yehia, H. M., Karam, L., Savvaidis, I. N. (2018). Effects of chitosan and natamycin on vacuum-packaged phyllo: A pastry product. *Journal of Food Protection*, 81(12), 1982-1987.
- [7] Bahmanpour, H., Sowti Khiabani, M., Pirsā, S. (2024). Improving the microbial and physicochemical shelf life of yufka paste using *Lactobacillus plantarum* and calcium propionate. *Food Science & Nutrition*, 12(3), 1635-1646.
- [8] Arda, Ş., Aydın, A., (2011). A study on the relationship of thin sheet of dough microbiological quality between quality of raw material and some hygiene parameters. *J. Fac. Vet. Med. İstanbul Univ.* 37(2): 135-147.
- [9] Tsiraki, M. I., Karam, L., Abiad, M. G., Yehia, H. M., Savvaidis, I. N. (2017). Use of natural antimicrobials to improve the quality characteristics of fresh “Phyllo”—A dough-based wheat product—shelf life assessment. *Food Microbiology*, 62, 153-159.
- [10] Basman, A., Köksel, H. (2001). Effects of barley flour and wheat bran supplementation on the properties and composition of Turkish flat bread, yufka. *European Food Research and Technology*, 212, 198-202.
- [11] Anonim, (2000). Gıda Mikrobiyolojisi ve Uygulamaları. Ankara Üniversitesi Ziraat Fakültesi Gıda Mühendisliği Bölümü Yayını. Sim Matbaası, 522 s, Ankara.
- [12] Gorbunova, E.V., Chertov, A.N., Petukhova, D.B., Alekhin, A.A., Korotaev, V.V. (2015). Research of principles for estimating the freshness of meat products by color analysis method. In *Photonic Instrumentation Engineering II* (Vol. 9369, pp. 180-186). SPIE.
- [13] Andrés-Bello, A., Barreto-Palacios, V., García-Segovia, P., Mir-Bel, J., Martínez-Monzó, J. (2013). Effect of pH on color and texture of food products. *Food Engineering Reviews*, 5, 158-170.
- [14] Saraç, S., Saraç, D., Yüzbaşıoğlu, E., (2006). Evaluation of the color stability of the acrylic base resins in different food colorant solutions. *The Official Journal of Gazi University Faculty of Dentistry/Acta Odontologica Turcica*, 23 (2), 111-116.

- [15] Mamat, H., Hardan, M.O.A., Hill, S.E. (2010). Physicochemical properties of commercial semi-sweet biscuit. *Food Chemistry*, 121(4), 1029-1038.
- [16] Chowdhury, T.H. (2022). Review on the pre-treatment methods of waste for anaerobic digestion. *The Seu Journal of Electrical and Electronic Engineering (SEUJEEE)*, 2(1), 46-51.
- [17] Su, L., Nian, Y., Li, C. (2023). Microencapsulation to improve the stability of natural pigments and their applications for meat products. *Food Materials Research*, 3(1).
- [18] Paulsen, G.W. (1962). Preservation and stratigraphic distribution of pigments in minnesota lake sediments. In partial fulfillment of the requirements for the degree master of science. The Faculty of the Graduate School of the University of Minnesota.
- [19] Wyk, A.A.V., (2004). Time-temperature interaction on postharvest rind colour development of citrus. In partial fulfillment of the requirements for the degree of master of science. Agriculture at the University of Stellenbosch.
- [20] Donoso, G., Cabas, P., Paredes, M. S., Becerra, V., Balzarini, M. G. (2015). Cold tolerance evaluation of temperate rice (*Oryza sativa* L. ssp. japonica) genotypes at seedling stage. *Gayana Bot.* 72(1): 1-13.
- [21] Erdemir E, Karaoğlu M.M. (2021). A review on methods of determining textural properties of meat and meat products instrumentally and texture profile analysis. *Journal of the Institute of Science and Technology*, 11(4): 2836-2848.
- [22] Giannou, V., Kessoglou, V., Tzia, C. (2003). Quality and safety characteristics of bread made from frozen dough. *Trends in Food Science & Technology*, 14(3), 99-108.
- [23] Vigoureux, D., Vigoureux, J. M. (2018). How can freezing water burst pipes and containers?. *European Journal of Physics*, 39(4), 045808.
- [24] Urugami, T., Chakraborty, S., Piemonte, V., Di Paola, L. (2013). Biocatalytic membrane reactors: Principles, preparation and biotechnological, pharmaceutical and medical applications. In *Handbook of Membrane Reactors* (pp. 846-887). Woodhead Publishing.
- [25] Moy, A., Nkongolo, K. (2022). Influence of decreasing temperature on soil microbial activity in a boreal shield ecozone. *American Journal of Environmental Sciences*, 42-51.
- [26] Koehler, P., Wieser, H. (2012). Chemistry of cereal grains. In *Handbook on sourdough biotechnology* (pp. 11-45). New York, NY: Springer US.
- [27] Blomquist, C.L. (1977). Effects of freezing and thawing on sensory quality and thiamin content of spaghetti and meat sauce after reheating in conventional or microwave oven. Master's Thesis, Department of Foods and Nutrition, Kansas State University, Kansas.
- [28] Funami, T., Nakauma, M., (2022). Instrumental food texture evaluation in relation to human perception. *Food Hydrocolloids* 124, 107253.

- [29] Boz, H., (2019). Effect of flour and sugar particle size on the properties of cookie dough and cookie. *Czech Journal of Food Sciences*, 37(2).
- [30] Dai, Y., Gao, H., Zeng, J., Liu, Y., Qin, Y., Wang, M. (2022). Effect of subfreezing storage on the qualities of dough and bread containing pea protein. *Journal of the Science of Food and Agriculture*, 102(12), 5378-5388.
- [31] Gupta, R. K., Sharma, A., Sharma, R. (2007). Instrumental texture profile analysis (TPA) of shelled sunflower seed caramel snack using response surface methodology. *Food Science and Technology International*, 13(6), 455-460.
- [32] Mumyapan, M., Aktaş, N., Gerçekaslan, K. E. (2022). Seed pumpkin flour as a dietary fiber source in Bologna-type sausages. *Journal of Food Processing and Preservation*, 46(7), e16586.
- [33] Feng, T., Gu, Z., Jin, Z., Zhuang, H., (2010). Rheological properties of cereal starch gels and mesona blumes gum mixtures. *Starch Staerke* 62 (9), 480–488.
- [34] Saha, D., Bhattacharya, S., (2010). Characteristics of gellan gum based food gels. *J. Texture Stud.* 41 (4), 459–471.
- [35] Hanoğlu, A., Karaoğlu, M. M. (2024). The effect of different pulp powders incorporation on the instrumental texture and rheological properties of Turkish delight. *International Journal of Gastronomy and Food Science*, 35, 100872.
- [36] Zeybekoğlu Baş, N., (2018). Determination of some quality characteristics of wheat varieties/ lines suitable for İzmir and coastline yufka production and determination of new wheat varieties /lines suitable for yufka. Doctoral Thesis, Ege University, Institute of Sciences, İzmir.
- [37] Sert, S., (2000). Genel Mikrobiyoloji, Atatürk Üniversitesi, Ziraat Fakültesi Ders Yayınları No: 195, Erzurum.
- [38] Karamah, E.F., Wajdi, N. (2018). Application of ozonated water to maintain the quality of chicken meat: effect of exposure time, temperature, and ozone concentration. In *E3S Web of Conferences* (Vol. 67, p. 04044). EDP Sciences.
- [39] Wei, A.A.Q. (2020). The effect of temperature on microorganisms growth rate. *The Expedition*, 10.
- [40] Can, N., Velioglu, S. D. (2018). Microbial Quality and Presence of Mycotoxins in Herbal Teas. *Erzincan University Journal of Science and Technology*, 11(3), 362-380.
- [41] Okcu, Z., Abanoz, Y. Y. (2021). Determination of some quality properties of blueberry fruit coated with edible coating (*Vaccinium Arctostaphylos*). *Erzincan University Journal of Science and Technology*, 14(3), 979-992.

Block-Based Forgery Detection: Performance Comparison Using HOG, LBP and MBF

Yıldız AYDIN^{1*}, Yunus BABACAN²

¹Department of Computer Engineering, Erzincan Binali Yıldırım University, Erzincan, 24000

²Department of Electrical and Electronics Engineering, Erzincan Binali Yıldırım University, Erzincan, 24000

Received: 19/09/2024, **Revised:** 23/10/2024, **Accepted:** 07/11/2024, **Published:** 31/12/2024

Abstract

One of the types of forgery performed on digital images is copy-move forgery (CMF). This type of forgery is carried out by pasting a region copied from the same image over another region of the image. It is very important to determine whether there is any forgery on these images, as they can be used as evidence in many fields. In this study, an analysis of forgery detection is performed using Histogram of Oriented Gradients (HOG), Local Binary Patterns (LBP), and Multiscale Basic Features (MBF) for block-based copy-move forgery detection. The performance of various features, both individually and in combination, is evaluated. Combinations such as HOG+LBP, HOG+MBF, and MBF+LBP were tested, but the expected performance improvement was not achieved. Although the performance increase was not significant, the highest results were generally obtained with the LBP+MBF hybrid feature, resulting in an F1 score of 88.5%. Additionally, while HOG and LBP features are frequently used in block-based approaches, the use of the MBF feature has not been found in the literature. This study contributes to the existing methods in the field of block-based forgery detection and highlights the effectiveness of various features and feature combinations.

Keywords: Copy-move forgery, HOG, LBP, MBF

Blok Tabanlı Sahtecilik Tespiti: HOG, LBP ve MBF Kullanılarak Performans Karşılaştırması

Öz

Dijital görüntüler üzerinde yapılan sahtecilik türlerinden biri de kopyala-yapıştır sahteciliğidir (CMF). Bu sahtecilik türü, aynı görüntüden kopyalanan bir bölgenin, görüntünün başka bir bölgesi üzerine yapıştırılmasıyla gerçekleştirilir. Bu görüntüler, birçok alanda delil olarak kullanılabilenlerinden, üzerinde herhangi bir sahtecilik olup olmadığının belirlenmesi oldukça önemlidir. Bu çalışmada, blok tabanlı kopyala-yapıştır sahteciliği tespiti için Yönlendirilmiş Gradyanların Histogramı (HOG), Yerel İkili Örüntüler (LBP) ve Çok Ölçekli Temel Öznitelikler (MBF) kullanılarak sahtecilik tespiti üzerine bir analiz yapılmıştır. Çeşitli özniteliklerin hem tek başına hem de birlikte performansları değerlendirilmiştir. HOG+LBP, HOG+MBF ve MBF+LBP gibi kombinasyonlar denenmiş, ancak beklenen performans artışı sağlanamamıştır. Performans artışı çok büyük olmasa da, en yüksek sonuçlar genellikle LBP+MBF hibrit özelliği ile elde edilmiş ve %88,5'lik bir F1 puanı ile sonuçlanmıştır. Ayrıca, HOG ve LBP özellikleri blok tabanlı yaklaşımlarda sıkça kullanılsa da, MBF özneteliğini kullanan yaklaşımlara literatürde rastlanmamıştır. Bu çalışma, blok tabanlı sahtecilik tespiti alanındaki mevcut yöntemlere katkı sağlamak ve çeşitli öznitelik ve öznitelik kombinasyonlarının etkinliğini vurgulamaktadır.

Anahtar Kelimeler: Kopyala yapıştır sahteciliği, HOG, LBP, MBF.

1. Introduction

The rapid development of technology has significantly increased the use of digital images and the operations performed on these images. Along with this increase, studies on forgery detection systems on digital images have become increasingly important. In particular, the widespread use and ease of use of image editing applications such as Photoshop has led to a rapid increase in the number of forged images, making it crucial to accurately and reliably detect whether such images are forged or not, as they can be used as evidence in many areas, such as forensic cases.

To make it difficult to detect forgeries, various post-processing operations such as blurring, noise addition, and illumination modification are performed on forged images. This makes forgery detection more challenging and increases the need for the development of a reliable copy-move forgery detection system. Therefore, the focus of much research in this area has been the development of robust and effective detection methods against forged images.

Methods used in copy-move forgery detection (CMFD) systems are generally divided into two groups: keypoint-based methods and block-based methods. Keypoint-based methods have the disadvantage that the boundaries of the forged region cannot be precisely determined. In block-based methods, the entire image information is used, but this can negatively affect the accuracy rate. In the literature, various studies have been conducted in order to improve the performance of copy-move forgery (CMF) detection systems, but research on the use of hybrid features in block-based approaches has been very limited.

In the field of image processing, the use of hybrid features has been widely investigated in keypoint-based methods, where successful results have been achieved [1–3]. However, the lack of emphasis on the potential benefits of hybrid features in block-based approaches points to an important gap in this field. The main objective of this study is to investigate the use of hybrid features in block-based CMFD systems to address the challenges of detecting forgery region boundaries and to present a new method aimed at improving performance.

Main Contributions of the Proposed Method to the Literature:

- The proposed method introduces a new CMFD (Copy-Move Forgery Detection) approach that compares the use of HOG, LBP, MBF, and hybrid features in block-based forgery detection systems.
- The problem of not being able to detect forgery zone boundaries, which is frequently encountered in keypoint-based methods, has been solved.

In this research, we propose a CMFD system that utilizes various hybrid features in a block-based approach. Thus, the aim is to compare the performance of these features while addressing the disadvantage of not being able to detect forgery boundaries, which is often encountered in keypoint-based methods. The rest of this paper is organized as follows: In the second section of this article, the related work on copy-move forgery detection methods are detailed. In the third section, the stages of the proposed method are explained. In the fourth section,

experimental results and comparisons of the proposed method with other methods in the literature are presented. Finally, in the fifth section, the results of the study and future studies are detailed.

2. Related Work

Copy-move forgery detection is a popular area of research that is being intensively studied. The methods developed for forgery detection in digital images with evidentiary value can be basically divided into 3 categories. These categories are keypoint-based, block-based and hybrid approaches.

In key-point based CMFD systems, in the first stage, identifiers are created on the key points detected on the image. The keypoint-based descriptors (local features) obtained from the whole image are compared with each other. As a result of this comparison, if there are local features that match each other, the locations of these features are marked as forged regions. Amerini et al. [4] used the SIFT feature, which is invariant to post-processing such as scaling differences, illumination differences and rotation changes, in their proposed CMFD system. In the application, forgery detection was performed by taking into account the matches between the extracted SIFT features.

In recent years, many studies have been conducted to increase the success rate by using hybrid features [1,5,6]. In the study by Aydın [7] keypoint locations are detected using the DOG detector and a LIOP descriptor is built on these keypoints. Thanks to this hybrid feature, higher performance was achieved on different datasets. In the method proposed by Wang et al. [8], simple linear iterative clustering (SLIC) and the K-multiple-means methods are used to detect keypoint locations. They obtained a hybrid feature using Fast Quaternion Generic Polar Complex Exponential Transform (FQGPCET) and Graylevel co-occurrence matrix (GLCM) as features. They obtained a high precision value in the experimental results of their proposed method.

In block-based approaches, the image is decomposed into fixed-size blocks and features are extracted from each block, and forgery defects persist throughout these features. Fridrich et al. [9] were among the pioneers in this area, proposing a method where the image is divided into blocks, and Discrete Cosine Transform (DCT) feature vectors are extracted. These vectors are then lexically filtered and compared to detect forgeries. Ganguly et al. [10] suggested an approach where local tetra pattern-based texture descriptors are extracted from the blocks, which are then compared to identify forgery. This method has shown increased robustness to common post-processing and has been particularly effective in detecting small forgeries that traditional methods miss. Shehin et al. [11] present a method that combines the Discrete Cosine Transform (DCT) with eigenvalues to enhance the detection and localization of forgery, especially in images subjected to post-processing operations like rotation. This method processes overlapping blocks of the image, extracting features using DCT and eigenvalues, and applies cumulative DCT features for more robust detection, even against rotation attacks. Weng et al. [12] proposed a new CMFD method based on UCM-Net, a U-Net-like architecture for the problem of forgery detection, which is difficult to solve due to the photometric similarities

between forged regions and original regions. In particular, the method treats large and small forged regions differently and uses various deep networks and techniques to extract the features of these regions and localize the forged regions more precisely. UCM-Net provided higher accuracy rates in the face of operations such as blurring, rotation, and noise that make forgery detection difficult. Experiments have shown that UCM-Net outperforms existing best practices.

3. The Proposed Method

This paper proposes a three-stage method for the detection of copy-move forgery: (i) decomposition of the image into overlapping blocks, (ii) feature extraction and fusion of the extracted features, (iii) detection of forgery regions. There are several studies in the literature that apply various histogram-based local features using block-based approaches [10,13]. However, the combination of different feature extraction techniques such as Local Binary Pattern (LBP), Histogram of Oriented Gradients (HOG) and Multiscale Basic Features (MBF) and performance comparisons are limited. In Aydın's skin cancer recognition study [14], the combination of these features has been shown to yield better results.

In recent years, keypoint-based features have been widely used in copy-move forgery [15,16], and hybrid methods developed by combining different keypoint based methods are becoming widespread [1, 8]. In this study, the performance comparison of the features used in block-based approaches and the fusion features obtained by combining these features in various combinations was performed. Figure 1 presents the flowchart of the proposed method, which shows the general operation of the proposed method.

In the first stage of the proposed method, the analyzed image is divided into overlapping 8x8 blocks. The 8x8 block size is chosen because it is widely used in block-based approaches in the literature [10, 18]. While smaller blocks require higher computational costs and increased memory consumption, larger blocks may result in a loss of detail and decreased detection accuracy.

In the second stage, Local Binary Pattern (LBP), Histogram of Oriented Gradients (HOG) and Multiscale Basic Features (MBF) are extracted separately from each block. For each of these methods, 9-dimensional feature vectors are obtained from LBP and HOG, and 1536-dimensional feature vectors are obtained from MBF. In order to evaluate the performance of hybrid features, these individual features are combined to form new feature sets. For example, the HOG+LBP combination provides 18-dimensional feature vectors, HOG+MBF provides 1545-dimensional feature vectors and LBP+MBF provides 1545-dimensional feature vectors. These hybrid features are named as HOG+LBP, HOG+MBF and LBP+MBF, respectively.

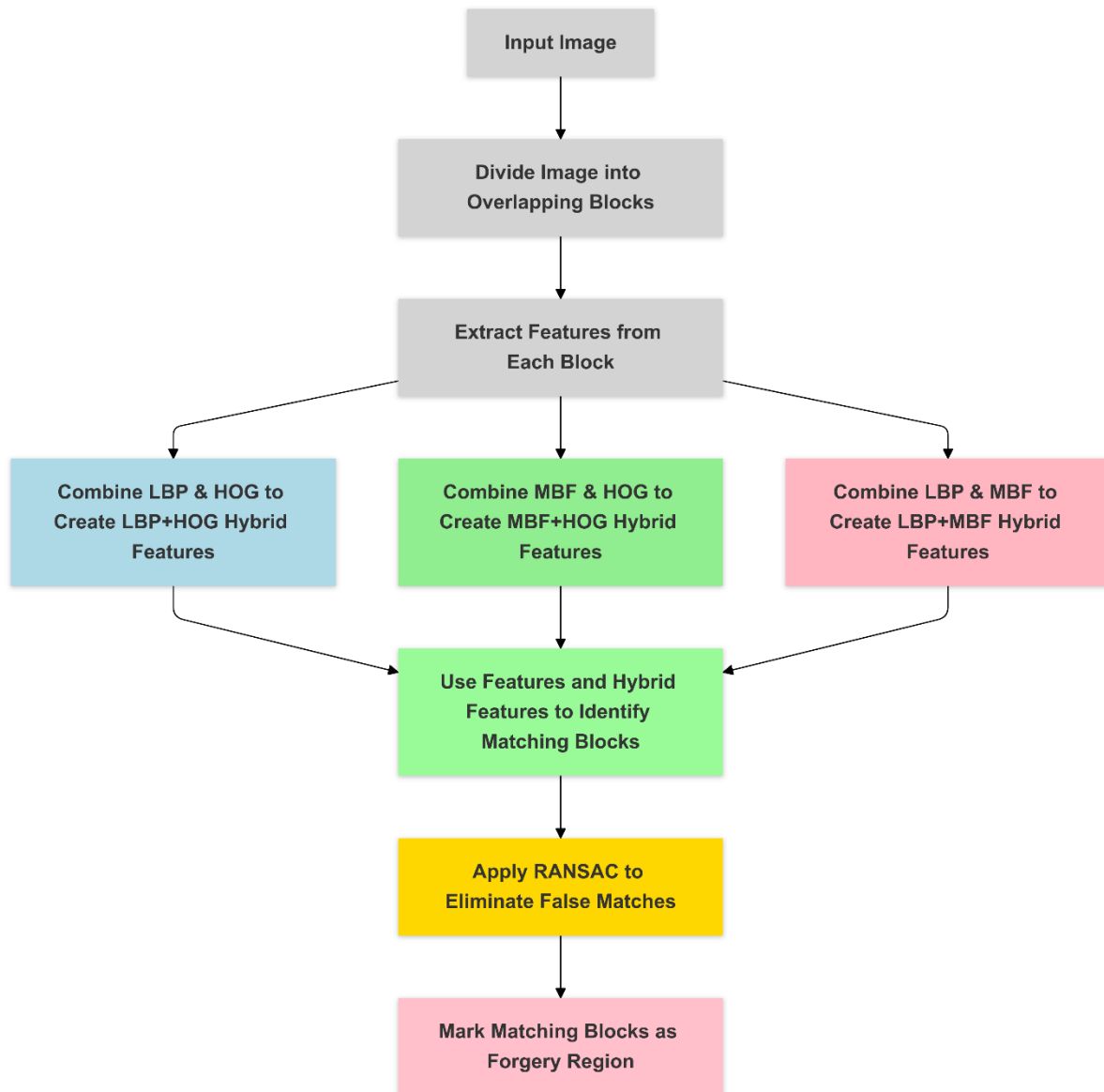


Figure 1. Flowchart of the suggested approach

In the last stage, all extracted features in the second stage are stored in the M matrix and sorted according to the dictionary order. If the Euclidean distance between each feature vector and the other vectors in the M matrix is less than the previously determined threshold value, these vectors are considered to be matched and the relevant blocks are labeled as copy-move forgery regions. In this method, hybrid features obtained by combining the features frequently used in keypoint-based methods are used in the block-based approach.

3.1 Dataset

The CoMoFoD dataset is a rich database that is widely used in research on digital image forgery and contains different forms of forgery. For each 40 images in the CoMoFoD dataset, a total of 200 images were created by applying operations such as translation, rotation, scaling, distortion, combination. In addition, different types of attacks such as image blurring (IB), color reduction (CR), JPEG-compression, contrast adjustment (CA) and changes in brightness (BC) were

applied to these 200 images in the CoMoFoD dataset. The final number of all these 512x512 images is 10,400. In this study, only the first 40 images containing translation in the CoMoFoD (Copy-Move Forgery Detection) dataset were used to measure the performance of the application developed for copy-move forgery detection.

4. Experimental Results

In this study, experiments were conducted to compare the performance of various features for the copy-move forgery detection problem. The experiments were performed on a computer with an Intel i5 processor and 8 GB of RAM, using the Python programming language. In this context, HOG, LBP, MBF and combinations such as HOG+LBP, HOG+MBF, and LBP+MBF were included as features.

The experiments were conducted on 40 plain copy-move forgery applied images with a resolution of 512x512 from the CoMoFoD dataset. Precision, recall, F1-score, and accuracy were used as performance metrics. Precision measures the ratio of pixels that are actually fake among all pixels labeled as fake, while recall measures the ratio of correctly predicted fake pixels to the total fake pixels. In short, precision focuses on the false positives, while recall focuses on the rate of forgery detection. Since both metrics are important, the harmonic mean of precision and recall is calculated as the F1-score. Lastly, the accuracy is calculated as the ratio of correctly labeled pixels to the total number of pixels. The calculation formulas for precision, recall, F1 score and accuracy metrics are given in Equations 1, 2, 3 and 4, respectively.

$$recall(r_c) = \frac{TP}{TP+FN} \quad (1)$$

$$Precision(p_r) = \frac{TP}{TP+FP} \quad (2)$$

$$F1\ Score = 2 * \frac{Recall * Precision}{Recall + Precision} \quad (3)$$

$$Accuracy = \frac{TP+TN}{TP+FP+TN+FN} \quad (4)$$

Table 1 shows the results of the experiments performed using 40 plain copy-move forgery images from the CoMoFoD dataset.

Table 1. Results of experiments

Method	Precision	Recall	F1 Score	Accuracy
HOG	0.297	0.928	0.451	0.799
LBP	0.868	0.894	0.881	0.986
MBF	0.895	0.869	0.882	0.990

Method	Precision	Recall	F1 Score	Accuracy
HOG+LBP	0.879	0.871	0.875	0.989
HOG+MBF	0.874	0.873	0.874	0.989
LBP+MBF	0.878	0.891	0.885	0.990

As shown in Table 1, the experiment using the HOG feature resulted in a high recall value but a low precision value. This shows that the HOG feature tends to over-detect fake regions, which leads to a large number of false positives.

Table 2 presents the performance comparison of the proposed method with other methods in the literature. The performance results in Table 2 are obtained using 40 plain copy-move forged images from the CoMoFoD dataset. Except for the proposed method, other method results are taken from [10]

Table 2. Comparative analysis for plain copy-move forgery applied to 40 forged images in CoMoFoD dataset.

Method	Year	Precision	Recall	F1 Score
Li et al. [18]	2014	0.418	0.833	0.557
Silva et al. [19]	2015	0.492	0.775	0.602
Liu et al. [20]	2018	0.455	0.802	0.581
Kumar et al. [21]	2022	0.910	0.818	0.844
Proposed Method		0.878	0.891	0.885

The precision and recall values obtained in the experiments performed using the LBP and MBF features are consistent and higher. These methods have shown an effective performance in detecting fake and non-fake regions. In the experiments conducted with the HOG+LBP, HOG+MBF, LBP+MBF methods obtained by the combination of features, they showed slightly better performance than the individual methods. The best overall performance was obtained by LBP+MBF with 0.878 precision, 0.891 recall and 0.990 accuracy.

In Figure 2, some prediction images obtained from the experiment performed with the LBP+MBF features, which obtained the highest performance, are given.

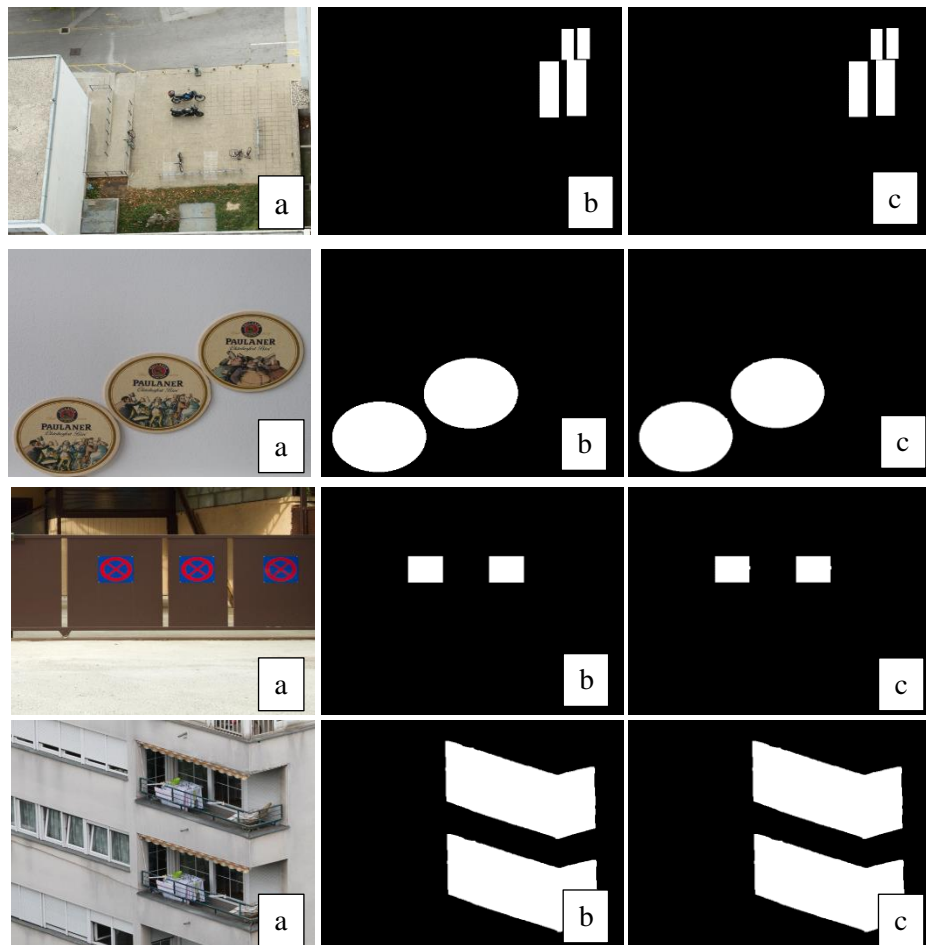


Figure 2. Results of the suggested approach on plain copy-move forgery images from the CoMoFoD dataset: a) counterfeit image, b) ground truth, c) detection result of the proposed method.

5. Conclusions

In this study, the performances obtained by using HOG, LBP, MBF features and different combinations of these features in the block-based approach were compared for the copy-move forgery detection problem. The experiments were carried out by measuring the similarities of HOG, LBP, MBF and HOG+LBP, HOG+MBF and LBP+MBF features on 40 forged images in the CoMoFoD dataset. In the performance evaluation performed using precision, recall, f1-score and accuracy evaluation metrics, the application performed with LBP+MBF provided the highest performance. The lowest performance was obtained in the experiment performed using the HOG feature. In the future, the use of more robust features and machine learning models will be investigated to improve the detection rate in the block-based approach.

Ethics in Publishing

There are no ethical issues regarding the publication of this study.

Author Contributions

All authors contributed equally to all stages of the study, including its conceptualization, methodology, data collection, analysis, and writing.

Acknowledgements

This project was supported by the Scientific Research Projects (BAP) program under project number 1004 FBA-2024-1004, titled 'Block-based Copy-move forgery Detection,' and conducted at Erzincan Binali Yıldırım University"

References

- [1] Niyishaka, P., Bhagvati, C. (2020). Copy-move forgery detection using image blobs and BRISK feature. *Multimed. Tools Appl.* 10.1007/s11042-020-09225-6.
- [2] Aydın, Y. (2024). Automated identification of copy-move forgery using Hessian and patch feature. *J. Forensic Sci.* 69, 131–138.
- [3] Sunitha, K., Krishna, A.N., Prasad, B.G. (2022). Copy-move tampering detection using keypoint based hybrid feature extraction and improved transformation model. *Appl. Intell.*, 15405–15416. 10.1007/s10489-022-03207-x.
- [4] Amerini, I., Ballan, L., Caldelli, R., Del Bimbo, A., Serra, G. (2011). A SIFT-based forensic method for copy-move attack detection and transformation recovery. *IEEE Trans. Inf. Forensics Secur.* 6, 1099–1110. 10.1109/TIFS.2011.2129512.
- [5] Kumar, N., Meenpal, T. (2022). Salient keypoint-based copy-move image forgery detection. 10.1080/00450618.2021.2016964.
- [6] Aydın, Y. (2022). Comparison of color features on copy-move forgery detection problem using HSV color space. *Aust. J. Forensic Sci. early acce.* 10.1080/00450618.2022.2157046.
- [7] Aydın, Y. (2022). A new Copy-Move forgery detection method using LIOP. *J. Vis. Commun. Image Represent.* 89, 103661. 10.1016/j.jvcir.2022.103661.
- [8] Wang, X. yang, Wang, X. qi, Niu, P. pan, Yang, H. ying (2024). Accurate and robust image copy-move forgery detection using adaptive keypoints and FQGPCET-GLCM feature (Springer US) 10.1007/s11042-023-15499-3.
- [9] Fridrich, J., Soukal, D., Lukáš, J. (2003). Detection of Copy-Move Forgery in Digital Images. *Proc. Digit. Forensic Res. Work.*, 133–162. 10.1109/ICMLA.2015.137.
- [10] Ganguly, S., Mandal, S., Malakar, S., Sarkar, R. (2023). Copy-move forgery detection using local tetra pattern based texture descriptor. *Multimed. Tools Appl.* 82, 19621–19642. 10.1007/s11042-022-14287-9.

- [11] Shehin, A.U., Sankar, D. (2024). Copy Move Forgery detection and localisation robust to rotation using block based Discrete Cosine Transform and eigenvalues. *J. Vis. Commun. Image Represent.* 99, 104075. 10.1016/j.jvcir.2024.104075.
- [12] Weng, S., Zhu, T., Zhang, T., Zhang, C. (2024). UCM-Net: A U-Net-Like Tampered-Region-Related Framework for Copy-Move Forgery Detection. *IEEE Trans. Multimed.* 26, 750–763. 10.1109/TMM.2023.3270629.
- [13] Nawaz, M., Mehmood, Z., Nazir, T., Masood, M., Tariq, U., Munshi, A.M., Mehmood, A., Rashid, M. (2021). Image authenticity detection using DWT and circular block-based LTrP features. *Comput. Mater. Contin.* 69, 1927–1944. 10.3233/JIFS-191700.
- [14] Aydin, Y. (2023). A Comparative Analysis of Skin Cancer Detection Applications Using Histogram-Based Local Descriptors. *Diagnostics* 13. 10.3390/diagnostics13193142.
- [15] Hailing, H., Weiqiang, G., Yu, Z. (2008). Detection of copy-move forgery in digital images using sift algorithm. *Proc. - 2008 Pacific-Asia Work. Comput. Intell. Ind. Appl. PACIIA 2008 2*, 272–276. 10.1109/PACIIA.2008.240.
- [16] Raj, R., Joseph, N. (2016). Keypoint Extraction Using SURF Algorithm for CMFD. *Procedia Comput. Sci.* 93, 375–381. 10.1016/j.procs.2016.07.223.
- [17] Popescu, A.C., Farid, H. (2004). Exposing Digital Forgeries by Detecting Duplicated Image Regions. *Tech. Report, TR2004-515, Dep. Comput. Sci. Dartmouth Coll. Hanover, New Hampsh.*, 1–11.
- [18] Li, J., Li, X., Yang, B., Sun, X. (2015). Segmentation-based image copy-move forgery detection scheme. *IEEE Trans. Inf. Forensics Secur.* 10, 507–518. 10.1109/TIFS.2014.2381872.
- [19] Silva, E., Carvalho, T., Ferreira, A., Rocha, A. (2015). Going deeper into copy-move forgery detection: Exploring image telltales via multi-scale analysis and voting processes. *J. Vis. Commun. Image Represent.* 29, 16–32. 10.1016/j.jvcir.2015.01.016.
- [20] Liu, Y., Guan, Q., Zhao, X. (2018). Copy-move forgery detection based on convolutional kernel network. *Multimed. Tools Appl.* 77, 18269–18293. 10.1007/s11042-017-5374-6.
- [21] Kumar, S., Mukherjee, S., Pal, A.K. (2023). An improved reduced feature-based copy-move forgery detection technique. *Multimed. Tools Appl.* 82, 1431–1456. 10.1007/s11042-022-12391-4.

Comparison of models on basic passive circuit components

Murat GÜLNAHAR^{ID*1}, Yunus BABACAN^{ID 2}, Müslüm GÜR^{ID 2}

^{*1}Erzincan Binali Yıldırım University, Vocational School, Department of Electrics and Energy, 24100, Erzincan, Turkey

²Erzincan Binali Yıldırım University, Faculty of Engineering Architecture, Department of Electric and Electronic Engineering, 24100, Erzincan, Turkey

Received: 08/03/2023, Revised: 03/08/2024, Accepted: 08/10/2024, Published: 31/12/2024

Abstract

In this model, the models created by Chua and Wang about high and low order basic passive circuit elements are mentioned and the advantages and disadvantages of these models are commented comparatively. In the Chua model, voltage, current, flux and load are considered as fundamental quantities and these circuit elements are placed with a quadratic method. On the other hand, in the Wang model, a new model is put forward on the grounds that voltage and current are not fundamental quantities, and therefore the quadratic model is not completely correct. According to this model, only flux and load are considered as basic quantities and circuit elements are positioned with a triangular model. However, since there are some deficiencies/errors in the placement of the elements in these two models, we think that both models are not completely correct. Thus, we come to the conclusion that accurately defining the advantages and disadvantages of both models will form an important basis for creating a more accurate model.

Keywords: Memristor, Chua's model, Wang's model

Temel pasif devre elemanları üzerine modellerin karşılaştırılması

Öz

Bu çalışmada, yüksek ve düşük dereceli temel pasif devre elemanları hakkında Chua ve Wang tarafından oluşturulan modellerden bahsedilerek bunların avantajları ve dezavantajlarından mukayeseli olarak bahsedilmektedir. Chua modelinde gerilim, akım, akı ve yük temel büyüklük olarak düşünülerek bu devre elemanları karesel bir metodla yerleştirilmektedir. Buna karşın Wang modelinde ise, gerilim ve akımın temel büyüklük olmadığı ve bundan dolayı karesel modelin tam manasıyla doğru olmadığı gerekçesiyle yeni bir model ortaya konulmaktadır. Bu modele göre, sadece akı ve yük temel büyüklük olarak düşünülmemekte ve üçgensel bir model ile devre elemanları konumlandırılmaktadır. Ancak bu iki modelde de elemanların yerleştirilmesinde bazı eksikler/hatalar bulunduğu için her iki modelin tam olarak doğru olmadığını düşünmekteyiz. Böylece her iki modelin avantajları ve dezavantajlarının doğru olarak tanımlanmasıyla daha doğru bir modelin oluşturulmasında önemli bir temel oluşturacağı düşüncesine ulaşmaktayız.

Anahtar Kelimeler: Hafızalı Direnç, Chua modeli, Wang modeli

1. Introduction

It was thought that the basic circuit elements were now completed, the starting with the invention of the capacitor by Ewald Georg Von Kleist in 1745, and then continuing with the resistor in 1827 by Georg Simon Ohm, and a few years later with the proposal of the coil by Michael Faraday in 1831. However, considering the relations between voltage, current, flux and load, which are accepted as basic quantities by Chua in 1971, it was stated that there should be a circuit element that should establish the relationship between flux and load [1]. After this study [1], researchers began to focus on both this proposed new circuit element and its different derivatives. Afterwards, the relationship between these elements and which basic quantities should be became a matter of debate, and as a result, two separate models were proposed in this field [2,4].

Chua's Model: The first model about circuit elements was proposed by Chua [2]. Chua first created the quadratic model shown in Figure 1 in 1971, the fourth of which he called memristor, and which showed a symmetrical connection between four circuit elements, including the other three basic circuit elements: resistor, capacitor and inductor [1,2]. All elements shown in the same color in Figure 1 are defined as belonging to the same circuit type, that is; They are the forms which are frequency dependent resistors (red), inductors (blue), negative resistors (orange) and capacitors (green) [2]. In this way, when establishing relationships between circuit elements, Chua accepted that there are four different quantities: current, voltage, load and magnetic flux.

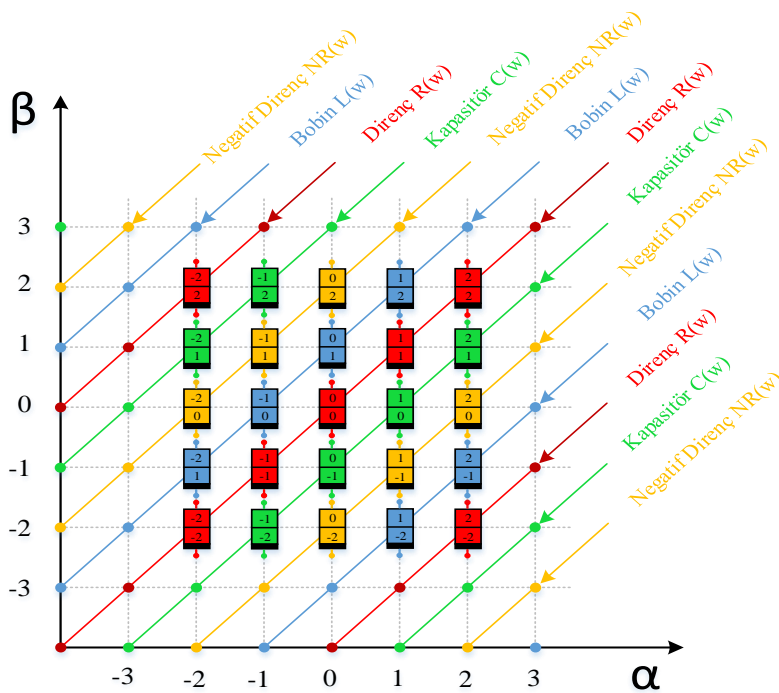


Figure 1. Periodic table of circuit elements developed by Chua [2] in the form of two terminals (α, β).

It is mentioned that in this model, there is a circuit element that establishes a linear connection between each of the four quantities. According to this, a resistor is a circuit element that establishes a relationship between current and voltage, a capacitor between load and voltage, and a coil between flux and current. Chua mentioned this connection in her work in 1971, where he stated that there is no element that provides a connection between the flux and the load, and that this is the memristor, which is a missing circuit element [1,3]. In consequence, Chua created a model by mentioning that the basic elements are not limited to just four, as shown in Figure 1, but are much more.

According to Chua's model, α denotes voltage, β denotes current, and the change along the axis indicates the degree of derivative or integral of current or voltage. In addition, in the model, resistance is considered as [0,0] since it is an element that has a direct relationship with current and voltage. The capacitor is included in the table as [0,-1] since it is the integral of voltage and load (integral of current), and the coil is included in the table as [-1,0] because it establishes the relationship between flux (integral of voltage) and current. Here, the (-) sign denotes the integral and the (+) sign denotes the derivative. For example, according to this model, there is a circuit element that reveals the [-2,+3] relationship, and it provides the relationship between the second-order integral of the current and the third-order derivative of the voltage. As seen in Figure 1 [2], the elements arranged diagonally are of the same type; for example, all of the red colored elements represent the series of elements that show resistor properties, the blue colored elements show coil properties, the green colored elements show capacitor properties, and finally the yellow colored elements represent the series of elements that show negative resistance properties.

Wang's Model: Wang [4], in her Chua model [5], claimed that the Chua model was not correct by explaining some asymmetric and abnormal situations and listed these claims as follows:

a. Unitary Abnormality: While the passive circuit elements resistor, capacitor and coil have their own units such as Ohm, Farad and Henry respectively, a different unit cannot be recommended for the memristor in the Chua model, and the use of ohm as the unit of the memristor gives the impression that this model is incomplete or incorrect [4].

b. Nonlinearity Anomaly: When Chua's model is examined, it can be said that the elements consist of two different groups. One of these groups consists of linear passive circuit elements such as resistors, capacitors and inductors, and the other group consists of non-linear behavior, including the memristor. In this case, the memristor, which is the element in the second group, should show non-linearity. Otherwise, it can be concluded that the memristor should have the same characteristics as a resistor [1,4].

c. *Status of Fundamental Quantities:* Chua model was developed on the basis of two fundamental relations: voltage and current. It is stated that these relations have the equation forms which are $i = dq/dt$ and $v = d\phi/dt$. However, Wang [4] states that this assumption is completely incomplete or wrong.

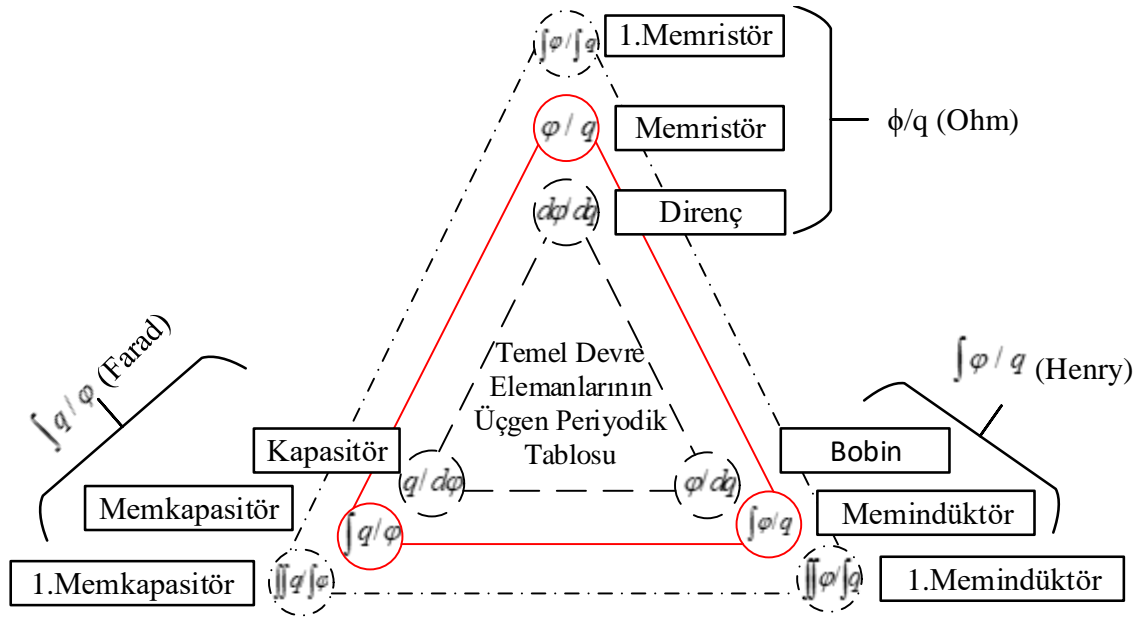


Figure 2. Triangular model developed by Wang for basic circuit elements [4].

d. *Presence of Negative Element:* In the Chua model [2], there is a negative resistance and the presence of this element causes the inconsistency between active and passive elements. Because negative resistance can be achieved with some active elements.

This model, developed by Wang as an alternative to Chua's model due to the anomalies or deficiencies mentioned by Wang about the Chua model above, is not square but has a triangular format, unlike Chua [4,6]. As a result, it is possible to depict the Wang model, which has two basic quantities and three basic circuit elements, as shown in Figure 2, as schematized by Wang [4].

2. Results and Discussions

In his proposed model, Chua accepted elements such as resistors, capacitors, coils and negative resistors as basic elements, and it is possible to depict the current-voltage curves of these elements as suggested by Chua [2,3], as shown in Figure 3. As seen in Figure 3, the precisely known elements are resistor, capacitor, inductor and memristor. As stated in this figure, the relationship between current and voltage is linear in the resistor, and hysteresis in the oval

memristor, capacitor and inductor. Also, if you pay attention, when the voltage is zero in the resistor and memristor, the current is also zero, and in the capacitor and coil it is different from zero. This means that there is no phase difference in the resistor and memristor and they do not store energy, while there is a phase difference in the capacitor and coil and they store energy [7].

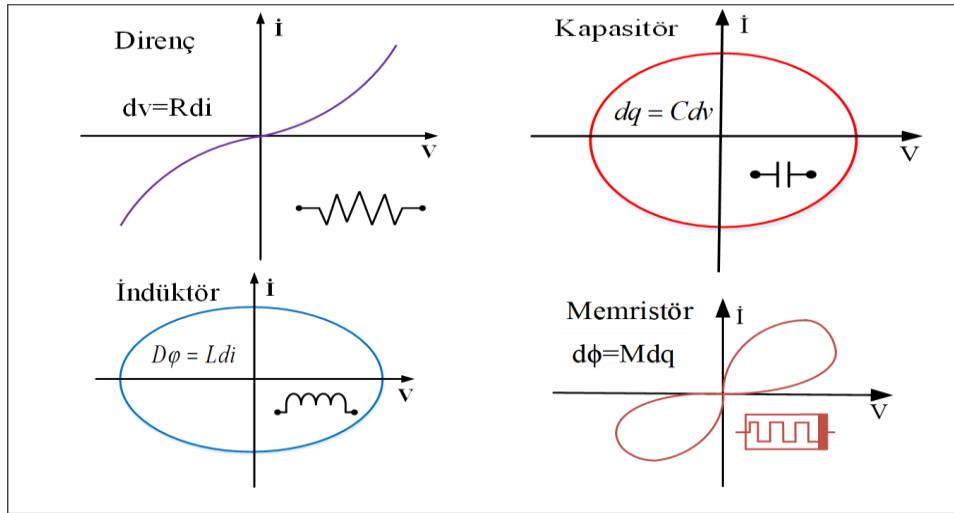


Figure 3. Current-voltage graph of the four basic passive circuit elements, according to Chua's idea.

In addition, since these four elements, the capacitor, inductor and memristor, have frequency-dependent properties, it can be said that these three elements have the ability to store information. When the voltage-current, voltage-load and current-flux curves of memristors, memcapacitors and meminductors, which are considered as memelements, are examined among themselves, respectively, it can be seen in Figure 3 that the hysteresis curve is obtained. Additionally, when Figure 3 is examined, it can easily be said that the four passive circuit elements are a group or have similar features. It is also possible to observe these changes in different literature studies [8].

Due to the anomalies or deficiencies in the Chua model, the model developed and explained by Wang as an alternative to Chua has a triangular format that not square, unlike the Chua model, as depicted in Figure 2 [4,6]. According to this format, neither resistor, capacitor nor coil are basic circuit elements, but memristor, memcapacitor and meminductor are accepted as basic circuit elements. Another difference of this model from the Chua model is that voltage and current are not accepted as fundamental quantities, and these quantities are only the time derivatives of flux and charge and they are not thought to be separate quantities.

As seen in Figure 2, according to Wang's model, each corner of the triangle represents a different type of basic circuit element. In other words, there are three types of elements as basic circuit elements and the other elements are derivatives of these three elements. For example,

memcapacitor is the basic circuit element and but capacitor or 1st order memcapacitor is a derivative of it.

Table I. Compatibility of the relationship between charge (q) and flux (ϕ) with the new element, according to Wang's idea [4,7].

Relationship between q and ϕ	Compatibility with the new element recipe.
$q - \phi$	It fits.
$\frac{dq}{dt} - \phi$	
$q - \frac{d\phi}{dt}$	
$\frac{dq}{dt} - \frac{d\phi}{dt}$	It does not fit.

According to Wang's idea [4,9], the fundamental quantities are only charge (q) and flux (ϕ). Therefore, the number of new elements will also decrease as the number of basic sizes decreases. According to Wang's approach, for an element to be a basic circuit element, elements that provide a connection either between the load and flux, or between the derivative or integral of only one of them and itself, can be new elements. As a result, this situation is shown briefly in Table I.

Thus, when these two models are compared, it is possible to say that both models have missing and advantageous parts. In the Chua model, which is the first mentioned model, the basic quantities are accepted as four. At this point, "Are voltage and current a fundamental quantity, or are voltage derived from the derivative of the flux and current from the time derivative of the load, respectively?" It is natural that the question comes to mind. If voltage and current are accepted as quantities, it can be said that the initial assumption of Chua's model is correct and the model proposed by Wang is wrong. However, if voltage and current are not fundamental quantities, then it comes to mind why only charge and flux are fundamental quantities. If it is said that voltage is the time-dependent derivative of flux and current is the time-dependent derivative of the load, then it can be assumed that the flux is the integral of the voltage and the load is the integral of the current. Therefore, this situation cannot be considered as either a completely correct or completely wrong assumption.

Another situation is that negative resistance is present in Chua's theorem but not in Wang's theorem. If the resistor is a new element, the negative resistance is expected to be accepted as a new element. However, this element is present in Chua's table but not in Wang's table.

On the other hand is that Wang did not accept resistor, capacitor and coil as a basic element, and instead memristor, memcapacitor and meminductor were accepted. While a behavior such as resistance exists in almost all elements, it remains a question mark why it is not considered a basic element. The same applies to capacity and coil. Therefore, it will be difficult to accept Wang's theorem as correct in this respect.

Again, three basic elements were accepted by Wang and the other elements were considered as different versions of these three basic elements. This reveals the situation that there will be no new element, which cannot be said to be completely true. In addition, in Wang's theorem, it is assumed that there is no connection between the second order derivative and the first order derivative of an element. In other words, there is always a relationship between the degree of derivative or integral of something and the derivative or integral of that degree.

In Chua's theorem, it has revealed a contradiction the fact that the units of elements such as memristors and memcapacitors are the same as those of resistors and capacitors. Therefore, it can be said that this situation is one of the weakest points of the Chua model.

3. Conclusion

In this study, the Chua and Wang models, which are the two main models proposed so far on passive basic circuit elements, are commented in the terms of circuit elements. These circuit elements, including the basic circuit elements resistor, inductor, capacitor, and the smart resistor (memristor) proposed in their context, are examined in these two models, and the models are compared to each other in terms of circuit elements such as current, voltage and flux.

In the Chua model, current, voltage, flux and charge are considered as fundamental quantities. However, in the Wang model, voltage and current are not fundamental quantities and elements such as flux and charge are considered as fundamental quantities. But, due to our opinion of the fact that there are some deficiencies and errors in the placement of the elements in both models, we conclude that it is not possible to interpret that both models are completely correct in the placement of the elements and their association with each other.

Resultantly, the necessity of new elements increases day by day, but it is of great importance to define and model them mathematically correctly. Predicting the behavior of higher order elements is delayed due to the inadequacy of the presented models. Although both models offered to eliminate this deficiency have disadvantages and advantages, it is important to come up with a new model to overcome this bottleneck. As a result, if a model is to be created, it must first be well defined exactly what the required quantities will be, and the model must be built on it.

Ethics in Publishing

There are no ethical issues regarding the publication of this study.

Author Contributions

Murat Gülnahar: Designed and wrote the manuscript, and commented conclusions,

Yunus Babacan: carried out interpretation of the figures and models,

Müslüm Gür: interpreted figures.

References

- [1] Chua, L. (1971) Memristor—The missing circuit element, *IEEE Transactions on Circuit Theory*, CT-18 (5), 507–519.
- [2] Chua, L. (2003) Nonlinear circuit foundations for nanodevices. Part I: The four-element torus. *Proceedings of the IEEE*, 91 (11), 1830–1859.
- [3] Chua, L. and Kang, S. (1976) Memristive devices and systems, *Proceedings of the IEEE*, 64, 209–223.
- [4] Wang, Frank Z. (2013) A triangular periodic table of elementary circuit elements. *IEEE Transactions on Circuits and Systems*, 60(3), 616-623.
- [5] Chua, L. (2011) Resistance switching memories are memristors. *Applied Physics A: Materials Science & Processing*, 102, 765–783.
- [6] Wang, F. Z., Helian, N., Wu, S., Lim, M., Guo, Y., and Parker, A. (2010) Delayed switching in memristors and memristive systems. *IEEE Electron Device Letter*, 31 (7), 755–757.
- [7] Gürsul, S., & Hamamci, S. E. (2019) Comparison of different memristor emulators on low-pass filter circuit. In *2019 3rd International Symposium on Multidisciplinary Studies and Innovative Technologies (ISMSIT) IEEE*, 1-4.
- [8] Barraç, I., Mestiri, H., & Masmoudi, M. (2024) Overview of Memristor-Based Design for Analog Applications. *Micromachines*, 15(4), 505-508.
- [9] Wang, F. Z., Helian, N., Guo, Y., Wu, S., Yang, X., Lim, M. and Rashid, M. (2011) Delayed switching applied to memristor neural networks. *Journal of Applied Physics*, 111 (7), 07E317–07E317-3.

Voltage Controlled Oscillator Realisation with Temperature and Source Independent Circuits

Müslüm GÜR^{1*}, Yunus BABACAN²

¹Çankırı Karatekin University, Vocational School, Department of Electronics and Automation, 18100, Çankırı, Turkey

²Erzincan Binali Yıldırım University, Faculty of Engineering and Architecture, Department of Electrical and Electronics Engineering, 24100, Erzincan, Turkey

Received: 04/07/2024, **Revised:** 28/08/2024, **Accepted:** 18/09/2024, **Published:** 31/12/2024

Abstract

In this article, a square wave was generated with a voltage-controlled oscillator circuit (VCO) using a bandgap reference voltage circuit and a low drop-out (LDO) circuit. The band gap reference circuit can generate a constant 500mV voltage between -40°C and +125°C. The LDO circuit is driven by a bandgap reference voltage circuit and exhibits a stable output even at different voltage levels. The last circuit, VCO, is driven by the LDO circuit. It can generate square waves between 1200MHz and 1600MHz at the output. Simulations using 130nm TSMC technology parameters have been successfully achieved.

Keywords: Bandgap reference voltage circuit, low dropout regulator circuit, voltage controlled oscillator circuit.

Sıcaklıktan ve Kaynaktan Bağımsız Devreler ile Voltaj Kontrollü Osilatör Gerçeklenmesi

Öz

Bu makalede, band aralığı referans gerilim devresi ve düşük düşümlü regülatör devresi (LDO) kullanılarak gerilim kontrollü salıncı devresi (VCO) ile kare dalga üretildi. Band aralığı referans devresi -40°C ile +125°C arasında sabit 500mV gerilim üretebilmektedir. LDO devresi ise band aralığı referans gerilim devresi ile sürülmekte olup farklı gerilim seviyelerinde bile kararlı bir çıkış sergilemektedir. Son devre olan VCO ise LDO devresi tarafından sürülmektedir. Çıkışta 1200MHz ile 1600MHz arasında kare dalga üretebilmektedir. 130nm TSMC teknoloji parametreleri kullanılarak yapılan benzetimler başarılı bir şekilde elde edilmiştir.

Anahtar Kelimeler: Bant aralığı referans gerilim devresi, düşük çıkışlı regülatör devresi, gerilim kontrollü osilatör devresi.

1. Introduction

In order to obtain circuits to operate with good performance, voltage reference circuits that are independent of temperature and power supply fluctuations are required [1],[2]. It is possible to find many reference voltage circuits with different features in the literature [3-6]. Especially, it is important to design sub-1v supply circuits [7].

Low drop-out (LDO) circuits are used as power supplies in RF, analog and mixed signal applications [8]. In noise-sensitive systems, a low-output regulator is generally used after the DC-DC converter stage to meet the power need. In LDO circuits, wide loop bandwidth and fast response time are important at the design stage, and studies that take these parameters into consideration can be easily found in the literature[9-10].

Voltage controlled oscillators (VCO) are circuits that are widely used in many applications and can produce square waves even at high frequencies. Ring oscillators and LC oscillators can also be used as voltage-controlled oscillators. Ring oscillators are types of oscillators obtained by connecting the last delay stage to the first delay stage [11]. If the delay multiples increase, the frequency of the produced signal decreases and its cost increases[12-13].

In this study, the band gap reference voltage circuit, LDO circuit and VCO circuit found in the literature were rearranged for the desired purposes and turned into a block that can work together. Bandgap reference circuit exhibited high performance from -40°C to 125°C. LDO circuit also exhibited similar performance under connected capacitor and current source as load. The last circuit, VCO, generated a close to ideal square wave at the desired frequencies even under load. For all simulations, TSMC 130nm parameters were used to analyze the circuits and all results are obtained with high performance.

2. Material and Methods

2.1. Bandgap Reference Voltage Circuit

While designing the bandgap reference voltage circuit, the opposite temperature coefficients of PMOS and NMOS transistors were used. There are many transistor models, and in this study, mathematical analyzes were made using the α power model [14]. V_{GS} voltage,

$$V_{GS_ZTC} = V_{TH0} - \eta T + \frac{\alpha \eta T_0}{\beta} \left(\frac{T}{T_0} \right)^{\frac{\beta}{\alpha}} \quad (2.1)$$

When the first order derivative of the above expression is taken with respect to temperature,

$$\frac{dV_{GS_ZTC}}{dT} = -\eta + \eta \left(\frac{T}{T_0} \right)^{\left(\frac{\beta}{\alpha} - 1 \right)} \quad (2.2)$$

Similarly, when the above expression is derived one more degree with respect to temperature,

$$\frac{d^2V_{GS_ZTC}}{dT^2} = \left(\frac{\beta}{\alpha} - 1\right) \eta T_0^{\left(\frac{\beta}{\alpha}-1\right)} T^{\left(\frac{\beta}{\alpha}-2\right)} \quad (2.3)$$

Here, V_{TH0} is the threshold voltage at zero Kelvin, η , α , β are constant coefficients, and when the second order derivative is equal to zero, the β value must be equal to the α value. This ensures that transistors operate independently of temperature. Although the β value is fixed and 1.5, the α value varies between 1 and 2. For a value equal to 1, the transistor must be operated in the active region, and for a value greater than 1, it must be operated in the saturation region. Since both values (α , β) must be equal, the two values become equal thanks to the saturation operation of the transistors.

As seen in Figure 1, the tail current of the OTA (Operational Transconductance Amplifier) circuit is created by the M_{A9} transistor driven by the voltage created with the help of the M_{A1} - M_{A4} transistors. A simple OTA structure was used, consisting of OTA M_{A5} - M_{A9} transistors, and its output was connected to the gate terminals of M_{A10} - M_{A11} transistors to drive them. In addition, the required current for the LDO circuit was created with the help of M_{A14} - M_{A16} transistors.

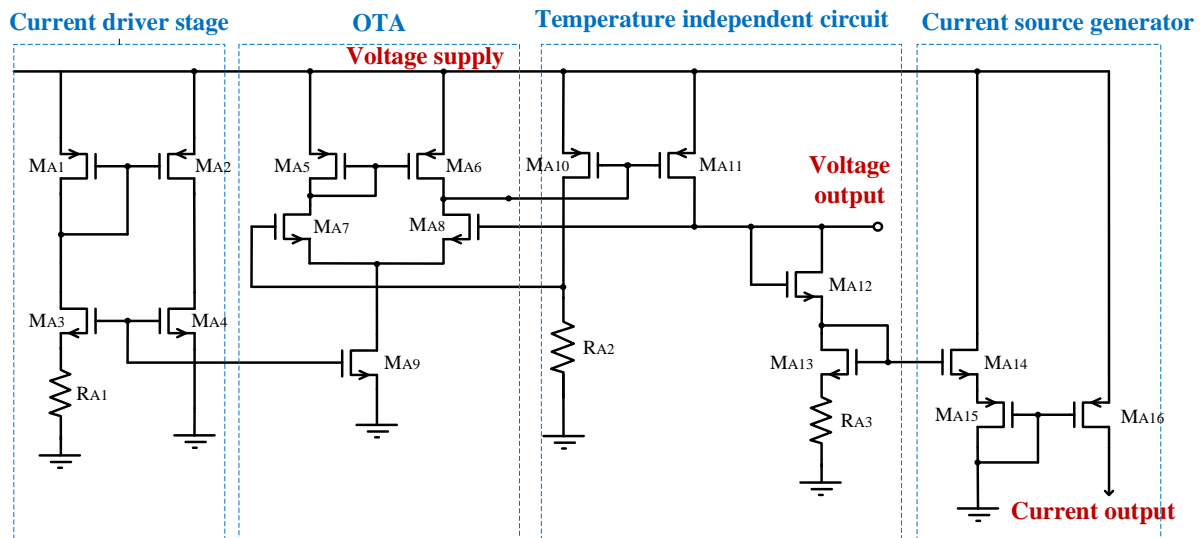


Figure 1. Modified temperature independent bandgap reference circuit[14]

The dimensions of the transistors in the circuit and the values of the elements used are important to obtain the 500mV voltage value. Table 1 contains information about circuit elements.

Table1. Element dimensions and values of the circuit.

Circuit Element	W(μm)	L(μm)	Circuit Element	W(μm)	L(μm)
M_{A1-A2}	2	1	M_{A12}	16.1	1.3
M_{A3-A4}	4	4	M_{A13}	8.1	1
M_{A5-A6}	16	4	M_{A14}	10	1

M_{A7-A8}	16	2	$M_{A15- A16}$	1	1
M_{A9}	3	1	R_{A1}	10 k Ω	
M_{A10}	16	2	R_{A2}	110 k Ω	
M_{A11}	16.2	2	R_{A3}	120 Ω	

As seen in Figure 2a, a temperature-independent voltage value of 500mV was successfully obtained. The temperature changed from -40°C to 125°C with 5°C temperature steps.

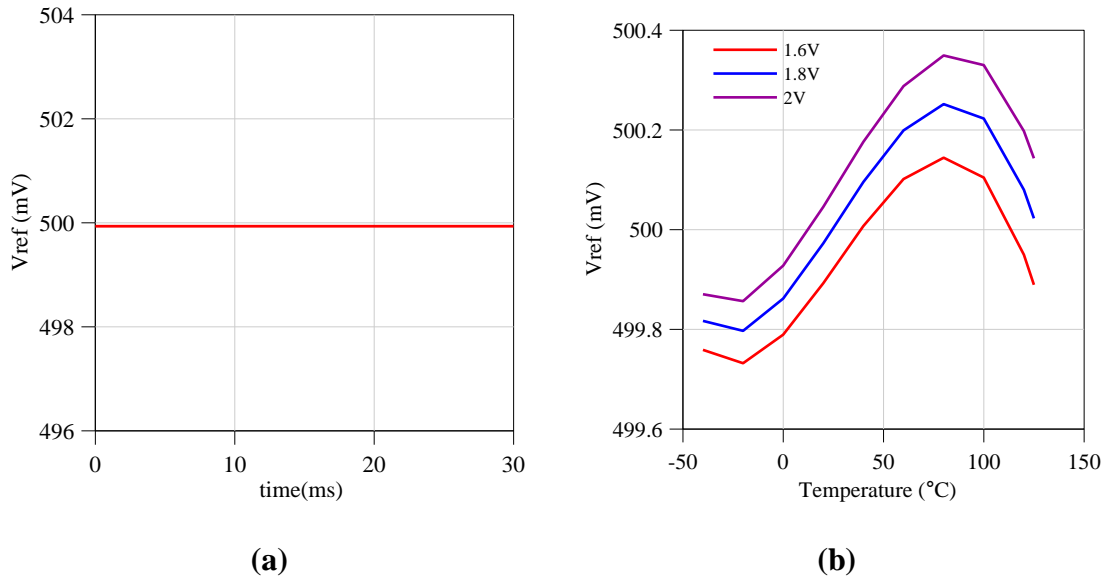


Figure 2. a) Time-dependent reference voltage output b) the reference voltage output for different supply voltages.

The output voltage of the circuit according to different supplies is seen in Figure 2b. As can be seen from the figure, the circuit exhibits a very stable output despite the wide temperature range, showing a change of 5.5 ppm/°C. Finally, the frequency-dependent variation of the power supply rejection ratio (PSRR) value was obtained in Figure 3 and was found to be -20dB on average.

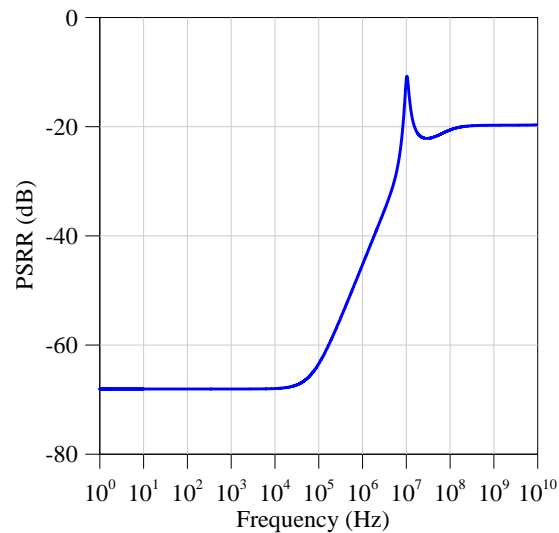


Figure 3. The change of PSRR value depending on frequency.

2.2. LDO Voltage Regulator Circuit

Low output regulator (LDO) circuits are used extensively in many analog circuits due to their features such as low power consumption, high power supply rejection ratio (PSRR) and high current capability [8]. Many different types of LDO circuits can be found in the literature [15-18]. The LDO circuit [19] found in the literature, which will be used for the square wave generator, has been modified. The block diagram of the circuit is shown in the figure 4. Here, while reference voltage is applied from the positive input of the opamp, feedback is provided from the other input. A high current block was added to the circuit to provide the high current (a few mA) required for the oscillator circuit.

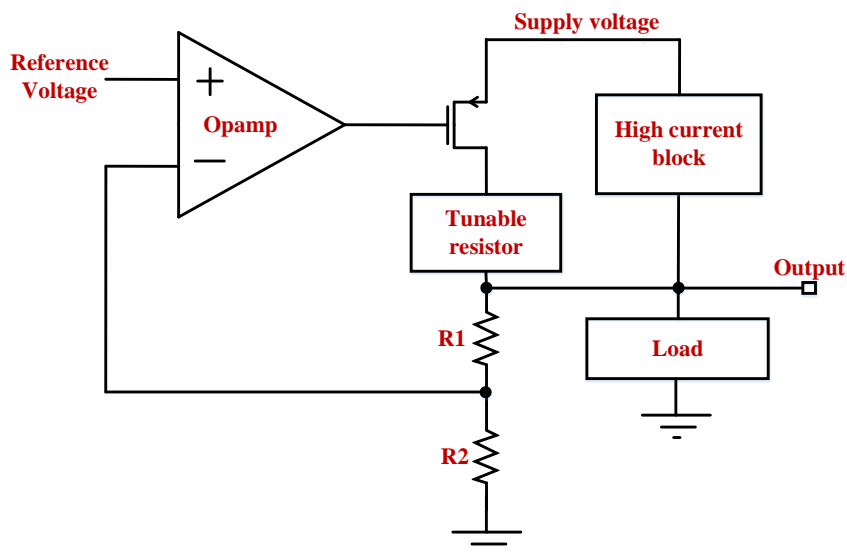


Figure 4. Block diagram of the LDO circuit.

As seen in the circuit in figure 5, the LDO circuit consists of three blocks. These are the opamp section where amplification and comparison are performed, the variable and fixed resistance region for feedback and voltage level control, and the high current block to provide high current.

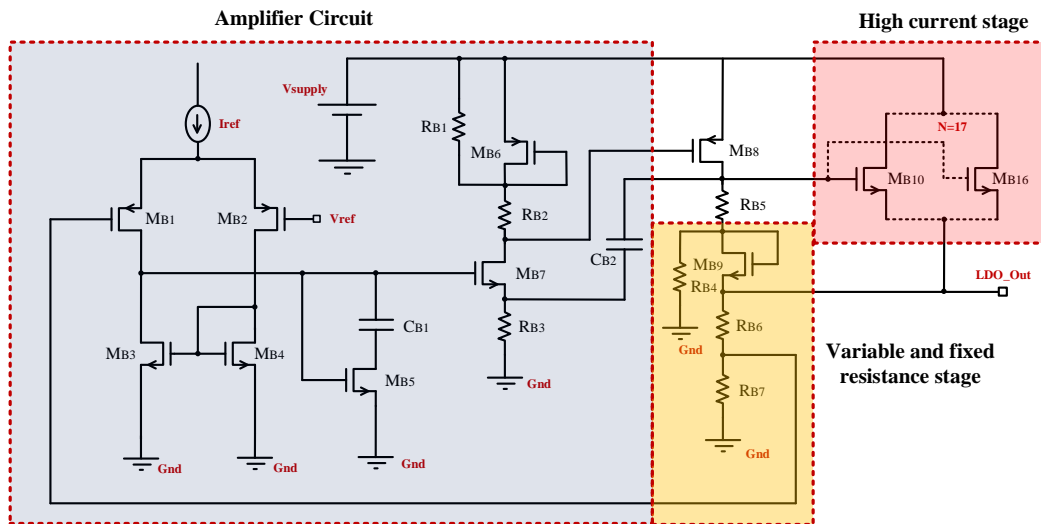


Figure 5. Modified LDO circuit diagram [19].

Here, capacitor C_{B1} provides impedance matching thanks to its high resistance at low frequencies and low resistance at high frequencies. C_{B2} capacitor is also used to improve the power supply rejection ratio (PSRR) value. M_{B6} - M_{B9} transistors are transistors used to adjust the current given to the load at the output. The current drawn by the load occurs through the M_{B8} and M_{B9} transistors and the R_{B5} resistor. Here, resistors R_{B2} and R_{B5} are used to limit unnecessary current flow and therefore excessive power consumption. Resistors R_{B1} and R_{B4} are also used to regulate current flow when there is no load. M_{B8} transistors, generally called power transistors, are implemented with PMOS transistors. However, in this design, NMOS transistor was used due to its higher electron mobility and lower parasitic capacitances compared to PMOS transistor. The dimensions and element values of the elements of the circuit are given in table 2. Here, care has been taken to create a circuit suitable for chip implementation, especially by choosing low capacitor values.

Table 2. Element dimensions and values of the circuit.

Circuit Element	W(μm)	L(μm)	Circuit Element	Element values
$M_{B1-2,6}$	2	1	C_{B1}	3pF
$M_{B3-5,7,9}$	1	1	C_{B2}	10pF
M_{B10-16}	30	0.25	R_{B1}	100k Ω
R_{B2}	30k Ω		R_{B3}	1k Ω
R_{B4}	10k Ω		R_{B6}	146k Ω
R_{B5}	200k Ω		R_{B7}	110k Ω

When the input is 1.8V, the output voltage is measured as 1.2V. As seen in Figure 6a, the output was measured as a stable and constant value when 500pF load capacitor is connected. Likewise, when the input voltage was set to 2.5V, the time-dependent change of the output voltage was measured. It can be easily seen in Figure 6b, even if the input voltage changes radically, the output voltage changes very little.

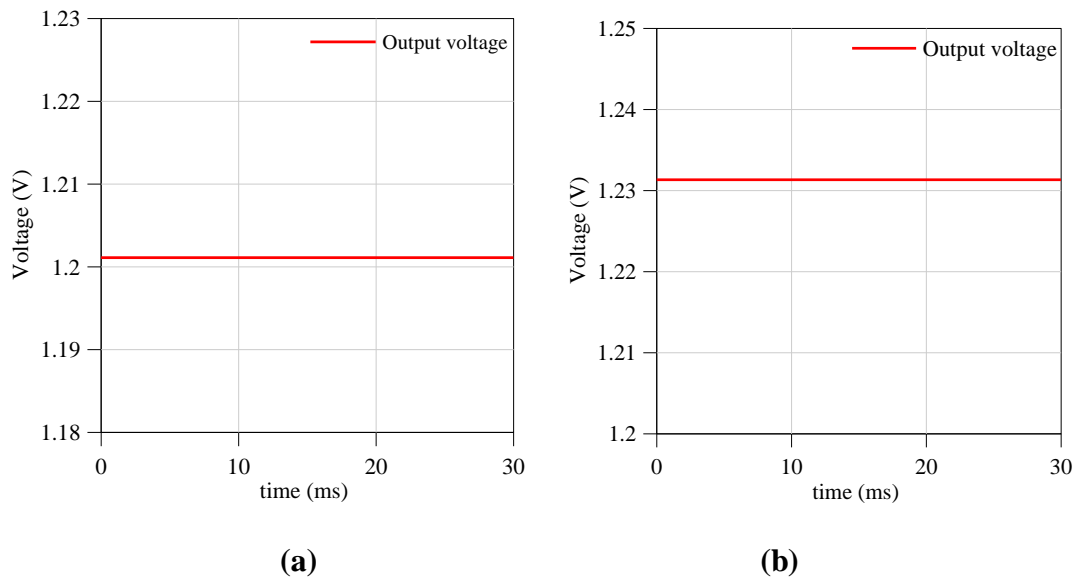


Figure 6. a) The variation of output voltage with time when the input voltage is 1.8V and **b)** 2.5V.

When the loop gain and phase margin of the LDO circuit are analyzed, it appears as shown in Figure 7. It is desired that the gain and phase angle of the LDO circuit be high. As seen in Figure 2.8, 108.06dB and 117.07° were obtained.

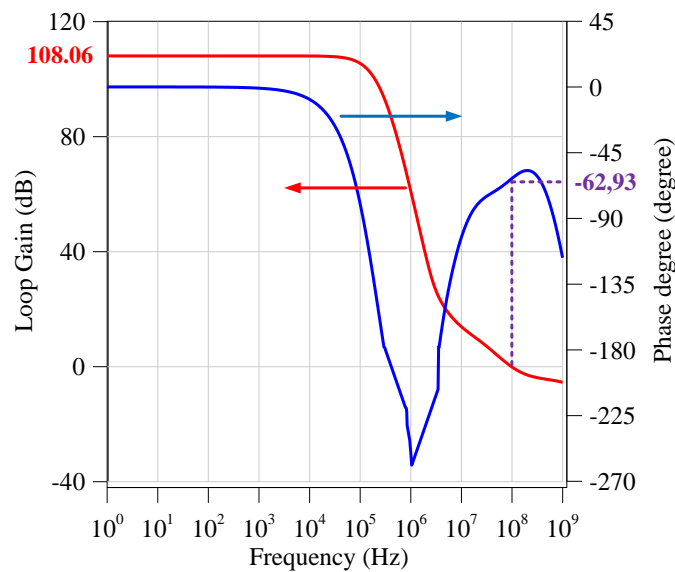


Figure 7. Loop gain and phase margin changes.

2.3. Voltage Controlled Oscillator (VCO) Circuit

Voltage controlled oscillator (VCO) circuits are advantageous circuit types due to their low power consumption and suitability for VLSI circuits. There are different types of VCO circuits in the literature [20-22]. In this study, the modified circuit is seen in Figure 8 and consists of two basic blocks. The first block is the part where the square wave signal is produced, and the second block is the block required to provide enough current when the load is connected. The first block consists of 3 parts. The first part; It consists of the current supply stage, the inverter stage where the signal is generated, and the current limiting stage that provides current limitation. As the number of inverter stages increases, the generated signal decreases inversely. To operate at high frequencies, inverter stages must be increased.

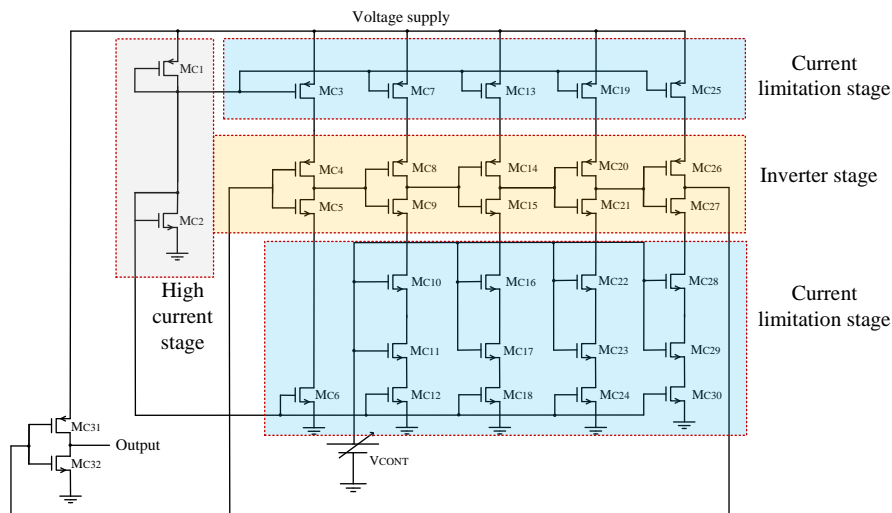


Figure 8. Modified VCO circuit [20]

In addition, M_{C11} , M_{C17} , M_{C23} and M_{C29} transistors enable the K_{VCO} value to be improved. These transistors take an active role in reducing the effect of changing the V_{CONT} value. Transistor dimensions and element values of the designed circuit are given in table 3.

Table 3. The element dimensions and values for the circuit.

Circuit Element	W(μ m)	L(μ m)	Circuit Element	W(μ m)	L(μ m)
M_{C1}	2	1	$M_{C16,17,22,23}$	0.7	0.2
M_{C2}	1	2	M_{28}	2	0.2
M_{C3}	25	0.5	M_{C29}	1	0.2
$M_{C4-5,8-9,14,15,20,21,26,27}$	0.3	0.2	M_{C31-32}	1	0.3
M_{C10-11}	0.5	0.2	M_{C33-34}	3	0.3
$M_{C6,12,18,24,30}$	14	0.35	M_{C35-36}	10	0.3
$M_{C7,13,19,25}$	15	0.5	M_{C39-64}	30	0.3

The VCO circuit is supplied with 1.2V supplied from the LDO circuit. It has been successfully achieved that the designed circuit produces a square wave between 0V-1.1V and its frequency is controlled with a voltage source. Here, the control voltage value was set to 0.6V to generate the signal and the signal at 1.2GHz was produced as seen in figure 9. Likewise, when the control voltage was set to 1.1V, the output voltage was easily obtained as 1.6GHz without distorting the signal shape.

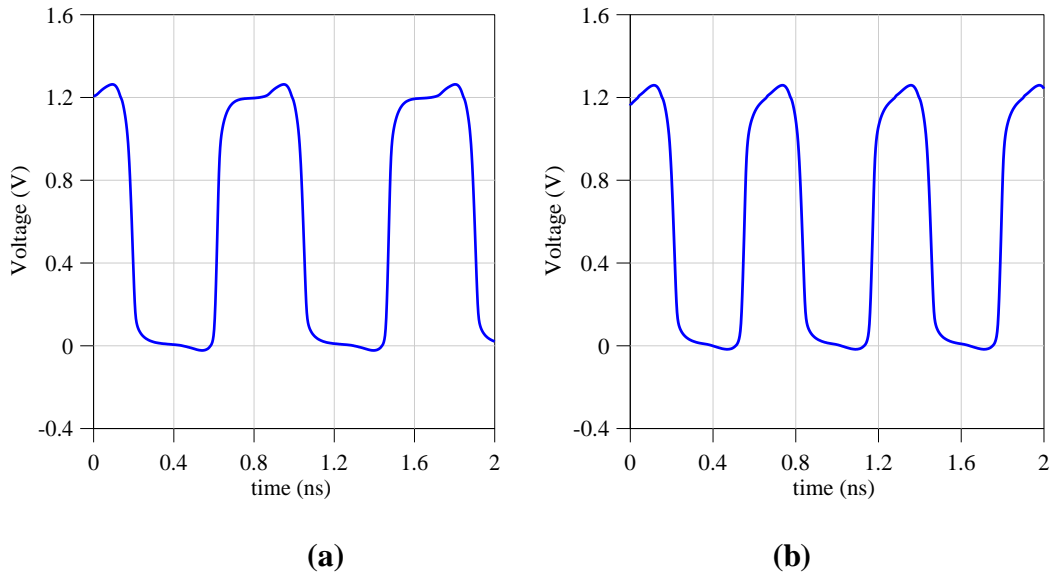


Figure 9. Signal generated by the VCO circuit a) 1.2GHz b) 1.6GHz.

K_{VCO} value is a quantity that indicates the relationship between the control voltage and the produced frequency. It is desirable that the generated frequency is not too sensitive to the control voltage. Figure 10 shows the change in the frequency generated by the control voltage.

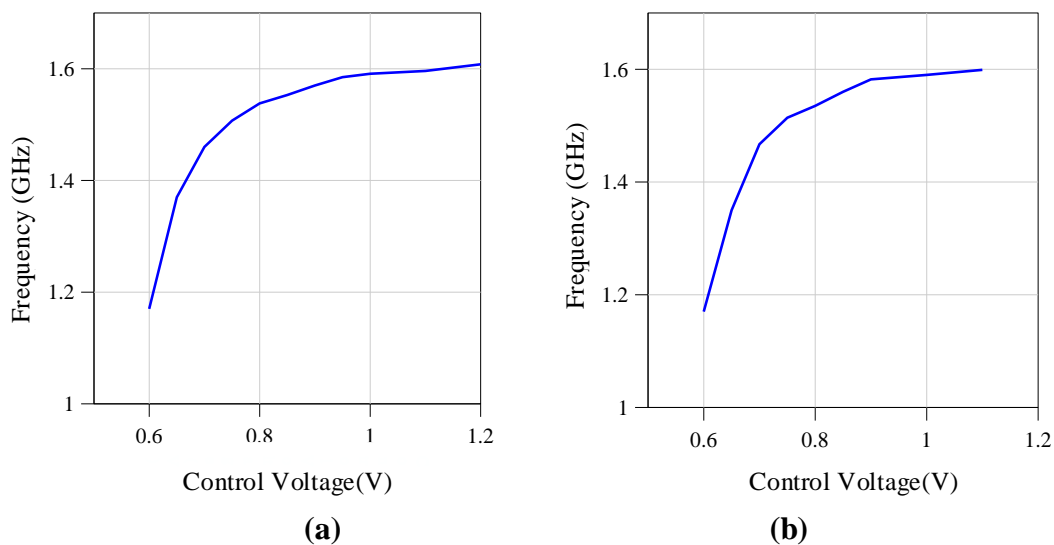
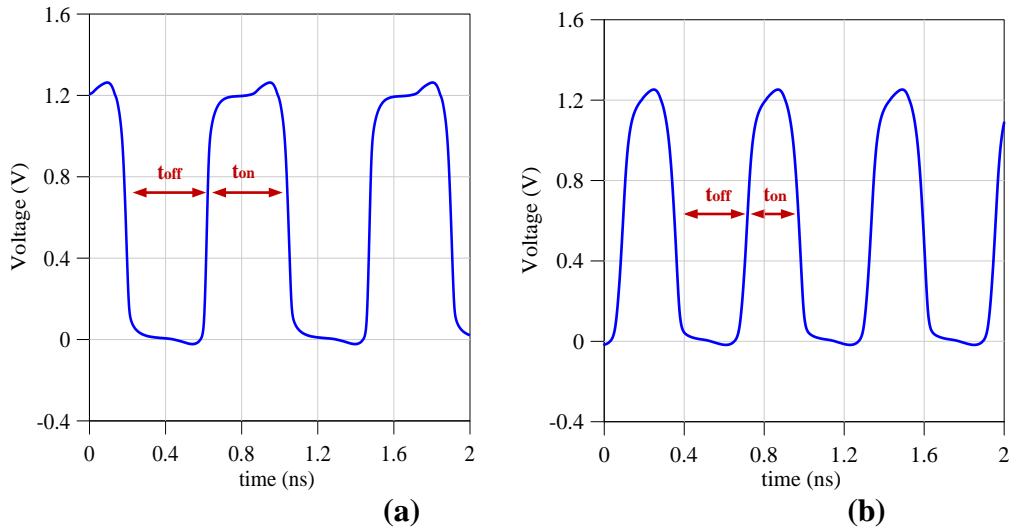


Figure 10. Variation of frequency with control voltage a) with no load b) with 0.6pF load. Here, the K_{VCO} value is 730 MHz/V.

Another important advantage of the modified VCO circuit is the duty cycle value of the produced square wave. Here, if these ratios for 1200MHz and 1600MHz frequencies are calculated as in figure 11, the results are obtained as follows.



Şekil 11. a) 1200MHz and b) 1600MHz signal output.

The duty cycle ratios for 1200MHz and 1600MHz signals are shown in table 4. As shown, the duty cycle for 1200MHz signal is very good, is in acceptable limits for 1600MHz signal output.

Table 4. Duty cycle ratios of signal outputs of the VCO circuit.

Frequency	ton (ps)	toff(ps)	Duty cycle ratio
1200 MHz	391.934	430.924	%47.63
1600 MHz	250.813	369.683	%40.376

3. Results and Discussion

As seen in Figure 12, the LDO circuit was fed by the current and voltage produced by the temperature-independent bandgap reference circuit. Afterwards, the voltage source required by the VCO circuit was produced with LDO. Thus, all blocks were fed with a single source and the desired square wave production was achieved.

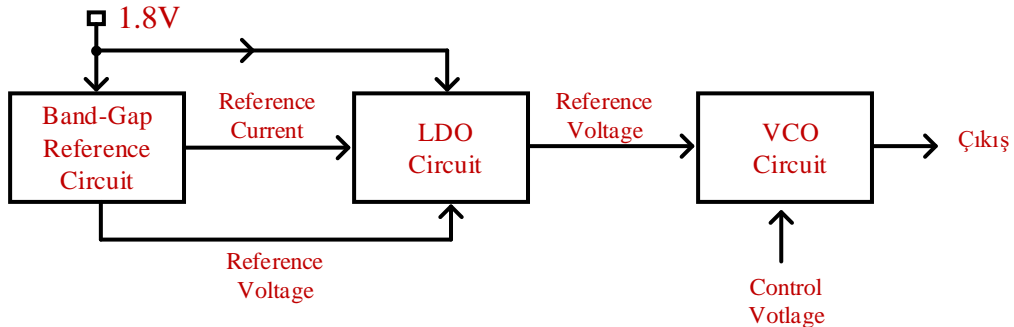


Figure 12. The connection diagram of all presented circuits.

When the band gap reference circuit, LDO circuit and VCO circuit are combined, oscillation is achieved without much performance degradation. All circuits are connected to each other and while the VCO circuit is driving a 0.4pF load, the current provided by the band gap reference

circuit to the LDO circuit is seen in figure 13. Figure 13a shows the current drawn while producing a 1200MHz signal. The pins seen here are a systematic problem caused by the program and do not represent circuit performance. Additionally, as can be seen, the supplied current exhibits a very stable behavior. A similar situation can be seen in figure 13b.

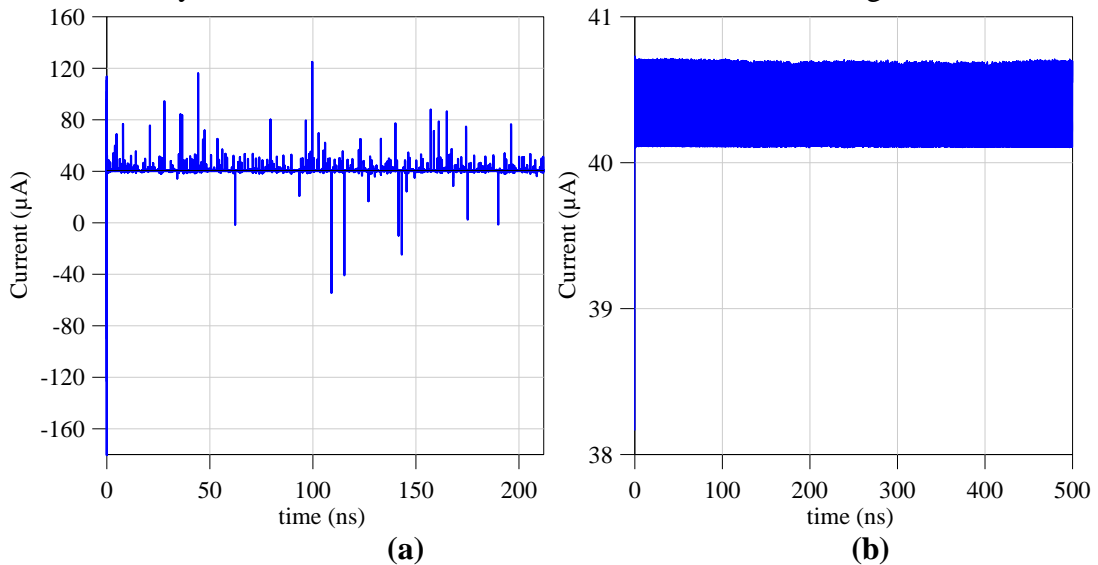


Figure 13. Entire system is interconnected **a)** 1200MHz and **b)** 1580MHz currents provided by the band gap reference circuit for signal outputs.

When all circuits are combined, the outputs of the LDO circuit are seen in the graphs below for 1200MHz and 1580MHz. As can be seen, both LDO outputs give almost the same result. From here it is understood that the LDO circuit is stable.

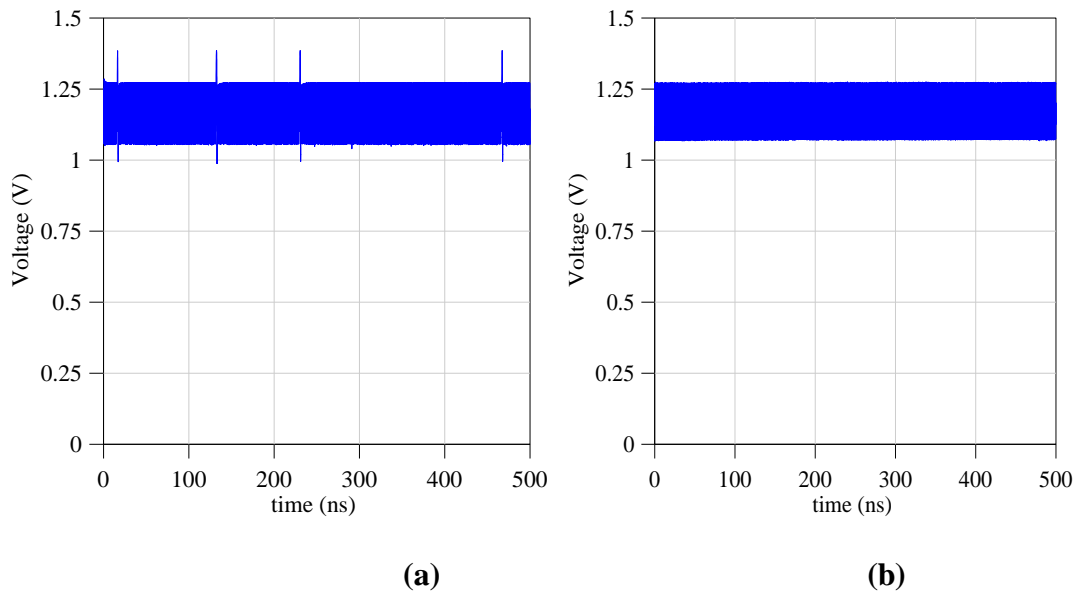


Figure 14. Entire system is interconnected **a)** 1200MHz and **b)** voltage provided by the LDO circuit for 1580MHz signal outputs.

Finally, the VCO output is obtained when all circuits are connected to each other. As seen in Figure 15, it is understood that the square wave shape of the signals produced at both frequencies does not change.

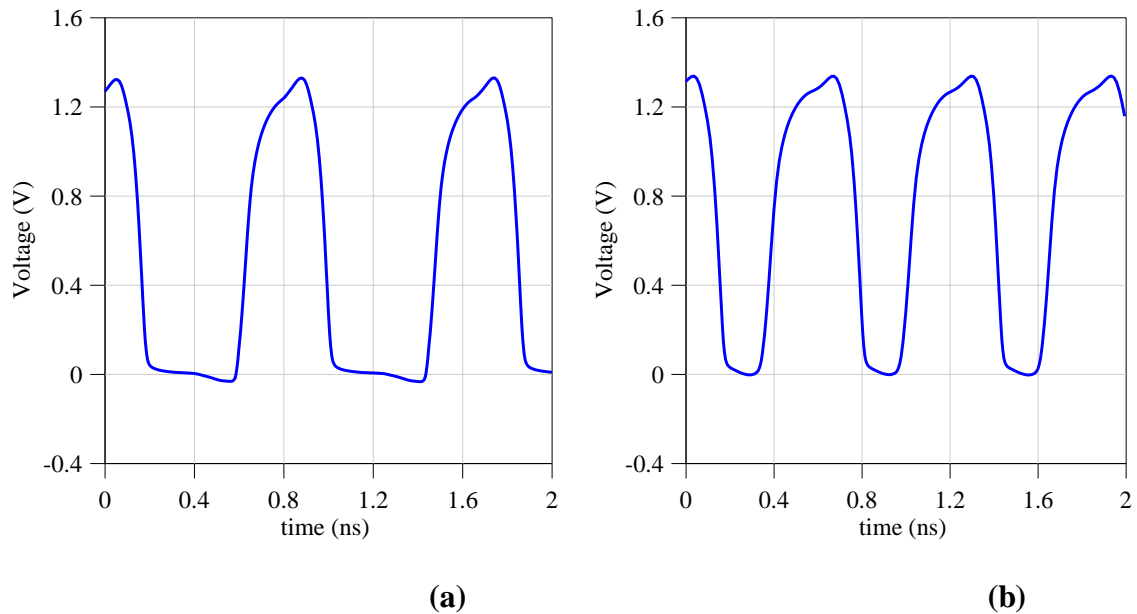


Figure 15. Entire system is interconnected **a)** 1200MHz and **b)** output generated by the VCO circuit for 1580MHz signal outputs.

4. Conclusion

In this study, a bandgap reference voltage circuit was realized by taking advantage of the opposite temperature coefficients of PMOS and NMOS transistors. The circuit exhibited a stable behavior between $-40\text{ }^{\circ}\text{C}$ and $125\text{ }^{\circ}\text{C}$ and the temperature change was obtained as $5.5\text{ ppm}/^{\circ}\text{C}$. The frequency-dependent variation of the PSRR value of the designed circuit between 1 Hz and 10 GHz was found to be -20 dB on average. While the input voltage of the LDO circuit is 1.8 V , the output voltage is measured as 1.2 V . A square wave between 0 V - 1.1 V was produced with the VCO circuit, and signals at 1.2 GHz and 1.6 GHz frequencies were obtained with the help of a voltage source. A 0.4 pF load was easily driven by the generated square wave. This study shows that the performance of the VCO circuit does not change when examined both under load and no load. Finally, all circuits were connected to each other, the performance of the entire system was examined, and the circuit block fed by a single high-performance source was successfully operated.

Ethics in Publishing

There are no ethical issues regarding the publication of this study.

Author Contributions

Müslüm GÜR: Circuit Designs, Evaluation of the results, Writing – original draft preparation.
Yunus BABACAN: Circuit Designs, Evaluation of the results, Supervision, reviewing and editing.

References

- [1] Lin, T., Chong, K. S., Chang, J. S., & Gwee, B. H. (2012) An Ultra-Low Power Asynchronous-Logic In-Situ Self-Adaptive V_{DD} System for Wireless Sensor Networks. *IEEE Journal of Solid-State Circuits*, 48 (2), 573-586.
- [2] Guo, L., Ge, T., & Chang, J. S. (2014) A 101 dB PSRR, 0.0027% THD+N and 94% power-efficiency filterless class D amplifier. *IEEE Journal of Solid-State Circuits*, 49 (11), 2608-2617.
- [3] Lee, I., Sylvester, D., & Blaauw, D. (2017) A subthreshold voltage reference with scalable output voltage for low-power IoT systems. *IEEE Journal of Solid-State Circuits*, 52 (5), 1443-1449.
- [4] Wang, Q., Wang, X., Li, J., & Liu, Y. (2022) A bandgap reference voltage source design for wide temperature range. In *2022 7th International Conference on Integrated Circuits and Microsystems (ICICM)* (pp. 245-250). IEEE.
- [5] Jain, S., Kanchetla, V. K., & Zele, R. (2022) A Sub-1V, current-mode bandgap voltage reference in standard 65 nm CMOS process. In *2022 IEEE 15th Dallas Circuit And System Conference (DCAS)* (pp. 1-5). IEEE.
- [6] Basyurt, P. B., Bonizzoni, E., Maloberti, F., & Aksin, D. Y. (2017) A low-power low-noise CMOS voltage reference with improved PSR for wearable sensor systems. In *2017 IEEE International Symposium on Circuits and Systems (ISCAS)* (pp. 1-4). IEEE.
- [7] Shrivastava, A., Craig, K., Roberts, N. E., Wentzloff, D. D., & Calhoun, B. H. (2015) 5.4 A 32nW bandgap reference voltage operational from 0.5 V supply for ultra-low power systems. In *2015 IEEE International Solid-State Circuits Conference-(ISSCC) Digest of Technical Papers* (pp. 1-3). IEEE.
- [8] Lu, Y., Wang, Y., Pan, Q., Ki, W. H., & Yue, C. P. (2015) A fully-integrated low-dropout regulator with full-spectrum power supply rejection. *IEEE Transactions on Circuits and Systems I: Regular Papers*, 62 (3), 707-716.
- [9] Bu, S., Leung, K. N., Lu, Y., Guo, J., & Zheng, Y. (2018) A fully integrated low-dropout regulator with differentiator-based active zero compensation. *IEEE Transactions on Circuits and Systems I: Regular Papers*, 65 (10), 3578-3591.
- [10] Qu, W., Singh, S., Lee, Y., Son, Y. S., & Cho, G. H. (2016) Design-oriented analysis for Miller compensation and its application to multistage amplifier design. *IEEE Journal of Solid-State Circuits*, 52 (2), 517-527.
- [11] Rajalingam, P., Jayakumar, S., & Routray, S. (2021) Design and analysis of low power and high frequency current starved sleep voltage controlled oscillator for phase locked loop application. *Silicon*, 13 (8), 2715-2726.

- [12] Aranda, M. L., Díaz, O. G., & Álvarez, C. R. B. (2013) A performance comparison of CMOS voltage-controlled ring oscillators for its application to generation and distribution clock networks. *Sci J Circuits Syst Sig Process*, 2 (2), 56-66.
- [13] Hwang, I. C., Kim, C., & Kang, S. M. (2004) A CMOS self-regulating VCO with low supply sensitivity. *IEEE Journal of Solid-State Circuits*, 39 (1), 42-48.
- [14] Jiang, J., Shu, W., & Chang, J. S. (2016) A 5.6 ppm/° C temperature coefficient, 87-dB PSRR, sub-1-V voltage reference in 65-nm CMOS exploiting the zero-temperature-coefficient point. *IEEE Journal of Solid-State Circuits*, 52 (3), 623-633.
- [15] Sobhan Bhuiyan, M. A., Hossain, M. R., Minhad, K. N., Haque, F., Hemel, M. S. K., Md Dawi, O., & Ooi, K. J. (2022) CMOS low-dropout voltage regulator design trends: an overview. *Electronics*, 11 (2), 193.
- [16] Kang, J. G., Park, J., Jeong, M. G., & Yoo, C. (2021) Digital low-dropout regulator with voltage-controlled oscillator based control. *IEEE Transactions on Power Electronics*, 37(6), 6951-6961.
- [17] Kang, J. G., Park, J., Jeong, M. G., & Yoo, C. (2021) Digital low-dropout regulator with voltage-controlled oscillator based control. *IEEE Transactions on Power Electronics*, 37(6), 6951-6961.
- [18] Silva-Martinez, J., Liu, X., & Zhou, D. (2020) Recent advances on linear low-dropout regulators. *IEEE Transactions on Circuits and Systems II: Express Briefs*, 68(2), 568-573.
- [19] Cao, H., Yang, X., Li, W., Ding, Y., & Qu, W. (2021) An impedance adapting compensation scheme for high current NMOS LDO design. *IEEE Transactions on Circuits and Systems II: Express Briefs*, 68(7), 2287-2291.
- [20] Annamma, K., Saxena, S., & Patel, G. S. (2022) Sleepy Stack CSVCO with wide tuning and low power for PLL applications. In *Journal of Physics: Conference Series* (Vol. 2327, No. 1, p. 012013). IOP Publishing.
- [21] Panigrahi, J. K., Acharya, D. P., & Nanda, U. (2022) Performance Analysis of Dual Threshold CMOS based Current Starved Voltage Controlled Oscillator-A Review. In *2022 2nd International Conference on Artificial Intelligence and Signal Processing (AISP)* (pp. 1-4). IEEE.
- [22] Prajapati, A., & Prajapati, P. P. (2014) Analysis of Current Starved Voltage Controlled Oscillator using 45nm CMOS Technology. *International Journal of Advanced Research in Electrical, Electronics and Instrumentation Engineering*, 3(3), 8076.

Radioprotective Effect of Umbelliferon Against Radiation-Induced Myocardial Damages

Nurdan DUMLU¹, Fatime GEYİKOĞLU¹, Suat ÇOLAK^{2*}

¹Department of Biology, Faculty of Sciences, Atatürk University, 25240, Erzurum, Turkey

²Department of Biochemistry, Faculty of Pharmacy, Erzincan Binali Yıldırım University, 24002, Erzincan, Turkey

Received: 24/09/2024, **Revised:** 11/10/2024, **Accepted:** 01/11/2024, **Published:** 31/12/2024

Abstract

Radiation at the high dose may attenuate myocardial functions while presenting the therapeutic effect on cancer cells and thus can life-threatening. There are numerous phytotherapeutic studies in the literature to reduce or eliminate tissue damage. Therefore, the current study was planned to evaluate the role of umbelliferone radiation-induced cardiac injury using biochemical and histological data. Rats will be divided into eight different groups as control, radiation and treatment groups. Radiation exposure to the rats induced oxidative stress, inflammation, pathological changes and vascular dysfunction in cardiac tissue. Whereas umbelliferone in high dose (100 mg/kg) pretreatment supported the anti-oxidant activity and also reduced inflammatory response and histopathologic damage in heart tissue against radiation-associated toxicity. In conclusion, it was shown that umbelliferon (100 mg/kg) pretreatment can be used against the side effects of radiotherapy.

Keywords: Radiation, umbelliferone, oxidative stress, cardiotoxicity, rat

Umbelliferon'un Radyasyona Bağlı Miyokard Hasarlarına Karşı Radyoprotektif Etkisi

Öz

Yüksek dozda uygulanan radyasyon, kanser hücreleri üzerinde tedavi edici etki gösterirken miyokardiyal fonksiyonları zayıflatmakta ve yaşamı tehdit etmektedir. Literatürde doku hasarını azaltmak veya gidermek için çok sayıda fitoterapötik çalışma vardır. Bu çalışma ile biyokimyasal ve histolojik yöntemler kullanarak umbelliferonun radyasyona bağlı kalp hasarındaki rolünün değerlendirilmesi hedeflenmiştir. Bu amaçla, Sıçanlar kontrol, radyasyon ve tedavi grupları olmak üzere sekiz farklı gruba ayrılmıştır. Sıçanların kalp doku örneklerinde radyasyon maruziyetinin oksidatif strese artma, inflamasyon, patolojik değişiklikler ve vasküler disfonksiyona neden olduğu görülmüştür. Yüksek dozda (100 mg/kg) umbelliferon uygulanan grupta ise anti-oksidan aktivite desteklenmiş ve radyasyonla ilişkili toksisiteye karşı kalp dokusunda inflamatuvar yanıtı ve histopatolojik hasarı azalttığı görülmüştür. Sonuç olarak, umbelliferon (100 mg/kg) ön tedavisinin radyoterapinin yan etkilerine karşı kullanılabileceğini göstermiştir.

Anahtar Kelimeler: Radyasyon, umbelliferon, oksidatif stres, kardiyotoksisite, sıçan

*Corresponding Author: scolak@erzincan.edu.tr
Nurdan DUMLU, <https://orcid.org/0009-0009-1658-6484>
Fatime GEYİKOĞLU, <https://orcid.org/0000-0003-2488-1757>
Suat ÇOLAK, <https://orcid.org/0000-0001-8320-3038>

1. Introduction

According to the report published by the World Health Organisation in 2021, cardiovascular diseases are in the first place among the causes of death. In second place are respiratory system diseases due to the Covid-19 pandemic that we experienced between 2019-2021. Cancer cases, which were in the top 3 among the causes of death in previous years, decreased to 6th place among the causes of death with the global epidemics [1]. By 2035, It is estimated that there will be 24 million new cancer cases worldwide [2]. Surgery, chemotherapy, radiotherapy methods and their combinations are still frequently used in cancer treatments. Radiotherapy (RT), one of them, remains the most widely used method of cancer treatment and is estimated to be given to a round 60% of cancer patients [3]. Although ionizing radiation therapy has beneficial effects on living cells, it has also been reported that it has many side effect that develop depending on dose and duration and finally this effects reduced quality of life [4]. Furthermore, these adverse effects have also been linked to developing metabolic disorders, which may cause to serious complications such as renal failure, impairment in lung function, liver injury, neuropathy, atherosclerosis or cardiac damage [5-9].

Many of these toxic effects result from excessive Reactive Oxygen Species (ROS) that induce oxidative stress caused by ionising rays used in radiotherapy [10]. Our body has an antioxidant enzymatic defense system such as catalyze (CAT), superoxide dismutase (SOD) and glutathione peroxidase (GPx). These prevent oxidative stress by directly scavenging reactive oxygen species or reducing their effect [11]. In cases where this system is insufficient, the intake of primarily plant-derived dietary antioxidants is thought to play an important role in protecting human health [12-14].

The coumarins are biologically active compounds that have heterocyclic structure and belonging to the class of benzopyrone. Coumarins and their derivatives have recently been studied extensively and found to have many biological properties, including antibacterial, anti-inflammatory, antioxidant, antitumor, antiviral, and especially anticoagulant [15-17]. Umbelliferone (UMB), known as 7-hydroxycoumarin, is a naturel coumaric compound that found in many plant [18]. Although there are many theories to explain how umbelliferone works, the most widely accepted is that it has antioxidant properties [19]. Studies have reported that it is effective against myocardial ischaemia damage [20], liver damage [21], testicular dysfunction [22] and diabetic nephropathy [23].

In recent years, the discovery of new agents of natural and herbal origin has become increasingly popular among researchers due to the lack of complete treatment of human diseases and undesirable side effects. From this point of view, this study aimed to determine whether umbelliferone pretreatment reduces radiation-induced myocardial damage. Thus, our study for the first time reveals the novel therapeutic role of umbelliferone in cardiac tissue against radiation-induced injury.

2. Materials and Methods

Umbelliferone and chemicals

Umbelliferone (purity $\geq 98\%$) and other chemicals have been purchased from Merck Healthcare KGaA (Darmstadt, Germany). Thromboxane B2 (TXB2) was obtained from Cell Signaling Technology (Danvers, MA, USA). TAC (Randox, UK), TOS commercial kits (Rel Assay Diagnostics; Mega Tip, Gaziantep, Turkey) were purchased from commercial sources.

Animals care and maintenance

In this experimental study, fifty six male Sprague Dawley rats (weighing 280-300 g) were obtained from Animal Center of Atatürk University. The animals were housed in an air-conditioned room (20- 24°C) with 12-hour light-dark cycle. The rats were provided free access to standard feed and water ad libitum. All experimental procedures were approved by Institutional Ethical Committee for Animal Care and Use at Atatürk University, Erzurum, Turkey (Code number: 263, 26.12.2019B.30.2.ATA.0.23.85-11) and were conducted in accordance with the National Institutes of Health Guide for Care and Use of Laboratory Animals [24].

Experimental design

The experimental groups were formed as 7 groups with 8 animals in each group. The groups were administrated different doses as follows:

Group I: (Control group) given physiological saline,

Group II: (Radiation group) exposed a single high dose of 12 Gy of gamma rays,

Group III, IV and V: (Umbelliferone groups) Administered umbelliferone (30, 60 and 90 mg/kg body weight/day) alone,

Group VI, VII and VIII: (treatment groups) received umbelliferone orally (30, 60 and 90 mg/kg body weight/day) for 5 days prior to radiation exposure.

The umbelliferone doses were determined based on the literature and our pilot studies [25]. After treatment for 24 h, the animals were anesthetized by injections of 12 mg/kg xylazine and 80 mg/kg ketamine and were sacrificed to collect heart tissues. The tissue samples were carefully collected and divided into two parts: one part was fixed in 10% formalin solution for histopathological studies and the second part was stored as a lysate for biochemical and other analysis.

Ionizing radiation exposure

The cardiac irradiation model was established as previously described by researchers [26,27]. According to the this procedure, a Theratron 780-C source (AECL, Ontario, Canada) with a dose rate of 0.78 Gy/min was used to deliver a single 12 Gy dose to whole body. The applications were carried out in the Radiotherapy Unit of Atatürk University Medical College

Hospital, Erzurum, Turkey. A tissue-equivalent ionisation chamber was used to calibrate the exposure setup by physical measurement. The homogenous irradiation field measured 30 × 30 cm, exhibiting uniformity within 1%. Each rat was placed in a ventilated circular holder during irradiation to minimize movement, ensuring that the whole body received a uniform dose of radiation.

Total Antioxidant Capacity and Total Oxidant Status

Total antioxidant capacity (TAC) and total oxidative status (TOS) assay kits were used to measure oxidative stress and resistance to oxidants. Measurements were conducted according to the protocols of TAC and TOS kits [28,29]. The TAC and TOS results were given as mmol trolox equivalent/L and $\mu\text{mol H}_2\text{O}_2$ equivalent/L, respectively.

TNF-a and Thromboxane B2 (TXB2)

Rat heart tissue samples (approximately 2 g) were weighed and then stored at -80 °C. After, tissue samples were homogenized into phosphate-buffered saline (PBS) and centrifuged at 10,000g, 4 °C for 10 minutes. The supernatants (40 μl) were collected and promptly transported to -80 °C. Thromboxane B2 (TXB2) and tumor necrosis factor alpha (TNF-a) levels were tested using commercially available ELISA kits, according to the manufacturer's instructions.

Histopathological studies

Rat heart tissue samples were fixed in buffered 10% formalin for 48 h and then embedded in paraffin blocks. The heart tissues were sectioned at 5 μm and stained using Haematoxylin-Eosin (H&E), Congo Red and Periodic Acid-Schiff (PAS) methods. The slides were examined under a light microscope. Changes in heart tissue were scored in twenty different areas for each section. The cardiac lesions (congestion, infiltration, haemorrhage and apoptotic) in the groups were scored out of a maximum of 18. These lesions were scored as 1 if less than 30%, 2 if between 30-60% and 4-5 if more than 60% [30].

Statistical Method

Data analysis of TAC, TOS, TNF-a, TXB2 parameters was performed using SPSS 24.0 for Windows software (SPSS Inc., Chicago, IL). Data are expressed as means \pm SE. Since, all results followed a normal distribution comparisons between the groups were carried out using one-way parametric ANOVA. The data were commented according to the significance level of 0.05.

Results and Discussion

Evaluation of biochemical parameters

TAC, TOS, TNF-a, TXB2 tissue levels in all experimental groups are presented in Table I according to the groups. In the RAD group (group II), TOS levels in rat heart tissue increased while TAC levels decreased compared to the control group. This is a clear indication that the

Radioprotective Effect of Umbelliferone Against Radiation-Induced Myocardial Damages

oxidative balance in the heart tissue was impaired. However, no significant difference was found between the control and RAD+UM25 and RAD+UM50 treated groups. Furthermore, it was observed that these levels returned to control levels in UM100-treated rats.

We also evaluated the anti-inflammatory activity of UMB by determining the TNF- α value. While the level of TNF- α was significantly up-regulated in the radiation-exposed group, the group pretreated with UMB100 showed a marked down-regulation of TNF- α in the heart tissue sample ($p < 0.05$).

TXB2 levels were significantly higher in the irradiated group compared to the other groups ($p < 0.05$). This increase is an important evidence of vascular injury. In the rats treated with different doses of UMB, the level of TBX2 did not change level of the control group ($p > 0.05$).

Table 1. Effects of Umbelliferone on TAC, TOS, TNF- α and TXB2 levels

Groups	TAC	TOS	TNF- α	TXB2
	(mmol Trolox Equiv./L)	(μ mol H ₂ O ₂ Equiv./L)	(pg/mg tissue)	(pg/mg)
Control	7.94 \pm 0.80	5.01 \pm 0.24	3.90 \pm 0.29	429 \pm 19
Rad	3.90 \pm 0.10 ^a	8.10 \pm 0.01 ^a	6.30 \pm 0.27 ^a	645 \pm 15 ^a
Umb25	8.17 \pm 0.12 ^b	5.13 \pm 0.06 ^b	3.81 \pm 0.12 ^b	411 \pm 19
Umb50	8.29 \pm 0.27 ^b	5.13 \pm 0.11 ^b	3.78 \pm 0.05 ^b	407 \pm 13
Umb100	8.42 \pm 0.10 ^b	5.05 \pm 0.19 ^b	3.83 \pm 0.12 ^b	404 \pm 8
Umb25+Rad	4.80 \pm 0.16 ^{a,b,c}	4.79 \pm 0.05 ^{a,b,c}	5.10 \pm 0.15 ^{a,b,c}	596 \pm 13 ^{a,b}
Umb50+Rad	4.64 \pm 0.14 ^{a,b,c}	4.50 \pm 0.05 ^{a,b,c}	4.40 \pm 0.17 ^{a,b,c}	495 \pm 16 ^{a,b,c}
Umb100+Rad	7.57 \pm 0.23 ^{b,c,d}	4.97 \pm 0.01 ^{b,c,d}	3.83 \pm 0.08 ^{b,c,d}	469 \pm 12 ^{a,b,c,d}

Data are presented as means \pm SD (n=7). ^{a,b,c,d} The groups in the same column with different letters are statistically significant ($p < 0,05$). Abbreviation used: Rad: Radiation, Umb25: 25 mg/kg Umbelliferone, Umb50: 50 mg/kg Umbelliferone; Umb100: 100 mg/kg Umbelliferone

Many researchers are currently working on the development of new methods in cancer treatment. But, as of today, radiotherapy is one of the most effective and preferred methods in cancer treatment. Unfortunately, although the number of patients treated with this method is increasing day by day, the side effects of the method have not been reduced [31,32]. In a clinical application, ionizing radiation such as gamma rays or X-rays are frequently preferred. However,

The type and dose of radiation have an important role in the development of cardiotoxicity seen with radiation [33].

It has been demonstrated that exposure to ionizing radiation causes oxidative stress by increases ROS production, reduces antioxidant capacity, and inducing apoptosis [34, 35]. The main impacts of oxidative stress on cardiotoxicity induced by radiation involve several kinds of molecular pathways and oxidative damage to organic macromolecules such as proteins, lipids, and DNA. Excessive production of ROS also contributes to this impact. [31, 33]. Many of these possible effects have been ameliorated by the presence of different antioxidants, both enzymatic and non-enzymatic, including GSH-Px, SOD, vitamin E, melatonin and zinc [35]. The TOS is frequently included in the set of parameters used to characterize cellular stress responses [36]. From our experimental data, we found that the level of TOS in rat heart tissues increased significantly with the application of irradiation. On the contrary, it was noticed that TAC levels decreased. This indicates that irradiation increases oxidative stress in rat heart tissue and that this stress depletes antioxidant stores. In the current study, high dose of umbelliferone pretreatment increased TAC levels through umbelliferone supplementation, which is important for the redox modulation of heart tissue after high-dose radiation exposure. Considering the data, the results of our study clearly demonstrate that umbelliferone has a radioprotective effect on the rat heart by decreasing the formation of reactive oxygen species

An essential intermediate and second messenger such as interleukin-1 (IL-1) and tumor necrosis factor (TNF) are formed by irradiation-induced ROS [37]. Multifunctional proinflammatory cytokine TNF- α is primarily created by activated mononuclear phagocytes, however it can also be produced occasionally by T lymphocytes, smooth muscle cells, and activated polymorphonuclear endothelial cells [38]. The anti-inflammatory effect of umbelliferone detected by biochemically measuring expression of TNF- α levels on irradiation-induced cardiac tissue damage. There are some articles indicating that inflammation occurs after irradiation applied to rat heart tissue [39,40]. The results of our study are similar to those of these studies, and there was a significant increase in TNF- α levels in the patient group of animals. However, pretreatment with high dose of umbelliferone prevented significant increases in TNF- α in cardiac muscle cells and markedly reduced inflammation induced by acute irradiation. TNF- α and other cytokines promote inflammation not only through the recruitment of white blood cells but also through the activation of NF- κ B. [41]. The inhibition of TLR/NF- κ B signaling during myocardial ischemia is believed to be connected to umbelliferone's radioprotective function [42]. We attempted to demonstrate in this experimental investigation that umbelliferone, in addition to its antioxidant properties, plays an important role in the inflammatory response in irradiation-induced heart damage.

Strong blood vessel constrictor Thromboxane A₂ (TxA₂) has been linked to the etiology of a number of cardiovascular disorders. The half-life of TxA₂ is very short and therefore is rapidly metabolized to form the relatively stable but inactive TXB₂ [38, 43]. In this work, the concentration of TXB₂ level was measured to reflect the quantity of TxA₂. In the current investigation, it was indicated that, in contrast to the control values, TXB₂ levels were considerably enhanced following acute radiation exposure. On the other hand, umbelliferone injection dramatically reduces the rising radiation-mediated TXB₂ levels in rats. This finding

suggested that radiation exposure causes the secretion of pro-inflammatory cytokines and may reduce vascular damage in the heart tissue. This finding could point to the potential of umbelliferone as a novel endovascular treatment for heart damage.

Evaluation of histopathological changes

Histological examinations were performed on cardiac tissue from irradiated rats using different staining techniques, and examples of result are given in Figs. 1, 2 and 3. Firstly, H&E staining results showed that the heart tissues of the control group rats had a normal morphology and appearance. In the radiated patient groups, there were more light stained and necrotic areas throughout the cardiac muscle tissue. This is an indication of weakened cardiac muscle tissue. The presence of cylindrical shaped cell nuclei, oedema, congestion and infiltration were among other important findings. Severe degeneration was also observed around the vessels, On the opposite, in the Rad+UMB100 group, the heart tissue had a well-preserved appearance and shape. The pathological changes, such as the presence of necrotic areas, congestion and edema, were observed less frequently. The results in UMB25 and UMB50 groups were not given because they were similar to the patient group (Fig 1).

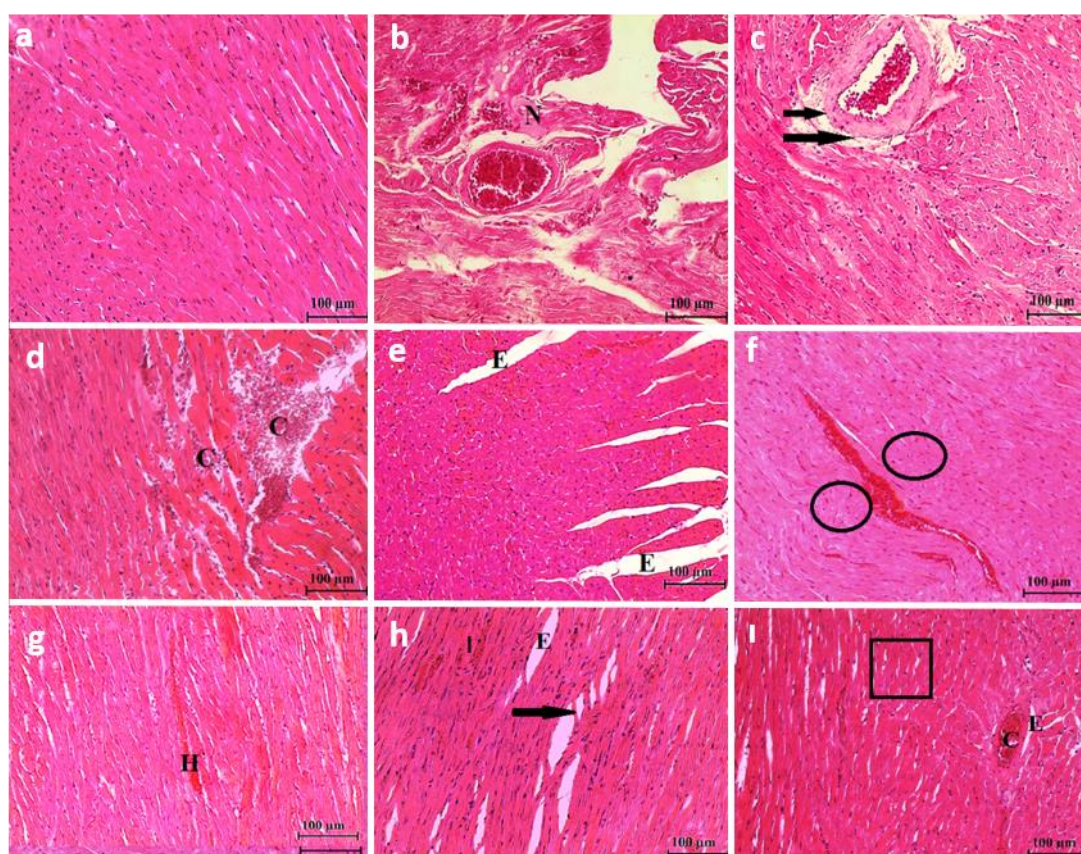


Fig. 1. Heart tissue section. **a)** The control group had normal architecture; The heart tissue of Rad group was shown a severe damage in figure b-h. **C;** Congestion, **N;** Nekrosis, **E;** Edema, **H;** Haemorrhage, **I;** Infiltration, **double black arrows;** Artery wall damage, **black arrows;** Reduced edema area, **Circle;** Apoptotic cells, **Frame;** Vacuolization **i)** Slight renal injury in group given umbelliferone (100 mg/kg) before irradiated,. (H&E), Bar: 100 µm

According to the PAS staining results, the presence of light stained areas and a decrease in glycogen content were observed in rat heart tissues exposed with radiation compared to the control group. PAS staining also revealed edema and vessel wall degeneration, which were present in H&E staining (Fig 2).

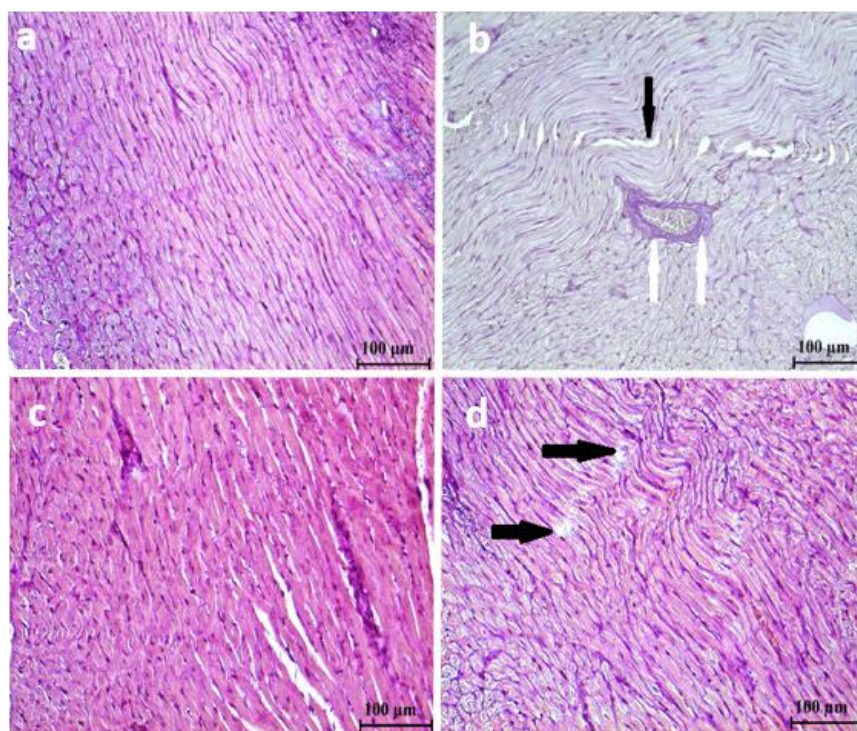


Fig. 2. Heart tissue section staining with PAS. **a)** The control group had normal architecture. **b)** Reduced glycogen content in the irradiated group. **Black arrow;** Muscle cell degeneration, **White arrow;** Intense PAS-positive staining around the vessel. (PAS), Bar: 100 µm.

With Congo red staining method, several histopathologic changes such as marked protein accumulation was observed in cardiac muscle cells and vascular endothelium. However, this was not observed in the UMB100-treated patient groups and histological results were similar to the control group (Fig 3).

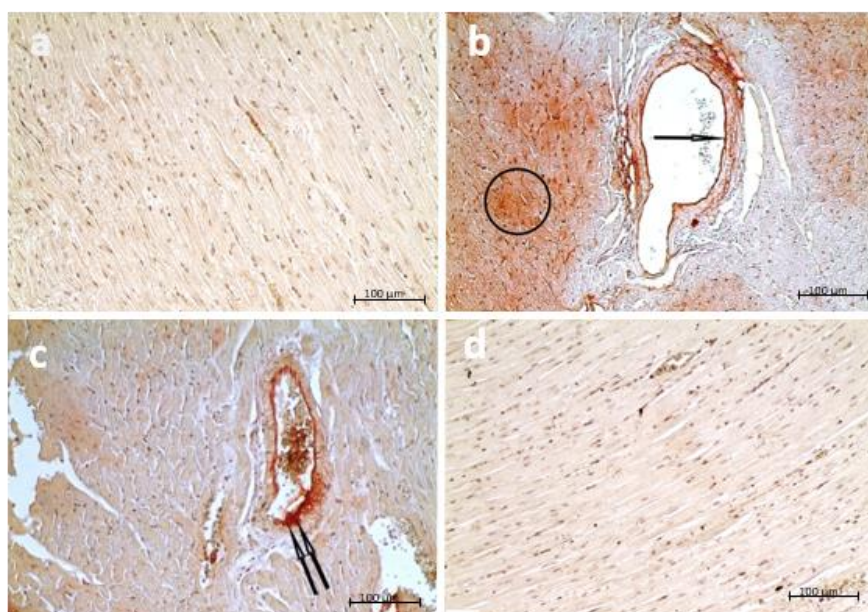


Fig 3. **a)** The control group had normal architecture. **b and c)** The amyloid aggregations in heart tissue (Circle) and vascular area (Arrow) **d)** Normal histological appearance of kidney in group given umbelliferone before irradiated. (Congo red), Bar: 100 µm.

In order to provide more accurate and clear evidence of histopathological findings in rat heart tissue, a semi-quantitative scoring system was performed and the results are presented in Table 2. As a result of radiation exposure, congestion, inflammation, haemorrhage and apoptotic cells increased in myocardial tissue and this result was statistically significant ($p < 0.05$). Whereas in the Umb100 pretreated group, pathological conditions could be restored.

Table 2. Comparison of histomorphologic scores between groups in heart tissue

Groups	Congestion	Infiltration	Haemorrhage	Apoptosis
Control	0,00±0,00	0,00±0,00	0,00±0,00	0,00±0,00
Rad	5,49±0,50 ^a	4,81±0,62 ^a	4,50±0,91 ^a	4,86±0,64 ^a
Umb25	0,00±0,00 ^b	0,00±0,00 ^b	0,00±0,00 ^b	0,00±0,00 ^b
Umb50	0,00±0,00 ^b	0,00±0,00 ^b	0,00±0,00 ^b	0,00±0,00 ^b
Umb100	0,00±0,00 ^b	0,00±0,00 ^b	0,00±0,00 ^b	0,00±0,00 ^b
Umb25 +Rad	3,96±0,34 ^{a,b}	4,69±0,47 ^{a,b}	4,43±0,73 ^{a,b}	4,72±0,52 ^{a,b}
Umb50+Rad	3,84±0,41 ^{a,b}	3,00±0,26 ^{a,b,c}	1,80±0,44 ^{a,b,c}	1,70±0,40 ^{a,b,c}
Umb100+Rad	1,41±0,19 ^{a,b,c}	1,60±0,11 ^{a,b,c}	1,57±0,21 ^{a,b,c}	1,92±0,24 ^{a,b,c}

Data are presented as means ± SD (n=7). ^{a,b,c,d} The groups in the same column with different letters are statistically significant (p< 0,05). Abbreviation used: Rad: Radiation, Umb25: 25 mg/kg Umbelliferone, Umb50: 50 mg/kg Umbelliferone; Umb100: 100 mg/kg Umbelliferone

Cardiac dysfunction may result from radiation-induced cardiac fibrosis and remodeling [9]. Our pathological findings demonstrated numerous tissue damage such as widespread interstitial edema, vacuolization, degenerations in arteries, widespread hemorrhagic formations, degenerations in contraction bands, congestion in large and small capillaries, muscle fiber degenerations, intense infiltration areas, decrease in glycogen content in muscle cells, amyloid accumulations in the lumens of vessels and between muscle fibers. In line with our result, El-Benhawy et al., (2021) found that, radiation exposure resulted in irregular longitudinal cardiac muscle fibers with areas of destructive and necrotic myocytes, interstitial mononuclear cellular infiltration, dilated congested blood vessels and dilated spaces between the cardiac muscle fibers in heart tissue [44]. Also, with the work done by Sarhan and Naoum who showed distorted cardiac muscle fibres of the irradiated rats with deeply stained nuclei (pyknotic) and highly thickened and elongated arterial Wall [45].

In addition to all the findings, Hemnani and Parihar (1998) reported that the production of superoxide anions and their derivatives, which cause peroxidation of lipids in cell membranes, is responsible for the radiation-induced cardiotoxicity mechanism [46]. Damaged cardiac tissue observed in the present study may be due to increased oxidative stress. Radiation-induced

histopathological changes in rat heart tissue are significantly attenuated by pretreatment with umbelliferone.

Conclusion

As a result, Current study reflects new and beneficial evidence about the role of umbelliferone against heart injury before radiation exposure. Umbelliferone has a beneficial role in reducing oxidative stress and cardio-toxicity induced by radiation exposure. Moreover, It has also been shown to have a protective effect on biochemical, inflammation and pathological parameters. Researchers should focus more on the development of new therapeutic agents for patients harmed by IR exposure during radiotherapy.

Ethics in Publishing

All experimental procedures were performed according to approval of the Institutional Ethical Committee for Animal Care and Use at Atatürk University, Erzurum, Turkey (Code number: 263, 26.12.2019B.30.2.ATA.0.23.85-11)

Author Contributions

ND and FG were responsible for the design and execution of the experiments. FG and SC performed data analysis, drafting and editing.

Acknowledgements

No financial support has been provided for the carrying out of this study. There is no conflict of interest regarding the publication of this paper.

References

- [1] <https://www.who.int/news-room/fact-sheets/detail/the-top-10-causes-of-death>, 16.09.2024
- [2] Pilleron, S., Sarfati, D., Janssen-Heijnen, M., Vignat, J., Ferlay, J., Bray, F., & Soerjomataram, I. (2019) Global cancer incidence in older adults, 2012 and 2035: a population-based study. *International Journal of Cancer*, 144(1), 49-58.
- [3] Simcock, R., Fallowfield, L., Monson, K., Solis-Trapala, I., Parlour, L., Langridge, C., Jenkins, V. Aris. (2013) A Randomised Trial of Acupuncture V Oral Care Sessions in Patients with Chronic Xerostomia Following Treatment of Head and Neck Cancer. *Annual Oncology*, 24 (3), 776–783.
- [4] Konak, M., Cincik, H., Erkul, E., Kucukodaci, Z., Gungor, A., Ozdemir, S., Cekin, E., Arisan, V., Mutluoglu, M., Salihoglu, M. (2016) The Protective Effects of Different Treatments on Rat Salivary Glands after Radiotherapy. *European Archives of Oto-Rhino-Laryngology*, 273 (12), 4501–4506.
- [5] Huang, Y., Zhang, W., Yu, F., Gao F. (2017) The Cellular and Molecular Mechanism of Radiation-Induced Lung Injury. *Medical Science Monitor*, 15(23), 3446-3450.

- [6] Azmoonfar, R., Khosravi, H., Rafieemehr, H., Mirzaei, F., Dastan, D., Ghiasvand, M. R., Khorshidi, L., Pashaki, A. S. (2023) Radioprotective effect of *Malva sylvestris* L. against radiation-induced liver, kidney and intestine damages in rat: A histopathological study. *Biochemistry and Biophysics Reports*, 34, 101455.
- [7] Aras, S., Efendioğlu, M., Wulamujiang, A., Ozkanli, S. S., Keleş, M. S., Tanzer, İ.O. (2021) Radioprotective effect of melatonin against radiotherapy-induced cerebral cortex and cerebellum damage in rat. *International Journal of Radiation Biology*, 97(3), 348-355.
- [8] Kaplan, M., Demir, E., Yavuz, F., Kaplan, G. I., Taysi, M. R., Taysi, S., Sucu, M.M. (2022) Radioprotective effect of *nigella sativa* oil on heart tissues of rats exposed to irradiation. *International Journal of Cardiovascular Sciences*, 35(2), 214-219.
- [9] Zhang, J., He, X., Bai, X., Sun, Y., Jiang, P., Wang, X., Li, W., Zhang, Y. (2020) Protective effect of trimetazidine in radiation-induced cardiac fibrosis in mice. *Journal of Radiation Research*, 61(5), 657-665.
- [10] Adaramoye, O., Okiti, O., Farombi, E. (2011) Dried fruit extract from *Xylopiiæthiopica* (Annonaceae) protects Wistar albino rats from adverse effects of whole body radiation. *Experimental and Toxicologic Pathology*, 63 (7-8), 635-39.
- [11] Şener, G., Kabasakal, L., Atasoy, B.M., Erzik, C., Velioglu-Öğünç, A, Çetinel, Ş., Contuk, G., Gedik, N., Yeğen, B.Ç. (2006) Propylthiouracil-induced hypothyroidism protects ionizing radiation-induced multiple organ damage in rats. *Journal of Endocrinology*, 189 (2), 257-62.
- [12] Benzie, I.F. (2000) Evolution of antioxidant defence mechanisms. *European Journal of Nutrition*, 39, 53-61.
- [13] McCord, J.M. (2000) The evolution of free radicals and oxidative stress. *The American Journal of Medicine*, 108(8), 652-659.
- [14] Ames, B.N. (2001) DNA damage from micronutrient deficiencies is likely to be a major cause of cancer. *Mutation Research/Fundamental And Molecular Mechanisms Of Mutagenesis*, 475(1-2), 7-20.
- [15] Kasaian, J., Mohammadi, A. (2018) Biological activities of farnesiferol C: a review. *Journal of Asian Natural Products Research*, 20 (1), 27-35.
- [16] Garg, S.S., Gupta, J., Sharma, S., Sahu, D. (2020) An insight into the therapeutic applications of coumarin compounds and their mechanisms of action. *European Journal of Pharmaceutical Sciences*, 152, 105424.
- [17] Küpeli Akkol, E., Genç, Y., Karpuz, B., Sobarzo-Sánchez, E., & Capasso, R. (2020) Coumarins and coumarin-related compounds in pharmacotherapy of cancer. *Cancers*, 12 (7), 1959.
- [18] Mazimba, O. (2017) Umbelliferone: Sources, chemistry and bioactivities review. *Bulletin of Faculty of Pharmacy, Cairo University*, 55 (2), 223-232.
- [19] Althunibat, O. Y., Abduh, M. S., Abukhalil, M. H., Aladaileh, S. H., Hanieh, H., & Mahmoud, A. M. (2022) Umbelliferone prevents isoproterenol-induced myocardial injury by

upregulating Nrf2/HO-1 signaling, and attenuating oxidative stress, inflammation, and cell death in rats. *Biomedicine & Pharmacotherapy*, 149, 112900.

- [20] Dikmen, M. (2016) Antiproliferative and apoptotic effects of aprepitant on human glioblastoma U87MG cells. *Marmara Pharmaceutical Journal*, 21(1), 156-164.
- [21] Mahmoud, A. M., Hozayen, W. G., Hasan, I. H., Shaban, E., & Bin-Jumah, M. (2019) Umbelliferone ameliorates CCl₄-induced liver fibrosis in rats by upregulating PPAR γ and attenuating oxidative stress, inflammation, and TGF- β 1/Smad3 signaling. *Inflammation*, 42, 1103-1116.
- [22] Alotaibi, M. F., Al-Joufi, F., Abou Seif, H. S., Alzoghaibi, M. A., Djouhri, L., Ahmeda, A. F., Mahmoud, A. M. (2023) Umbelliferone Inhibits Spermatogenic Defects and Testicular Injury in Lead-Intoxicated Rats by Suppressing Oxidative Stress and Inflammation, and Improving Nrf2/HO-1 Signaling [Retraction]. *Drug Design, Development and Therapy*, 17, 1153-1154.
- [23] Wang, H.Q., Wang, S.S., Chiufai, K., Wang, Q., Cheng, X.L. (2019) Umbelliferone ameliorates renal function in diabetic nephropathy rats through regulating inflammation and TLR/NF-kappaB pathway. *Chinese Journal of Natural Medicine*, 17(5), 346-354.
- [24] Council, N.R. (2011) National Institutes of Health guide for the care and use of laboratory animals.
- [25] Cruz, L. F., De-Figueiredo, G.F., Pedro, L.P., Amorin, Y.M., Andrade, J.T., Passos, T. F., Rodrigues, F. F., Souza, I.L.A., Gonçalves, T.P.R., Dos Santos Lima, L.A.R., Ferreira, J.M.S., Freitas Araújo, M. G. (2020) Umbelliferone (7-hydroxycoumarin): A non-toxic antidiarrheal and antiulcerogenic coumarin. *Biomedicine & Pharmacotherapy*, 129, 110432.
- [26] Sproull, M., Kramp, T., Tandle, A., Shankavaram, U., Camphausen, K. (2017) Multivariate analysis of radiation responsive proteins to predict radiation exposure in total-body irradiation and partial-body irradiation models. *Radiation Research*, 187 (2), 251-258.
- [27] Jacobs, E. R., Narayanan, J., Fish, B. L., Gao, F., Harmann, L. M., Bergom, C., Tracy, G., Jennifer, S., Medhora, M. (2019) Cardiac remodeling and reversible pulmonary hypertension during pneumonitis in rats after 13-Gy partial-body irradiation with minimal bone marrow sparing: effect of lisinopril. *Health physics*, 116 (4), 558-565.
- [28] Erel, O. (2004) A novel automated method to measure total antioxidant response against potent free radical reactions. *Clinical Biochemistry*, 37 (2), 112-119.
- [29] Erel, O. (2005) A new automated colorimetric method for measuring total oxidant status. *Clinical Biochemistry*, 38 (12), 1103-1111.
- [30] Akyazi, I., Eraslan, E., Gülçubuk, A., Ekiz, E. E., Çıraklı, Z. L., Haktanir, D., Bala D.A., Özkurt, M., Matur, E., Özcan, M. (2013) Long-term aspirin pretreatment in the prevention of cerulein-induced acute pancreatitis in rats. *World Journal of Gastroenterology*, 19 (19), 2894-2903.

- [31] Ping, Z., Peng, Y., Lang, H., Xinyong, C., Zhiyi, Z., Xiaocheng, W., Hong, Z., Liang, S. (2020) Oxidative stress in radiation-induced cardiotoxicity. *Oxidative Medicine and Cellular Longevity*, 2020(1), 3579143.
- [32] Armanious, M.A., Mohammadi, H., Khodor, S., Oliver, D.E., Johnstone, P.A., Fradley, M.G. (2018) Cardiovascular effects of radiation therapy. *Current Problems in Cancer*, 42 (4), 433–442.
- [33] Puukila, S., Lemon, J. A., Lees, S. J., Tai, T.C., Boreham, D.R., Khaper, N. (2017) Impact of ionizing radiation on the cardiovascular system: a review. *Radiation Research*, 188 (4.2), 539–546.
- [34] Vona, R., Gambardella, L., Cittadini, C., Straface, E., Pietraforte, D. (2019) Biomarkers of oxidative stress in metabolic syndrome and associated diseases. *Oxidative Medicine and Cellular Longevity*, 1, 8267234,
- [35] Karlioglu, I., Ertekin, M. V., Kocer, I., Taysi, S., Sezen, O., Gepdiremen, A., & Balci, E. (2004) Protective role of intramuscularly administered vitamin E on the levels of lipid peroxidation and the activities of antioxidant enzymes in the lens of rats made cataractous with gamma-irradiation. *European Journal of Ophthalmology*, 14(6), 478-485.
- [36] Dilber, B., Akbulut, U. E., Alver, A., Mentese, A., Kolaylı, C. C., & Cansu, A. (2021) Plasma and erythrocyte oxidative stress markers in children with frequent breath-holding spells. *Klinische Pädiatrie*, 233 (04), 173-180.
- [37] Elahi, M.M., Kong, Y.X., Matata, B.M. (2009) Oxidative stress as a mediator of cardiovascular disease. *Oxidative Medicine and Cellular Longevity*, 2(5), 259-269.
- [38] Zhang, C., Chen, H., Xie, H. H., Shu, H., Yuan, W. J., & Su, D. F. (2003) Inflammation is involved in the organ damage induced by sinoaortic denervation in rats. *Journal of Hypertension*, 21(11), 2141-2148.
- [39] Luo, N., Zhu, W., Li, X., Fu, M., Peng, X., Yang, F., Zhang, Y., Yin, H., Yang, C., Zhao, J., Yuan, X., Hu, G. (2022) Impact of Gut Microbiota on Radiation-Associated Cognitive Dysfunction and Neuroinflammation in Mice. *Radiation Research*, 197 (4), 350-364.
- [40] Guo, D.B., Zhu, X.Q., Li, Q.Q., Li, G.M., Ruan, G.P., Pang, R.Q., Chen, Y.H., Wang, Q., Wang, J.X., Liu, J.F., Chen, Q., Pan, X.H. (2018) Efficacy and mechanisms underlying the effects of allogeneic umbilical cord mesenchymal stem cell transplantation on acute radiation injury in tree shrews. *Cytotechnology*, 70 (5), 1447-1468.
- [41] Brasier, A. R. (2010) The nuclear factor- κ B–interleukin-6 signalling pathway mediating vascular inflammation. *Cardiovascular Research*, 86 (2), 211-218.
- [42] Gan, J., Qian, W., Lin, S. (2018) Umbelliferone alleviates myocardial ischemia: the role of inflammation and apoptosis. *Inflammation*, 41, 464-473.
- [43] Danborn, A.M., Monnet, P. L., Orr, A.J. (2020) TxA2 Receptor Antagonist (SQ29548) attenuates Endothelium-Independent recovery from Thromboxane A2 Contraction of Isolated Rabbit Aorta. *Journal of African Association of Physiological Sciences*, 8(1), 8-15.

- [44] El-Benhawy, S. A., Morsi, M. I., El-Tahan, R. A., Matar, N. A., & Ehmaida, H. M. (2021) Radioprotective effect of thymoquinone in X-irradiated rats. *Asian Pacific Journal of Cancer Prevention*, 22(9), 3005.
- [45] Sarhan, H., Naoum, L. (2020) Protective role of royal jelly against gamma radiation induced oxidative stress, cardio-toxicity and organ dysfunctions in male rats. *The Egyptian Journal of Hospital Medicine*, 78(1), 62-67.
- [46] Hemnani, T., Parihar, M.S. (1998) Reactive oxygen species and oxidative DNA damage. *Indian Journal of Physiology and Pharmacology*, 42, 440-452.

Modeling, Analysis, and Comparison of Rectangular Waveguide Structures Having Glide Symmetrical Step Discontinuity with Periodic Dielectric Loading

Agâh Oktay ERTAY^{1*}

¹Erzincan Binali Yıldırım University, Faculty of Engineering and Architecture, Department of Electrical and Electronics Engineering, 24002, Erzincan, Türkiye

Received: 09/10/2024, Revised: 21/11/2024, Accepted: 28/11/2024, Published: 31/12/2024

Abstract

This paper presents an analysis of the dispersion and $|S_{21}|$ frequency characteristics of three periodic structures constructed in rectangular waveguides. Unit cells with dielectric-loaded step discontinuities based on double steps, symmetric double steps, and glide-symmetric double steps were investigated using full-wave electromagnetic simulation software. All dispersion diagram results obtained from the three different models are compared to each other by fixing the period of the unit cell ($p = 13.68mm$) for each periodic structure. $|S_{21}|$ frequency characteristics of the first propagating mode are examined for finite implementations of all considered structures. The transmission characteristics of different numbers of periodic arrangements of each periodic unit cell were investigated. Then, the effect of geometric variations, including glide symmetry, on the transmission characteristics is investigated by keeping the number of unit cells constant ($N = 10$). Furthermore, the filter performance characteristics of the proposed structure are compared with those of the reported studies in the open literature.

Keywords: dispersion analysis, glide symmetry, periodic structures, rectangular waveguides, step discontinuity

Periyodik Dielektrik Yüklü Kayma Simetrik Adım Süreksizliğine Sahip Dikdörtgen Dalga Kılavuzu Yapılarının Modellenmesi, Analizi ve Karşılaştırılması

Öz

Bu makale, dikdörtgen dalga kılavuzlarında oluşturulan üç periyodik yapının dispersiyon ve $|S_{21}|$ frekans karakteristiklerinin analizini sunmaktadır. Çift adım, simetrik çift adım ve kayma-simetrik çift adıma dayalı dielektrik yüklü adım süreksizliğine sahip birim hücreler, tam dalga elektromanyetik benzetim yazılımı kullanılarak incelenmiştir. Üç farklı modelden elde edilen tüm dispersiyon diyagramı sonuçları, her periyodik yapı için birim hücrenin periyodunu sabitleyerek ($p = 13.68mm$) birbirleriyle karşılaştırılmıştır. Tüm dikkate alınan yapıların sonlu yapıları için ilk yayılan modun $|S_{21}|$ frekans karakteristikleri incelenmiştir. Her periyodik birim hücrenin farklı sayıdaki periyodik dizilimlerinin iletim karakteristikleri incelenmiştir. Sonra, birim hücre sayısı sabit tutularak ($N = 10$) kayma simetrisi de dâhil olmak üzere geometrik değişimlerin iletim karakteristikleri üzerindeki etkisi incelenmiştir. Ayrıca, önerilen yapının filtre performans özellikleri açık literatürde rapor edilen çalışmalarla karşılaştırılmıştır.

Anahtar Kelimeler: adım süreksizliği, dikdörtgen dalga kılavuzları, dispersiyon analizi, kayma simetrisi, periyodik yapılar

1. Introduction

The investigation of electromagnetic wave propagation and its effects on periodic structures is a current and interesting research area [1]. By appropriately selecting the dimensions of the geometries and medium properties in periodic structures, passband/stopband regions can be obtained. These properties are widely exploited in waveguides [2, 3], substrate-integrated waveguides [4], microstrip [5] type filters, and leaky wave antennas [6]. In recent years, the investigation of the dispersion characteristics of unit cell designs of dielectric-loaded metallic rectangular [7] and corrugated parallel-plate waveguide [8–10] periodic structures has become a popular topic. Higher-symmetry unit cell modeling of such structures is frequently preferred due to its features, which provide benefits in applications such as low dispersion, wider stopbands, and passbands [11–13].

In dielectric-loaded rectangular waveguides, step discontinuity structures are used for purposes such as examining field distribution changes [14] and obtaining passband/stopband regions [15, 16]. It is well known that the use of multiple-step discontinuities in rectangular waveguide unit cells creates deeper stopbands and passband fluctuations when the structure is connected in a finite number of cascades [15, 16]. However, to the best of our knowledge, the modeling and analysis of the unit cell structure with glide-symmetric step discontinuity in dielectric-loaded rectangular waveguides has not been investigated. To fill this gap in the literature, systematic modeling and analysis results are presented in this study. First, a unit cell with classical step discontinuity is modeled. In the second stage, a second-step discontinuity is modeled in the opposite direction to the step discontinuity region of the model used in the first stage. In the final stage, the glide symmetry approach is applied to the model created in the second stage. Dispersion diagrams of the structures are obtained, and the passband/stopband regions of periodic structures are analyzed. A finite periodic implementation is performed for all models, and frequency characteristics are examined. The details of these modellings and the results are given in the following sections.

2. Material and Methods

In this section, the dispersion properties of the selected unit cell models will be analyzed.

2.1. Considered Unit Cell Geometries for the Analysis

A periodic structure with glide symmetry is a structure that is invariant under the translation of the half-period of the structure in the periodicity direction and mirroring with respect to the glide plane [9, 10]. Accordingly, the glide operator (G) for a periodic structure with a direction period p can be written as [17]:

$$G = \begin{cases} x \rightarrow -x \\ y \rightarrow y \\ z \rightarrow z + p/2 \end{cases} \quad (1)$$

Figure 1 shows the geometries of the investigated unit cell models. From Figure 1(a) to Figure 1(c), the step-by-step application of the glide symmetry operation (G) given in equation (1) in

a rectangular waveguide with step discontinuity is given. Figure 1(a) shows the rectangular waveguide unit cell structure with conventional step discontinuity, with examples from the literature [14-16]. Figure 1(b) shows the unit cell of the rectangular waveguide geometry with a symmetric double-step discontinuity [18]. Figure 1(c) shows the newly proposed rectangular waveguide unit cell with double-step discontinuity generated by glide symmetry. All models were homogeneously loaded with the same dielectric material. To obtain the dispersion diagrams of the unit cell models, the generalized scattering matrices of these structures were obtained using the CST Microwave Studio Frequency Domain Solver based on the Finite Element Method (FEM). All waveguides consist of metallic walls with a thickness of t as indicated in Figure 2. The interior of the structure is filled with a dielectric material with $\epsilon_r = 4.8$. The boundary conditions in x and y are assigned as electric ($E_t = 0$) since all side walls are metallic. All unit cell structures are excited by a waveguide port operating in 10 modes from the input and output reference planes. To find the Floquet modes and stop bands supported by each unit cell, the obtained generalized scattering matrix elements are substituted into the eigenvalue equation [3]:

$$\begin{bmatrix} I & -S_{11} \\ \mathbf{0} & -S_{12} \end{bmatrix} \begin{bmatrix} \mathbf{b}_1 \\ \mathbf{a}_1 \end{bmatrix} + \lambda \begin{bmatrix} -S_{12} & \mathbf{0} \\ -S_{22} & I \end{bmatrix} \begin{bmatrix} \mathbf{b}_1 \\ \mathbf{a}_1 \end{bmatrix} = \mathbf{0} \quad (2)$$

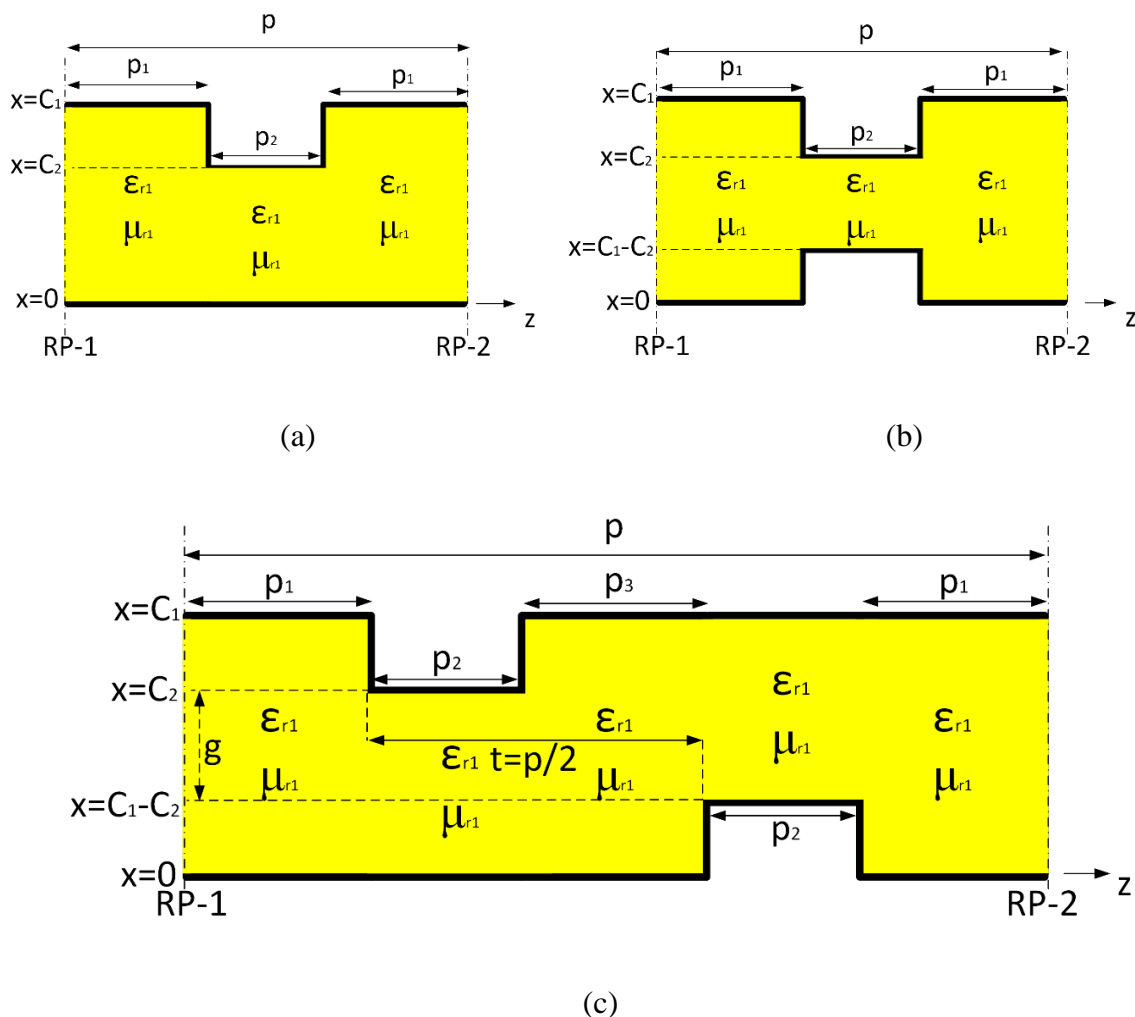


Figure 1. Unit cell of periodic rectangular waveguide with the following different geometries: (a) one step discontinuity with symmetric dielectric loading (conventional structure – 1 (CS - 1)) (b) Two symmetric step discontinuity with dielectric loading (conventional structure – 2 (CS - 2)) (c) glide symmetric step discontinuity with dielectric loading (proposed structure (PS)). p depicts the period of given unit cell geometries. μ_{r1} is taken as 1.

I , (S_{ii}, S_{ij}) and $(\mathbf{a}_1, \mathbf{b}_1)$ in Equation (2) denote the unit matrix, block S-matrix elements, and complex amplitudes incident and reflected from reference plane-1 (RP-1), respectively. For single Floquet mode propagation, eigenvalue λ is defined as $\lambda_{1,2} = e^{\pm j\theta}$, $\theta = \beta p \in 0, \pi$ where β is Floquet phase factor [3, 19]. With fine frequency scanning, the passband and stopband regions can be determined by finding whether there is at least one propagating mode corresponding to the eigenvalue pair at each step.

2.2. Dispersion Diagram Analysis

Figures 2-4 shows the first passband/stopband regions of dispersion diagrams of the unit cell geometries of CS-1, CS-2, and PS in Figure 1. There is a two-stage flow for obtaining these graphs. In the first stage, the investigated unit cells are simulated in CST using the simulation details given in the previous subsection. In the second stage, the dispersion diagrams of the unit cells are obtained by substituting the obtained generalized scattering matrices into Equation 2 and solving this equation. The parameters of all models are presented in Figure 1, and the values of these parameters are given in Figures 2-4. The period of each unit cell was kept constant at the same value to observe the effects of the modification of each stage and the glide symmetry on the dispersion diagrams and transmission characteristics. Despite the homogeneous dielectric loading, the step discontinuities in the cross-sections caused high-order mode interactions.

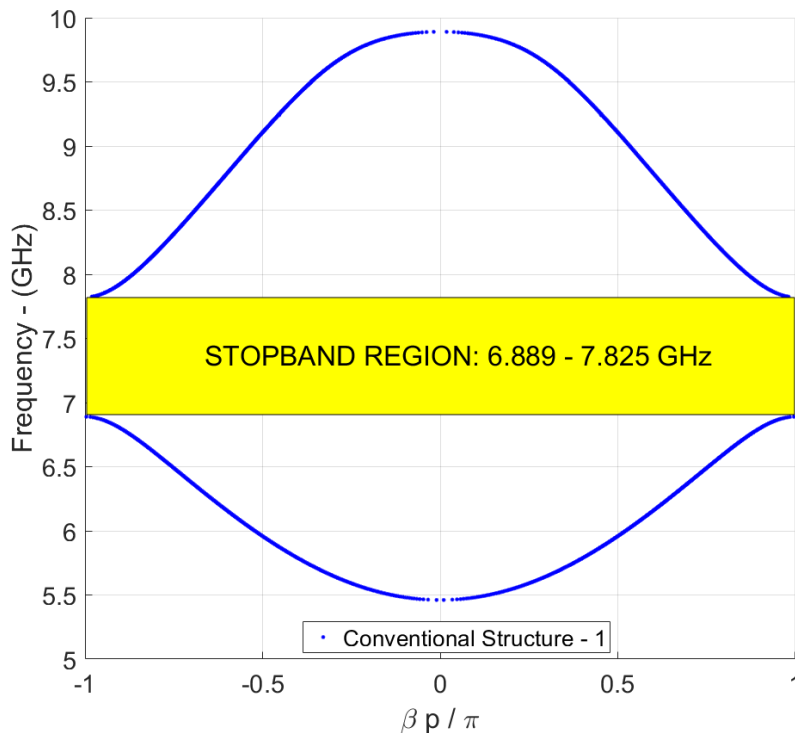


Figure 2. Dispersion diagram of conventional structure-1 given in Figure 1 (a) with the following parameters: $C_1 = 14.8\text{mm}$, $C_2 = 0.7C_1$, $p_1 = 0.416C_1$, $p_2 = 0.0925C_1$, $h = 0.5\text{mm}$, $t = 0.035\text{mm}$, $\epsilon_{r1} = 4.8$, $p = 2p_1 + p_2 = 0.9245C_1$. t and h are the thickness and the height (in the y -direction) of the rectangular waveguide walls, respectively.

To monitor these effects on the mode of the periodic structure, 10 excitation modes are considered sufficient. The first Floquet mode of CS-1 started at approximately 5.5 GHz and

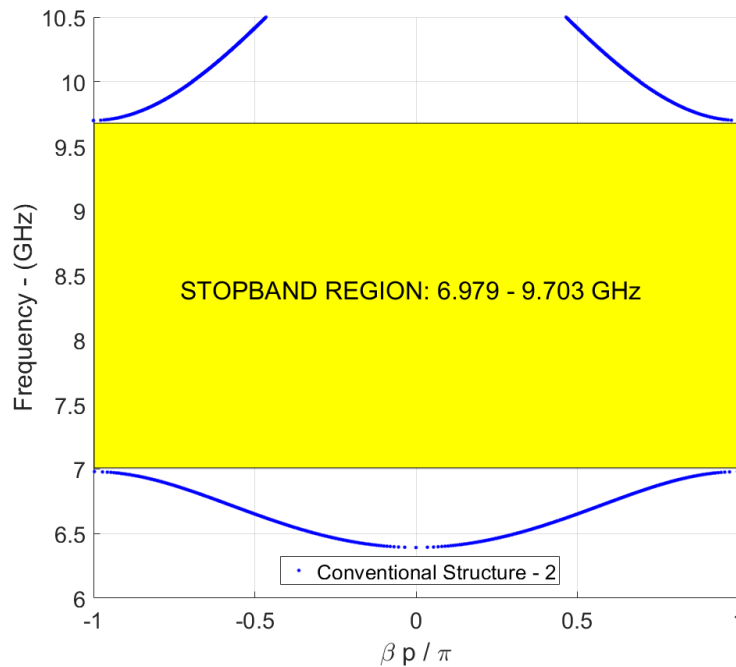


Figure 3. Dispersion diagram of conventional structure-2 given in Figure 1 (b) with the following parameters: $C_1 = 14.8\text{mm}$, $C_2 = 0.7C_1$, $p_1 = 0.416C_1$, $p_2 = 0.0925C_1$, $h = 0.5\text{mm}$, $t = 0.035\text{mm}$, $\epsilon_{r1} = 4.8$, $p = 2p_1 + p_2 = 0.9245C_1$.

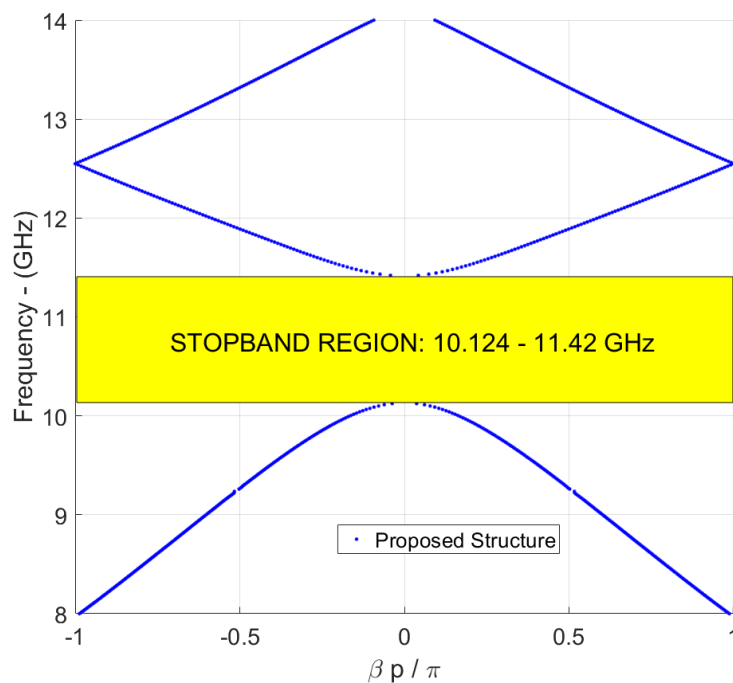
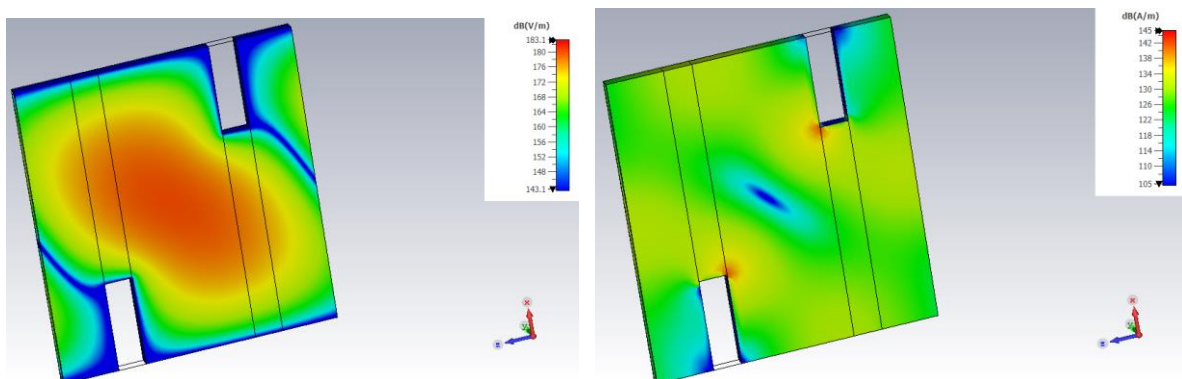
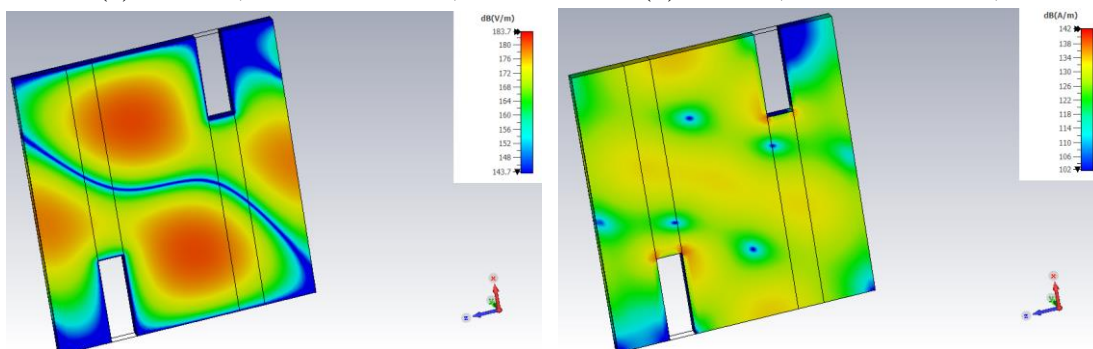


Figure 4. Dispersion diagram of proposed structure given in Figure 1 (c) with the following parameters: $C_1 = 14.8\text{mm}$, $C_2 = 0.7C_1$, $p_1 = 0.18541C_1$, $p_2 = 0.0925C_1$, $p_3 = 0.37C_1$, $h = 0.5\text{mm}$, $t = 0.035\text{mm}$, $\epsilon_{r1} = 4.8$, $p = 2p_1 + 2p_2 + p_3 = 0.9245C_1$.

ended at 6.889 GHz, and the first stopband of this periodic structure occurs at 6.889-7.825 GHz, as shown in Figure 2. Unlike CS-1, CS-2 has a symmetric step discontinuity, starting from $x = 0$ and extending to $(C1-C2)$ is formed in CS-2. The effect of this change on the dispersion diagram of the periodic structure is shown in Figure 3, where a wider stopband is slightly shifted to the upper frequency. Because of these modeling and simulations given in Figure 1(c), the dispersion diagram shown in Figure 4 can be obtained. Glide-symmetric modeling caused the stopband of the periodic structure to increase to higher frequencies and narrowed it with respect to CS-2. Figure 5 shows the electric and magnetic field distributions of two propagating Floquet modes obtained using the CST Eigenmode Solver. It is seen from Figure 5 that the first propagating mode is TE_{10} and the second mode is TE_{20} from the field patterns. In addition, it is observed in Figure 5 that in the electric and magnetic field distributions, one is mostly at maximum in the regions where the other is at minimum. In addition, changes in the cross-section of the unit cell change the cut-off frequencies of the propagating Floquet modes in the unit cell. In addition, the length of each waveguide region along the z -axis seen in Figure 5 is also very important in the formation of passband/stopband regions according to the guided wavelength of the waveguide in the relevant region [15, 16].



(a) E-field, The First Mode, 7.98GHz (b) H-field, The First Mode, 7.98GHz



(c) E-field, The Second Mode, 12.55GHz (d) H-field, The Second Mode 1, 12.55GHz

Figure 5. Electric and magnetic field distributions of propagating Floquet modes for different frequencies.

3. Results and Discussions

In this section, the frequency characteristics of various numbers of cascade-connected unit cells, whose dispersion properties were determined in Section 2, will be analyzed.

3.1. Finite Modeling of Periodic Dielectric Loading of Rectangular Waveguides with glide symmetric step discontinuity

To observe the bandstop or bandpass filter characteristics, simulations of all the studied models with a finite number of periodic arrays are given in Figures 6-8. First, the frequency characteristics of the first mode of $|S_{21}|$ of the 10 waveguide modes were plotted for all models. As it is well known, it is expected that as the periodic sequence increases, a stopband region very close to the stop band obtained in the dispersion diagram of the periodic structure is formed. In addition, a deeper level of suppression appears as the number of unit cells increases. However, increasing the number of unit cells increased the ripple levels in the passband. Figure 6 shows $|S_{21}|$ frequency characteristics of CS-1 for $N = 10$, $N = 15$, and $N = 20$, where N is the number of unit cells.

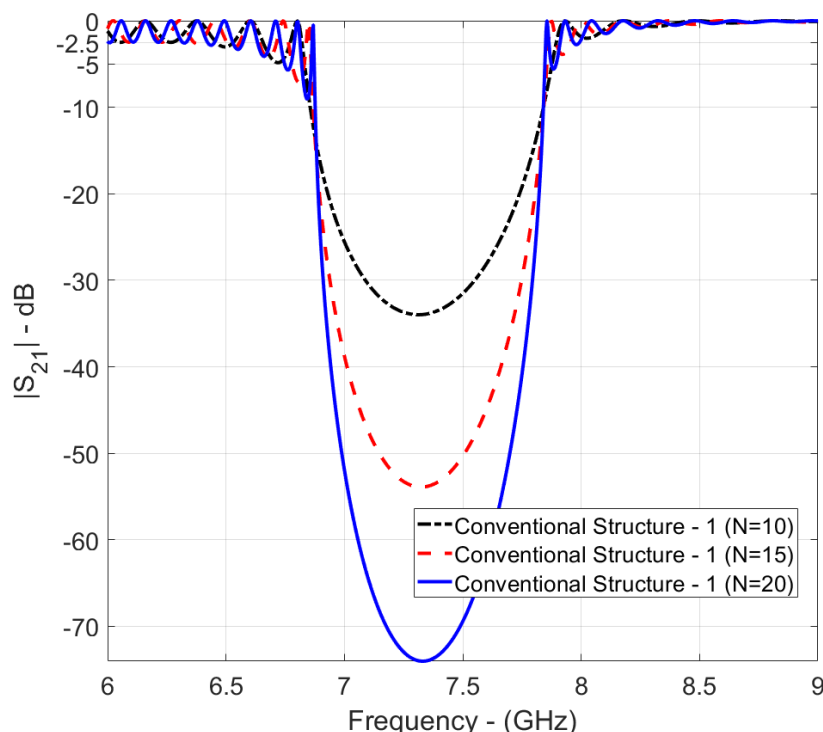


Figure 6. $|S_{21}|$ frequency characteristics of conventional structure - 1 given in Figure 1(a) with given parameters in Figure 2 for different cascaded scenarios.

Figures 7 and 8 show $|S_{21}|$ frequency characteristics of CS-2 and PS for $N = 3$, $N = 5$, $N = 7$, and $N = 10$, respectively. It can be clearly observed that the occurrence of symmetric step discontinuity (CS-2) leads to a wider and deeper stopband with fewer unit cells; however, this

leads to higher levels of fluctuations in the passband (close to -15dB). Switching from symmetric step discontinuity (CS-2) to glide symmetric step discontinuity (PS) with fewer unit cells results in a wider passband (7 – 10 GHz) and lower ripple levels (maximum -2.5 dB) in this passband, as shown in Figures 7 and 8. However, the stopband region has shifted, and the formation of a passband at higher frequencies is no longer valid. To compare the three models at the same dimensions, the number of unit cells was kept as high as possible to obtain a sufficiently deeper stopband.

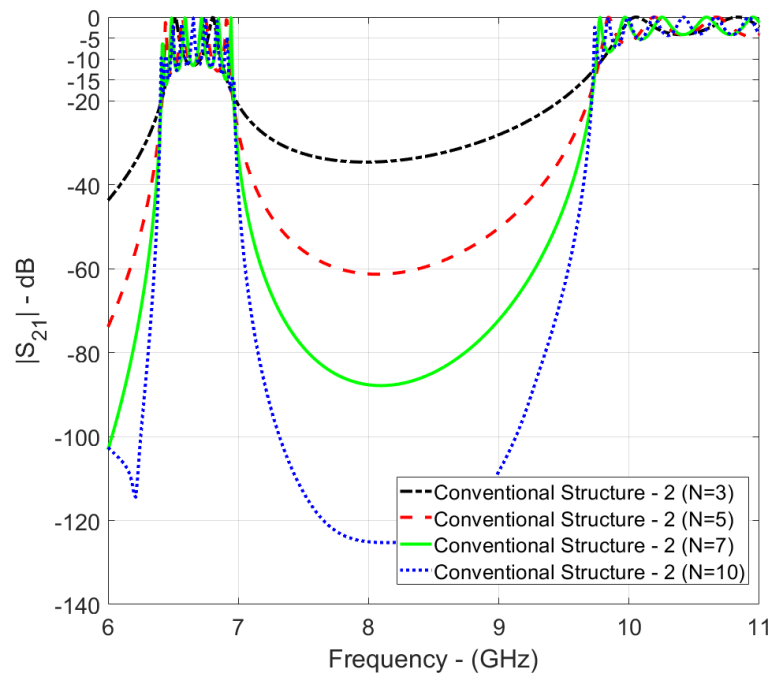


Figure 7. $|S_{21}|$ frequency characteristics of conventional structure - 2 given in Figure 1(b) with given parameters in Figure 3 for different cascaded scenarios.

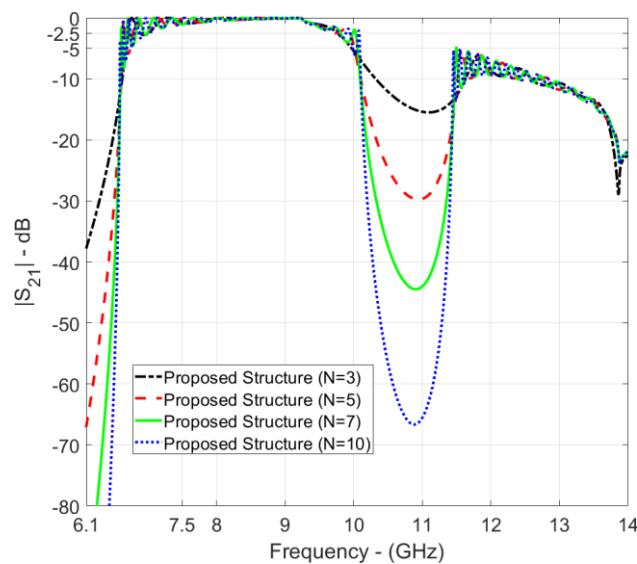
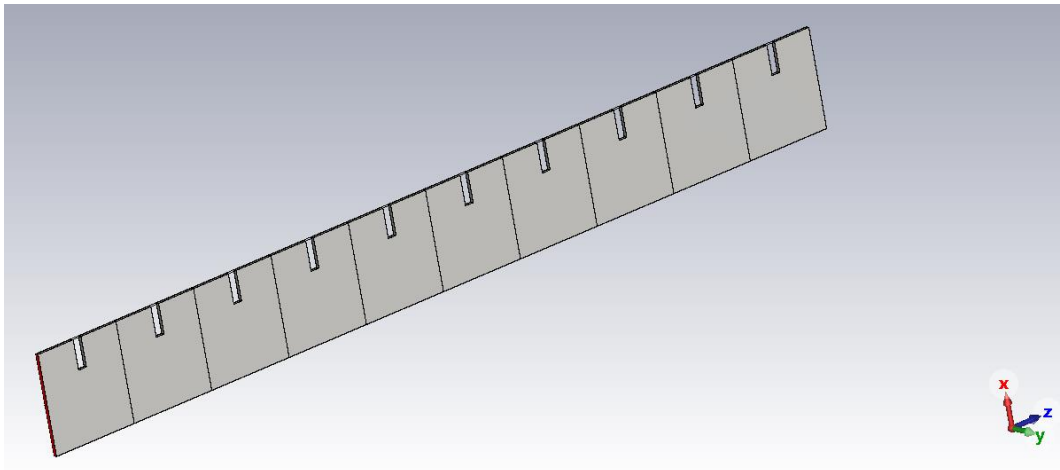


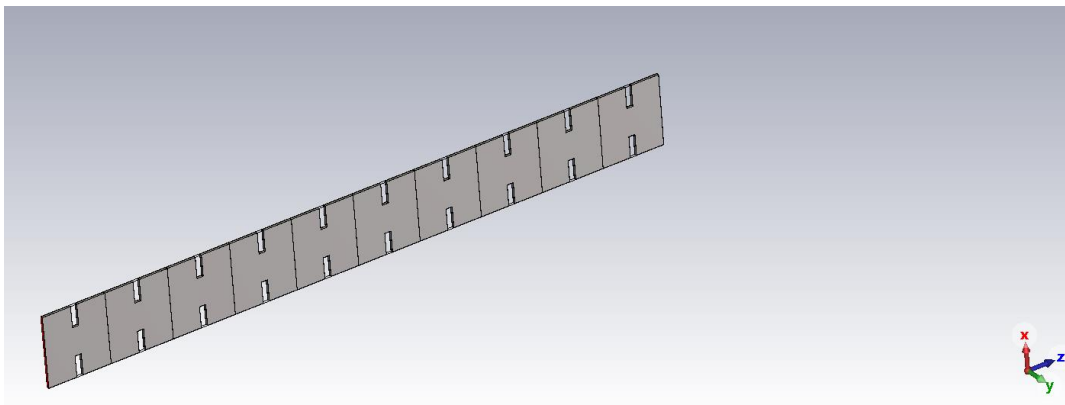
Figure 8. $|S_{21}|$ frequency characteristics and the proposed structure given in Figure 1(c) with given parameters in Figure 4 for different cascaded scenarios.

Modeling, Analysis, and Comparison of Rectangular Waveguide Structures Having Glide Symmetrical

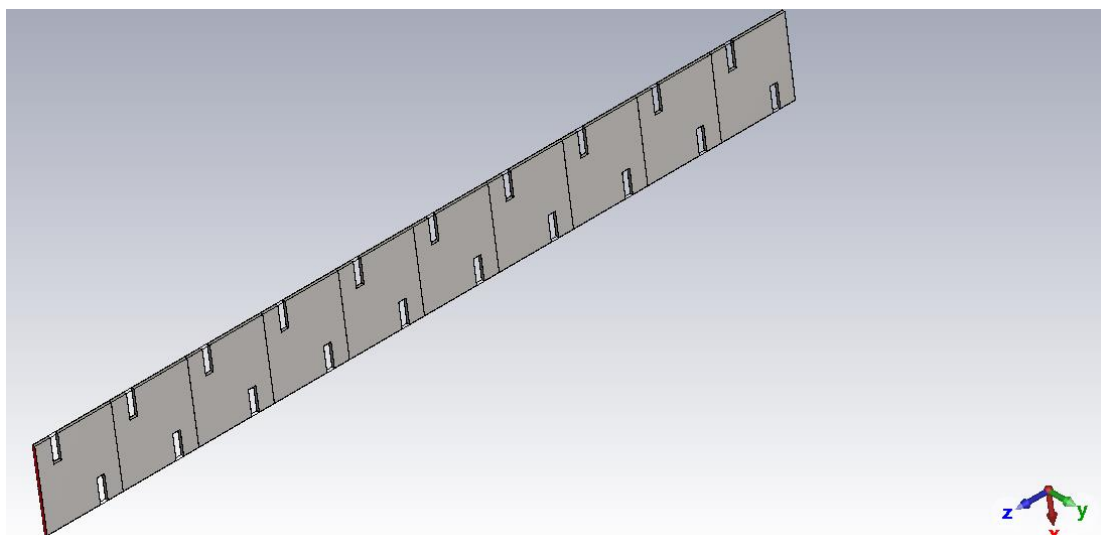
To compare and understand the frequency effects of different unit cell models called CS-1, CS-2, and PS, finite implementations of these structures for $N=10$ are carried out in CST Microwave Studio as shown in Figure 9. The parameter t is critical to understand the evaluation of the frequency response in the proposed structure. For this purpose, a parametric analysis showing the effect of the parameter t for $N=10$ is shown in Figure 10. In the curves ranging from $t=0$ to $t=p/2$, the passband in the range of 6.2 - 7.5 GHz and the fluctuations occurring there gradually decreased and reached very low levels. In addition, Figure 10 shows that in the



(a)



(b)



(c)

Figure 9. 3D view of cascaded-connected considered unit cells for $N=10$ in CST Microwave Studio.

same curves, the stopband between 7-9.8 GHz is replaced by a passband around 6.5-10 GHz. It is also possible to see in Figure 10 that the passband fluctuations gradually decrease at higher frequencies. It is clear from Figure 10 that this level of double step discontinuity given in this paper causes very high levels of fluctuations in the passband of the structure. In addition, gliding the one-step discontinuity region along the periodicity axis without changing the period of the unit cell reduces both the passband ripple levels. It also results in a wider passband and a shift of the stopband to higher frequencies.

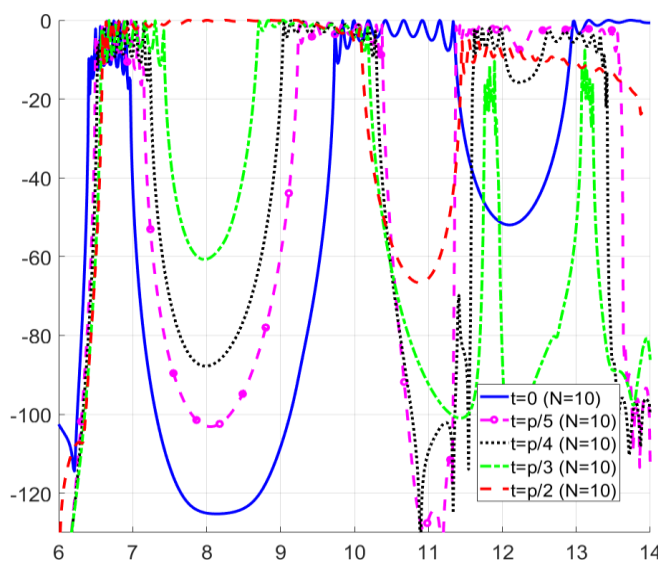


Figure 10. The effects of t parameters on the interested structure.

Accordingly, Figure 11 shows $|S_{21}|$ frequency characteristics of all three models for $N = 10$. According to Figure 11, the glide symmetric model allowed for a wider passband, as shown in Figure 11. In addition, the application of glide symmetry to the considered structure improved the fluctuation levels in the passband.

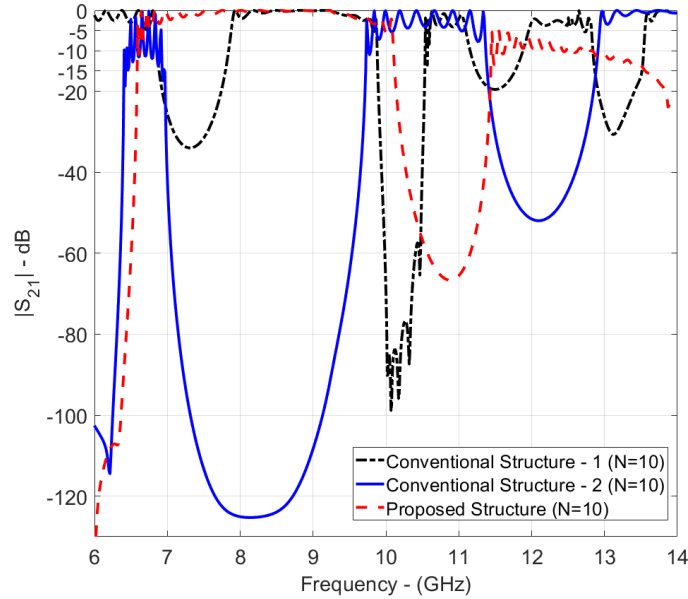


Figure 11. Comparison of $|S_{21}|$ frequency characteristics of given structures for $N=10$.

The frequency characteristics of the PS $N=10$ model were compared with those of similar designs in the literature, and the results are given in Table 1. According to the literature with very similar stopband characteristics, the best suppression level was obtained in the proposed study (PS, $N=10$). On the other hand, the proposed structure ranked second after [20] in terms of compactness in the compared studies.

Table 1. Comparison of the proposed structure with previous studies.

<i>Studies</i>	<i>Bandstop Region for -20 dB S_{21}</i>	<i>% FBW for -20 dB</i> *	<i>Suppression level min S_{21} (dB)</i>	<i>Circuit Size (mm × mm × mm)</i>
[2], fig. 5	10-11.32	12.38	-48	10.16 × 22.86 × 301.84
[20], fig. 20	10.7-10.85	1.39	-30	10.16 × 22.86 × 16.957
PS $N=10$	10.14-11.429	11.95	-66	14.8 × 0.5 × 136.826

*FBW can be calculated as follows: $\%FBW = (f_2 - f_1) / f_0$ where $f_0 = (f_2 + f_1) / 2$. f_0 , f_1 and f_2 are center, lower and upper frequency of the stopband region with respect to -20 dB.

4. Conclusion

In this paper, a comparative analysis of a rectangular waveguide unit cell with homogeneous dielectric-loaded glide symmetric step discontinuity and conventional structures is presented, and its implications for filter design are investigated. The glide-symmetric unit cell structure produced a narrower stopband (between 10.124 and 11.42 GHz) than the other considered models. For $N = 10$, a wider passband with a lower ripple level (between 7-10 GHz and less than -2.5 dB) was obtained among all the modeled structures. The passband/stopband characteristics of the proposed structure demonstrate that these structures can be used in filter applications. Classical filter theory or direct coupling matrix synthesis approaches [21] can be used in each unit cell design of the proposed structure to minimize passband ripples and achieve the filter design goals. Higher-order symmetries can play an important role in achieving a wider passband. In this respect, different types of higher-order symmetries [12, 13] can be applied to rectangular waveguides with homogeneous dielectric-loaded step discontinuity in future studies.

Ethics in Publishing

There are no ethical issues regarding the publication of this study.

Author Contributions

Agah Oktay Ertay prepared organization and concept of the paper, wrote the whole paper; materials, methods, simulations, results and discussions and conclusions.

References

- [1] Brillouin L., (1953) *Wave Propagation in Periodic Structures*, 2nd ed. New York: Dover.
- [2] Şimşek, S., Topuz, E., Niver, E. (2012) A novel design method for electromagnetic bandgap based waveguide filters with periodic dielectric loading. *AEU-International Journal of Electronics and Communications*, 66(3), 228-234.
- [3] Simsek, S., Topuz, E. (2007) Some properties of generalized scattering matrix representations for metallic waveguides with periodic dielectric loading. *IEEE transactions on microwave theory and techniques*, 11(55), 2336-2344.
- [4] Coves, A., San-Blas, A. A., Bronchalo, E. (2021) Analysis of the dispersion characteristics in periodic Substrate Integrated Waveguides. *AEU-International Journal of Electronics and Communications*, 139, 153914.
- [5] Mesa, F., Rodríguez-Berral, R., Medina, F. (2018) On the computation of the dispersion diagram of symmetric one-dimensionally periodic structures. *Symmetry*, 10(8), 307.

- [6] Zuo, L., Wang, K., Li, Y., Liang, Z., Zheng, S. Y., Long, Y. (2020) The periodic leaky-wave antenna with different unit cells based on consistent fundamental mode. *IEEE Transactions on Antennas and Propagation*, 68(12), 7794-7802.
- [7] Palomares-Caballero, Á., Alex-Amor, A., Padilla, P., Valenzuela-Valdés, J. F. (2020) Dispersion and filtering properties of rectangular waveguides loaded with holey structures. *IEEE Transactions on Microwave Theory and Techniques*, 68(12), 5132-5144.
- [8] Valerio, G., Sipus, Z., Grbic, A., Quevedo-Teruel, O. (2017) Accurate equivalent-circuit descriptions of thin glide-symmetric corrugated metasurfaces. *IEEE Transactions on Antennas and Propagation*, 65(5), 2695-2700.
- [9] Sipus, Z., Bosiljevac, M. (2019) Modeling of glide-symmetric dielectric structures. *Symmetry*, 11(6), 805.
- [10] Tomić, D., Šipuš, Z. (2024) Rigorous Coupled Wave Analysis of Parallel-Plate Waveguides Loaded With Glide-Symmetric Dielectric Structures. *Ieee Transactions on Microwave Theory and Techniques*.
- [11] Quevedo-Teruel, O., Chen, Q., Mesa, F., Fonseca, N. J., Valerio, G. (2021) On the benefits of glide symmetries for microwave devices. *IEEE Journal of Microwaves*, 1(1), 457-469.
- [12] Quevedo-Teruel, O., Valerio, G., Sipus, Z., Rajo-Iglesias, E. (2020) Periodic structures with higher symmetries: their applications in electromagnetic devices. *IEEE Microwave Magazine*, 21(11), 36-49.
- [13] Dahlberg, O., Mitchell-Thomas, R. C., Quevedo-Teruel, O. (2017) Reducing the dispersion of periodic structures with twist and polar glide symmetries. *Scientific reports*, 7(1), 10136.
- [14] Fayzi, A., (2002) Dikdörtgen kesitli dalga kılavuzunda kesim ötesi değişikliklerin incelenmesi, İstanbul Teknik Üniversitesi Fen Bilimleri Enstitüsü, Yüksek Lisans Tezi.
- [15] Berksoy, Z., (2013) SIW dalga kılavuzlarının analizi ve tasarım uygulamaları, İstanbul Teknik Üniversitesi Fen Bilimleri Enstitüsü, Yüksek Lisans Tezi.
- [16] Bayraktar, F. A., (2013) Periyodik olarak yüklü dikdörtgen dalga kılavuzlarında bloch empedansı ve uygulamaları, İstanbul Teknik Üniversitesi Fen Bilimleri Enstitüsü, Yüksek Lisans Tezi.
- [17] Hessel, A., Chen, M., Oliner, A. A. (1973) Propagation in periodically loaded waveguides with higher symmetries. *Proceedings of the IEEE*, 61(2), 183-195.
- [18] Hamid, A. K. (1988) Moment method solution for multiple-step discontinuities in waveguides. University of Manitoba, Master thesis.

- [19] Ertay, A. O., Şimşek, S. (2018). A comprehensive auxiliary functions of generalized scattering matrix (AFGSM) method to determine bandgap characteristics of periodic structures. *AEU-International Journal of Electronics and Communications*, 94, 139-144.
- [20] Mrvić, M. V., Potrebić, M. M., Tošić, D. V. (2017) Compact h-plane dual-band bandstop waveguide filter. *Journal of computational electronics*, 16, 939-951.
- [21] Cameron R. J., Kudsia C. M., Mansour R. R., (2018) *Microwave filters for communication systems*. Hoboken, NJ, USA: John Wiley & Sons, Ltd. Inc.

Determination of Uric Acid Using 2D-MoS₂ Modified GCE

Güliden ASAN^{1*}, Hüseyin ÇELİKKAN²

¹Hitit University Vocational School of Technical Sciences, Çorum, 19030, Türkiye.

²Gazi University, Faculty of Science, Ankara, 06500, Türkiye.

Received: 24/10/2024, **Revised:** 16/12/2024, **Accepted:** 23/12/2024, **Published:** 31/12/2024

Abstract

Uric acid (UA) is the end product of purine metabolism in the human body. The determination of the amount of uric acid in biological samples is made by many analytical methods. However, due to the high cost and time consumption of these methods, many sensors have been developed for the determination of uric acid by electrochemical methods. Analysis of biological samples using electrochemical methods is possible in a shorter time and with cheaper devices. In this study, electrochemical determination of uric acid was performed by modifying the glassy carbon electrode with two-dimensional molybdenum disulfide using two different methods (drop-coating and electrochemical coating). From the uric acid determination with the MoS₂(1)/GCE numbered electrode, the sensitivity was found to be 11.4 $\mu\text{A}\cdot\text{mM}^{-1}$, the linear operating range from 4 μM to 520 μM , and the detection limit was 0.8 μM . With MoS₂(2)/GCE, the 1st linear working range against Uric acid was found to be 0.1 μM – 20 μM , the sensitivity was 331 $\mu\text{A}\cdot\text{mM}^{-1}$ and the detection limit was 6.7×10^{-8} M. The 2nd linear operating range was 20 μM - 687 μM , and the sensitivity was determined as 62.4 $\mu\text{A}\cdot\text{mM}^{-1}$. In order to determine the efficiency of uric acid determination with MoS₂(2)/GCE, Uric acid determination in blood serum samples obtained from the hospital was successfully performed with MoS₂(2)/GCE with a relative error of 3.7%.

Keywords: Uric acid, Two-Dimensional Molybdenum disulfide, Electrochemical Determination

2D-MoS₂ ile Modifiye Edilen GCE Kullanılarak Ürik Asit Tayini

Öz

Ürik asit (UA) insan vücudundaki pürin metabolizmasının son ürünüdür. Biyolojik örneklerde ürik asit miktarının belirlenmesi birçok analitik yöntemle yapılmaktadır. Ancak bu yöntemlerin yüksek maliyet ve zaman tüketimi nedeniyle elektrokimyasal yöntemlerle ürik asit tayini için birçok sensör geliştirilmiştir. Biyolojik numunelerin elektrokimyasal yöntemlerle analizi daha kısa sürede ve ucuz cihazlarla mümkün olmaktadır. Bu çalışmada, camsı karbon elektrotun iki farklı yöntem (damlatarak kaplama ve elektrokimyasal kaplama) kullanılarak iki boyutlu molibden disülfür ile modifiye edilmesiyle ürik asidin elektrokimyasal tayini yapıldı. MoS₂(1)/GCE numaralı elektrot ile yapılan ürik asit tayininde duyarlılığın 11,4 $\mu\text{A}\cdot\text{mM}^{-1}$, doğrusal çalışma aralığının 4 μM ile 520 μM arasında olduğu ve tespit limitinin 0,8 μM olduğu belirlendi. MoS₂(2)/GCE ile ürik aside karşı 1. doğrusal çalışma aralığı 0,1 μM – 20 μM , hassasiyet 331 $\mu\text{A}\cdot\text{mM}^{-1}$ ve tespit limiti $6,7\times 10^{-8}$ M olarak bulunmuştur. 2. doğrusal çalışma aralığı 20 μM - 687 μM , duyarlılığı ise 62,4 $\mu\text{A}\cdot\text{mM}^{-1}$ olarak belirlendi. MoS₂(2)/GCE ile ürik asit tayininin etkinliğini belirlemek amacıyla hastaneden alınan kan serum örneklerinde Ürik asit tayini MoS₂(2)/GCE ile %3,7 bağıl hata ile başarılı bir şekilde gerçekleştirildi.

Anahtar Kelimeler: Ürik asit, İki Boyutlu Molibden disülfür, Elektrokimyasal Tayin.

1. Introduction

Molybdenum disulfide (MoS₂): It is one of the important two-dimensional (2D) transition metal dichalcogenides from graphene analogues. MoS₂ is the most interesting material of this group with its graphite-like structure [1]. Transition metal dichalcogenides (TMD) are denoted by the general formula MX₂ (M = Mo, W, V, Nb, Ta, Ti, Zr, Hf and X = S, Se, Te). They have found a very wide application area by forming an interesting group of materials with unique electronic, optical, thermal, mechanical and electrical properties and structures similar to graphene [2]. For example; such as in lubricants, hydrogen storage, catalysts, transistors, optics, nanoelectronics. TMDs contain aggregates in planar structure with weak van-der-waals-force. In recent years, the most studied of the transition metal dichalcogenides are MoS₂ and WS₂. The layered structure of MoS₂ is shown in Figure 1 [3].

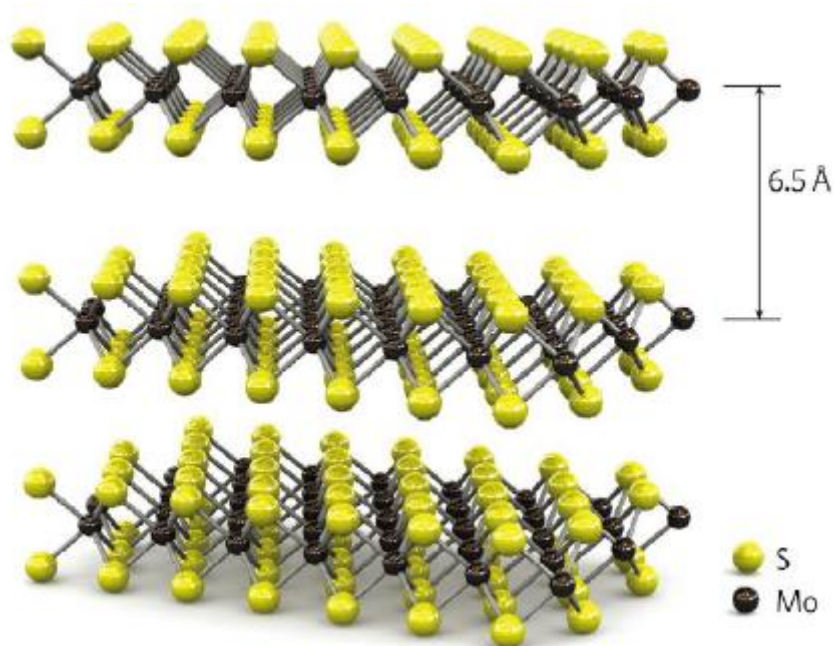


Figure 1. Layered structure of MoS₂, monolayer thickness 6.5 Å

MoS₂ has a hexagonal layer configuration. Atoms in the layer are connected by strong covalent bonds, the layers are connected to each other by weak forces, as in graphite, and each molybdenum layer is sandwiched between two sulfur layers [4]. In this study, glassy carbon electrode was modified using two-dimensional MoS₂ and used for uric acid determination. The amount of uric acid in the blood, which is the end product of purine metabolism in the human body [5]; It indicates the balance between the production of uric acid in the liver and intestine and its excretion through the kidneys. Most of the uric acid is excreted by the kidneys, and a small amount is excreted through the intestines. Depending on the foods and their uric acid content, the amount of uric acid in the blood constantly changes. In a healthy adult, blood uric acid levels range between 4-7 mg/100 mL in men and 3-6 mg/100 mL in women [6]. An increase in uric acid can be an indicator of many diseases. Determination of uric acid level is an important examination in the treatment of gout, but it also provides information about many other diseases. An increase in uric acid is seen in many diseases such as leukemia (blood

cancer), some anemia, lymphatic system cancers, and some hormonal disorders such as hyperthyroidism (overwork of the thyroid gland). In such cases, detecting the uric acid concentration in the urine is useful for early diagnosis of the disease. Electrochemical determination of uric acid is possible. Figure 2 shows the electrochemical oxidation of uric acid [7].

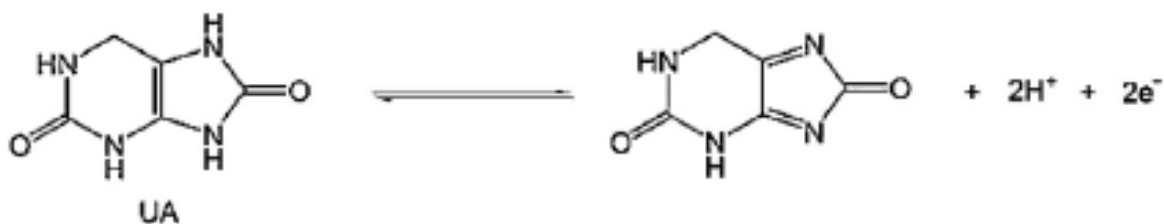


Figure 2. Electrochemical oxidation of uric acid

Electro-analytical techniques allow the qualitative and quantitative determination of a large number of inorganic and organic substances. These techniques have been developing more rapidly in recent years due to some of their superiorities over other analytical techniques (spectroscopy, chromatography, etc.) and find application areas. These superiorities are sensitivity, speed, ease of sample preparation, selectivity, low detection limit and low cost. Uric acid determination can be determined by different methods such as chromatographic [8,9] and spectrophotometric [10,11]. However, due to the superiorities mentioned above, an increase in the determination of uric acid by electrochemical method [12-16] has been observed in recent articles.

In this study, MoS₂ modified electrodes were prepared by drop coating and electrochemical coating techniques and exploited for uric acid determination in blood sample.

2. Materials and Methods

Electrochemical measurements were done in a three-electrode system with a computer-controlled CHI 660E potentiostat. Glassy carbon electrode (GCE) and modified glassy carbon electrodes (MoS₂(1)/GCE electrode and MoS₂(2)/GCE electrode) were used as working electrode, platinum wire as counter electrode and saturated calomel electrode (SCE) as reference electrode. MoS₂ in powder form was obtained from Özdogu Madencilik Ltd.Şti. and uric acid was obtained from Sigma Aldrich. Standard solutions of uric acid were prepared in phosphate buffer pH=7. Phosphate buffer solution (pH=7) was used as the supporting electrolyte. For the preparation of MoS₂(1)/GCE electrode and MoS₂(2)/GCE electrode, drop coating method and electrochemical coating method were applied. Uric acid was determined using the MoS₂(1)/GCE electrode prepared by taking 5 μL of the coating suspension. Since the preparation of the MoS₂(1)/GCE electrode prepared by the drop coating method was given in detail in our previous publication [17]. Electrochemical coating method was used for the preparation of the MoS₂(2)/GCE electrode. In another study, the cleaned surface of GCE electrodes was coated in three different times and the optimum time determination was determined as 3600 seconds (18). For this reason, 3600 seconds was preferred as the duration

in this study. The coating was carried out by keeping the GCE in 0.5 M NaOH containing the coating suspension (10% v/v) at constant potential (1.0 V) for 60 minutes. Detailed information on how the MoS₂(2)/GCE electrode is prepared can be found in doctoral thesis [18]. The differential pulse voltammetry (DPV) method was used for uric acid determination.

3. Results and Discussions

3.1. Determination of Uric Acid with MoS₂(1)/GCE

Uric acid determination was made with MoS₂(1)/GCE electrode prepared. The differential pulse (DP) voltammograms versus increasing uric acid concentrations with MoS₂(1)/GCE (in pH=7 phosphate buffer) are given in Figure 3 and the calibration curve produced from the peak currents of DP voltammograms is given in Figure 4.

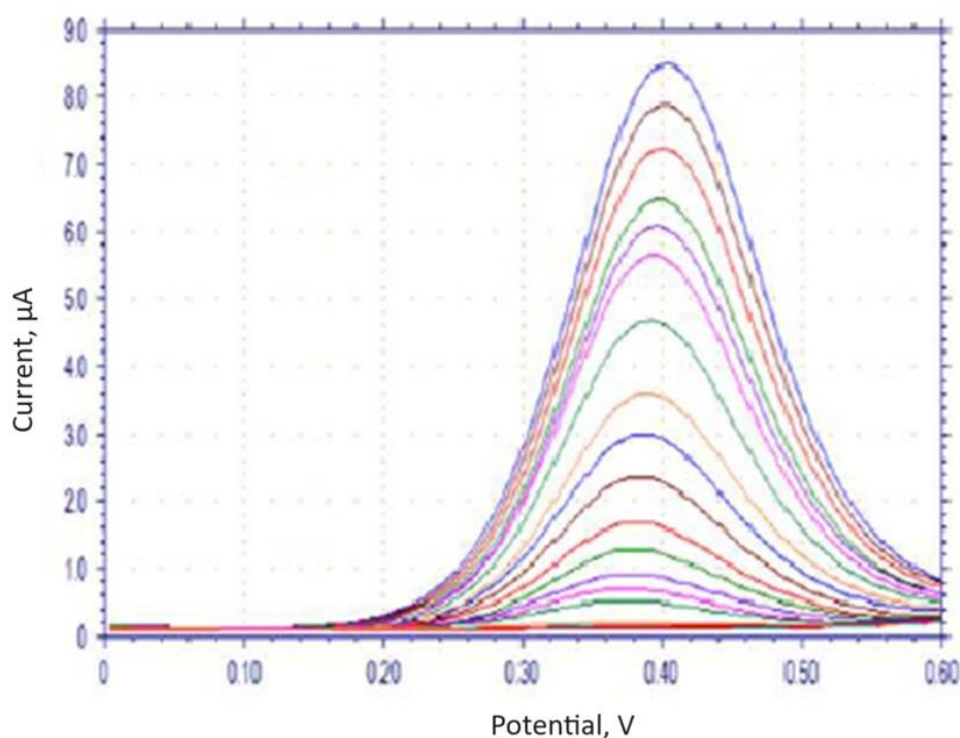


Figure 3. DP voltammograms at different concentrations for Uric Acid determination with MoS₂(1)/GCE

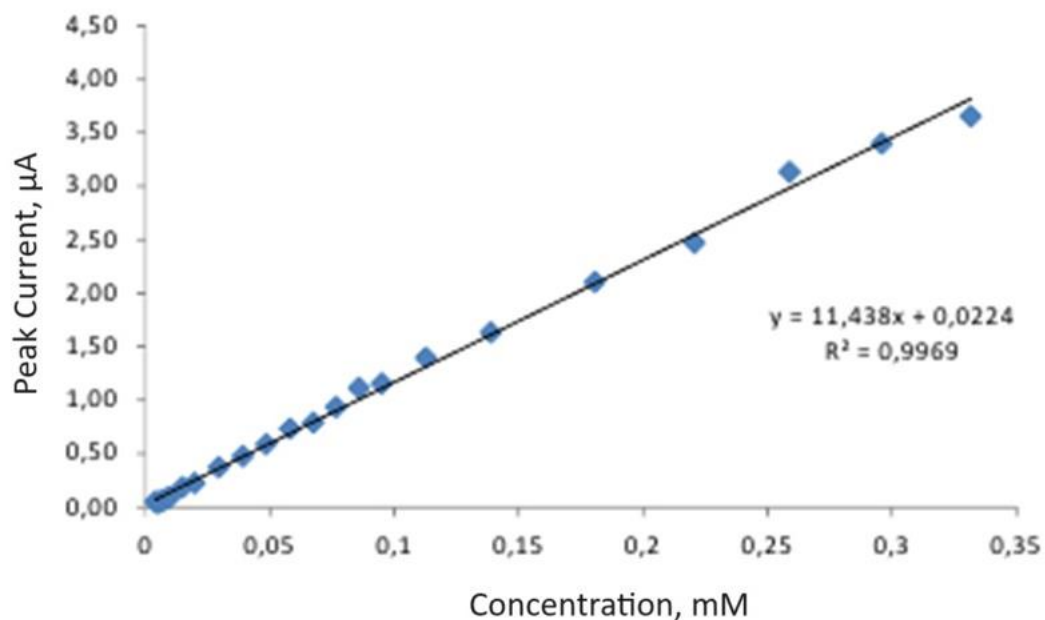


Figure 4. The plot of peak currents versus UA concentration measured by MoS₂(1)/GCE

For comparison, differential pulse voltammograms against increasing uric acid concentrations in pH=7 phosphate buffer with GCE were given in Figure 5 and concentration versus peak currents plot is given in Figure 6.

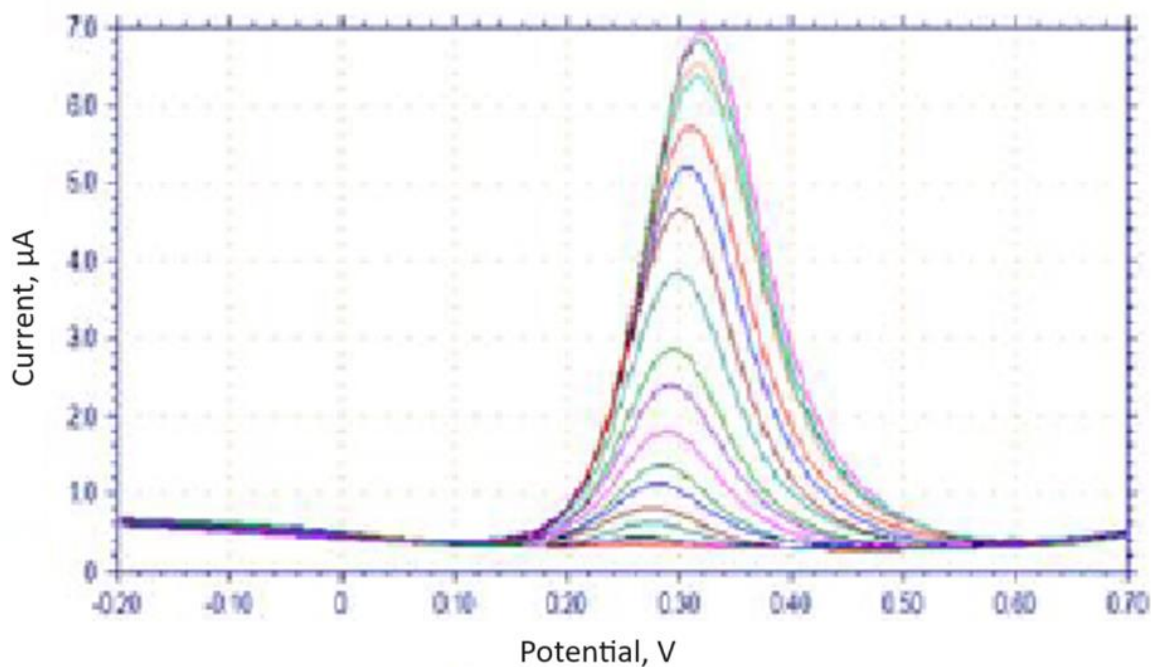


Figure 5. DP voltammograms at different concentrations for UA determination by GCE

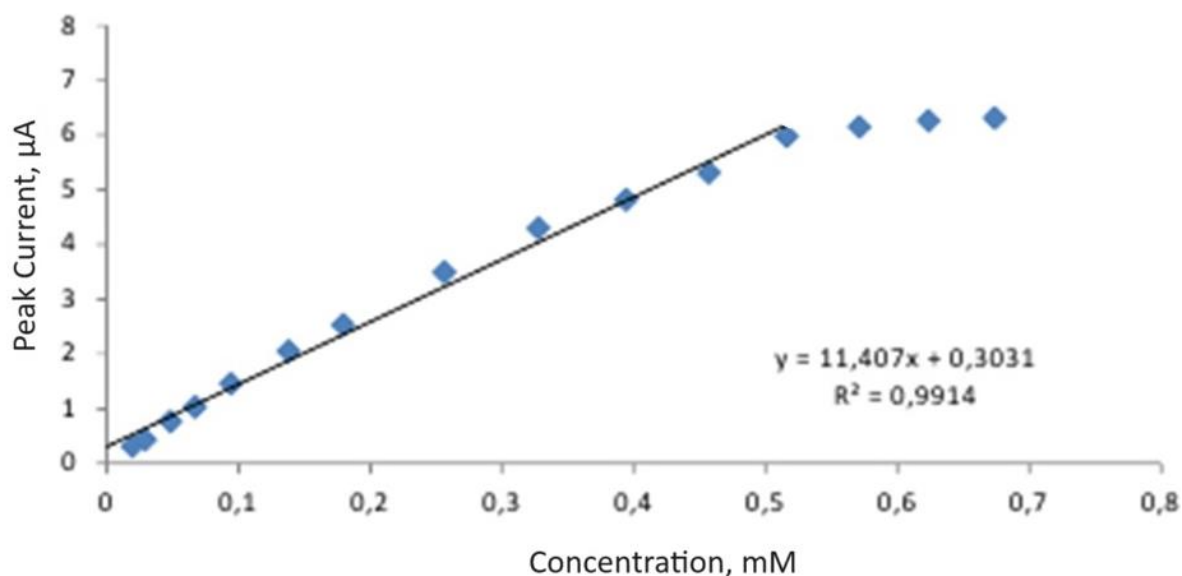


Figure 6. The plot of peak currents versus UA concentration measured by GCE

When Table 1 is examined, the sensitivity value for MoS₂(1)/GCE and uric acid was found to be 11.44 µA/mM, and the sensitivity value for GCE for uric acid was 11.41 µA/mM. It showed almost the same catalytic efficiency for uric acid with MoS₂(1)/GCE compared to GCE.

Table 1. Comparison of the values obtained in the determination of UA with MoS₂(1)/GCE and GCE

	Electrode Name	
	GCE	MoS ₂ (1)/GCE
Linear Operating Range (µM)	4-520	4-520
Line Equation (µA/ mM)	y=11.407x +0.3031	y=11.438x +0.0224
R ²	0.9914	0.9969
Sensitivity (µA/ mM)	11.41	11.44

Analytical performance values for uric acid with MoS₂(1)/GCE were given in Table 2.

Table 2. Analytical performance values for uric acid with MoS₂(1)/GCE

Linear Working Range (µM)	4 - 520
Sensitivity (µA.mM ⁻¹)	11.4
LOD (µM)	0.84
LOQ (µM)	2.81

After taking the differential pulse voltammograms at varying uric acid amounts with MoS₂(2)/GCE, they were superimposed and the resulting graph is given in Figure 7, and the peak currents against concentration are plotted in Figure 8. As seen in Figure 8, first a linear

interval with a higher slope and then a second linear interval with a lower slope were found for the concentration range studied. The 1st linear operating range is presented in Figure 9 and the 2nd linear operating range is presented in Figure 10.

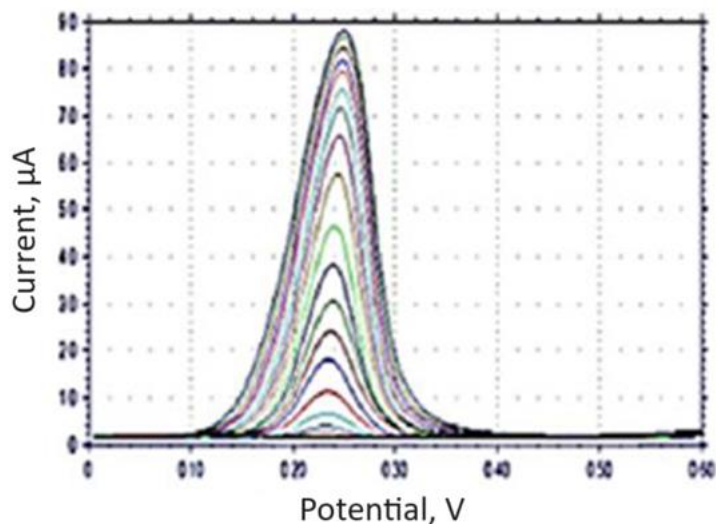


Figure 7. DP voltammograms at different concentrations for UA determination with MoS₂(2)/GCE

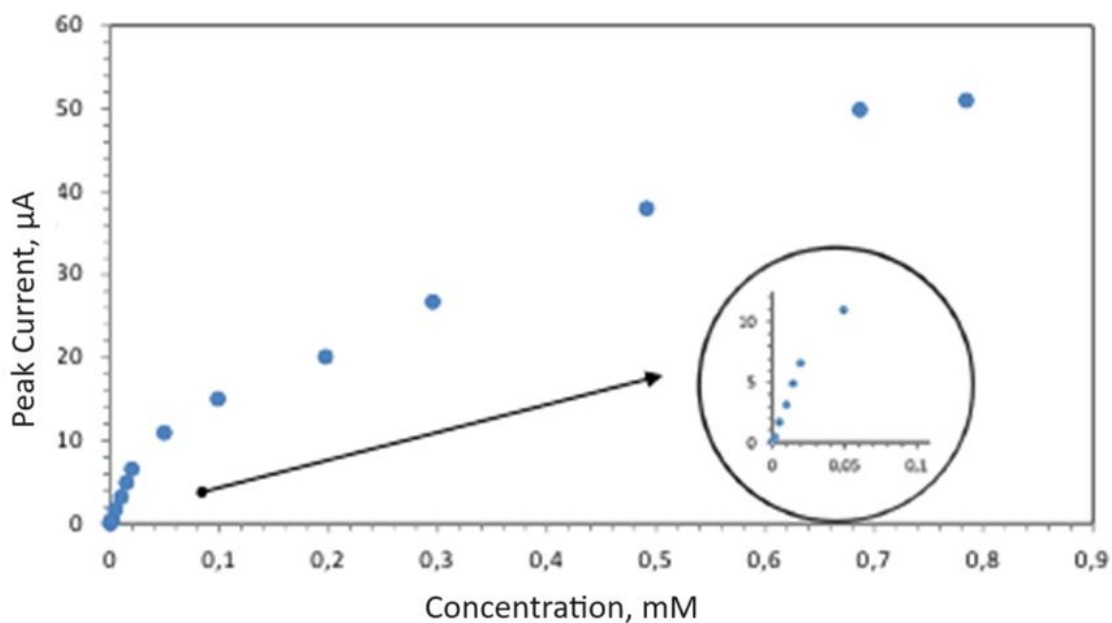


Figure 8. The plot of peak currents versus UA concentration measured by MoS₂(2)/GCE

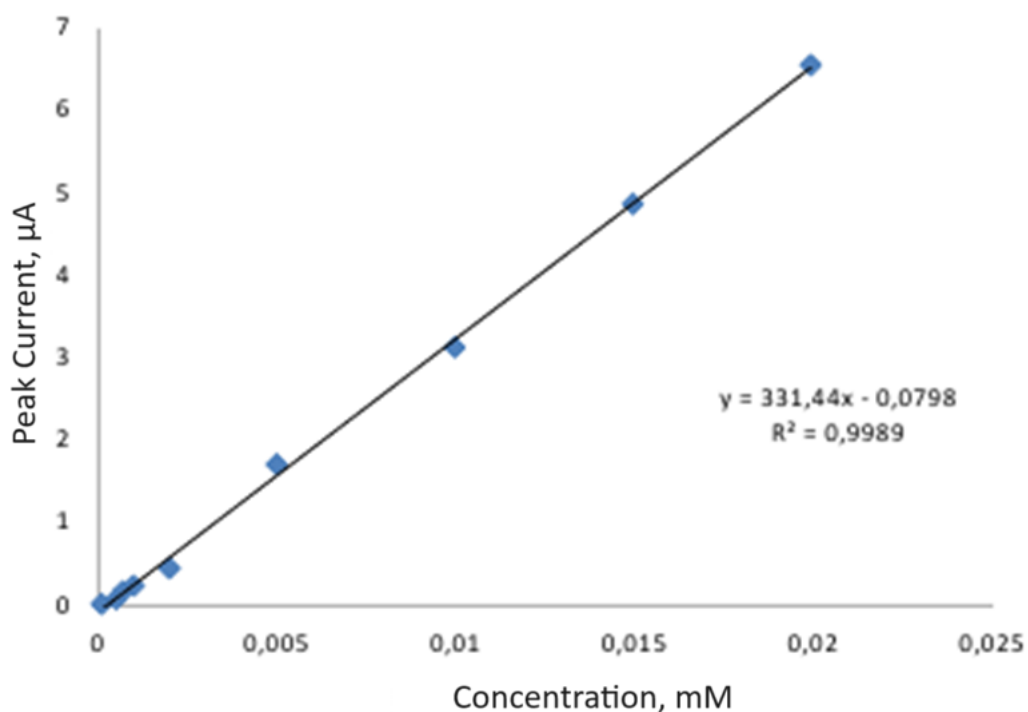


Figure 9. 1st linear operating range for UA determination with MoS₂(2)/GCE

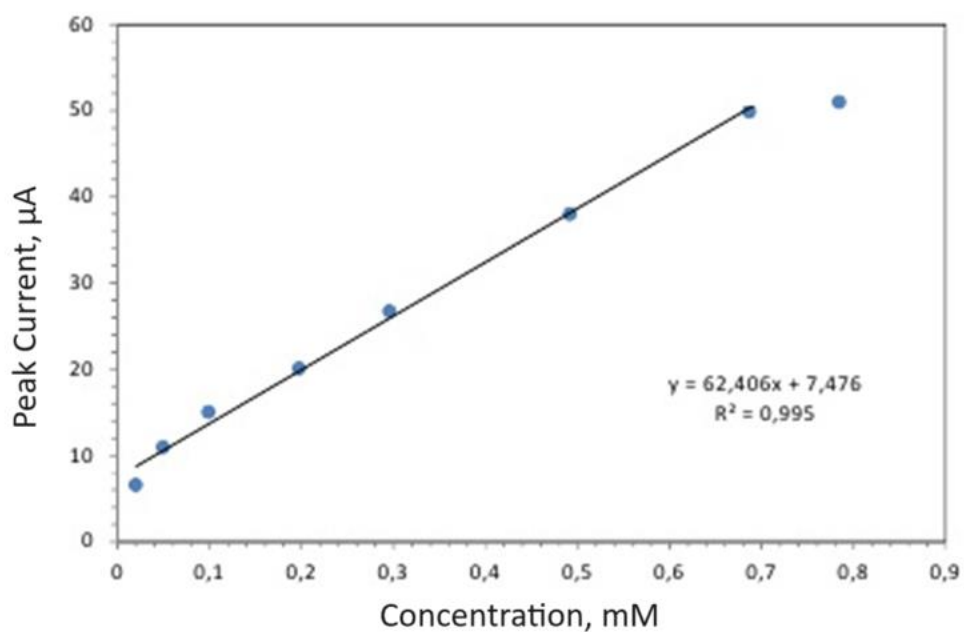


Figure 10. 2nd linear operating range for UA determination with MoS₂(2)/GCE

Table 3 has been prepared to compare electrode sensitivity with GCE and MoS₂(2)/GCE.

Table 3. Comparison of MoS₂(2)/GCE values obtained in uric acid determination with GCE

	Electrode Name		
	GCE	MoS ₂ (2)/GCE	MoS ₂ (2)/GCE
Linear Operating Range (μM)	20 - 520	0.1 – 20	20 – 687
Line Equation (μA/mM)	y=11.407x+0.3031	y = 331.44x-0.798	y = 62.406x+7.4757
R ²	0.9914	0.9989	0.9948
Sensitivity (μA/ mM)	11.41	331.4	62.4

When Table 3 is examined, it was observed that the sensitivity of MoS₂(2)/GCE and uric acid determination increased 29 times in the 1st linear operating range compared to GCE. In addition, it was found that the sensitivity value in the 2nd linear operating range with MoS₂(2)/GCE increased by 5.5 times compared to GCE. As can be seen, it has been possible to determine uric acid in a wide range from very low to very high concentrations with MoS₂(2)/GCE and with high sensitivity. Analytical performance values of MoS₂(2)/GCE for uric acid are presented in Table 4.

Table 4. Analytical performance values for uric acid with MoS₂(2)/GCE

1.Linear Working Range(LWR) (μM)	0.1 – 20
(1. LWR) Sensitivity (μA.mM ⁻¹)	331.4
2.Linear Working Range(LWR) (μM)	20 – 687
(2. LWR) Sensitivity (μA.mM ⁻¹)	62.4
LOD (nM)	67
LOQ (nM)	224

3.2. Determination of Uric Acid in Blood Samples with MoS₂(2)/GCE

For the determination of uric acid in blood serum with MoS₂(2)/GCE, DP voltammograms were produced from 1 mL of sample by adding 9 mL of pH=7 phosphate buffer. This process was repeated three times. Then, uric acid solutions were prepared at known concentrations in pH=7 buffer solution. Concentrations were calculated for three samples by taking the DP voltammograms by the standard addition method. The received DP voltammograms are superimposed and presented in the concentration-peak current graphs. Concentration-peak current graphs for sample 1, sample 2 and sample 3 are given in Figure 11, Figure 12 and Figure 13, respectively.

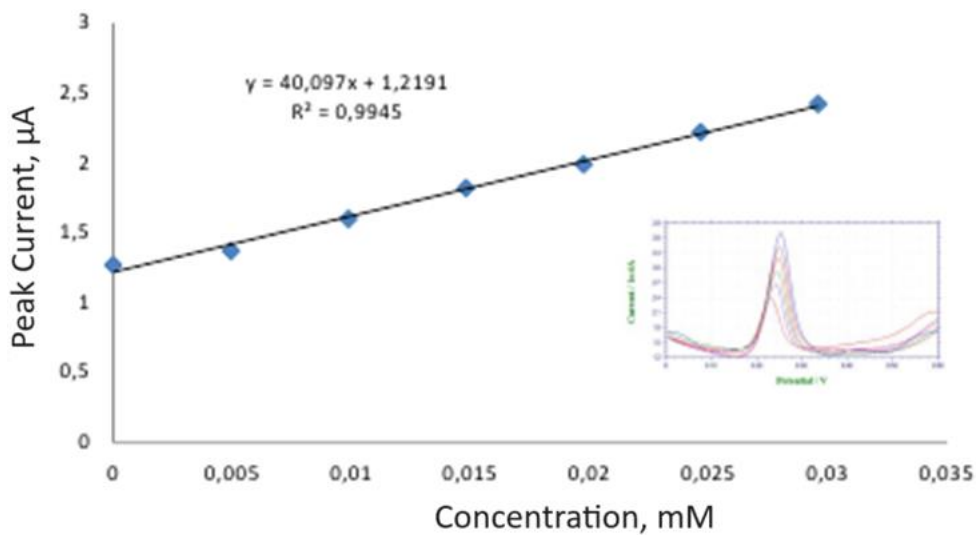


Figure 11. By standard addition method in the blood serum sample 1 with MoS₂(2)/GCE uric acid determination

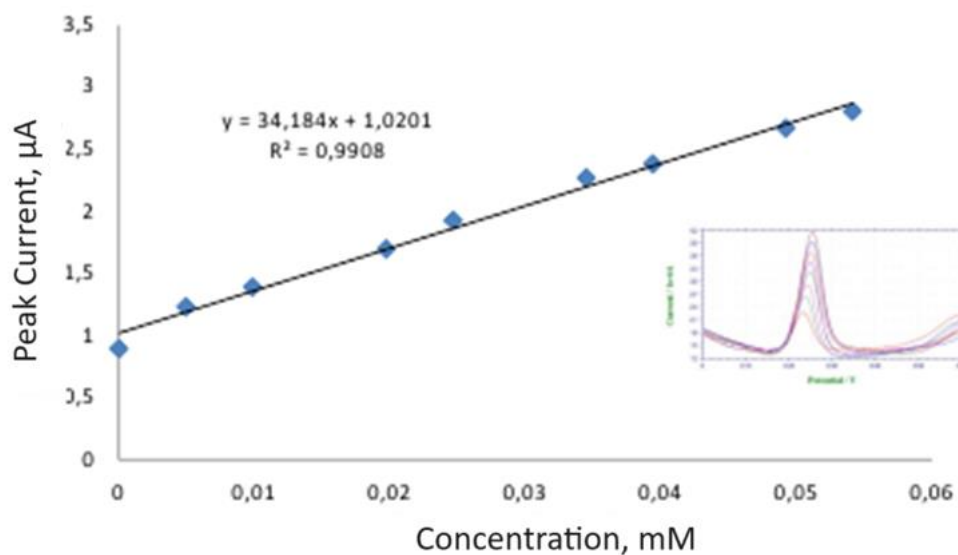


Figure 12. By standard addition method in the blood serum sample 2 with MoS₂(2)/GCE uric acid determination

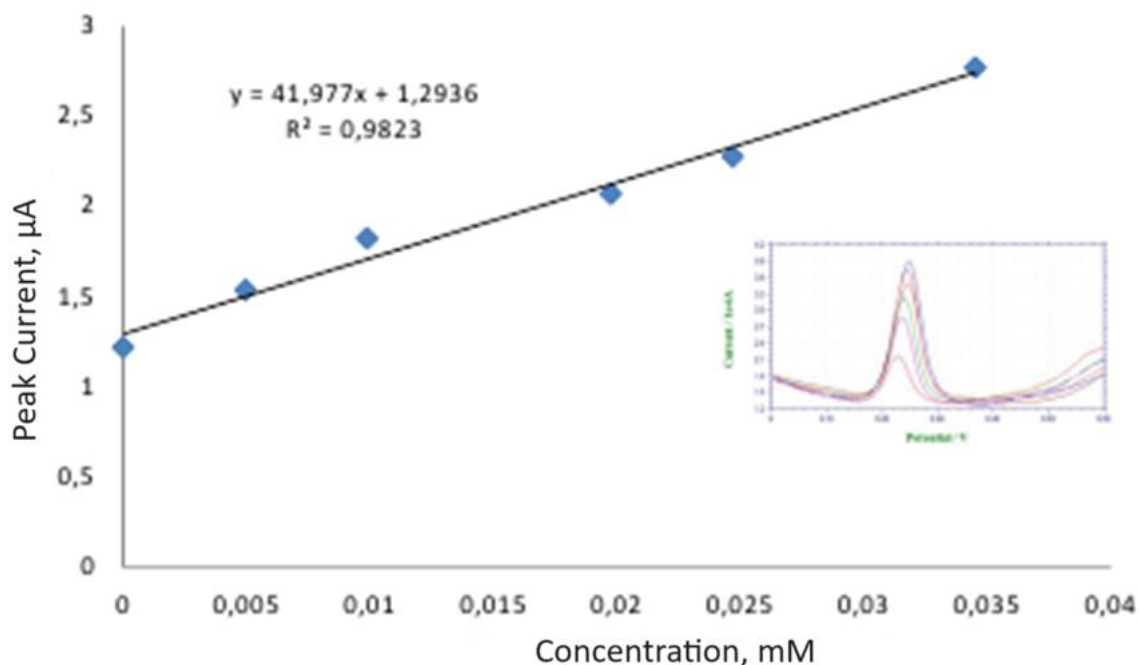


Figure 13. By standard addition method in the blood serum sample 3 with MoS₂(2)/GCE uric acid determination

In Table 5, uric acid values obtained from real samples are presented with their relative errors.

Table 5. Uric acid concentrations obtained from real samples with MoS₂(2)/GCE, with their relative errors

Sample	Calculated UA Concentration (mM)	UA Values in Blood (mg/100mL)	Real Value (mg/100 mL)	% Relative Error
1	0.03040	5.11	5.3	3.6
2	0.02984	5.02	5.3	5.3
3	0.03082	5.18	5.3	2.3

(X) average = 5.10 mg, t = 4.30 (at 95% Confidence level)

95% Confidence Level = 5.10 ± 0.20 mg

The real value is 5.3 mg/100 mL which is in between the range of given confidence level. Results can be given at 95% confidence intervals.

4. CONCLUSIONS

In the determination of uric acid with the modified electrode (MoS₂(1)/GCE) obtained by the drop-coating method; sensitivity was found to be 11.4 $\mu\text{A}\cdot\text{mM}^{-1}$, linear operating range from 4 μM to 520 μM , and the detection limit was 0.8 μM . In the determination of uric acid with the electrode (MoS₂(2)/GCE) obtained by electrochemical coating method, the 1st linear working range was found to be 0.1 μM – 20 μM , the sensitivity was 331 $\mu\text{A}\cdot\text{mM}^{-1}$, and the detection limit was 6.7×10^{-8} M. The 2nd linear operating range was 20 μM - 687 μM , the sensitivity was determined as 62.4 $\mu\text{A}\cdot\text{mM}^{-1}$. In order to determine the effectiveness of uric acid determination with MoS₂(2)/GCE, uric acid determination in blood serum samples obtained from the hospital was successfully performed with MoS₂(2)/GCE with a relative error of 3.7%.

Ethics in Publishing

There are no ethical issues regarding the publication of this study

5. REFERENCES

- [1] Zhou, K., Liu, J., Wen, P., Hu, Y., Gui, Z. (2014) A noncovalent functionalization approach to improve the dispersibility and properties of polymer/MoS₂ composites. *Applied Surface Science*, 316 (1), 237-44.
- [2] Zhang, S.L., Choi, H.H., Yue, H.Y., Yang, W.C. (2014) Controlled exfoliation of molybdenum disulfide for developing thin film humidity sensor. *Current Applied Physics*, 14 (3), 264-8.
- [3] Tang, Q., Zhou, Z. (2013) Graphene-analogous low-dimensional materials. *Progress in Materials Science*, 58 (8), 1244-315.
- [4] Huang, K.J., Wang, L., Liu, Y.J., Gan, T., Liu, Y.M., Wang, L.L., Fan, Y. (2013) Synthesis and electrochemical performances of Layered tungsten sulfide-graphene nanocomposite as a sensing platform for catechol, resorcinol and hydroquinone. *Electrochimica Acta*, 107, 379-87.
- [5] Zhang, Y., Xu, R.X., Li, S., Zhu, C.G., Guo, Y.L., Sun, J., Li, J.J. (2015) Lipoprotein subfractions partly mediate the association between serum uric acid and coronary artery disease. *Clinica Chimica Acta*, 441, 109-114.
- [6] Mayer, F.J., Mannhalter, C., Minar, E., Schillinger, M., Chavakis, T., Siegert, G., Arneth, B.M., Koppensteiner, R., Hoke, M. (2015) The impact of uric acid on long-term mortality in patients with asymptomatic carotid atherosclerotic disease. *Journal of Stroke and Cerebrovascular Diseases*, 24 (2), 354-61.
- [7] Cai, W., Lai, T., Du, H., Ye, J. (2014) Electrochemical determination of ascorbic acid, dopamine and uric acid based on an exfoliated graphite paper electrode: A high performance flexible sensor. *Sensors and Actuators B: Chemical*, 193, 492-500.

- [8] Kand'ár, R., Drábková, P., Hampl, R. (2011) The determination of ascorbic acid and uric acid in human seminal plasma using an HPLC with UV detection. *Journal of Chromatography B: Analytical Technologies in the Biomedical and Life Sciences*, 879 (26), 2834-9.
- [9] Li, X., Franke, A.A. (2009) Fast HPLC-ECD analysis of ascorbic acid, dehydroascorbic acid and uric acid. *Journal of Chromatography B: Analytical Technologies in the Biomedical and Life Sciences*, 877 (10), 853, 6.
- [10] Marquardt, R.R. (1983) A Simple Spectrophotometric Method for the Direct Determination of Uric Acid in Avian Excreta. *Poultry Science*, 62 (10), 2106-8.
- [11] Rocha, D.L., Rocha, F.R.P. (2010) A flow-based procedure with solenoid micro-pumps for the spectrophotometric determination of uric acid in urine. *Microchemical Journal*, 94 (1), 53-9.
- [12] Lakshmi, D., Whitcombe, M.J., Davis, F., Sharma, P.S., Prasad, B.B. (2011) Electrochemical Detection of Uric Acid in Mixed and Clinical Samples: A Review. *Electroanalysis*, 23(2), 305-20.
- [13] Aafria, S., Kumari, P., Sharma, S., Yadav, S., Batra, B., Rana, J.S., Sharma, M. (2022) Electrochemical biosensing of uric acid: A review. *Microchemical Journal*, 182, 107945.
- [14] Sheng, Z.H., Zheng, X.Q., Xu, J.Y., Bao, W.J., Wang, F.B., Xia, X.H. (2012) Electrochemical sensor based on nitrogen doped graphene: Simultaneous determination of ascorbic acid, dopamine and uric acid. *Biosensors and Bioelectronics*, 34 (1), 125-31.
- [15] Zhang, B., Huang, D., Xu, X., Alemu, G., Zhang, Y., Zhan, F., Shen, Y., Wang, M. (2013) Simultaneous electrochemical determination of ascorbic acid, dopamine and uric acid with helical carbon nanotubes. *Electrochimica Acta*, 91, 261-266.
- [16] Tatlı, F., Calam, T.T., Uzun, D., Hasdemir, E. (2020) The determination of uric acid in the presence of ascorbic acid and dopamine using [(1H-1,2,4-triazole-3-ylimino) methyl]naphthalene-2-ol modified platinum electrode. *Journal of the Faculty of Engineering and Architecture of Gazi University*, 35 (4), 2013-2022.
- [17] Asan, G. Çelikkan, H. (2017) Askorbik Asitin MoS₂ Esaslı Elektrotla Elektrokimyasal Tayini. *Gazi Üniversitesi Mühendislik-Mimarlık Fakültesi Dergisi*, 32 (3), 617-625.
- [18] Asan, G. (2015) MoS₂ İle Modifiye Edilmiş Camsı Karbon Elektrot Kullanılarak Askorbik Asit, Dopamin Ve Ürik Asit'in Elektrokimyasal Yöntemlerle Tayini. Doktora Tezi, Gazi Üniversitesi.

Investigation of Influencing Factors on Power Generation Performance in Reverse Electrodialysis

Aydın CİHANOĞLU^{1,2*}

¹Department of Chemical Engineering, Faculty of Engineering, Ege University, İzmir, 35100, Türkiye

²Refinery and Petrochemical Technology, Aliğa Vocational School, Ege University, İzmir, 35800, Türkiye

Received: 04/11/2024, **Revised:** 15/12/2024, **Accepted:** 23/12/2024, **Published:** 31/12/2024

Abstract

The importance of meeting energy demands from renewable sources is growing daily. Reverse electrodialysis (RED) is a membrane-based technology that produces energy using electrolyte solutions with different salinities. This study has generated energy from the RED system using the commercial Fujifilm Type II ion exchange membranes (IEMs). Many parameters affect the power generation performance of the RED system. This study systematically investigated the parameters, the presence of divalent ions and organic molecules, the electrolyte solution concentration, and the flow velocity. The flow velocity results indicated that energy efficiency increased with increasing flow velocity of the electrolyte solutions. The presence of divalent ions created uphill transport. The results showed that increasing the mole ratio of divalent ions in the feed electrolyte solutions dramatically decreased the RED system performance due to increasing resistances. The organic fouling test of the anion exchange membranes (AEMs) was carried out using a real humic and fulvic acid mixture under static conditions. The results indicated that fouling layers formed in the AEMs structure, and these layers decreased by 30% of RED performance. Lastly, the RED system's long-term performance was tested for 4 hours at a constant current density of 8 A/m² before and after AEM fouling experiments. The results revealed the fouling layers severely reduced the power generation performance of the RED system.

Keywords: reverse electrodialysis, ion exchange membrane, uphill transport, organic fouling, blue energy.

Ters Elektrodializde Güç Üretim Performansını Etkileyen Faktörlerin Araştırılması

Öz

Enerji taleplerini yenilenebilir kaynaklardan karşılamının önemi her geçen gün artmaktadır. Ters elektrodializ (RED), farklı tuzluluklara sahip elektrolit çözeltileri kullanarak enerji üreten membran tabanlı bir teknolojidir. Bu çalışmada ticari Fujifilm Tip II iyon değiştirici membranlar (IEMs) kullanılarak RED sisteminden enerji üretilmiştir. RED sisteminin güç üretim performansını birçok parametre etkilemektedir. Bu çalışmada, iki değerlikli iyonların ve organik moleküllerin varlığı, elektrolit çözelti konsantrasyonu ve akış hızı sistematik olarak araştırılmıştır. Akış hızı sonuçları, elektrolit çözeltilerinin akış hızının artmasıyla enerji verimliliğinin arttığını göstermiştir. Çift değerlikli iyonların varlığı konsantrasyon gradyanının tersine taşınım yarattı. Sonuçlar, besleme elektrolit çözeltilerindeki iki değerlikli iyonların mol oranının artırılmasının, artan dirençler nedeniyle RED sistem performansını önemli ölçüde azalttığını gösterdi. Anyon değiştirici membranların (AEMs) organik kirlenme testi, statik koşullar altında gerçek hümik ve fulvik asit karışımı kullanılarak gerçekleştirildi. Sonuçlar, AEM yapısında kirlenme tabakalarının oluştuğunu ve bu tabakaların RED performansını %30 oranında azalttığını gösterdi. Son olarak, RED sisteminin uzun vadeli performansı, AEM kirlenme deneylerinden önce ve sonra 8 A/m² sabit akım yoğunluğunda 4 saat boyunca test edildi. Sonuçlar, kirlenme katmanlarının RED sisteminin güç üretim performansını ciddi şekilde azalttığını ortaya koydu.

Anahtar Kelimeler: ters elektrodializ, iyon değiştirici membran, konsantrasyon gradyanı tersine taşınım, organik kirlilik, mavi enerji.

1. Introduction

Access to energy is one of the most fundamental human rights required to improve people's living standards and ensure sustainability. The meeting energy demand of the rapidly growing population with fossil fuels is a huge problem for all living due to its hazardous impact on the environment. Salinity gradient energy (SGE), also called blue energy, is considered a promising technology since its efficiency and sustainability are not dependent on external conditions, and it does not produce solid, liquid, or gas waste. This technology produces energy by converting chemical potential into electrical or mechanical energy [1-4]. The potential source of this technology is the sea and river water and the place where the junction of these two sources. Theoretical studies based on Gibbs's free energy calculations report that the global potential of SGE considering entire regions that could be used is around 1.4-2.6 TW. This is equivalent to 20% of total demand [2,3,5]. Using the full potential of SGE could reduce energy-related CO₂, CH₄, and N₂O emissions by 25%, 27%, and 8% respectively [6]. The SGE technology includes three different techniques, RED, PRO (pressure retarded osmosis), and CapMix (capacitive mixing) [1]. Of the mentioned techniques, RED is considered the most promising of those proposed so far because of its high power density and functionality [7-9]. Technically, a RED stack consists of AEMs and CEMs (cation exchange membranes) placed in succession between electrodes, and a spacer and gasket separate these membranes. The concentrate and dilute electrolyte solutions are fed to compartments between IEMs. The salinity difference across IEMs creates a Nernst potential, and this potential is converted to electricity by a redox reaction at electrodes.

Many researchers have been working on renewable energy harvesting from the RED system using standard commercial IEMs and NaCl salt ions [10-12]. Further, the effect of membrane type [11,12], flow rate [13,14], spacer thickness [15], electrode system [16-18], and feed concentration [19] on power generation was comprehensively investigated. However, few studies are focused on the effect of multivalent ions and organic substances on power generation performance. The studies in the literature that used NaCl do not accurately shed the actual industrial-scale RED energy harvesting performance because the electrolyte solutions in the actual applications do not include only monovalent ions. The multivalent ions decrease the power generation, depending on the concentration in the feed electrolyte solutions. The reason for performance loss is the uphill transport that occurs in the presence of multivalent ions, creating high resistance in the RED system. In this transport, multivalent ions are transported against the concentration gradient, whereas monovalent ions are transported through the concentration gradient. This counter-current transport of ions creates electroneutrality, resulting in potential differences reduction between the compartments and a loss of power density by increasing the resistance [20]. For instance, Vermaas et al. reported that almost 50% loss of power density in the RED system, where Fujifilm IEMs were located, was obtained when the 10% MgSO₄ and 90% NaCl of mole fraction were in the feed electrolyte solution in both concentrate and dilute compartments [21]. Similarly, Pintossi et al. studied the effect of multivalent ions on the RED performance using commercial FujiFilm IEMs. They concluded the presence of multivalent ions increases the resistance of the RED system and decreases the permselectivity of the IEMs [22]. Organic fouling is another problem in power generation from

the RED system on an industrial scale. The presence of organic substances, a source of fouling, creates a fouling layer in the membrane structure, reducing the power generation performance by increasing resistance and decreasing the permselectivity of the IEMs. For instance, the first laboratory-scale RED fouling test results, using sea and river water as the electrolyte solution, showed a high-pressure drop during operation even though pretreatment was applied to the feed solutions with a 20-micron filter [23]. This was attributed to organic fouling layer formation, especially in the AEMs structure.

This work aims to systematically study four fundamental parameters that affect the power generation performance of the RED system using commercial Fujifilm IEMs. These parameters are i) the flow velocity of electrolyte solutions, ii) electrolyte solution concentrations, iii) the presence of divalent ions, and iv) the presence of organic acids. To this end, three different flow velocities and two different electrolyte solution concentrations were used. The effect of divalent ions was first investigated using the same concentration in concentrate and dilute compartments. Then, the compartment composition effect was studied by changing the divalent ion concentrations in the compartments. The organic fouling tendency of AEMs was tested using a real humic and fulvic acid mixture solution under static conditions. The long-term energy generation performance of the RED system was determined before and after the organic fouling test of AEMs.

2. Material and Methods

2.1. Materials and chemicals

This study used commercially available AEMs (Fujifilm Type II) and CEMs (Fujifilm Type II) from Fujifilm manufacturers as ion exchange membranes (IEMs). IEMs were washed with deionized water and stored in 0.5 M NaCl solution for at least one day before use. The properties of IEMs are given in Table 1. Analytical grade $K_3Fe(CN)_6$, $K_4Fe(CN)_6$, and NaCl were used to prepare the electrode solution and NaCl and Na_2SO_4 for electrolyte solutions. All chemicals used in electrode and electrolyte solutions preparations were supplied from Merck (Germany) and used without further purification. The real (not model) humic and fulvic acid mixture (Ant, Türkiye) was used for the fouling test. All solutions were prepared with deionized water.

2.2. Experimental set-up

A schematic view of the RED system (STT Products B.V. BA Schiedam, Netherlands) is given in Figure 1. The electrodes in the system are Ti/Ru-Ir alloyed mesh-type anode and cathode. The polyamide 6-based spacers (Sefar, Switzerland) with 450-micron thickness, 71% porosity, and 38% open areas and silicon rubber gasket were used to separate the membranes with a 10cm x 10cm active area in the RED system [24]. Three repeat units (one repeat unit consisting of one AEM and one CEM) were used in the study. Dilute and concentrate solutions were represented as low and high salinity, respectively. The electrode solution was fed as a closed loop circulated to the electrodes. Two peristaltic pumps were operated for the dilute, concentrate, and electrode solutions feeding speed adjustment in the RED system. The feeding speed of the electrolyte solutions was changed during the study, but the electrode feeding speed

was constant at a 300 mL/min volumetric flow rate. Electrochemical measurements were carried out using Gamry Instrument Reference 3000 (USA). All RED tests were carried out at room temperature (25 °C). RED test experiments were repeated four times, and the standard deviations of the power were obtained on the order of 10^{-4} . Since the standard deviation values were too small, they did not add to the values.

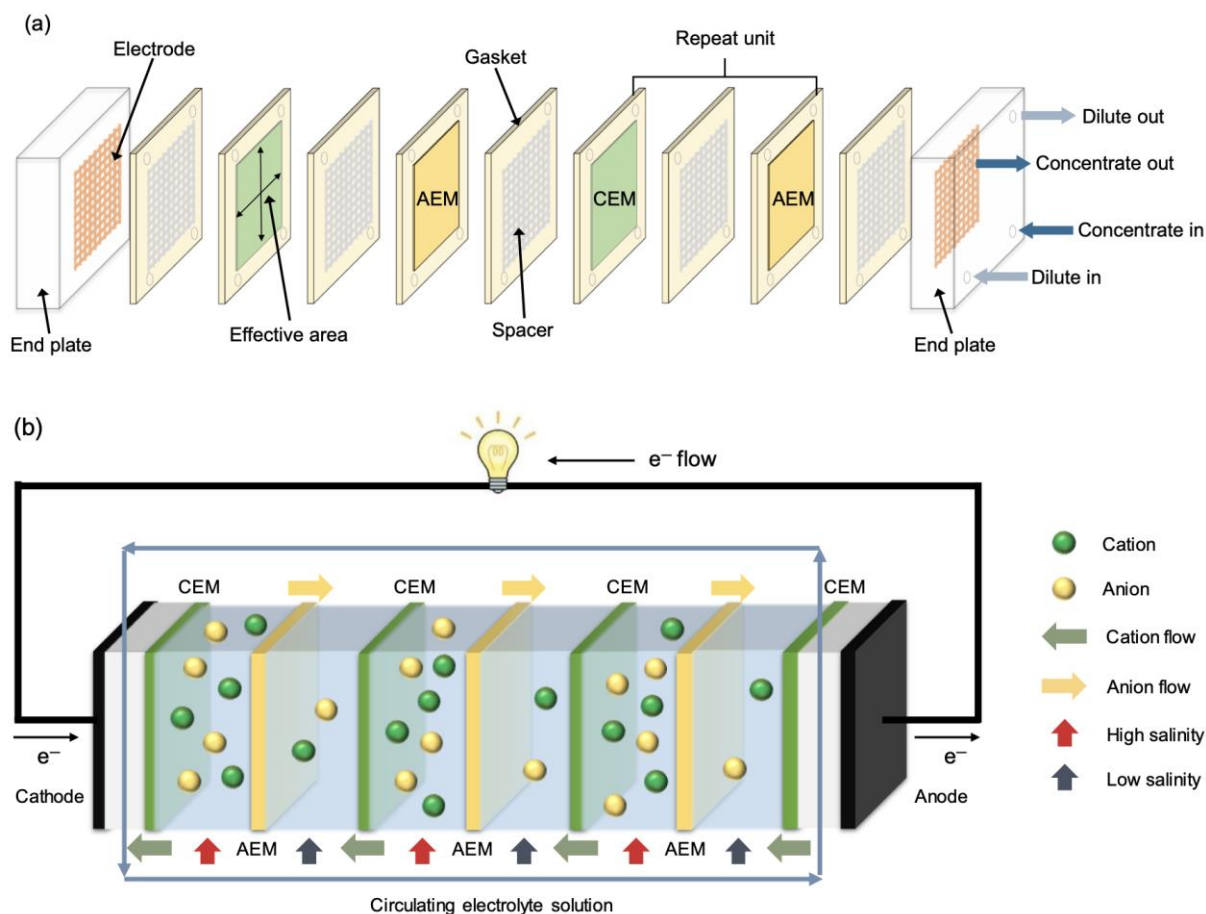


Figure 1. A schematic view of the RED system, a) components, and b) working principle. The figure is reprinted with permission from [25] (Copyright 2020, Elsevier).

2.3. Electrode and electrolyte solution preparation

The electrode solution (2 L) was prepared using 0.05 M $K_3Fe(CN)_6$, 0.05 M $K_4Fe(CN)_6$, and 0.25 M NaCl ions. To this end, all chemicals were well mixed using deionized water at room temperature (25 °C). Then, the mixture was put in a sunlight-proof tank for use. Two different electrolyte solutions, dilute and concentrate, are used in the RED system. The 0.017 M NaCl (dilute) / 0.513 M NaCl (concentrate) solution pair and 0.1 M NaCl (dilute) / 2.5 M NaCl (concentrate) solution pair were separately used as electrolyte solution pairs. On the other hand, in the experiments where monovalent (NaCl) and multivalent ions (Na_2SO_4) were present simultaneously, only a 0.017 M NaCl / 0.513 M NaCl solution pair was used. The Na_2SO_4 concentration was adjusted to be 10% and 50% mole of the total solution concentration. Multivalent ions were added to both dilute and concentrate electrolyte solution compartments.

The label was coded as 90% NaCl+10% Na₂SO₄ and 50% NaCl+50% Na₂SO₄ for 10% and 50% mole ratios, respectively.

2.4. Theoretical background

The salinity difference between the compartments creates a potential difference known as the Nernst potential. The theoretical open circuit voltage (OCV) (V) (when no current is allowed) of each compartment in the presence of monovalent and multivalent ions is calculated using Equations 1 and 2, respectively [26].

$$OCV_{theoric} = \left(\frac{\alpha_{AEM}}{z_-} + \frac{\alpha_{CEM}}{z_+} \right) * \frac{RT}{F} * \ln \left(\frac{m_c \gamma_c}{m_d \gamma_d} \right) \quad (1)$$

$$OCV_{theoric} = \left[\left(\frac{\alpha_{CEM}}{z_{Na^+}} \right) * \frac{RT}{F} * \ln \left(\frac{m_c^{Na^+} \gamma_c^{Na^+}}{m_d^{Na^+} \gamma_d^{Na^+}} \right) \right] + \left[\left(\alpha_{AEM} \right) * \frac{RT}{F} * \left[\frac{1}{z_{Cl^-}} * \ln \left(\frac{m_c^{Cl^-} \gamma_c^{Cl^-}}{m_d^{Cl^-} \gamma_d^{Cl^-}} \right) + \frac{1}{z_{SO_4^{2-}}} \ln \left(\frac{m_c^{SO_4^{2-}} \gamma_c^{SO_4^{2-}}}{m_d^{SO_4^{2-}} \gamma_d^{SO_4^{2-}}} \right)^{1/2} \right] \right] \quad (2)$$

α_{AEM} and α_{CEM} are the membrane permselectivity, z_- , and z_+ are the negative and positive ion valence, respectively, R is the universal gas constant (8.31 J/mol K), T is the temperature (K), F is the Faraday constant (96485 C/mol), m is the molality of the electrolyte solution, γ is the activity coefficient of the ion. The subscripts c and d of constants in the equations represent the concentrated and dilute compartments.

The maximum net power density (P_{Net}) (W/m²) is calculated as the difference in power densities created by the RED system and consumed by the pumps (P_{Pump}). Equations 3-8 are used for the calculations of P_{Net} [27,28].

$$P_{Net} = \frac{(OCV)^2}{4 R_{Cell}} - P_{Pump} \quad (3)$$

$$P_{Pump} = \frac{\sum \Delta P_i * \phi_i}{A_{Membrane}} = \frac{\Delta P_c * \phi_c + \Delta P_d * \phi_d}{A_{Membrane}} \quad (4)$$

$$\Delta P = \frac{12 * \mu * L^2}{\left(\frac{1}{4} \right) * d_h^2 * t_{res}} \quad (5)$$

$$d_h = \frac{4 * \varepsilon}{\left(\frac{2}{h} \right) + (1 - \varepsilon) * \left(\frac{8}{h} \right)} \quad (6)$$

$$t_{res} = \frac{L}{U} \quad (7)$$

$$U = \frac{\phi}{w * h * \varepsilon * N} \quad (8)$$

R_{Cell} is the total resistance of the RED stack ($\Omega \text{ cm}^2$), ΔP is the pressure difference over the feed water compartment (Pa), Φ volumetric flow rate (m³/s), $A_{Membrane}$ is the total membrane area (m²), μ is the viscosity of the electrolyte solution (Pa s), L is the cell length (m), d_h is the hydraulic diameter of the channel (m), t_{res} is the residence time of the electrolyte solution in the

RED stack (s), ε is the porosity of the spacer, h is the intermembrane distance (m), U is the linear flow velocity (m/s), w is the membrane width (m) and N is the membrane number.

The flow regime (Reynolds number, Re) of electrolyte solutions is determined by Equation 9.

$$Re = \frac{2*\phi*\rho}{w*\mu*\varepsilon} \tag{9}$$

ρ is the electrolyte solution density (kg/m³).

Table 1. Properties of Fujifilm Type II IEMs used in the RED stack [29].

Properties	AEM	CEM
Reinforcement	Polyolefin	Polyolefin
Thickness dry (μm)	160	160
Electrical resistance (Ω cm ²)	5	8
Perm selectivity (%)	95	96
Ion exchange capacity (meg/g)	0.9	1.1
pH stability	2-10	4-12
Temperature stability (°C)	40	40

2.5. Fouling test

The fouling tendency of the commercial AEMs was tested in the presence of a real (not model) humic and fulvic acid mixture (Ant, Türkiye). The humic and fulvic acid mixture is an organic acid, and it is commonly present in sea and river water. To this end, the membranes were immersed in the solution with a 20-ppm acid mixture under static conditions for 7 days at room temperature (25 °C). Then, membranes were washed with deionized water to desorb weakly adsorbed organic molecules in the membrane structure. After simple rinsing, the power generation performance of the fouled membranes in the RED system was tested using a 0.017 M NaCl / 0.513 M NaCl electrolyte solution pair under a constant flow velocity of 0.52 cm/s at room temperature (25 °C).

2.6. Long-term test

The long-term power generation performance of IEMs was tested before and after fouling experiments using a constant current density of 8 A/m² and a flow velocity of 0.52 cm/s with a 0.017 M NaCl / 0.513 M NaCl electrolyte solution pair. The experiments took 4 hours and were at room temperature (25 °C). The current density that achieved the highest power density has been identified as the optimum current density value used in long-term performance tests.

Table 2 summarizes the experimental conditions and parameters used in the energy generation performance in the reverse electrodialysis system.

Table 2. Experimental conditions for energy generation from the RED stack.

Membranes	The electrolyte solution concentration	Flow velocity (cm/s)	T (°C)	Presence of divalent ions (moles %)	Presence of organic compound (ppm)*
Fujifilm Type II AEM & CEM	0.017 M NaCl & 0.513 M NaCl	0.26	25	10% Na ₂ SO ₄	20
		0.52		50% Na ₂ SO ₄	
Fujifilm Type II AEM & CEM	0.1 M NaCl & 2.5 M NaCl	2.09		-	-

* The effect of organic compound presence on energy generation performance was tested only using 0.017 M NaCl & 0.513 M NaCl electrolyte solution concentration with 0.52 cm/s solution velocity conditions.

3. Results and Discussion

In this study, the RED performance of the commercially available Fujifilm Type II IEMs was tested using different electrolyte solution concentrations, flow velocities, the presence of multivalent ions, and organic foulants. The effect of these four variables on the RED system performance is crucial. The power generation performance is based on creating a maximum potential difference between the compartments by transporting the ions from the concentrate to dilute compartments and a minimum total resistance during the operation. The theoretical OCV in Equations 1 and 2 indicate that the solution concentration is the most significant parameter since it influences the created potential difference logarithmically [26]. On the other hand, the resistances in the RED system consist of ohmic and non-ohmic. Membrane resistance, spacer properties, electrolyte solution conductivity, inter-membrane distance, and electrode resistance are significant parameters in determining the ohmic resistances. The non-ohmic resistances are based on two fundamental phenomena: boundary layer area resistance and area resistance due to bulk concentration changes. The flow velocity of the electrolyte solution is one of the most significant parameters, reducing these two resistances by decreasing concentration polarization on the membrane surface [13].

In real applications, the feed electrolyte solutions include multivalent ions and organic molecules that trigger the membrane fouling, reducing the power generation performance [23]. The presence of multivalent ions causes uphill transport. In this transport, three scenarios negatively affect the RED system performance: i) transport of multivalent ions from the dilute to concentrate compartments, ii) binding the multivalent ions to a single fixed-charged group, iii) binding the multivalent ions to multiple fixed-charged groups in the membrane structure. In the first scenario, the transport of multivalent ions creates electroneutrality by dropping the potential difference between the compartments because two monovalent ions (Cl⁻) are equal to one divalent ion (SO₄²⁻) in the opposite transport direction. In the second scenario, a multivalent ion stack inside the membrane cross-section structure decreases the ion exchange capacity and permselectivity. In the third scenario, multivalent ions located within the membrane cross-

section cause severe membrane resistances since they reduce the free volume of the membrane, resulting in the reduction of the ion exchange capacity. [20-22]. Lastly, organic molecules in the feed solution create fouling layers in the membrane structure, and the layers prevent ion transport by increasing membrane resistance. These layers also cause an increased pressure drop, increasing the pumping power of the electrolyte solution to the RED system. Therefore, the P_{Net} produced by the RED system is reduced by increased energy consumption [27]. This study investigated the effects of the parameters above-mentioned on power generation performance in detail.

3.1. Effect of concentration and flow velocity of electrolyte solution on RED performance

Table 3 indicates the power generation performance, where only NaCl salt ions were used. The power density values in Table 3 are the maximum values obtained from the RED system. The maximum power density was obtained at a current density of 4 A/m^2 for the $0.017 \text{ M NaCl} / 0.513 \text{ M NaCl}$ electrolyte solution pair while at a current density of 6 A/m^2 for the $0.1 \text{ M NaCl} / 2.5 \text{ M NaCl}$ electrolyte solution pair. The results indicated that the power density increased with increasing flow velocity at both concentration pairs. Similarly, the same trend in the effect of flow velocity and feed electrolyte concentration on power generation performance was observed in the literature [7, 29]. Increasing the flow velocity allows for decreasing the non-ohmic resistances formed in the membrane structure [13]. The thickness of the boundary and bulk concentration layers, known as non-ohmic resistances, increase on the membrane surface on time, especially at low flow velocities, and create a mass transfer resistance [28]. Decreasing t_{res} (Equation 7) and increasing Re (Equation 9) cause the acceleration of ion transport across the membrane cross-section, increasing the generated power density since boundary and bulk concentration layer thicknesses decrease. Similarly to the power density values, the experimental OCV and calculated average membrane permselectivity (%) values shown in Figure 2 also increase as the flow velocity increases due to decreasing non-ohmic resistances.

Further, Table 3 points out no significant difference in power density between the solution pairs with different salinities at flow velocities of 0.26 cm/s and 0.52 cm/s , even though there was a statistical difference in the theoretical and experimental OCV values at these velocities between the solution pairs. However, the generated power density at the flow velocity of 2.09 cm/s in the $0.017 \text{ M NaCl} / 0.513 \text{ M NaCl}$ electrolyte solution pair was higher than the $0.1 \text{ M NaCl} / 2.5 \text{ M NaCl}$ electrolyte solution pair. This result is consistent with the OCV and permeability in Figure 2.

It is known that the power density produced by the RED system also includes the P_{Pump} . Therefore, calculating the P_{Net} produced by the system is extremely important in determining the system's efficiency. Table 3 shows the highest power density value was obtained at a 2.09 cm/s flow velocity in both electrolyte solution pairs. In parallel with this result, the power consumed by the pump at the highest flow velocity was also calculated as the highest. At this point, although the RED system produced the highest power value at a flow velocity of 2.09 cm/s , considering the P_{Pump} , it was found that the P_{Net} generated at a flow velocity of 0.52 cm/s was the optimum value for the RED system. Also, the system yield calculations show that the highest efficiency was achieved at a flow velocity of 0.52 cm/s for both solution pairs.

Investigation of Influencing Factors on Power Generation Performance in Reverse Electrodialysis

Considering the results in this section, 0.017 M NaCl / 0.513 M NaCl electrolyte solution pair was selected as the optimum for the remainder of the studies due to the higher yield obtained from the RED system. This choice also serves the idea of using the RED system in real applications at the junction of sea (0.513 M NaCl) and river (0.017 M NaCl) on a model scale.

Table 3. The RED performance of Fujifilm Type II IEMs in the presence of monovalent ions.

Feed Compositions	Flow velocity (cm/s)	Re	t_{res} (s)	Power density (W/m ²)	P_{Pump} (W/m ²)	P_{Net} (W/m ²)	* $P_{Theoric}$ (W/m ²)	**Yield (%)
0.017M (NaCl) & 0.513M (NaCl)	0.26	2.30	38.4	0.156	0.001	0.155	0.270	57.4
	0.52	4.70	19.1	0.175	0.004	0.171		63.3
	2.09	18.7	4.80	0.197	0.066	0.131		48.5
0.1 M (NaCl) & 2.5 M (NaCl)	0.26	2.30	38.4	0.160	0.001	0.159	0.387	41.1
	0.52	4.70	19.1	0.174	0.004	0.170		43.9
	2.09	18.7	4.80	0.177	0.066	0.111		28.7

* $P_{Theoric} = OCV_{Theoric} \times Current$, **Yield (%) = ($P_{Net} / P_{Theoric}$) x 100, $OCV_{Theoric}$ data given in Figure 2a.

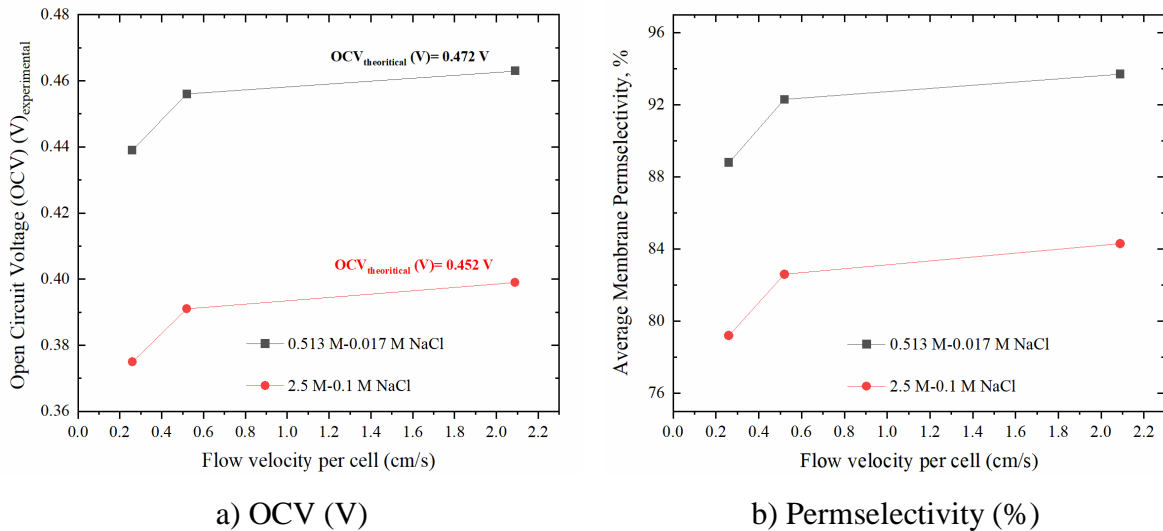


Figure 2. a) Experimental OCV (V), b) Average membrane permselectivity (%). Average membrane permselectivity was calculated as the ratio of experimental and theoretical OCV values ($OCV_{experimental}/OCV_{theoretical}$) (Theoretical OCV values were embedded in Figure 2a).

3.2. Effect of multivalent ion and flow velocity of electrolyte solution on RED performance

In real energy harvesting applications, monovalent and multivalent ions are present simultaneously in the feed electrolyte solutions [19-23]. Therefore, examining the multivalent ions' effect on the power generation performance is essential. In this section, the power densities of the RED system in the presence of divalent ions (SO_4^{2-}) were determined using different electrolyte solution concentrations and flow velocities. Table 4 indicates the power density and

P_{Net} values produced by the RED system and power loss (PL) when SO_4^{2-} are in different mole ratios in concentrate and dilute electrolyte solution compartments. The PL values in Table 4 show the power density difference of the RED system performed in the presence and absence of SO_4^{2-} ions.

The results indicated the power density increased as the flow velocity increased in all feed solution compositions, like the monovalent (Cl^-) ion study. However, it has been shown that the power density produced in the presence of SO_4^{2-} ions was lower compared with the presence of Cl^- ions (Table 3). These results indicate a decrease in generated power density when SO_4^{2-} ions are used. There are two fundamental reasons for the occurrence of PL. The first is the uphill transport created by the SO_4^{2-} ions since the membranes have low permselectivity against $\text{Cl}^-/\text{SO}_4^{2-}$ ions, and the second is the increasing membrane resistances in the presence of SO_4^{2-} ions. Further, the PL also varies depending on the SO_4^{2-} ion concentrations and the compartments in which it is used (Table 4). To this end, the effect of SO_4^{2-} ion concentration and the compartment composition on the PL was investigated by applying two different strategies in detail.

In the first strategy, the same amount of SO_4^{2-} ions was used in the dilute and concentrate compartments (Table 4). The results showed that increasing the amount of SO_4^{2-} ions from 10% mole to 50% mole in the total electrolyte solution decreased the power density dramatically and parallelly increased the PL. Pintossi et al. [20, 22] reported similar results and observed that power density decreased when the mole ratio of SO_4^{2-} ions increased in the feed electrolyte solution. These results can be explained by the three different transport: i) low permselectivity of AEMs ($\text{Cl}^-/\text{SO}_4^{2-}$), ii) reduced fixed charge group numbers in AEMs, and iii) increased membrane resistance. Increasing the multivalent ion concentrations in the feed electrolyte solution made these three transports more dominant, resulting in a heavy loss of power density. Figure 3 shows the theoretical and experimental OCV values and the average membrane permselectivity as a function of SO_4^{2-} ion concentrations using three different flow velocities. The difference between the theoretical and experimental OCV values shows a measure of total resistances formed on the membrane and $\text{Cl}^-/\text{SO}_4^{2-}$ permselectivity. Although the theoretical OCV value of the system when using the 50% mole of SO_4^{2-} ions in both compartments' solution was the highest, the experimental OCV values were the lowest at three different flow velocities. This means high SO_4^{2-} ion concentrations create more total resistances by decreasing membrane permselectivity, resulting in a loss of power density.

The second strategy used different SO_4^{2-} ion concentrations in the dilute and concentrate compartments to understand the compartment composition's effects on the RED performance. High ion concentration was first used in the dilute and then in the concentrate compartments (Table 4). The results showed that when the high SO_4^{2-} ion concentration was used in the dilute compartment, the power density values at three flow velocities decreased more than the low SO_4^{2-} ion concentration used in the same compartment. The reason is that electroneutrality is the dominant transport mechanism when using high SO_4^{2-} ion concentration in dilute compartments rather than the resistances. In summary, the PL results in Table 4 indicate divalent ions in the feed electrolyte solution cause heavy power density loss due to creating uphill transport, increasing total resistance, and decreasing membrane permselectivity.

Table 4. The RED performance of Fujifilm Type II IEMs in the presence of multivalent ions.

Membranes	Flow velocity (cm/s)	Re	t_{res} (s)	Power density (W/m ²)	P_{pump} (W/m ²)	P_{Net} (W/m ²)	*PL (%)
0.017 M (90% NaCl+10% Na ₂ SO ₄) & 0.513 M (90% NaCl+10% Na ₂ SO ₄)	0.26	2.30	38.4	0.115	0.001	0.114	26.5
	0.52	4.70	19.1	0.142	0.004	0.138	19.3
	2.09	18.7	4.80	0.183	0.066	0.117	10.7
0.017 M (50% NaCl+50% Na ₂ SO ₄) & 0.513 M (50% NaCl+50% Na ₂ SO ₄)	0.26	2.30	38.4	0.085	0.001	0.084	45.8
	0.52	4.70	19.1	0.093	0.004	0.089	47.9
	2.09	18.7	4.80	0.111	0.066	0.045	65.6
0.017 M (50% NaCl+50% Na ₂ SO ₄) & 0.513 M (90% NaCl+10% Na ₂ SO ₄)	0.26	2.30	38.4	0.114	0.001	0.113	27.1
	0.52	4.70	19.1	0.116	0.004	0.111	35.1
	2.09	18.7	4.80	0.133	0.066	0.067	48.9
0.017 M (90% NaCl+10% Na ₂ SO ₄) & 0.513 M (50% NaCl+50% Na ₂ SO ₄)	0.26	2.30	38.4	0.122	0.001	0.121	22.0
	0.52	4.70	19.1	0.128	0.004	0.124	27.5
	2.09	18.7	4.80	0.152	0.066	0.086	34.4

*PL (%) = ((P_{NET})_{NaCl} - (P_{NET})_{NaCl+Na₂SO₄}) / (P_{NET})_{NaCl}, (P_{NET})_{NaCl} data given in Table 2.

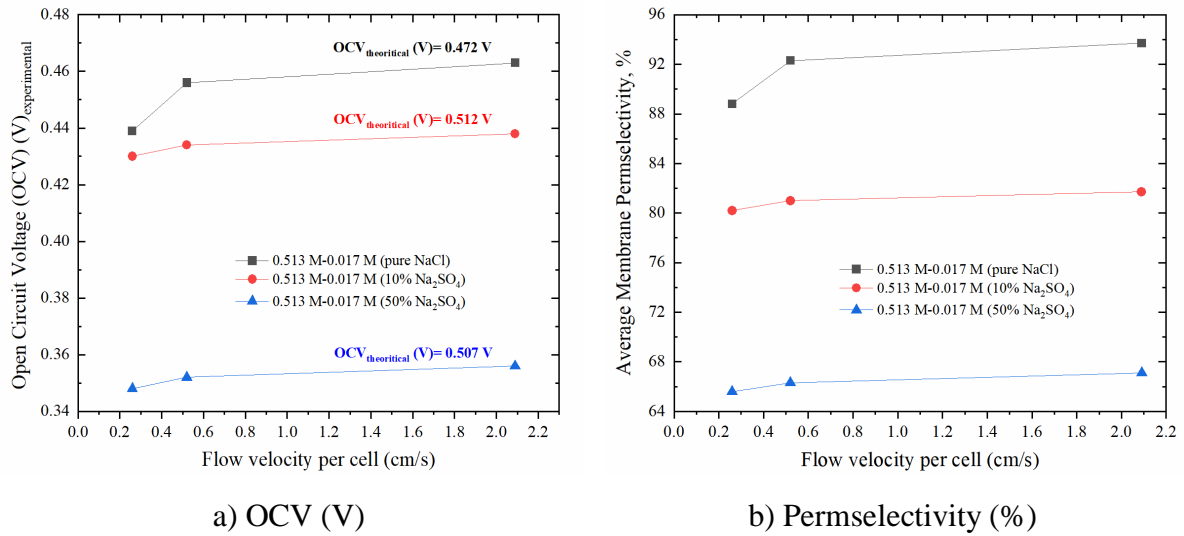


Figure 3. a) Experimental OCV (V), b) Average membrane permselectivity (%). Average membrane permselectivity was calculated as the ratio of experimental and theoretical OCV values ($OCV_{experimental}/OCV_{theoretical}$) (Theoretical OCV value was embedded in Figure 3a).

3.3. Organic fouling tendency and long-term performance of IEMs

The determination of the fouling behavior of membranes is of such importance for guiding real applications. It is well known that organic, inorganic, and biological substances are commonly present in natural water sources, and these substances play a significant role in membrane fouling, decreasing performance and shelf life and increasing operating costs [23]. In the scope of this study, the organic fouling behavior of AEMs was tested using a real (not model) humic and fulvic acid mixture solution. The main reason for examining the fouling behavior of AEMs is that their structures have a positive charge. Most of the substances in nature have a negative charge. Therefore, the electrostatic interactions between the negatively charged substances and positively charged AEMs surfaces become more dominant and trigger fouling exponentially. Since CEMs have a negative charge, electrostatic repulsion occurs between the contaminant and the membrane surface. Therefore, CEMs do not get fouled as much as AEMs. For this reason, there is a vigorous effort in the literature to produce fouling-resistant AEMs.

Figure 4 shows the P_{Net} values of the RED system before and after exposure of the AEMs to the humic and fulvic acid mixture solution. The maximum P_{Net} values were obtained at a current density of 8 A/m^2 for both conditions. However, a 30% decrease was observed in the maximum P_{Net} values after membrane fouling. This is because organic acid molecules are present in the membrane structure even after washing. Figure 5 shows AEM surface images before and after the fouling test. While the non-fouled membrane is white, the fouled membrane is yellow-brown. The color change refers to the presence of organic molecules in the membrane structure, decreasing the power generation performance of the RED system by reducing permselectivity and increasing resistances. Vital et al. [30] used natural water in reverse electrodialysis for energy generation and observed fouling on the membrane surface since the membrane color changed dramatically after the operation, like ours. Further, they applied the pre-treatment protocol to the feed water to mitigate the membrane fouling, and the results indicated the pre-treatment worked to prevent fouling. Similarly, Vermaas et al. [23] investigated the effect of natural seawater and river water for the feed electrolyte solution on the energy generation performance from the RED system with a long-term study. They reported that power density dropped approximately 40% at the end of the first day due to the organic fouling layers on the membrane structures.

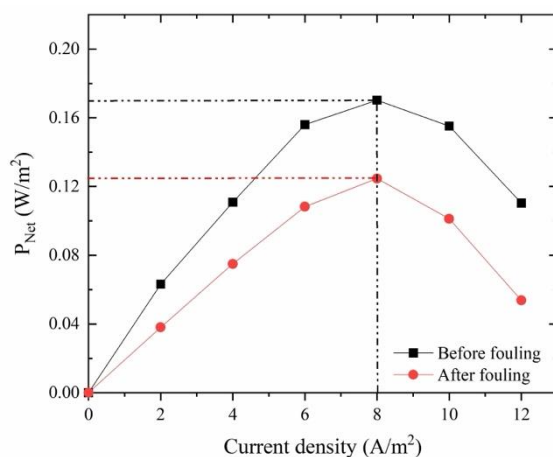


Figure 4. Effect of organic foulants on the power generation performance. (0.52 cm/s constant flow velocity and 0.017 M NaCl / 0.513 M NaCl electrolyte solution pair)

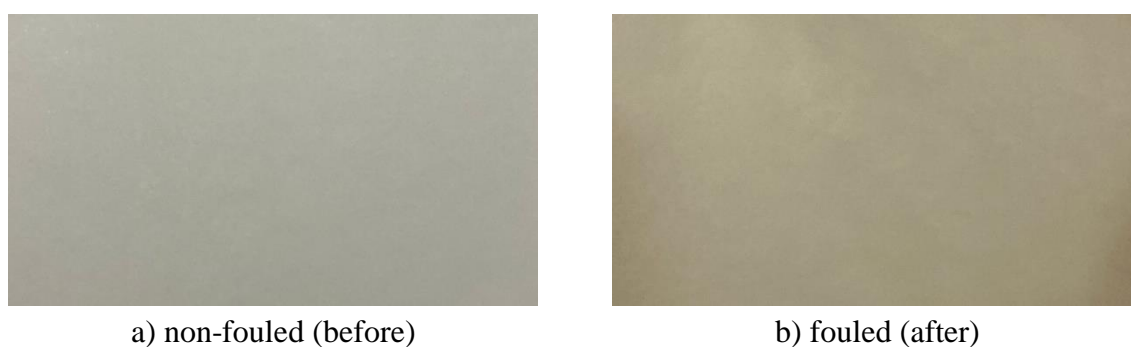


Figure 5. Membrane surface images a) before and b) after exposure to organic acid mixture.

Testing membranes' long-term performance is critical in determining their usability in industrial-scale systems. To this end, the RED system was operated for 4 hours nonstop with a constant current density of 8 A/m² and flow velocity of 0.52 cm/s with a 0.017 M NaCl / 0.513 M NaCl electrolyte solution pair. Figure 6 shows the RED system's long-term power generation performance. The result indicates that the initial P_{Net} value of the RED system where non-fouled membranes are used decreased gradually until 2 hours. Then, the value almost reached a stable and kept constant. The reason for the drop in performance in the first 2 hours is the accumulation of salt ions in the membrane structure over time. This means that fouling slowly occurred in the membrane structure. This period can be defined as the time required for the system to reach a steady state. On the other hand, the initial P_{Net} of the RED system where fouled membranes decreased sharply by almost 30%, and the value was constant during the operation. These obtained results show that membrane fouling significantly reduces the power generation performance of the RED system.

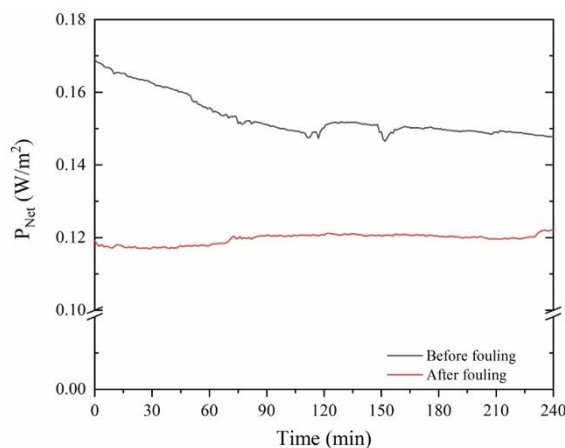


Figure 6. Long-term stability test of the RED system.

4. Conclusion

This study showed the effect of divalent ions, organic acids, electrolyte solution concentration, and flow velocity, significantly affecting the power generation performance in real applications. The flow velocity effect results indicated that the power generation performance decreased as the flow velocity reduced due to increased system resistances with decreasing flow velocity, especially non-ohmic resistances. The general projection for industrial-scale RED applications is to use sea and river water as feed electrolyte solutions. In this respect, the solution concentration pair used in this study, which corresponds to sea and river salinity, is of a nature that will shed light on industrial-scale studies. This study also indicated that divalent ions and organic substances seriously affected the power generation performance negatively. In particular, a significant drop in performance was observed as the concentration of divalent ions used in the compartments was increased. In addition, studies on the effect of composition in the compartments have shown that high divalent ion concentrations used in the dilute compartments have a more negative on performance. These results reveal that electrolyte solutions must be pretreated before feeding them to the RED system. In addition to the pretreatment protocol, coating the membrane surfaces with fouling-resistant materials, especially organic and biofouling, will reduce fouling and increase monovalent ion selectivity, increasing energy efficiency.

Ethics in Publishing

There are no ethical issues regarding the publication of this study.

Author Contributions

The author contributed to the study in terms of data curation, investigation, conceptualization, writing-original draft, funding acquisition, and project administration.

Acknowledgments

This study was supported by the Scientific and Technological Research Council of Turkey (TÜBİTAK) under the 2218 National Postdoc Project (Grant Number: 118C549). The author thanks TÜBİTAK for their support. I acknowledge FUJIFILM Manufacturing Europe BV for sending Fujifilm Type II IEMs and Assoc. Prof. Dr. Enver GÜLER for his effort in providing them. I want to acknowledge Prof. Dr. Nalan KABAY for providing me with all the equipment I need to use in my work.

References

- [1] Yip, N. Y., Brogioli, D., Hamelers, H. V. M., Nijmeijer, K. (2016) Salinity gradients for sustainable energy: primer, progress, and prospects. *Environmental Science & Technology*, 50 (22), 12072-12094.
- [2] Logan, B. E., Elimelech, M., (2012) Membrane-based processes for sustainable power generation using water. *Nature*, 488, 313-319.
- [3] Ramon, G. Z., Feinberg, B. J., Hoek, E. M. V. (2011) Membrane-based production of salinity gradient power. *Energy & Environmental Science*, 4, 4423-4434.
- [4] Weinstein, J. N., Leitz, F. B. (1976) Electric power from differences in salinity: the dialytic battery. *Science*, 191, 557-559.
- [5] Veerman, J., Saakes, M., Metz, S. J., Harmsen, G. J. (2010) Electrical power from sea and river water by reverse electrodialysis: a first step from the laboratory to a real power plant. *Environmental Science & Technology*, 44, 9207-9212.
- [6] Kuleszo, J., Kroeze, C., Post, J., Fekete, B. M. (2010) The potential of blue energy for reducing emissions of CO₂ and non-CO₂ greenhouse gases. *Journal of Integrative Environmental Sciences*, 7, 89-96.
- [7] Długołęcki, P., Antoine, G., Nijmeijer, K., Wessling, M. (2009) Practical potential of reverse electrodialysis as process for sustainable energy generation. *Environmental Science & Technology*, 43 (17), 6888-6894.
- [8] Tristan, C., Fallanza, M., Ibanez, R., Ortiz, I. (2020) Recovery of salinity gradient energy in desalination plants by reverse electrodialysis. *Desalination*, 496, 114699.
- [9] Tian, H., Wanga, Y., Peia, Y., Crittenden, J. C. (2020) Unique applications and improvements of reverse electrodialysis: A review and outlook. *Applied Energy*, 262, 114482-114506.
- [10] Audinos, R. (1983) Electrodialyse inverse. Etude de l'energie electrique obtenue a partir de deux solutions de salinites differentes. *Journal of Power Sources*, 10, 203-217.

- [11] Długolecki, P., Nijmeijer, K., Metz, S., Wessling, M. (2008) Current status of ion exchange membranes for power generation from salinity gradients. *Journal of Membrane Science*, 319, 214-222.
- [12] Veerman, J., de Jong, R. M., Saakes, M., Metz, S. J., Harmsen, G. J. (2009) Reverse electrodialysis: comparison of six commercial membrane pairs on the thermodynamic efficiency and power density. *Journal of Membrane Science*, 343, 7-15.
- [13] Długolecki, P., Ogonowski, P., Metz, S. J., Saakes, M., Nijmeijer, K., Wessling, M. (2010) On the resistances of membrane, diffusion boundary layer and double layer in ion exchange membrane transport. *Journal of Membrane Science*, 349, 369-379.
- [14] Veerman, J., Saakes, M., Metz, S. J., Harmsen, G. J. (2011) Reverse electrodialysis: a validated process model for design and optimization. *Chemical Engineering Journal*, 166, 256-268.
- [15] Vermaas, D. A., Saakes, M., Nijmeijer, K. (2011) Doubled power density from salinity gradients at reduced intermembrane distance. *Environmental Science & Technology*, 45, 7089-7095.
- [16] Burheim, O. S., Seland, F., Pharoah, J. G., Kjelstrup, S. (2012) Improved electrode systems for reverse electro-dialysis and electro-dialysis. *Desalination*, 285, 147-152.
- [17] Veerman, J., Saakes, M., Metz, S. J., Harmsen, G. J. (2010) Reverse electrodialysis: evaluation of suitable electrode systems. *Journal of Applied Electrochemistry*, 40, 1461-1474.
- [18] Vermaas, D. A., Bajracharya, S., Sales, B. B., Saakes, M., Hamelers, B., Nijmeijer, K. (2013) Clean energy generation using capacitive electrodes in reverse electrodialysis. *Energy & Environmental Science*, 6, 643-651.
- [19] Tedesco, M., Brauns, E., Cipollina, A., Micale, G., Modica, P., Russo, G., Helsen, J. (2015) Reverse electrodialysis with saline waters and concentrated brines: a laboratory investigation towards technology scale-up. *Journal of Membrane Science*, 492, 9-20.
- [20] Pintossi, D., Chen, C-L., Saakes, M., Nijmeijer, K., Borneman, Z. (2020) Influence of sulfate on anion exchange membranes in reverse electrodialysis. *npj Clean Water*, 3, 29.
- [21] Vermaas, D. A., Veerman, J., Saakes M., Nijmeijer, K. (2014) Influence of multivalent ions on renewable energy generation in reverse electrodialysis. *Energy & Environmental Science*, 7, 1434-1445.
- [22] Pintossi, D., Simoes, C., Saakes, M., Borneman, Z., Nijmeijer, K. (2021) Predicting reverse electrodialysis performance in the presence of divalent ions for renewable energy generation. *Energy Conversion and Management*, 243, 114369.
- [23] Vermaas, D. A., Kunteng, D., Saakes, M., Nijmeijer, K. (2013) Fouling in reverse electrodialysis under natural conditions. *Water Research*, 47, 1289-1298.

[24] <https://www.sefar.com/en/>, 01.10.2024.

[25] Jang, J., Kang, Y., Han, J. H., Jang, K., Kim, C. M., Kim, I. S. (2020) Developments and future prospects of reverse electrodialysis for salinity gradient power generation: Influence of ion exchange membranes and electrodes. *Desalination*, 491, 114540.

[26] Emdadi, A., Hestekin, J., Greenlee, L. F. (2021) Salt screening analysis for reverse electrodialysis. *Sustainable Energy & Fuels*, 5, 6135-6144.

[27] Golubenko, D. V., Van der Bruggen, B., Yaroslavtsev, A. B. (2021) Ion exchange membranes based on radiation-induced grafted functionalized polystyrene for high-performance reverse electrodialysis. *Journal of Power Sources*, 511, 230460.

[28] Vermaas, D. A., Guler, E., Saakes, M., Nijmeijer, K. (2012) Theoretical power density from salinity gradients using reverse electrodialysis. *Energy Procedia*, 20, 170-184.

[29] Altıok, E., Kaya, T. Z., Güler, E., Kabay, N., Bryjak, M. (2021) Performance of reverse electrodialysis system for salinity gradient energy generation by using a commercial ion exchange membrane pair with homogeneous bulk structure. *Water*, 13, 814.

[30] Vital, B., Torres, E. V., Sleutels, T., Gagliano, M. C., Saakes, M., Hamelers, H. V. M. (2021) Fouling fractionation in reverse electrodialysis with natural feed waters demonstrates dual media rapid filtration as an effective pre-treatment for fresh water. *Desalination*, 518, 115277.

Enhanced Classification of Skin Lesions Using Fine-Tuned MobileNet and DenseNet121 Models with Ensemble Learning

Yasin SANCAR ^{1*}

¹Ataturk University, Faculty of Open and Distance Education, Department of Information Systems, Erzurum, Türkiye

Received: 08/11/2024, **Revised:** 27/11/2024, **Accepted:** 30/11/2024, **Published:** 31/12/2024

Abstract

This study presents a deep learning approach for early detection of melanoma, one of the most dangerous skin cancers. In this article, all pre-trained models of the Keras library are trained with the ISIC skin cancer dataset available on Kaggle and the accuracy of each model is analyzed in detail. With the results obtained from the trained models, the models were fine-tuned to further optimize the performance of each model. After re-evaluation with fine-tuning, the accuracy rates were compared: DenseNet121 and MobileNet were found to be the two best models with high accuracy among the fine-tuned models. As such, these two models were combined in an ensemble approach to achieve a better overall accuracy. The skin cancer detection rate obtained with this ensemble approach is 93.03%. Therefore, the deep learning-based ensemble method appears to be a reliable and powerful technique that can be used to diagnose serious diseases such as skin cancer. This model can be used to provide a powerful support system with great potential to assist dermatologists in the early detection phase by easing workload and improving patient outcomes.

Keywords: Transfer learning, skin cancer classification, fine tuning, model ensemble

Topluluk Öğrenmesi ile İnce Ayarlı MobileNet ve DenseNet121 Modelleri Kullanılarak Cilt Lezyonlarının Geliştirilmiş Sınıflandırılması

Özet

Bu çalışma, en tehlikeli cilt kanserlerinden biri olan melanomun erken teşhisi için bir derin öğrenme yaklaşımı sunmaktadır. Bu makalede, Keras kütüphanesinin önceden eğitilmiş tüm modelleri, Kaggle'da bulunan ISIC cilt kanseri veri kümesi ile eğitilmiş ve her modelin doğruluğu ayrıntılı olarak analiz edilmiştir. Eğitilen modellerden elde edilen sonuçlarla, her modelin performansını daha da optimize etmek için modellere ince ayar yapılmıştır. İnce ayar ile yeniden değerlendirme yapıldıktan sonra doğruluk oranları karşılaştırılmıştır. DenseNet121 ve MobileNet, ince ayarlı modeller arasında yüksek doğruluk oranına sahip en iyi iki model olarak bulunmuştur. Bu nedenle, bu iki model daha iyi bir genel doğruluk elde etmek için bir topluluk yaklaşımında birleştirilmiştir. Bu topluluk yaklaşımı ile elde edilen cilt kanseri tespit oranı %93,03. Bu nedenle, derin öğrenme tabanlı topluluk yöntemi, cilt kanseri gibi ciddi hastalıkların teşhisinde kullanılabilecek güvenilir ve güçlü bir teknik olarak görünmektedir. Bu model, iş yükünü hafifleterek ve hasta sonuçlarını iyileştirerek erken teşhis aşamasında dermatologlara yardımcı olmak için büyük potansiyele sahip güçlü bir destek sistemi sağlamak için kullanılabilir.

Anahtar Kelimeler: Transfer öğrenme, cilt kanseri sınıflandırma, ince ayar, model birleştirme

1. Introduction

Ultraviolet or ultraviolet rays with wavelengths between 100 and 400 nanometers have a significant effect on skin cancer [1]. These rays are divided into three categories: UV-A, UV-B and UV-C. UV-C rays are relatively less harmful than other rays and cannot reach the skin surface because they are absorbed by the atmosphere [2]. However, if UV-B and UV-C rays come into contact with the skin, it can cause damage to the skin tissue and cancer. Melanoma, a type of skin cancer, is divided into two types: benign and malignant, with an irregular structure containing several colors [3]. Early detection of malignant melanoma allows dermatologists to recommend surgical removal of the affected skin area to prevent the spread of the malformation in melanoma cells. Automatic disease recognition and diagnosis systems with machine learning and deep learning methods have been rapidly increasing in medical applications in recent years [4, 5, 6, 7]. These applications help specialists and significantly reduce their workload. Similarly, pre-diagnostic decision support systems have been proposed for skin cancer detection. In this study, a deep learning-based skin lesion detection mechanism is developed using images from the ISIC archive on Kaggle. In order to compare the performance of the proposed model with state-of-the-art models for early detection of malignant melanomas, only studies using the same dataset are evaluated.

1.1. Related studies

In a study by Basaran and Celik [8], the ISIC dataset was first trained with the EfficientNetB0 model and then deep features were obtained using Particle Swarm Optimization (PSO) and Genetic algorithm (GA) with the fully connected layer of this model. The features selected over different feature combinations were classified with Support Vector Machine, one of the classical machine learning methods, and an accuracy rate of 89.1% was achieved. Anand et al. [9] aimed to improve model accuracy by adding a flat layer, two dense layers with an activation function called LeakyRelu, and a sigmoid layer to a pre-trained VGG16 model and achieved 89.09% accuracy on the ISIC dataset. Sethanan et al. [10] classified melanoma, vascular lesions, melanocytic nevus, cutaneous fibromas, benign keratosis, and different carcinomas and skin moles using the HAM10000 dataset along with the ISIC dataset. In the proposed model, the input images are passed through the CNN model by applying image segmentation methods such as U-net, RP-Net, Threshold method, Edge detection and data augmentation such as rotation, shifting, and flipping in a dual artificial multiple intelligence system (AMIS). The proposed model outperformed the traditional CNN models with 98.4% on the hybrid dataset. Hussein et al. [11] applied various transfer learning networks such as AlexNet, ResNet-18, SqueezeNet, and ShuffleNet to the ISIC dataset and observed that the ResNet-18 model performed relatively better than other models with an accuracy of 89.9%. On the other hand, when precision, sensitivity and specificity values were compared, it was seen that the specificity rate exceeded 90% in the SqueezeNet model and surpassed the other models. Precision values showed slight differences in other models except ShuffleNet. However, when the F1 score value is analyzed, it is seen that the ResNet

model has better performance than the other transfer learning models in general. Tuncer et al. [12] presented a CNN model called TurkerNet, which aims to improve classification performance by minimizing the number of trainable parameters by working on four basic components: input block, residual bottleneck block, efficient block and output. Since the proposed model shows high performance with an accuracy of 92.12% even with low trainable parameters, it can be frequently preferred in medical applications as a low-weight CNN model. Bazgir et al. [13] proposed an optimized Inception model for skin cancer based on the InceptionNet architecture with data augmentation and the addition of base layers. The proposed model was applied to the dataset from the ISIC archive and achieved 84.39% and 85.94% accuracy rates in Adam and Nadam optimizations, respectively. In another recent study presenting a deep learning-based approach, Prasad et al. [14] applied EfficientNet-B3, a deep transfer learning model, to ISIC data with rescaling, brightness, and contrast equalization preprocessing in the range of 20%. As a result of the experimental studies, 90.62% accuracy, 90.21% recall, 91.33% F1-score and 91.91% precision were obtained. A general comparison of the studies using the raw dataset I used in this study is presented in Table 1.

Table 1. Comparison of Classification Methods for Skin Lesion Analysis

Year	Study	Method	Classifier	Accuracy
2022	Basaran and Celik [8]	PSO-GA	SVM	89.1%
2022	Anand et al. [9]	VGG16	Softmax	89.09%
2022	Alfi et al. [15]	CNN	Softmax	92%
2023	Ramya and Sathiyabhama [16]	Enhanced genetic algorithm	SVM	89.19%
2023	Hussein et al. [11]	ResNet-18	Softmax	89.39%
2023	Shekar and Hailu [17]	DenseNet-169, local binary pattern	Random Forest	89.70%
2024	Bazgir et al. [13]	Optimized InceptionNet	Softmax	85.94%
2024	Prasad et al. [14]	EfficientNet-B3	Softmax	90.62%
2024	Turker et al. [12]	TurkerNet	Softmax	92.12%
	This study	Ensemble of Fine Tuned MobileNet and DenseNet121	Softmax	93.03%

1.2. Research Contributions

The main research contributions of this work are listed below: • The proposed MobileNet-DenseNet ensemble model outperforms other works in the literature using the same dataset, making significant progress in skin lesion diagnosis.

- The experimental results are presented in comparison with widely used pre-trained network models that have shown successful results in the literature.

- The highest performance was achieved by combining the DenseNet and MobileNet architectures from the pre-trained transfer learning models, and this achievement was compared with different studies in the literature using the same dataset.

- A fusion-based pre-trained transfer learning approach is proposed to improve skin lesion classification performance.

The flow diagram of the hybrid model combining DenseNet and MobileNet transfer learning networks with CNN is given in Figure 3.

2. Materials and Methods

2.1. Dataset

For the study, the Kaggle skin cancer dataset, an open-source platform containing 1800 images of benign and malignant skin lesions sized 224*224, was used [18]. This special dataset consists of training and test sets containing images divided into two classes: benign and malignant. Figure 1 shows a representative example of the dataset. Data augmentation included random rotations, zoom, and contrast adjustments to simulate diverse real-world scenarios, improving model robustness.

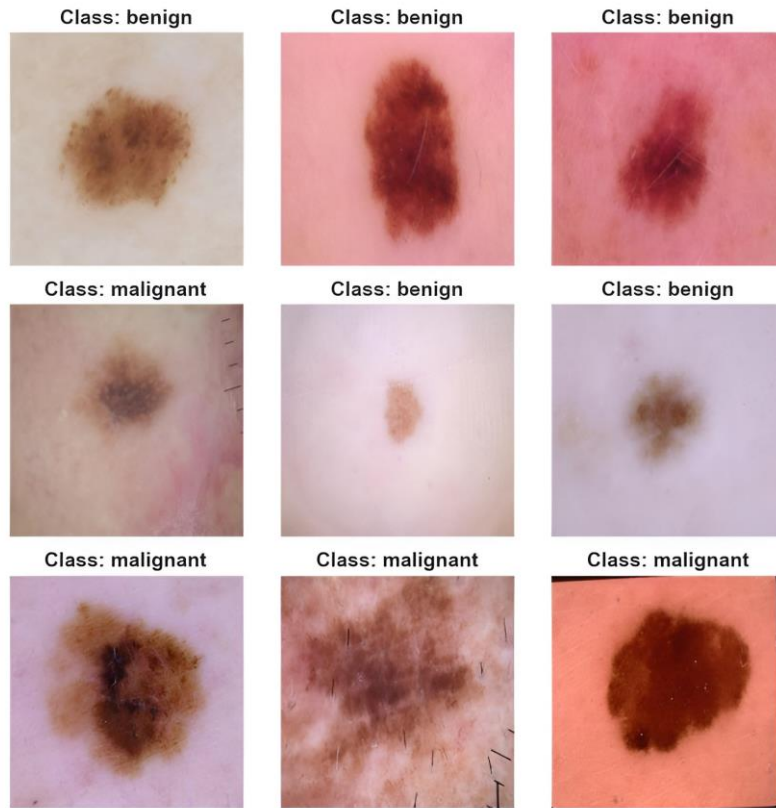


Figure 1. ISIC Archive sample skin lesions

As seen in Figure 2, the dataset of this study has been divided into training and test sets according to class labels. The benign dataset contains 360 images for testing and 1440 images for training. Similarly, for malignant training, 1197 training and 300 test images have been allocated.

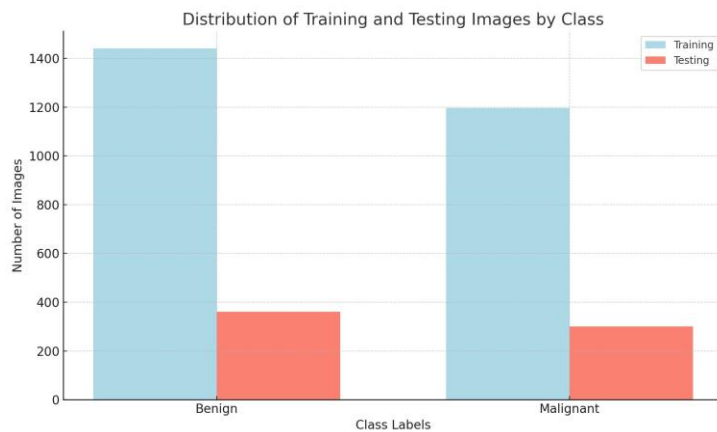


Figure 2. The number of benign and malignant lesions in the training and test dataset

2.2. The proposed ensemble transfer learning model

The use of pre-trained transfer learning models in the field of healthcare has significantly improved classification performance in recent years. The hyper-parameters of these models and the fact that the datasets on which the deep learning approaches are trained are balanced and contain a sufficient number of data affect the classification performance. In this study, I propose a hybrid use of a pre-trained deep learning approach on original data for skin lesion classification. Figure 3 shows the general flowchart of the proposed MobileNet-DenseNet ensemble model. In the proposed model, all layers in MobileNet are made trainable and fine tuned without any preprocessing of the original data set. Then, using the CNN architecture, GlobalAverageMaxPooling2d, Dense 1024, Batch Normalization, Dropout (0.5), Dense 64 and Dense 2 layers were used to reduce the number of classes to two, malignant and benign, by gradually reducing the layers in order not to lose the features obtained from the pre-trained model. As a second model, the last 171 layers of the DenseNet121 model out of a total of 427 layers are trainable and subjected to fine tuning. After the same CNN operations, the output obtained from both models was combined end-to-end to obtain a hybrid ensemble model.

The Global Average Pooling layer is a process that calculates the average output of the feature map in the previous layer. As shown in Figure 3, a

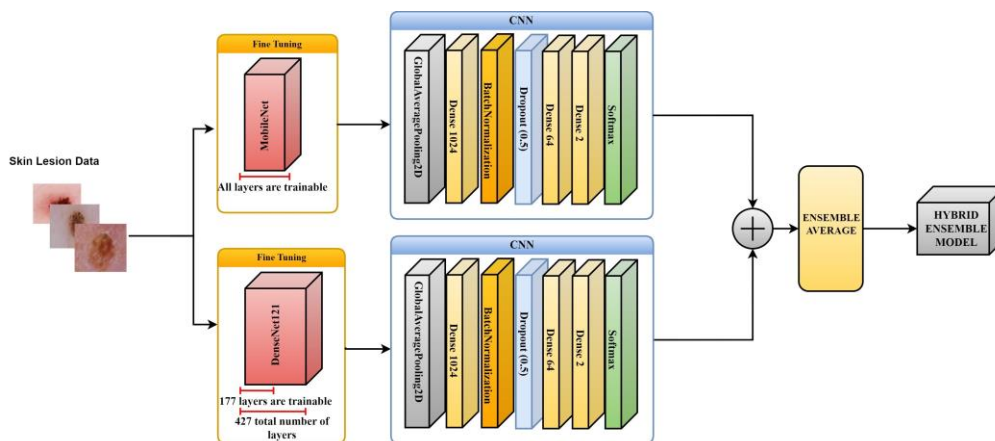


Figure 3. The diagram of the proposed ensemble transfer learning model

Global Average Pooling layer preceding the Dense layer fully connected layer is used to extract features from the trainable layers where fine tuning is performed. With this average calculation, the features are significantly reduced, preparing the model for the final classification layer. In Global Average Pooling, overfitting is avoided by averaging the feature map. A dropout layer is used to reduce overfitting during the training process. It is the elimination of some memorizing nodes in the network to prevent the network from being memorized. Thus, the memorization of the network is tried to be eliminated. The dropout layer is a flattening layer for fully connected layers. Dropout increases the smoothing ability

of the neural network. With dropout, neurons in the network are randomly assigned a zero weight value. For this process, the dropout rate is set to 0.5 to make the model robust to small changes in the input and to ensure high performance models. Dense fully connected layers, which are added after the dropout process, are gradually reduced to 2 classes in order to prevent the loss of features and these features are given to the Softmax layer to give the classification result. The training process employed the Adam optimizer with a learning rate of 0.001, chosen for its balance between convergence speed and stability. Other hyperparameters, such as batch size (32) and dropout rates (0.5), were fine-tuned through cross-validation to avoid overfitting.

2.2. Mathematical Model for Global Average Pooling, Dropout, and Average Ensemble

Let F represent the output feature map of the preceding layer, as follows:

$$F = \begin{bmatrix} f_{1,1} & f_{1,2} & \cdots & f_{1,n} \\ f_{2,1} & f_{2,2} & \cdots & f_{2,n} \\ \vdots & \vdots & \ddots & \vdots \\ f_{m,1} & f_{m,2} & \cdots & f_{m,n} \end{bmatrix}$$

where the output of the j -th channel of the i -th feature map is represented by $f_{i,j}$.

The average output for every channel is determined by the Global Average Pooling operation:

$$G = \frac{1}{H \times W} \sum_{h=1}^H \sum_{w=1}^W F_{h,w}$$

where H and W represent the feature map's height and width, respectively, to create a vector G that represents the feature map's summary. This technique works well to lessen overfitting. [19]

In order to avoid overfitting, the Dropout layer then randomly changes a fraction p of the input units to zero during training:

$$Y = D(F) = \begin{cases} F & \text{with probability } 1 - p \\ 0 & \text{with probability } p \end{cases}$$

This technique helps to improve the generalization of neural networks [20].

Finally, the Dense layer receives the output from the Dropout layer and uses C units for classification:

$$Z = W \cdot Y + b$$

where, prior to applying the Softmax activation function, Z is the output, b is the bias vector, W is the weight matrix, and Y is the input from the Dropout layer:

$$P = \text{Softmax}(Z)$$

where P gives the predicted probabilities for each class.

To employ an average ensemble strategy to integrate many models, let M represent the number of models and O_i represent the output of the i-th model:

$$O_i = \text{Softmax}(Z_i)$$

The final ensemble output O_{ensemble} can be computed as the average of the outputs from all models:

$$O_{\text{ensemble}} = \frac{1}{M} \sum_{i=1}^M O_i$$

This averaging method is a common ensemble strategy used to enhance predictive performance. [21].

3. Experimental Results

In the study, the dataset was initially trained on pre-trained models and accuracy rates were obtained. These models were first tested without any modifications and the accuracy rates for each were determined. After the initial training phase, fine-tuning was applied to each model to further optimize model performances. Fine-tuning was used to adjust model weights in pre-trained models to improve their ability to generalize from training data. After fine-tuning, the models were trained and the accuracy rates were redetermined. After this step, the DenseNet121 and MobileNet models had the highest accuracy among the fine-tuned models. Table 2 shows the 5 models with the highest accuracy. Fine-tuning adjusts pre-trained model parameters to better adapt to specific datasets, improving performance on new tasks.

Table 2. Individual performance of transfer learning models after fine tuning and CNN applications

Model	Precision	Recall	F1 Score	Accuracy	Epoch
MobileNet	0.9242	0.9242	0.9241	0.9242	22
DenseNet121	0.9232	0.9227	0.9228	0.9227	68
ResNet50V2	0.8803	0.8803	0.8800	0.8803	63
VGG19	0.8787	0.8787	0.8787	0.8787	49
Xception	0.8713	0.8712	0.8709	0.8712	68

The graphs of training and test accuracy, training and validation loss values of the DenseNet121 model according to the number of epochs are given in Figure 4. As can be seen from the figure, while the training accuracy increases rapidly when the number of epochs is

increased up to 20, it reaches a more regular accuracy rate after 60 epochs. Similarly, the test accuracy varied at each step, but it reached over 90% after the 60th epoch. When comparing the training and validation loss values, the training loss value decreased in the opposite direction of the accuracy rate as the number of epochs increased and progressed more consistently than the test loss.



Figure 4. Training and Test Accuracy/Loss graphs for DenseNet121 according to the number of epochs

Figure 5 shows the training-test accuracy and training-validation loss graphs of the MobileNet model according to the number of epochs. Similar to the DenseNet graph, while more stable accuracy and loss rates are determined on the train data, large differences are observed between 20 and 40 epochs in the test set. Therefore, the number of epochs was truncated at 22 to minimize test loss.



Figure 5. Training and Test Accuracy/Loss graphs for MobileNet according to the number of epochs

An ensemble approach was used to further improve the accuracy of the classification system. Ensemble learning involves combining the predictions of multiple models to improve overall performance and robustness. In the study, the fine-tuned outputs of several transfer learning models were combined together to create a more comprehensive and accurate classification

mechanism. The ensemble method exploits the unique strengths of each model, reducing the weaknesses that any one model may have. This method reduced the probability of misclassification and increased the model's ability to generalize across different data samples. The result is a significant improvement in accuracy and reliability, as demonstrated by the MobileNet and DenseNet121 ensemble, which reached an accuracy of 93.03%. Table 3 shows the results obtained by combining the models with the highest accuracy with the ensemble method. For model ensembling, the average method was used, where the outputs of the individual models, MobileNet and DenseNet121, were averaged to make the final prediction. This approach leverages the complementary strengths of the models: MobileNet's efficiency and DenseNet121's ability to extract deep features. By averaging their outputs, the ensemble model reduces the impact of potential biases or weaknesses of individual models, leading to improved robustness and accuracy. This method ensures that each model contributes equally to the final decision, making it an effective and computationally efficient strategy for combining predictions in a classification task.

Table 3. The performances of ensemble models

<i>Model</i>	<i>Precision</i>	<i>Recall</i>	<i>F1 Score</i>	<i>Accuracy</i>
MobileNet + DenseNet121	0,9307	0,9303	0,9303	0,9303
MobileNet + Xception	0,9218	0,9212	0,9209	0,9212
DenseNet121 + VGG19	0,9148	0,9136	0,9137	0,9136
MobileNet + ResNet50V2	0,9121	0,9121	0,9121	0,9121
MobileNet + VGG19	0,9120	0,9121	0,9120	0,9121
DenseNet121 + ResNet50V2	0,9120	0,9121	0,9120	0,9121
DenseNet121 + Xception	0,9030	0,9030	0,9030	0,9030
ResNet50V2 + VGG19	0,8984	0,8984	0,8984	0,8984
Xception + VGG19	0,8940	0,8939	0,8937	0,8939
ResNet50V2 + Xception	0,8842	0,8833	0,8828	0,8833

In Figure 6, the performance of DenseNet121, MobileNet and DenseNet121+ MobileNet hybrid transfer learning model on skin cancer is measured classwise in confusion matrices. In distinguishing two very similar classes, the total number of misclassifications of the DenseNet121 model is 51 while the number of misclassifications of MobileNet is 50. The total number of misclassifications obtained as a result of the combination of both models is reduced to 46. It can be said that the proposed ensemble model is effective in classifying data that are very similar to each other.

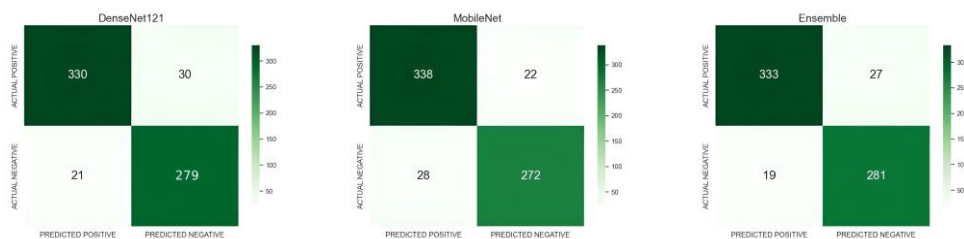


Figure 6. MobileNet, DenseNet121 and proposed model’s confusion matrices

4. Discussion

The results of this study show that the performance of pre-trained deep learning models in the classification of skin lesions is enhanced by the ensemble technique. By fine-tuning the MobileNet and DenseNet121 models and then creating an ensemble, superior performance metrics have been achieved compared to individual models or other ensemble combinations. The ensemble model combining MobileNet and DenseNet121 has achieved the highest precision, recall, F1 score, and accuracy, surpassing other commonly used models such as ResNet, VGG19, and Xception. One of the most significant strengths of this approach is its hybrid structure that combines the strengths of both MobileNet and DenseNet. MobileNet is known for its efficiency and speed, complementing DenseNet’s ability to leverage deeper feature representations. While fine-tuning the last 171 layers of DenseNet121, allowing all layers in MobileNet to be trainable ensured that both models adapted to the unique characteristics of the skin lesion dataset without overfitting. The use of dropout layers and global average pooling also contributed to the overall performance of the model. These techniques reduced overfitting and ensured that the model memorized the training data, which is crucial in medical imaging tasks where generalization to new, unseen data is vital. Additionally, instead of relying on a simple voting scheme, the end-to-end combination of the models’ outputs ensured the full utilization of each model’s strengths and provided a robust classification output. Experimental results further emphasize that independent models like ResNet50V2 and Xception perform reasonably well, but they cannot distinguish between benign and malignant skin lesions as effectively as the ensemble model. Confusion matrices reveal that the combination of MobileNet and DenseNet121 reduces misclassification errors, especially when distinguishing between classes with very similar features, compared to individual models. This is very important in the field of healthcare, where accurate classification can lead to significant clinical outcomes.

Despite these promising results, there are some limitations in our approach. For example, while our ensemble model achieved high performance metrics, the computational complexity and training time were higher compared to individual models. Especially the DenseNet121 model required more epochs to stabilize compared to MobileNet, indicating that future studies should explore more efficient ways to combine deep learning models so that the computational load does not increase significantly.

5. Conclusion

This model, which proposes a hybrid ensemble model combining MobileNet with DenseNet121, was used for the classification of skin lesions. The approach here was to leverage the strengths of both models. By fine-tuning the final layers of the models, better learning was achieved. Subsequently, high accuracy was achieved using the merging method. Thanks to this, it has reached the latest technological performance in classifying skin lesions as benign or malignant. It has been determined that such hybrid approaches can provide better results compared to individual models obtained from transfer learning and other ensemble combinations. This study demonstrates the potential of transfer learning in healthcare applications, particularly in the classification of skin lesions. The reduction in misclassifications with the collective approach underscores its value, especially in a clinical setting where accurate diagnosis is paramount. However, further research is needed on the optimal computational efficiency of this approach, especially for its use in real-time applications. Large-scale and more diverse datasets will further validate the generalization of the proposed model. These promising results enable the investigation of community methods on medical images in many other applications where appropriate and efficient classification, which is absolutely necessary for the clinical decision-making process, is required. The proposed ensemble model significantly reduced misclassification rates compared to individual models, demonstrating its potential in medical imaging. By leveraging MobileNet's efficiency and DenseNet121's deeper feature extraction, the ensemble achieved higher accuracy and generalization.

Ethics in Publishing

There are no ethical issues regarding the publication of this study

Author Contributions

Yasin SANCAR: Designed and wrote the manuscript, carried out the experimental studies, conclusions and interpretation of the experiment.

References

- [1] Nisar, D.M., Amin, R., Shah, N.H., Al Ghamdi, M. A., Almotiri, S. H., & Alruily, M. (2021). Healthcare techniques through deep learning: issues, challenges and opportunities. *IEEE Access*, 9, 98523–98541.
- [2] Alfi, I. A., Rahman, M. M., Shorfuzzaman, M., & Nazir, A. (2022) A non-invasive interpretable diagnosis of melanoma skin cancer using deep learning and ensemble stacking of machine learning models. *Diagnostics*, 12(3), 726.
- [3] Anand, V., Gupta, S., Koundal, D., & Singh, K. (2023) Fusion of U-Net and CNN model for segmentation and classification of skin lesion from dermoscopy images. *Expert Systems with Applications*, 213, 119230.
- [4] Başaran, E., & Çelik, Y. (2022) Skin cancer diagnosis using CNN features with Genetic Algorithm and Particle Swarm Optimization methods. *Transactions of the Institute of Measurement and Control*, 01423312241253926.
- [5] Bazgir, E., Haque, E., Maniruzzaman, M., & Hoque, R. (2024) Skin cancer classification using Inception Network. *World Journal of Advanced Research and Reviews*, 21(2), 839–849.
- [6] Dimen, L., Tahâs, V.-S., Borşan, T., & Ferencz, Z. (2016) Ultraviolet Rays and Its Environmental Effects. *International Multidisciplinary Scientific GeoConference: SGEM*, 1, 787–792.
- [7] Hussein, Z. J., Hussein, A. M., Maki, G. I., & Ghenni, H. Q. (2023) Improved model for skin illnesses classification utilizing gray-level co-occurrence matrix and convolution neural network. *Journal of Advances in Information Technology*, 14(6), 1273–1279.
- [8] Ker, J., Wang, L., Rao, J., & Lim, T. (2017) Deep learning applications in medical image analysis. *Ieee Access*, 6, 9375–9389.
- [9] Kilic, U., Karabey Aksakalli, I., Tumuklu Ozyer, G., Aksakalli, T., Ozyer, B., & Adanur, S. (2023) Exploring the Effect of Image Enhancement Techniques with Deep Neural Networks on Direct Urinary System (DUSX) Images for Automated Kidney Stone Detection. *International Journal of Intelligent Systems*, 2023(1), 3801485.
- [10] Latif, J., Xiao, C., Tu, S., Rehman, S. U., Imran, A., & Bilal, A. (2020) Implementation and use of disease diagnosis systems for electronic medical records based on machine learning: A complete review. *IEEE Access*, 8, 150489–150513.

- [11] Mohania, D., Chandel, S., Kumar, P., Verma, V., Digvijay, K., Tripathi, D., Shah, D. (2017) Ultraviolet radiations: Skin defense-damage mechanism. *Ultraviolet Light in Human Health. Diseases and Environment*, 71–87.
- [12] Sethanan, K., Pitakaso, R., Srichok, T., Khonjun, S., Thannipat, P., Wanram, S., ... Others. (2023) Double AMIS-ensemble deep learning for skin cancer classification. *Expert Systems with Applications*, 234, 121047.
- [13] Shekar, B. H., & Hailu, H. (2023) Fusion of features extracted from transfer learning and handcrafted methods to enhance skin cancer classification performance. In *Computer Vision and Machine Intelligence: Proceedings of CVMI 2022*, Springer, 243–257.
- [14] Tumpa, P. P., & Kabir, M. A. (2021) An artificial neural network based detection and classification of melanoma skin cancer using hybrid texture features. *Sensors International*, 2, 100128.
- [15] Tuncer, T., Barua, P. D., Tuncer, I., Dogan, S., & Acharya, U. R. (2024) A lightweight deep convolutional neural network model for skin cancer image classification. *Applied Soft Computing*, 111794.
- [16] Panneerselvam, R., Balasubramaniam, S. (2023) Multi-Class Skin Cancer Classification using a hybrid dynamic salp swarm algorithm and weighted extreme learning machines with transfer learning. *Acta Informatica Pragensia*, 12(1), 141–159.
- [17] Prasad, C. R., Bilveni, G., Priyanka, B., Susmitha, C., Abhinay, D., & Kollem, S. (2024) Skin Cancer Prediction using Modified EfficientNet-B3 with Deep Transfer Learning. 2024 IEEE International Conference for Women in Innovation, Technology & Entrepreneurship (ICWITE), 519–523.
- [18] Srivastava, N., Hinton, G., Krizhevsky, A., Sutskever, I., & Salakhutdinov, R. (2014) Dropout: a simple way to prevent neural networks from overfitting. *The Journal of Machine Learning Research*, 15(1), 1929–1958.
- [19] Dietterich, T. G. (2000) Ensemble methods in machine learning. *International Workshop on Multiple Classifier Systems*, Springer, 1–15.
- [20] Lin, M. (2013) Network in network. *arXiv Preprint arXiv:1312. 4400*.
- [21] Fanconi, C. (2019) Skin cancer: malignant vs. benign-processed skin cancer pictures of the ISIC archive.

A Mobile Secure Content Development Application for Children in the Software Development Life Cycle Framework

İsakhan KARABAŞ^{1*}, Fulya ASLAY¹, Elif ÖKSÜZ¹

¹Department of Artificial Intelligence and Robotics, Institute of Science and Technology, Erzincan Binali Yıldırım University, 24030, Erzincan, Türkiye.

Received: 08/11/2024, Revised: 16/12/2024, Accepted: 16/12/2024, Published: 31/12/2024

Abstract

This study focuses on the software development process of a mobile application that aims to support children's learning, development and entertainment processes while ensuring their safety in the online environment. The project, which was carried out within the framework of the Software Development Life Cycle (SDLC), adopted a systematic approach that included requirements analysis, design, development, testing and maintenance phases. This systematic structure enabled the project to proceed in a planned manner and effective use of resources. The project aims to minimize digital security risks, provide appropriate content for children and enable parents to safely control their children's internet use. Extreme Programming (XP) methodology was preferred in the SDLC development phase. The principles specific to this methodology such as pair programming, test-driven development (TDD) and continuous integration were effectively applied. The use of XP enabled user feedback to be processed quickly and the application to be continuously improved. Thus, the software adapted not only to technical requirements, but also to user experience and security needs. This process, which successfully completed security and performance tests, demonstrates that effective management of the entire process, not just coding, in software development projects directly contributes to project success. The study aims to contribute to the literature on children's digital safety and to provide a basis for future research in this field.

Keywords: Methodology, SDLC, Software Engineering, Software Testing, XP

Yazılım Geliştirme Yaşam Döngüsü Çerçevesinde Çocuklar için Bir Mobil Güvenli İçerik Geliştirme Uygulaması

Öz

Bu çalışma, çocukların çevrimiçi ortamda güvenliğini sağlarken, öğrenme, gelişim ve eğlence süreçlerini desteklemeyi amaçlayan bir mobil uygulamanın yazılım geliştirme sürecini ele almaktadır. Yazılım Geliştirme Yaşam Döngüsü (SDLC) çerçevesinde yürütülen proje; gereksinim analizi, tasarım, geliştirme, test ve bakım aşamalarını içeren sistematik bir yaklaşımı benimsemiştir. Bu sistematik yapı, projenin planlı bir şekilde ilerlemesini ve kaynakların etkili kullanımını mümkün kılmıştır. Proje, dijital güvenlik risklerini minimize ederek çocuklara uygun içerik sunmayı ve ebeveynlerin çocuklarının internet kullanımını güvenle kontrol edebilmesini sağlamayı hedeflemektedir. SDLC geliştirme aşamasında Ekstrem Programlama (XP) metodolojisi tercih edilmiştir. Bu metodolojiye özgü olan çift programlama, test odaklı geliştirme (TDD) ve sürekli entegrasyon gibi prensipler etkin bir şekilde uygulanmıştır. XP'nin kullanımı, kullanıcı geri bildirimlerinin hızlı bir şekilde işlenmesini ve uygulamanın sürekli iyileştirilmesini sağlamıştır. Böylece yazılım, yalnızca teknik gereksinimlere değil, aynı zamanda kullanıcı deneyimi ve güvenlik ihtiyaçlarına da uyum sağlamıştır. Güvenlik ve performans testlerini başarıyla tamamlayan bu süreç, yazılım geliştirme projelerinde yalnızca kodlama değil, tüm sürecin etkin yönetiminin proje başarısına doğrudan katkı sağladığını ortaya koymaktadır. Çalışma, çocukların dijital güvenliği alanındaki literatüre katkı sunmayı ve bu alanda gelecekte yapılacak araştırmalar için bir temel oluşturmayı hedeflemektedir.

Anahtar Kelimeler: Metodoloji, SDLC, Yazılım Mühendisliği, Yazılım Testi, XP

*Corresponding Author: isakhan.karabas@ogr.ebyu.edu.tr

İsakhan KARABAŞ, <https://orcid.org/0009-0006-0852-1996>

Fulya ASLAY, <https://orcid.org/0000-0001-5212-6017>

Elif ÖKSÜZ, <https://orcid.org/0009-0002-8743-2676>

1. Introduction

The process of developing a software product is considered as the software life cycle and consists of various phases such as planning, analysis, design, implementation, testing and maintenance [1,2]. These phases are implemented sequentially through a model. The software development model expresses the strategy for the realization of the software and this strategy includes a set of activities, objects, transformations and events [3]. The software process includes all activities involved in software development. All activities of specification, development, verification and evolution are part of all software processes. In addition to the functionality and performance that customers expect, a good software product is expected to be easily modifiable according to changing customer requirements. In other words, a good software product should be maintainable, reliable, efficient and acceptable. In order for a software product to be successful, all activities planned throughout the software lifecycle process must be realized within the planned time and cost scope.

Today, a wide variety of software such as operating systems, mobile applications, web applications, cloud-based applications are being developed. The developed software can appeal to very different audiences. The software development process should be implemented by choosing the right methodology according to the scope and scale of the software. In today's digital world, it is of great importance to ensure that children use the internet safely, to provide them with appropriate safe and educational content, and to enable parents to safely control their children's internet use. For this reason, it is necessary to have applications that contain safe content for children. At the same time, content producers should be guided in this area. Managing the software processes required for the realization of such applications is also of great importance in terms of both time and cost. For this reason, this study focuses on a medium-sized mobile software application that contains safe content for children. In today's digital world, it is of great importance to ensure that children use the internet safely, to provide them with appropriate safe and educational content, and to enable parents to safely control their children's internet use. For this reason, it is necessary to have applications that contain safe content for children. At the same time, content producers should be guided in this area. Managing the software processes required for the realization of such applications is also of great importance in terms of both time and cost.

The term digital security is often used interchangeably with internet security, cyber security, online security, information security and data security. While some researchers in the field of early childhood education see the benefits of digital technology in supporting children's learning and social interactions, others have concerns about its negative impacts on children's health and development. Children growing up in the digital age from an early age are exposed to digital technology and overshadowed by digital security threats. According to the OECD (2021), digital security risks in children can be divided into 4Cs (concerning contact, content, conduct, and contract risks). Children also have privacy risks, advanced technology risks, and health and well-being risks. This often causes parental concern and tends to discourage children's use of technology. There is an important need to raise parents' awareness about the

impact of digital devices on children's health and development and to ensure that they use the internet safely [4].

Cyberbullying is increasingly recognized as a threat to the mental health of children and young people. Children, young people and their families may not know how to stay safe online or how to respond to unsafe online experiences. Child and Adolescent Mental Health Physicians believe that new generations should be guided by education from a young age, but it is impossible to reach everyone [5].

In this study, the software of a mobile application that will support children's learning, development and entertainment processes while keeping them safe in the online environment was realized within the framework of the Software Development Life Cycle (SDLC). This process was carried out by progressing step by step with the principles of continuous improvement within the framework of the software development life cycle. Within the scope of the study, requirements determination, system design, development, testing and maintenance phases are included.

2. Software Development Life Cycle

The Software Development Life Cycle (SDLC) is a systematic process that covers all phases of software projects from planning to deployment and maintenance. Careful and meticulous work at every stage of the software development lifecycle and the application of the right methodologies contribute significantly to the successful completion of the project by improving the quality of the software [6].

SDLC is used in the software industry to design, develop and produce high-quality, reliable, cost-effective and timely software products. It is also called the software development process model [6]. SDLC models form the backbone of software engineering practice by guiding a systematic and structured approach to creating high quality software products. As technology evolves and market demands become more dynamic, software development organizations are faced with the challenge of selecting the most appropriate SDLC model to meet project requirements efficiently and effectively. Developers, project managers, and quality engineers should have a thorough understanding of the advantages, disadvantages, and applicability of various SDLC models in the context of software quality engineering in order to make informed decisions [7].

The SDLC is a fundamental framework that guides the process of building software applications, including mobile applications. It consists of a series of well-defined phases designed to ensure the development of high-quality software that meets or exceeds customer expectations [7,8].

2.1 SDLC Methodology Phases

SDLC methodologies provide a structured framework that guides the process of designing, developing and implementing software solutions. These methodologies are diverse and each offers an approach tailored to a specific project needs, complexity and objectives. One of the key aspects of the SDLC is its ability to adapt to the unique requirements and constraints of

different software projects, including mobile applications [10,11]. A visualized description of the stages in the SDLC is presented in Figure 1 [9].

- Planning
 1. Define project scope, objectives and requirements
 2. Identify stakeholders and roles
 3. Create a project plan, including timelines and resources
- Analysis
 1. Collect and document detailed requirements from users and stakeholders
 2. Analyze the information collected to understand the functional and non-functional requirements of the system
 3. Develop use cases, user stories or functional specifications
- Design
 1. Create an architectural design that defines how software components interact
 2. Develop detailed technical specifications
 3. Designing the user interface
- Application (Coding)
 1. Writing the actual code based on design and specifications
 2. Perform unit tests to ensure that individual components function as intended
 3. Integrate code modules as needed
- Testing and Merging
 1. Conduct various tests, including integration testing, system testing and user testing
 2. Identify and correct defects and problems
 3. Verify that the software meets the completed requirements
- Maintenance and Sustainability
 1. Monitoring and maintenance of the software
 2. Addressing and correcting reported problems or defects
 3. Make necessary updates, enhancements and patches

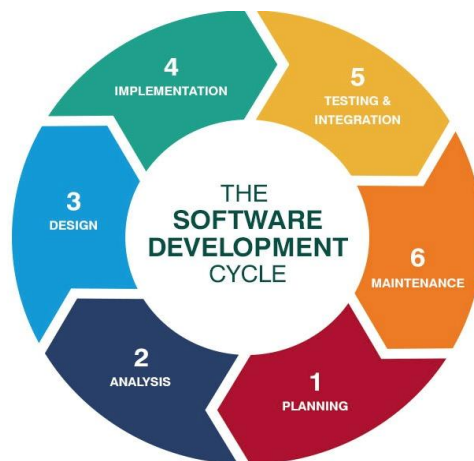


Figure 1. Software lifecycle.

2.2 Using Decision Support Matrix for Selection of SDLC Methodologies

In software development, selecting an appropriate SDLC methodology is a critical decision that significantly impacts project outcomes [10]. To effectively carry out this decision-making process, the use of a decision support matrix is invaluable. A decision support matrix provides a structured approach to evaluate and compare various SDLC methodologies based on their compatibility with project-specific factors, enabling stakeholders to make informed and strategic choices [11].

A decision support matrix considers several key factors that influence the suitability of an SDLC methodology for a given project:

Project Complexity: The complexity of a project's requirements, architecture and technology stack can influence the choice of SDLC methodology. Projects with high complexity can benefit from methodologies that allow iterative development and frequent adaptations [12].

Stability of Requirements: The stability of project requirements is a very important consideration. Projects with well-defined and stable requirements may tend towards a linear approach, while projects with evolving requirements may prefer Agile methodologies [6].

Customer Involvement: The extent to which customers or end users should be involved throughout the development process plays an important role. Agile methodologies emphasize regular customer feedback, while traditional methodologies may involve customers primarily in the requirements phase [12].

Flexibility and Adaptability: The project's capacity to accommodate changes and adapt to evolving needs is an important factor. Agile methodologies excel in providing flexibility, while traditional methodologies may struggle to accommodate late-stage changes [6].

Timeline and Predictability: The timeline requirements of the project and the organization's need for predictability in terms of project milestones and deadlines are considered. Traditional methodologies offer a relatively predictable timeline, while Agile methodologies embrace change and evolution [13].

Creation of Decision Support Matrix;

Factor Weighting: Assign relative weights to each factor based on its importance to the project [14]. For example, if customer engagement is very important, it may receive a higher weight.

Scoring Criteria: For each factor, scoring criteria can be defined, usually on a scale from low to high or inadequate to excellent [15,16].

Methodology Assessment: Evaluate each SDLC methodology against factors and criteria and points are awarded based on compliance [17].

Calculation of Weighted Scores: Multiply the assigned weights by the scores for each factor for each methodology. Sum these weighted scores for each methodology to obtain the total weighted score [18,19].

Selection: The methodology with the highest overall weighted score is the recommended choice [11].

The general structure of the decision support matrix is shown in Figure 2.

Decision Support Matrix		Methodologies	
Scoring Criterias	Factor Weights	Agile Methods	Traditional Methods
A1			
A2			
A3			
Decision			

Figure 2. Decision support matrix.

2.3 Software Development with SDLC Methodologies

2.3.1 Traditional Software Development Methodologies

It is an approach that generally follows the planning, design, development, testing and maintenance phases in a sequential and systematic way. It is used in complex projects where requirements are clear, large teams are working and complex projects. The most common traditional software development models include the cascade model, the V-process model and the spiral model.

The cascade model is one of the oldest methods used in software development processes. It is an approach in which project steps are sequential and progressive, one step is not completed until the next step is completed, and it is difficult to go back to the previous step.

The V process model is considered an improved version of the waterfall model. The software development process has a test phase corresponding to each development phase. Thus, each phase is verified. It is preferred in projects with high quality requirements.

The spiral model places great emphasis on risk analysis and risk management, which are ignored in the waterfall model. The project is divided into cycles and each cycle is detailed and its risks are assessed separately. Therefore, it is suitable for high-risk projects. It is also close to contemporary models.

2.3.2 Agile Software Development Methodologies

They are software development approaches that enable fast and effective response to customer requirements and can easily adapt to all kinds of changes [20]. It allows software development projects to be developed in short cycles by dividing them into small, manageable parts. It is used in situations where it is difficult to predict the detailed roadmaps and designs of projects. The most common agile software development methods include Scrum, Kanban, Extreme Programming (XP) and Lean software development [21].

The Scrum model is an agile software development model and its general characteristic is that it is observer, developer and iterative. The Scrum model is used when it is difficult and complex to plan a software project completely from the beginning. According to this method, a team is formed for the software development process and a scrum master responsible for the team is determined. This enables teams to work faster and more efficiently. Scrum teams ensure the progress of the project by holding sprint meetings at certain intervals [22].

Kanban is a visual management methodology that aims to make production processes and workflows more efficient. It is used in software development processes in the form of scheduling to control the phases [23].

XP is an agile software development methodology designed to improve software quality and responsiveness to changing customer requirements. XP is particularly effective in dynamic environments where requirements are likely to change because it encourages adaptability and communication. Team roles in XP vary, but key positions include developers, customers (or their representatives), coaches and monitors who collectively prioritize tasks, write user stories and evaluate progress. XP increases productivity and fosters innovation by fostering a culture of trust and shared responsibility, making it a valuable methodology for teams that want to deliver high-quality software in a flexible, customer-centric way [24].

Lean software development is adapted from lean manufacturing principles and aims to make software development processes more efficient and effective. It is a methodology used to minimize waste in software development processes, maximize customer value and ensure continuous improvement [25].

3. Mobile Application Project Management

Mobile application project management is the management of the processes and tools used in the development of mobile applications. This enables both organizing software development teams and achieving specific business goals. Successful mobile app project management ensures that the development process is completed on time and within budget, ensuring that the app meets the targeted quality and user experience standards.

In this project, a mobile application will be developed to create a clean platform for children that is easy to use, has a high level of security and at the same time does not contain inappropriate content. The application is designed to work on iOS and Android platforms. The stages of the application within the scope of SDLC are presented below;

3.1 Software Methodology Selection

XP stands out as one of the agile software development methodologies. Developed by Kent Beck in the 1990s, this methodology aims to maximize customer satisfaction, improve teamwork and adapt to changing requirements in software projects. XP is a particularly suitable approach for projects with frequently changing requirements and where fast deliveries are critical [24]. XP is built on a set of fundamental principles. These principles include small and frequent releases, test-driven development (TDD), pair programming, continuous integration, simple design, continuous feedback, code standards and the 40-hour work week. These

principles are designed to make the software development process more efficient and agile. For example, through small and frequent releases, software is delivered in such a way that customers can provide early feedback [26]. TDD ensures that tests are written before the coding process and bugs are detected early [27]. Pair programming improves code quality by encouraging developers to work together [28]. Continuous integration ensures that new code is continuously integrated into the main code base and that this process is tested [29]. Many advantages are gained through the use of XP. These include fast feedback, quality coding and flexibility to change. Frequent deliveries and customer involvement allow the software to be improved in the early stages [30].

Agile software development methodologies include Scrum, Kanban and Feature-Driven Development (FDD). A decision-making matrix was created to decide which software development method to use for the application planned to be made within the scope of this project, and as a result, it was deemed more appropriate to use the XP software development process in our software project due to the different sections it contains. XP was chosen especially because of its advantages of handling user feedback quickly, continuous improvement of the system through frequent releases and maintaining high quality standards. According to this software development process, each section is designed, coded and tested separately. After the testing phases of the sections are completed, all sections are merged. This user-oriented method contributed to the app providing an effective solution to ensure children's digital safety.

3.2 Software Requirements Analysis

Requirements analysis is critical to the success or failure of a software project. Requirements analysis should be performed in order to determine customer expectations in the initial phase of software projects and to minimize the errors that may occur in the later stages of the software project. The requirements determined in the early stages of the project may change as the project progresses. Therefore, they are dynamic. They are divided into two as functional and non-functional requirements. The steps of requirements analysis are as follows;

- Requirements Gathering: Gathering needs from users and stakeholders. This can be done through surveys, interviews and observations.
- Requirements Definition: Analyzing the information collected and transforming it into specific, measurable and achievable requirements.
- Requirements Documentation: Detailed documentation of requirements. These documents serve as a guide for the project team.
- Requirements Verification and Validation: Checking the accuracy and completeness of requirements and validation by stakeholders.
- Requirements Management: Monitoring requirements and managing changes throughout the project [31,32].

These steps ensure that the project achieves its goals and meets user needs. Some common techniques used in the requirements analysis process include flow diagrams and prototyping [33].

For the development of the application, requirements were first analyzed. For this, the functional and non-functional requirements that make up the software were identified. Then, a feasibility study was conducted for the analysis and it was decided whether the project should be carried out or not. Cost and time analysis were made within the scope of the feasibility study.

3.2.1 Functional Requirements

Requirements are expressed as services provided directly to the user in order to meet the user's needs and expectations. It defines what the system should do. Some functional requirements of the software developed in the study are presented below;

- Users should be able to register and login to the application with e-mail and password.
- Users should be able to create multiple child profiles and set age-appropriate content filters for each profile.
- The system should be opened according to the authorization level of the logged in user.
- Users should be able to search for content in the system using the content search feature.
- The user should be able to update their profile information (name, profile photo, etc.).
- Users should be able to access detailed information about each content such as author, publication date, age group.
- The user should be able to play the game of their choice within the app and track their achievements in the games.
- Users should be able to play online multiplayer games with other players.
- The user should be able to watch the cartoon of their choice within the application.
- The user should be able to read the books they have selected within the application or listen to them as audiobooks.
- The user should be able to add any content to their favorite list.
- Parents should be able to limit the usage time of the app and view viewing and reading history.
- If there is a problem with the password, a password renewal link should be sent to the e-mail address.

3.1.2 Non-Functional Requirements

It is a performance requirement that addresses the quality and correct operation of the software, not the service provided directly to the user. It defines how the system should perform. Non-functional requirements help to ensure that the user's needs are met, that it is reliable. It also helps to make it easier to use and maintain.

- The system must be secure against unauthorized access. It should ask for member login.
- The application should scale to serve 100000 users at the same time.
- Access to the application should be provided via the internet.
- The app's response time to user requests should not exceed 2 seconds.
- Loading and playback of books, videos and games in the app should not exceed a maximum of 3 seconds.
- Age verification mechanisms should be in place to control access to content.

- The user interface should be simple and colorful so that children can use it easily.
- There should be a feedback mechanism where users can easily report bugs in the application.
- The application should work flawlessly on all operating systems.
- The application should be suitable for commonly used web browsers.
- If there is a problem with the password, a password renewal link should be sent to the e-mail address.
- The app should be maintained on a monthly basis so that new content and updates can be easily added.
- The application should be tested weekly for vulnerabilities.

3.3 Software Feasibility Analysis

In software projects, a feasibility analysis should be performed to evaluate the feasibility of the project by taking into account all factors related to the project. This analysis aims to identify resources, risks and opportunities to increase the chances of success of the project. In feasibility analysis, evaluation is made from various angles and it is aimed to increase the efficiency of the project. Within the scope of this project, cost analysis and time analysis were conducted.

3.3.1 Cost Analysis

In general, cost estimation is one of the most difficult steps in project management. It is very important to accurately calculate the resources and schedule needed. The software costing process includes calculating the size of the software to be produced, calculating the effort required, developing the project schedule, and finally calculating the cost of the entire project [34]. There is a wide variety of cost estimation methods for evaluating projects, and there are quite a few studies that favor the COCOMO model for software projects. A study covering 115 different software projects highlighted that costs and timelines are often under- or overestimated, often due to a lack of structured estimation methods. By applying COCOMO, this study addressed common problems such as frequent changes made by users, missed tasks, and inadequate analysis, and helped to improve estimation accuracy by considering complexity, system size, and team capabilities [35]. In a study focused on creating an online bookstore, the COCOMO model was used to estimate development efforts. The project included 14 web pages written in HTML and JavaScript, and the application was categorized under the “organic” mode using both the basic and intermediate COCOMO sub-models. This approach assisted in effort estimation based on 2.9 KLOC (thousands of lines of code) and adjusted the predictions using cost drivers such as reliability, database size, and team experience [36]. The COCOMO model is used to estimate the cost, duration, and workforce requirements of a software project by considering its size and complexity. It was developed by Barry W. Boehm in 1981, based on the principle that the required effort is proportional to an exponential function of the program's size [12]. COCOMO estimates workload in software projects by considering developers' skills, software complexity, and the technologies used. The structure of the COCOMO model is presented in Figure 3 [37].



Figure 3. COCOMO model.

The COCOMO model has three fundamental types based on different project types and complexity levels: discrete, semi-detached, and embedded. The effort and duration formulas for these three models are shown in Table 1 [37,38]. Discrete projects are those developed by small, experienced teams, characterized by a well-understood scope and low complexity. Semi-detached projects refer to projects of medium size and complexity, typically managed by expert teams. Embedded projects are very large, complex projects that require specialized equipment or hardware.

Table 1. COCOMO model effort and duration formulas.

Mode	Effort	Schedule
Organic	$E=2.4*(KDSI)^{1.05}$	$TDEV=2.5*(E)^{0.38}$
Semidetached	$E=3.0*(KDSI)^{1.12}$	$TDEV=2.5*(E)^{0.35}$
Embedded	$E=3.6*(KDSI)^{1.20}$	$TDEV=2.5*(E)^{0.32}$

The cost multiplier in the model is obtained from the product of 15 cost drivers.

COCOMO equations; $E=a \times (KLOC)^b$ [12]

E: Effort, **KLOC:** Lines of Code, **a ve b:** Constants Determined by Model Type

The cost multiplier for the mobile application developed in the study has been determined as shown in Table 2.

Table 2. Mobile application cost drivers

COST DRIVERS		RATINGS						PROJECT
		VERY LOW	LOW	NOMINAL	HIGH	VERY HIGH	EXTRA HIGH	
PRODUCT ATTRIBUTES	RELY : Required software reliability	0,75	0,88	1	1,15	1,4	-	1
	DATA : Size of application database	-	0,94	1	1,08	1,16	-	1,08
	CPLX : Complexity of the product	0,7	0,85	1	1,15	1,3	1,65	1
HARDWARE ATTRIBUTES	TIME : Run time performans constraints	-	-	1	1,11	1,3	1,66	1
	STOR : Memory constraints	-	-	1	1,06	1,21	1,56	1
	VIRT : Volatility of the virtual machine environment	-	0,87	1	1,15	1,3	-	1
	TURN : Required turnabout time	-	0,87	1	1,07	1,15	-	1,07
PERSONNEL ATTRIBUTES	ACAP : Analyst capability	1,46	1,19	1	0,86	0,71	-	1
	AEXP : Applications experience	1,29	1,13	1	0,91	0,82	-	1
	PCAP : Software engineer capability	1,42	1,17	1	0,86	0,7	-	1,17
	VEXP : Virtual machine experience	1,21	1,1	1	0,9	-	-	1
	LEXP : Programlama dili deneyimi	1,14	1,07	1	0,95	-	-	0,95
PROJECT ATTRIBUTES	MODP : Application of software engineering methods	1,24	1,1	1	0,91	0,82	-	0,91
	TOOL : Use of software tools	1,24	1,1	1	0,91	0,83	-	1,1
	SCED : Required development schedule	1,23	1,08	1	1,04	1,1	-	1

In this context, the effort coefficient for the software project has been calculated as follows;

$$C = C1 * C2 * C3 * \dots * C15 = 1,28$$

The size of the software is approximately 15000 LOC=15 KLOC and it is evaluated as a semi-detached application.;

$$\text{Effort} = 3 * 15^{1.28} = 96 \text{ man/month}$$

$$\text{Duration} = 2.5 * 96^{0.35} = 12,3 \text{ month}$$

$$N = 96/12,3 = 7,8 = 8$$

Accordingly, it has been estimated that the project can be developed by a team of 8 people in approximately 12 months.

3.3.2 Time Analysis

Time analysis is an evaluation that includes planning and monitoring the steps required to complete a software project within the targeted duration, the time allocated for these steps, and the business processes involved. Through time analysis, it helps determine when the project will start and finish, identify critical paths, and recognize potential delays, contributing to the timely and budget-compliant completion of the project. One of the most common methods for time analysis is the Gantt chart. A Gantt chart visualizes the start and end dates of specified time periods as horizontal bars. It is a simple and clear visual tool for tracking and managing project progress. Considering the duration obtained for the project within the framework of the COCOMO model, a time analysis has been conducted and is illustrated in Figure 4 using a Gantt chart. The chart shows the time analysis for the 12 months required to complete the project based on the planned tasks. Accordingly, customer meetings and target audience analysis were completed in the first month, followed by the determination of requirements. A cost analysis was performed based on the identified requirements, and immediately after that, the design phase commenced. After the design, the implementation phase—the longest phase of the project—began, during which testing was conducted for each unit as the application was developed. Performance and security testing started after the application was developed, and once these tests were completed, the software project was launched with a beta version. Subsequently, the project entered the maintenance phase with feedback from end users and requests for software updates, finalizing the software.

Gantt Chart	Month 1	Month 2	Month 3	Month 4	Month 5	Month 6	Month 7	Month 8	Month 9	Month 10	Month 11	Month 12
Customer meetings												
Target audience analysis												
Determination of the project team												
Requirements identification												
Cost analysis												
Database design												
User interface design												
Application development												
Unit tests												
User testing												
Performance and security testing												
Adding beta version												
Updates												
Adding new features												

Figure 4. Gantt diagram for the developed application.

3.4 Software Design

The software design phase is one of the most critical and important stages in the software development process, occurring before the coding phase. There are three different software design models: Architectural design, which involves designing program models using UML (Unified Modeling Language) graphic language and GUI (Graphical User Interface) design. Each model generates various sub-models. Architectural design is created by establishing the foundations of the software and connecting these building blocks to form the design. This involves determining how the software's modules and sub-modules relate to the database and other structures, thereby designing how the system will operate. Here, client-server architecture, layered architecture, and repository architecture can be employed [39].

The study plans to develop the software for mobile platforms. Mobile software development requires rapid updates and enhancements to meet the varying capacities of different customers in a mobile environment, which is subject to failures and a series of constraints. The evolving constraints also include existing limitations such as technology, resources, bandwidth, and coverage area in the future [40].

In object-oriented design, specialized design tools are used. UML is a standard modeling language commonly preferred for modeling systems where object-oriented programming techniques are planned to be used. UML is employed to provide standards for complex programs that require the consideration of both software and hardware, especially in situations where the code will be developed by multiple developers [41].

UML diagrams are graphical representations that illustrate different aspects and features of a system. When modeling a system, the appropriate diagram is selected and drawn based on the specific aspect that needs to be examined. Depending on the specialized needs of the developers, some programmers maintain a strict approach and take great care in using all the diagrams and definitions from the Object Management Group (OMG), potentially wasting time on unnecessary drawings. In contrast, others may settle for just using use case and class diagrams [41]. Use Case diagrams are a sub-module of UML diagrams, and during the software design development process, a use case diagram is used to model how a system interacts with its users. This diagram aims to visualize the functions offered by the system, the users who will utilize these functions, and the relationships between the functions. In software development processes, use case diagrams help simplify the visualization of complex system functionalities, enabling users to understand the system easily [42,43]. Accordingly, when creating the diagram, the functions that the system will offer and the users who will utilize the system are determined. Based on the functions provided by the system or the expectations of the users from the system, use cases are created, visualizing the relationships between the users and the use cases.

A general use case diagram illustrating the actors and their permissions for the mobile application developed in the study is displayed in Figure 5.

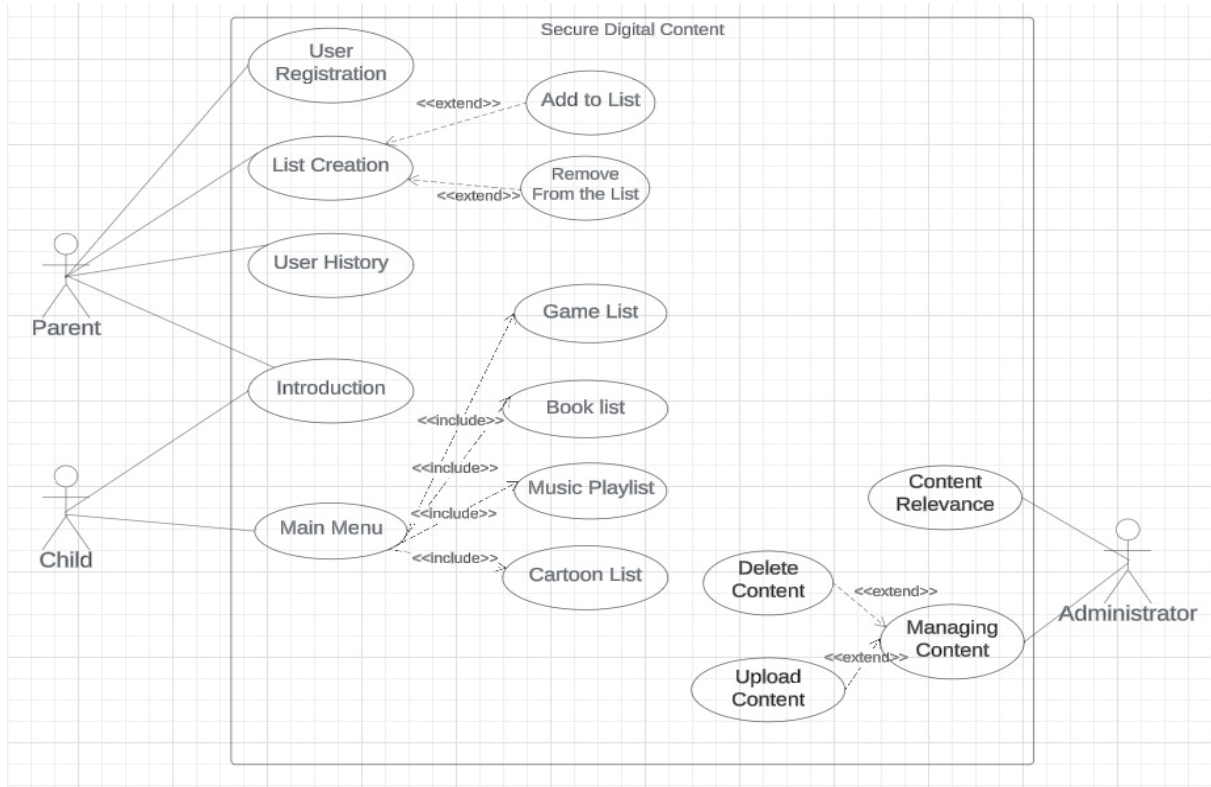


Figure 5. Use case diagram of the application.

Accordingly, a user with "Administrator" privileges can perform content compliance and addition/deletion operations. The registration and list creation processes are carried out by the "Parent" user, while the "Child" can access the created lists. This access helps prevent the child from navigating inappropriate content.

3.5 Software Testing

The testing phase, which is a part of the software development process, is a crucial stage for ensuring the functionality and quality of the software. The aim of the testing phase is to identify and rectify any potential errors in the software beforehand. Some of the tests conducted during the software development process include unit tests, integration tests, performance tests, user tests, security tests, and acceptance tests [44].

When the testing process begins, it is essential to plan in advance which tests will be conducted, how they will be performed, when they will take place, who will conduct them, and which tools will be used. Tests should be executed, results recorded, and necessary improvements made. Following these improvements, the tests should be repeated, and after all these testing stages, the success of the system should be evaluated.

Within the scope of the study, it is planned to test each module of the application separately for different content sections. For example, in the application's book list section, it will be tested whether the pages of the books displayed change individually and within a specified time frame. Based on the results, improvements will be made if necessary.

When the sections are integrated, it is essential to verify how the system works together and to check the data flow and compatibility between them. Additionally, since further additions to the created application are planned, it is intended to ensure the appropriateness of each content that is considered for inclusion.

It is planned to test the response times of each content section of the application, assess its performance under extreme conditions, identify any security vulnerabilities, and evaluate whether it is user-friendly.

Finally, it is planned to test whether the entire system operates according to its requirements across different devices, browsers, and operating systems. Each of these tests is critical to ensuring the application's functionality. Additionally, it is necessary to carefully analyze the results of these tests to manage the continuous improvement process with feedback at every stage.

3.6 Software Maintenance

In software development projects, the maintenance phases encompass activities aimed at ensuring the software operates effectively and reliably throughout its lifecycle after development. The maintenance phases are critical for the sustainability and longevity of a project. Specifically, regular maintenance activities lead to performance improvements and the resolution of security vulnerabilities [45,46]. Types of maintenance to be implemented in the study;

- **Preventive Maintenance:** Periodic security updates and system enhancements will be performed to improve the application's security and performance. Preventive maintenance is designed to prevent future issues with the software.
- **Corrective Maintenance:** Rapid identification and resolution of errors reported by users will be ensured. This type of maintenance is critical for enhancing the software's user experience. Additionally, regular updates will be planned based on user feedback.
- **Performance Maintenance:** Performance optimizations will be implemented to enhance the speed and efficiency of the application. The software's response times, resource usage, and other performance metrics will be regularly analyzed.
- **Test Maintenance:** This involves updating and maintaining software tests. Test scenarios need to be updated to accommodate new features or changes in the software.
- **Training Maintenance:** Training processes and materials will be developed to enable users to utilize the application most effectively. This aims to ensure that users are informed about the system and can troubleshoot potential issues.

In the study, rapid identification and resolution of errors reported by users will be ensured. Considering user feedback allows for updates to the system according to user needs, thereby continuously enhancing the application's speed and efficiency. Regular updates will be released to address security vulnerabilities and implement performance improvements. Conducting regular updates ensures the platform's resilience and security against technological advancements. Performance optimizations will be carried out to enhance the application's speed and efficiency. User feedback will be collected and evaluated regularly. This will ensure that

the application remains a long-lasting and secure platform, adapting to user needs and technological developments [45].

In a software lifecycle, the maintenance phase is continuous, meaning that every request (such as software bugs, new plugin requests, etc.) leads the lifecycle back to the beginning, and the software development process continues through the same stages. Therefore, this process takes the form of a cycle.

4. Conclusion & Discussion

In the study, the software development phases of a mobile application that ensures children's safety in the online environment while supporting their learning, development, and entertainment processes have been managed. Within the framework of the software development lifecycle, phases such as requirement identification, feasibility analysis, system design, development, testing, and maintenance have been prepared.

In the initial phase of the project, the needs of children and parents were analyzed in detail to determine requirements, leading to the design of a user-friendly, safe, and educational interface. By adopting the XP methodology, a lifecycle process aimed at continuous improvement has been implemented.

Security and performance tests of the application have been conducted to ensure smooth operation across all systems. During the maintenance phase, quick responses to user feedback have been provided to keep the application continuously updated and secure. Additionally, with the chosen methodology, the mobile application developed in the study will continue to be enhanced in line with the principles of continuous improvement, and updates will be planned to incorporate new features based on user feedback.

In software development projects, the code development phase is often considered the most important. However, the successful completion of a project relies on effective process management throughout all phases, from the project's inception to its final stages. Continuing the maintenance processes with the same steps after the project is completed enhances the project's success.

Life cycle models need to be rigorously applied to ensure that software projects meet user requirements [47]. He emphasized that digital security is a key element for developing more reliable apps, especially for vulnerable user groups such as children [48].

Studies on SDLC and secure digital content development projects for children prove the importance of security-focused SDLC methodologies. For example, threat modelling and security testing applied in Microsoft's Secure Development Lifecycle (SDL) model helps teams developing content for children to identify and eliminate security vulnerabilities at an early stage [49].

Research by Snyk shows that security assessments integrated into each phase of the secure SDLC improve the security of the software. As stated in Snyk's work on SDLC practices,

implementing security controls at the requirement and design stages significantly reduces the cost of changes to be made at later stages and increases security. In addition, they emphasize that the adaptation of SDLC in secure mobile applications for children is effective in protecting children's online safety and privacy rights [50].

Existing research shows that providing safe content for children is not only a software development issue, but also a critical issue for children's health and development. This study contributes to this literature and argues that analyzing user requirements, enabling parental control mechanisms and conducting digital security tests are necessary in the process of developing safe content for children [6,47,48,51].

In the literature, there are similar studies on digital security, software development processes and creating safe digital content for children. This study will contribute to the literature by combining digital security and user experience in the field of safe mobile content development for children. In the future, more comprehensive research on the personalization of applications for different age groups, the development of parental control tools, and the integration of digital safety tools with educational content can be recommended.

This study contributes to the literature by combining digital safety and user experience in the field of developing safe mobile content for children. However, there are some limitations. First, the study only addressed the development of a generic mobile application for children of a certain age group. It is thought that personalized solutions for different age groups may be more effective. Secondly, parental control mechanisms and digital safety tools could be expanded to analyze children's interactions with different digital environments in more detail. Furthermore, the methodology developed in this study has not been tested for its applicability to larger or different scale projects. For future research, it is recommended to conduct more comprehensive studies on customizing applications for different age groups, developing parental control tools, and integrating digital safety tools with educational content. In addition, it would be useful to conduct long-term studies to evaluate the impact of the developed applications on user satisfaction and safety in the long term. Such studies will contribute to the improvement of both software development processes and user experience.

Ethics in Publishing

There are no ethical issues regarding the publication of this study

Author Contributions

In the preparation of the publication, the authors have acted jointly in all parts.

References

- [1] Curtis, B., Krasner, H., Iscoe, N., (1988). A field study of the software design process for large systems. *Commun ACM*; 31: 1268–1287.

- [2] Rod S. BEGINNING Software Engineering, Second Edition, (2024). Beginning Software Engineering, Second Edition; 1–685.
- [3] Setyantoro A. Process Models in Software Engineering. https://www.academia.edu/36272460/Process_Models_in_Software_Engineering.
- [4] Sari, P.I., Rahmawati, I., Mariyana, R., Charmeida, N. (2024) The Correlation Between Parental Awareness and Concern to The Early Childhoods' Digital Safety. Kiddo: Jurnal Pendidikan Islam Anak Usia Dini, 5, 310–326.
- [5] Lonergan, A., Moriarty, A., McNicholas, F., Byrne, T. (2023) Cyberbullying and internet safety: a survey of child and adolescent mental health practitioners. Ir J Psychol Med; 40: 43–50.
- [6] Pressman, R.S., Maxim, B.R. (2015) The Software Engineer's Responsibility. Software Engineering: A Practitioner's Approach, 865–867.
- [7] Software development life cycle methods | by Chathurika Dhananjani | Medium. <https://chathurikadhananjani97.medium.com/software-development-life-cycle-methods-712be36f6aae>.
- [8] DevOps Puppet. In a simple word a Puppet is a... | by Sidhant Suryavansham | Medium. <https://sidhant-suryavansham.medium.com/devops-puppet-78400f04696b>.
- [9] Software Development Life Cycle | Benefits, Phases, Process & Models. <https://www.weetechsolution.com/blog/software-development-life-cycle>.
- [10] Comparative Analysis of Software Development Life Cycle Models https://www.researchgate.net/publication/286134213_Comparative_Analysis_of_Software_Development_Life_Cycle_Models.
- [11] Wang, Y.M., Elhag, T.M.S. (2006) Fuzzy TOPSIS method based on alpha level sets with an application to bridge risk assessment. Expert Syst Appl, 31, 309–319.
- [12] Boehm, B.W. (1988) A Spiral Model of Software Development and Enhancement. Computer (Long Beach Calif), 21,: 61–72.
- [13] McConnell, S. R. (2010) Development: Taming Wild Software Schedules. Microsoft Press, 6, 680.
- [14] Saaty, T.L. (1990) How to make a decision: The analytic hierarchy process. Eur J Oper Res, 48, 9–26.
- [15] Liberatore, M.J., Nydick, R.L. (2008). The analytic hierarchy process in medical and health care decision making: A literature review. Eur J Oper Res, 189, 194–207.
- [16] Aniley, D.B., Jalew, E.A., Agegnehu, G.A. (2024) Selection of Software Development Life Cycle Models using Machine Learning Approach. Int J Comput Appl, 186, 36–43.
- [17] MIH (2023) Software Development Life Cycle (SDLC) Methodologies for Information Systems Project Management. IJFMR - International Journal For Multidisciplinary Research; 5.

- [18] Brans, J.P., Vincke, P. (1985). Note—A Preference Ranking Organisation Method. *Manage Sci*, 31, 647–656.
- [19] Islam, A.K.M.Z., Ferworn, DrA. (2020). A Comparison between Agile and Traditional Software Development Methodologies. *Global Journal of Computer Science and Technology*; 20: 7–42.
- [20] Keskinç, M. & Kahveci, F. (2019) Yazılım Mühendisliğinde Çevik Yöntemler Üzerine Kavramsal Bir İnceleme ve Sınıflandırma. *Atatürk Üniversitesi Sosyal Bilimler Enstitüsü Dergisi*, 23(3), 1067-1091.
- [21] Herdika, H.R., Budiardjo, E.K. (2020) Variability and Commonality Requirement Specification on Agile Software Development: Scrum, XP, Lean, and Kanban. *International Conference on Computer and Informatics Engineering*, 323–329.
- [22] Schwaber, K., Sutherland, J. (2020) *The Scrum Guide The Definitive Guide to Scrum: The Rules of the Game*.
- [23] Ahmad, M.O., Markkula, J., Oivo, M. (2013) Kanban in software development: A systematic literature review. *Proceedings- 39th Euromicro Conference Series on Software Engineering and Advanced Applications, SEAA*, 9–16.
- [24] Beck K. *Praise for Extreme Programming Explained, Second Edition*.
- [25] *Lean Software Development: An Agile Toolkit: Poppendieck, Mary, Poppendieck, Tom: 0785342150780: Amazon.com: Books.* <https://www.amazon.com/Lean-Software-Development-Agile-Toolkit/dp/0321150783>.
- [26] Fowler, M., Beck, K. (2018) *Refactoring : Improving the Design of Existing Code, Second Edition* Fowler, Martin.
- [27] *Test Driven Development: By Example: Beck, Kent: 8601400403228: Amazon.com: Books.* <https://www.amazon.com/Test-Driven-Development-Kent-Beck/dp/0321146530>.
- [28] Williams, L., Kessler, R.R., (2003) *Pair Programming Illuminated*, 265.
- [29] *Continuous Integration: Improving Software Quality and Reducing Risk: Paul M. Duvall, Steve Matyas, Andrew Glover: 9780321336385: Amazon.com: Books.* <https://www.amazon.com/Continuous-Integration-Improving-Software-Reducing/dp/0321336380>.
- [30] Cohn, M. (2009). *What is a User Story? User Stories Applied*, 4.
- [31] *Yazılım Gereksinim Analizi | AppMaster.* <https://appmaster.io/tr/blog/yazilim-gereksinimleri-analizi>.
- [32] *Mobil Uygulama Geliştirme Rehberi | Vayes.* <https://www.vayes.com.tr/tr/blog/mobil-uygulama-gelistirme-rehberi>.
- [33] *Gereksinim yönetimi - Vikipedi.* https://tr.wikipedia.org/wiki/Gereksinim_y%C3%B6netimi.

- [34] Albrecht, A.J., Gaffney, J.E., (1983) Software Function, Source Lines of Code, and Development Effort Prediction. *IEEE Transactions on Software Engineering*, SE-9, 639–648.
- [35] Milicic, D. (2004) Applying COCOMO II- A case study.
- [36] Albakri, M.M., Rizwan, M., Qureshi, J. Empirical Estimation of COCOMO I and COCOMO II Using a Case Study.
- [37] Yazılımcılar Dünyası: COCOMO (Constructive Costing Model).
<https://www.yazilimcilar dunyasi.com/2017/01/cocomo-constructive-costing-model.html>.
- [38] Rush, C., Roy, R. (2023) Analysis of cost estimating processes used within a concurrent engineering environment throughout a product life cycle. *Advances in Concurrent Engineering*; 58–67.
- [39] Baresi, L., Pezzè, M. (2006) An Introduction to Software Testing. *Electron Notes Theor Comput Sci*, 148, 89–111.
- [40] Corral, L., Sillitti, A., Succi, G. (2013) Agile Software Development Processes for Mobile Systems: Accomplishment, Evidence and Evolution. *Lecture Notes in Computer Science (including subseries Lecture Notes in Artificial Intelligence and Lecture Notes in Bioinformatics)*, 8093 LNCS: 90–106.
- [41] Dobing, B., Parsons, J. (2006) How UML is used. *Commun ACM*, 49:109–113.
- [42] Faitelson, D., Tyszberowicz, S. (2017) UML Diagram Refinement (Focusing on Class-And Use Case Diagrams). *Proceedings - International Conference on Software Engineering*; 735–745.
- [43] Jayasiriwardene, S., Meedeniya, D. (2021) Architectural framework for an interactive learning toolkit. *Proceedings - International Research Conference on Smart Computing and Systems Engineering*; 14–21.
- [44] Li, S., Lei, Y., Jia, Z., Boukhelif, M., Hanine, M., Kharmoum, N. (2023) A Decade of Intelligent Software Testing Research: A Bibliometric Analysis. *Electronics*, 12.
- [45] Umudova, S. (2019) Analysis of Software Maintenance Phases. *Noble International Journal of Scientific Research*; 3: 62–66.
- [46] The Unified Modeling Language Reference Manual, (2nd Edition): Rumbaugh, James, Jacobson, Ivar, Booch, Grady: 9780321718952: Amazon.com: Books.
<https://www.amazon.com/Unified-Modeling-Language-Reference-paperback/dp/032171895X>.
- [47] Curtis, B., Krasner, H., Iscoe, N. (1988) A field study of the software design process for large systems. *Commun ACM*, 31, 1268–1287.
- [48] Setyantoro A. Process Models in Software Engineering.
https://www.academia.edu/36272460/Process_Models_in_Software_Engineering.

- [49] Children’s online activities, risks and safety: A literature review by the UKCCIS Evidence Group - GOV.UK. <https://www.gov.uk/government/publications/childrens-online-activities-risks-and-safety-a-literature-review-by-the-ukccis-evidence-group>.
- [50] Secure Development Lifecycle for App Security - AppSOC. <https://www.appsoc.com/blog/understanding-the-secure-development-lifecycle-sdlc-for-app-security>.
- [51] Lonergan, A., Moriarty A, McNicholas F, Byrne T, (2023) Cyberbullying and internet safety: a survey of child and adolescent mental health practitioners. *Ir J Psychol Med*; 40: 43–50.